Imperial College London

Department of Mechanical Engineering

A multiscale modelling framework to capture atomically resolved interfacial processes at experimentally relevant timescales.

Stavros Ntioudis

Submitted in part fulfilment of the requirements for the degree of Doctor of Philosophy (PhD) in Mechanical Engineering of the Imperial College, June 2025

Statement of originality

I, Stavros Ntioudis, confirm that the work presented in this thesis is my own, except where explicit reference is made to the work of others. Proper acknowledgement has been given to all sources, including published and unpublished materials, in accordance with academic integrity standards.

Copyright declaration

The copyright of this thesis rests with the author. Unless otherwise indicated, its contents are licensed under a Creative Commons Attribution-Non Commercial 4.0 International Licence (CC BY-NC). Under this licence, you may copy and redistribute the material in any medium or format. You may also create and distribute modified versions of the work. This is on the condition that: you credit the author and do not use it, or any derivative works, for a commercial purpose. When reusing or sharing this work, ensure you make the licence terms clear to others by naming the licence and linking to the licence text. Where a work has been adapted, you should indicate that the work has been changed and describe those changes. Please seek permission from the copyright holder for uses of this work that are not included in this licence or permitted under UK Copyright Law.

Declaration of published work

Portions of this thesis are adapted from my previously peer-reviewed published articles and preprints. The adapted papers are:

1. Ntioudis, Stavros and Ewen, James P. and Dini, Daniele and Turner, C. Heath. A hybrid off-lattice kinetic Monte Carlo/molecular dynamics method for amorphous thin film growth. ChemRxiv, April 2023. doi: 10.26434/chemrxiv-2023-9fl0k-v2. Reproduced (adapted) under the terms Creative Commons CC-BY-NC-ND 4.0 License.

2. Ntioudis, Stavros and Ewen, James P. and Dini, Daniele and Turner, C. Heath. A hybrid off-lattice kinetic Monte Carlo/molecular dynamics method for amorphous thin film growth. Computational Materials Science, 229:112421, October 2023. doi: 10.1016/j.commatsci.2023.112421. Reproduced (adapted) under the terms of the Creative Commons CC-BY license.

3. Ntioudis, Stavros and Ewen, James P. and Dini, Daniele and Turner, C. Heath. PAPRECA: A parallel hybrid off-lattice kinetic Monte Carlo/molecular dynamics simulator. Journal of Open Source Software, 9(98):6714, June 2024. doi: 10.21105/joss.06714. Reproduced (adapted) under the terms of the Creative Commons Attribution 4.0 International License.

Abstract

Molecular-level simulations are crucial in deepening our understanding of complex systems in the energy sector. Computational techniques such as density functional theory (DFT) and molecular dynamics (MD) help uncover the physical, chemical, electronic, and morphological characteristics of materials interfaces such as the thin films formed from lubricant additives, solid electrolyte interphases (SEIs), energy storage devices, catalysts, and porous media. However, traditional MD simulations are computationally demanding and are limited to timescales of roughly a few microseconds (μs). In this thesis, we introduce a hybrid off-lattice kinetic Monte Carlo/molecular dynamics (kMC/MD) scheme capable of extending simulation timescales beyond the temporal limits of MD. The scheme can describe elementary atomistic processes such as reactions, adsorption/desorption, or diffusion. The introduced kMC/MD model was utilised to investigate the thermal decomposition of tricresyl phosphate (TCP) on iron. Kinetic, chemical, and morphological results generated from the model agree well with previous experimental and MD simulation results. Additional spacer layer imaging method (SLIM) and x-ray photoelectron spectroscopy (XPS) experiments were performed to further validate the thermal decomposition model. It was found that the upper layer of the thin film from TCP was rich in carbon-based and iron oxide compounds with diminished phosphate content. On the other hand, the film growth rates were in good agreement with rates reported in other studies and the hybrid kMC/MD predictions. The model was extended to a general hybrid off-lattice kMC/MD simulator called PAPRECA. PAPRECA is fully parallelised and distributed under an open-source license. The developed software is used for the fine-tuning of the thermal decomposition model and the investigation of the effects of temperature and diffusion hopping distance. Finally, a PAPRECA model for accelerated hybrid kMC/MD simulations on the mechanochemical decomposition of TCP is presented and compared to existing MD studies.

Acknowledgements

I would like to thank my supervisors, Prof. Daniele Dini and Dr. James Ewen, for their valuable support, insights, and time throughout my PhD. I would also like to express my gratitude to Prof. C. Heath Turner from the University of Alabama. Heath kindly shared code and ideas and smoothly collaborated with us over the past years. Thank you for your guidance and for inspiring me with your passion for kinetic Monte Carlo simulations.

Many thanks to Dr. Huw Shiel for dedicating effort to assist with not only the execution of the XPS experiments but also the analysis as well as understanding of the relevant results. A warm thank you to Egheosa Ogbomo, who kindly shared additional data from his computational work on the decomposition of lubricant additives. This helped me to further investigate the applicability of my models.

Additionally, I would like to thank my parents (Christos and Fotini), sister (Iro), and partner (Rafaela). With their unconditional emotional support, they encouraged me through challenges and celebrated my achievements every step of the way.

Thank you to the members of the Tribology group for making this journey an enjoyable experience.

Special thanks go to the EPSRC and the inFUSE prosperity partnership. This program not only funded my PhD studies but also gave me the opportunity to be part of a diverse group that shares a passion for research.

Finally, I am grateful to the UK MMM Hub for computational resources, which is partially funded by EPSRC, United Kingdom (EP/T022213/1, EP/W032260/1 and EP/P020194/1). I also acknowledge computational resources provided by the Imperial College Research Computing Service.

Contents

1 Introduction **22**

1.1 Motivation and impact . . . 22
1.2 Research objectives . . . 23
1.3 Thesis structure . . . 24

2 Background **26**

2.1 Literature Review . . . 26
2.1.1 Critical materials interfaces in engineering and physics . . . 26
2.1.1.1 Solid Electrolyte Interphases (SEIs). . . . 26
2.1.1.2 Carbon dioxide capture . . . 29
2.1.1.3 Thin films from lubricant anti-wear additives . . . 31
2.1.2 Multiscale modelling methods . . . 39
2.1.3 Concluding remarks and motivation for thesis . . . 44
2.2 Theory of numerical algorithms . . . 44
2.2.1 MD . . . 44
2.2.1.1 Basics of MD . . . 44
2.2.1.2 Lennard-Jones, DREIDING, and ReaxFF potentials . . . 45
2.2.1.3 Basics of QEq . . . 47
2.2.2 KMC . . . 48
2.2.2.1 Fundamentals of kMC . . . 48
2.2.2.2 KMC catalog of rates and limitations of latticed-based and non-lattice-based schemes . . . 51

3 Off-lattice hybrid kMC/MD model for thin films from lubricant additives **53**

3.1 Introduction . . . 53
3.2 The proposed hybrid off-lattice kMC/MD framework with predefined transition events 53
3.3 A benchmark application: Polyphosphate film growth from the thermal decomposition of TCP molecules on a Fe(110) substrate. . . . 57
3.3.1 Background . . . 57
3.3.2 Overview of modelling details . . . 58
3.3.3 Details of the MD stage . . . 59
3.3.4 Details of the predefined events of the kMC stage . . . 59
3.3.5 Post-processing of results . . . 70
3.3.6 Computational efficiency . . . 71

3.3.7 Results & discussion . . . 72
3.4 Conclusions & Future work . . . 81

4 Experimental Validation **83**
4.1 Introduction . . . 83
4.2 Methods . . . 83
4.2.1 Thermal decomposition setup . . . 83
4.2.2 Selection of materials . . . 86
4.2.3 XPS measurements . . . 87
4.2.4 Spacer-layer imaging method (SLIM) measurements . . . 88
4.2.5 Film growth rate and activation energy estimation . . . 89
4.3 Results and discussion . . . 90
4.3.1 Surface structure analysis with XPS . . . 90
4.3.2 Film height analysis with SLIM . . . 95
4.4 Conclusions and further work . . . 101

5 General off-lattice hybrid kMC/MD model: PAPRECA **103**
5.1 Motivation for open-source implementation . . . 103
5.2 Introduction . . . 104
5.3 Hybrid (kMC/MD) parallel algorithms . . . 106
5.3.1 MD stage . . . 106
5.3.1.1 Partitioning . . . 106
5.3.1.2 Communication . . . 109
5.3.1.3 Neighbour lists . . . 110
5.3.2 KMC stage . . . 112
5.3.2.1 Off-lattice rejection-free kMC, mobile sites and predefined table of events . . . 112
5.3.2.2 Overview of supported atomistic events . . . 115
5.3.2.3 Supported atomistic events: reactions . . . 116
5.3.2.4 Supported atomistic events: molecular and monoatomic deposition 119
5.3.2.5 Supported atomistic events: monoatomic desorption . . . 124
5.3.2.6 Supported atomistic events: diffusion hops . . . 125
5.3.3 Utility operations . . . 129
5.3.3.1 Film-height estimation . . . 129
5.3.3.2 Removal of disconnected atoms . . . 130
5.3.3.3 Files output . . . 133
5.3.3.4 Estimation of event rates . . . 134
5.3.4 Hybrid kMC/MD implementation . . . 135
5.4 Flexible, extendable, and user-friendly design . . . 140
5.4.1 User interface through input files . . . 140
5.4.2 PAPRECA and LAMMPS libraries . . . 140
5.4.3 Object-oriented design . . . 142
5.4.4 Open source implementation . . . 144
5.5 Example PAPRECA applications . . . 147

5.5.1 Diffusion in solvent . . . 147
5.5.1.1 Background . . . 147
5.5.1.2 Methods . . . 148
5.5.1.3 Results and discussion . . . 150
5.5.1.4 Conclusions and further work . . . 155
5.5.2 Monoatomic adsorption and desorption . . . 156
5.5.2.1 Background . . . 156
5.5.2.2 Methods . . . 156
5.5.2.3 Results and discussion . . . 157
5.5.2.4 Conclusions and further work . . . 159
5.6 Scalability of PAPRECA . . . 160
5.7 Limitations and further plans for development . . . 161
5.8 Summary and conclusions . . . 164

6 Revisiting the model for thin films from lubricant additives 167
6.1 Introduction . . . 167
6.2 Thermal decomposition of TCP on iron . . . 167
6.2.1 Methods . . . 167
6.2.2 Results and discussion . . . 169
6.2.3 Conclusions and future work . . . 173
6.3 Mechanochemistry of TCP molecules on ferrous surfaces . . . 173
6.3.1 Methods . . . 173
6.3.2 Results and discussion . . . 175
6.3.3 Conclusions and future work . . . 178

7 Summary, conclusions, and future work 179
7.1 Summary and key thesis conclusions . . . 179
7.2 Further work . . . 181

Bibliography 183

Appendices 219
Appendix A: Example PAPRECA input files: Phosphate Film Growth from TCP on Fe110219
Appendix B: Analytic solution for non-reactive monolayer surface coverage . . . 221
Appendix C: Decomposition of TCP on iron: Growth profiles for hopping distance of 5.14468 Å . . . 223
Appendix D: Copies of permission documents to reproduce copyrighted material . . . 223

List of Figures

2.1 Evolution of morphology of SEI film on highly oriented pyrolytic graphite (HOPG). Reprinted (adapted) with permission from Cresce et al. [4]. Copyright © 2014 American Chemical Society. 26

2.2 SEI films grown at various electrode potentials. Reprinted (adapted) with permission from Harris and Lu [12]. Copyright © 2013 American Chemical Society. . . . 27

2.3 Ethylene carbonate (EC) decomposition pathways captured from eReaxFF simulations at **(a)** 0 and **(b)** 25 ps. C, H, O, Li^+ species are drawn with cyan, white, red, and purple. Blue is used to illustrate electrons. Reprinted (adapted) with permission from Islam and Van Duin [24]. Copyright © 2016 American Chemical Society. 28

2.4 **(a)** HRTEM image of MIL-101-NA. **(b)** Magnification of dashed region. **(c)** Schematic illustration of MIL-101 showing the supercell comprising TO_4 tetrahedrals. Reprinted (adapted) with permission from Li et al. [40]. Copyright © 2019 American Chemical Society. 30

2.5 Qualitative Stribeck curve illustrating the various regimes of lubrication. Adapted from Hutchings and Shipway [48]. 32

2.6 TEM images of ZDDP tribofilms on steel. Adapted from Dawczyk et al. [57]. Reprinted under the terms of the Creative Commons CC BY license. 33

2.7 Adsorption sequence of a ZDDP molecule on iron surfaces with varying oxygen coverages. Adapted from the DFT study of Benini, Restuccia, and Righi [62]. Reprinted under the terms of the Creative Commons CC-BY license. 34

2.8 AFM images for pristine and lubricated with 5% TCP in ester solvent on pure Fe and 304SS substrates. Reprinted from Acharya et al. [89], Copyright © 2018 with permission from Elsevier. 37

2.9 Reaction steps (A-D) involved in a hydrolytic decomposition pathway of m-TCP on Fe(110) and relevant free energies. Reproduced from Osei-Agyemand, Berkebile, and Martini [90] with permission from Springer Nature. 38

2.10 Simulation techniques across the scales and selected scale-bridging methods. The figure contains adapted images reprinted from Peguiron et al. [94], Deng, Morgan, and Szlufarska [95], Jalali et al. [96], and Phlipot and Kochmann [97], Copyright © with permission from Elsevier. Images reprinted with permission from Islam and Van Duin [24], and Abbott and Hanke [98], Copyright © American Chemical Society. Images obtained from Benini, Restuccia, and Righi [62], and Chacón, Bresme, and Tarazona [99], and Trageser et al. [100], and Wiriyasart et al. [101] are reproduced under the Creative Commons CC-BY license. Images used from Weiand et al. [102], and O'Malley et al. [103] are reproduced under the Creative Commons Attribution 3.0 Unported License. 39
2.11 Qualitative graph of the Potential Energy (U) versus a reaction coordinate (r). 2D representation of the PES. **(Left)** Detailed transition simulated using schemes of molecular-level resolution (e.g., MD or DFT). The system vibrates around valley S_1 and eventually reaches the transition state (S_T) and relaxes to a new valley S_2. **(Right)** Basin-to-basin transition described by the Markovian Master equation (expressed in 2.20). From our pre-print on cheRxiv © reproduced under the CC BY NC ND 4.0 license. 49
2.12 Flowchart summarizing the workflow of the standard kMC algorithm. 51

3.1 Schematic comparison between on-lattice, proposed off-lattice with predefined table of rates, and on-the-fly off-lattice kMC schemes. *(Top)* Standard on-lattice approaches examine the feasibility of an event (contained in the predefined table of events) through mechanism searches centred on fixed lattice sites. The rates of detected transitions are then passed on to the kMC algorithm. *(Middle)* The introduced off-lattice methodology retains the predefined table of events philosophy but substitutes fixed lattice sites with mobile event sites attached to the system atoms. (Bottom) On-the-fly off-lattice approaches detect basin-to-basin transitions by causing a localised perturbation and then searching for adjacent minima (along with their corresponding transition states) on the PES. Reproduced under the CC BY NC ND 4.0 license from our published preprint on ChemRxiv [233]. 54
3.2 Flowchart summarising the workflow of the proposed kMC/MD methodology. . . . 55
3.3 Adsorption radius (r_{mol} in Eq. 3.5) for mmm-TCP. 60
3.4 Three-layered Fe(110) substrate used in the current study and long bridge adsorption site dimensions ($d_{Fe-Fe}(sb) = 2.488$Å and $d_{Fe-Fe}(lb) = 3.071$ Å) values obtained from Xu et al. [247]. 62
3.5 Flowchart of an adsorption event. 63
3.6 Flowchart of the P-O bond breaking event. 64
3.7 Flowchart of the C-O bond breaking event. 65
3.8 Natural logarithm of rate versus the inverse of temperature for the C-O (a) and P-O (b) dissociation events. The activation energies and attempt frequencies can be extracted from the slope and the intercept of the best linear fit. 66
3.9 Flowchart of a bond formation event adapted from our preprint on the hybrid kMC/MD method [233]. 67
3.10 Flowchart of a diffusion event. 69

3.11 Post-processing flowchart adapted from our preprint on the hybrid kMC/MD method [233]. Reproduced under the CC BY NC ND license. 70
3.12 Block (i.e., 9 kMC and 1 MD step) CPU time versus number of atoms of the performance run (used for comparison with the ReaxFF scheme). 72
3.13 (a) Example growth profile from run 1 along with best linear fits for the first, second, and third stages of growth. (b-d) Evolution of total (cumulative) kMC event rates of run 1. The total rates are calculated by summing the rates of all the detected events of the respective event family. Evolution of time increment (Δt as in Eq. 3.2 at each hybrid kMC/MD step) for run 1. 73
3.14 Example film growth snapshots for run 1 at different times. (a-f) Snapshots at 0, 12, 24, 36, 48, and 60 seconds. 73
3.15 Growth rates and standard deviations of the 3 stages. The dashed line represents the growth rate for TCP molecules on Fe(110) from the experimental study of Acharya et al. [89]. 74
3.16 RMS roughness versus kMC time. The vertical bars represent the standard deviation of four hybrid kMC/MD runs. 75
3.17 Surface height profiles and relevant 2D radially averaged PSDs of the four (a-d) kMC/MD runs. The FD of individual hybrid kMC/MD runs is obtained from the slope of the respective power spectrum versus wavevector graph. The average FD is 2.301 ± 0.0112. 76
3.18 RDFs (a) Hybrid kMC/MD simulations at 60 seconds and standard deviations. (b) Al-Hasni and Mountjoy [262], RDF of $40Fe_2O_3$. (c) Al-Hasni and Mountjoy [262], RDF of 40FeO. Offsets of 30 and 70 $g_{ij}(r)$ are used for curves (b) and (a), respectively. 77
3.19 Film elemental composition graphs. (a) Hybrid kMC/MD simulations. The shadowed regions represent the standard deviation of four runs. (b) Approximate atomic percentage versus film depth from Auger depth profile for a thermally decomposed film formed from tri(tert-butylphenyl) phosphate (t-BPP) molecules at 698.15K after 2 hours of exposure. Experimental data adapted from Johnson and Morrow [67]. The x-axis was converted from sputter time to film depth using the sputter rate (80Å /min) reported. 79
3.20 Illustration of (PO_4) phosphate chain structures. 80
3.21 Phosphate chain lengths at about 12, 24, 36, 48, and 60 seconds, respectively and relevant standard deviation. Percentage of atoms with 0, 1, 2, 3, and 4 bridging oxygens, corresponding to Q^0, Q^1, Q^2, Q^3, and Q^4, respectively. 81

4.1 CAD rendered **(left)** and actual **(right)** experimental setup for the thermal decomposition of TCP on iron. 84
4.2 Exploded view of a steel rod assembly. A clamping knob facilitates the handling of the assembly. A steel glass holder secures the assembly on the rim of the borosilicate glass tube. A set of nuts allows for adjustments to the position of the 52100 specimen to ensure proper sample wetting. 84
4.3 Detailed flowchart depicting the experimental procedure (preparing, testing, and measuring) for the study of thermal decomposition of TCP on iron. Certain icons and vectors were adapted from [272] and [273], respectively. 85

4.4 Survey spectra for Pristine (specimen i), Low T GLT-3 (specimen ii), High T GLT-3 (specimen iii), Low T DIDA (specimen iv), and High T DIDA (specimen v) 52100 balls with annotated (dotted lines) regions of detailed elemental scans (Fe, O, C, P, respectively). 90

4.5 Detailed XPS scans illustrating contributions from **S atoms** for Low T DIDA (sample iv - **left**) and High T DIDA (sample v - **right**). 91

4.6 XPS survey spectra for Pristine (specimen i), Low T GLT-3 (specimen ii), High T GLT-3 (specimen iii), Low T DIDA (specimen iv), and High T DIDA (specimen v) between 704 and 740 eV revealing contributions from **iron**. 91

4.7 Detailed XPS scans illustrating contributions from **O atoms** for Low T GLT-3 (sample ii), High T GLT-3 (sample iii), Low T DIDA (sample iv), and High T DIDA (sample v). 92

4.8 Detailed XPS scans illustrating contributions from **C atoms** for Low T GLT-3 (sample ii), High T GLT-3 (sample iii), Low T DIDA (sample iv), and High T DIDA (sample v). 93

4.9 Detailed XPS scans illustrating contributions from **P atoms** for Low T GLT-3 (sample ii), High T GLT-3 (sample iii), and Low T DIDA (sample iv). 94

4.10 Colourimetric images of our SLIM measurements for samples reacted at 185 °C , 190 °C , 195 °C , 200 °C , and 205 °C . The colourbar on the right was generated using the calibration file of the PCS offline software. 96

4.11 Mean film height of thermally reacted thin films from mixtures of 1% TCP in GTL-3 along with associated parabolic fits. Figs. **(a-f)** correspond to tests at 185°C , 190 °C , 195 °C , 200 °C , 205 °C , and Fig. **(f)** shows the parabolic fit model retrieved from our analysis. The error bars quantify uncertainties originating from spatial height variations, loading cycles, ageing (for all samples), and repeated tests (only for specimens reacted at 195 °C and 205 °C). 97

4.12 Violin plots quantifying the contributions of different classes of experimental uncertainties to the SLIM height measurements. Generated in origin with a smooth kernel and a Scott bandwidth. 98

4.13 Film growth rates calculated using scaled averages **(left)** and parabolic fits **(right)** using Eqs. 4.1 and 4.3, respectively. 99

4.14 Rate versus inverse of temperature graphs along with corresponding linear fits for the scaled average **(left)** and parabolic approaches **(right)** using Eqs. 4.1 and 4.3, respectively. Note that $r_0 = 1s^{-1}$ and $r_0 = 1s^{-0.5}$ for the scaled average and parabolic fits, respectively. 99

4.15 Experimentally obtained film-growth rates. An Arrhenius-type model is used to extrapolate data beyond the tested temperatures (185 °C-205 °C). Additional data points correspond to the studies of Acharya et al. [89], Johnson and Morrow [67], Ntioudis et al. [270], and Saba and Forster [77]. 100

5.1 2D projection of a regular 4x4x1 processor grid along the x-, y-, and y-dimensions, respectively. Snapshots of a toy-system at the 0^{th} **(left)**, 1000^{th} **(middle)**, and 1000000^{th} **(right)** step. The solid black lines mark the non-intersecting MPI subdomains, while the blue dotted lines mark an example ghost-atom regime for the 1^{st} MPI rank. The thin film grows while maintaining uniform atomic density across the MPI processes. 107

5.2 Top view of a regular 4x3x1 processor grid along the x-, y-, and y-dimensions, respectively. Snapshots of a toy system at the 0^{th} **(left)**, 1000^{th} **(middle)**, and 1000000^{th} **(right)** step. The solid black lines mark the non-intersecting MPI subdomains, while the blue dotted lines mark an example ghost-atom regime for the 5^{st} MPI rank. Islands and patches are visible at steps 1000 **(middle)** and 1000000 **(right)**, and particles are non-uniformly distributed across the MPI ranks. 107

5.3 Top view of irregular ("tiled") 12-process grid. The RCB partitioning strategy results in improved load balancing than that offered by a regular subdomain decomposition (see **right** image of Fig. 5.2). The solid black lines mark the non-intersecting MPI subdomains, while the blue dotted lines mark an example ghost-atom regime for an MPI rank. 108

5.4 2D communication strategy for regular MPI grids. Communication occurs sequentially and in two phases along the x-direction **(left)** and y-direction **(right)**. In the y-dimension phase, "ghost" attributes (denoted with dark blue) are transferred alongside "owned atom" data (annotated with bright blue). Adapted from Thompson et al. [26]. 110

5.5 2D communication strategy for irregular MPI grids. Communication occurs sequentially and in two phases along the x-direction **(left)** and y-direction **(right)**. In the y-dimension phase, "ghost" attributes (denoted with dark blue) are transferred alongside "owned atom" data (annotated with bright blue), but solely if the relevant data are not communicated during the x-phase. Adapted from Thompson et al. [26]. 110

5.6 **(Left)** "Half" neighbours list approach where each pair of atoms is listed once. Atom 2 is retained in the neighbours list of atom 1, but atom 1 is not stored in the list related to atom 2. **(Right)** "Full" neighbours list approach where each pair of atoms is listed in both neighbours lists. 111

5.7 Assembly of local *tables of detected events* on MPI ranks and calculation of cumulative rates of MPI processes (R_i, with i being the MPI rank). Example with 4 MPI processes and n_i discovered events on each rank. 112

5.8 Communication of local cumulative rates R_i to the master MPI process and estimation of global rate of kMC step R_{global}. Example with 4 MPI ranks. 113

5.9 Stochastic selection of elementary event (e.g., reaction, adsorption) on *event rank* and communication of information related to the atomistic process to all MPI ranks. In this example, rank 2 is the *event rank* and there are a total of 4 MPI processes. 114

5.10 Summary of steps involved in the parallelised kMC stage of PAPRECA. 115

5.11 Summary of key steps involved in bond-breaking events (type i). 117

5.12 Summary of key steps involved in bond-formation events (type ii). Bond-formation image **(top left)** adapted from our preprint on the hybrid kMC/MD method [233]. 118

5.13 Deposition sites as generated by the `random_depovecs` command. **(Top left):** random_depovecs YES 2D places sites on the surface of the northern hemisphere above the parent atom. **(Top right):** `random_depovecs YES 3D` unlocks sites on both hemispheres. **(Bottom left):** `random_depovecs NO 2D` and **(bottom right):** `random_depovecs NO 3D` generate sites directly above or both above and below the parent atom, respectively. 120

5.14 Summary of key steps involved in deposition events (type iii). Overlap and parent atom detection images adapted from our previous work on the hybrid kMC/MD off-lattice method [270]. 122

5.15 Summary of key steps involved in monoatomic desorption events (type iv). 124

5.16 Types of supported diffusion hop events in PAPRECA. **(Top):** initial diffusion hop step with identification of parent atom. **(Bottom left):** *displacive* diffusion hop where the parent atom moves from its initial position. **(Bottom right):** *non-displacive* diffusion hop where the parent atom is not modified and a new atom is placed in the simulation box at a separation distance of ΔL_k. 125

5.17 Deposition sites as generated by the `random_diffvecs` command. **(Top left):** random_diffvecs YES 2D places diffusion sites on the surface of the northern hemisphere above the parent atom. **(Top right):** `random_diffvecs YES 3D` unlocks sites on both hemispheres. **(Bottom left):** `random_diffvecs NO 2D` and **(bottom right):** `random_diffvecs NO 3D` generate diffusion sites directly above or both above and below the parent atom, respectively. 127

5.18 Flowchart summarising the main steps of diffusion hop events. 128

5.19 Film height determination on global mass bins (of dimensions L_x, L_y, and t). Image adapted and reproduced under the CC BY NC ND 4.0 license from our preprint on the hybrid kMC/MD method [233]. 129

5.20 Removal of atoms via the `desorption command`. **(Top):** initial desorption step with identification of atoms located above h_{cut}. **(Bottom left):** `LAMMPS_region` command that solely deletes atoms with $z \geq h_{cut}$. **(Bottom right):** `gather_all` and `gather_local` features removing atoms with $z \geq h_{cut}$ as well as bonded atoms. 131

5.21 Summary of steps involved in the PAPRECA hybrid off-lattice kMC/MD program. 139

5.22 Structure of table of predefined events (PAPRECA::PredefinedEventsCatalog class). The *predefined table of events* contains as many unordered maps as the types of predefined events in PAPRECA (i.e., five corresponding to bond-formation, bond-breaking, deposition, monoatomic desorption, and diffusion hops). Each map maps an atom ID (of integer C++ type) to a pointer to the predefined event object. . . 142

5.23 Inheritence tree of `PAPRECA::Event` classes. `PAPRECA::Event` is the parent class of all event classes. `PAPRECA::Reaction` class is the parent of both `PAPRECA::BondForm` and `PAPRECA::BondBreak` classes. 143

5.24 Flowchart of GitHub versioning workflow. 146

5.25 Snapshots of the **pure kMC** model at various timesteps. 150

5.26 Spatial distributions of the **pure kMC** model at various timesteps. The distributions were procured using spatial binning along the z-direction of the simulation box (as explained in Section 5.3.3.1). 151
5.27 Variance versus time for **pure kMC**. Variances were calculated with Eq. 5.33 from the applied Gaussian fit ("Gauss" model of Origin Pro). 152
5.28 Snapshots of **hybrid kMC/MD** model at different simulation times. 153
5.29 Final snapshot of pure MD **(left)** and hybrid kMC/MD **(right)** simulations. The pure MD model reaches $10^{-7}s$ with 8.54 hours of walltime, while the hybrid kMC/MD scheme in PAPRECA reaches 5.75 10^{-5} s in 5.48 hours. 154
5.30 Final (steady state) snapshots (at $t = 50$ s) of kMC simulations for different ratios of adsorption/desorption rates (r_a/r_d). Type 1 and type 2 atoms are illustrated as grey and red, respectively. 157
5.31 Surface coverage (θ) as a function of time for different ratios of adsorption/desorption rates (r_a/r_d). The kMC data and theoretical solution (see Eq. 5.34) are depicted with solid orange and dotted black lines, respectively. 158
5.32 Average error for different ratios of adsorption to desorption (r_a/r_b). The error at each time step was calculated as $\frac{|\theta_{analytic}-\theta_{kMC}|}{\theta_{analytic}}$ 159
5.33 Hybrid kMC/MD scalability tests of PAPRECA for TCP on Fe(110) conducted on a workstation **(left)** and on the CX3 cluster at Imperial College **(right)**. 160

6.1 Height versus time for different temperatures with a diffusion hopping distance for substrate iron atoms (ΔL_k) fixed at 7.14468 Å. Results from hybrid kMC/MD simulations in PAPRECA. Extrapolating lines and fit predictions at 3600 s are obtained from linear fits on the final 100 seconds of the respective run. Experimental results come from our investigation presented in Chapter 4. 170
6.2 Elemental distribution across the film thickness as calculated from the hybrid kMC/MD model on the decomposition of TCP on Fe(110) and at different temperatures. All distributions were generated from the final snapshot (i.e., at 350 s) and for a thickness range of [0,h_m], where h_m is the maximum film height of the run. . 171
6.3 Example micrograph segments for 205 °C at 0.5, 1, 4, and 8.3 nm. 172
6.4 Mechanochemical system snapshots at different stages of the simulation. 175
6.5 Normalised number densities obtained from hybrid kMC/MD runs and at different stages of the simulation. 176
6.6 Normalised probability density from ReaxFF simulations on the mechanochemistry of TCP on iron. Data were retrieved using ReaxFF simulations by Egheosa Ogbomo [92] and kindly shared with permission to be included in the current PhD thesis. . 177

C.1: Height versus time for different temperatures with a diffusion hopping distance for substrate iron atoms (ΔL_k) fixed at 5.14468 Å. Results from the refined model for the study of the thermal decomposition of TCP on iron (see Chapter 6). 223

List of Tables

4.1 Selected binding energies (BE) of detected contributions for Pristine (i), Low T GLT-3 (ii), High T GTL-3 (iii), Low T DIDA (iv), and High T DIDA (v) specimens. 94
4.2 Activation energies (E_a) and attempt frequencies (ν) evaluated using the scaled average (Eq. 4.1) parabolic fit (Eq. 4.3) methods. 99

6.1 Hybrid kMC/MD simulation output data for different temperatures. Revisited model for the thermal decomposition of TCP on Fe(110). 170
6.2 Summary of reaction events used for the PAPRECA study of mechanochemical decomposition of TCP on iron. The rate-determining reactions and their relevant rates correspond to 1 GPa normal pressure and 10 m/s sliding speeds. Data were retrieved using ReaxFF simulations by Egheosa Ogbomo [92] and kindly shared with permission to be included in the current PhD thesis. 174

Nomenclature

AA All-atom

ABF Adaptive biasing force

AES Auger electron spectroscopy

AFM Atomic force microscopy

$AIMD$ Ab-initio molecular dynamics

$akMC$ Adaptive kinetic Monte Carlo

$ATR-FTIR$ Fourier-transform infrared spectroscopy

CAD Computer-aided design

CCS Carbon capture and storage

CG Coarse-graining

CG Conjugate gradient

CN Coordination number

COF Coefficient of friction

COM Centre of mass

DD Domain decomposition

$DDFT$ dynamic density functional theory

DFT Density functional theory

$DIDA$ Diisodecyl adipate

EA Electron affinity

EAM Embedded atom model

EC Ethylene carbonate

EHL Elastohydrodynamic lubrication

EV Electric vehicle

FCC Face-centred cubic

FD Fractal dimension

FEA Finite element analysis

$GCMC$ Grand canonical Monte Carlo

GP Gaussian process

GS Ground state

HL Hydrodynamic lubrication

HMM Heterogeneous multiscale method

HPC High-performance computing

$HRTEM$ High-resolution transmission electron microscopy

I/O Input/Output

$inFUSE$ Interface with the Future Underpinning Science to support the Energy transition

IP Ionisation potential

$IPCC$ Intergovermental Panel on Climate Change

KDE kernel density estimation

kMC kinetic Monte Carlo

$LAMMPS$ Large-scale Atomic/ Molecular Massively Parallel Simulator

LIB Lithium-ion battery

LJ Lennard-Jones

MC Monte Carlo

MD Molecular dynamics

ML Machine learning

MMC Metropolis Monte Carlo

MOF Metal-organic framework

MPI Message passing interface

MSD Mean-squared distance

MTM Mini-traction machine

$MuMMI$ Multiscale Machine-Learned Modeling Infrastructure

$NEMD$ Non-equilibrium molecular dynamics

OOP Object-oriented programming

$PAPRECA$ PArallel PREdefined CAtalog

PBC Periodic boundary conditions

PDE Partial differential equation

PES Potential energy surface

PFM Phase field method

PRD Parallel replica dynamics

PSD Power spectral density

QC Quasicontinuum

QCM Quartz crystal microbalance

QM Quantum mechanics

RCB Recursive coordinate bisectioning

RDF Radial distribution function

$rkMC$ Rejection-free kinetic Monte Carlo

RMS Root meat squared

SE Schrödinger equation

SEI Solid electrolyte interphase

SEM Scanning electron microscopy

$SIMD$ Single instruction, multiple data

$SLIM$ Spacer layer imaging method

$SPPARKS$ Stochastic Parallel PARticle Kinetic Simulator

SS Stainless steel

STD Standard deviation

$t-BPP$ tri(tetr-butylphenyl) phosphate

$TBPP$ Tertiary-butyl phenyl phosphate

TCP Tricresyl phosphate

TEM Transmission electron microscopy

$TNBP$ tri-n-butyl phosphate

TPP triphenylphosphate

VMD Visual molecular dynamics

VPL Vapour phase lubrication

XPS X-ray photoelectron spectroscopy

$ZDDP$ Zinc dithiophosphate

Chapter 1

Introduction

1.1 Motivation and impact

Climate change is one of the major challenges that humanity faces. National and international regulations are established to ensure a livable climate for future generations and mitigate the effects of human activities on global warming. Nonetheless, current projections by the United Nations (as of 2025) show that global greenhouse gas emissions will only be reduced by 2.6 per cent by 2030. Note that, to accomplish the goals outlined by the Paris Agreement, greenhouse gas emissions must be lowered by 45% by 2030.

The energy sector is responsible for approximately 75% of the global greenhouse gas emissions [1]. Therefore, the mobilisation of researchers in the energy sector is paramount to reaching net-zero CO_2 targets introduced by governments. Specifically, scientists and engineers must not only contribute towards clean and alternative energy solutions but also in the direction of elevating the efficiency of existing technologies. Examples include, but are not limited to, the reduction of frictional losses in key energy systems (engines, bearings, and tyres), increase of the efficiency of combustion engines as well as electric motors, enhancement of the stability and prolonging of lifetime of materials, boosting of capacity in storage devices (e.g., batteries), and lowering of the greenhouse gas emissions associated with the extraction, storage, and transportation of fuels.

Optimisation of the aforementioned processes demands tools capable of providing in-depth insights into materials interfaces at the molecular level [2]. Various computational methods possess the necessary accuracy and can be utilised to investigate the properties and behaviour of energy systems under different environmental conditions (e.g., temperature and pressure). Nevertheless, such methods are numerically expensive, with the relevant computational cost typically being proportional to the accuracy of the method. As such, simulation tools with molecular-level resolution are not suitable when it comes to investigating long timescales (e.g., seconds, minutes, and hours) or large systems (e.g., volumes in the order of mm^3), even with the use of modern supercomputers [3]. The inability of traditional methods with molecular-level resolution to capture the physicochemical processes occurring at materials interfaces over experimentally relevant time- and length-scales limits progress in materials research. This creates obstacles in the direction of accomplishing goals established by environmental policies.

This work is predominantly motivated by the necessity for an open-source multiscale computational tool capable of performing molecular-resolution simulations on energy interfaces over

experimentally relevant timescales. Emphasis is given to the importance of scalability and computational efficiency in software engineering. We understand that every additional simulated second bridges even further the gap between experimental and modelling timescales.

This work is associated with the Interface with the future underpinning science to support the energy transition (InFUSE) EPSRC Prosperity Partnership. InFUSE is an interdisciplinary project between Imperial, Shell, and Diamond Light Source, which investigates interfaces linked to geomaterials, catalysts, mobility, and lubrication. As part of InFUSE, the present PhD work aims to provide fellow scientists and engineers with a user-friendly, flexible, and extensible software suitable for simulations of molecular-level resolution at experimentally relevant timescales. Such software will be useful not only to the modellers but also to the experimentalists involved in the InFUSE project. The software will provide means for validation as well as a thorough understanding of atomistic phenomena at energy interfaces. Most importantly, a novel multiscale workflow can shed light on the link between atomistic processes and long-timescale properties of energy interfaces. Moreover, a novel multiscale methodology is essential for the industrial partners of InFUSE. Specifically, the efficiency of existing systems can be elevated through simulation-experimentation-industrial application cycles. Overall, InFUSE promises to aid the UK government in achieving its net-zero targets by providing sustainable solutions in the energy sector through a thorough understanding of materials interfaces. Consequently, this PhD work and its active involvement in the InFUSE partnership can benefit society and global efforts to mitigate the environmental impact of human activities.

The current project is linked to the lubricants and e-fuels branch of the inFUSE project. As such, the development of the multiscale package will be oriented towards applications of interest in tribology and lubrication. A user-friendly and open-source multiscale package with molecular-level resolution is necessary for tribologists and surface scientists. It will enable long-timescale investigations on lubricated contacts and virtual screening of next-generation lubricants. The latter becomes increasingly important due to the immediate need for ashless oils, as the decomposition of lubricants from existing formulations can lead to highly toxic (for humans, ecosystems, and the environment) deposits containing heavy metals. Effectively, a novel multiscale package is demanded by the tribology community to shed light on interfacial phenomena governing lubricated surfaces and their connection to key properties of tribological interest. Such properties include, but are not limited to, surface roughness, elemental composition, film-growth rates, bonding environment, or even viscosity. Additionally, a multiscale methodology is necessary to bridge the gap between experiments and theory, as experimentally relevant timescales are not attainable by traditional methods of molecular-level resolution. Overall, this project promises to provide tools for lubrication scientists and engineers to holistically study complex tribological systems of multiphysics and multiscale character.

1.2 Research objectives

The **overarching goals** of this work are the development and validation of a multiscale methodology that enables computationally efficient simulations at key materials interfaces of the energy sector. The developed model aims to unlock molecular-level resolution simulations at long timescales (i.e., seconds, minutes, and hours), bridging the gap between theory and experiments. A series of

specific research objectives is established to address the overarching goal:

1. **Identify a key application in tribology and lubrication.** Thorough understanding of the physics associated with this application should demand long-timescale insights from a multiscale methodology. The key application will be used as a proof of concept to test the proposed modelling framework.

2. **Develop a specialised multiscale model dedicated to capturing the physics of the identified key application (see goal 1).**

3. **Validate the developed model.** On a first level, the results should be compared to data from relevant studies available in the literature.

4. **Perform experiments to further validate the developed model.** On a second level, experiments must be performed on the key system. This will provide better control over the experimental details and the measured system properties. Overall, this will enable direct and appropriate comparison between experimental results and data generated by the multiscale methodology.

5. **Generalise the specialised code.** Here, the code must be extended to a general and user-friendly open-source software capable of modelling materials interfaces in the energy sector beyond the tribologically-relevant system studied in **objectives 1, 2, 3, 4.** This research objective is of paramount importance when it comes to achieving the central goal of the PhD project. Such a goal is to provide fellow researchers and members of the inFuse project with a reliable multiscale framework to capture the physics at interfaces at experimentally relevant timescales.

6. **Improve the computational efficiency, scalability, and extensibility of the general code.** Emphasis must be given on the lowering of the numerical cost of the open-source software, and the implementation of efficient parallelisation techniques. This objective is important as every additional simulated second diminishes even further the gap between model and experimental timescales.

1.3 Thesis structure

This thesis is organised as follows. A literature review is presented in Chapter 2. The review covers a broad range of topics. Firstly, crucial energy materials, interfaces, and tribological systems are discussed. Also, the use of computer simulations in the direction of understanding such crucial systems is analysed. Moreover, the problem of the separation of timescales is outlined. In particular, we address the fact that certain models are suitable to capture the physics of a system, but solely on a narrow range of length and timescales. Then, multiscale modelling approaches are discussed and emphasis is given to their importance in holistically understanding the underlying complex phenomena across different length and timescales. The motivation to develop and test hybrid kinetic Monte Carlo/Molecular dynamics (kMC/MD) models is provided in Section 2.1.3 after analysing the available multiscale techniques in the bibliography. Also, in Section 2.2,

the kMC and MD methods (the two theories involved in our hybrid kMC/MD methodology) are introduced and a relevant theoretical background is provided.

Chapter 3 is based on our initial publication on the hybrid kMC/MD model. The multiscale framework is introduced, and a benchmark application is used as a proof of concept. In particular, the thermal decomposition of tricresyl phosphate (TCP) molecules on Fe(110) is studied. Specifics on the implementation of the novel hybrid kMC/MD technique are given. The long-timescale behaviour of the system is captured beyond the limits of MD. Results from our simulations are compared to relevant data from the bibliography on phosphate films or the decomposition of phosphate esters on ferrous surfaces.

An in-house experimental setup designed to study oil oxidation and thermal decomposition of lubricants on metallic surfaces is presented in Chapter 4. The aforementioned setup is deployed to provide further insights into thin films from TCP on iron. Results on the film growth rates and film composition are validated against the hybrid kMC/MD model (presented in Chapter 3) and other data originating from equivalent studies in the bibliography.

A general open-source hybrid off-lattice kMC/MD model is presented in Chapter 5. A detailed discussion of the parallel kMC, MD, and hybrid algorithms is provided. Emphasis is given to the coupling of the kMC and MD solvers through effective interfacing and on the extensibility, scalability, and user-friendliness of the software. Also, the transferability of the code is discussed, and examples are given to showcase its usage in systems beyond the thermal decomposition of TCP on iron.

In Chapter 6 the newly introduced open-source software is deployed to refine our model on the thermal decomposition of TCP on iron. In particular, conclusions drawn from our initial in-silico study on the system (as outlined in Chapter 3) and from our experimental investigation (as presented in Chapter 4) are utilised to refine the relevant model and improve its accuracy. Here, simulations are performed in a computationally efficient manner using the parallelised and optimised software presented in Chapter 5. Finally, the general conclusions and outcomes of this PhD work are given in Chapter 7. The thesis is discussed as a whole, the success of the project is examined, and suggestions for further work are provided.

Chapter 2

Background

2.1 Literature Review

2.1.1 Critical materials interfaces in engineering and physics

This section presents critical applications involving materials interfaces in the energy sector. The discussed systems are associated with projects affiliated with the inFUSE prosperity partnership. Overall, a multiscale methodology capable of modelling such systems would benefit members of the inFUSE projects as well as relevant industrial collaborators.

2.1.1.1 Solid Electrolyte Interphases (SEIs).

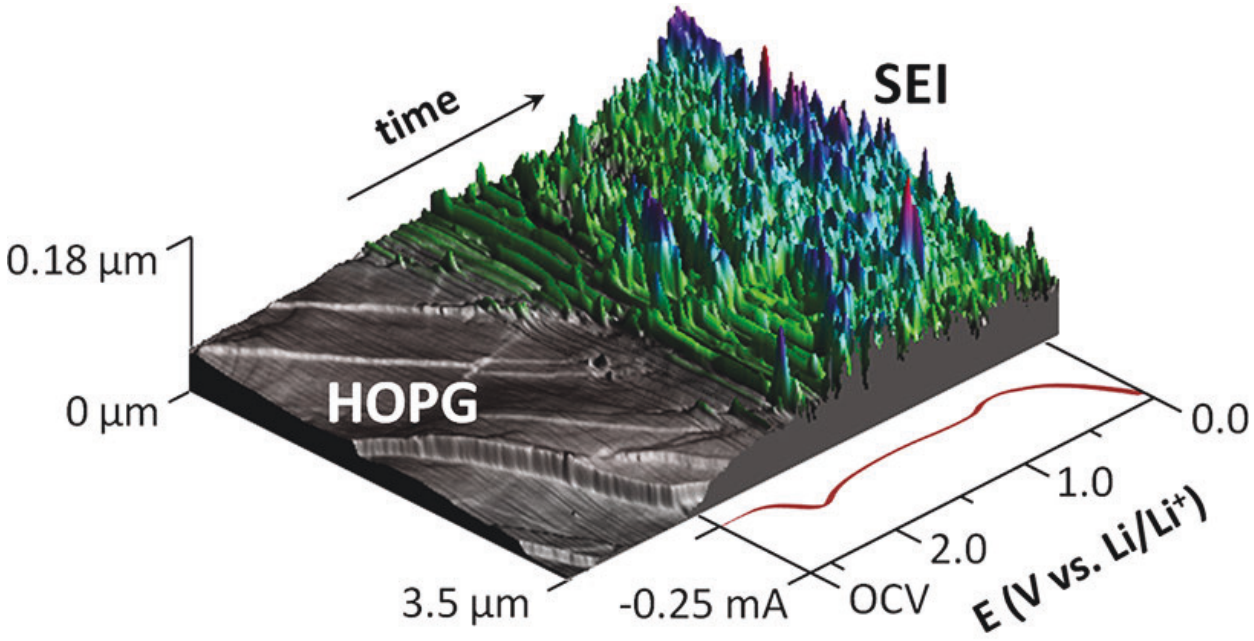


Fig. 2.1: Evolution of morphology of SEI film on highly oriented pyrolytic graphite (HOPG). Reprinted (adapted) with permission from Cresce et al. [4]. Copyright © 2014 American Chemical Society.

Rechargeable Li-ion batteries (LIBs) are utilised as energy storage devices in applications ranging from smart watches and mobile phones to electric vehicles (EV). LIBs comprise two electrodes (i.e., an anode and a cathode) separated by a liquid electrolyte. During battery operation, solvent salts and impurities react with Li. As a result, a nanometer-thick film called the solid electrolyte

interphase (SEI) decomposes on the solvent/electrode interface. Note that SEIs form more readily on anode than cathode interfaces due to the thermodynamic instability of solvent constituents at lower operating voltages [5]. In any case, the formation of SEIs consumes Li-ions present in both the solvent and the cathode. This leads to irreversible capacity as well as power density losses [5, 6]. Patil et al. estimated that about 10% of Li-ions are depleted during the initial charging cycle [7]. Nevertheless, solvent decomposition and the subsequent growth of SEI leading to capacity fade can occur throughout the lifetime of the energy storage device.

Despite consuming Li-ions, SEIs are vital for the performance, safety, and continuous operation of LIBs. During the battery's operation, SEIs act as passivating layers on electrodes, inhibiting further solvent decomposition [8]. This preserves Li-ion inventory, suppresses dendrite formation, and overall, enhances the electrochemical stability of the energy storage device. Various studies investigated the structure and morphology of SEIs and demonstrated that these films feature layered characteristics. A layer permeable to Li-ions but impermeable to solvent molecules is in contact with the electrode. In contrast, a porous layer allowing the transport of both solvent and Li-ions is in contact with the liquid electrolyte [9–11]. SEIs are three-dimensional structures exhibiting mosaic features as shown in the in-situ atomic force microscopy (AFM) study of Cresce et al [4]. Fig. 2.1 illustrates the morphological characteristics of an SEI as it evolves through charge-discharge cycles. Scanning electron microscopy (SEM) images of SEIs formed at different electrode potentials from the study of Harris and Lu [12] reveal the porous characteristics of the thin films (see Fig. 2.2).

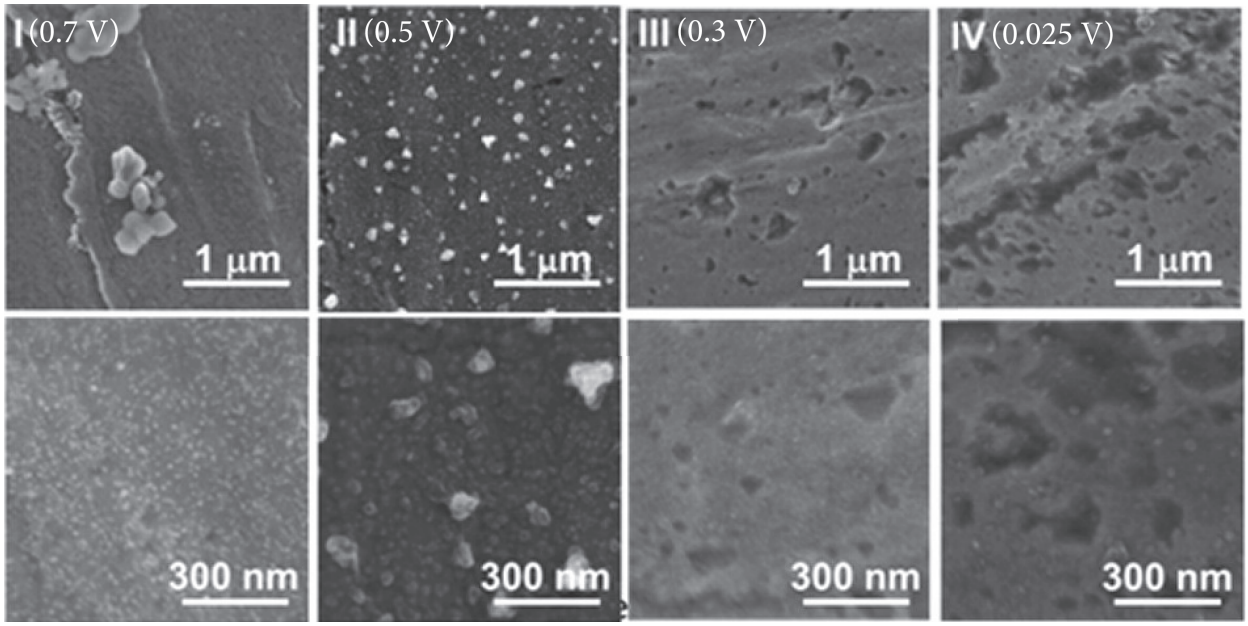


Fig. 2.2: SEI films grown at various electrode potentials. Reprinted (adapted) with permission from Harris and Lu [12]. Copyright © 2013 American Chemical Society.

Extensive research exists to enable SEI engineering aimed at achieving desirable properties such as increased Li-ion permeability, decreased electronic mobility, and electrochemical stability of the electrolyte/electrode interface. SEI engineering necessitates an in-depth understanding of the elementary atomistic processes (e.g., reaction pathways) leading to the growth of these thin films. Elucidation of formation mechanisms can aid towards the derivation of structure-property relationships for SEIs. Nevertheless, the formation and growth of SEIs are influenced by a broad

range of factors. For instance, the composition of SEIs is dictated by the choice of anode [13, 14] and electrolyte [15–17]. Note that the electrolyte itself is a mixture of base oils and additives. This adds to the complexity of deriving structure-property relationships for SEIs as each additive can modify the composition as well as morphology of the thin film [18]. Furthermore, operating environmental conditions (e.g., temperature, pressure) and manufacturing practices (e.g., first-cycle charging potential) affect the structure of the formed SEI, which in turn, impacts the performance of the LIB [19]. Finally, SEIs can grow after the initial charging cycle [20, 21]. The fact that the properties of SEIs are dynamic and evolve through the operation of LIBs introduces obstacles to the thorough understanding of SEI formation mechanisms.

Progress on the understanding of formation mechanisms of SEIs is also influenced by the intrinsic aspects associated with the experimental investigation of SEIs. For instance, Li-ions react with oxygen upon atmospheric exposure [22]. This introduces artefacts in ex-situ experimental studies. Consequently, sophisticated in-situ investigations must be performed to accurately capture the characteristics of the thin films, which elevates implementation complexity [8]. Moreover, rate-determining reactions contributing to the growth of SEIs typically occur in picosecond (i.e., 10^{-12} s) timescales, which is below the resolution limit of available experimental techniques [23].

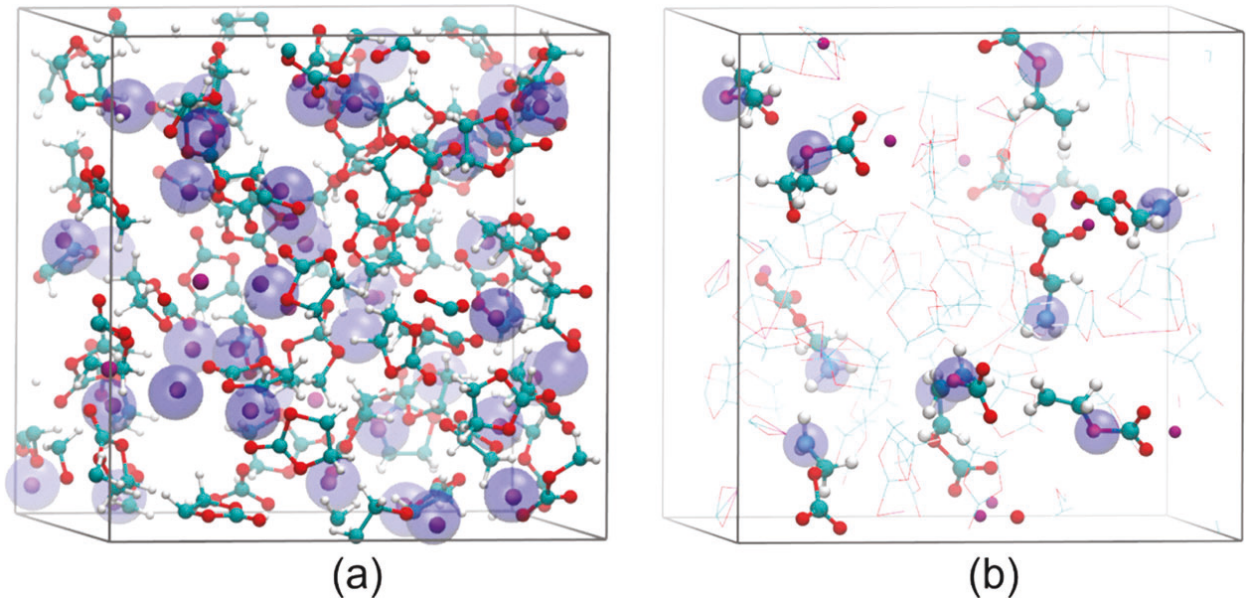


Fig. 2.3: Ethylene carbonate (EC) decomposition pathways captured from eReaxFF simulations at **(a)** 0 and **(b)** 25 ps. C, H, O, Li^+ species are drawn with cyan, white, red, and purple. Blue is used to illustrate electrons. Reprinted (adapted) with permission from Islam and Van Duin [24]. Copyright © 2016 American Chemical Society.

Methods of atomic-scale resolution, such as the density functional theory (DFT), ab-initio molecular dynamics (AIMD), and molecular dynamics (MD), can be utilised to capture the dynamics of SEI growth at the picosecond timescales [23]. Hence, significant contributions to our understanding regarding SEIs are enabled due to the use of atomistic simulations. For instance, Islam and van Duin deployed eReaxFF MD simulations that explicitly captured electron transfer to gain further insights into the decomposition pathways of ethylene carbonate (EC) solvents [24]. Their simulations featured a reduction process triggered due to electron transfer, followed by C-O scission. The latter reaction step produced EC anion as well as Li cation radicals. The EC decomposition pathway ended with the termination of the generated radicals. Snapshots from their

molecular dynamics simulations are provided in Fig. 2.3. Furthermore, Jorn et al. conducted MD simulations on $LiPF_6$ systems in EC to investigate the influence of imposed electric fields on the composition and thickness of an SEI[25]. They discovered significant polarisation effects on Li-ion adsorption [25].

Nevertheless, the aforementioned methods (i.e., DFT, AIMD, MD) are computationally expensive and cannot typically be deployed for studies beyond μs and system sizes exceeding 10^6 atoms, even with the use of modern supercomputers [26]. It can be concluded that multiscale methods of atomic-scale resolution are of paramount importance to the investigation of the long-term evolution of SEIs beyond the picosecond timescales. In other words, multiscale methods are necessary to shed light on the interplay between environmental operating conditions, electrolyte/-electrode choice and key LIB properties such as capacity, capacity retention, and power density at experimentally relevant timescales (i.e., seconds, minutes, and hours). This promises to reduce manufacturing costs and elevate the performance of LIBs, thus benefiting a variety of modern technological systems in electric motion and energy storage. In addition, multiscale modelling can enable in vivo engineering of SEIs through the virtual screening of next-generation electrolytes and anode materials for energy storage devices [23].

2.1.1.2 Carbon dioxide capture

Carbon capture and storage (CCS) refers to a family of frameworks dedicated to capturing CO_2 emitted from industrial sites and potentially permanently storing it. CCS technologies promise to directly contribute towards the reduction of greenhouse gas emissions in pivotal operations, including but not limited to fuel extraction/processing/transportation/storage, fertiliser and ammonia generation, wastewater management, and steel or cement production. This is essential when it comes to achieving the goals of the Paris Agreement linked to the reduction of greenhouse gas emissions. Furthermore, CCS offer attractive solutions to climate change as they promise to balance the negative consequences of elevated demand for energy sourcing from fossil fuels [27].

In 2005, the Intergovernmental Panel on Climate Change (IPCC) argued that released CO_2 from power plants can be reduced by as much as 90% through the implementation of CCS technologies [28, 29]. Of course, the use of CCS elevates the energy requirements of the production plan. In 2008, a report illustrated that the relevant theoretically minimum increase in energy consumption for a 90% reduction in CO_2 emissions is about 3.5%. However, in reality, the utilisation of CCS in power plants leads to energy penalties that are higher by approximately 20% than the theoretical minimum [30]. This does not render CCS economically viable in most practical applications.

A variety of materials have been investigated and are suitable for use in CCS technologies, including:

- **Microporous and mesoporous materials.** Zeolites (e.g., Zeolite 13X [31]) are the most popular CO_2 adsorbents of this material class. Zeolites are crystalline aluminosilicates with a general formula of $(MAlO_2)(SiO_2)_x(H_2O)_y$, where M^+ typically represents a hydrogen or sodium cation [32, 33].

- **Carbonaceous Adsorbents** (e.g., coal), which are preferred in high-pressure applications due to their increased adsorption efficiency at elevated pressures. These materials are also cheaper than alternative choices for CO_2 adsorption (e.g., Microporous materials). Another

advantage of carbonaceous adsorbents is their stability in moisture-intensive environments [32, 34].

- **Organic Solids**. Typically non-porous self-assembled (e.g., p-tetrbutylcalix[4]arene [35]) or crystalline porous organic materials (e.g., $C_{25}H_{24}B_4O_8$ [36]) have been investigated as CO_2 adsorbent candidates.

- **Metal-organic frameworks (MOFs)**, which are porous crystalline three-dimensional networks featuring metallic cations (e.g., Cu^{2+}, Zn^{2+}, or Al^{3+}) bridged by organic ligands (e.g., carboxylates). MOFs are attractive for CO_2 adsorption due to their low weight, elevated surface area, and thermal as well as chemical stability. Furthermore, MOFs are preferred due to their potential for engineering [29] and functionalization [37]. In essence, each combination of organic bridging ligament and metal node results in varying properties (e.g., pore size, density) and CO_2 selectivity. Certain examples of MOFs are $[Zn_4O(btb)_2]$ (btb = benzene-1,3,5-tribenzoate) and $[Al(OH)(ndc)]$ (ndc^{2-} = 1,4-napthalenedicarboxylate) [38, 39]. A high-resolution transmission electron microscopy (HRTEM) of a MOF MIL101 from the study of Li et al. is provided in Fig. 2.4 [40].

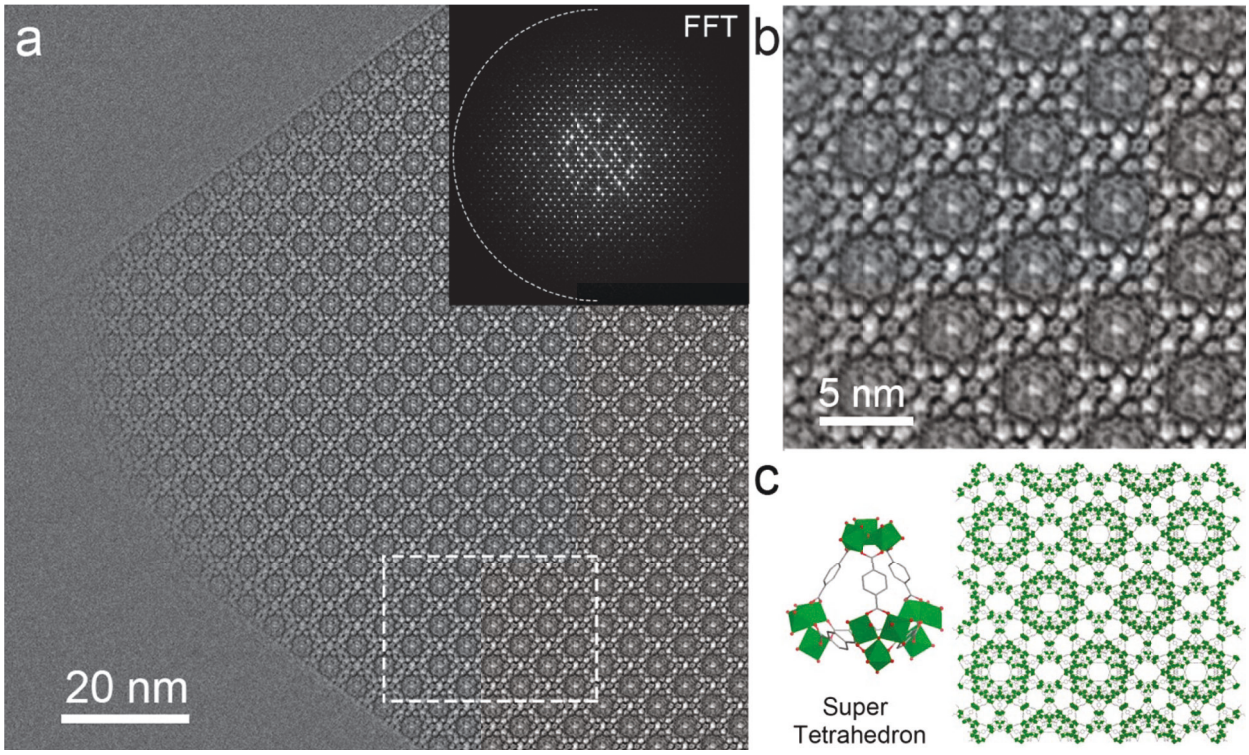


Fig. 2.4: **(a)** HRTEM image of MIL-101-NA. **(b)** Magnification of dashed region. **(c)** Schematic illustration of MIL-101 showing the supercell comprising TO_4 tetrahedrals. Reprinted (adapted) with permission from Li et al. [40]. Copyright © 2019 American Chemical Society.

Advances in the materials classes listed above drive progress in CCS technologies. In that respect, methods of molecular-level resolution are essential to shed light on CO_2 adsorption mechanisms and provide insights into structure-property relationships. For instance, Yazaydın et al. reported that the presence of water in the cavity of $[Cu_3(btc)_2]$ can enhance the CO_2 selectivity of the MOF material [41]. Yazaydın et al. performed Grand canonical Monte Carlo (GCMC) simulations and successfully experimentally validated their results by synthesising hydrated MOFs and

reproducing the relevant CO_2 adsorption isotherms. Overall, atomistic simulations (e.g., GCMC or MD) enable the virtual screening of different classes of materials for CCS technologies. For example, combinations of bridging ligands and metal nodes can be simulated to accelerate the discovery of novel MOFs. Furthermore, the effect of functional groups on CO_2 selectivity under various environmental conditions (e.g., pressure, temperature, humidity) can be investigated with molecular-level resolution through atomistic simulations. The above are of paramount importance considering the need for highly optimised and readily synthesizable materials capable of reducing the added energy consumption (or cost) associated with the implementation of CCM technologies in power plants.

Nevertheless, numerical schemes of atomistic resolution (such as MD) are incapable of simulating representative timescales or lengthscales [26] for CCS-related materials under actual operating conditions (i.e., minutes, hours, days). Hence, traditional methods of atomic-level accuracy cannot be utilised to examine the long-term stability of zeolites, carbonaceous adsorbents, organic solids, and MOFs. These methods are also unsuitable when it comes to providing insights regarding the long timescale evolution of other key CCS materials, such as pore size evolution, or CO_2 uptake. The above underline the necessity for multiscale frameworks possessing atomic-scale resolution. Such frameworks can be used to shed light on the elementary processes, such as reaction pathways, diffusion hops, and adsorption site selectivity, associated with novel materials for CCS at experimentally relevant timescales. Multiscale frameworks could also become useful in providing solutions for the existing limitations of CCS materials. For instance, multiscale simulations could be utilised to address the reported instabilities linked to zeolites after multiple adsorption cycles [42].

2.1.1.3 Thin films from lubricant anti-wear additives

Lubrication refers to the application of lubricant oils to contacting surfaces in relative motion to decrease friction and surface wear. Lubrication regimes are classified according to the value of the dimensionless film thickness parameter, $\lambda = \frac{h}{\sigma}$, where h is the lubricant film thickness and σ is the combined root-mean-square (RMS) surface roughness of the contacting bodies. Specifically, the lubrication regimes are [43]:

- **Boundary lubrication**: occurring when $\lambda < 1$. Here, the lubricant film thickness is lower than the intrinsic surface roughness. Consequently, surfaces are in direct contact, which results in elevated values of the coefficient of friction (COF) [44].

- **Mixed lubrication**: characterised by $1 < \lambda < 5$. Within this regime, lubricant film thickness allows for partial surface separation. Nevertheless, frictional load is supported by both the lubricant and the surface asperities [45].

- **Elastohydrodynamic lubrication (EHL)**: typically associated with $3 < \lambda < 10$, EHL occurs in non-conformal, high-pressure contacts (e.g., gears, rolling bearings). In this regime, significant elastic deformation of the contacting surfaces and a sharp increase in lubricant viscosity under pressure lead to the formation of a full fluid film. EHL overlaps with the mixed and hydrodynamic regimes and provides low coefficients of friction [46].

- **Hydrodynamic lubrication (HL)**: manifesting for $\lambda > 5$ and associated with total surface separation. In hydrodynamic lubrication, friction is governed by viscous shear within the fluid [47].

A qualitative Stribeck curve depicting the various lubrication regimes is provided in Fig. 2.5. Note that the Stribeck curve illustrates the variation of the COF with the non-dimensional **Hersey number**, defined as $\frac{\eta\nu}{P}$, where η, ν, and, P represent the dynamic viscosity, sliding velocity, and contact pressure, respectively [43].

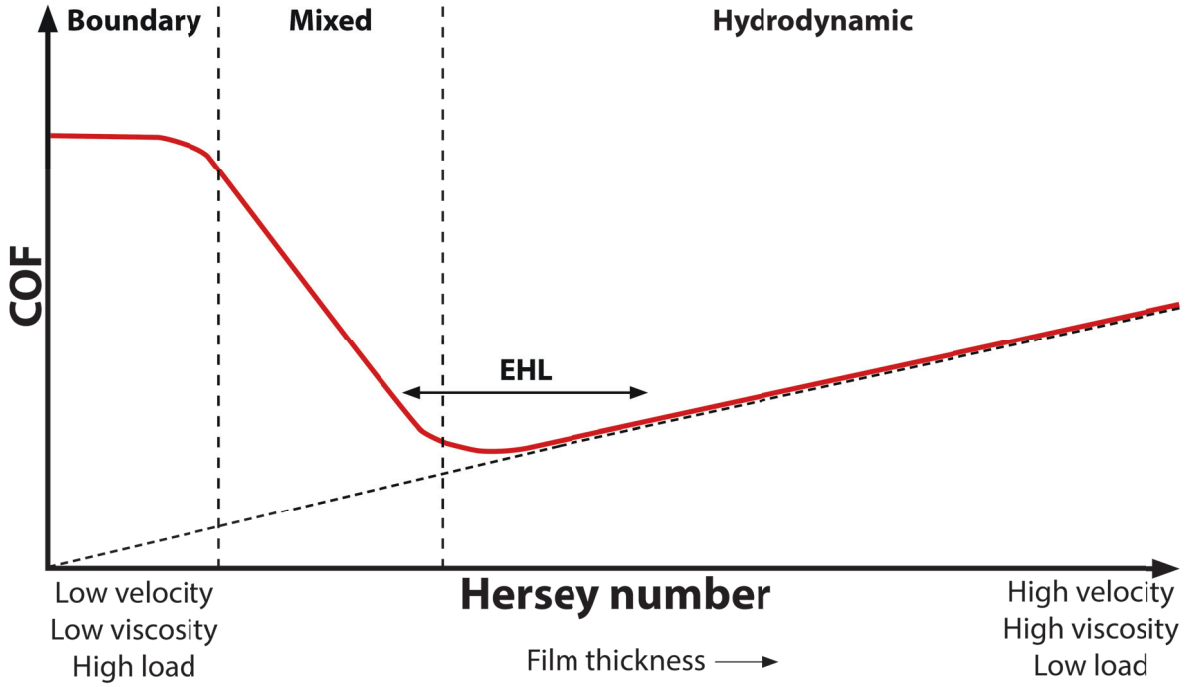


Fig. 2.5: Qualitative Stribeck curve illustrating the various regimes of lubrication. Adapted from Hutchings and Shipway [48].

Modern lubricants are blends of base oils and additives. Additives are essential to the fine-tuning of specific lubricant properties. Additionally, additives are vital to the reliable operation of lubricants in any lubrication regime (see Fig. 2.5) and are typically grouped into the following classes [49]:

- **Detergents** used to prevent the deposition of carbonaceous compounds on lubricated interfaces.
- **Dispersants** deployed to tackle the aggregation of solid impurities in the lubricant.
- **Anti-foam agents** added to eliminate bubble formation due to the use of dispersant and detergent additives.
- **Antioxidants** acting as inhibitors of base oil oxidation.
- **Anti-wear additives** used to reduce frictional wear in metallic interfaces.
- **Friction modifiers** utilised to diminish friction in rubbing surfaces.

- **Corrosion inhibitors** used to prevent the oxidation and corrosion of lubricated metallic surfaces.
- **Viscosity index improvers** deployed to diminish the viscosity of the base oil.
- **Pour point depressants** added to guarantee the continuous flow of lubricant at lower temperatures.

Anti-wear additives decompose on metallic lubricated surfaces, usually under friction, forming protective thin films. Such protective films inhibit direct metal-to-metal contact and effectively contribute to the reliable operation of critical modern engineering systems (e.g., combustion engines). Zinc dithiophosphate (ZDDP) is a popular anti-wear additive in automotive applications [50]. Thermally grown films from ZDDPs can develop at temperatures typically higher than 140°C [51–53]. The decomposition rate of ZDDP scales exponentially with not only temperature, but also applied shear stress. Specifically, the applied shear stress reduces the activation energy for ZDDP decomposition, rendering the growth of the relevant thin films a mechanochemically controlled process [54, 55]. Note that tribofilms develop between sliding interfaces. They are assisted by shear stress and therefore, can develop at significantly lower temperatures than thermal films [56] (e.g., at 25 °C [51]).

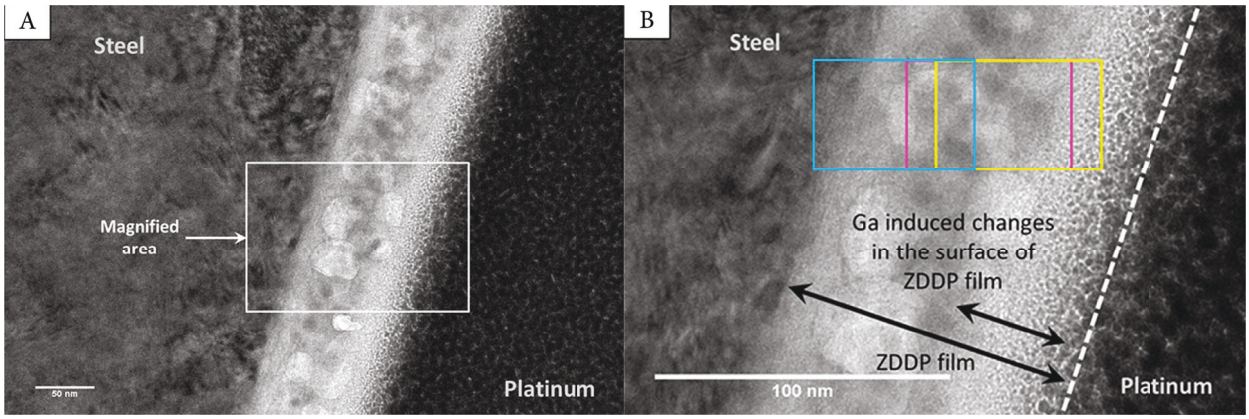


Fig. 2.6: TEM images of ZDDP tribofilms on steel. Adapted from Dawczyk et al. [57]. Reprinted under the terms of the Creative Commons CC BY license.

The thickness of ZDDP tribofilms ranges between 50 and 150 nm. A thin layer rich in Fe or Zn sulphides is present in contact with the substrate. Thicker (0.15-5 μm) glassy Fe/Zn phosphate as well as polyphosphate patches are grown on top of the sulphide layer. Note that the layer of phosphate chains gradually decreases from the uppermost layers of the ZDDP film to the sulphide layer formed on the metallic substrate [50, 58]. Transition electron microscopy (TEM) images of a ZDDP film on a steel substrate from the experimental investigation of Dawczyk et al. [57] are provided in Fig. 2.6. Previous experimental work provided insights on the tribofilm growth sequence, which exhibits five stages [59]. Firstly, ZDDP deposits on the metallic substrate. Then, adsorbed ZDDP molecules react on the surface to produce the lowermost layer of FeS or FeS/$FeSO_4$. After the formation of the bottom layer, alkyl groups can transfer from oxygen to the sulphur species. Following, thiophosphates as well as phosphates polymerise on the bottom layer to grow glassy polyphosphate pads. Finally, rubbing can trigger the depolymerisation of the polyphosphate pads, which produces nanocrystalline structures with enhanced resistance to wear [58].

Atomistic simulations have been deployed to provide further insights into the decomposition of ZDDPs on metallic substrates. For instance, Mosey et al. used AIMD to investigate the influence of pressure in systems comprising triphosphate as well as zinc phosphate molecules [60]. They observed that the number of zinc neighbours to oxygen atoms was analogous to the applied pressure. They showed that at pressures as high as 17 GPa cross-linking can be triggered, resulting in the formation of polyphosphate chains that elevate hardness. In 2022, Peeters et al. investigated the initial film growth stages of ZDDP additives on light alloys with ab initio methods [61]. They showed that ZDDP molecules deposit readily on various Al and Mg surfaces. They also illustrated that ZDDPs on $Mg_{17}Al_{12}$ substrates can undergo pressure-assisted decomposition to produce dithiophosphate compounds. Benini, Restuccia, and Righi used DFT to shed light on the adsorption and decomposition energetics of ZDDP under shear stress on ferrous substrates [62]. They found that the initial surface adsorption step was necessary to render decomposition reactions energetically favourable. Furthermore, they illustrated that shear and normal loads can trigger the dissociation of organophosphorus compounds from the Zn-S central blocks of ZDDPs. Finally, Benini and coworkers [62] demonstrated that oxidised surfaces can inhibit ZDDP adsorption. A graphical illustration of such a phenomenon is provided in Fig. 2.7 (adapted from the relevant paper).

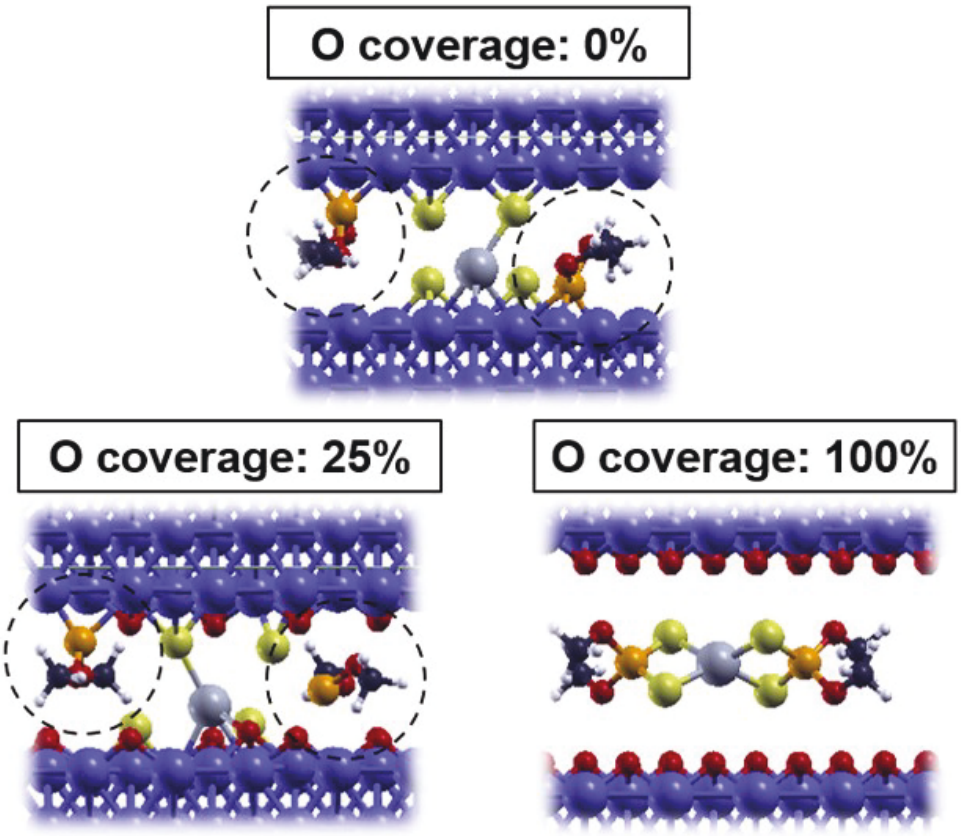


Fig. 2.7: Adsorption sequence of a ZDDP molecule on iron surfaces with varying oxygen coverages. Adapted from the DFT study of Benini, Restuccia, and Righi [62]. Reprinted under the terms of the Creative Commons CC-BY license.

It becomes clear that a variety of experimental as well as computational studies investigate thin films from ZDDPs. The distinct stages leading to the growth of such coatings (i.e., adsorption,

decomposition, polymerisation/depolymerisation) have been identified in the literature. Nevertheless, the exact atomic-scale mechanisms linked to the aforementioned stages and driving the formation of thin films from ZDDP additives are still debated. For instance, the adsorption steps and reaction pathways associated with the growth of the lowermost film layer (rich in metallic compounds) and the effects of ZDDP variants (e.g., primary or secondary) are not yet understood. Also, additional research is required to clarify the reaction pathways leading to the decomposition of ZDDP molecules and the formation of polyphosphate structures in the anti-wear additive film. Finally, optimisation and enhancement of anti-wear properties necessitate a better understanding of the failure mechanisms of ZDDP films. Note that traditional methods of molecular-level accuracy (e.g., DFT, AIMD, MD) cannot be utilised to investigate ZDDP films beyond the initial stages of growth. This is a direct consequence of the intrinsic timescale and lengthscale limitations associated with the relevant numerical schemes. Consequently, simulations capturing the entire decomposition pathway beginning with the deposition of ZDDP on the substrate and followed by sulphide film and organophosphate pad growth cannot be performed with standard atomistic methods. This underlines the necessity for multiscale methods of atomic-scale resolution capable of modelling larger systems and longer timescales than AIMD and MD.

Regardless of its widespread use, ZDDP contains zinc, an element known to damage exhaust aftertreatment systems [63]. The degradation of exhaust components can be mitigated with the utilisation of zinc-free additives. Examples of relevant additives include, but are not limited to phosphate and thiophosphate esters such as tri-n-butyl phosphate (TNBP), tertiary-butyl phenyl phosphate (TBPP), and triphenylphosphate (TPP) [64–67]. Tricresyl phosphate (TCP) is a different zinc-free lubricant additive. Despite toxicity concerns, particularly associated with the tri-o-cresyl isomer [68], TCP is predominantly used in aerospace applications [69]. It forms protective thin films (approximately 100 nm) on metallic lubricated interfaces. TCPs can also be utilised as lubricant additives in vapour phase lubrication (VPL) conditions [70]. In VPL applications, the lubricant is delivered as a homogeneous gas that interacts with the underlying surface. VPL can be applied as a lubrication solution for limited-life, gas turbine engines [71–73]. The exact decomposition sequence leading to the formation and growth of thin films from TCP additives depends on a series of factors ranging from the environmental conditions (e.g., temperature, pressure, humidity), the shear rate of the lubricant, and importantly, the underlying substrate. Specifically, on ferrous surfaces, the protective coatings from TCP molecules typically form by (a) corrosion, (b) thermal decomposition, or (c) hydrolytic decomposition [69].

In 1965, Godfrey postulated that the presence of phosphoric acid in the vicinity of the steel surface is integral to the growth of thin films from TCP [74]. Godfrey stated that phosphoric acid can be produced from the decomposition of TCP due to rubbing at the ferrous surface or originate from anti-wear additive impurities. In 1968, the chromatography experiments of Bieber, Klaus, and Tewksbury confirmed the presence of phosphoric acid in TCP additives [75]. The same authors performed transition-load experiments and reported that wear was inversely proportional to the percentage of acid phosphate in TCP. Therefore, they theorised that thin films from TCP grow due to reactions involving phosphoric acid and iron. In 1982, Gauthier, Montes, and George supported that theory [76]. These authors performed plane-on-plane tribometer experiments on 52100 bearing steel and summarised the decomposition process as follows. Firstly, acids (impurities as well as wear products) deposit on the steel surface. This triggers corrosive wear on the iron substrate that

generates ferrous phosphate. After a critical surface concentration of ferrous phosphate is reached, impurities in TCP decompose further on the substrate and produce a polyphosphate film.

The thermal decomposition of TCPs on ferrous substrates initiates with the physical adsorption of TCP molecules and proceeds with the homolytic scission of P-O as well as C-O bonds [67, 77, 78]. The cleavage of P-O and C-O bonds generates oxygen radicals, which in turn react with Fe or P species, producing Fe-O as well as P-O bonds. Overall, such a sequence leads to the formation and growth of polyphosphate or iron polyphosphate films [79].

A different adsorption mechanism is linked to the influence of water molecules on the decomposition of TCP. Specifically, humidity in the vicinity of lubricated contacts can lead to the deposition of H_2O on ferrous surfaces. It is hypothesised that adsorbed water molecules and $O-H$ radicals reduce the activation energy for $P-O$ dissociation and result in the substitution of $P-O$ bonds by phosphoric hydroxyl groups (i.e., $P-OH$). The reacted hydroxyl groups attach to the ferrous surface to produce a hydrolysed polyphosphate film. The aforementioned mechanism was inspired by the findings of Bieber, Klaus, and Tewksbury [75]. These authors performed tribometer studies and revealed that transition loads were analogous to the concentration of hydrolysed products in the lubricated contact under friction. Hence, they concluded that hydrolysed TCP compounds exhibited superior anti-wear properties compared to non-hydrolysed TCP blends. Nevertheless, such a conclusion was not supported by another experimental study that revealed comparable wear-scar diameters linked to similar anti-wear performance for hydrolysed and non-hydrolysed TCP formulations [80].

The study of Klaus et al. [81] revealed that crystallites comprising Fe, C, and P species are present in proximity to the substrate. Amorphous coating layers of diminished Fe content dominated the surface layers of the protective film. Nonetheless, there is no general agreement regarding the exact composition of thermally-grown films from TCP additives. For instance, a recent study of 2024 argued that TCPs form interconnected carbon-rich coatings [82].

The diffusion of Fe ions originating from the substrate and progressing through the protective coating is considered a rate-determining mechanism for films grown from phosphate ester additives under VPL conditions. Such a conclusion is experimentally supported by a previous Auger electron spectroscopy (AES) analysis conducted by Forster on bearing steel surfaces lubricated by TBPP [83]. Forster claimed that the mass transport of metal (e.g., Fe) cations enables the growth of thin films beyond the initial stages of formation. In essence, it was hypothesised that metal cations facilitate the equilibration of unbalanced surface charges due to the condensation of phosphate ions at the film/lubricant interface. Further experimental studies underline the catalytic role of Fe species in the thermal decomposition of TCP films e.g., the Fourier-transform infrared spectroscopy (ATR-FTIR) investigation of Sasaki et al. [84], the work of Wheeler and Faut [85] using X-ray Photoelectron Spectroscopy (XPS) techniques, or the AES investigation of Shaeffer [86].

Note that the previously discussed mechanisms for the decomposition of TCP on ferrous surfaces were hypothesised purely based on experimental results. The control of certain experimental parameters, such as impurities in lubricants, the influence of other additives, or humidity in the vicinity of the surface, is a non-trivial endeavour. Even the choice of base oil dissolving the anti-wear additive can alter the phosphate content of the relevant coatings, as demonstrated in the studies of Arezzo and coworkers [87, 88]. Moreover, the choice of surface can affect the anti-wear properties of TCP. For instance, Acharya et al. performed quartz crystal microbalance (QCM)

experiments on Fe and 304SS surfaces lubricated with 5% TCP in ester solvents [89]. Their results showed that lubrication with TCP increased and reduced the RMS roughness of the surface for Fe and 304SS, respectively. The relevant atomic force microscopy (AFM) images are provided in Fig. 2.8.

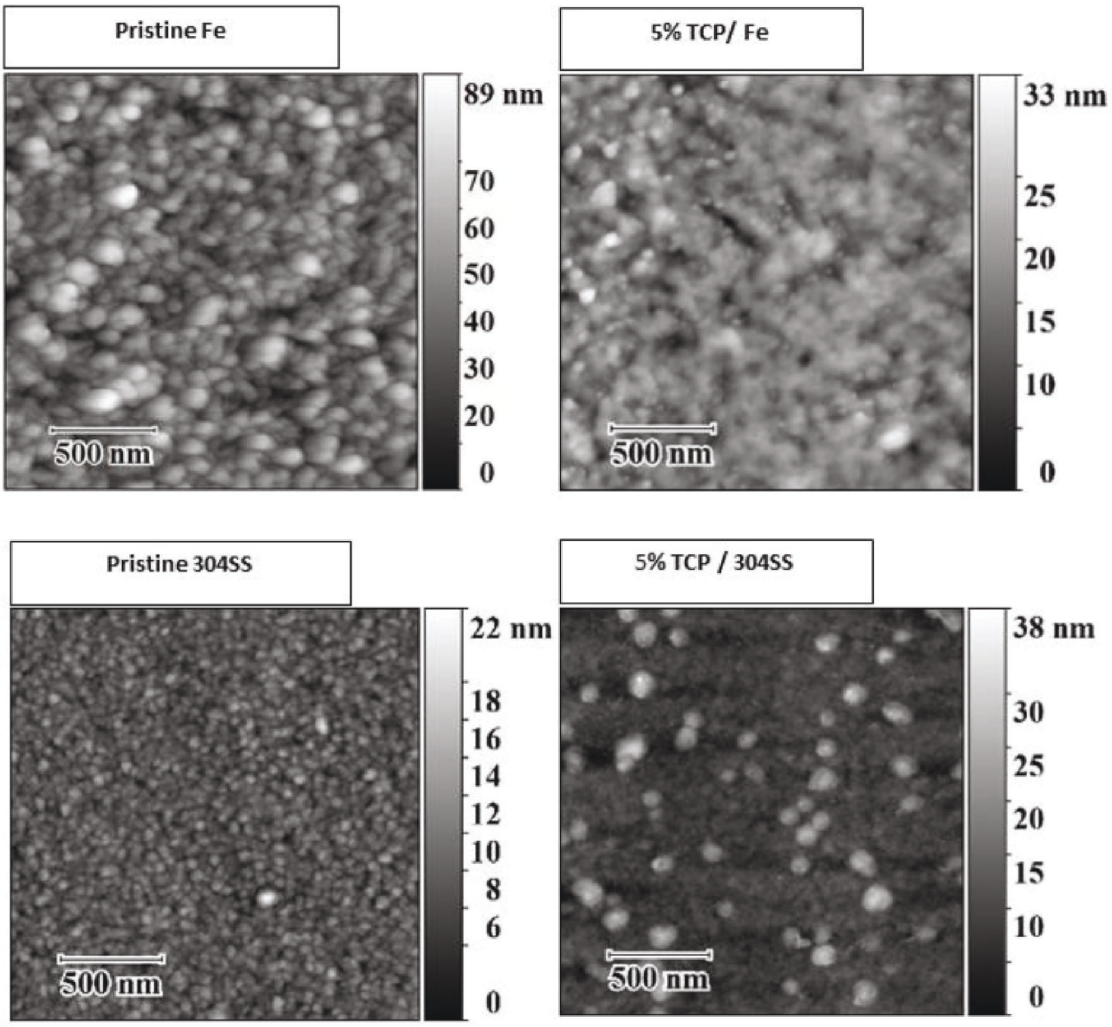


Fig. 2.8: AFM images for pristine and lubricated with 5% TCP in ester solvent on pure Fe and 304SS substrates. Reprinted from Acharya et al. [89], Copyright © 2018 with permission from Elsevier.

The above factors introduce obstacles to the thorough understanding of the mechanisms of TCP decomposition. Overall, the exact thin-film formation mechanism is not fully elucidated [69]. Furthermore, it becomes difficult to distinguish between the different decomposition mechanisms (e.g., corrosion, thermal decomposition, hydrolysis). It is unclear which mechanism is expected to dominate under various environmental conditions (e.g., temperature, pressure, humidity) or due to the use of different lubricant mixtures. Finally, an interplay between the various thin-film decomposition mechanisms might exist. The above underline the importance of simulations of molecular-level resolution in the direction of providing further insights into the formation of thin films from TCP.

For instance, Osei-Agyemang, Berkebile, and Martini studied the experimentally proposed decomposition pathways of m-TCP on Fe(110) using DFT calculations [90]. The simulations revealed the existence of multiple exothermic and energetically favourable reaction pathways associated with

the acidic reservoir, thermal decomposition, and nucleophilic attack by H_2O (hydrolysis) mechanisms (discussed above). Fig. 2.9 depicts the steps and relevant free energies linked to a hydrolysis decomposition pathway from the study of Osei-Agyemang and colleagues. The ReaxFF simulations performed by Khajeh et al. revealed that TCP reacts with ferrous surfaces mainly through the decomposition of aromatic groups (i.e., cresols) [91]. The same authors complemented their ReaxFF simulations with nudged-elastic band calculations to estimate the activation energies for the dominant P-O scission events. They found that decomposition through hydroxylation is more energetically favourable than direct P-O scission. Ogbomo et al. [92] confined TCP molecules between ferrous surfaces to computationally investigate the effect of pressure and sliding speeds on the decomposition. They discovered that the scission rate of the anti-wear additive featured an exponential dependence on shear stress and temperature. Additionally, they revealed that the TCP decomposition rate is elevated in pure iron than in iron oxide/carbide substrates.

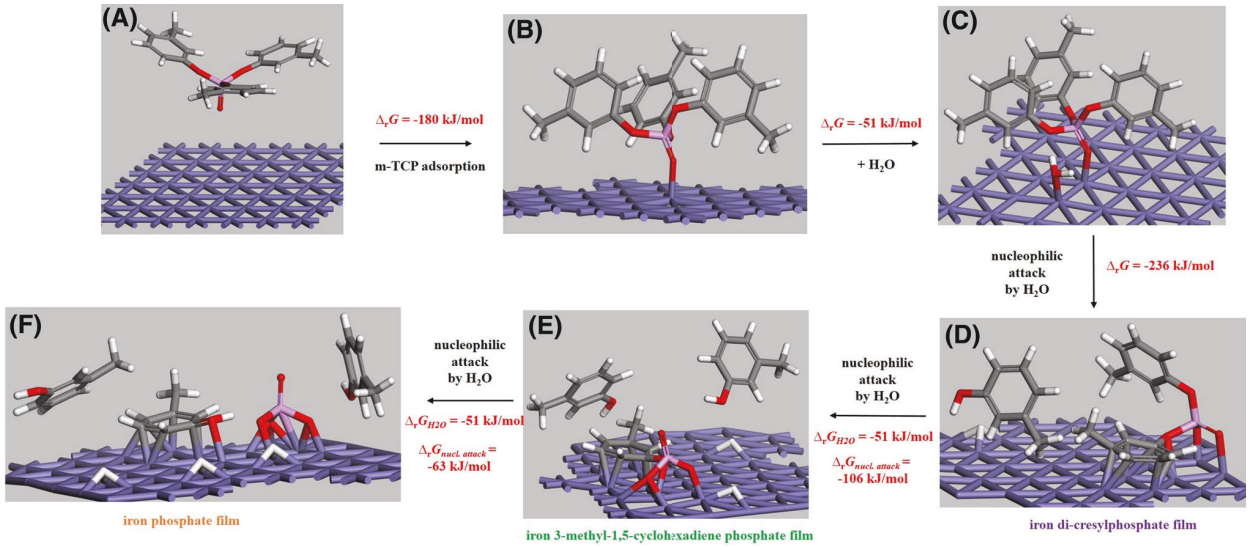


Fig. 2.9: Reaction steps (A-D) involved in a hydrolytic decomposition pathway of m-TCP on Fe(110) and relevant free energies. Reproduced from Osei-Agyemand, Berkebile, and Martini [90] with permission from Springer Nature.

Overall, experiments and simulations provided valuable insights into the reaction pathways of anti-wear additives (e.g., ZDDP, TCP) on metallic surfaces and revealed the underlying composition of the generated thin films. However, a gap in the literature exists when it comes to the link between atomic-scale mechanisms (e.g., reactions, adsorption, diffusion) and macroscopic properties (e.g., viscosity, friction, roughness, wear) of lubricated contacts. Multiscale methods of atomistic resolution are of paramount importance to address such a gap. Specifically, numerical schemes capable of overcoming the timescale limitations of MD while retaining a degree of molecular-level accuracy have to be developed. These schemes will be used to link elementary processes to experimentally measurable quantities, thus bridging the gap between theory and experiments. Furthermore, multiscale modelling can become beneficial in the screening of next-generation lubricant additives. Note that the discovery of alternatives to ZDDP and TCP is necessary to address the environmental (e.g., ecotoxicity), health (e.g., neurotoxicity), and performance (e.g., catalyst deactivation due to thiophosphates) issues associated with conventional phosphate-containing anti-wear additives [64, 68, 93].

2.1.2 Multiscale modelling methods

Section 2.1.1 discussed a few critical materials interfaces in the energy sector. A variety of experimental and computational studies shed light on the composition and properties of the relevant systems. Nevertheless, a gap exists associated with the influence of atomic-scale mechanisms (e.g., reaction pathways, adsorption/desorption steps) on material properties at experimentally relevant timescales. This delays progress in energy storage devices, carbon capture materials, and next-generation lubricant additives. Moreover, the aforementioned gap inhibits the in-depth understanding of the critical materials interfaces (see Section 2.1.1) and introduces hurdles to deriving structure-property relationships. To the best of our knowledge, this gap in the literature is linked to the intrinsic limitations of atomistic simulations, rendering them incapable of capturing timescales beyond a few μs [26].

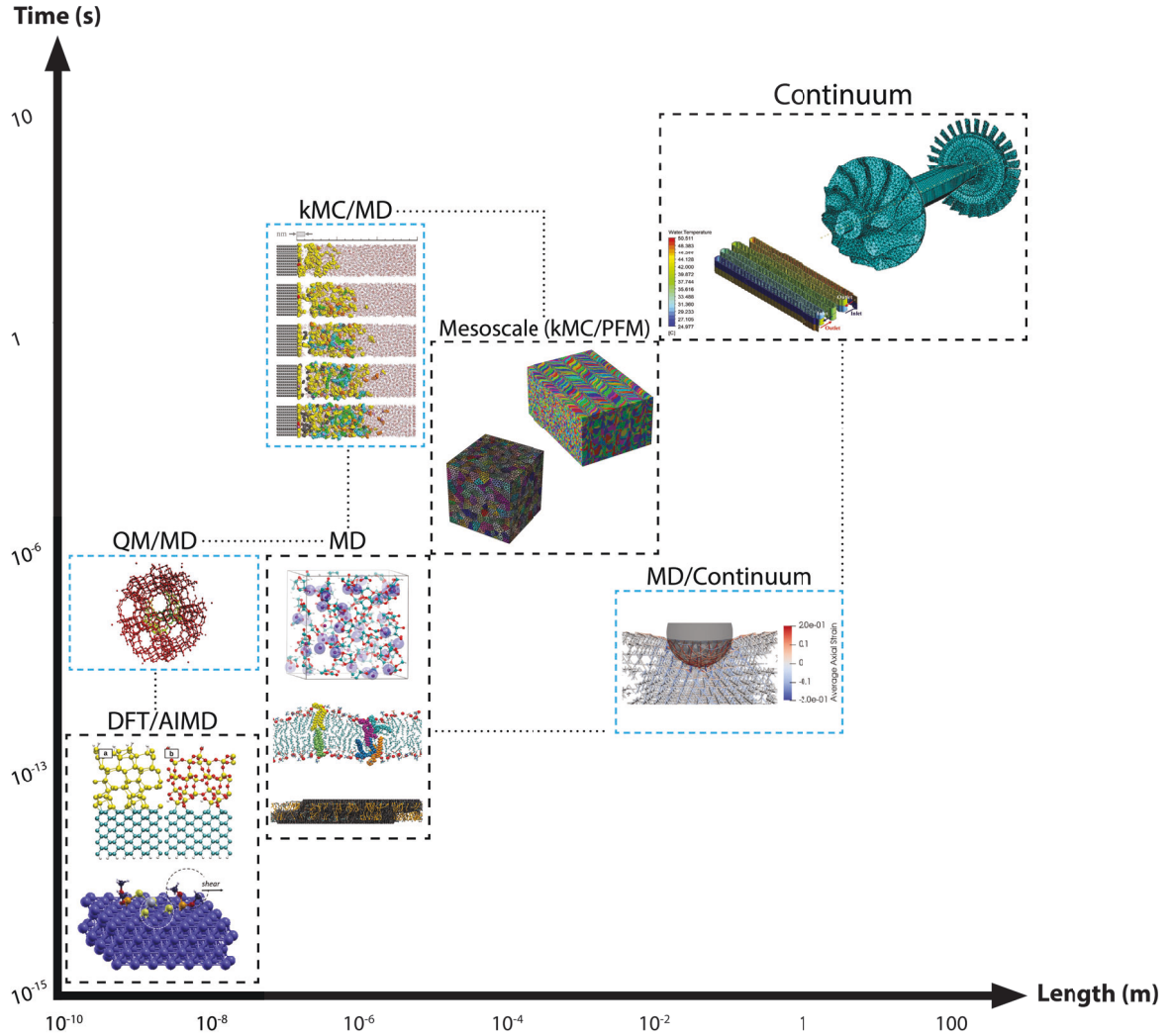


Fig. 2.10: Simulation techniques across the scales and selected scale-bridging methods. The figure contains adapted images reprinted from Peguiron et al. [94], Deng, Morgan, and Szlufarska [95], Jalali et al. [96], and Phlipot and Kochmann [97], Copyright © with permission from Elsevier. Images reprinted with permission from Islam and Van Duin [24], and Abbott and Hanke [98], Copyright © American Chemical Society. Images obtained from Benini, Restuccia, and Righi [62], and Chacón, Bresme, and Tarazona [99], and Trageser et al. [100], and Wiriyasart et al. [101] are reproduced under the Creative Commons CC-BY license. Images used from Weiand et al. [102], and O'Malley et al. [103] are reproduced under the Creative Commons Attribution 3.0 Unported License.

Fig. 2.10 illustrates the characteristic spatiotemporal scales linked to popular simulation techniques in engineering and physics. Quantum mechanical (QM) schemes provide a numerical solution to the Schrödinger equation (SE). Self-consistent calculations in DFT can resolve the ground state (GS) energy of a system. Ab initio (DFT) studies have been deployed to provide insights into the mechanochemistry of diamonds [94], catalysts [104], oxidation potentials of organic solvents [105], reduction of EC electrolytes [106], carbon capture in open-site MOFs [107], and decomposition of anti-wear lubricant additives [61, 62, 90]. AIMD can be deployed to capture the temporal evolution of systems up to a few ps ($10^{-12}s$) [23, 108]. AIMD is inspired by the Born-Oppenheimer approximation. This approximation exploits the fact that electronic motion occurs in significantly lower timescales than nuclear motion. Effectively, this allows the separation of nuclear and electronic motion due to their vastly different timescales. In particular, nuclei are treated classically through Newton's equations of motion, while the GS electronic structure is obtained by solving the SE for the significantly lighter electrons. In essence, accurate interatomic forces are computed via electronic structure calculations and utilised to displace atoms in the simulation box. AIMD simulations have been used to investigate the structure and dynamics of water [109], ammonia [110], and molten salts [111], or to shed light on polymeric chain rupture [112], HIV-1 protease inhibition [113], solvation of hydroniom as well as hydroxyl ions [114], and ZDDP adsorption [60].

MD methods can be utilised for simulations beyond the limits of AIMD. Similar to AIMD, MD treats atomic nuclei as classical objects whose instantaneous positions can be predicted from Newton's equations. Nevertheless, traditional MD methods do not involve QM calculations to resolve the GS electronic structure and estimate interatomic forces. Instead, forces between atoms are calculated through an equation that describes the potential energy of the system as a function of atomic nuclei coordinates (i.e., the interatomic potential). Previous MD studies investigated a variety of systems in materials science, physics, chemistry, biology, and engineering such as protein unfolding [115], bilayers [99, 116], antibodies [117], adsorption in biomimetic surfaces [102], thermal transport in iron oxide-hydrocarbon interfaces [118], polymers in shear flow [119], energetics of anti-wear lubricant additives [92, 120, 121], and SEIs [24, 25]. Overall, MD schemes are scalable and can be deployed to capture system sizes of approximately 10^6 atoms at timescales in the order of μs [26].

Investigations on longer timescales and larger lengthscales necessitate the utilisation of mesoscale techniques. Mesoscale refers to the spatiotemporal domain bridging the MD and continuum scales. The phase field method (PFM) is prevalent in the mesoscopic domain. PMF deploys a diffuse interface concept, where a field variable (the phase field) describes varying material phases or states without explicitly modelling the interface at the molecular level. Different free energy functionals (typically derived from thermodynamic principles), such as the Cahn-Hillard or Allen-Cahn equations, can be deployed to capture the evolution of the phase field variable [122–124]. PFM simulations have been utilised to investigate solidification in binary alloys [125, 126], martensitic transformations [127] as well as phase transformation in ferroelectric thin films [128], anisotropic grain growth [129, 130], crack propagation [131, 132], and dislocation dynamics [133].

KMC is another mesoscopic technique. KMC assumes that the system evolution is driven by rare atomic-scale mechanisms (i.e., events whose activation energies are by 1-2 orders of magnitude greater than k_bT). KMC is a stochastic technique that selects and executes rare events to update the positions of atoms. The respective transition probabilities are analogous to the frequencies of

the relevant atomic-scale mechanisms. Effectively, the kMC method can be deployed to neglect trivial system transitions around minima on the potential energy surface (PES) [134] and extend the simulation timescales beyond the limits of AIMD and MD. The kMC method has been successfully applied to study a wide range of applications from deposition processes [135, 136], to heterogenous catalysis [137–139], nanoparticle growth [140], additive manufacturing microstructures [100], grain boundary diffusivity [95], and even interstellar grain chemistry [141].

Under the continuum assumption, atoms are not modelled explicitly. Instead, it is postulated that they operate collectively to give rise to macroscopic phenomena such as deformation, fluid flow, and electrostatic interactions. Continuum methods offer solutions to partial differential equations (PDEs) describing a phenomenon. For instance, the finite element analysis (FEA) [142, 143] can numerically solve the PDEs corresponding to stress-strain relationships (e.g., linear elasticity, plasticity) in solid mechanics, fluid flow (e.g., Navier-Stokes, Reynolds), or electromagnetism (e.g., Maxwell's equations). Furthermore, multiphysics models can provide a simultaneous solution to a system of PDEs describing varying macroscopic phenomena (e.g., fluid flow coupled with thermal transport). Since continuum schemes do not explicitly model atoms, they are usually less computationally expensive than methods of molecular-level resolution. Therefore, continuum approaches can be utilised to simulate complete engineering systems and capture experimentally relevant timescales as well as lengthscales. However, they are less detailed than lower-scale methods (e.g., kMC, PFM, MD, AIMD, and DFT). Previous studies deploying continuum models have investigated electrode materials for Li-ion batteries [144], cooling in energy storage devices [101], rotors [96], thin films from additives and lubricated contacts [145, 146], CO_2 separation [147], and diffusion of nanoparticles in the brain white matter [148].

Overall, single-scale methods of atomistic resolution (e.g., AIMD or MD) are not numerically tractable to enable long-timescale investigations on the aforementioned critical materials interfaces. On the other hand, simulation techniques of the continuum can address experimentally relevant time or lengthscales, but do not possess the required accuracy to investigate the effect of elementary processes (e.g., reactions, diffusion, adsorption) on the evolution of the system. Multiscale methods are required to reach experimentally relevant timescales while maintaining a degree of molecular-level accuracy. By definition, multiscale schemes involve multiple levels of resolution and spatiotemporal scales. Multiscale schemes are necessary to investigate systems evolving by phenomena manifesting at varying scales (see Sections 2.1.1.1, 2.1.1.2, and 2.1.1.3).

Quantum mechanical/molecular mechanical (QM/MM) models are hybrid multiscale schemes aiming to extend AIMD simulations to the characteristic timescales and lengthscales associated with MD. QM/MM algorithms are based on a domain decomposition (DD) concept. In essence, the computational domain is divided into QM and MM regions performing DFT/AIMD and MD calculations, respectively [108, 149]. The AIMD solver typically describes an interface of interest where QM-level accuracy is necessary, while the MD solver captures interatomic interactions in the bulk through a force field. QM/MM simulations have been successfully deployed to model surface reactions of solvents on metallic substrates [150], adsorption as well as methoxylation of Zeolites [103, 151], nanoparticles [152–154], and defects in metallic oxides [155–157]. QM/MM calculations are also significant in biological applications and shed light on the catalytic effect of enzymes [158] or the dynamics of proteins (e.g., myoglobin [159, 160]). Overall, QM/MM approaches can be utilised to perform QM simulations beyond the spatiotemporal scale limits of

AIMD. Nevertheless, the timescales and lengthscales of QM/MM schemes are at best comparable to MD-relevant scales.

The timescales of MD simulations can be extended to the $\mu s - ms$ regime through enhanced sampling methods [161]. Monte Carlo (MC)-based as well as MD-based enhanced sampling methods exist in the literature [162] and include but are not limited to Wang-Landau [163], umbrella sampling [164], multicanonical sampling [165], and hyperdynamics [166]. The aforementioned enhanced sampling methods are conceptually similar. They aim at biasing and subsequently elevating the probability of sluggish elementary processes inaccessible to traditional MD simulations. These elementary processes are the so-called rare events (e.g., reactions or adsorption steps) and are typically associated with high activation energies. Nevertheless, there are usually no analytic or straightforward approaches to derive or select the appropriate biasing potential for a system of choice studied with enhanced sampling techniques [167].

Accelerated MD schemes can be deployed to extend the MD timescales without the need to directly bias the probabilities of rare events. For instance, the adaptive biasing force (ABF) [168] method introduces an equal and opposite force to the mean force acting along a reaction coordinate. This process smoothens valleys along the PES and facilitates system transitions to nearby states. Nonetheless, the exploration of the PES with ABF is influenced by the choice of reaction coordinate or collective variable. ABF-MD schemes have been deployed to shed light on fuel deposits [169] and surfactant adsorption [170]. Parallel replica dynamics (PRD) [171] is a different parallelised technique that generates a system replica on each parallel process. Initially, a decorrelation stage ensures that each replica features a different starting point. Then, the replica trajectories are evolved independently until a rare event is observed and the cumulative elapsed time of the replicas is added to the simulation clock. The simulation resumes from the replica in which the rare event manifested with another decorrelation-replication sequence. PRD simulations have been previously utilised to study sluggish chemical reactions in compressed liquid benzene [172]. Overall, enhanced sampling and accelerated dynamics approaches can be deployed to overcome high energy barriers and reach $\mu s - ms$ timescales in MC as well as MD simulations.

Hybrid kMC/MD schemes can be utilised to advance the simulation clock beyond the timescale limits of enhanced sampling or accelerated MD with molecular-level resolution. The kMC method deploys a variable timestep that is inversely proportional to the cumulative rate of events on a given step [173]. For example, if the total rate of events at each step is in the order of 10^6 Hz, then the relevant timestep would be in the order of μs. In this example, about 10^3 kMC steps would be sufficient to access timescales of ms. Of course, the lower the cumulative rate of events, the less detailed the trajectory. For instance, in the aforementioned example featuring cumulative rates of 10^6 Hz, the kMC model would be incapable of capturing molecular-level elementary processes manifesting at frequencies in the order of fs (e.g., atomic vibrations). To address that and, therefore, unlock long-timescale simulations with molecular-level resolution, the kMC algorithm can be coupled with an MD scheme in a hybrid kMC/MD formulation. By doing so, the MD method can be utilised to model phenomena occurring in fs timescales, while the kMC solver can capture rare events. A hybrid kMC/MD model dedicated to the modelling of 2-chlorobutane racemisation in solution was published by Nagaoka et al. [174]. In 2020, Gissinger and colleagues presented the REACTER algorithm, which is essentially a kMC/MD scheme that enabled reactive MD simulations with classical interatomic potentials [175]. In 2022, Abbot and Hanke [98] deployed hybrid kMC/MD

simulations to investigate the structure of SEIs. Nonetheless, the aforementioned schemes are designed to model solely bond formation and breaking in the kMC stage and cannot capture other classes of rare events, such as adsorption/desorption steps or diffusion hops. These events can be fundamental in the thorough understanding of the long-timescale evolution of critical interfaces in the energy sector (see Section 2.1.1). Moreover, the lengthscales of hybrid kMC/MD schemes are still dictated by the simulation box size and, therefore, are comparable to MD lengthscales.

The bridging of the molecular-continuum lengthscales is more appropriately achieved through coarse-graining (CG) techniques. CG methods map collections of atoms into particles or onto a lattice. This process diminishes the dimensionality of atomistic simulations and allows them to reach lengthscales well beyond the limits of traditional MD methods [176–180]. CG simulations have been used to investigate a variety of hierarchical systems, such as membranes for hydrogen fuel cells [181], protein unfolding [180], soft matter [182], and human hair [183]. Overall, CG models can extend the lengthscales of atomistic simulations. However, the timescales of CG techniques are slightly longer but typically similar to that of MD schemes. For instance, stable integration with MARTINI CG force fields for various biomolecular systems demands timesteps in the order of tens of fs [184].

Unlocking simulations on systems with characteristic scales greater than ms and μm usually necessitates the coupling of methods of atomistic or quantum resolution with continuum models [185]. Similarly to QM/MM techniques, a variety of continuum/molecular approaches are based on the DD concept [186]. In particular, MD simulations are deployed to offer molecular-level resolution detail at a boundary of interest (e.g., solid/liquid interface), while a continuum (e.g., FEA) scheme provides a less detailed solution for the rest of the system. For instance, Tadmor and colleagues developed the quasicontinuum (QC) method [187]. This method coupled FEA with MD to investigate defects in crystalline materials. Other hybrid FEA schemes with molecular/quantum detail domains were successfully utilised to study crack propagation and tip dislocation nucleation [188, 189], and hierarchical metamaterials [190]. Besides DD-based techniques, multigrid coupling schemes can bridge atomistic and continuum scales. In these approaches, macroscopic PDEs are solved on a coarse grid to capture continuum-level behaviour, while progressively finer grids resolve atomistic effects [186]. Multigrid techniques have been utilised to shed light on diffusion processes [191] or the structure of composite materials [192, 193]. Both DD-based and multigrid simulations exhibit a tradeoff between accuracy and the ability to model larger lengthscales and longer timescales [194, 195]. Specifically, incorporating longer molecular-level simulations or extending the MD domain can elevate the accuracy of the methods. Nevertheless, this can increase the numerical cost of the relevant multiscale techniques and impede their ability to capture long timescale system behaviour and properties (e.g., viscosity, diffusivity).

Machine learning (ML)-based methods are becoming popular in the field of multiscale modelling. For example, in 2023, Ingólfsson et al. developed the Multiscale Machine-Learned Modeling Infrastructure (MuMMI) [196]. In their relevant publication, they demonstrated how MuMMI can be deployed to bridge three different spatiotemporal scales to investigate protein binding. A dynamic density functional theory (DDFT) [197, 198] approach was utilised at the top level to model particles at timescales of ms and lengthscales of μm, while CG and all-atom (AA) schemes were used at the intermediate and finer scales. ML models classified DDFT structures based on their diversity importance [199] to occasionally launch CG simulations. On the other hand, structural

criteria (e.g., orientation and tilt of protein) derived from histograms were deployed to generate initial structures from the CG models and communicate them to the AA scales. A feedback loop enabled adaptive modification of CG force field parameters from data derived from the finest scales, while CG properties such as radial distribution functions (RDFs) were passed to the DDFT scale to update the top-level simulation.

Holey, Gumbsch, and Pastewka recently presented a different active learning ML-based scheme suitable for continuum/MD modelling of lubricant flow [200]. In their heterogeneous multiscale method (HMM) technique, a continuum-scale solver calculates the momentum and mass densities from conservation laws. Non-equilibrium MD (NEMD) simulations are deployed to provide accurate estimates for the stress tensor at a given point in the spatial domain. Gaussian process (GP) surrogate models [201] dynamically trained on NEMD are used as a numerically cheap approach to interpolate between NEMD data and populate the stress tensor for every point in the computational domain. Additional NEMD calculations are occasionally triggered based on a GP prediction uncertainty criterion. This allows for continuum-level simulations with molecular-level detail, leveraging an assumed separation of timescales to overcome the limitations of conventional MD timescales.

2.1.3 Concluding remarks and motivation for thesis

In Section 2.1.2, we reviewed the state-of-the-art in multiscale modelling. Specifically, a discussion regarding traditional simulation techniques and advanced scale-bridging algorithms was presented. The hybrid kMC/MD method is a technique of molecular-level accuracy with the potential to access any timescale. As previously discussed, this is associated with the fact that the timestep of the kMC method is variable and depends on the total rate of events at a given step. Nevertheless, the hybrid kMC/MD algorithms identified in the bibliography specialise in bond-formation and bond-breaking events. In the present thesis, we aim to unlock hybrid kMC/MD simulations in experimentally relevant timescales with different classes of events (adsorption, diffusion, etc.). This will enhance the applicability of the hybrid kMC/MD method in critical systems in physics, chemistry, materials science, and engineering (see Section 2.1.1 for examples).

2.2 Theory of numerical algorithms

As motivated in Section 2.1.3, this work will mainly focus on developing and testing a hybrid kMC/MD methodology capable of simulating different classes of predefined events. This section provides the theoretical background for the simulation techniques that constitute the hybrid kMC/MD model.

2.2.1 MD

2.2.1.1 Basics of MD

As briefly mentioned in Section 2.1.2, MD postulates that atomic nuclei are classical objects. MD deploys Newton's second law of motion to update the positions of atoms at each step. The equations of motion can be expressed in differential form as follows [202]:

$$\mathbf{F_i} = m_i \frac{d^2\mathbf{r_i}}{dt^2} \tag{2.1}$$

Where $\mathbf{F_i}$ is the force acting on the i^{th} atom with mass m_i located at $\mathbf{r}_i = (x_i, y_i, z_i)$. Note that bold and regular symbols represent vectors and scalars, respectively. Given initial atomic positions and velocities $\mathbf{r}_i(t)$ and $\mathbf{v}_i(t)$, the velocity-Verlet algorithm is typically utilised to integrate Newton's equations and predict $\mathbf{r}_i(t + \Delta t)$ and $\mathbf{v}_i(t + \Delta t)$ [203] from the following expressions:

$$\mathbf{r}_i(t + \Delta t) = \mathbf{r}_i(t) + \mathbf{v}_i(t)\Delta t + \frac{1}{2m_i}\mathbf{F}_i(t)\Delta t^2 \tag{2.2}$$

$$\mathbf{v}_i(t + \Delta t) = \mathbf{v}_i(t) + \frac{1}{2m_i}\left[\mathbf{F}_i(t + \Delta t) + \mathbf{F}_i(t)\right]\Delta t \tag{2.3}$$

The relevant forces acting on atoms are obtained from the gradient of the potential energy:

$$\mathbf{F_i} = -\nabla_i U \tag{2.4}$$

Here, the potential energy is a function of the instantaneous positions of N atoms (i.e., $U = U(\mathbf{r}_1, \mathbf{r}_2, .., \mathbf{r}_N)$). The resolution and, therefore, the computational cost of MD depend on the choice of interatomic potential function. A variety of force fields are available in the literature, including but not limited to ML, reactive, many-body, and pairwise [26]. An extensive analysis of the advantages, disadvantages, and approximations associated with the different classes of U is addressed in previous reviews (e.g., Müser, Sukhomlinov, and Pastewka [204]) and is beyond the scope of this section. Here, we briefly discuss the force field expressions used in this work.

2.2.1.2 Lennard-Jones, DREIDING, and ReaxFF potentials

The 12-6 Lennard-Jones (LJ) force field is a widely utilised empirical potential function [205]. It expresses the interatomic potential energy as:

$$U(\mathbf{r}_{ij}) = 4\epsilon_{ij}\left[\left(\frac{\sigma_{ij}}{r_{ij}}\right)^{12} - \left(\frac{\sigma_{ij}}{r_{ij}}\right)^{6}\right] \tag{2.5}$$

Where r_{ij}^{-12} is a repulsive term (arising from Pauli's exclusion principle) and r_{ij}^{-6} is an attractive term associated with van der Waals interactions. Also, ϵ_{ij} is a coefficient with units of energy controlling the strength of interactions, while σ_{ij} is another parameter expressing the equilibrium interatomic distance (i.e., $U(\sigma_{ij}) = 0$).

The DREIDING potential uses the LJ 12-6 expression and additionally includes Coulombic terms to account for electrostatic interactions between atoms [206]:

$$U_{nb}(\mathbf{r}_{ij}) = 4\epsilon_{ij}\left[\left(\frac{\sigma_{ij}}{r_{ij}}\right)^{12} - \left(\frac{\sigma_{ij}}{r_{ij}}\right)^{6}\right] + \frac{q_i q_j}{4\pi\epsilon_0 r_{ij}} \tag{2.6}$$

Here, q_i represents the static charge of the i_{th} atom, and ϵ_0 is the vacuum permittivity. Note that fixed atomic charges are typically assumed in MD algorithms. Alternatively, atomic charges can be continuously updated throughout the MD simulation via semi-empirical charge equilibration schemes parametrised from QM calculations. An example of such a scheme is the charge equilibration method (QEq) briefly discussed in Section 2.2.1.3, which updates the atomic charges by

minimising the system's electrostatic energy [207]. The bonded DREIDING interactions comprise bond stretch (E_B), bond-angle bend (E_A), dihedral angle torsion (E_T), and inversion (E_I) terms expressed as follows:

$$E_B = \frac{1}{2}K_B(r_{ij} - r_0)^2 \tag{2.7}$$

Where K_B is a spring constant and r^0 is the equilibrium bond distance.

$$E_A = \frac{1}{2}K_A[cos(\theta_{ijk}) - cos(\theta_j^0)]^2 \tag{2.8}$$

Here, K_A is a harmonic spring bond-angle parameter, θ_{ijk} is the angle between atom pairs i-j and j-k, and θ_j^0 is the equilibrium bond-angle, which is independent of the positions of atoms i, j, and k.

$$E_T = \frac{1}{2}K_T\left\{1 - \cos\left[n_{JK}(\phi - \phi_{JK}^0)\right]\right\} \tag{2.9}$$

With ϕ being the dihedral angle between planes IJK and JKL, ϕ_{JK}^0 represents the equilibrium angle, n_{JK} is an integer expressing the periodicity, and K_{JK} is the torsional energy barrier.

$$E_I = \frac{1}{2}K_I(\psi - \psi_0) \tag{2.10}$$

Here, K_I is the inversion spring constant, ψ is the angle between the IL bond and the JIK plane, and ψ^0 is the equilibrium distance. The potential energy of bonded interactions is given as follows:

$$U_b = E_B + E_A + E_T + E_I \tag{2.11}$$

Overall, the total potential energy is the sum of non-bonded (Eq. 2.6) as well as bonded (Eq. 2.11) potential energies. Occasionally, hydrogen bond terms (i.e., U_{hb}) can be included as contributions to the potential energy:

$$U_{DREIDING} = U_{nb} + U_b + U_{hbond} \tag{2.12}$$

The DREIDING potential is computationally efficient. Nevertheless, it uses fixed bonded interactions that cannot be altered during the simulation. Hence, the DREIDING force field cannot capture reactions (e.g., bond-formation or bond-breaking). Reactive potentials were introduced to address the aforementioned issue linked to interatomic potentials of predefined connectivity between atoms. ReaxFF is a popular reactive force field that expresses the energy of the system as follows [208, 209]:

$$E_{ReaxFF} = E_{bond} + E_{angle} + E_{tors} + E_{vdWaals} + E_{Coulomb} + E_{specific} \tag{2.13}$$

Where E_{bond}, E_{angle}, and E_{tors} represent contributions from two-body, three-body, and four-body terms, respectively. E_{over} is an over-coordination penatly energy. $E_{Coulomb}$ and $E_{vdWaals}$ are energies associated with Coulombic as well as van der Waals interactions. Finally, $E_{specific}$ is an optional term to account for energy contributions in specific systems (e.g., lone-pair, hydrogen binding [209]). To capture reactivity, ReaxFF deploys a bond-order formulation. In particular, the following empirical equation is used, accounting for σ, π, and $\pi\pi$ contributions:

$$BO_{ij} = BO_{ij}^{\sigma} + BO_{ij}^{\pi} + BO_{ij}^{\pi\pi} = e^{p_{bO1}(\frac{r_{ij}}{r_0^{\sigma}})^{p_{BO2}}} + e^{p_{bO3}(\frac{r_{ij}}{r_0^{\pi}})^{p_{BO4}}} + e^{p_{bO5}(\frac{r_{ij}}{r_0^{\pi\pi}})^{p_{BO6}}} \tag{2.14}$$

Here, BO is the bond order between species i and j, p_{BO} are empirical ReaxFF coefficients, and r_0^{σ}, r_0^{π}, $r_0^{\pi\pi}$ correspond to equilibrium bond distances for the relevant bond-type contributions.

2.2.1.3 Basics of QEq

QEq is a technique introduced by Rappé and Goddard [207] dedicated to the dynamic prediction of partial atomic charges in atomistic simulations. The QEq method can elevate the accuracy of MD simulations in cases where the charge distribution within molecules is unknown. Furthermore, QEq accounts for alterations in the local atomic environment (e.g., modifications to the geometry of a molecule or changes in atom neighbours). Consequently, dynamically updated partial charges calculated with QEq are preferred over static Coulombic charges in reactive MD simulations [120, 210, 211].

An in-depth derivation of the QEq equations and a thorough discussion on the QEq variants are beyond the scope of this thesis. For further information, the reader is advised to refer to the original work of Rappé and Goddard [207] or the review of Ongari et al. [212]. This section provides an overview of the QEq equations along with a summary of the relevant QEq parameters and fundamental approximations.

QEq is based on the principle of electronegativity equalisation [213, 214]:

$$\frac{\vartheta E(\mathbf{r}, \mathbf{q})}{\vartheta q_i} = -\mu \tag{2.15}$$

Where E is the total electrostatic energy of the system expressed as a function of instantaneous atomic positions ($\mathbf{r}$) and charges ($\mathbf{q}$). Effectively, Eq. 2.15 demands that the electronegativity (i.e., the partial derivative of electrostatic energy) at an atomic site is equal to the negative of the chemical potential (μ) of system electrons. QEq uses an atomic chemical potential based on shielded electrostatic interactions as well as three experimentally obtained parameters:

1. **Atomic ionisation potentials (IP)**: The energy required to remove the outermost (valence) electron from a neutral, isolated gaseous atom.
2. **Electron affinities (EA)**: The energy change (typically released) when an electron is added to a neutral, isolated gaseous atom.
3. **Covalent atomic radii (R_a)**: The effective size of an atom, often defined as half the distance between the nuclei of two identical atoms bonded together.

The QEq method deploys a second-order Taylor expansion of the total energy with respect to the atomic charge fluctuations. IP and EA are utilised in partial derivatives of the total electrostatic energy. Specifically, the first-order derivative represents the electronegativity (χ), quantifying an atom's tendency to attract electron density:

$$\chi_i = \frac{1}{2}(IP + EA) \approx \frac{\vartheta E}{\vartheta q_i} \tag{2.16}$$

The second-order derivative is the atomic hardness (η), which expresses the atom's resistance to charge deformation:

$$\eta_i = IP - EA \approx \frac{\vartheta^2 E}{\vartheta q_i^2} \tag{2.17}$$

On the other hand, R_a is used to define an effective smeared-out charge distribution that replaces point charges, leading to "shielded" Coulombic interactions. This regularisation prevents the divergence of electrostatic interactions when the interatomic distance (R_{ij}) approaches zero (i.e., $R_{ij} \rightarrow 0$), thereby eliminating short-range instabilities in the energy expression. Nevertheless, versions of QEq exist that deploy point charges instead of smeared-out distributions for computational efficiency purposes. Such an approach is used in the `qeq/point` fix of the Large-scale Atomic/Molecular Massively Parallel Simulator (LAMMPS) [26].

Finally, the total electrostatic energy is expressed as

$$E(\mathbf{r}, \mathbf{q}) = \sum_i (q_i \chi_i + \frac{q_i^2}{2} \eta_i) + \sum_{i \neq j} q_i q_j J_{ij}(\mathbf{r}) \tag{2.18}$$

With the "shielded" Coulombic interaction (J) defined as:

$$J_{ij}(\mathbf{r}) = \left\langle \phi_i \phi_j \left| \frac{1}{|\mathbf{r}_i - \mathbf{r}_j|} \right| \phi_i \phi_j \right\rangle \tag{2.19}$$

Where ϕ can represent a Slater function or a smeared Gaussian.

2.2.2 KMC

2.2.2.1 Fundamentals of kMC

KMC schemes assume that the evolution of the underlying system is driven by rare atomic-scale mechanisms (e.g., diffusion, deposition, dissociation). The activation energies associated with such mechanisms are approximately 1-2 orders of magnitude greater than $k_b T$ (i.e., $\Delta E \gg k_b T$, where k_b and T are the Boltzmann constant and temperature, respectively). The dynamic trajectory linked to systems driven by low-barrier events is dominated by thermal fluctuations in the neighbourhood of PES basins with infrequent jumps to adjacent minima. Therefore, the spatial coordinates of atoms are thermalised adequately between successive rare events, and the local configuration reaches thermodynamic equilibrium before transitioning to a different bottleneck region. Ergo, the system evolution can be modelled as a sequence of occasional jumps between deep PES valleys. This underlines the suitability of a Markovian chain (i.e., a memoryless process) in the direction of predicting state-to-state transitions along the PES. Specifically, the Markovian Master equation can be used to describe the temporal evolution of $P(S_i, t)$, which expresses the probability of finding the system at state S_i at time t [134]:

$$\frac{dP(S_i, t)}{dt} = -\sum_{i \neq j} W_{ij} P(S_i, t) + \sum_{i \neq j} W_{ji} P(S_j, t) \tag{2.20}$$

Where W_{ij} is the transition frequency from state i to state j, with $W_{ij} \geq 0$ and $\sum_j W_{ij} = 1$. Relation 2.20 is essentially a system of coupled PDEs based on a continuity condition (i.e., the balancing of the probabilities of transitioning in and out of the current state S_i). Such a condition establishes the conservation of the total transition frequency for any value of *"t"* (i.e., $\sum_i P(S_i, t) = 1, \forall t \in R$). Notice that the principle of detailed balance is satisfied in stationary

conditions i.e., $\sum_{i \neq j} W_{ij} P_{eq}(S_i, t) = \sum_{i \neq j} W_{ji} P_{eq}(S_j, t)$ when $dP/dt \equiv 0$, with $P_{eq}(S_i, t)$ and $P_{eq}(S_j, t)$ representing the equilibrium state probabilities [215].

It becomes important to underline that equation 2.20 captures solely rare events (realised as transitions between local minima on the PES) and neglects the low activation energy mechanisms (e.g., atomic vibrations) in the vicinity of valleys on the PES. This fact implies that Markovian trajectories (obtained by solving equation 2.20) are less detailed than trajectories generated using theories of molecular level resolution, such as DFT or MD simulations. Nonetheless, the inability of the Markovian Master equation to generate a complete system trajectory is balanced by its potential to advance the system clock by several orders of magnitude beyond the microsecond $(10^{-6}s)$ scale, which is typically the limit of MD [26, 216]. Figure 2.11 illustrates a schematic comparison between state-to-state transitions obtained from lower-level theories and the Markovian Master Equation.

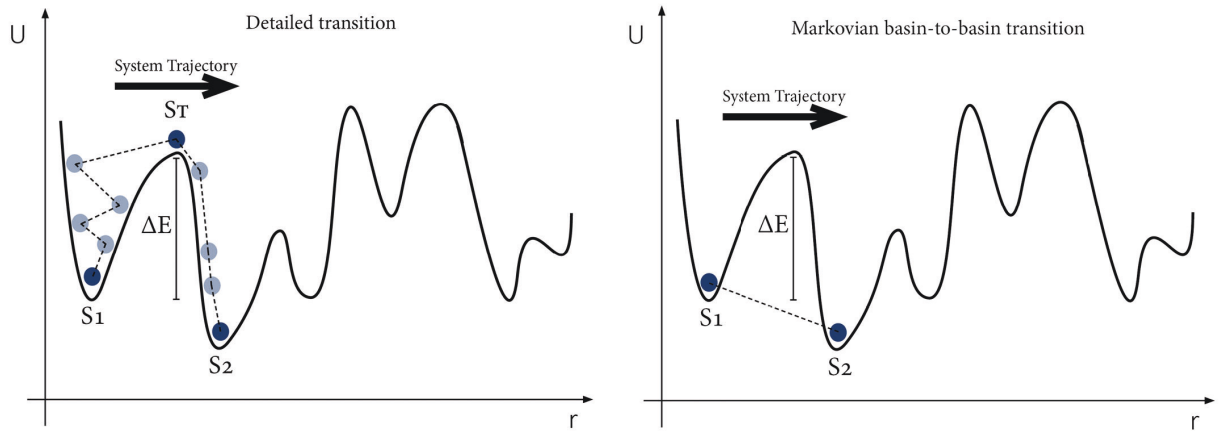


Fig. 2.11: Qualitative graph of the Potential Energy (U) versus a reaction coordinate (r). 2D representation of the PES. **(Left)** Detailed transition simulated using schemes of molecular-level resolution (e.g., MD or DFT). The system vibrates around valley S_1 and eventually reaches the transition state (S_T) and relaxes to a new valley S_2. **(Right)** Basin-to-basin transition described by the Markovian Master equation (expressed in 2.20). From our pre-print on cheRxiv © reproduced under the CC BY NC ND 4.0 license.

Now, the total number of states of a system following a Markovian process can be expressed as:

$$N = n^m \tag{2.21}$$

where n and m are the possible occupation states of each surface site and the total system sites, respectively. Relation 2.21 implies that the transition frequency matrix (W) is an N by N array with $n^m n^m = n^{2m}$ elements. This justifies the fact that obtaining an analytic solution for the system of PDEs of relation 2.20 becomes impractical for most physics and engineering applications. As an example, consider a simplistic system of 50 lattice sites (m=*50*) and 3 atomic species. Then assume that each surface site can be unoccupied or singly occupied by any of the 3 species (i.e., each surface site has 4 occupation states and n=*4*). In this example, W is a matrix of $n^{2m} = (4^{50})^2 \approx 1.61 \times 10^{60}$ elements. Therefore, attempting to diagonalise W becomes impracticable. From a numerical point of view, even storing and performing basic arithmetic operations on 1.61×10^{60} elements can be considered challenging, if not impossible. Consequently, the acquisition of an analytic solution for equation 2.20 is infeasible even for trivial examples. Undoubtedly, solving equation 2.20 for critical

energy interfaces and materials science problems involving amorphous films (elevates the number of available surface sites m) as well as multiple species and atomic scale processes (increases the number of possible occupation states n) becomes unrealistic.

The aforementioned remarks underline the necessity for an approximation in the direction of describing the temporal evolution of $P(S_i, t)$ (probability of finding the system at state S_i at time t). Such necessity motivated the development of kMC approaches. KMC is an umbrella term that encompasses probabilistic algorithms such as the n-fold way [217] and the Direct Method [218]. KMC algorithms capture the temporal evolution of $P(S_i, t)$ by displacing the system from the current basin (S_i) to a neighbouring state (S_j) and estimating the average time required to overcome the relevant energy barrier (ΔE_{ij}) at each time step. Specifically, it can be proven that treating the mean escape time from state S_i (sojourn time) as an exponentially distributed random variable allows for the calculation of the time increment associated with a transition from state S_i and time t_{S_i} to state S_j and time t_{S_j} [173]:

$$\Delta t = -\frac{\ln(\rho_1)}{W_{tot}} \tag{2.22}$$

Where $\Delta t = t_{S_j} - t_{S_i}$, ρ_1 represents a uniformly distributed random number with $\rho_1 \in [0, 1]$, and W_{tot} describes the cumulative rate for the n possible escape processes from state S_i (i.e., $W_{tot} = \sum_{j=1}^{n} W_{ij}$). Then, an atomic scale mechanism that displaces the system out of the current state S_i is selected, such as:

$$\sum_{j=1}^{p} W_{ij} \geq \rho_2 W_{tot} \geq \sum_{j=1}^{p-1} W_{ij} \tag{2.23}$$

where p is an integer corresponding to the selected transition mechanism (with a rate of W_{ip}) and ρ_2 is a second uniformly-distributed number in the [0,1] interval. Inequality 2.23 ensures that faster atomic scale mechanisms (those of elevated W_{ij} value) are selected more frequently than slower processes. Specifically, the event selection probability can be written as [137]:

$$P_{S_i \to S_j} = \frac{W_{ij}}{W_{tot}} \tag{2.24}$$

Generally, kMC algorithms generate a stochastic basin-to-basin trajectory on the PES. This allows for the description of the temporal evolution of $P(S_i, t)$ through ensemble averaging over multiple stochastic trajectories, without the requirement for a direct solution of equation 2.20. Such a fact contributes to the time-advancing efficiency of the kMC method. The standard (n-fold way) kMC algorithm, which is the basis of the computational framework presented in Section 3, is summarised in the flowchart of Figure 2.12. In the beginning, an array containing the rates of basin-to-basin transition events is assembled and the cumulative transition rate (W_{tot}) is estimated. Following, two random numbers (ρ_1,ρ_2 $\in$[0,1]) are drawn to advance the system clock (by Δt as in relation 2.22) and stochastically select an atomic scale process (by satisfying inequality 2.23). Then, the selected event is executed and the system moves from the current state to a neighbouring state. The algorithm reaches an end when the system time (t_{clock}) exceeds the user-defined end time (t_{end}).

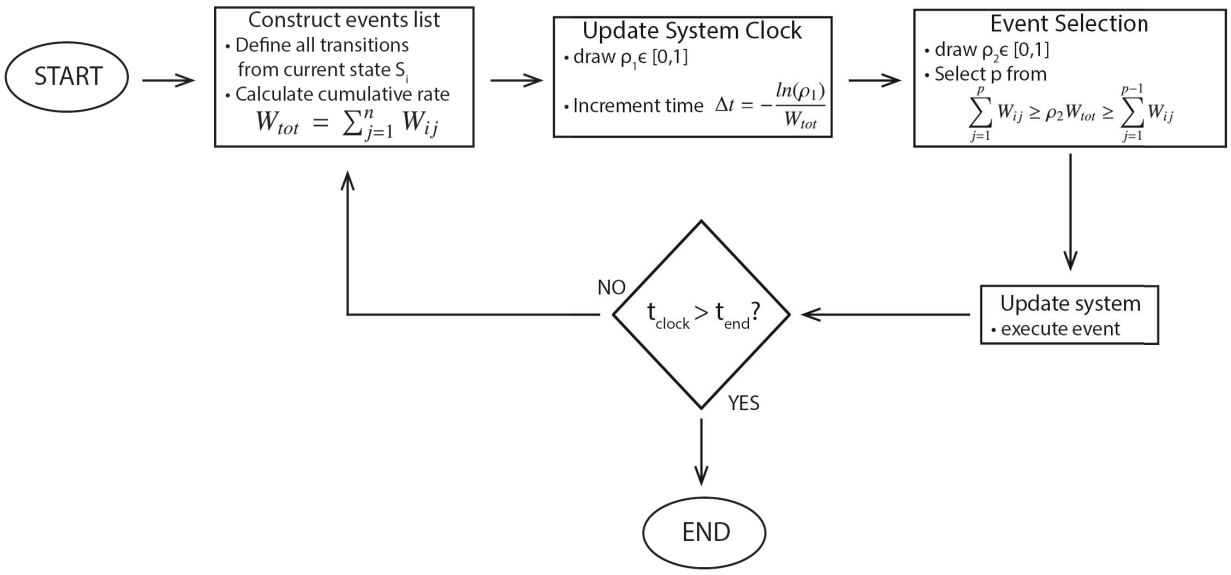


Fig. 2.12: Flowchart summarizing the workflow of the standard kMC algorithm.

2.2.2.2 KMC catalog of rates and limitations of latticed-based and non-lattice-based schemes

From a practical perspective, the implementation of the standard kMC algorithm is a trivial endeavour. Regardless, the number of distinct elementary processes dictating the concentrations of surface species in materials science as well as chemistry applications are typically in the order of thousands [219]. This fact elevates the numerical effort associated with calculating and storing the state-to-state transition rates (i.e., components of the W matrix in equation 2.20). Such effort can be diminished by introducing a list of transition events that remains fixed during the kMC run (i.e., a predefined catalog of events). Typically, any uncompetitive steps [220] that are unlikely to meaningfully propagate the system are excluded and solely rate-determining atomic scale mechanisms are considered in the predefined catalog of events. Nonetheless, the predefined catalog of events approximation necessitates the prior determination of the important transition mechanisms along with their corresponding rates for the studied system (obtained from laboratory studies or supplementary simulations). In such instances, the kMC schemes become semi-empirical in nature, since only a set of predefined elementary processes are simulated and no additional atomic-scale events are discovered during the course of the simulation [216, 221].

The number of elements included in the W matrix can be further reduced by the exploitation of any translational or rotational symmetries present in the underlying system. Specifically, in crystalline materials, the computational domain can be discretised to ensure that any species can occupy predefined lattice sites. Restricting atoms to specific spatial positions naturally diminishes the overall number of atomic-scale processes demanded to accurately describe the evolution of the system [222–224]. However, the lattice approximation introduces obstacles into the investigation of ordered materials. Simulation of amorphous materials through the kMC method requires an off-lattice scheme. Off-lattice kMC algorithms in the present literature commonly deploy an on-the-fly strategy to populate the transition frequency matrix (W) [225], [226, 227]. Effectively, at each time step, the configurational space in the vicinity of the current state is scanned, neighboring valleys on the PES are discovered, and the activation energies of transition events are calculated. Those

operations can be realised through the implementation of a minimum-mode following method (e.g., Activation Relaxation Technique nouveau [228] or the dimer method [229]). Another option is the use of high-temperature MD [230] followed by occasional quenching and ultimately application of the nudged elastic band method [231] to acquire the coordinates of the saddle point and the respective activation energies of transition events.

On-the-fly off-lattice models are analytic and capable of discovering elementary processes during the course of the simulation. Even so, those models are associated with a series of shortcomings. Firstly, on-the-fly schemes become numerically tractable only if they are coupled with a method dedicated to recycling atomic-scale processes throughout the course of the simulation [216]. In other words, transition events discovered at each time step should be identified and executed in subsequent time steps, without the need for additional searches on the PES. An on-the-fly model should also include an algorithm devoted to storing and managing arrays containing the rates (i.e., the on-the-fly catalog of rates) and the positions of atom(s) participating in any transition mechanism of the kMC run. Undoubtedly, the necessity for supplementary numerical schemes aimed at the storage, detection, and reuse of rates of elementary processes elevates the complexity associated with the practical implementation of on-the-fly off-lattice kMC methods.

Moreover, on-the-fly schemes discover transition mechanisms by identifying saddle points on the PES. Consequently, the modelling of systems that are dominated by transition events of elevated entropic contributions to the free energy is expected to result in inaccurate long-timescale properties [216]. Besides, certain atomic-scale processes involving the insertion of atoms (e.g., adsorption) cannot be directly described by interatomic potentials. On the other hand, the explicit description of reactions demands the use of numerically expensive interatomic potentials (e.g., ReaxFF [209]) or an implicit approach where bonded interactions are defined through cutoff distances between the bonded species [232].

Chapter 3

Off-lattice hybrid kMC/MD model for thin films from lubricant additives

3.1 Introduction

In Section 2.2.2, the theory of kMC was introduced. Then, in Section 2.2.2.2 we compared on-the-fly and predefined catalogue kMC schemes. In this chapter, we present a numerically efficient and easy-to-implement kMC/MD framework that unlocks the possibility for off-lattice simulations on amorphous systems involving different classes of atomistic processes. The applicability of the introduced methodology is examined through a benchmark application involving a non-crystalline system. Specifically, the thermal decomposition of lubricant additive TCP molecules on a Fe(110) surface and the subsequent growth of an amorphous polyphosphate film are simulated using our off-lattice kMC/MD model. The obtained results are compared with previous experiments as well as other simulation studies.

3.2 The proposed hybrid off-lattice kMC/MD framework with predefined transition events

To reduce the computational cost and lower the implementation complexity of typical off-lattice kMC methods based on on-the-fly approaches (see Section 2.2.2.2), we introduce an off-lattice framework featuring a list of transition events that remains fixed during the kMC run (i.e., a predefined catalog of events). As discussed in Section 2.1.2, previous off-lattice kMC schemes with a predefined catalog of events can solely describe reactions. Here, we propose an off-lattice kMC framework that extends the concept of the predefined table of events to complex materials science problems involving virtually any transition mechanism from adsorption/desorption and diffusion steps to complex reaction pathways.

Since atomic-scale events cannot be discovered during the kMC run, our methodology becomes less accurate and less analytic than conventional on-the-fly schemes. Furthermore, the applicability of the introduced model is subject to the availability of information linked to the rate-determining elementary events of the studied system. Specifically, the user must be capable of estimating the rates of different events prior to the initiation of a kMC run. Moreover, the implementation of our off-lattice scheme necessitates an explicit description of any alterations in the current atomic

configuration (e.g., addition, removal, or displacement of atoms, change in bonded interactions between species) as a consequence of a basin-to-basin transition.

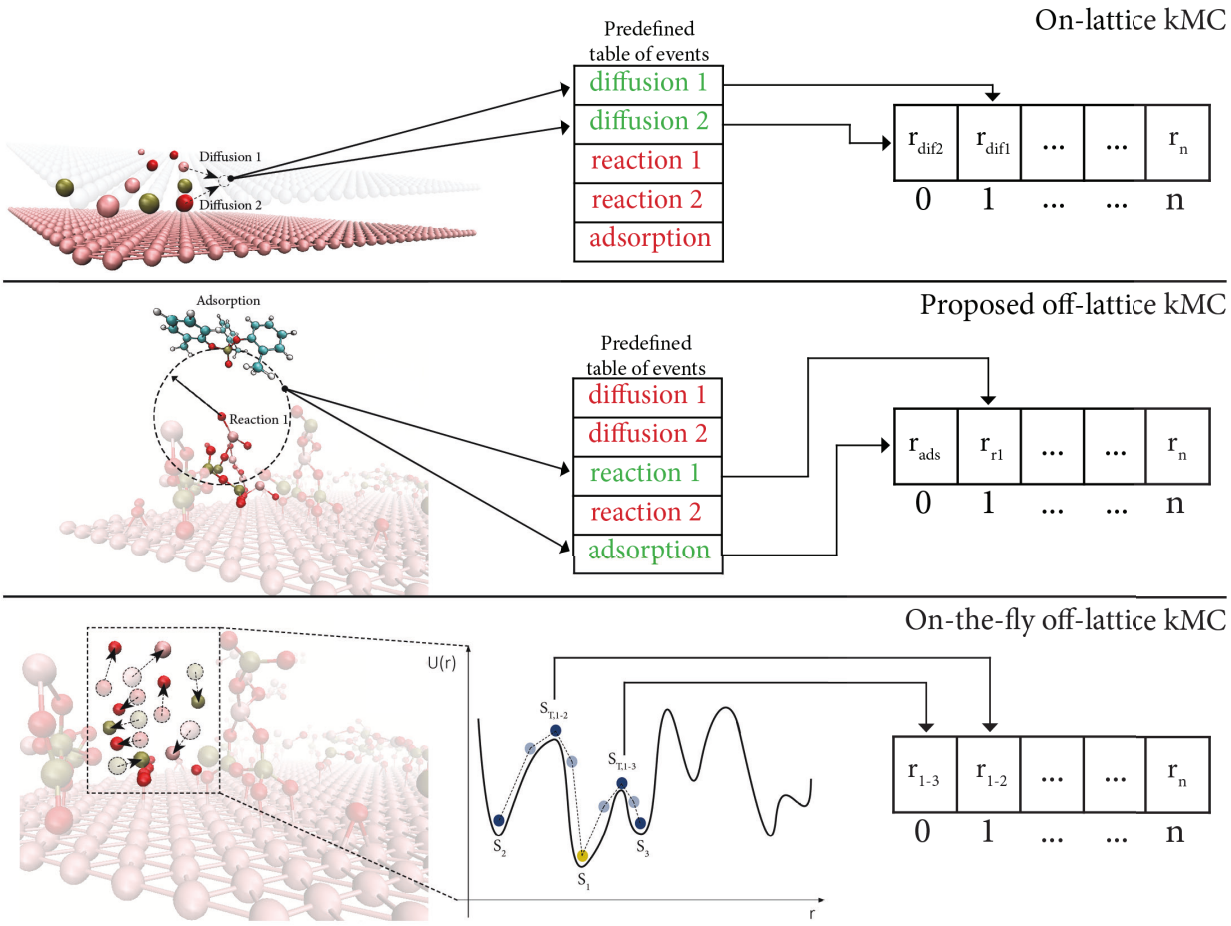


Fig. 3.1: Schematic comparison between on-lattice, proposed off-lattice with predefined table of rates, and on-the-fly off-lattice kMC schemes. *(Top)* Standard on-lattice approaches examine the feasibility of an event (contained in the predefined table of events) through mechanism searches centred on fixed lattice sites. The rates of detected transitions are then passed on to the kMC algorithm. *(Middle)* The introduced off-lattice methodology retains the predefined table of events philosophy but substitutes fixed lattice sites with mobile event sites attached to the system atoms. (Bottom) On-the-fly off-lattice approaches detect basin-to-basin transitions by causing a localised perturbation and then searching for adjacent minima (along with their corresponding transition states) on the PES. Reproduced under the CC BY NC ND 4.0 license from our published preprint on ChemRxiv [233].

In cases where the explicit *a priori* description of elementary processes is not possible, a bottom-up multi-scale approach has to be deployed and simulations on lower scales (e.g., MD, DFT, or even on-the-fly kMC [216]) have to be performed to populate the predefined table of events. Overall, our method sacrifices some of the accuracy and predictive power of on-the-fly approaches for the sake of significantly boosting the computational efficiency of the off-lattice kMC algorithm. Such sacrifice enables long-timescale off-lattice kMC runs with the ability to resolve various classes of elementary processes.

Our model assumes that the rates of elementary processes obey an Arrhenius-type equation (a common practice in kMC simulations [137]) of the following form:

$$r = \nu \, \exp\left(\frac{-\Delta E}{RT}\right) \tag{3.1}$$

Where r represents the event rate (in units of 1/s), ΔE is the activation energy, ν is the Arrhenius prefactor (attempt frequency), and R and T are the universal gas constant and system temperature, respectively. Then, a central model assumption is that system transition events can be grouped into families of mechanisms with identical activation energies (ΔE) and attempt frequencies (ν). For example, the family of decomposition reactions involving species A and B (i.e., AB→A+B) would be assigned with a unique set of ΔE and ν values. It is acknowledged that such modelling choice may result in the inaccurate estimation of mechanism rates since the ΔE and ν values could depend on variables such as the local atomic environment or the bonded interactions between species (e.g., bond length or angle). Regardless, the model accuracy can be elevated by deploying variable ΔE and ν as functions of critical parameters (e.g., distance from a catalyst or the substrate, bond length, bond angles). Obtaining such expressions for ΔE and ν typically requires supplementary simulations at smaller scales.

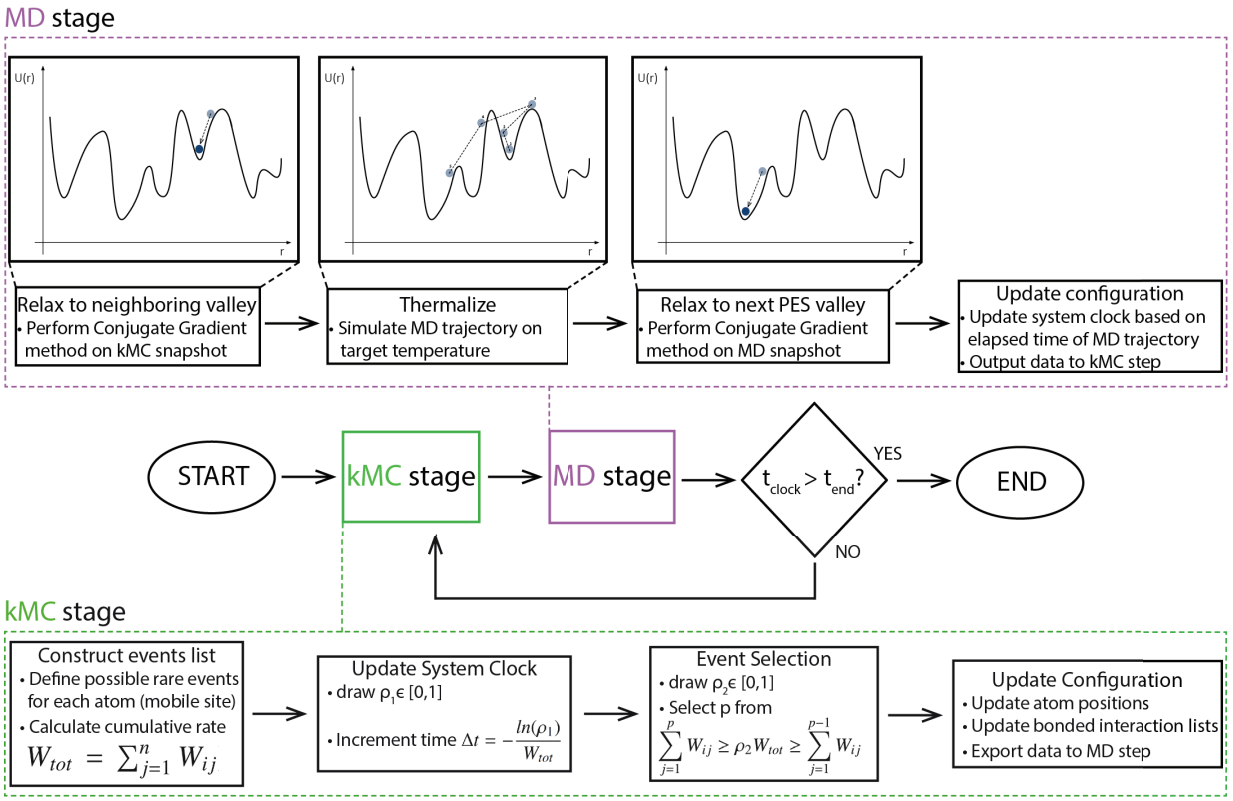


Fig. 3.2: Flowchart summarising the workflow of the proposed kMC/MD methodology.

The concept of an event site had to be revised to allow for off-lattice simulations with a predefined table of events. Effectively, the proposed kMC algorithm uses mobile instead of rigid event sites. In the introduced model, event sites are attached to and migrate with atoms throughout the course of the simulation. Specifically, at each time step, the local environment of every atom is scanned to assess the feasibility of user-defined atomic-scale mechanisms. This is equivalent to the event search in traditional on-lattice kMC algorithms with a predefined table of rates. The critical difference in our approach is associated with the fact that event searches are not performed on lattice sites but are centred around freely moving atoms in the 3D space. A schematic comparison between the conventional on-lattice kMC methods, proposed off-lattice kMC framework with a predefined table of events, and on-the-fly kMC implementations is provided in Fig. 3.1.

Furthermore, for the sake of simulating the realistic evolution of thin films, it becomes important to consider fast atomic-scale mechanisms (e.g., bond stretching, bond angle bending, reorientation of adsorbates, surface reconstructions, electrostatic or solvent/heat bath interactions [135, 234, 235]) typically manifesting in timescales between 10 and 100 fs (i.e., frequencies of 10^{13}-10^{14} Hz) [236]. However, directly inserting such fast processes into the predefined table of events is expected to hinder the kMC algorithm from accessing timescales beyond the limits of MD schemes, as trivial transitions would dominate over interesting rare mechanisms. This is justified by acknowledging that the rate and the selection probability of a kMC event are analogous (i.e., $p = \frac{W_{ij}}{W_{tot}}$ in Eq. 2.24) [173].

In this work, to account for rare events as well as explicitly simulate high-frequency (above 10^{12} Hz) elementary mechanisms, we couple our algorithm with an MD scheme. In essence, the kMC stage is deployed to execute rare transitions of high activation energies, while a short MD trajectory between the kMC steps is simulated to relax any residual atomic forces and analytically describe fast concerted moves. A complete schematic flowchart of the proposed hybrid kMC/MD methodology is provided in Fig. 3.2.

The introduced hybrid methodology begins with the kMC stage. Firstly, the feasibility of predefined events is assessed for every mobile event site (one for every system atom), and the global event matrix is assembled. Additionally, each element of the global event array is associated with the characteristic (for that family of mechanisms) activation energy (ΔE), attempt frequency (ν), and effective rate (calculated through Eq. 3.1). Once the global event matrix is assembled, the kMC algorithm is deployed to stochastically advance the simulation clock as well as select and execute an atomic-scale process [173]. Specifically, the time increment (Δt) is estimated as:

$$\Delta t = -\frac{\ln(\rho_1)}{W_{tot}} \tag{3.2}$$

where $\Delta t = t_{S_j} - t_{S_i}$, ρ_1 represents a uniformly distributed random number with $\rho_1 \in [0, 1]$, and W_{tot} describes the cumulative rate for the n possible escape processes from state S_i (i.e., $W_{tot} = \sum_{j=1}^{n} W_{ij}$). An atomic-scale process is selected, such as:

$$\sum_{j=1}^{p} W_{ij} \geq \rho_2 W_{tot} \geq \sum_{j=1}^{p-1} W_{ij} \tag{3.3}$$

where p is an integer corresponding to the selected transition mechanism (with a rate of W_{ip}) and ρ_2 is a second uniformly distributed number in the [0,1] interval. Finally, the position as well as bonded interaction lists of each atom are updated to reflect the changes as a result of the basin-to-basin transition.

The MD stage of the framework is initiated immediately after the kMC stage. Note that it is not necessary to deploy the MD stage after every kMC stage. For example, the user might choose to solely initiate an MD stage after 5 or 10 kMC stages. This boosts the computational efficiency of the methodology at the expense of model accuracy. In any case, the MD part of the framework begins by implementing the conjugate gradient (CG) method [237] on the current configuration (output of the kMC method). Applying the CG method is critical for the sake of relaxing any residual forces between atoms. Such forces can become significant since our off-lattice implementation permits atoms to freely move in the 3D space. Effectively, this might lead to

short interatomic distances, which in turn can result in numerical instabilities in the MD stage. Also, the equilibration of the remaining interatomic forces and the stability offered by the CG method allow the utilisation of larger time steps in the MD algorithm. Of course, this increases the computational efficiency as well as enhances the time-advancing capabilities of the introduced methodology.

After the relaxation of residual forces, a short MD trajectory is simulated. Since the number of particles is conserved during the MD stage, the user is given the freedom to select from a wide range of ensembles (e.g., microcanonical, canonical, isoenthalpic-isobaric, or isothermal-isobaric) that appropriately fit the application of interest. The overall duration of the MD trajectory is also user-selected and depends on the studied system. Typically, a trajectory of a few hundred or thousand fs (approximately $10^{-13} - 10^{-12}$ s) is sufficient to capture fast elementary events of frequencies in the order of 10^{12} Hz and above. Moreover, the deployed interatomic potential should be chosen by the user. It is advised to deploy numerically inexpensive interatomic expressions (e.g., the 12-6 LJ potential [205]). Such a choice ensures that the MD stage is numerically efficient and means that the proposed hybrid kMC/MD framework remains computationally tractable. Of course, the selected interatomic potential should accurately describe the physics of any fast elementary processes simulated through the MD stage.

Following the simulation of the short MD trajectory, the configuration is relaxed to the nearest PES valley using the CG method. This instance removes the residual forces induced by the MD trajectory and prepares the system for the next kMC basin-to-basin transition. The hybrid algorithm terminates once the user-defined simulation ending time (t_{end}) is reached.

The next section is devoted to a benchmark application. The benchmark application section showcases how the proposed hybrid kMC/MD framework can be implemented to investigate the polyphosphate film growth from the thermal decomposition of TCP molecules on an iron surface.

3.3 A benchmark application: Polyphosphate film growth from the thermal decomposition of TCP molecules on a Fe(110) substrate.

3.3.1 Background

The present work focuses on the investigation of thin films generated from the thermal decomposition of TCP molecules on pure iron surfaces. Such a system is considered an appropriate benchmark application for our introduced hybrid kMC/MD methodology since it has been thoroughly investigated both experimentally [67, 77–79] and computationally [91, 120]. Furthermore, the thermal decomposition pathway can evolve without activation from pressure or frictional sliding and the presence of acids, H_2O molecules. The aforementioned factors simplify the modelling of surface interactions, which renders the thermal decomposition mechanism ideal for benchmarking.

A detailed literature review regarding the TCP decomposition mechanisms is provided in Chapter 2.1 (Section 2.1.1.3). Nonetheless, a clear lack of understanding is identified when it comes to the link between elementary events and macroscopic properties of thermally decomposed TCP films. This is justified by the fact that such protective films require seconds, minutes, or hours to grow and form [89]. Experimental methods and models of the continuum are capable of reaching

the relevant timescales but typically lack the ability to precisely resolve atomic-scale processes. On the other hand, numerical schemes of molecular-level accuracy (e.g., MD or DFT) are usually incapable of simulating timescales beyond the microsecond (10^{-6} s) limit. Ultimately, our proposed hybrid kMC/MD methodology promises to shed light on the effect of elementary transitions on the macroscopic morphological (e.g., RMS roughness, fractal dimension) as well as chemical/structural (e.g., RDFs, species distribution) characteristics of the polyphosphate films by the thermal decomposition of TCP molecules.

The following sections provide an overview of the important modelling details of the introduced hybrid methodology. The specifics of the MD stage of the hybrid framework are outlined in Section 3.3.3. Section 3.3.4 describes the methods used to simulate the relevant atomistic events (adsorption, bond breaking/formation, and diffusion) within the kMC stage of the newly proposed hybrid kMC/MD framework. Specifically, a brief discussion is featured related to (a) the algorithms implemented for the sake of adding/removing, updating the positions/velocities/charges/bonded interaction lists of atoms as well as (b) the numerical procedures and assumptions involved in the calculation of the rates of the different classes of basin-to-basin transitions. Finally, Section 3.3.5 outlines the post-processing methods, Section 3.3.6 discusses the computational efficiency of the methodology, and Section 3.3.7 presents the obtained results.

3.3.2 Overview of modelling details

This work focuses on the study of thermally decomposed mmm-TCP molecules. The system temperature is set at $T = 528.15K$. Such a temperature value exceeds the boiling point of mmm-TCP at 101.325 kPa. An adsorbate partial pressure (P in equation 3.8) of 0.01 kPa is used to estimate the deposition rate of mmm-TCP molecules on the iron substrate (see Section 3.3.4 for additional details). Such a partial pressure value was selected to simulate the vacuum conditions present in VPL. Generally, the mmm-TCP molecules interact with the underlying Fe(110)/film surface through a solid/gas interface. Four individual hybrid kMC/MD runs are performed in the direction of producing ensemble statistics.

The present study is performed on a 3-layered $\alpha - Fe(110)$ substrate. A lattice constant of 2.866 Å is used, as reported in the pseudopotential plane-wave study of Milman et al. [238]. The length and width of the substrate are $L_x = 59.39$Å and $L_y = 62.20$Å, respectively. Prior to the beginning of the kMC/MD simulation, the CG method is deployed together with the DREIDING [206] force field to relax the residual forces of the generated surface. Following the removal of remaining stresses, the substrate is frozen. This reduces the computational cost of the MD stage within the hybrid framework, albeit at the expense of capturing detailed near-surface Fe–TCP interactions. Overall, the substrate atoms are fixed in space but are allowed to interact (through the DREIDING force field) with each other as well as with other atoms of the growing film. Moreover, the fixed surface atoms are active event sites in the kMC stage (i.e. local environment searches are conducted on substrate atoms to assess the feasibility of atomic-scale processes). Finally, a short MD trajectory of 10 ps is simulated to equilibrate surface charges via the QEq method (see Sections 2.2.1.3 and 3.3.3 for details on the QEq method and the MD setup).

The kMC stage of the hybrid kMC/MD methodology is realised through an in-house code written in Fortran95. On the other hand, the MD stage is implemented in LAMMPS [26], which is written in C/C++. Overall, an MD stage is simulated every 9 kMC stages (i.e., a block of

kMC/MD steps comprises 9 kMC stages and 1 MD stage).

3.3.3 Details of the MD stage

The MD stage (realised in LAMMPS) uses the DREIDING [206] force field, which was also utilised in a previous study of Mosey et al. [239] on phosphate-containing species. The LAMMPS Data-File generator (a nanoHUB tool [240]) is deployed to generate the force field coefficients and the bonded interaction parameters of the Fe/mmm-TCP system. The Lorentz-Barthelot mixing rules are used to evaluate the cross terms of the DREIDING force field. The cutoff distance for non-bonded interactions (d_{cut}) is fixed at 12 Å. The time step of the MD stage is set at 1 fs ($10^{-15}s$). The velocity-Verlet [203] algorithm is applied to integrate the equations of motion. The QEq method [207] (briefly discussed in section 2.2.1.3) is utilised to equilibrate the atomic charges at every time step. The relevant QEq method parameters (χ and η) are extracted from the ReaxFF coefficients of Khajeh et al. [121]. Note that, in this example, the QEq method is preferred over static Coulombic charges to better account for the dynamic nature of the simulations, which involve the addition and removal of atoms and molecules during kMC stages [207].

Additional harmonic bond angle rules are implemented to capture the bond-bending interactions of polyphosphate chains within the growing film. Particularly, a harmonic bond angle rule is applied to the P-O-P and O-P-O pairs. The corresponding spring constant (K) and equilibrium angle (θ_0) values for the P-O-P and O-P-O are $K^{POP} = 88.03$ kcal/mol, $\theta_0^{POP} = 141.179°$ and K^{OPO}=38.72 kcal/mol, $\theta_0^{OPO} = 109.470°$, respectively (as obtained from Di Tomasso et al. [241]). The length and width of the simulation box are identical to those of the generated Fe(110) substrate ($L_x = 58.39$Å and $L_y = 61.20$Å as given in Section 3.3.2). The height of the simulation box is a function of the film height and is defined as $L_z = h + 70$Å. Note that the instantaneous film height (h) is defined as a line parallel to the xy plane and below which 50% of the film's total density is contained. Periodic boundary conditions (PBCs) are applied in the x- and y-directions. A reflective boundary is utilised at a variable distance of $d_{zR} = h + 26$Å on the xy-plane to prevent atoms from escaping the simulation box.

The complete general flowchart of the MD stage is presented in Section 3.2 (flowchart 3.2). To summarise, the MD stage begins with a relaxation step (using the CG method), followed by a thermalisation step, and ends with an additional relaxation step on the final snapshot of the thermalised configuration. The thermalisation step of the MD stage consists of two parts. Both parts generate trajectories from the NVT ensemble and deploy the Nosé–Hoover [242, 243] thermostat with a damping parameter of 100 fs. For the first thermalisation step, the temperature is linearly ramped from 400K to 528.15K (the target temperature) over 600 fs. This ensures that the system is equilibrated at the target temperature and eliminates instabilities due to the addition/removal of atoms in the kMC stage (i.e., through adsorption, bond breaking, and diffusion events). In a second thermalisation step, the temperature is maintained at 528.15 K for a total duration of 600 fs. The overall trajectory duration of the MD stage is 1200 fs.

3.3.4 Details of the predefined events of the kMC stage

This section provides information related to the calculation of rates as well as the execution of kMC events. In the context of our benchmark application, we manually design the predefined catalog

of events. The design is based on remarks made on the growth of TCP films in the relevant literature. As discussed in Section 3.3.1, the thermal decomposition of TCP molecules on ferrous surfaces evolves through the following elementary processes: (a) adsorption of TCP molecules, (b) cleavage of the P-O and C-O bonds of TCP molecules, (c) P-O and Fe-O bond formation within the growing film, and (d) diffusion of Fe species from the underlying surface and through the developing coating. Consequently, the aforementioned atomistic processes are modelled within the kMC stage of our methodology and included in the fixed table of events. Note that the predefined table does not include the reverse process of every kMC event. This implies that the principle of detailed balance is not obeyed [215]. Hence, the benchmark application refers to a non-equilibrium system, and the hybrid kMC/MD simulations are exclusively deployed to describe the dynamic behaviour, rather than sample the equilibrium properties of the thin film [244].

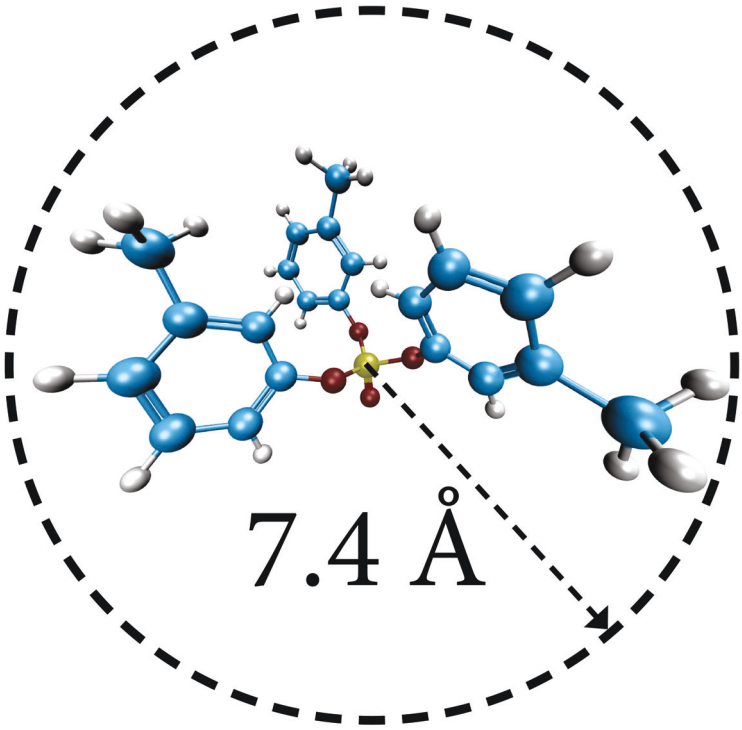


Fig. 3.3: Adsorption radius (r_{mol} in Eq. 3.5) for mmm-TCP.

The simulation of the adsorption event of the kMC stage requires the identification of surface atoms. The z-coordinate of any surface atom obeys the following inequality:

$$|z_j - h| \leq r_{ads} \tag{3.4}$$

Where h is the current film height and r_{ads} is the nominal adsorption radius:

$$r_{ads} = r_{w,j} + r_{mol} \tag{3.5}$$

Here, $r_{w,k}$ represents the van der Waals radius of the j^{th} system atom. In the present work, the respective r_w values are evaluated from the following equation:

$$r_w = 0.5\sigma_{j,j} \tag{3.6}$$

With $\sigma_{j,j}$ being a coefficient of the DREIDING force field. Moreover, the molecule radius r_{mol} is a hardcoded user parameter quantifying the size of the adsorbate. Specifically, r_{mol} is the radius

of the smallest sphere capable of covering the entire molecule and is located at the centre of mass of the adsorbate. The r_{mol} value for the mmm-TCP molecule used in this study was set at 7.4 Å (see Fig. 3.3).

Surface atoms act as parent atoms for kMC adsorption events. In detail, a homogeneous 20-point spherical grid of radius $r_{ads} = r_{w,j} + r_{mol}$ is generated around every surface atom. Here, the nominal deposition radius (r_{ads}) is deployed to guarantee that the distance between the parent atom and the adsorption site (i.e., the grid point) is sufficiently large to not only accommodate an adsorbate (because $r_{ads} > r_{mol}$) but also to prevent numerical instabilities (since $r_{ads} > r_{w,j}$). Following the grid generation, an mmm-TCP molecule is temporarily inserted into the system for the sake of performing a deposition test and ultimately assessing whether the generated grid point qualifies as a valid candidate adsorption site. The centre of mass of the tested adsorbate is coincident with the generated grid point coordinates. Also, the temporarily inserted adsorbate is oriented such that the centerline of the phosphorus-oxygen double bond of the mmm-TCP is perpendicular to the underlying Fe(110) substrate. The tested molecule is given this particular orientation to ensure that the doubly bonded oxygen atom of the mmm-TCP is the species that eventually physisorbs on the underlying substrate/film surface, as suggested in previous studies (experimental and computational) on the thermal decomposition of TCP molecules on ferrous substrate (discussed in Section 3.3.1).

Note that it is advised to relax the mmm-TCP molecule prior to the initiation of the proposed kMC/MD algorithm to ensure that any residual intermolecular forces are removed. This usually reduces the numerical effort of the MD stage of the hybrid methodology and guarantees that spurious motions due to local fluctuation of the potential energy are eliminated. In the present work, the CG algorithm is deployed (in vacuum) to the spatial atomic coordinates of the adsorbate, using an identical (DREIDING) force field as the one deployed in the MD stage of the kMC/MD methodology (specific details are given in Section 3.3.3). The PACKMOL [245] software is deployed to translate the relaxed local atomic coordinates of mmm-TCP to the global system coordinates and provide the adsorbate with the preferred orientation (i.e., P=O bond centerline perpendicular to the substrate) during the adsorption tests of the kMC stage.

Overall, a grid point qualifies as a valid candidate adsorption site if and only if none of the atoms of the temporarily inserted mmm-TCP molecule overlaps with existing system atoms. It is assumed that an overlap occurs when:

$$d_{j,k} \leq \sigma_{j,k} \tag{3.7}$$

With $d_{j,k}$ being the interatomic distance between an atom j on the substrate/film and an atom k of the tested adsorbate. The DREIDING force field parameter $\sigma_{j,k}$ corresponds to the j^{th} substrate/film atom and the k^{th} tested adsorbate atom. The above criterion (Eq. 3.7) is imposed to filter and reject adsorption events that may lead to interatomic distances capable of causing instabilities and crashes in the MD stage of the proposed hybrid kMC/MD framework.

Each detected overlap-free grid point corresponds to a valid kMC adsorption event. The kMC rates of such adsorption events are calculated from the kinetic theory of gases. Particularly, the Hertz-Knudsen equation is used [246]:

$$r_{ads} = \frac{\sigma(\theta, T) P A}{\sqrt{2\pi m k_b T}} \tag{3.8}$$

Where r_{ads} is the rate (units of $[T]^{-1}$) of a single adsorption event. Moreover, k_b and T are the Boltzmann constant and system temperature, respectively, m is the molecular weight of the adsorbate (m=368.37 g/mol for mmm-TCP), and P is the partial pressure of the adsorbate.

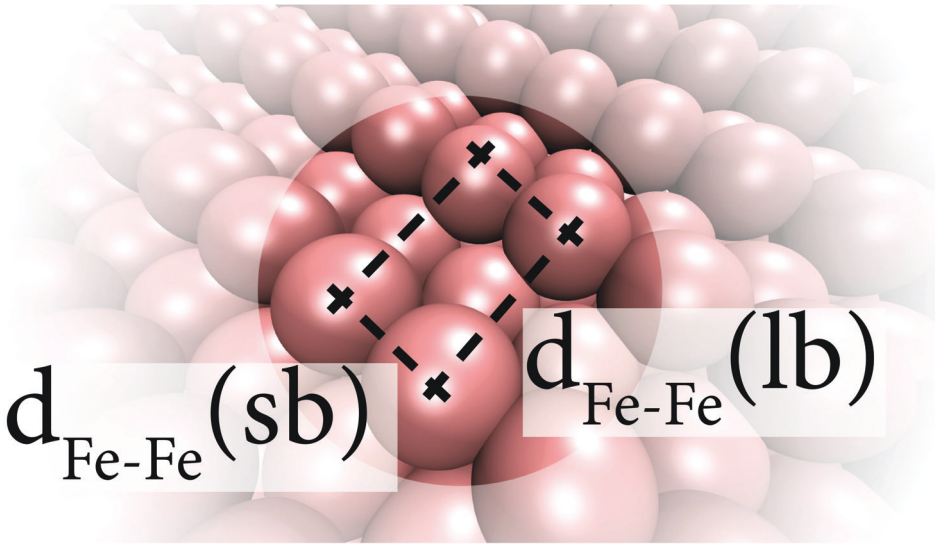


Fig. 3.4: Three-layered Fe(110) substrate used in the current study and long bridge adsorption site dimensions ($d_{Fe-Fe}(sb) = 2.488$Å and $d_{Fe-Fe}(lb) = 3.071$ Å) values obtained from Xu et al. [247].

Our model assumes that all adsorption sites are identical. The area A of each adsorption site is fixed at 7.648 Å^2. Such value corresponds to the area of a parallelepiped of base $d_{Fe-Fe}(sb) = 2.488$Å and height $d_{Fe-Fe}(lb) = 3.071$Å that encompasses the long bridge (lb) adsorption site of an oxygen atom on a Fe(110) surface. As discussed in Section 3.3.1, the double-bonded oxygen atom is the adsorbing species in the initial stages of the thermal decomposition of TCP molecules on ferrous substrates. The Fe-Fe distances $d_{Fe-Fe}(sb)$ and $d_{Fe-Fe}(lb)$ along the short bridge and long bridge directions, respectively (as depicted in Fig. 3.4), used for the estimation of the parallelepiped surface area, were retrieved from the DFT study of Xu et al. [247].

Different works suggest that adsorbed oxygen atoms preferentially occupy the long bridge sites at oxygen surface coverage of about 0.25 monolayer (ML) [247–249]. Nonetheless, it is acknowledged that the use of a non-variable surface area in Eq. 3.8 may lead to inaccuracies when it comes to the estimation of the adsorption rate due to the following considerations. Firstly, the preferred adsorption site (e.g., long bridge, short bridge, pseudo threefold hollow) for oxygen species on Fe(110) depends on the surface coverage [250]. Therefore, the adsorption surface area also becomes a function of the surface coverage. Secondly, the energetically favourable adsorption site may differ for the cases of atomic oxygen adsorption and adsorption of double-bonded oxygen species of mmm-TCP molecules.

The sticking coefficient ($\sigma(\theta, T)$ in Eq. 3.8) is a function of both the fraction of occupied adsorption sites (θ) and the system temperature. In the absence of an analytic expression for $\sigma(\theta, T)$ we approximate the sticking coefficient as:

$$\sigma(\theta, T) = \sigma_0(1 - \theta) \tag{3.9}$$

With σ_0 being the initial sticking coefficient. Of course, $\sigma_0 = 1$ since all surface sites are unoccupied at the beginning of the simulation. The fractional coverage (θ) at a given time step is estimated

by dividing the number of overlapping grid points (adsorption sites which do not obey Eq. 3.7) by the total number of grid points (i.e., 20 per surface atom).

Overall, each valid adsorption event is associated with an overlap-free mmm-TCP molecule as well as with a corresponding adsorption rate. A flowchart summarising the steps involved in the identification of adsorption events is illustrated in Fig. 3.5. The introduced mmm-TCP molecules are given a bias velocity of -0.02 Å/fs in the z-direction to ensure that the added adsorbates move toward the growing film. Finally, the initial charges of the inserted atoms are set to zero. The charges are updated in the next MD stage of the hybrid kMC/MD framework using the QEq method.

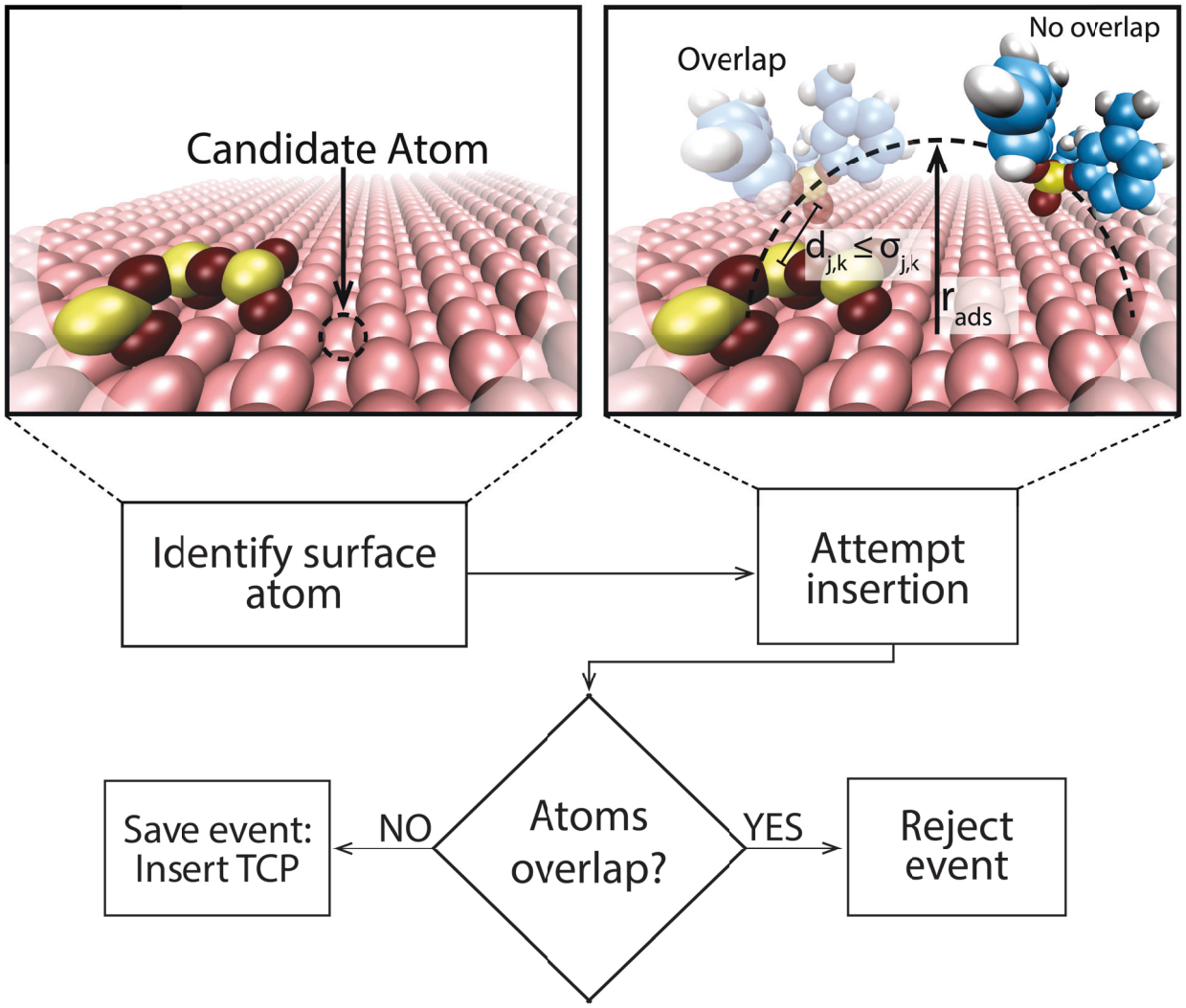


Fig. 3.5: Flowchart of an adsorption event.

Additionally, the kMC stage captures bond dissociation events between P-O and C-O pairs of mmm-TCP molecules. The flowchart of Fig. 3.6 provides a graphical representation of the workflow linked to the simulation of a P-O bond dissociation event. The specific steps involved in the simulation of the P-O bond-breaking event are different, depending on whether a C-O cleavage has already occurred on the same branch of the adsorbed mmm-TCP. If no prior C-O scission took place on the same mmm-TCP branch, then the P-O bond dissociation event produces a dehydrogenated cresol fragment (as seen in Fig. 3.6.b). Alternatively, the P-O scission event

releases a lone oxygen in the system.

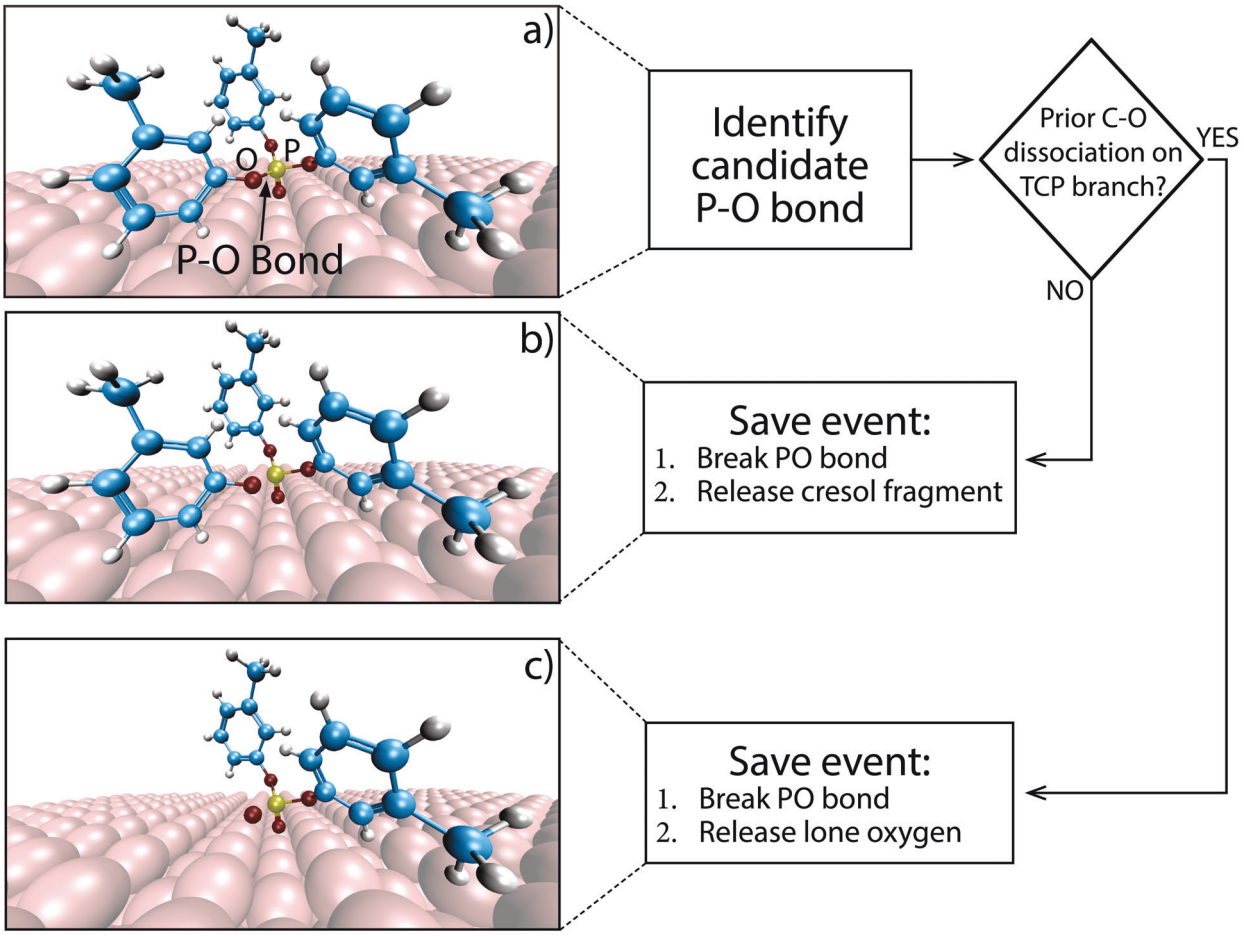


Fig. 3.6: Flowchart of the P-O bond breaking event.

Fig. 3.7 summarises the steps associated with the modelling of the C-O bond dissociation event. Cleaved C-O bonds of dehydrogenated cresol fragments (resulting from previous P-O scission events) produce lone oxygens (see Fig. 3.7.b). In this case, the remaining m-tolyl group is assumed to desorb and gets deleted from the system. It is acknowledged that this approximation can lead to inaccuracies regarding the elemental composition of the growing film since certain carbon species can adsorb on the underlying substrate/film system (instead of desorbing). Nonetheless, the approximation above is implemented for a couple of reasons. Firstly, it guarantees the growth of pure iron polyphosphate films, which can be viewed as the central focus of the present benchmark application. Secondly, it reduces the total number of atoms in the system and therefore enhances the computational efficiency of the introduced kMC/MD framework. The C-O scission event linked to m-tolyl groups attached to adsorbed mmm-TCP molecules (as observed in Fig. 3.7.c) results in an oxygen radical as well as an m-tolyl group. Once again, the m-tolyl group is removed from the system, for identical reasons to the case of the dehydrogenated cresol fragment.

The activation energies and attempt frequencies of the P-O and C-O bond dissociation events are not available in the literature. Therefore, supplementary ReaxFF/MD simulations (in LAMMPS [26]) are conducted prior to the hybrid kMC/MD runs, to capture the relevant ΔE and ν values of the bond-breaking events. The reaxFF MD setup deployed to evaluate the activation energies and attempt frequencies of the bond-breaking events is almost identical to that used in the work

of Ewen et al. [120] on the thermal decomposition of aryl phosphates on ferrous surfaces. The differences between the MD configuration of the current work and that of Ewen et al. are associated with the total duration of the production runs and the investigated temperature range. Specifically, in this work, simulations are conducted for $T \in [1100, 1600]K$ and up to $t_{end} = 1ns$. The following paragraphs provide an overview of the critical modelling parameters of the preliminary MD simulations. For further information, the reader is advised to consult the original work of Ewen et al. [120].

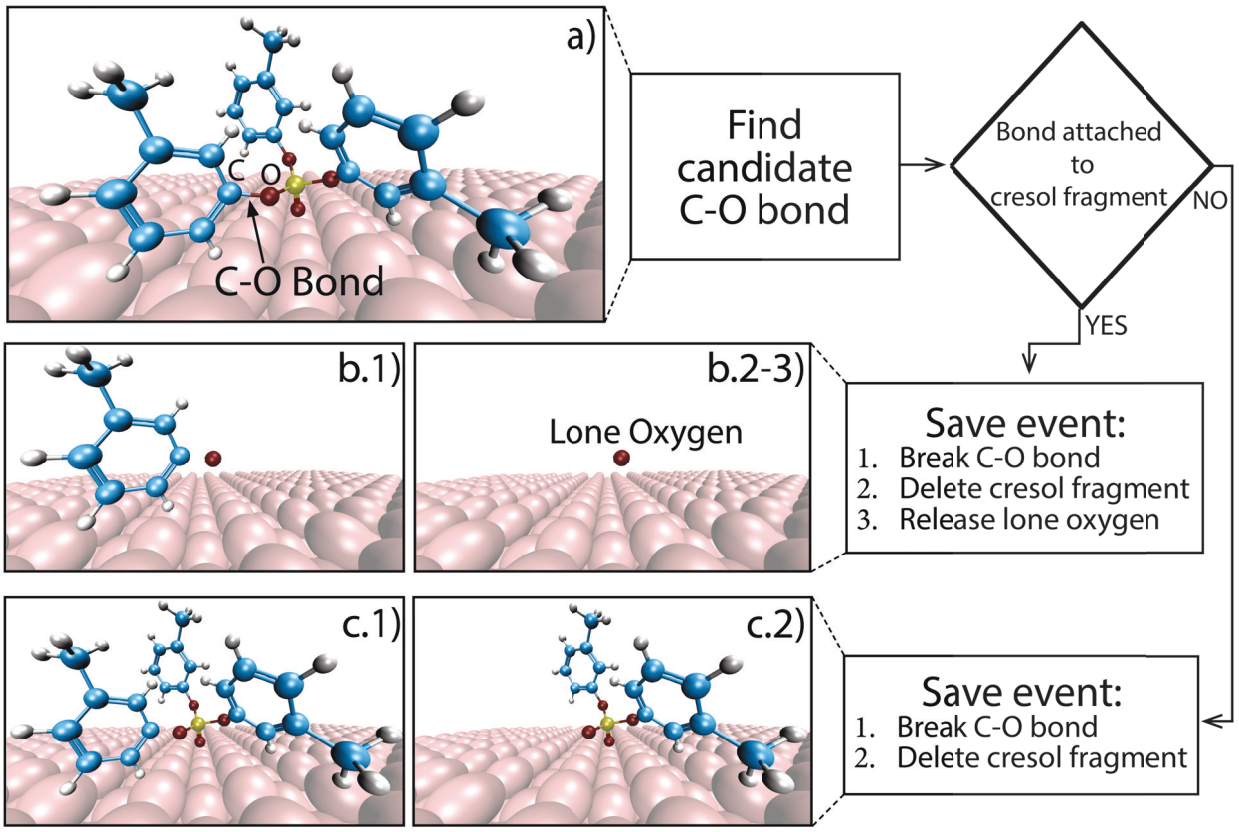


Fig. 3.7: Flowchart of the C-O bond breaking event.

The initial configuration of the system features 16 mmm-TCP molecules, placed at a distance of 3 Å above the surface of the Fe(110) substrate. The dimensions of the substrate along the x-, y-, and z-directions are 50 Å, 50 Å, and 15 Å, respectively. PBCs are used on the x- as well as y-directions, and a reflective wall is placed at a distance of z = 50 Å (on the xy-plane). The bottom layer of atoms is fixed during the simulation. The velocity-Verlet [203] integration scheme is utilised with a time step of 0.25 fs, and the Nosé–Hoover thermostat is used to control the temperature of the system atoms [242, 243] with a damping parameter of 25 fs. The MD simulations in this study use the ReaxFF interatomic potential introduced by Chenoweth et al. [251]. This bond-order potential is capable of capturing bond formation and dissociation events during the course of the MD run. The force field parameters (for the C/H/O/Fe/P interactions) are taken from Khajeh et al. [121].

The reduction in the number of P-O and C-O bonds is monitored throughout the MD production run (for $t \in [t_{start}, t_{end}]$, with $t_{start} = 0$ and $t_{end} = 1ns$). The P-O and C-O bond cleavage rates (r_{ReaxFF}) of each production run are evaluated from the following equation, which is used in other ReaxFF studies of organic species (e.g., Chen et al.[210], Si et al. [211]).

$$r_{ReaxFF} = \frac{\ln N_0 - \ln N_{teq}}{t_{eq}} \tag{3.10}$$

Where N_0 and N_{eq} are the initial and equilibrium number of bonds, and t_{eq} represents the time required for the number of bonds to reach a stable (equilibrium) value. Three independent MD runs at each investigated temperature ($T \in [1100, 1600]$ in steps of 100) are utilised to produce ensemble statistics.

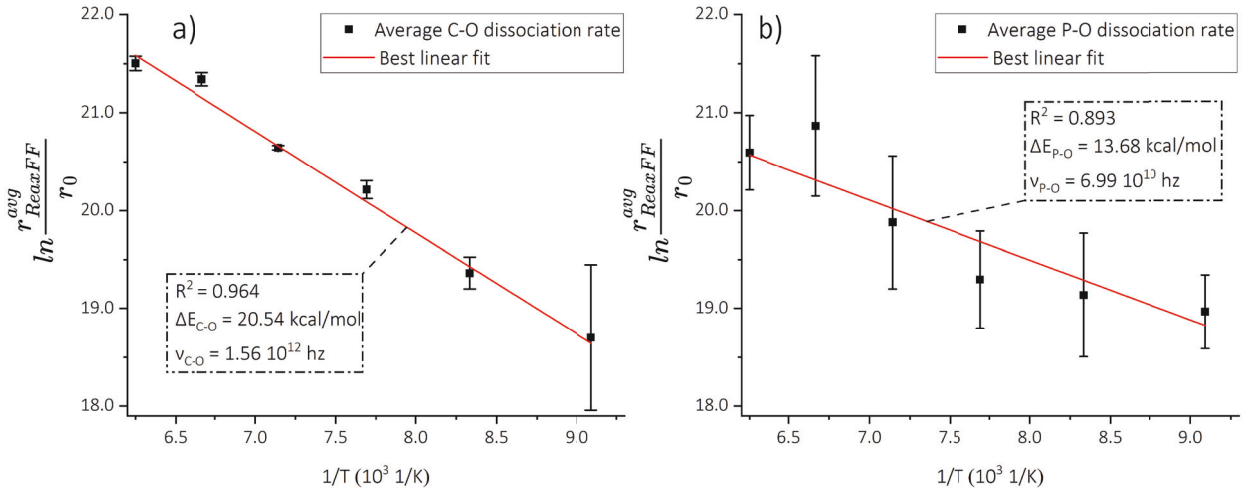


Fig. 3.8: Natural logarithm of rate versus the inverse of temperature for the C-O (a) and P-O (b) dissociation events. The activation energies and attempt frequencies can be extracted from the slope and the intercept of the best linear fit.

Fig. 3.8 shows the results of the MD simulations. Here, the natural logarithm of the bond dissociation rate is plotted against the inverse of temperature (1/T). Each plotted point represents the average rate ($\ln \frac{r^{avg}_{ReaxFF}}{r_0}$) value of the three production runs at a specific target temperature. Also, $r_0 = 1s^{-1}$ is introduced to ensure that the exponentials and logarithms are non-dimensional. The vertical bars represent the standard deviation (STD) of the three runs. Note that the STDs linked to P-O events are elevated compared to those of C-O events. Such a higher statistical variability indicates that the energetics of the P-O bond-breaking events are more sensitive to changes in the local atomic environment. For example, the activation energy for a P-O cleavage event might be altered by the orientation of the dissociating TCP molecule or the presence of neighbouring iron atoms. The above can influence the kinetics of dissociation events and lead to rate variability among the different ReaxFF runs, as demonstrated by the elevated errors in graph 3.8.b).

The activation energies and attempt frequencies linked to the P-O and C-O cleavage event are estimated from the slope and the intercept of the best linear fit applied to the relevant $\ln \frac{r^{avg}_{ReaxFF}}{r_0}$ versus 1/T data. Specifically, the activation energy is evaluated as ΔE = -Ra, with R and a being the universal gas constant and the slope of the best linear fit, respectively. On the other hand, the attempt frequency is evaluated as $\nu = e^b r_0$, where b is the intercept of the best linear fit. These expressions can be derived by equating the best linear fit equations associated with the $\ln \frac{r^{avg}_{ReaxFF}}{r_0}$ versus 1/T graphs (Fig. 3.8) to the Arrhenius equation (see Section 4.2.5 and Eq. 4.4).

The obtained activation energies and attempt frequencies of the P-O and C-O bond-breaking reactions are ΔE_{P-O} = 13.68 kcal/mol, ν_{P-O} = 6.99 10^{10} Hz and ΔE_{C-O} = 20.54 kcal/mol, ν_{C-O} = 1.56 10^{12} Hz for P-O and C-O, respectively. The rate of a kMC transition through a bond

dissociation event (i.e., $r_{scission}$) at a specific temperature can be estimated using the relevant ΔE and ν values in Eq. 3.1. Note that the estimated ΔE, ν, and consequently rate values correspond to the catalysed (by the Fe surface) P-O and C-O dissociation events. In this work, solely catalysed bonds are allowed to break. System bonds are classified as catalysed if the neighbour lists of the relevant bonded atoms include at least one Fe species.

It is acknowledged that a ReaxFF MD analysis is not as accurate as first-principles methods (e.g., DFT with the nudged elastic band [231] or the Activation Relaxation Technique [228]). Nonetheless, utilising a ReaxFF/MD approach to characterise the C-O and P-O bond-breaking energetics aligns with the overall philosophy of the proposed hybrid kMC/MD framework, which approximates kMC events as mechanism families of identical ΔE as well as ν values (as discussed in Section 3.2). Specifically, the ΔE and ν values obtained from ReaxFF/MD can be viewed as average values that summarise the effects of varying bond lengths, angles, and distances from the substrate as well as the local environment of atoms associated with the cleavage event.

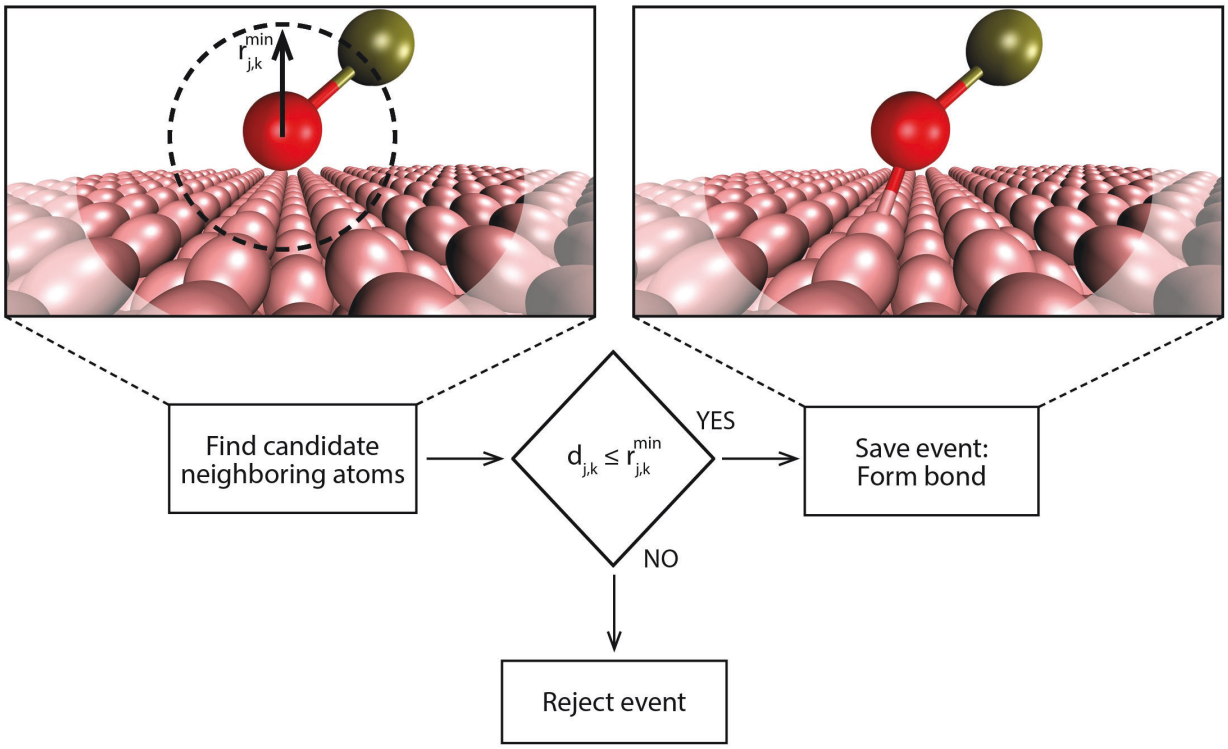


Fig. 3.9: Flowchart of a bond formation event adapted from our preprint on the hybrid kMC/MD method [233].

Furthermore, the kMC stage simulates bond-formation events within the growing film. Particularly, Fe-O, P-O, and O-O pairs whose distances obey the following inequality are associated with potential bond formation events:

$$d_{j,k} \leq r_{j,k}^{min} \tag{3.11}$$

Here, $r_{j,k}^{min}$ represents the interatomic distance which minimises the potential energy of the diatomic system of atoms j and k. Since the DREIDING force field uses a 12-6 LJ expression to model non-bonded interactions, the $r_{j,k}^{min}$ value is defined as $r_{j,k}^{min} = r_{j,k}^{min,LJ} = 2^{1/6}\sigma_{j,k}$. The DREIDING force field parameter $\sigma_{j,k}$ is associated with the j^{th} and k^{th} atoms. A summary of the bond formation

event is illustrated in Fig. 3.9.

As far as the O-O bond formation events are concerned, the paired lone oxygens (originating from prior C-O or P-O bond dissociation events) are assumed to volatilize and are removed from the system. P-O-P or O-P-O bond angles (as described in Section 3.3.3) are added to the system following certain P-O bond formation events. This occurs when a phosphorus or oxygen atom bonds to an existing P-O pair. To prevent clustering within the growing film (due to excessive bonding), the maximum number of formed bonds of each species is regulated. Particularly, phosphorus, oxygen, and iron atoms are allowed to form a total of 4, 2, and 6 bonds, respectively. Such criteria ensure that the formation of PO_4 as well as FeO_6 polyhedra within the growing film remains possible. Note that the PO_4 and FeO_6 structures are typically present in iron-phosphate glasses [252].

Radical species formed from C-O as well as P-O cleavage events are considered to be highly reactive. Therefore, in the present work, bond formation steps are modelled as spontaneous. Effectively, it is assumed that the rates of bond formation events in the growing film are by orders of magnitude faster than the rest of the simulated kMC events (i.e., adsorption, bond dissociation, diffusion). In detail, the activation energy of bond formation events is set to zero [98] and an attempt frequency of $\nu_{bond} = 10^{13}$Hz is used. This results in a bond-formation base rate of $r_{bond} = 10^{13}$Hz (though Eq. 3.1) at any given temperature. It is acknowledged that the barrierless bond formation approximation can lead to an overestimation of the growth rate of the thermally grown polyphosphate film. Regardless, the aforementioned assumption serves as a reasonable first-order approximation in the context of the proof-of-concept application for our proposed kMC/MD methodology.

Also, the kMC stage captures the diffusion of substrate Fe species towards the growing film. Simulation of the diffusion event necessitates the identification of vacant sites at each time step. Vacant sites are modelled as vacuum regions between four or more PO_4 tetrahedra. Such modelling choice can be justified by acknowledging that the Fe species of optimised iron-phosphate clusters typically occupy polyhedral sites surrounded by PO4 structures. The geometrical features of amorphous iron-phosphate glasses are discussed in the DFT/Raman spectroscopy study of Stoch et al. [252].

The kMC stage of the introduced methodology identifies vacant sites as follows. Firstly, the neighbour lists of surface iron species are scanned for the sake of identifying the nearest phosphorus atoms. Then, the bond lists of neighbouring atoms are utilised to assess whether the phosphorus atoms are bonded to four oxygen atoms. Essentially, this guarantees that a PO_4 tetrahedron exists in the neighbourhood of a substrate atom. If four or more PO_4 structures are detected in the vicinity of a surface iron, an algorithm performing insertion tests is deployed. Such an algorithm is similar to that implemented for the adsorption event. In essence, a 20-point spherical grid is generated around a Fe atom and test iron atoms are placed on the respective grid points. The spherical grid is centred on the parent iron atom with a radius equal to the minimum radius corresponding to a Fe-Fe pair (r^{min}_{Fe-Fe} as defined in Eq. 3.11). Once again, the overlap criterion of inequality 3.7 is utilised to reject diffusion events capable of causing numerical instabilities in the MD stage of the introduced hybrid kMC/MD framework.

As discussed in Section 3.3.2, the underlying Fe(110) substrate remains frozen throughout the kMC/MD run. Hence, Fe atoms are not allowed to migrate from the Fe(110) toward the growing

film. Nevertheless, it can be hypothesised that the mass of the Fe(110) substrate is considerably greater than that of the growing film. Effectively, it is assumed that the underlying Fe(110) surface becomes a source of Fe atoms diffusing within the thermally decomposed film. Under such an assumption, the diffusion event can be simulated by inserting an additional Fe atom on an overlap-free vacant site (as opposed to displacing a substrate Fe atom from the surface to the grid point). When a diffusion event is selected from the kMC stage of the hybrid kMC/MD methodology, the initial velocity and charge of the inserted Fe atom are zero. Both the velocity and the charge are updated in the subsequent MD stage. A flowchart illustrating the steps involved in the diffusion event is provided in Fig. 3.10.

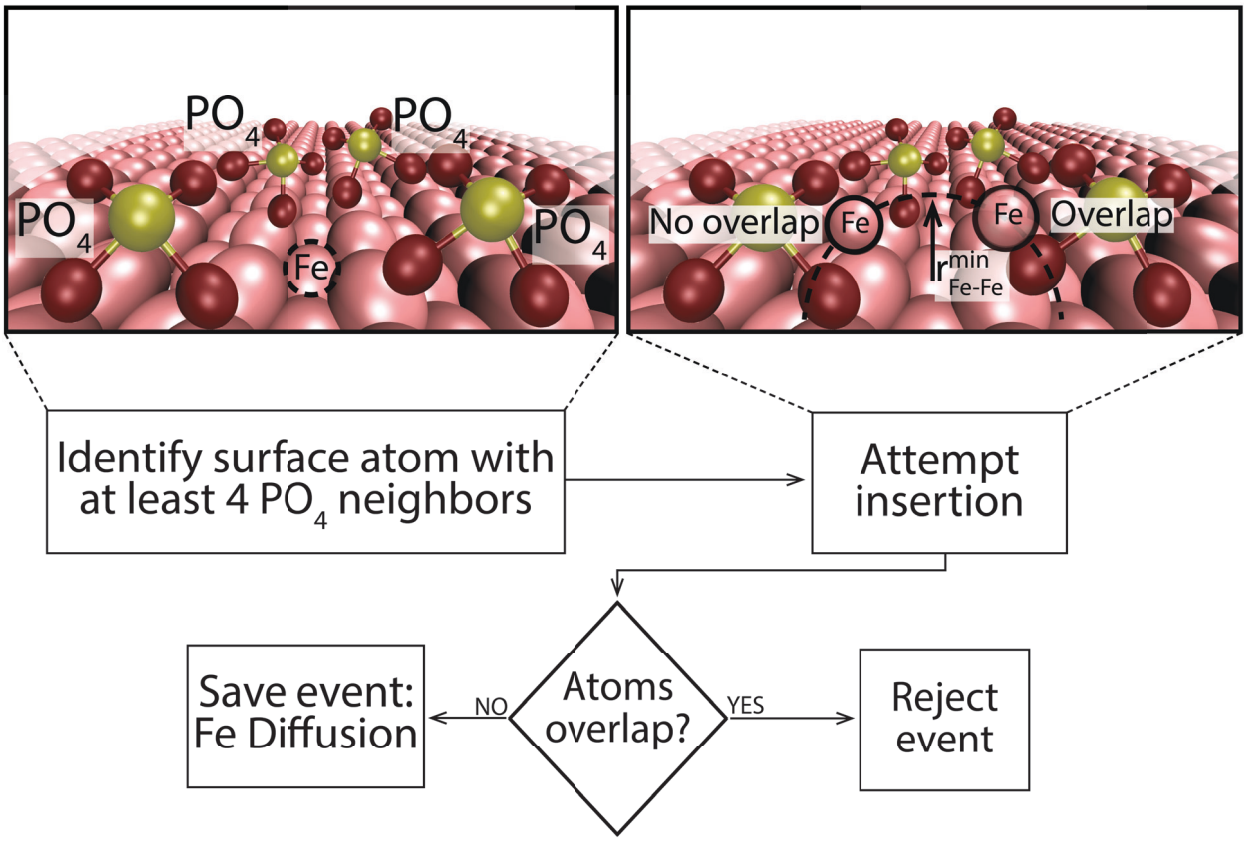


Fig. 3.10: Flowchart of a diffusion event.

The activation energy $\Delta E_{diff} = 11.53\,kcal/mol$ as well as attempt frequency $\nu_{diff} = 1.4\,10^{13}$ Hz linked to the diffusion event are obtained from the study of Kuss, Liang, and Schougaard [253]. Once again, the rate of a diffusion event (r_{diff}) is evaluated by using the respective ΔE_{diff} and ν_{diff} in Eq. 3.1. Note that such activation energy and attempt frequency values correspond to iron migration towards the M1 site of crystalline $FePO_4$ [254]. In the context of the current proof-of-concept application of this work, it is hypothesised that the diffusion energetics (i.e., ΔE and ν) of substrate iron in film $FePO_4$ are identical to those of Fe towards the M1 site of crystalline $FePO_4$.

To summarize, the kMC stage of our kMC/MD methodology simulates the following atomic-scale processes: (a) TCP adsorption (with a maximum base rate of $4.564\,10^3$ Hz, when $\sigma(\theta, T) = 1$), (b) P-O and C-O bond cleavage (with base rates of $1.525\,10^5$ Hz and 49.931 Hz, respectively), (c) P-O as well as Fe-O formation (considered barrierless with a rate of 10^{13} Hz), and (d) Fe diffusion

(with a base rate of $2.369\,10^8$ Hz). All the relevant base rates are obtained from the Arrhenius law (Eq. 3.1), except for the adsorption frequency, which is calculated from the kinetic theory of gases (Eq. 3.7). It can be observed that mechanisms (a), (b), and (d) are low-frequency events manifesting in timescales beyond the limits of MD. This justifies the fact that adsorption, bond dissociation, and diffusion events are simulated within the kMC stage of our kMC/MD framework.

On the other hand, the bond-formation events could be captured from the MD stage. Nonetheless, this would require the utilisation of an expensive interatomic potential capable of describing bond-association/dissociation (e.g., ReaxFF [251]). To favour the computational efficiency of our model, we simulate bond-formation events within the kMC stage. Finally, bond-formation events are grouped and executed concurrently. This prevents the kMC stage from becoming dominated by bond-formation events, which are by orders of magnitude faster than any other atomic-scale process [255].

3.3.5 Post-processing of results

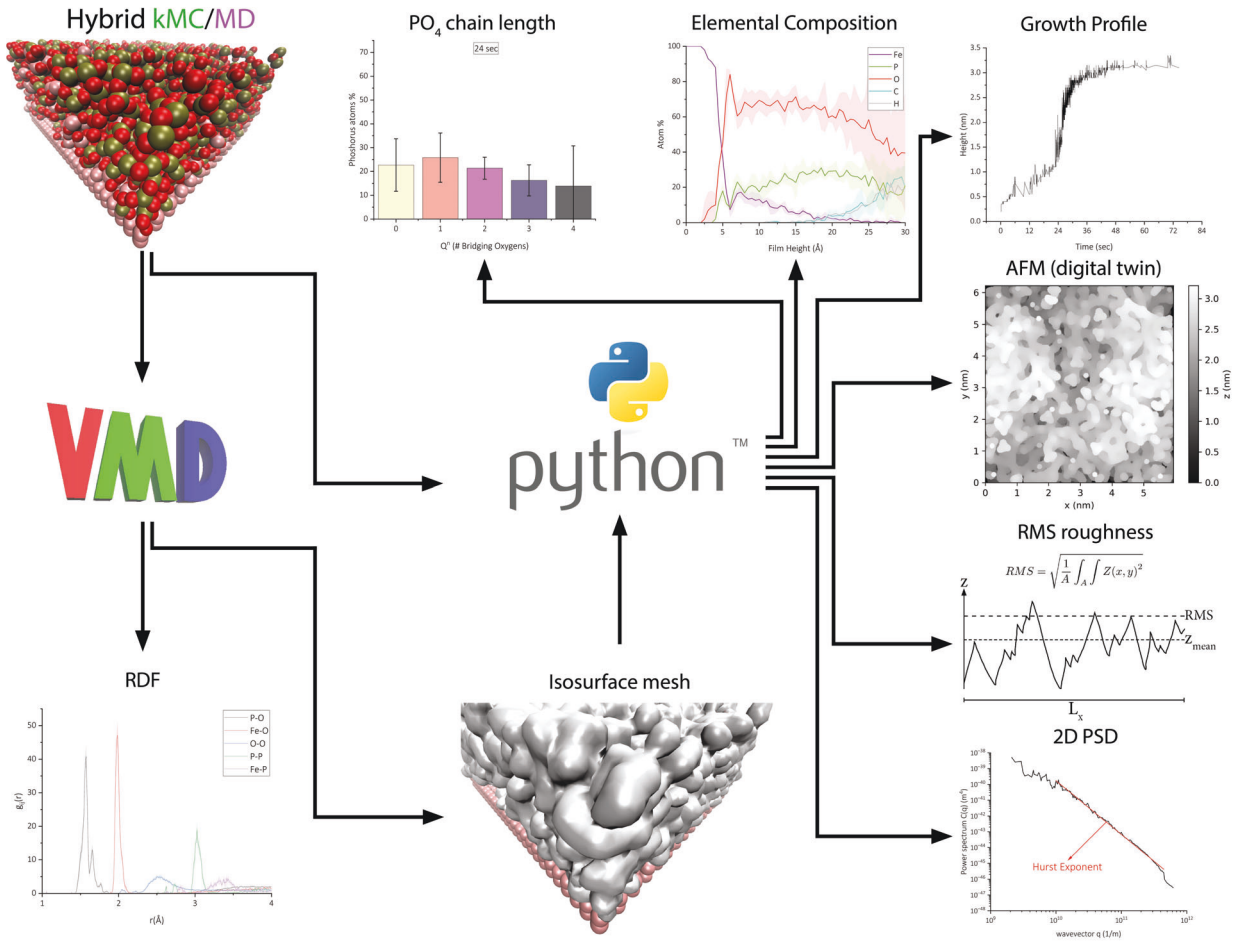


Fig. 3.11: Post-processing flowchart adapted from our preprint on the hybrid kMC/MD method [233]. Reproduced under the CC BY NC ND license.

The visual molecular dynamics (VMD) [256] is used to estimate the RDF for the species pairs contained in the grown film. The integrals of RDFs and, effectively, the coordination numbers (CN) of the species pairs are also obtained through VMD. Additionally, the volmap extension of VMD is deployed to generate a volumetric density map for each .xyz file. An isovalue of 0.6 is

selected, which ensures that the produced surface mesh reveals the morphological features of the grown film at lengthscales of approximately $10^{-9} - 10^{-10}$ m. Then, the coordinates of the grid points of the relevant isosurfaces are read by a Python script that converts each volumetric density map into a surface height map, which is used to calculate the RMS roughness.

Following, a 2D Hann window [27] is applied to the surface height map and the radially averaged 2D Power spectral density (2D PSD) is obtained [257]. The Hurst exponent (H) of the surface is calculated from the slope of the power spectrum-wavevector log-log graph ($H = -a/2 - 1$, with a being the graph slope). Note that the Hurst exponent is linked to the Fractal Dimension (FD) of the film ($FD = 3 - H$), which is a descriptor of the surface roughness.

Finally, a second Python script is deployed to evaluate the length distribution of the phosphate chains and calculate the atomic percentage of species at various film thicknesses. A flowchart summarising the post-processing procedure is provided in Fig. 3.11.

3.3.6 Computational efficiency

As expressed in Section 3.1, the central motivation of this work is the development of a computationally inexpensive algorithm capable of simulating amorphous thin film growth over experimentally relevant timescales with atomic-scale fidelity. In this section, we compare the computational efficiency of a hybrid kMC/MD run with the efficiency of the equivalent (at the same temperature $T = 528.15K$) ReaxFF MD simulation on thin films from TCP (deployed to acquire the activation energies of bond-breaking events). Such a comparison is performed in the direction of highlighting the time-advancing capabilities of our introduced hybrid kMC/MD framework.

The ReaxFF MD calculation features a fixed number of atoms (3632) and requires 20 h on the Young MMM Hub HPC cluster (200 cores @ 2.5 GHz Intel Xeon) to access timescales of 1 ns (10^{-9} second). Consequently, the time-advancing efficiency of the ReaxFF MD method is $\Delta t_{eff,ReaxFF} = 7.2\,10^{13}$ CPU s/s.

On the other hand, a kMC/MD run finishes in approximately 5 h on a personal computer (Dell Precision Workstation, 18 cores @ 3.0 GHz Intel Xeon) and is capable of reaching simulation times of about 60 seconds. Overall, the kMC/MD simulation requires 1100 blocks of steps (i.e., 9 kMC steps and 1 MD step) to complete. Hence, 18.33 blocks of kMC/MD steps advance the simulation clock by 1 second (1100/60 blocks/s). Now, the number of atoms is not fixed on a kMC/MD run. Therefore, the CPU time per block of kMC/MD steps is variable. To enable a direct comparison between ReaxFF MD and kMC/MD, a CPU time per block of steps of 11.89 sec is considered, corresponding to a system of 3632 atoms (i.e., N_{atoms} of ReaxFF MD). Note that in the current version of the kMC/MD model, the CPU time per block of steps scales linearly with the number of system atoms (as observed in Fig. 3.12). In any case, the time-advancing efficiency of the kMC/MD model ($\Delta t_{eff,kMC/MD}$) with 3632 atoms is 217.94 CPU sec/sec (11.89 CPU sec/block $\times$ 18.33 block/sec).

The hybrid kMC/MD run uses fewer computational resources (i.e., 18 cores) than the equivalent ReaxFF MD simulation (i.e., 200 cores). Nonetheless, our hybrid kMC/MD framework is eleven orders of magnitude more efficient than the ReaxFF MD method. It is important to mention that the Δt_{eff} of the hybrid kMC/MD framework scales with the simulation temperature. This is justified by observing that the rate of a kMC event (e.g., adsorption, diffusion, reaction) and ultimately, the overall rate (W_{tot}) scale with the system temperature. Since time steps (Δt) are

calculated through Eq. 3.2, altering the system temperature is also expected to influence the time-advancing capabilities of the methodology.

Moreover, note that the kMC stage of our algorithm is currently not parallelised. Overall, the Δt_{eff} of the introduced kMC/MD methodology is expected to decrease further in future versions of the hybrid kMC/MD model by parallelising the kMC stage as well as optimising the communication interface between the kMC and MD stages.

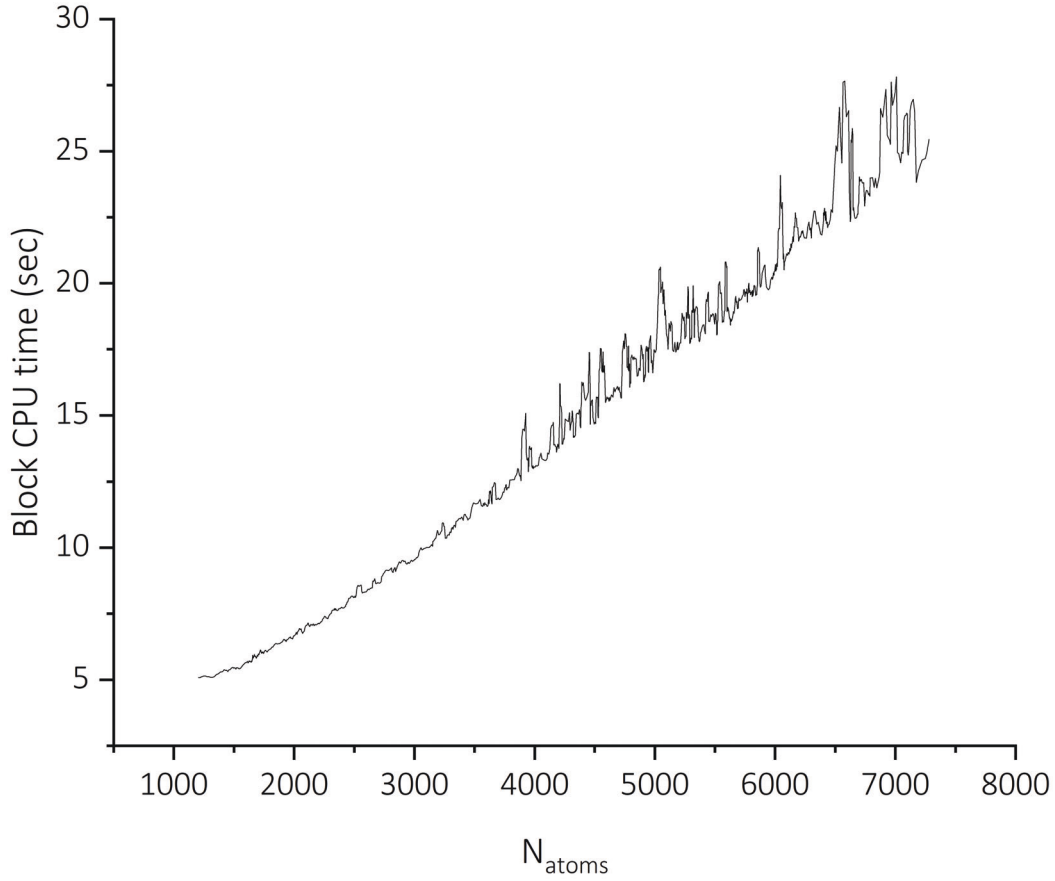


Fig. 3.12: Block (i.e., 9 kMC and 1 MD step) CPU time versus number of atoms of the performance run (used for comparison with the ReaxFF scheme).

3.3.7 Results & discussion

The growth profiles obtained from the four hybrid kMC/MD runs exhibit three roughly linear growth stages. An example growth profile curve (from run 1) is illustrated in Fig. 3.13.a). The relevant film snapshots of run 1 at different times are presented in Fig. 3.14. Initially, TCP molecules deposit on the Fe(110) substrate, which triggers dissociation [85] through P-O and C-O bond-scission events. The breaking of bonds releases phosphorus as well as oxygen species. This enables oxygen atoms to bond to surface Fe atoms and leads to the formation of PO_4 structures on the Fe(110) substrate. Adsorption events are characterised by relatively slower cumulative rates (sum of all adsorption event rates) compared to scission and (barrierless) bond-formation events (see Fig. 3.13). Notice that the probability of selection for a kMC event is proportional to W_{ij}/W_{tot} (see [173]). Therefore, the deposition probability is by orders of magnitude lower than the relevant probabilities of other event families. Hence, adsorption events typically occur

when further film growth necessitates the deposition of additional TCP molecules (i.e., after the execution of any available scission/formation event and when the relevant scission/formation rates drop to zero). Such an instance justifies the fact that the rate of deposition events dictates the shape of the growth profile. Effectively, adsorption events are performed when ($W_{tot} \approx W_{ads}$) directly influencing the time increment (Δt, as in Eq. 3.2) at a given kMC step. In essence, as the cumulative adsorption rate rises, so does the chance of generating a longer time increment Δt through Eq. 3.2.

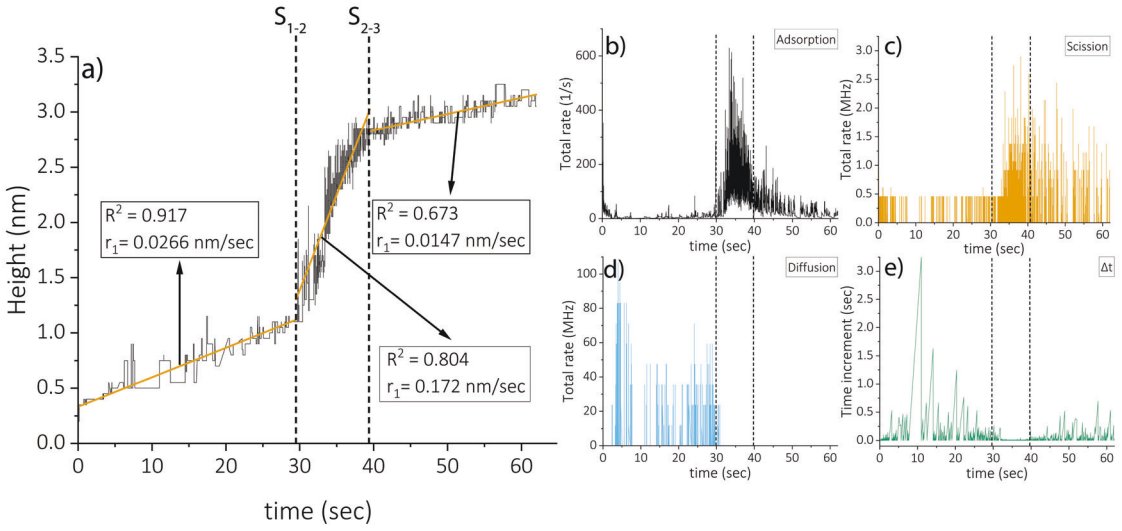


Fig. 3.13: (a) Example growth profile from run 1 along with best linear fits for the first, second, and third stages of growth. (b-d) Evolution of total (cumulative) kMC event rates of run 1. The total rates are calculated by summing the rates of all the detected events of the respective event family. Evolution of time increment (Δt as in Eq. 3.2 at each hybrid kMC/MD step) for run 1.

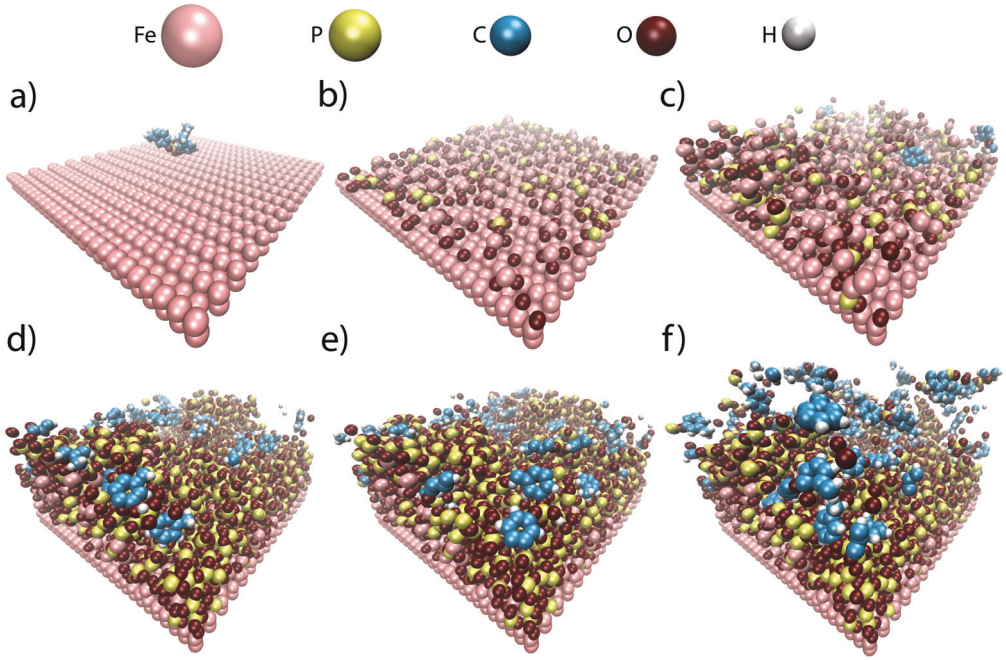


Fig. 3.14: Example film growth snapshots for run 1 at different times. (a-f) Snapshots at 0, 12, 24, 36, 48, and 60 seconds.

When at least four PO_4 structures are attached to the Fe(110) surface, the cumulative diffusion

rate becomes positive (as depicted in graph 3.13.d)) and Fe species begin to diffuse towards the growing film. Migrating atoms that do not form bonds with dangling oxygens can reach the film surface. This diminishes the availability of overlap-free adsorption sites and leads to the observed stage 1 growth plateau of the cumulative adsorption rate (i.e., the sum of the rates of all the adsorption events). This is illustrated in graph 3.13.b). Such a plateau can be considered responsible for the long time increments (see Fig. 3.13.e) and consequently, the slow, stable growth within stage one.

As the film grows, the number of overlap-free adsorption sites reduces. This results in a rise in the total adsorption rate since fewer Fe atoms obstruct TCP deposition sites. Of course, the increase of the cumulative adsorption rate leads to shorter time increments and faster stage 2 growth. The total deposition rate peaks within the second stage of growth, approximately when all the vacant sites for Fe diffusion are occupied (see Fig. 3.14.c).

Subsequent deposition beyond this point leads to the burying of Fe atoms within the thermally decomposed film. Note that non-catalysed P-O, as well as C-O bonds, are not permitted to break in the current study. Buried Fe species cannot catalyse P-O and C-O bond scission events. Consequently, a number of TCP molecules deposit on the growing front but remain intact and ultimately obstruct active adsorption sites (as seen in Fig. 3.14.d). This gradually diminishes the cumulative adsorption frequency and justifies the reduced growth within the third growth stage. Eventually, all Fe species become buried within the film and are incapable of further activating P-O or C-O bond-breaking reactions. Hence, the film ceases to grow and the height plateaus beyond the third stage of growth (see Figs. 3.14.e-f).

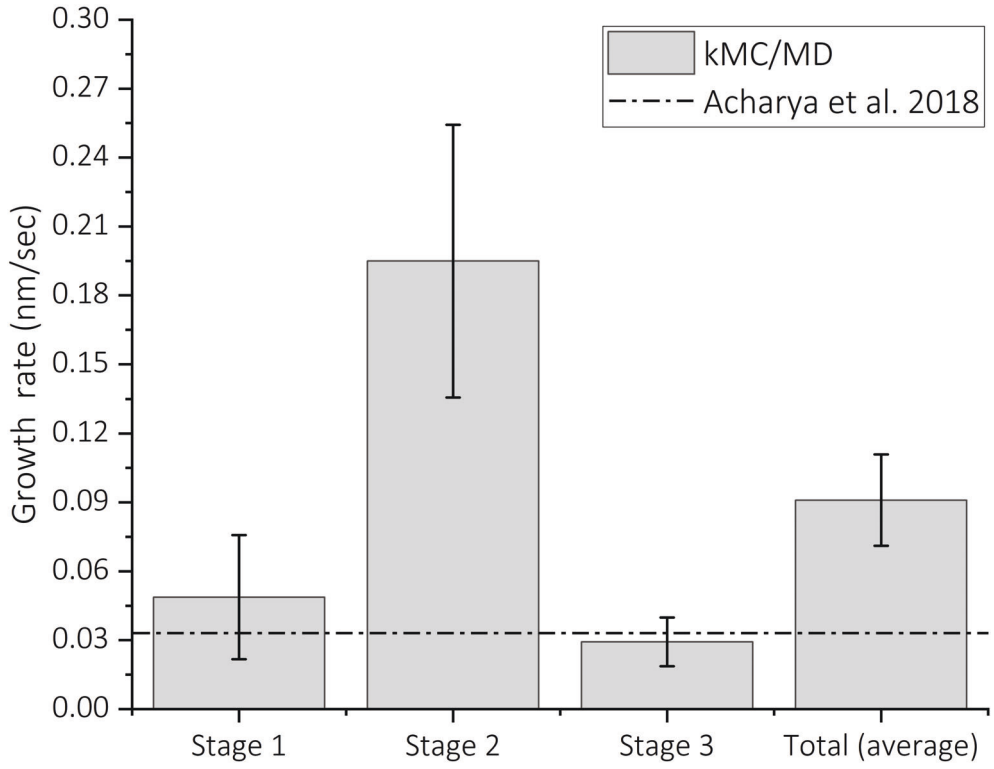


Fig. 3.15: Growth rates and standard deviations of the 3 stages. The dashed line represents the growth rate for TCP molecules on Fe(110) from the experimental study of Acharya et al. [89].

Overall, a sigmoidal growth profile (Fig. 3.13) is obtained, which has been observed in previous

modelling studies on film growth [258]. The bar chart presented in Fig. 3.15 exhibits the average growth rates along with the standard deviation of four hybrid kMC/MD runs. The horizontal dotted line corresponds to an experimentally obtained growth rate of 0.038 nm/sec for thermally decomposed TCP molecules on an iron substrate, as obtained from the work of Acharya et al. [89]. These authors did not provide the complete growth profile (height versus time graph), but instead assumed a linear behaviour and estimated the growth rate by dividing the final thickness by the total growth time associated with their QCM experiment. Since the growth behaviour observed in our simulations is not linear, a total growth rate is obtained for the sake of enabling the comparison between the hybrid kMC/MD and the experimental results. Particularly, we estimate the total growth rate as 0.09 ± 0.02 nm/sec (see Fig. 3.15) by averaging the rates of the three growth stages for each hybrid kMC/MD run. The evaluated total growth rate of the hybrid kMC/MD runs is approximately three times faster than the experimentally obtained value. Nonetheless, the kMC/MD and experimental growth rate values are of the same order of magnitude.

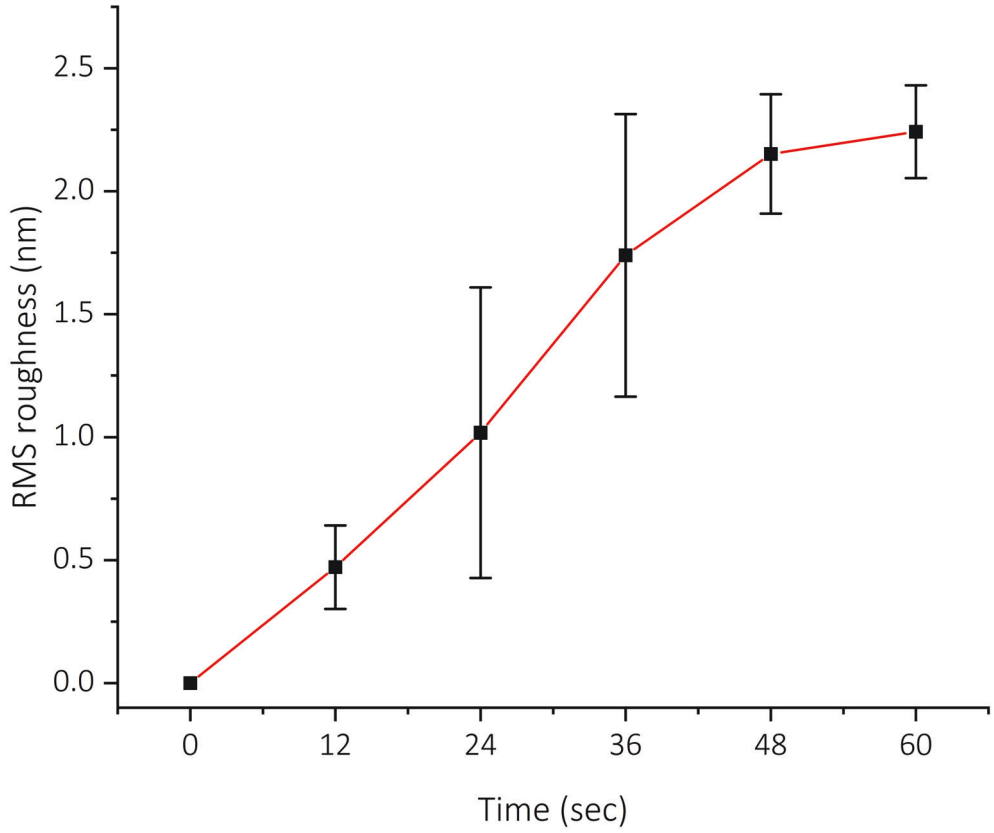


Fig. 3.16: RMS roughness versus kMC time. The vertical bars represent the standard deviation of four hybrid kMC/MD runs.

The disparity between the hybrid kMC/MD rate and the experimental value can be explained by the following differences. Firstly, the experiments were performed at 498.15 K, while the simulations were conducted at 528.15 K. Secondly, the experiments were conducted using a solution of 5% TCP in base oil, while our hybrid kMC/MD analysis assumes that TCP molecules approach the growing film from a vapour region (as analysed in Section 3.3.2). Thirdly, the experimental rates assume linear growth, rather than the sigmoidal growth profile observed by kMC/MD. Finally, the disparity between the experimental and computationally obtained growth rates may be linked to the central assumptions of our kMC/MD approach, such as considering the bond formation as

barrierless.

The evolution of the film RMS roughness is presented in Fig. 3.16. A steady rise in the RMS roughness value is observed within the first and second stages of growth. The roughness features of the film are almost fully developed when the system transitions from stage two to stage three growth. Essentially, the RMS roughness increases slightly within the third stage of growth and eventually reaches a maximum value of 2.242 ± 0.189 nm at 60 seconds. This is somewhat lower than the experimentally obtained value of 3.6 nm for 5% TCP dissolved in a base oil on a pure iron substrate (Acharya et al. [89]). Discrepancies between the computationally and experimentally obtained values may stem from the central assumptions implemented in our hybrid kMC/MD model. For example, in the present work, C-O bond-scission events may lead to the removal of carbon and hydrogen species from the system. Of course, such an instance alters the morphological characteristics of the thin film and can influence the value of RMS surface roughness.

Finally, relatively large uncertainties are observed in Fig. 3.16. However, this is justified by considering that the RMS roughness value is a function of film height and that the film height of individual hybrid kMC/MD runs can vary at a specific time. Such variation in film height can be non-negligible, especially if we acknowledge that the time increment (Δt) of the kMC method is non-constant (see Eq. 3.2).

Fig. 3.17 illustrates the height profile images from the four hybrid kMC/MD runs. Such images can be considered digital twins [259] of AFM images and can be used for visual comparison between computationally and experimentally grown thin films. The power spectrum of a digital twin image can be calculated by treating the height profile of the respective run.

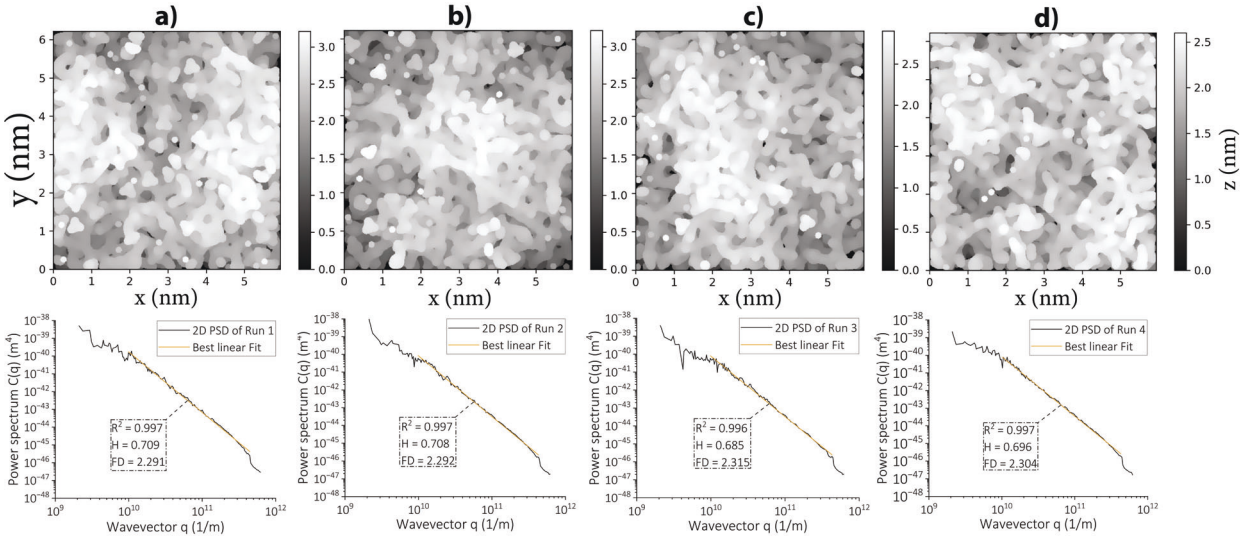


Fig. 3.17: Surface height profiles and relevant 2D radially averaged PSDs of the four (a-d) kMC/MD runs. The FD of individual hybrid kMC/MD runs is obtained from the slope of the respective power spectrum versus wavevector graph. The average FD is 2.301 ± 0.0112.

The associated FD (a surface roughness descriptor) can be estimated from the slope of the power spectrum (the treatment process is outlined in Section 3.3.5). Note that the radially averaged power spectrum is calculated, which assumes that the fractal characteristics of the film surface exhibit radial symmetry. In this work, a value of $FD = 2.30 \pm 0.001$ is obtained from the four hybrid kMC/MD runs. This is equal to the maximum FD limit of $FD_{max} = 2.3$ for self-affine surfaces of engineering interest (as outlined by Persson [260]). The FD value calculated from the

kMC/MD runs is also comparable to the FD of films grown on ferrous surfaces from phosphate-containing anti-wear additive molecules. For instance, in the study of Dorgham et al., [261], the FD of tribofilms formed from Zinc dialkyl dithiophosphates (ZDDP) molecules in the boundary lubrication regime ranged between 2.17 and 2.34 in 30% and 75% Relative Humidity conditions, respectively.

Fig. 3.18.a) illustrates the partial RDFs (g_{ij}) for the species pairs for the iron polyphosphate film obtained from kMC/MD at 60 s. Figs 3.18.c) and 3.18.d) correspond to the RDFs of two iron phosphate systems ($40Fe_2O_3$ and $40FeO$, respectively) as investigated in the MD study of Al-Hasni and Mountjoy [262]. Note that P-O and Fe-O pairs in the film interact not only through harmonic bonds, but also via thermostat and non-bonded interactions with other atoms (i.e., intact TPC molecules in the vicinity of the bond, other polyphosphate chains, etc.). Hence, the shapes (i.e., positions, numbers, and intensities of peaks) of the RDFs corresponding to the P-O and Fe-O pairs differ from the relevant (scaled) interatomic bond potential distributions (i.e., $p(r) \propto \exp^{\frac{k_0(r-r_0)^2}{2k_bT}}$, with k_0, r_0, k_b, and T being the harmonic spring constant, equilibrium bond distance, Boltzmann constant, and system temperature, respectively). The spring constants and equilibrium bond distances (as defined in the DREIDING force field) for the P-O and Fe-O pairs are $k_{0,P-O} = 350$ kcal/(mol Å^2), $r_{0,P-O} = 1.54$Å, and $k_{0,Fe-O} = 350$ kcal/(mol Å^2), $r_{0,Fe-O} = 1.935$Å.

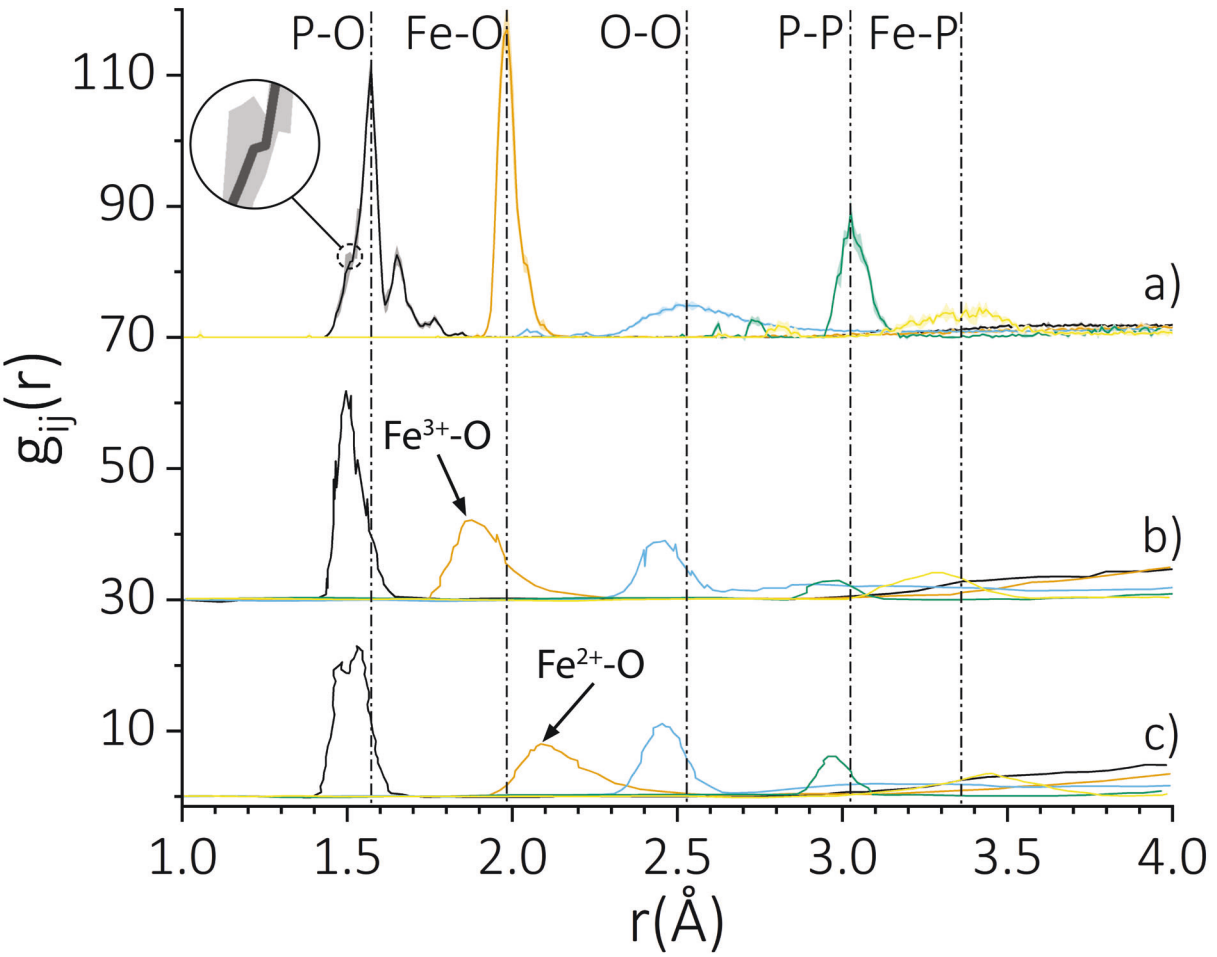


Fig. 3.18: RDFs (a) Hybrid kMC/MD simulations at 60 seconds and standard deviations. (b) Al-Hasni and Mountjoy [262], RDF of $40Fe_2O_3$. (c) Al-Hasni and Mountjoy [262], RDF of 40FeO. Offsets of 30 and 70 $g_{ij}(r)$ are used for curves (b) and (a), respectively.

The RDFs of the hybrid kMC/MD analysis are in reasonable qualitative agreement with the relevant MD RDFs (Figs. 3.18.c-d). The first two distinct P-O peaks of Fig. 3.18.a) at 1.519Å (zoomed-in region) and 1.573Å correspond to P-O bonds involving O_{NB} (non-bridging oxygens bonded to one or zero phosphorus atoms) and O_B (bridging oxygens bonded to two phosphorus atoms), respectively. The $P - O_{NB}$ bond length captured from our hybrid kMC/MD runs is somewhat longer than the experimentally obtained value of 1.432 ± 0.005Å from the study Hoppe et al. [263]. The $P - O_B$ from the same work of Hope et al. is 1.581 ± 0.003Å. Furthermore, the mean P-O value (average of $P - O_{NB}$ and $P - O_B$) from the hybrid kMC/MD simulations (Fig. 3.18.a) is 1.546Å. Such value is slightly greater than the average P-O length (1.50 ± 0.01Å) as reported in the study of Al-Hasni and Mountjoy [262] (see Figs. 3.18.b-c). Nonetheless, the mean kMC/MD P-O length value is within the P-O bond length limits reported in the Raman spectroscopy investigation of Zhang and Brow [264] (1.54-1.57Å).

A third P-O peak is depicted at 1.651Å. Such peak results from the influence of the m-tolyl groups of TCPs on adjacent P-O bonds of the growing film. Within the third stage of growth (see Fig. 3.13.a) and towards the end of a kMC/MD run, TCP molecules adsorb on the iron polyphosphate film and decompose partially or remain intact (depending on the number of the relevant activated P-O and C-O reactions). Using a Python script, we estimated that the length of P-O bonds in P-O-C or O=P-O-C structures is 1.651 ± 0.005Å. Such an average bond length coincides with the x-axis position of the third P-O peak. Note that, in the present work, carbon and hydrogen species are removed from the system following C-O dissociation events. Generally, obtaining a thorough understanding of the effect of cresol fragments on P-O bond lengths necessitates further simulations that allow C and H species to remain in the growing film.

The most probable O-O distance in the hybrid kMC/MD simulations is 2.515Å corresponding to a CN of 4.977 ± 0.06. The results are comparable to the relevant values obtained from diffraction studies on $40Fe_2O_3$ ($CN = 5.0 \pm 0.5$ and $d_{O-O} = 2.5 \pm 0.02$Å) [265, 266]. The CN obtained from the MD study of Al-Hasni and Mountjoy [262] is 4.3 for the $40FeO$ system (Fig. 3.18.a) and 3.7 for the $40Fe_2O_3$ glass (Fig. 3.18.b). Moreover, we observe longer P-P distances in the case of the hybrid kMC/MD simulations relative to the results of the study of Al-Hasni and Mountjoy [262]. This feature is potentially linked to the longer P-O bonds in the hybrid kMC/MD runs. This can be justified by considering that the thermally decomposed film simulated through kMC/MD is rich in P-O-P as well as O-P-O structures. Therefore, an elongation of P-O bonds can potentially result in the offset of the P-P peak towards higher distances. The predicted P-P CN of the MD simulations of Al-Hasni and Mountjoy is 2.34 and 1.0 for the $40FeO$ (Fig. 3.18.a) and $40Fe_2O_3$ (Fig. 3.18.c) systems, respectively. Note that the O:P ratios of the systems studied in the work of Al-Hasni and Mountjoy are 2.83 for FeO and 3.5 for $40Fe_2O_3$, while the O:P ratio of the kMC/MD runs at 60 seconds is 2.913 ± 0.122. The P-P CN value of the hybrid kMC/MD runs (2.361 ± 0.131) is similar to the relevant value of the $40FeO$ system of Al-Hasni and Mountjoy [262], which features a comparable O:P ratio.

As far as the Fe-O and P-O peaks are concerned, we notice that $r_{40Fe_2O_3} < r_{kMC/MD} < r_{40FeO}$. Such an instance is potentially linked to the central differences characterising the assumptions of the kMC/MD simulations and MD simulations of Al-Hasni and Mountjoy [262]. Specifically, the hybrid kMC/MD framework deploys a QEq method to equilibrate the atomic charges (as discussed in Section 3.3.3). Effectively, the Fe atoms inserted in the system (via diffusion events)

are in a mixed oxidation state during the hybrid kMC/MD runs. On the other hand, Al-Hasni and Mountjoy [262] utilised fixed charges meaning that the $40FeO$ and $40Fe_2O_3$ systems solely contain Fe ions in the 2+ (Fe^{2+}) and 3+ (Fe^{3+}) valence states, respectively. The kMC/MD Fe-O distance value is between the experimentally obtained Fe-O distances for $40Fe_2O_3$ (1.94 ± 0.01Å) and $40FeO$ (2.12 ± 0.02Å) [265, 267]. Finally, the hybrid kMC/MD CN for Fe-O (4.856 ± 0.145) is in good agreement with the experimentally obtained value of 5.0 ± 0.5 [265, 267].

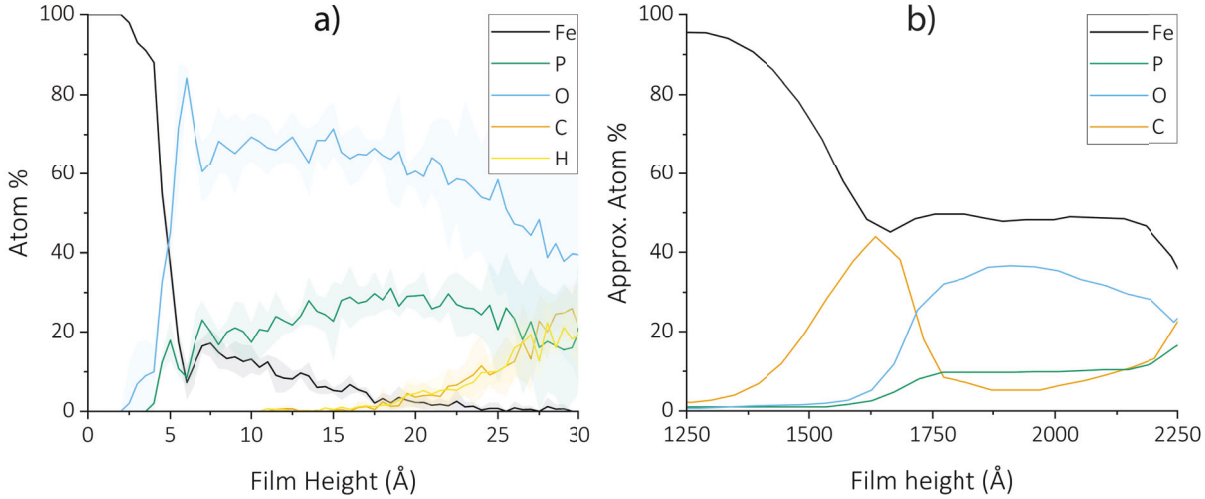


Fig. 3.19: Film elemental composition graphs. (a) Hybrid kMC/MD simulations. The shadowed regions represent the standard deviation of four runs. (b) Approximate atomic percentage versus film depth from Auger depth profile for a thermally decomposed film formed from tri(tert-butylphenyl) phosphate (t-BPP) molecules at 698.15K after 2 hours of exposure. Experimental data adapted from Johnson and Morrow [67]. The x-axis was converted from sputter time to film depth using the sputter rate (80Å /min) reported.

The elemental distribution (atomic percentage) across the growing film obtained from the hybrid kMC/MD is provided in Fig. 3.19.a). A reference Auger depth profile (from Johnson and Morrow [67]) for a film grown from tri(p-tert-butylphenyl) phosphate (p-TBPP) lubricant additive molecules on iron foils and in VPL conditions is illustrated in Fig. 3.19.b).

Firstly, we notice that the Fe atomic percentage in Fig. 3.19.b) is the highest through the film depth. On the contrary, when it comes to Fig. 3.19.a), Fe atoms dominate the film composition only in the neighbourhood of the Fe(110) surface. Such an instance is a consequence of the fundamental approximations relevant to the diffusion events of the kMC/MD model. Specifically, the diffusion of Fe species is enabled solely when a specific vacancy type is detected (empty space around at least 4 PO_4 as defined in Section 3.3.4). A more representative description of the diffusion process, especially in the case of non-crystalline films, demands the migration of species towards different vacant sites. Furthermore, the current iteration of our hybrid kMC/MD model does not consider the possible elongation of bonds in the vicinity of a vacancy. Such an instance can potentially allow for additional Fe species to migrate toward the growing film. Overall, the central assumptions of our kMC/MD diffusion processes justify the steep drop in the Fe atomic percentage. In essence, Fe species are abundant in the vicinity of the Fe(110) substrate. However, Fe vacancies become saturated in the early stages of growth (as observed in Fig. 3.13.a).

Moreover, the peak of the carbon curve close to the surface is not captured in hybrid kMC/MD runs. This is a result of the kMC/MD model assumptions regarding the C-O bond scission events. Essentially, our modelling choice to eject hydrogen and carbon atoms from the system after specific

bond cleavage events leads to zero carbon atomic percentage close to the substrate. The carbon content begins to rise steadily when approximately $h_{film} \geq 10$Å, as a larger number of TCP molecules deposit on the surface without decomposing fully. An increase in the atomic percentage of carbon is also observed in the relevant experimental curve (Fig. 3.19.b).

When it comes to the oxygen and phosphorus curves, we notice a reasonable qualitative match between the experimental and computational results. Both kMC/MD and AES graphs are richer in oxygen than phosphorus throughout the film thickness. The phosphorus content remains constant for the majority of the film. The oxygen and phosphorus curves in the case of Fig. 3.19.a) feature a slight drop in the vicinity of the film surface due to the rise of carbon percentage.

The connectivity of phosphate structures within the growing film can be described by the distribution of bridging oxygens (O_B) per P species. Specifically, P atoms are classified as Q^n, with $n \in [0, 4]$ being the number of O_B bonded to a P atom. The schematic depicted in Fig. 3.20 showcases examples of phosphate network structures.

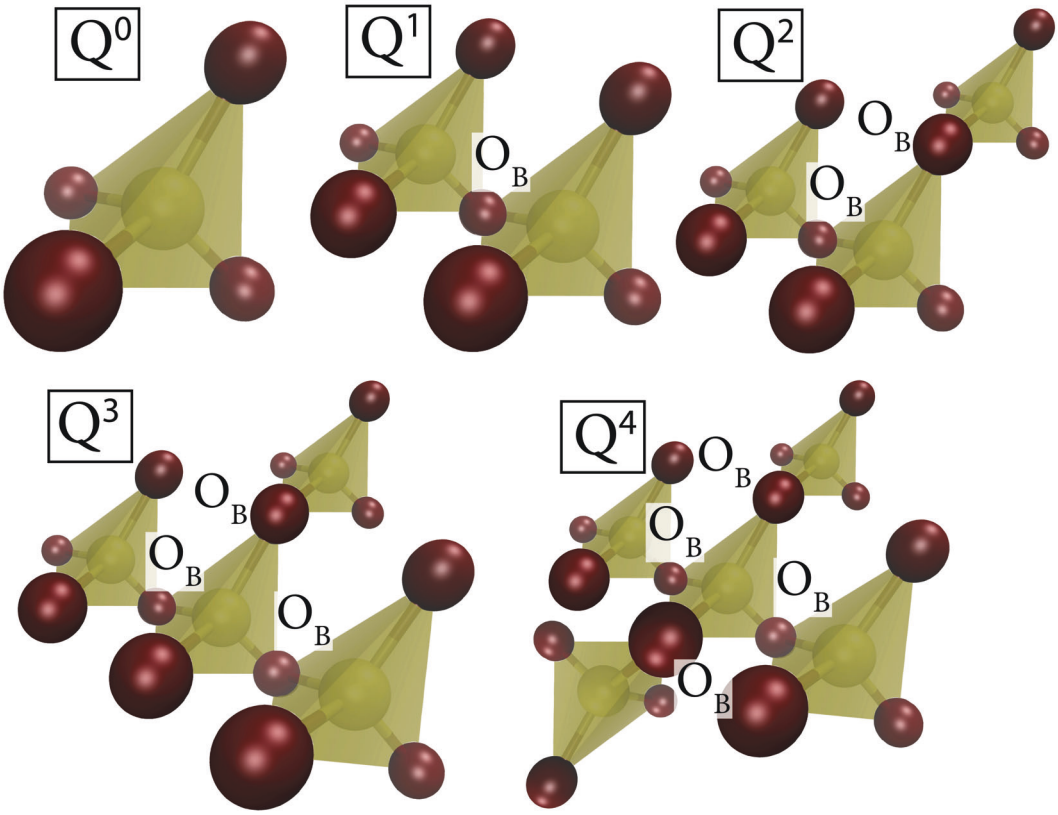


Fig. 3.20: Illustration of (PO_4) phosphate chain structures.

The relevant percentages of Q^n for the iron polyphosphate films of the kMC/MD runs at different snapshots are illustrated in Figs. 3.21a-d). In the early stages of growth (Fig. 3.21.a)) Q^0 structures dominate the system due to the low degree of polymerisation. The calculated O:P ratio of the kMC/MD simulations at 24 s is 4.90 ± 2.065. The corresponding distribution of Q^n structures at 24 seconds (as in Fig. 3.21.b)) shows that the two most probable phosphate network structures are Q^0 and Q^1. Such a result is in agreement with experimental studies on iron phosphate systems claiming that compositions with O:P ratios of 3.5 and above are dominated by Q^1 and Q^2 tetrahedra [264].

From 36 to 48 s (Figs. 3.21.b-e)) the percentage of Q^4 phosphorus species rises steadily, and

in the last snapshot (60 seconds - Fig. 3.21.d)), a left-skewed distribution is clearly depicted. The estimated O:P ratio at 60 seconds is 2.913 ± 0.122. Previous studies on phosphate systems suggest that at O:P ratios of approximately 3, iron phosphate films form glassy metaphosphates featuring long chains of Q^2 structures. Hence, the distribution depicted in Fig. 3.21.d) is not consistent with previous results on iron phosphate systems. Nonetheless, such inconsistency can be explained by acknowledging a couple of facts. Firstly, in the present work, we model bond formation as a barrierless event. Secondly, P-O and Fe-O bonds within the growing film are not permitted to break (see Section 3.3.4). In essence, iron-catalysed depolymerisation [59] is not currently considered in the present kMC/MD study, which explains the increase of bridging oxygens (O_B) within the growing films over time.

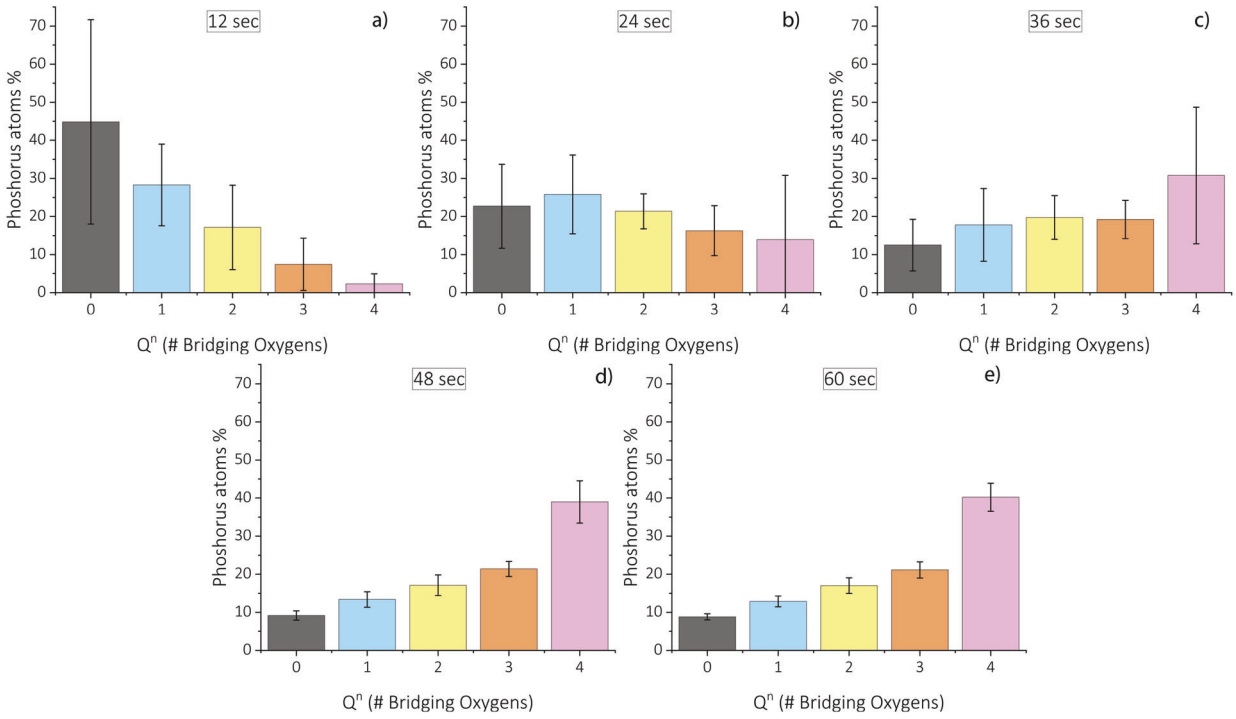


Fig. 3.21: Phosphate chain lengths at about 12, 24, 36, 48, and 60 seconds, respectively and relevant standard deviation. Percentage of atoms with 0, 1, 2, 3, and 4 bridging oxygens, corresponding to Q^0, Q^1, Q^2, Q^3, and Q^4, respectively.

3.4 Conclusions & Future work

We have introduced a 3D off-lattice hybrid kMC/MD methodology that bridges reactive MD simulation timescales with timescales linked to thin-film growth experiments. The stochastic kMC algorithm propagates the system through rare transitions, while a short NVT MD trajectory relaxes the system by accounting for the interactions between the atoms in the growing film (as discussed in Section 3.2). Utilisation of our kMC/MD implementation demands prior knowledge regarding the critical atomistic processes along with their associated rates. Essentially, our kMC/MD method is empirical in nature, meaning that it does not capture the detailed trajectory of the system. Therefore, it is not as accurate as other atomistic simulation methods (e.g., MD, DFT, or even on-the-fly off-lattice kMC). Nevertheless, we postulate that the predefined table of rates assumption of on-lattice kMC can be extended to off-lattice kMC approaches. This eliminates the requirement for

discovering as well as managing atomic-scale processes at every time step. This instance renders our kMC/MD methodology computationally efficient as well as easy to implement, especially compared to on-the-fly off-lattice approaches. Overall, the presented kMC/MD scheme serves as a tool that allows the user to potentially include any atomic-scale process of interest. Such a fact highlights the transferability of the proposed kMC/MD framework across different thin film systems of the energy sector (SEIs, catalysts, PVs, and tribofilms, as discussed in Section 2.1.1).

The thermal decomposition of TCP molecules on iron (see Section 3.3) was used as a proof-of-concept for our methodology. The growth rate, RMS roughness, FD, and RDF estimated from the hybrid kMC/MD model are in good agreement with the corresponding experimental and MD simulation results available in the literature. Also, we observed that our kMC/MD scheme was not capable of describing certain features related to the elemental composition as well as the distribution of polyphosphate chain length. Regardless, the accuracy of our kMC/MD methodology can be further improved by revising the central assumptions linked to the modelling of atomic-scale processes.

In that respect, our future work will primarily focus on conducting additional DFT as well as ReaxFF MD simulations on thin films generated from the decomposition of TCP molecules. Such simulations will enable us to reduce the uncertainty associated with the rates of the various events. Furthermore, supplementary simulations using ReaxFF MD or DFT will provide us with the necessary knowledge, allowing us to improve the fundamental approximations deployed to model the relevant rate-determining atomic-scale processes. For instance, the diffusion event could be revised to include more than one vacant site, and the C-O bond-scission event could be altered to retain C and H atoms within the growing film. In the direction of thoroughly corroborating the predictive capabilities of our kMC/MD framework, we also plan to design laboratory-based experiments on the thermal decomposition of TCP molecules on steel surfaces. These experiments will permit a more representative and direct comparison between the hybrid kMC/MD results and results of experiments conducted under the same conditions (e.g., temperature, pressure, partial pressure of TCP precursor, etc.).

Finally, we aim to optimise the computational efficiency of our hybrid kMC/MD algorithm. The kMC stage will be implemented in C++, and the kMC-MD communication interface (currently performed through reading/writing text files) will be revised to enable the direct passing of data from the kMC stage to LAMMPS. Then, the C++ kMC code will be parallelised. Both changes are expected to boost the computational efficiency of the hybrid kMC/MD framework even further, enabling the simulation of larger systems over longer timescales.

Data availability

Data from our hybrid kMC/MD runs on the thermal decomposition of TCP molecules are available at Mendeley data (DOI: 10.17632/p8bjyrg5jh.1) [268].

Chapter 4

Experimental Validation

4.1 Introduction

As discussed in Section 2.1.1.3, various experimental studies shed light on the formation mechanisms as well as the chemical (e.g., elemental composition, bonding environment) and morphological (e.g., roughness, friction coefficient) properties of TCP films on metallic surfaces ([69, 87, 89, 269]). Nonetheless, to the best of our knowledge, there is a gap in the literature regarding the in-depth understanding of kinetic properties (e.g., rate of formation) of thermally-grown coatings from TCP on iron.

The numerical model presented as part of this PhD thesis is kinetic. Its central aim is the bridging of experimental and molecular-resolution simulation timescales. Therefore, the experimental validation of the growth rates as well as thickness curves (see Figs. 3.13 and 3.15) produced by our hybrid kMC/MD workflow is paramount to the credibility of the method. In our previous work [270] (see Chapter 3), growth rates from TCP on iron from our kMC/MD model were compared to a formation rate reported in the study of Acharya et al. [89]. Nonetheless, that study assumed linear growth and estimated the formation rate by dividing the final thickness by the overall duration of the experiment.

For a more thorough investigation regarding the kinetics of the formation of TCP coatings on iron, we developed an in-house experimental setup aimed at the dynamic monitoring of thermally grown thin films. The following chapter discusses the materials used, conceptual design, methods, and limitations (Section 4.2) of our experimental setup. Next, Section 4.3 focuses on the presentation of experimental results and a comparison with in-silico data for TCP films grown by thermal decomposition on ferrous surfaces. Finally, conclusions and suggestions for further work are provided in Section 4.4.

4.2 Methods

4.2.1 Thermal decomposition setup

A computer-aided design (CAD) sketch and an actual image of the experimental arrangement utilised as part of this work are presented in Fig. 4.1. The experiments took place in a fume hood to prevent leakage of neurotoxic TCP vapours [68]. A round-bottom reaction vessel (sciLabware Quickfit 1000mL) was filled with silicone oil (Thermo Scientific Acros 316 °C flash point) and

secured on a heating mantle-stirrer (Electrothermal OMCA1000). A 100 PT RTD probe was connected to the mantle to measure and control the temperature of the silicone oil.

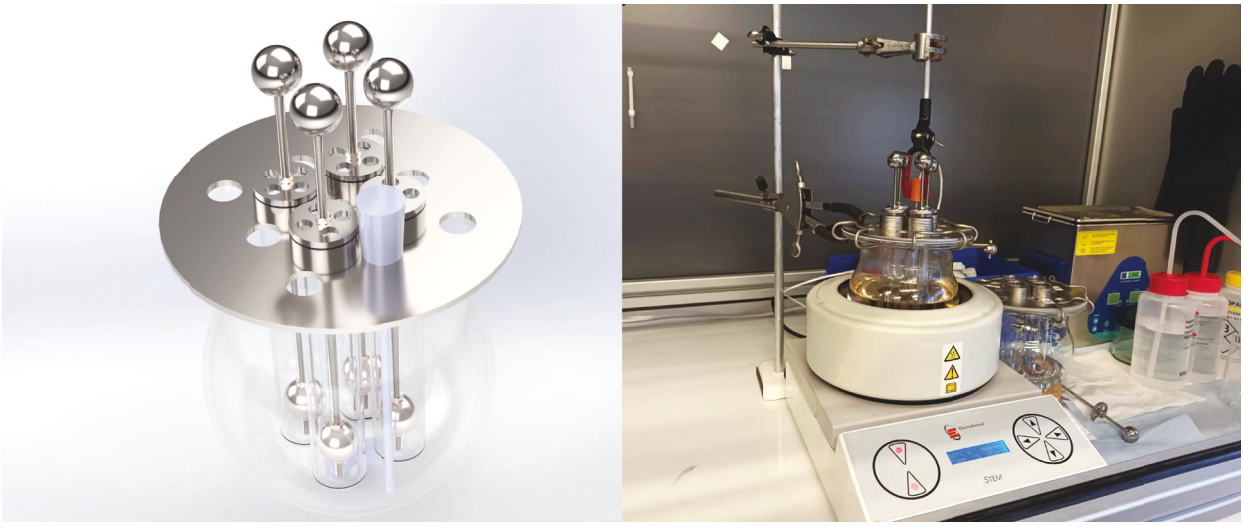


Fig. 4.1: CAD rendered **(left)** and actual **(right)** experimental setup for the thermal decomposition of TCP on iron.

Following, a laser-cut sheet metal (304S15 stainless steel) lid was mounted and secured on the rim of the round-bottom flask. Four rimmed glass tubes (DURAN borosilicate 3.3) were inserted into circular holes of the sheet metal lid, while smaller openings allowed silicone oil vapours to escape from the reaction flask in order to prevent pressure build-up. Spacers were used for height adjustment, ensuring that the borosilicate glass tubes were wetted by the silicone oil at all times.

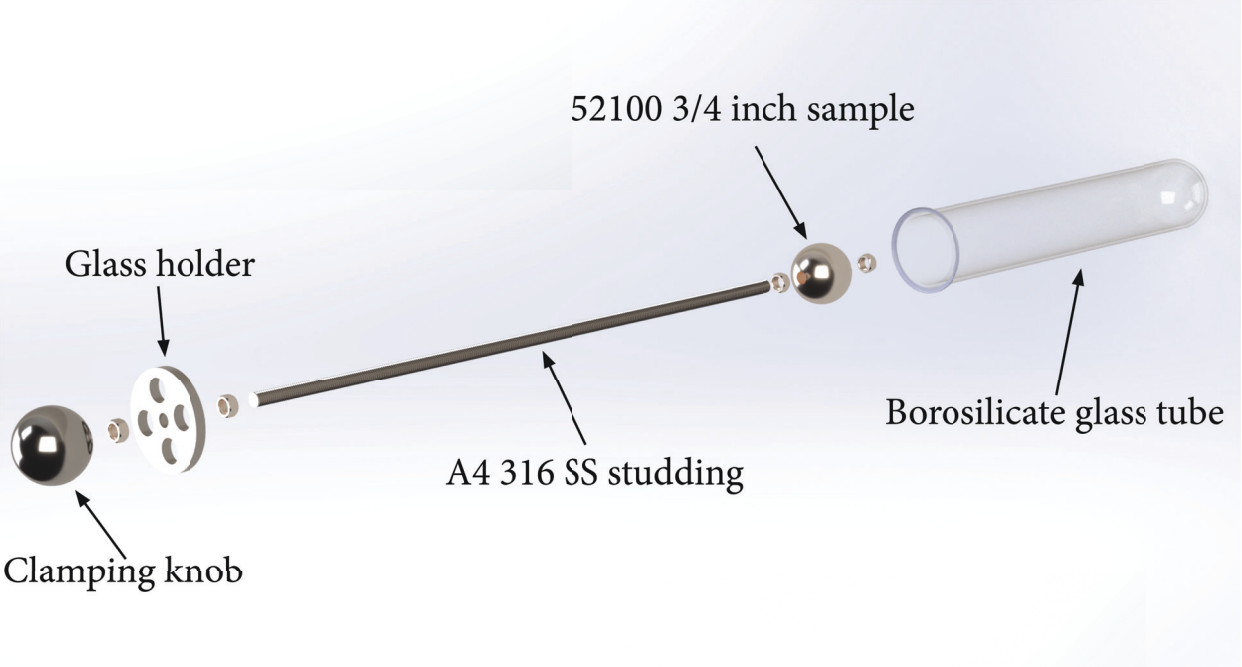


Fig. 4.2: Exploded view of a steel rod assembly. A clamping knob facilitates the handling of the assembly. A steel glass holder secures the assembly on the rim of the borosilicate glass tube. A set of nuts allows for adjustments to the position of the 52100 specimen to ensure proper sample wetting.

Next, four steel rod assemblies (as in Fig. 4.2) were placed on the rimmed glass tubes. Prior to each test, the assemblies were cleaned by rinsing with heptane and then with isopropanol. The

samples (52100 3/4 inch ball specimens from PCS instruments) fastened at the bottom of the assembly underwent a more thorough treatment to guarantee the removal of the stock grease as well as polar and non-polar contaminants from the surface of the spheres [271]. Specifically, the samples were sonicated sequentially in heptane, acetone, and finally isopropanol. Any part of the assembly in contact with the lubricant (i.e., studdings, nuts, and washers) was designed using A4 316 stainless steel (SS) to inhibit corrosion and oxidation.

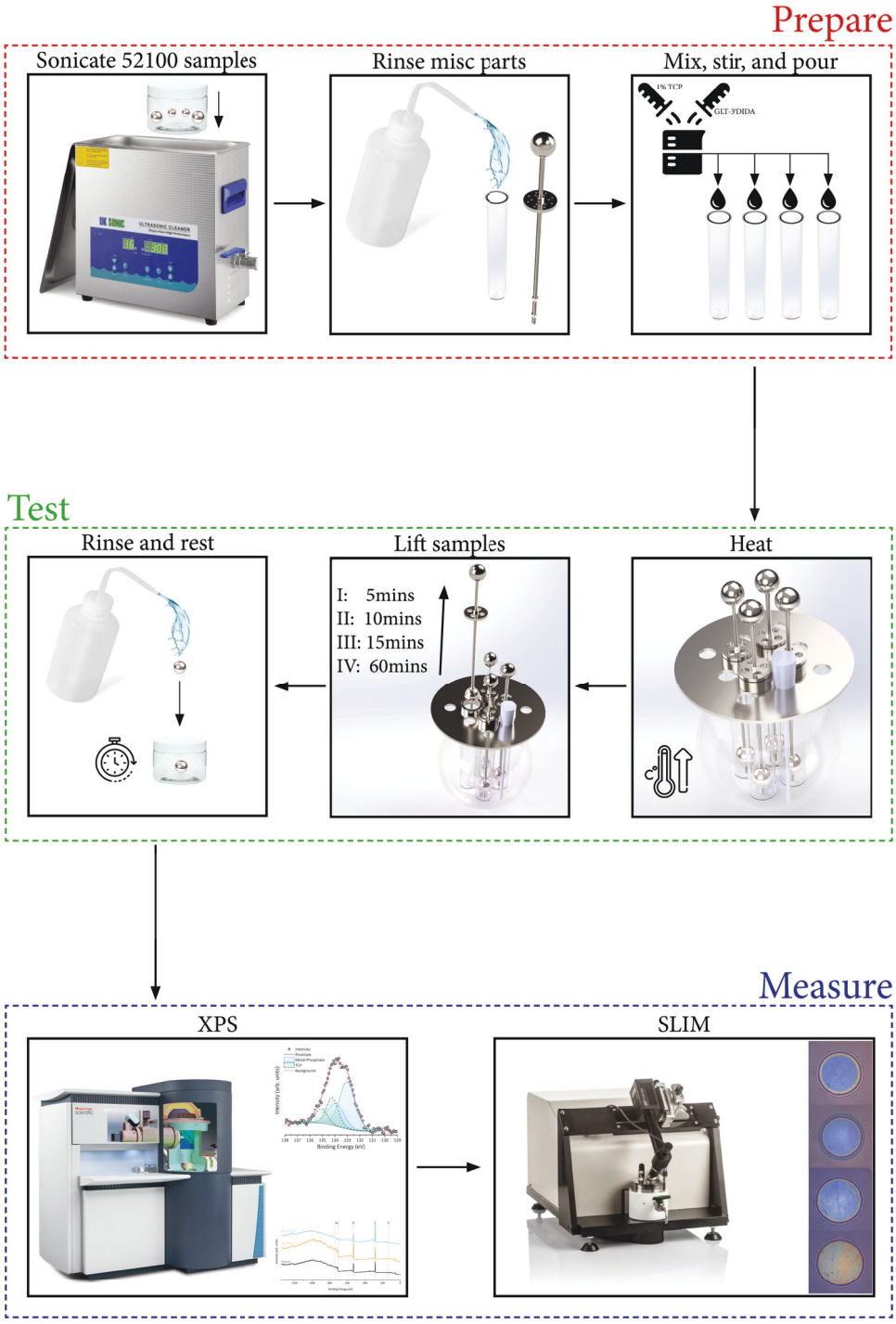


Fig. 4.3: Detailed flowchart depicting the experimental procedure (preparing, testing, and measuring) for the study of thermal decomposition of TCP on iron. Certain icons and vectors were adapted from [272] and [273], respectively.

The tests were performed with 6 mL solutions of 1 % tri-m-cresyl phosphate (Tokyo Chemical Industry). Two solvents were tested (see Section 4.2.2): GTL-3 solvent (Shell Global Solutions) and diisodecyl adipate (DIDA) from Tokyo Chemical Industry. All solutions were mixed as well as stirred at 70 °C for 1 hour, and poured into the glass tubes. Following, the heating mantle was set at the target temperature (125 °C , 185 °C , 190 °C , 195 °C , 200 °C , or 205 °C) and the magnetic stirrer at 1300 rpm. To study thin films in different stages of growth, 52100 ball samples were extracted from the assembly at various times after the silicone oil reached the target temperature. Immediately after each specimen lift-up, the 3/4 inch balls were rinsed with heptane to remove excess solvent from the sample surface. Finally, the specimens were sealed in soda-lime glass containers and allowed to cool down to room temperature.

The film height corresponding to each sample was measured using the spacer-layer imaging method (SLIM) [274]. Three test repetitions were performed at 190 °C as well as 205 °C to quantify the uncertainties and validate the reproducibility of the experimental procedure. Additional tests were conducted at 125 °C for 8 hours and analysed using XPS techniques to further understand the conditions favouring the formation and growth of phosphate films on iron (see Section 4.2.3). The flowchart depicted in Fig. 4.3 provides an overview of the experimental setup presented in this work.

4.2.2 Selection of materials

The choice of standardised spherical AISI 52100 precision super finish specimens (3/4 inch balls from PCS instruments) was motivated by:

i. The need to minimise the influence of roughness, small size, and geometrical asymmetries of the samples on the thin-film growth [275].

ii. The requirement for a material of elevated Fe content ($Fe_{\%} \approx 97\%$ for AISI 52100 [276]) to enable comparisons with our previously developed hybrid model [270] performed on an Fe(110) surface (see section 3).

iii. The desire to expedite the process of film-height measurements through the use of SLIM.

Nonetheless, utilising pure TCP to conduct the thermal growth experiments would not have been cost-effective. This can be justified by considering that submerging a 52100 3/4 inch MTM ball in pure mmm-TCP with a clearance of 3mm from the glass tube walls would demand approximately 15.3g of TCP (because $\rho_{TCP} = 1.247 g/cm^3$). Each run requires four 52100 specimens. Hence, a total weight of 61.2g of mmm-TCP that costs 1248.48 GBP (Tokyo Chemical Industry) would be necessary for each run. Therefore, we opted for mixtures of 1% mmm-TCP in base oils instead of pure TCP to render our experimental work financially viable.

Note that in our previous additive decomposition model (see Chapter 3), the solvent was not explicitly simulated [270]. Instead, solely mmm-TCP molecules reacted with the iron surface. Consequently, comparison of in-silico data with the corresponding experimental results would be valid solely by assuming that:

i. Solvent oxidation and blocking of TCP adsorption sites on the 52100 surface from decomposed base oil are negligible.

ii. Diffusion of TCP molecules through the solvent and towards the 52100 specimens is sufficiently rapid to not influence (or control) the overall film growth rate.

By taking the above assumptions into consideration and to diminish the influence of base oils on the formation and growth of thin films, we deployed XPS measurements (see Section 4.2.3) on the structure of mixtures of 1% TCP with the following base oils:

i. GTL-3 from Shell, which is a low-viscosity (6.5-11.0 mm^2/s at 40°C) as well as an oxidation-resistant solvent containing solely non-polar isomerised paraffins [277].

ii. DIDA from Tokyo Chemical Instruments, a synthetic dibasic ester featuring a flash point of 229 °C and a boiling point of 240 °C , both of which are greater than the maximum tested temperature of 205 °C.

4.2.3 XPS measurements

It is understood that the thorough investigation of the surface-layer structure of thin films grown using our experimental setup would demand XPS measurements performed on each reacted sample and for any tested temperature (i.e., 185 °C , 190 °C , 195 °C , 200°C , and 205 °C). However, due to the limited availability of access to the relevant equipment, we employed XPS in a complementary manner to the SLIM measurements. Effectively, XPS was performed prior to SLIM and on selected samples with the goal of validating that the obtained film composition was consistent with previous studies on the thermal decomposition of TCP on iron [77, 85, 87].

In particular, we opted to analyse five representative specimens:

i. Cleaned (as described in Section 4.2.1) 52100 ball used for reference (Pristine)

ii. Cleaned sample reacted with 1% TCP in GTL-3 at 125 °C for 8 hours (Low T GLT-3)

iii. Cleaned specimen reacted with 1% TCP in GTL-3 at 205 °C for 1 hour (High T GTL-3)

iv. Cleaned sample reacted with 1% TCP in DIDA at 125 °C for 8 hours (Low T DIDA)

v. Cleaned specimen reacted with 1% TCP in DIDA at 205 °C for 1 hour (High DIDA)

Moreover, for the sake of efficiently utilising our allocated time slot for XPS we performed detailed scans on selected species (Fe, C, O, P, S) and solely for samples ii, iii, iv, and v. Overall, the above representative specimens were selected after consulting the work of Arezzo [87] who reported that longer reaction times and reduced temperatures lead to an increase in the phosphate content of coatings formed on 52100 from TCP. To examine if phosphate thin films form under diverse experimental conditions we opted to analyze (with XPS) samples ii and iv which reacted at 80 °C lower but for 8 times longer than specimens iii and v. Note that 205 °C and 60 minutes (i.e., the conditions linked to specimens iii and v) correspond to the maximum testing temperature and elapsed time, respectively, for any sample imaged with SLIM.

All 52100 steel samples were measured in a Thermo K-alpha XPS system equipped with an Al kα X-ray source (hν=1486.6 eV). The spot size was fixed at 400 μm. A pass energy of 35 eV and 200 eV was used for core levels as well as surveys, respectively. The step size was set at

0.1 eV. The core-level spectra were fitted with Gaussian-Lorentzian convolution peaks and Smart-Shirley background [278] in Thermo Advantage software. Binding energies were determined with an uncertainty of approximately 0.1 eV. Peaks were calibrated utilising a C1s peak of 284.6 eV, and centres were referenced against the ThermoFisher Scientific [279] and NIST [280] XPS databases.

4.2.4 Spacer-layer imaging method (SLIM) measurements

The SLIM method uses a thin chromium layer to split white light into two paths. One beam reflects directly to a camera, while the other passes through the chromium and transparent film, reflects off a steel ball, and returns. As the beams recombine, their path difference creates interference patterns, forming coloured fringes that indicate variations in film thickness. These colours, captured by an RGB camera, are then matched to known thickness values to produce a detailed thickness map of the film [281].

In this work, a Mini-Traction Machine (MTM) from PCS instruments (MTM2) was utilised for the SLIM measurements. The MTM2 was equipped with the JAI CV-M9CL camera. The colour-height calibration curve was generated using a stationary contact profiling approach [274] through the MTM software (PCS instruments) on a clean 3/4 inch 52100 specimen (PCS instruments, decontamination process described in Section 4.2.1) with a height and distance of 131mm and 19mm, respectively. The load was fixed at 25N. The SLIM offline analysis software (PCS instruments) was deployed to estimate the film heights from the colourimetric images. Particularly, a least-squares search approach was implemented to obtain a height average over the sample area.

SLIM enables expeditious film height estimations with a resolution of a few nanometers (approximately 1nm for films thinner than 10nm) [282]. Nevertheless, such estimations can become error-prone due to the central assumptions associated with postprocessing colourimetric images to convert pixel colours to local film heights and subsequently to averaged-global film heights. Firstly, it is postulated that the adsorption spectra of the reacted samples match that of the pristine unreacted specimen deployed to capture the calibration curve. Secondly, SLIM assumes spatial (across all three directions) as well as temporal uniformity of the measured film's refractive index [281]. Finally, the refractive index is a function of the contact pressure [283].

The quantification of film-height estimation errors arising from the aforementioned assumptions (e.g., due to intensity shifts) demands an in-depth experimental analysis of adsorption spectra and refractive indexes of specimens reacted at various times and temperatures as well as measured at different contact pressures. Such a task was beyond the scope of the present work. Instead, further SLIM measurements were performed to quantify uncertainties associated with:

i. **Spatial height variations**. Two measurements were captured for each sample. Specifically, the second measurement was taken after rotating the specimen by 180° following the first measurement.

ii. **Loading cycles**. Two mapper steps (of 25N) were used for each specimen to investigate the effect of repeated loading/unloading on the generated colourimetric images.

iii. **Ageing**. All samples were stored in soda-lime containers and remeasured a week after the initial SLIM test.

iv. **Test repetitions**. Tests were repeated three times for specimens reacted with 1% TCP in GTL-3 at 190 °C and 205 °C (6 repetitions in total).

4.2.5 Film growth rate and activation energy estimation

Growth rates were calculated from the average height measurements at different times with two distinct methods. Firstly, a growth rate was estimated using a scaled (by the time interval) average formula:

$$r_{avg} = \sum_{i=0}^{N-1} \frac{h_{i+1} - h_i}{t_{i+1} - t_i} \tag{4.1}$$

Where N is the number of specimens measured at different times for the same run and h_i, t_i are the height and elapsed time of sample i, respectively. A second growth rate was estimated under the assumption of proportionality to the elapsed time:

$$\frac{dh}{dt} \propto t^{m-1} \tag{4.2}$$

Where $0 < m < 1$. Integration leads to the following equation:

$$h(t) = h_0 + r_{parabolic} t^m \tag{4.3}$$

Here, the growth rate $r_{parabolic}$ (in units of $[L][T]^{-m}$) can be obtained by interpolating the height versus time graphs (for the same run) with the parabolic fit (as in Eq. 4.3). Interpolations were performed utilising the non-linear fit function of Origin Pro software. Note that the literature shows evidence of parabolic growth behaviour for films from TCP and phosphate ester additives [81, 284]. Additionally, parabolic equations are widely used to fit height versus time data from experimental studies on a variety of thin-film coatings (e.g., hydrocarbons [285] as well as oxides and corrosion inhibitors [286–288]).

The attempt frequencies (ν) and activation energies (E_a) for film formation were evaluated by manipulating the Arrhenius equation as below:

$$r = \nu \exp \frac{-E_a}{RT} \Rightarrow \frac{r}{r_0} = \frac{\nu}{r_0} \exp \frac{-E_a}{RT} \Rightarrow ln\frac{r}{r_0} = ln(\frac{\nu}{r_0} \exp \frac{-E_a}{RT}) \Rightarrow ln\frac{r}{r_0} = ln\frac{\nu}{r_0} - \frac{E_a}{RT} \tag{4.4}$$

Where $r_0 = 1[T]^{-m}$ ($m = 1$ and $m = 0.5$ for scaled average and parabolic fits, respectively) is introduced to ensure that the exponentials and logarithms are non-dimensional. R is the universal gas constant and T represents the temperature. Eq. 4.4 is a linear expression of the form $y = ax+b$. Consequently, E_a and ν can be retrieved from the slope (a) and the intercept (b) of the $ln\frac{r}{r_0}$-1/T graph as:

$$E_a = -aR \tag{4.5}$$

$$\nu = e^b r_0 \tag{4.6}$$

The calculation procedure for the activation energies and attempt frequencies for film formation is similar to that followed to capture the C-O and P-O dissociation rates in our in-silico study of the thermal decomposition of TCP on iron (see Section 3.3.4 and Fig. 3.8) [270].

4.3 Results and discussion

4.3.1 Surface structure analysis with XPS

The XPS survey spectra of this study, along with the respective areas of detailed scans of thermally reacted samples (annotated with dotted lines), are presented in Fig. 4.4. The pristine sample (i) features contributions from Fe, O, and C species. Similar XPS spectra were obtained by Arezzo [87] where a clean 52100 specimen used as reference comprised 34.7 % and 46.7 % C and O, respectively. Generally, the strong carbon as well as oxygen signals can be attributed to the cleaning process (with heptane, acetone, and isopropanol as described in Section 4.2.1) or the polishing of the 52100 balls to achieve precision super finish. In the case of the thermally-reacted samples (ii, iii, iv, and v) such strong signals can be a consequence of the rinsing step leading to surface adsorption of heptane on the heated 52100 surface.

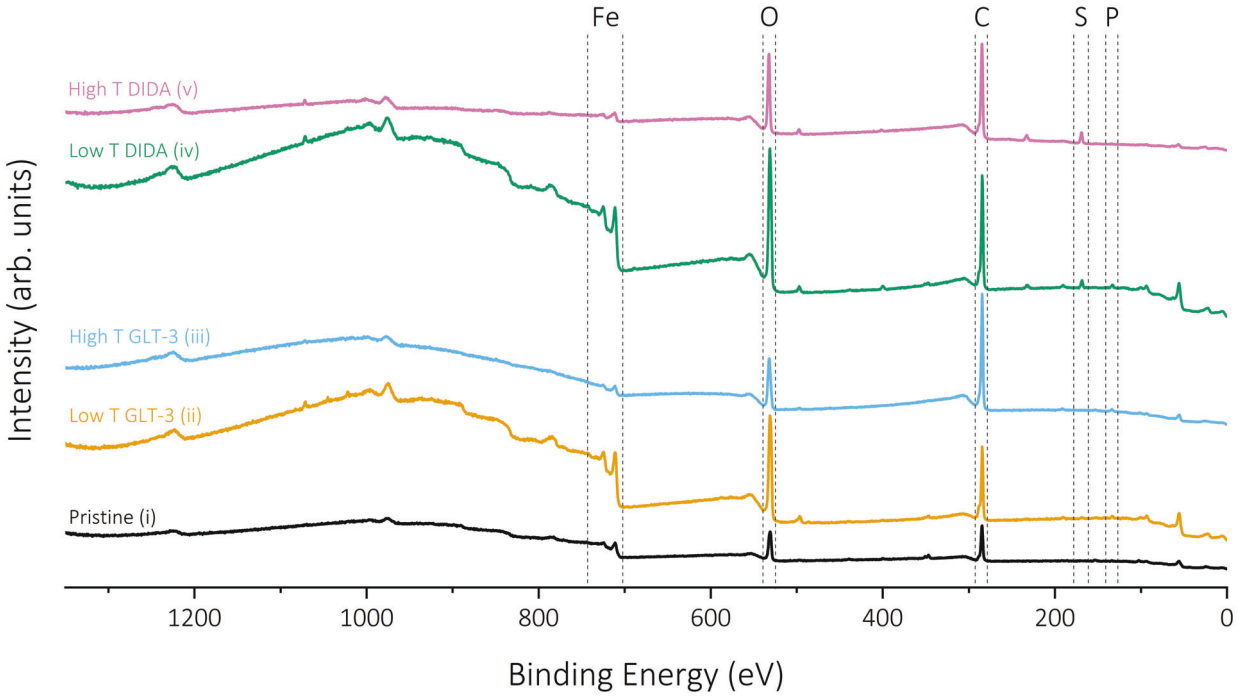


Fig. 4.4: Survey spectra for Pristine (specimen i), Low T GLT-3 (specimen ii), High T GLT-3 (specimen iii), Low T DIDA (specimen iv), and High T DIDA (specimen v) 52100 balls with annotated (dotted lines) regions of detailed elemental scans (Fe, O, C, P, respectively).

Samples ii, iii, and iv exhibit a P(2p) in addition to the Fe, O, and C peaks. Nonetheless, no phosphorus signal is detected on the High T DIDA specimen. Moreover, weak signals from Si (in samples i, iii, iv), Na (in specimens ii, iv, v), Zn (in sample ii), and N (in specimen v) indicate potential contamination of the 52100 balls during testing, transfer, or analysis in the XPS vacuum chamber. However, strong contributions from contaminant sulphur species are evident in both DIDA samples (iv and v). Detailed scans from 165-173 eV (illustrated in pictures 4.5) demonstrate that the relevant peaks of DIDA specimens are dominated by metallic sulphates.

Furthermore, from the XPS surveys (Fig. 4.4) it can be observed that the low temperature 52100 spheres (samples ii and iv) are dominated by oxygen species. By contrast, the high temperature samples (i.e., specimens ii and v) exhibit stronger contributions from carbon atoms. A separate graph for spectra with binding energies between 705 and 740 eV (associated with Fe

species) is illustrated in Fig. 4.6. The graph shows that samples ii, iii, and iv feature Fe(III). Contributions from both Fe(III) as well as Fe(II) are evident when it comes to the high-temperature DIDA sample. Finally, the pristine specimen additionally exhibits a weak metallic iron signal.

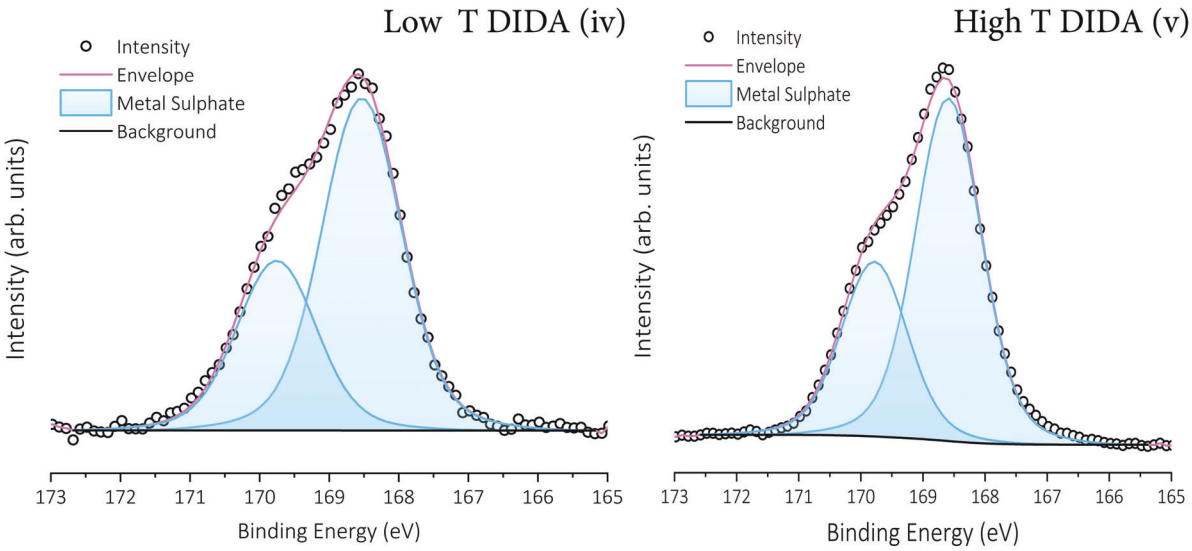


Fig. 4.5: Detailed XPS scans illustrating contributions from **S atoms** for Low T DIDA (sample iv - **left**) and High T DIDA (sample v - **right**).

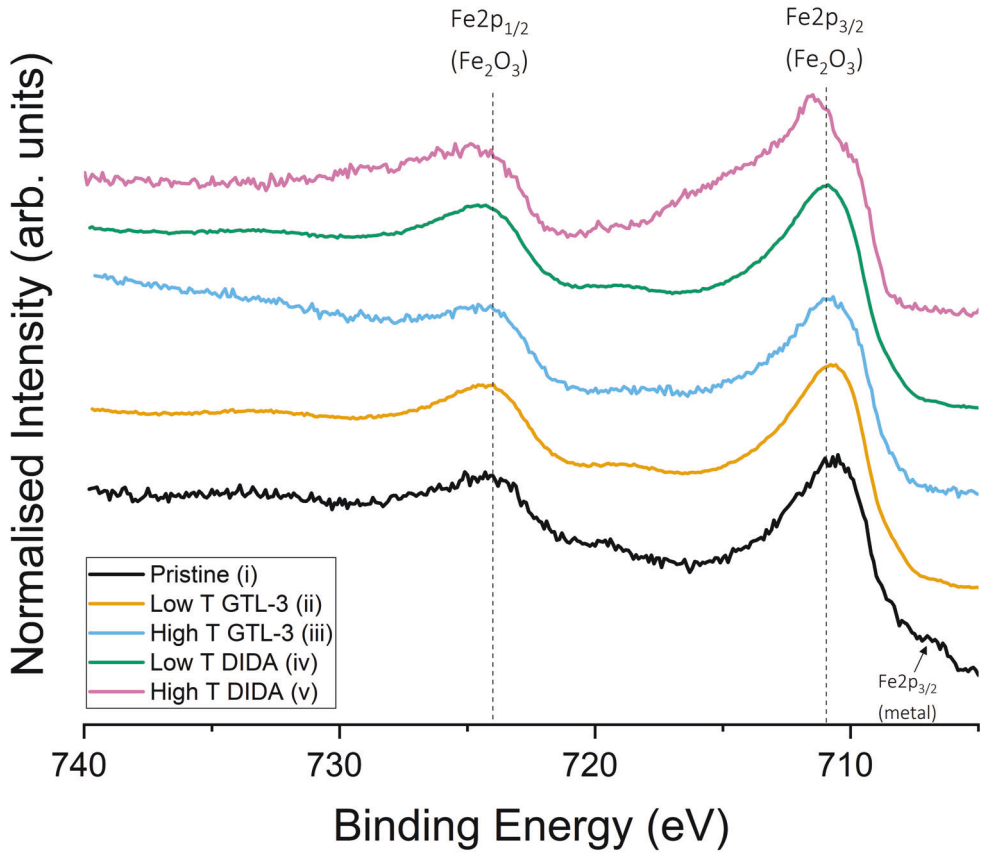


Fig. 4.6: XPS survey spectra for Pristine (specimen i), Low T GLT-3 (specimen ii), High T GLT-3 (specimen iii), Low T DIDA (specimen iv), and High T DIDA (specimen v) between 704 and 740 eV revealing contributions from **iron**.

Detailed scans of binding energies in the oxygen regime (527-536 eV) are presented in Figs. 4.7. Both low-temperature specimens (ii and iv) show contributions of similar intensity from C-O functional groups and iron oxides (Fe_2O_3). The high-temperature GTL-3 sample (iii) is dominated by C-O groups and shows a relatively reduced percentage of iron oxides, signifying the presence of a protective coating layer of elevated thickness. Ferrous oxides are not detected in the high-temperature DIDA sample (v), denoting that such a specimen features the thickest film of any measured 52100 sphere.

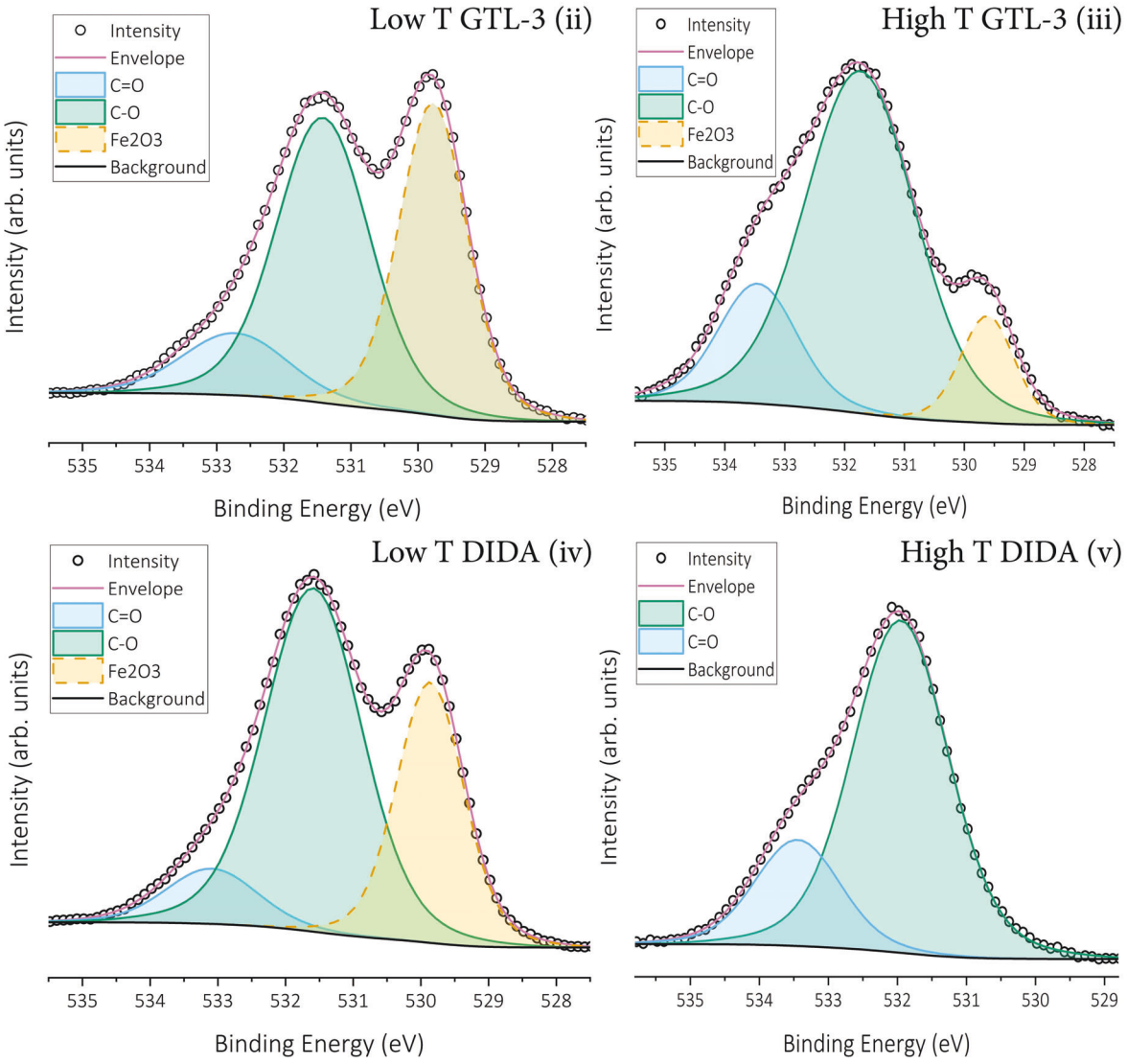


Fig. 4.7: Detailed XPS scans illustrating contributions from **O atoms** for Low T GLT-3 (sample ii), High T GLT-3 (sample iii), Low T DIDA (sample iv), and High T DIDA (sample v).

Images 4.8 illustrate detailed scans in the carbon region (281-291 eV). It is revealed that all samples have strong contributions from C-C functional groups. Furthermore, the high-temperature samples (iii and v) show more pronounced C-O than C=O bonds. In contrast, the low-temperature specimens (ii and iv) exhibit C-O and C=O signals of similar intensity.

Detailed scans for peaks associated with phosphorus species (129-138 eV) are provided in Fig. 4.9. Note that the high-temperature DIDA 52100 sphere (sample v) is excluded from images 4.9,

since no associated P(2p) peaks are identified. Specimens ii, iii, and iv feature metal-phosphate compounds at 133.09 eV, 133.02 eV, and 133.17 eV for Low T GLT-3, High T GTL-3, and Low T DIDA, respectively. The high-temperature GLT-3 sample exhibits further phosphorus contributions consistent with the literature report of Wheeler and Faut [85]. In particular, Wheeler and Faut investigated the XPS spectra of adsorbed TCP on iron and reported a characteristic P(2p) peak at 134.2 eV. A summary of the binding energies of P as well as S species centres for the various tested samples is given in Table 4.1.

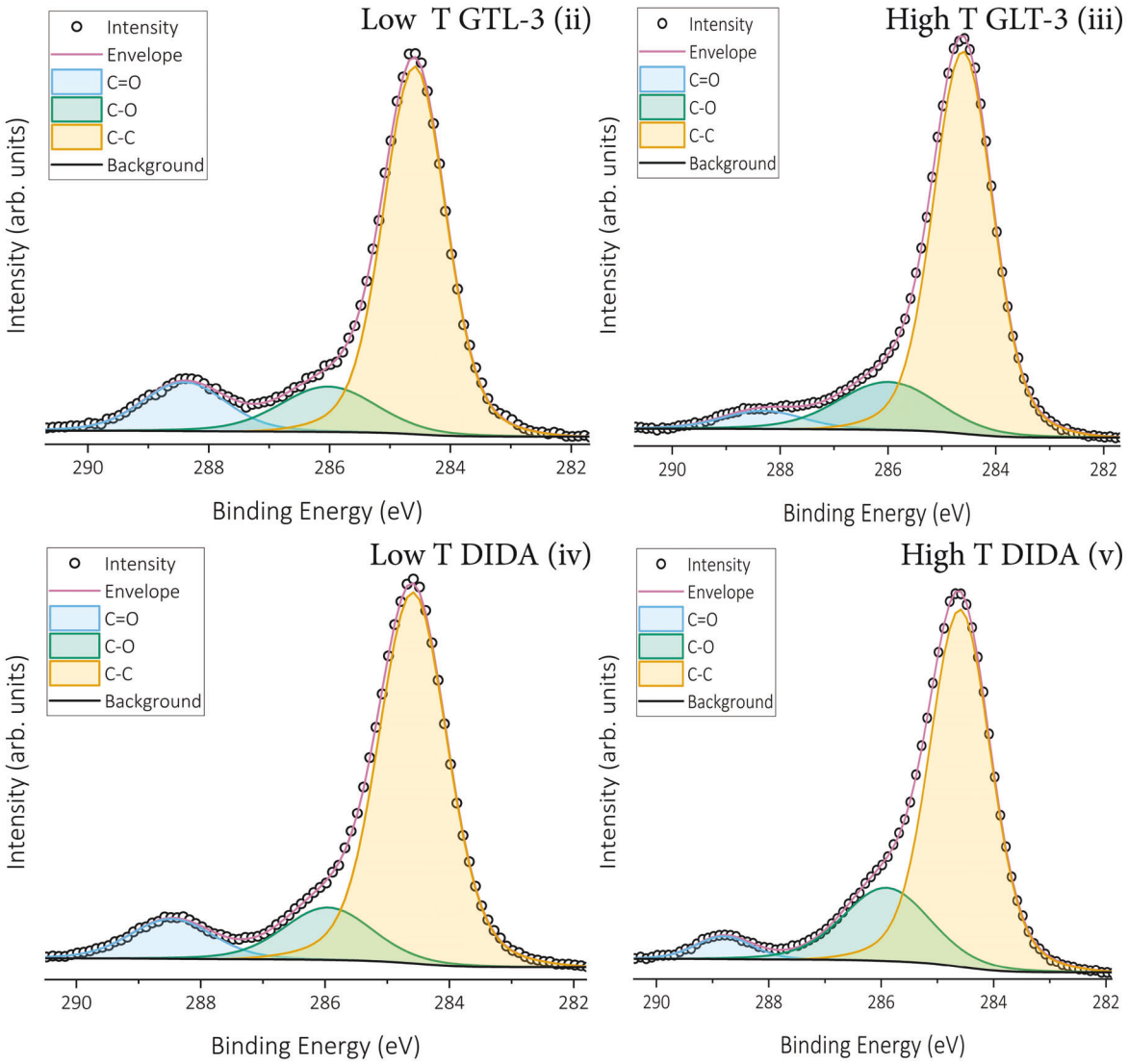


Fig. 4.8: Detailed XPS scans illustrating contributions from **C atoms** for Low T GLT-3 (sample ii), High T GLT-3 (sample iii), Low T DIDA (sample iv), and High T DIDA (sample v).

In any case, the additional P(2p) contributions indicate the presence of partially dissociated or unreacted TCP molecules on the surface of the high-temperature GTL-3 sample. Such observation underlines the influence of growth conditions on the structure of the phosphate films. Specifically, lower temperatures and longer reaction times appear to favour the complete decomposition of TCP molecules, leading to the formation of iron-phosphate coatings. In contrast, higher temperatures are linked to complexes comprising iron-phosphates and unreacted or partially decomposed TCP

molecules. Such behaviour could be associated with the fact that elevated temperatures can result in oxidation and subsequent surface adsorption of solvent. As such, GTL-3 adsorbates (along with their reaction products) can block TCP adsorption sites and therefore, hinder the activation and complete dissociation of TCP on the 52100 surface [69, 77, 78, 87].

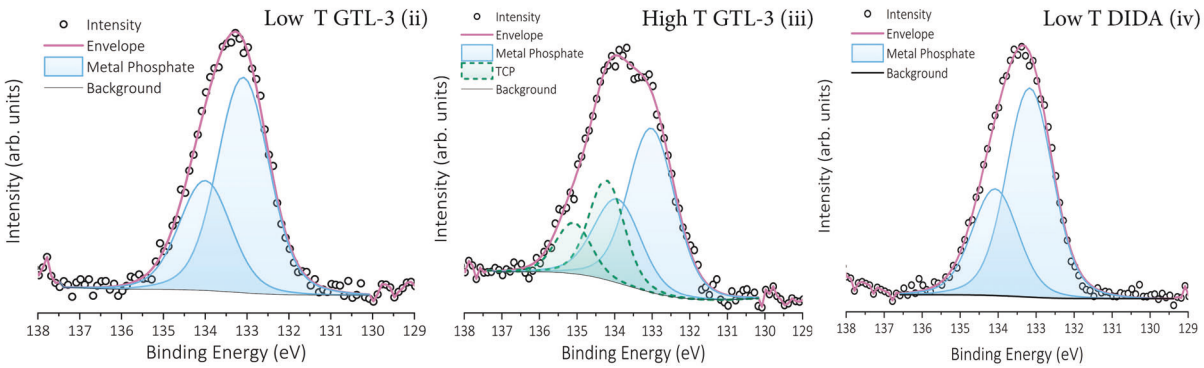


Fig. 4.9: Detailed XPS scans illustrating contributions from **P atoms** for Low T GLT-3 (sample ii), High T GLT-3 (sample iii), and Low T DIDA (sample iv).

Table 4.1: Selected binding energies (BE) of detected contributions for Pristine (i), Low T GLT-3 (ii), High T GTL-3 (iii), Low T DIDA (iv), and High T DIDA (v) specimens.

Sample	Phosphate BE (eV)	TCP BE (eV)	Sulphate BE (eV)
Pristine (i)	-	-	-
Low T GTL-3 (ii)	133.09	-	-
High T GLT-3 (iii)	133.02	134.2	-
Low T DIDA (iv)	133.17	-	168.63
High T DIDA (v)	-	-	168.59

Overall, the results obtained from our XPS analysis for all specimens except for the high-temperature DIDA sample (v) agree well with the findings of equivalent studies in the literature. For example, Arezzo [87] investigated the surface structure of films grown from aged mixtures of TCP with non-polar oils on 52100 discs. They reported that the top layers of the analysed samples were dominated by carbon as well as oxygen species, with lower-intensity ferrous and phosphate contributions. Similar results were obtained by Wheeler and Faut [85]. Their XPS analysis concluded that the surface of iron specimens reacted with TCP exhibited strong O(1s) ($\approx$ 57% peak area) as well as O(1s) signals ($\approx$ 38% peak percentage) with weaker P(2p) components ($\approx$ 5% peak percentage).

Moreover, Saba and Forster [77] studied the composition of fresh and oxidised 1010 steel coupons reacted with pure m-TCP at 475 °C under vacuum conditions. In their work, they revealed that the top layer of the thermally reacted films comprised ferrous oxides, carbonaceous compounds (originating from attached organic groups and/or TCP molecules), as well as various phosphate functional groups (e.g., P-O, P-O-P, P-O-C, iron phosphates). Nonetheless, caution should be exercised when it comes to the comparison of experimental studies related to thin films from neat TCP and mixtures of TCP with base oils, since evidence suggests that the structure of the resulting coatings can differ [88].

Additionally, the surface structure of the thin films obtained from samples ii, iii, and iv is similar to that reported in our previous hybrid kMC/MD work (see Chapter 3 and graph 3.19)

[270]. However, a central difference arises from the fact that our model predicted the strong presence of oxygen as well as carbon species, but not that of Fe atoms at the outermost layer of the protective coatings.

Conclusively, the structure of the films originated from our experimental setup for all samples (except for specimen V) is consistent with reports from the relevant literature. Specifically, no contributions from phosphates were identified in the high-temperature DIDA specimen. Such an instance is indicative of extensive solvent decomposition and deposition on the 52100 ball, which ultimately results in an oxidised base oil (i.e., DIDA) film rather than a coating from friction modifiers (i.e., TCP) [87].

Recall that the main goal of our experimental analysis was the validation of the growth rates obtained from our previous in-silico study [270] on the thermal decomposition of TCP on iron (see Section 4.1). Consequently, we opted to employ SLIM solely on mixtures of TCP with GLT-3 (see Section 4.3.2). This decision was motivated by the fact that the XPS analysis on coatings from GLT-3 yielded realistic top-layer compositions for a range of experimental conditions (i.e., both 125 °C for 8 hours and 205 °C for 1 hour) as expected for thermally reacted films from TCP on ferrous surfaces. In contrast, the structure of thin films from DIDA appears to be consistent with protective lubricant additive coatings solely when it comes to long reaction times and lower temperatures - conditions that inherently favour the formation of phosphate films [87].

4.3.2 Film height analysis with SLIM

The colourimetric images retrieved from the SLIM measurements on 1% TCP in GTL-3 mixtures for different temperatures and reaction times, along with a representative colourbar (reproduced using the calibration files as generated by the PCS offline analysis software), are depicted in Fig. 4.10. Generally, it can be observed that the film thickness increases at elevated temperatures as well as longer reaction times. Note that the maximum film height is 28.357 ± 6.295 nm corresponding to the sample collected at 60 minutes and 205 °C . Moreover, it is illustrated that certain specimens (e.g., 200 °C at 15 minutes or 195 °C at 10 minutes) exhibit non-uniform thickness. Nevertheless, the least-squares search approach averages the heights corresponding to each pixel of the interference pattern. As such, spatial non-uniformities are taken into consideration in the calculation of the mean film thickness.

The temporal evolution of the average film heights for the thermally grown films reacted at 185 °C , 190 °C , 195 °C , 200 °C , and 205 °C is presented in Figs. 4.11**a-e)**. Previous studies on the decomposition of TCP and phosphate ester additives reported that the deposit weight (in $\mu g/cm^2$) features a parabolic relationship with the reaction time [81, 284]. By extension, it can be assumed that the film thickness exhibits a parabolic behaviour with the growth time (see Eq. 4.3). In this regard, the parabolic fits generated for our experimental dataset (with a fit exponent m=0.5) are included in Figs. 4.11**a-e)**. Fig. 4.11**f)** depicts a parabolic model that describes the growth of the thin films resulting from mixtures of 1% TCP in GTL-3 on 52100 for temperatures between 185 °C and 205 °C.

The error bars on the y-axis quantify uncertainties linked to spatial height variations, loading cycles, and ageing (as discussed in Section 4.2.4). Specifically, the length of the error bars is the average of the standard deviations of the three aforementioned contributions to the uncertainty of the height measurements. Also, three test repetitions were performed at 195 °C and 205 °C (as

mentioned in Section 4.2.1). Therefore, the length of the error bars of the 195 °C and 205 °C data points is the mean of the standard deviations of uncertainties associated with height variations, loading cycles, ageing, as well as test repetitions.

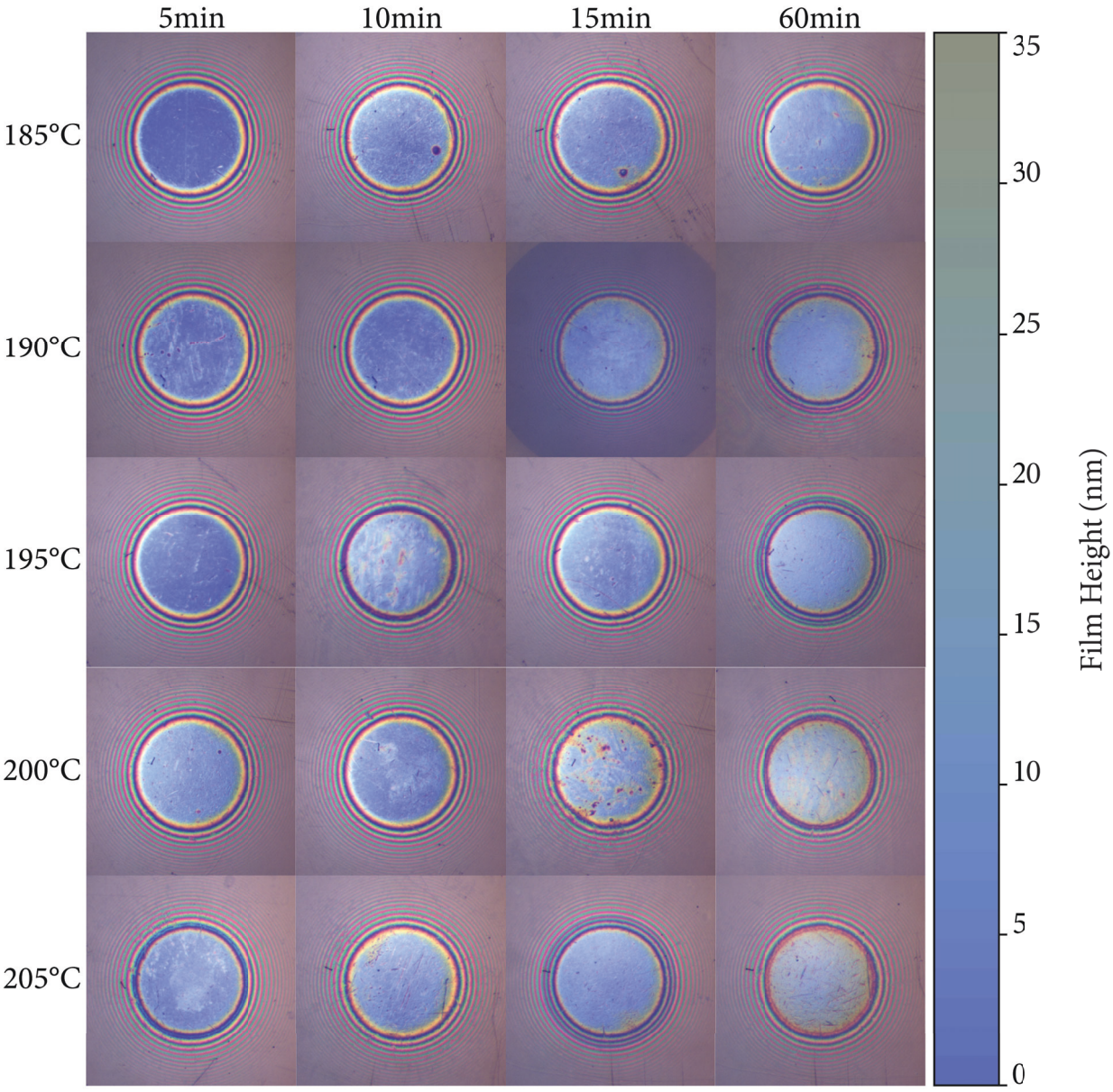


Fig. 4.10: Colourimetric images of our SLIM measurements for samples reacted at 185 °C , 190 °C , 195 °C , 200 °C , and 205 °C . The colourbar on the right was generated using the calibration file of the PCS offline software.

The violin plots of Fig. 4.12 provide a graphical representation of the effect of different sources of uncertainties in the height measurements. Once again, the loading cycles, height variations, and ageing plots include contributions from all measurements, while data points solely from the 195 °C and 205 °C tests were utilised for the test repetitions class.

It can be observed that the uncertainties specifically linked to the SLIM measurements (i.e., loading cycle and ageing with mean errors of 0.599 nm and 1.850 nm, respectively) are comparable to the intrinsic uncertainties associated with the microscopy technique ($\approx 1nm$ for films thinner than 10 nm [282]). Furthermore, the height variations category shows average errors of 1.567 nm.

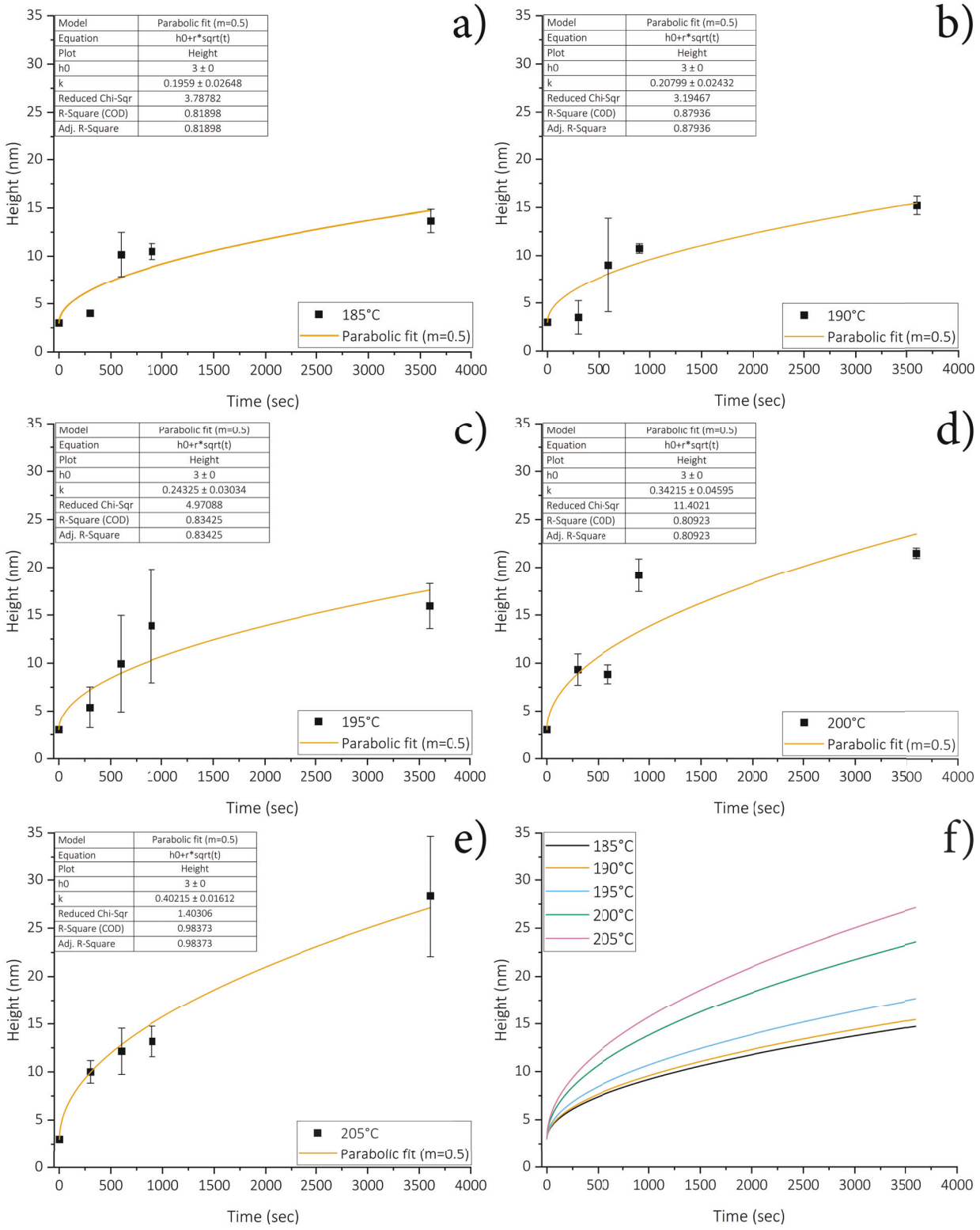


Fig. 4.11: Mean film height of thermally reacted thin films from mixtures of 1% TCP in GTL-3 along with associated parabolic fits. Figs. **(a-f)** correspond to tests at 185°C , 190 °C , 195 °C , 200 °C , 205 °C , and Fig. **(f)** shows the parabolic fit model retrieved from our analysis. The error bars quantify uncertainties originating from spatial height variations, loading cycles, ageing (for all samples), and repeated tests (only for specimens reacted at 195 °C and 205 °C).

Therefore, it can be concluded that the mean film thickness calculation method (i.e., least-squares) is not significantly influenced by the spatial non-uniformities of the grown thin films. Nonetheless,

the broader shape of the violin plot corresponding to height variations indicates higher uncertainty variability.

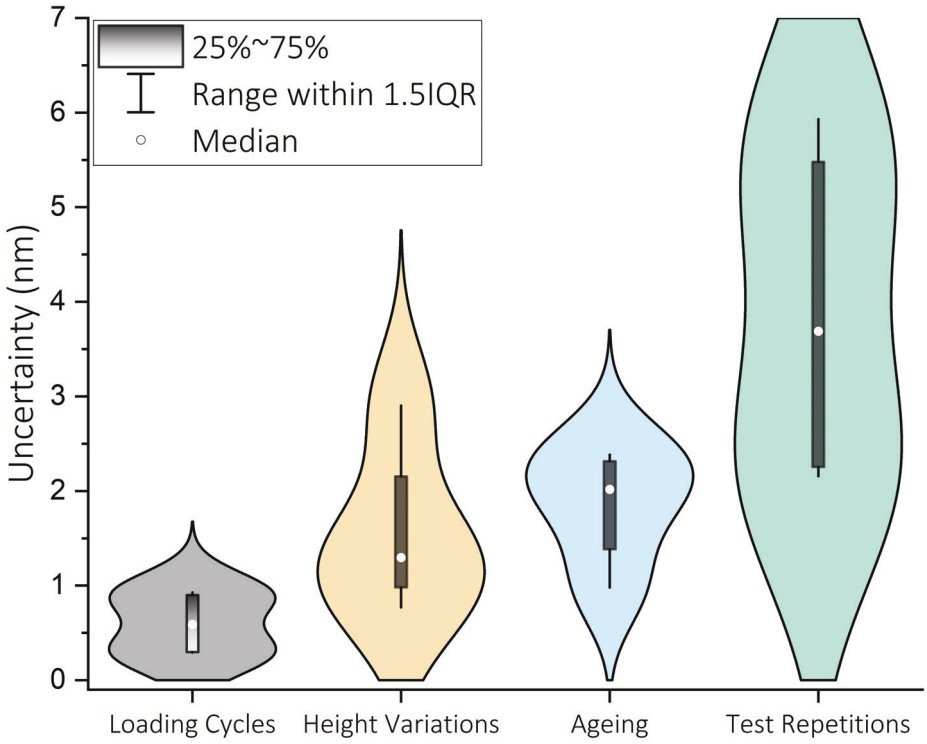


Fig. 4.12: Violin plots quantifying the contributions of different classes of experimental uncertainties to the SLIM height measurements. Generated in origin with a smooth kernel and a Scott bandwidth.

Finally, the test repetitions class exhibits relatively elevated variability and features the maximum mean error value of any quantified uncertainty source (3.867 nm). This observation can be justified by considering that both extrinsic as well as intrinsic factors linked to SLIM affect the uncertainties of test repetitions. Examples of extrinsic factors include specimen contamination during transferring or testing, adjustments to the cleaning procedure, or slight deviations in the execution of the sample lift-up step. On the other hand, oil entrapment between the specimen and the partially reflective window, age of equipment, and film-thickness estimation method can be listed as intrinsic uncertainty contributors to the test repetitions category [281].

The growth rates evaluated utilising the scaled average (see Eq. 4.1) and parabolic fit (see Eq. 4.3) approaches (see Section 4.2.5) are presented in Fig. 4.13. Note that the parabolic and scaled average rates have units of $nm\ sec^{-0.5}$ and $nm\ sec^{-1}$, respectively. Therefore, they are not directly comparable. Nevertheless, both rates yield useful insights since the scaled average rate can be effortlessly correlated with other literature reports. On the other hand, the parabolic rate describes more accurately the non-linear character of the temporal evolution of the thin films.

Assuming that the growth rates follow an Arrhenius-type relationship (Eq. 4.4) with the reaction temperature, the activation energies (E_a) and attempt frequencies (ν) associated with the film-formation rates can be obtained from the intercepts and the slopes (see Eqs. 4.5 and 4.6) of the linear fits illustrated in Fig. 4.14 (see Section 4.2.5). The results of such analysis are given in Table 4.2. Specifically, the scaled average approach resulted in an activation energy of 18.167 kcal/mol and an attempt frequency of 2.067 10^6 $nm\ sec^{-1}$, while the parabolic fit method yielded an activation energy of 16.820 kcal/mol and an attempt frequency of 1.908 10^7 $nm\ sec^{-0.5}$.

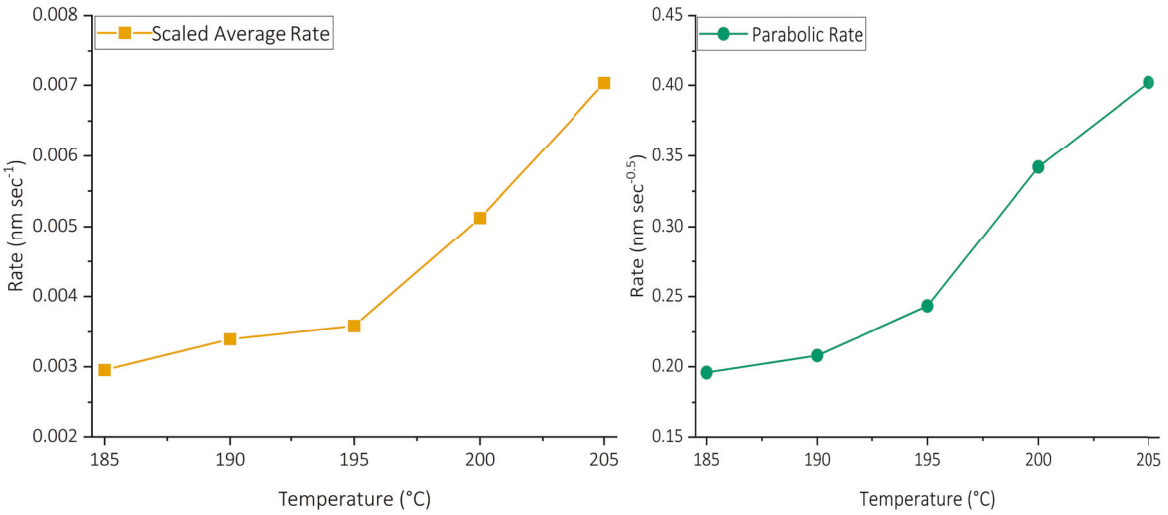


Fig. 4.13: Film growth rates calculated using scaled averages **(left)** and parabolic fits **(right)** using Eqs. 4.1 and 4.3, respectively.

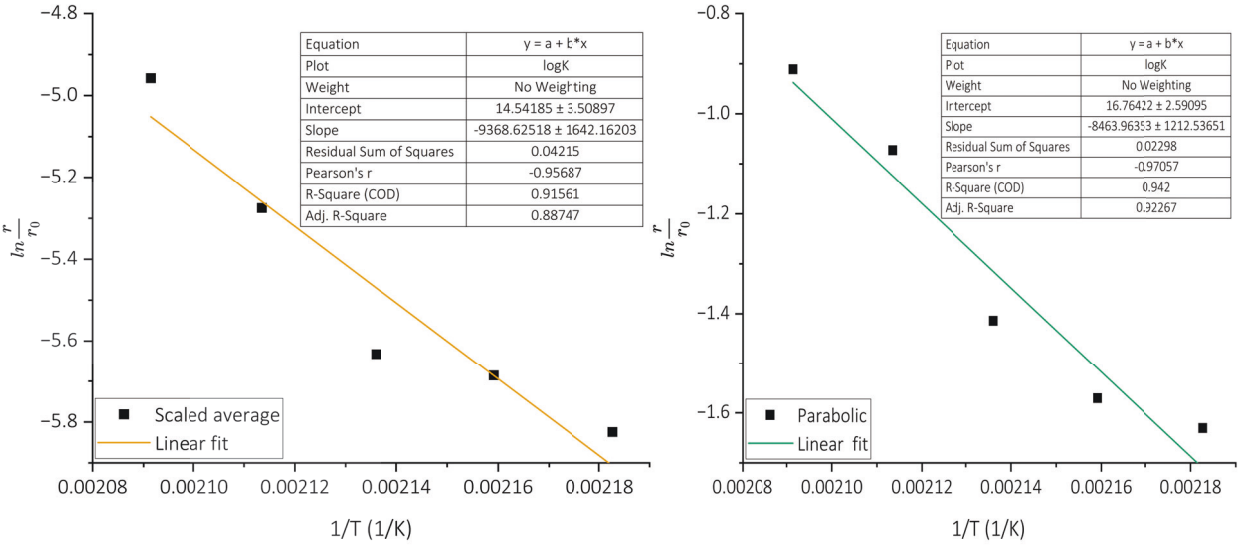


Fig. 4.14: Rate versus inverse of temperature graphs along with corresponding linear fits for the scaled average **(left)** and parabolic approaches **(right)** using Eqs. 4.1 and 4.3, respectively. Note that $r_0 = 1s^{-1}$ and $r_0 = 1s^{-0.5}$ for the scaled average and parabolic fits, respectively.

Table 4.2: Activation energies (E_a) and attempt frequencies (ν) evaluated using the scaled average (Eq. 4.1) parabolic fit (Eq. 4.3) methods.

Method	Scaled Average	Parabolic fit
E_a (kcal/mol)	18.617	16.820
ν ($nm\ sec^{-1}$ or $nm\ sec^{-0.5}$)	2.067 10^6	1.908 10^7

To enable comparisons with relevant results from the literature, the scaled average growth rates are extrapolated for temperatures beyond the experimentally-tested regime (185-205 °C). This is performed through the use of the associated E_a as well as ν values (Table 4.2) in the Arrhenius equation ($r = \nu \exp \frac{-E_a}{RT}$, with T being the temperature).

Fig. 4.15 illustrates the scaled average rates retrieved from our experimental setup. Additional data points on the graph depict:

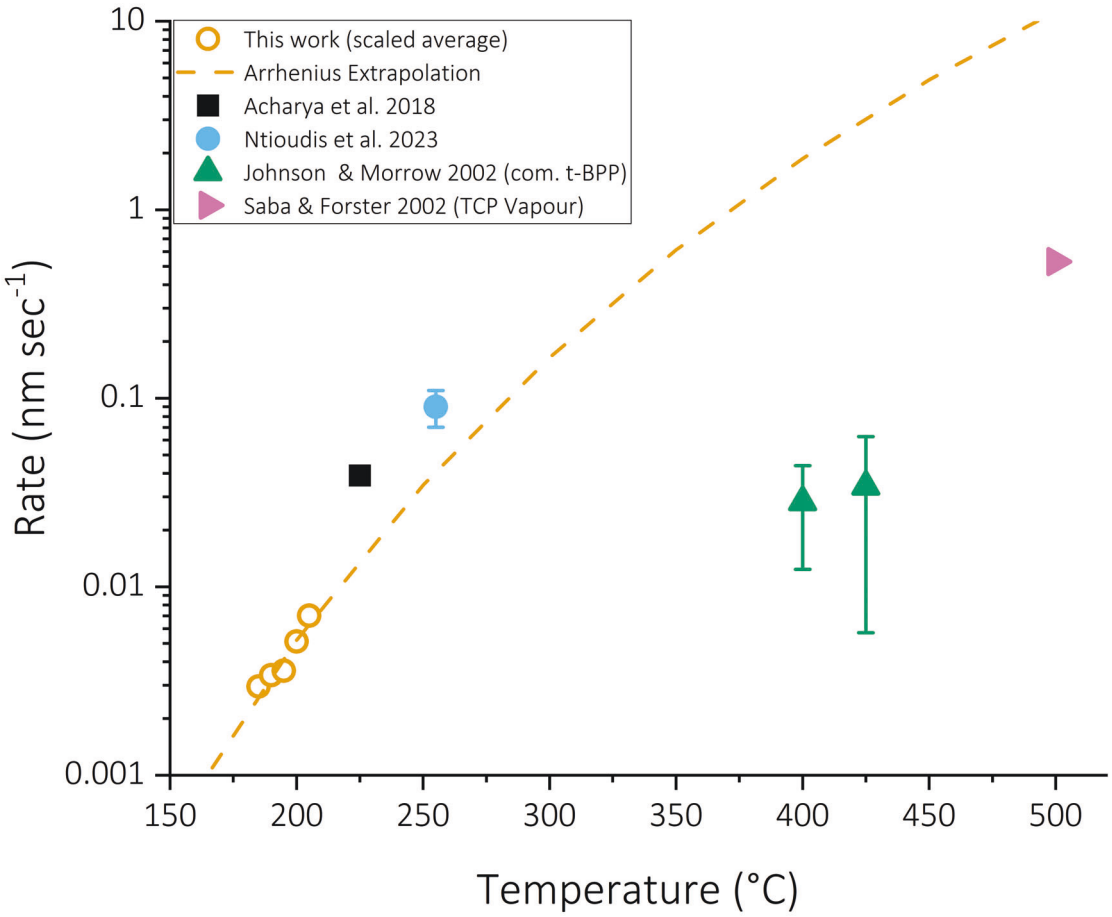


Fig. 4.15: Experimentally obtained film-growth rates. An Arrhenius-type model is used to extrapolate data beyond the tested temperatures (185 °C-205 °C). Additional data points correspond to the studies of Acharya et al. [89], Johnson and Morrow [67], Ntioudis et al. [270], and Saba and Forster [77].

- A rate of 0.039 nm/s (at 225 °C) estimated by Acharya et al. through QCM investigation [89].
- A rate of 0.09 ± 0.01992 nm/s (at 255 °C) obtained from our previous in-silico studies on the decomposition of TPC on Fe(110) (see Section 3) [270].
- Rates associated with the reaction of an iron foil with a phosphate ester lubricant (com. t-BPP) comprising predominantly meta and para TBPP compounds as well as TPP molecules [67]. The mean values and errorbars (0.02816 ± 0.01578 nm/s at 400 °C and 0.0341 ± 0.02839 nm/s at 425 °C) are linked to the average and STD of four measurements (at 15, 30, 60, 120 min as in Table 6 of the relevant paper).
- A rate of 0.53 nm/s obtained from the study of Johnson [67] for neat TCP vapours reacting with 1010 steel coupons.

It can be observed that our extrapolated rates are reduced compared to the rates of Acharya et al. [89] and Ntioudis et al. [270]. Specifically, the extrapolated rates are 0.014 nm/sec at 225 °C and 0.04 at 255 °C. Nonetheless, subtle differences in the underlying coating growth conditions exist between the current work and the aforementioned studies. For instance, the results of Acharya et al. [89] were performed on preoxidised ferrous surfaces and with 5% solutions of mixtures of

TCP isomers in DIDA. In contrast, cleaned (process described in Section 4.2) 52100 precision super finish specimens and 1% solutions of mmm-TCP in GTL-3 were used for the tests presented in the current work. Furthermore, our experiments were performed at atmospheric pressure, while a pressure of 0.01kPa was utilised in our hybrid off-lattice kMC/MD simulations on the thermal decomposition of mmm-TCP on iron [270].

Also, the extrapolated experimental rate is relatively elevated compared to those reported in the studies of Johnson & Morrow [67]. However, discrepancies between the rates of these studies are expected since the resulting thin films originated from two distinct mixtures of phosphate esters (i.e., TCP in GTL-3 for this work and com. t-PBB in the study of Johnson & Morrow [67]). Finally, the extrapolated rate at 500 °C is increased relative to the rate of Saba & Forster. This can be attributed to the following factors. Firstly, the extrapolated value at 500 °C is by 295 °C higher than the maximum tested temperature of this work (205 °C). A more accurate extrapolated estimate requires supplementary experiments at higher temperatures. Secondly, the experiments of Saba & Forster were performed in vacuum conditions and with neat TCP vapours. In contrast, the experiments of this work were performed with solutions of 1% in GTL-3 and at atmospheric pressure. Such differences in experimental details can influence the kinetics of thin-film formation and result in discrepancies in the estimated growth rates.

4.4 Conclusions and further work

In this chapter, we presented an experimental setup designed for the investigation of the kinetic (e.g., growth rate) as well as structural characteristics (e.g., top-layer composition) of thin films grown at solid-liquid interfaces. The setup was deployed for the study of protective coatings from mixtures of 1% TCP with two different solvents (i.e., DIDA and GTL-3) on 52100 samples. A gap was identified in the literature when it comes to the in-depth characterisation of the kinetic aspects of the thin films from the thermal decomposition of TCP on ferrous substrates. Therefore, the experimental study was motivated by the need to validate the results obtained from our previous hybrid off-lattice kMC/MD simulations on the surface adsorption of TCP on Fe(110).

Thin films grown from mixtures of 1% TCP (with DIDA and GLT-3) at 125 °C for 8 hours, as well as at 205 °C for 1 hour, were analysed with XPS. Such analysis showed that all samples were dominated by carbon and oxygen species. Moreover, the XPS results indicated that lower temperatures and longer reaction times can limit solvent oxidation and deposition on the substrate, thus favouring the formation of protective coatings containing metallic phosphates. In contrast, thin films grown at elevated temperatures and shorter reaction times (e.g., high-temperature GTL-3 sample reacted at 205 °C for 1 hour) feature P(2p) peaks with contributions from both metallic phosphates as well as partially decomposed or unreacted TCP molecules.

Furthermore, the surface-layer composition of both low-temperature samples (GTL-3 and DIDA) as well as that of the high-temperature GLT-3 specimen align well with structures associated with thin films from TCP on iron. Nonetheless, phosphates were not detected in the high-temperature DIDA sample. Overall, our XPS study suggests that mixtures of 1% TCP in DIDA could not produce phosphate-containing films under diverse experimental conditions (i.e., temperatures and reaction times). Consequently, SLIM measurements and subsequent calculations of growth rates were focused solely on solutions of 1% mmm-TCP in GTL-3.

The performed SLIM measurements on GTL-3 samples underline that the thin-film height exhibits a parabolic relationship with the reaction time. As expected, higher temperatures lead to faster growth rates and thicker thin films. The estimated growth rates were extrapolated beyond the maximum investigated temperature of 205 °C through an Arrhenius-type equation. The extrapolated rates compare well (within an order of magnitude) with a relevant experimental study and our off-lattice kMC/MD investigation on the thermal decomposition of TCP films on iron. Nonetheless, discrepancies between the evaluated growth rates can result from differences in the experimental conditions or the simulation parameters associated with the thermal decomposition of TCP on iron.

With that respect, an in-depth validation of our off-lattice hybrid kMC/MD model demands simulations to be performed at the same temperatures and pressure used for the experiments of this chapter. Furthermore, additional XPS analyses have to be conducted in the future in the direction of thoroughly understanding the effects of solvent as well as environmental conditions (e.g., pressure, temperature, reaction time) on the composition of the grown protective coatings. Finally, the elemental composition of such thin films must be investigated as a function of film thickness through ion-sputtering techniques. Such an investigation will enable the direct correlation of elemental composition maps as obtained from our kMC/MD model with experimental results.

Chapter 5

General off-lattice hybrid kMC/MD model: PAPRECA

5.1 Motivation for open-source implementation

In Chapter 3, we presented a hybrid off-lattice kMC/MD model to study the formation and growth of thin films on solid surfaces [270]. The model was validated through a benchmark application related to lubricant-additive decomposition. A computationally efficient (see Section 3.3.6) in-house code written in Fortran95 was utilised to perform the hybrid kMC/MD simulations. Nevertheless, it became apparent that certain practical aspects related to software implementation limited the transferability, scalability, and computational efficiency of the proposed hybrid kMC/MD model.

Firstly, the utilised code was specifically developed to capture the formation and growth of coatings from the thermal decomposition of TCP on iron Fe(110). In particular, the source code contained a series of parameters (e.g., rates, involved species) related to the predefined events of the kMC stage (e.g., adsorption/desorption, reactions, diffusion). Additional hardcoded parameters such as force field coefficients, spatial coordinates of surface and adsorbate atoms, thermostat as well as minimisation algorithm settings were included to describe the MD stage. As such, extension of the hybrid methodology to study other relevant applications beyond thin films from TPC molecules (e.g., catalysts [137], nanoparticles [140], or energy-storage devices [98], see Section 2.1.1) would necessitate a series of modifications directly performed on the source code. This impacted the transferability of our code and its extension to relevant projects of interest in materials science, chemistry, physics, biology, and engineering applications.

Moreover, the kMC stage of the hybrid code was not parallelised. Consequently, atomic information (e.g., positions, velocities, charges, neighbour lists) had to be serialised following every MD stage and subsequently, parallelised (by LAMMPS) after kMC stage. This introduced an efficiency overhead to our kMC/MD code. Furthermore, the serial implementation of the kMC stage negatively affected the scalability of the hybrid code and its performance in high-performance computing (HPC) services.

Limitations associated with interfacing between the kMC stage (written in Fortran95) and the MD stage (performed in LAMMPS) of the hybrid code further impacted the performance of the proposed (in Chapter 3) methodology [270]. Specifically, a simplistic interface based on text files was utilised to communicate information between the in-house Fortran95 code of the kMC stage

and LAMMPS. This elevated the implementation complexity of the code since the text files had to be correctly formatted at all times. Additionally, the use of text files introduced difficulties in the debugging process as detecting minor errors (e.g., when it comes to the coordinates of atoms) became more challenging due to the lack of strict data validation and the increased likelihood of formatting inconsistencies. In certain cases, interfacing through text files even rendered the execution of the hybrid kMC/MD code on HPC services impossible due to limitations linked to file reading, writing, and accessing speeds on clusters (e.g., CX3 cluster at Imperial College). Overall, such a simplistic communication approach hampered the computational efficiency due to excessive input/output (I/O) operations required to populate the neighbour and bond lists as well as store and export the positions, velocities, and charges of atoms at each timestep.

Finally, it can be reasoned that the extensibility of the hybrid kMC/MD code was restricted by the selection of the programming language of the kMC stage (i.e., Fortran95). Firstly, interfacing a Fortran95 code (i.e., in-house code of kMC stage) with a C/C++ codebase (LAMMPS used for the MD stage) is not straightforward and relies on C++ wrappers that allow the execution of C-style subroutines from Fortran95. Such wrappers may also introduce performance overhead and impact the computational efficiency and the scalability of the code. Secondly, the utilisation of Fortran95 for our hybrid kMC/MD code can increase the complexity of the software due to the lack of native interfacing between Fortran95 and C++ classes. This is justified by considering that additional C-style wrappers are required to access and modify C++ objects (e.g., classes and variables). Lastly, C/C++ can be preferred over Fortran95 in open-source implementations due to its active community, variety of available standard libraries (e.g., Boost, STL, Eigen, MPI, CUDA), implementation flexibility, and its native support for modern data structures and parallel computing [289].

The aforementioned limitations and considerations associated with the hybrid kMC/MD code used for the simulations of Chapter 3 motivated us to transition from a Fortran95 to a C/C++ implementation. Seamless integration and communication between the kMC and MD stages of the code were prioritised. User-friendliness was emphasised and a coordinated effort was made to render the newly introduced software as extendable as possible. Such software design choices aligned with our desire to contribute to the open-source community by enabling hybrid kMC/MD simulations for diverse applications of interest in materials science, chemistry, physics, biology, and engineering.

Section 5.2 provides a summary and a statement of need related to the newly presented open-source kMC/MD software. Following, specific aspects of the software implementation are analysed in sections 5.3 and 5.4. Example applications are discussed in Section 5.5. Finally, the scalability of the software is discussed in Section 5.6 and further plans for development and limitations are outlined in Section 5.7.

5.2 Introduction

As discussed in Section 2.2.2.2, on-lattice kMC models select atomistic events from a predefined table and execute them on fixed lattice sites [221]. The use of fixed lattice sites contributes to the computational efficiency of on-lattice algorithms but introduces obstacles associated with the study of unordered materials. Several lattice-based open-source kMC software are available, exam-

ples include the KMCLib [290], lattice_mc [291], KMC Lattice v2.0 [292], Excimontec v1.0 [293], MonteCoffee [294], and KIMERA [295]. Additionally, the Stochastic Parallel PARticle Kinetic Simulator (SPPARKS) [296] offers solely on-lattice kMC modelling capabilities, since the only currently available off-lattice solver is an MMC relaxation scheme. Furthermore, a wide range of on-lattice kMC packages such as kmcos [297], PyCD [298], VIS-A-VIS [299], MulSKIPS [300], Kimocs [301], KSOME [302], kMCpy [303], and Morphokinetics [304] are available in open-source software repositories.

EON [305] is the only identified off-lattice package distributed under an open-source license. This is an Adaptive kinetic Monte Carlo (AkMC) software that discovers as well as stores atomic-scale processes (e.g., reactions, diffusion) throughout the simulation instead of stochastically selecting transition events from a predefined table [225]. Such a feature elevates the accuracy of AkMC approaches but decreases their computational efficiency as well as increases their implementation complexity compared to predefined table kMC schemes.

To the best of our knowledge, a completely lattice-free kMC code with a predefined table of events is currently unavailable in open-source repositories. Therefore, we aim to fill that gap by providing the scientific community with a general and easy-to-use solution for performing long-timescale atomistic simulations on complex materials science, chemistry, physics, biology, and engineering problems involving amorphous materials or non-crystalline systems.

In this work, we introduce PArallel PREdefined CAtalog (PAPRECA) - a hybrid off-lattice kMC/MD simulator. PAPRECA is a parallelised software (uses the MPI protocol) that can capture four distinct classes of predefined transition events: 1) reactions (bonding and scission), 2) deposition (of molecules and atoms), 3) diffusion, and 4) monoatomic desorption. Virtually any system whose temporal evolution can be described by these atomic-scale processes can be effectively simulated by PAPRECA. Example applications of PAPRECA include but are not limited to: adsorption/desorption on catalytic surfaces, amorphous thin films (e.g., phosphate films, solid electrolyte interphases, oxide layers), and modelling self-diffusion of gases. Furthermore, PAPRECA allows for the extension of the source code to include other classes of transition events (e.g., reaction chains).

For accurate simulations of molecular-level resolution, it becomes necessary to model elementary steps of high frequency (10^{13}-10^{14} Hz and above [306]) such as atomic vibrations. These events cannot be explicitly included in the table of predefined events because they would dominate the system, thus preventing the simulation from reaching timescales beyond the limits of MD. This can be explained by considering that the higher the rate of a predefined elementary step, the greater its kMC selection probability [173]. To circumvent this issue, PAPRECA couples an off-lattice kMC solver with an MD solver (LAMMPS [26]) to enable hybrid off-lattice kMC/MD simulations. Effectively, atomistic processes of elevated activation energies are captured via the off-lattice kMC stage, while fast atomic-scale processes are treated by the MD stage.

Py-MCMD [307] is a different hybrid MC/MD workflow available in open-source repositories. Py-MCMD is a Python-based communication interface between the MC software GOMC [308] and the MD code NAMD [309]. The central difference between PAPRECA and py-MCMD is that the former implements a kMC approach, while the latter utilises an MMC scheme. Effectively, in the kMC stage of PAPRECA, predefined event probabilities are calculated based on their rates and an elementary process is selected and executed to overcome a high energy barrier. On the other

hand, during the MC phase of py-MCMD, trial moves (e.g., rigid-body displacements/rotations, intra-box swaps [310]) are attempted and accepted or rejected based on the Metropolis acceptance criterion [311].

5.3 Hybrid (kMC/MD) parallel algorithms

The kMC stage of PAPRECA, as well as the interface communicating information between the kMC and MD stages, are both realised by an in-house code written C/C++. On the other hand, the MD stage of PAPRECA is performed in LAMMPS [26]. Both stages use the message passing interface (MPI) to achieve memory-distributed parallelism.

Overall, PAPRECA is built with the LAMMPS library. As such, native LAMMPS subroutines are available to PAPRECA and are leveraged to perform fundamental tasks related to the hybrid kMC/MD model (domain decomposition, neighbour list management, treatment of periodic boundaries, modification of atom properties, time integration, etc.). Furthermore, PAPRECA is developed cohesively with LAMMPS. Effectively, PAPRECA classes are integrated with and access LAMMPS objects directly, facilitating data storage, transfer, and modification. Section 5.3.1 provides further details on the algorithmic aspects of the MD stage of PAPRECA (performed in LAMMPS). Section 5.3.2 focuses on the elements of the kMC solver. Section 5.3.3 discusses utility operations and functions. Finally, Section 5.3.4 focuses on the hybrid kMC/MD implementation and PAPRECA as a complete open-source software. Throughout the text, the terms "atom" and "particle" are interchangeable. "MPI process" and "MPI rank" are also interchangeable. Additionally, "atom types" refer to the LAMMPS atom types identified by unique numerical labels and exhibiting identical parameters (i.e., masses, interatomic potential coefficients, bonded interaction parameters). Note that "atom type" and "atom species" are not interchangeable since multiple types can be defined for the same species.

5.3.1 MD stage

5.3.1.1 Partitioning

Spatial decomposition is a key concept in MPI programs [312], referring to algorithms dedicated to distributing the computational workload across the MPI processes. Specifically, in atomistic simulations, each MPI rank is assigned a subdomain and performs operations (e.g., force calculations, position/velocity/charge updates) exclusively on atoms within it. Atoms are periodically redistributed to MPI processes as they migrate between different subdomains during the simulation [313].

The domain decomposition of PAPRECA is identical to that of LAMMPS. The details of the partitioning algorithms are discussed in detail in the relevant work of Plimpton [313]. In any case, spatial decomposition is initialised by LAMMPS at the beginning of the simulation and is managed entirely by the MD stage. Achieving uniform particle density is of paramount importance to the efficiency of the MD stage. To that respect, and to ensure that the number of atoms per MPI process is somewhat equal, PAPRECA fully supports both regular and irregular decomposition strategies as realised in LAMMPS [26].

The choice of decomposition strategy is strictly dictated by the underlying physics of the

modelled system. Regular (default) partitioning algorithms are preferred when it comes to systems exhibiting spatial uniformity of atomic density throughout the simulation. An example of such a system is illustrated in Figs. 5.1. The solid black lines denote the non-intersecting computational subdomains, whereas the dotted blue lines indicate the ghost atoms regime of an MPI process. It can be observed that the thin film of Fig. 5.1 grows over time. Nevertheless, the computational load is evenly distributed across the MPI processes since the number of atoms residing in each subdomain is roughly equal at every timestep.

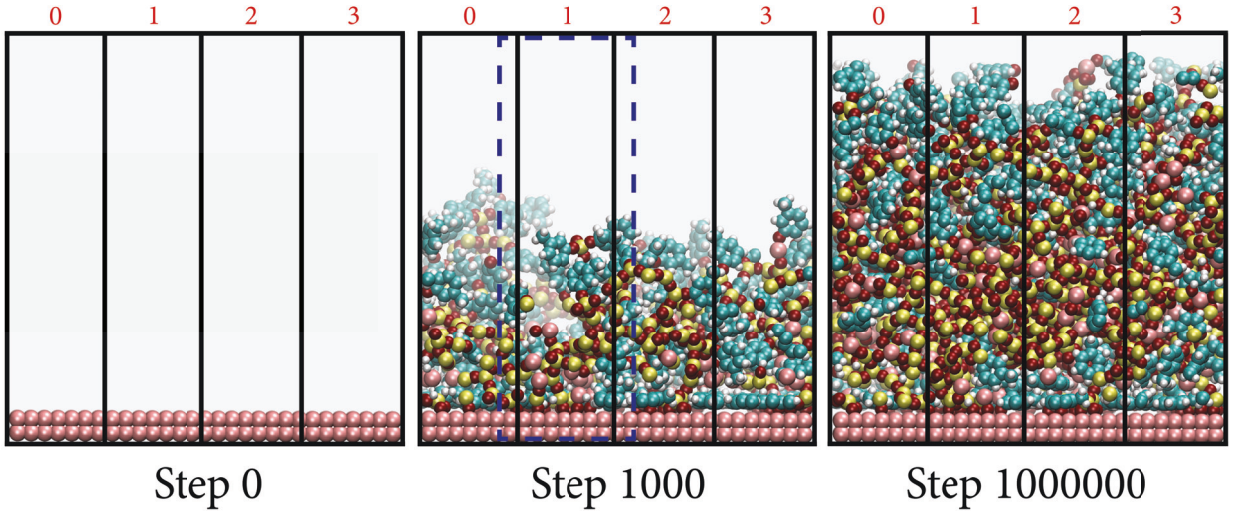


Fig. 5.1: 2D projection of a regular 4x4x1 processor grid along the x-, y-, and y-dimensions, respectively. Snapshots of a toy-system at the 0^{th} **(left)**, 1000^{th} **(middle)**, and 1000000^{th} **(right)** step. The solid black lines mark the non-intersecting MPI subdomains, while the blue dotted lines mark an example ghost-atom regime for the 1^{st} MPI rank. The thin film grows while maintaining uniform atomic density across the MPI processes.

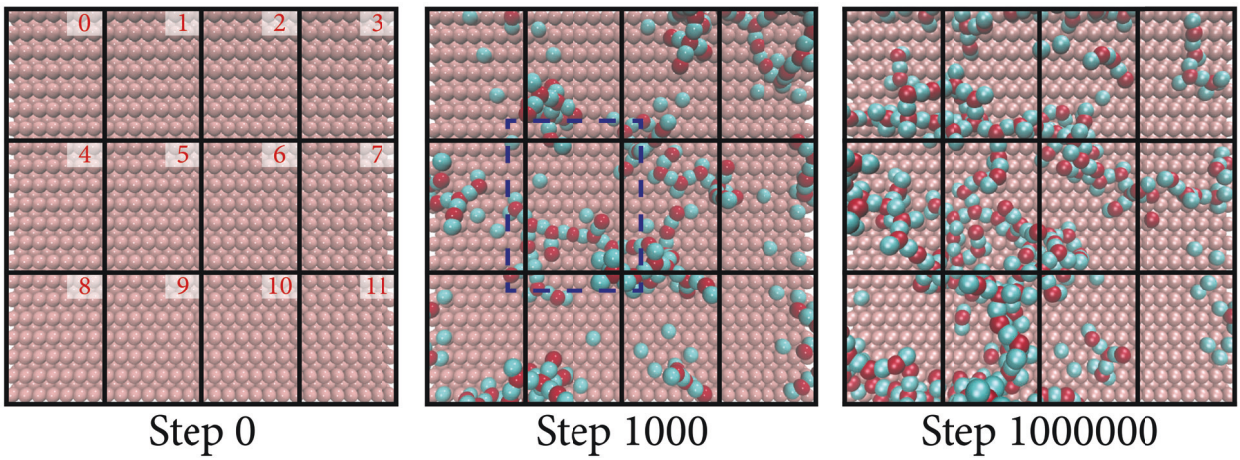


Fig. 5.2: Top view of a regular 4x3x1 processor grid along the x-, y-, and y-dimensions, respectively. Snapshots of a toy system at the 0^{th} **(left)**, 1000^{th} **(middle)**, and 1000000^{th} **(right)** step. The solid black lines mark the non-intersecting MPI subdomains, while the blue dotted lines mark an example ghost-atom regime for the 5^{st} MPI rank. Islands and patches are visible at steps 1000 **(middle)** and 1000000 **(right)**, and particles are non-uniformly distributed across the MPI ranks.

Note that regular MPI process grids in PAPRECA can either be orthogonal (i.e., with their edges parallel to the simulation box unit vectors) or triclinic [26]. This offers further flexibility

and provides load-balancing methods for systems exhibiting complex geometric arrangements (e.g., modelling of lubricant flow under shearing [314]). Finally, subdomains can deform while retaining identical dimensions relative to one another. Such a feature can aid towards the enhancement of the computational efficiency of simulations involving fluid compression (e.g., those shedding light on the mechanochemistry of lubricant additives [92, 315]).

Periodic and non-periodic domain boundaries are supported in PAPRECA. In the periodic case, atoms exiting a face are remapped to the opposite side of the simulation box. On the other hand, "fixed" non-periodic boundaries delete atoms exiting the relevant edges, while the dimensions of "shrink-wrapped" faces are continuously modified to encompass each particle at every step. A combination of periodic boundaries can be utilised during the MD stage of PAPRECA. For instance, the decomposition of additives on ferrous surfaces (see Chapter 3) can be modelled with periodic boundary conditions along the x- and y-dimensions and non-periodic "shrink-wrapped" faces on the z-axis to account for the change in system size due to thin-film growth.

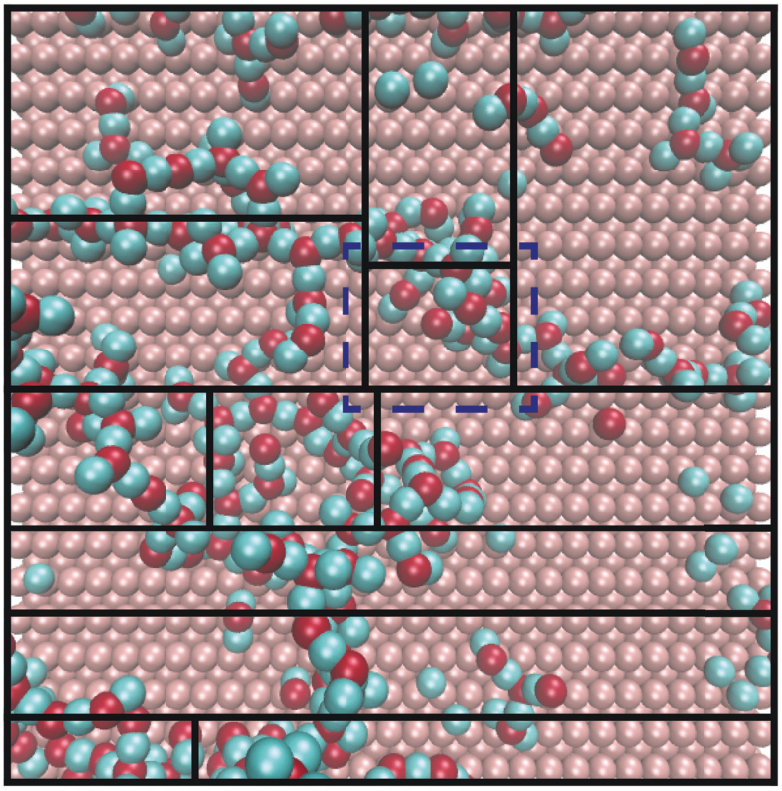


Fig. 5.3: Top view of irregular ("tiled") 12-process grid. The RCB partitioning strategy results in improved load balancing than that offered by a regular subdomain decomposition (see **right** image of Fig. 5.2). The solid black lines mark the non-intersecting MPI subdomains, while the blue dotted lines mark an example ghost-atom regime for an MPI rank.

In certain instances, regular partitioning approaches cannot guarantee a roughly equal atomic density for every MPI rank throughout the simulation. An example of such a system is given in Fig. 5.2. As the thin film becomes thicker, islands and rough surfaces appear, and particles are unevenly distributed on the subdomains. It is illustrated that MPI ranks #4, #5, and #9 are overloaded, whereas ranks # 3 and #11 encompass significantly fewer atoms. As such, the numerical efficiency of the simulation and the total computation rate (i.e., CPU time per timestep) are throttled by the slowest MPI rank, which corresponds to the subdomain with the highest particle count. To achieve

load-balancing in simulations exhibiting spatial non-uniformities in atomic density, irregular MPI grids can be employed. The MD stage of PAPRECA supports the recursive coordinate bisectioning (RCB) method as implemented in LAMMPS [26]. RCB is a dynamic load-balancing algorithm allowing for subdomains of varying dimensions. Fig. 5.3 provides a graphical illustration of an appropriate use of the RCB method to assist with load balancing at the 1000000^{th} step of the toy system presented in Fig. 5.2

5.3.1.2 Communication

This section focuses on aspects of inter-process communication related to the MD stage of PAPRECA. Communication during the kMC stage or between the MD and kMC stages is discussed in sections 5.3.2 and 5.3.4, respectively.

The PAPRECA MD stage communication is entirely controlled by LAMMPS. At every MD step, an MPI rank retains data (spatial coordinates, velocities, charges, bonded atoms, etc.) for each particle encompassed in its subdomain. These particles are referred to as "owned atoms" (e.g., atoms within the solid black lines in Figs. 5.1, 5.2, and 5.3). Each MPI process additionally retains partial copies of data for atoms located in neighbouring subdomains and within a cutoff distance. Such particles are known as "ghost atoms" (e.g., atoms within the dotted blue lines in Figs. 5.1, 5.2, and 5.3). Retaining data related to both "owned" as well as "ghost" atoms enhances the computational efficiency of the MD stage. This is achieved since the aforementioned data-storage strategy diminishes inter-process communication relevant to the computation of short-range pairwise interactions for particles residing in subdomain boundaries [26].

Two distinct types of inter-process communication are performed by LAMMPS in the MD stage of PAPRECA. "Forward" communication refers to the operation associated with the distribution of data from a parent rank (storing "owned" atoms) to nearby subdomains. In contrast, "reverse" communication occurs when "ghost atom" information is transferred to the parent MPI process. Both operations are vital and guarantee that all interatomic interactions are summed during the force calculation phase of the MD stage [26].

The diagrams presented in Figs. 5.4 and 5.5 provide graphical illustrations of the inter-process communication schemes of the MD stage. Communication is performed in as many phases as the dimensions of the MPI grid. In a 3-dimensional example, communication demands three sequential phases for the x-, y-, and z-dimensions. The 2-dimensional case is a special case of the 3D case where solely two phases are required (for the x- and y-directions).

In the 2D regular domain example of Fig. 5.4 MPI processes 2 and 3 transfer particle attributes to process 0 **(left)** during the x-dimension phase. Next, processes 3 and 4 transfer atom information to rank 0 in the y-direction phase. Note that, in the y-direction phase, "ghost atoms" transferred to MPI processes 3 and 4 can also be communicated to rank 0. After both communication phases, certain particles (e.g., "ghost atoms" located in the boundary between ranks 1 and 4 or 2 and 3) are transferred multiple times to the receiving subdomain (i.e., process 0).

When it comes to the irregular grid communication strategy, the central difference lies in the fact that MPI ranks receiving atomic data can feature several subdomain boundaries in each dimension. This is illustrated in Fig. 5.5. Once again, communication occurs on the x-direction and then on the y-direction. Nevertheless, "ghost atom" data transfer on the y-direction is performed from selected MPI ranks and solely if the relevant information is not communicated during the

x-direction phase. For instance, "ghost atom" attributes sent from MPI processes 3 to 4 and vice versa are not transferred to process 0 during the y-dimension communication phase [26].

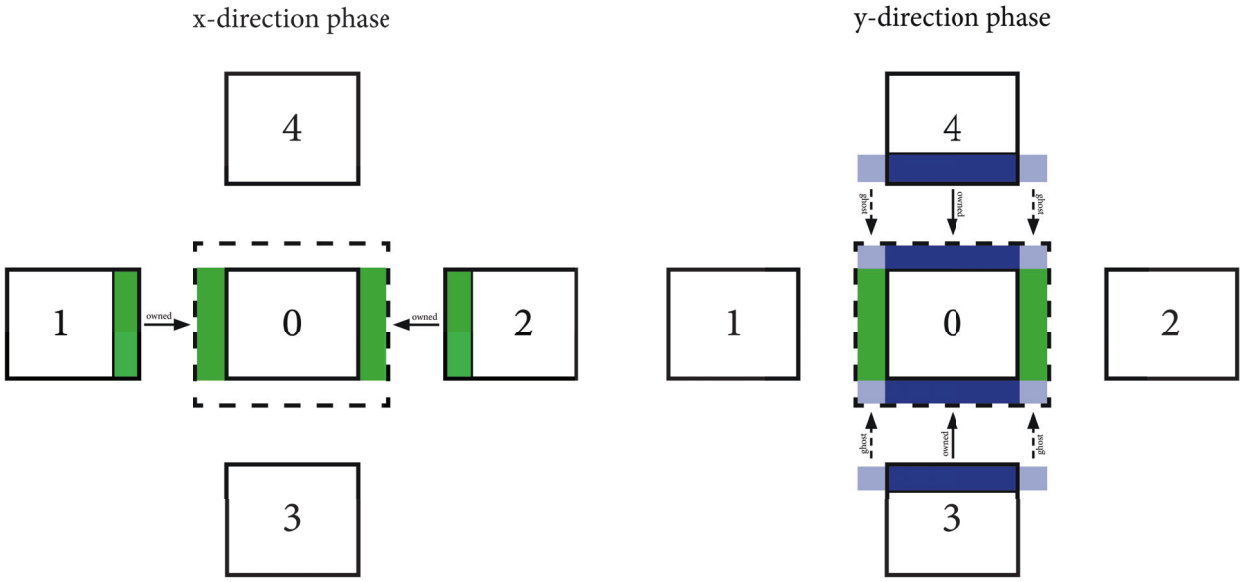


Fig. 5.4: 2D communication strategy for regular MPI grids. Communication occurs sequentially and in two phases along the x-direction **(left)** and y-direction **(right)**. In the y-dimension phase, "ghost" attributes (denoted with dark blue) are transferred alongside "owned atom" data (annotated with bright blue). Adapted from Thompson et al. [26].

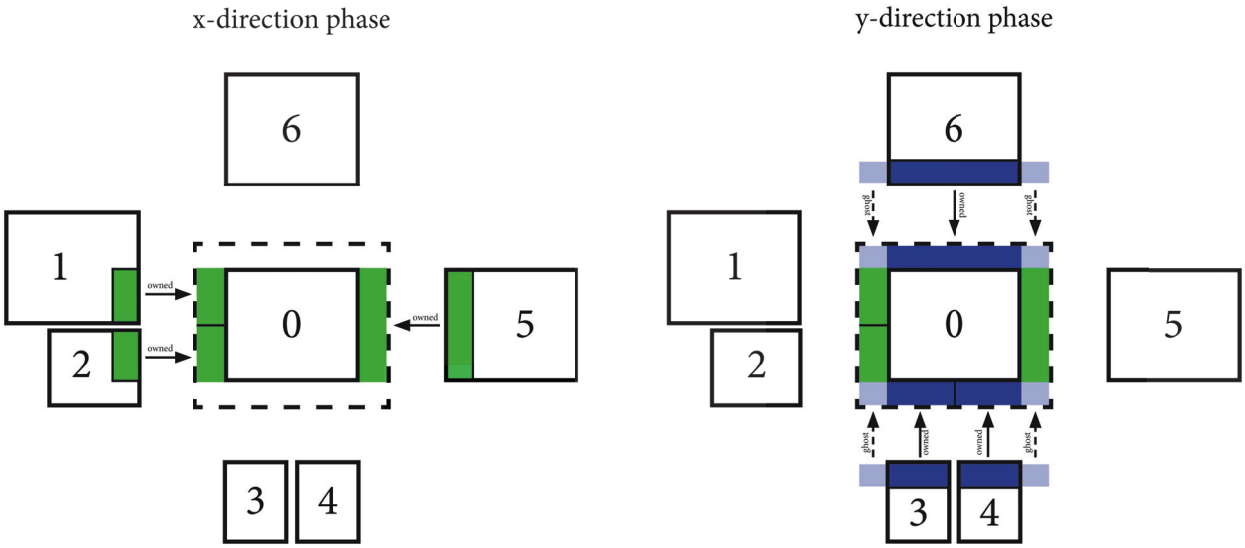


Fig. 5.5: 2D communication strategy for irregular MPI grids. Communication occurs sequentially and in two phases along the x-direction **(left)** and y-direction **(right)**. In the y-dimension phase, "ghost" attributes (denoted with dark blue) are transferred alongside "owned atom" data (annotated with bright blue), but solely if the relevant data are not communicated during the x-phase. Adapted from Thompson et al. [26].

5.3.1.3 Neighbour lists

Similarly to domain decomposition (see Section 5.3.1.1), neighbour lists in PAPRECA are managed by LAMMPS and the MD stage. This allows PAPRECA to leverage the continuously maintained and optimised parallel algorithms of LAMMPS dedicated to neighbour list building. The choice to

utilise such algorithms was driven by computational efficiency considerations and by acknowledging that neighbour list building and management can become one of the most memory-intensive processes in atomistic simulation codes [26, 313].

Neighbour lists are data structures associated with "owned" atoms (by an MPI rank). Effectively, each "owned" atom is linked to an array retaining the local indexes of nearby atoms ("owned" and "ghost") within a cutoff distance. In the MD stage of PAPRECA such indices are vital when it comes to accessing attributes of atoms in the vicinity of "owned" atoms and performing force computations. A Verlet-style neighbouring strategy is deployed with a neighbour list cutoff distance as [203]:

$$D = D_{ff} + D_s \tag{5.1}$$

Where D_{ff} is the force cutoff of the selected force field. D_s represents a "skin" distance which extends the neighbouring region beyond D_{ff}. By including additional neighbours in the lists of "owned" atoms, re-neighbouring can be triggered less frequently. This can boost the numerical efficiency of the MD stage. By default, re-neighbouring is performed if a particle is displaced by at least $D_s/2$ during a single step. Such a strategy guarantees that neighbour lists are properly updated, even in cases of rapid temporal evolution in local atomic environments. Note that, additional neighbour list builds are executed with a user-defined frequency regardless of whether atoms move by more than $D_s/2$. Overall, re-neighbouring algorithms based on binning strategies are implemented that allow list building in O(N) complexity (with N being the total number of particles owned by an MPI rank) [26].

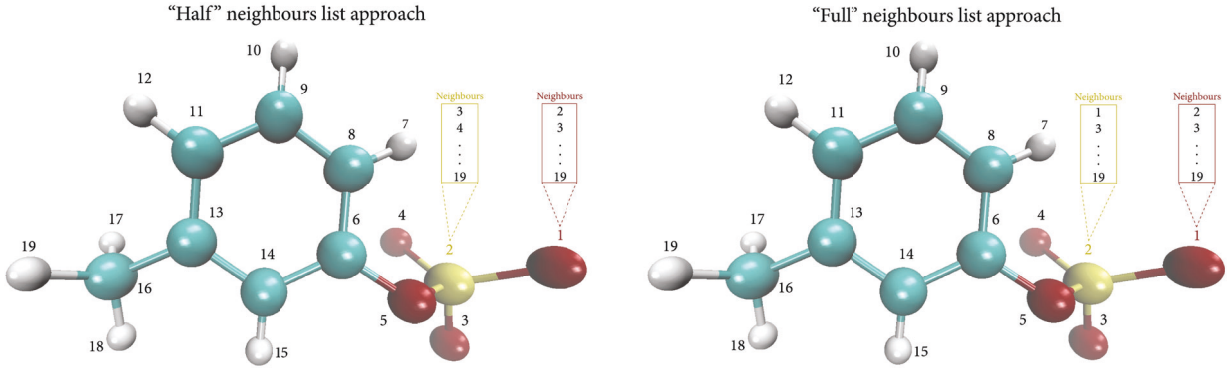


Fig. 5.6: (Left) "Half" neighbours list approach where each pair of atoms is listed once. Atom 2 is retained in the neighbours list of atom 1, but atom 1 is not stored in the list related to atom 2. **(Right)** "Full" neighbours list approach where each pair of atoms is listed in both neighbours lists.

The most commonly used type of neighbour list in the MD stage of PAPRECA (and by extension in LAMMPS) is the "half" list. In this approach, atom j is stored in the neighbours list of i, or vice versa. However, information is never retained in both lists. In contrast, in a "full" list strategy, each pair of nearby atoms is stored twice (i.e., in the lists of both atoms i and j). A graphical illustration of "half" and "full" neighbouring strategies is given in Fig. 5.6. Note that a "half" and a "full" neighbours list are used in the kMC stage of PAPRECA. The rationale behind this software design choice is discussed in detail in Section 5.3.2. In any case, a new LAMMPS fix was introduced to create, build, and maintain both neighbour lists during a hybrid kMC/MD run. The fix is named "fix PAPRECA" and is available from version v2.0.0 (released on the 17^{th} of September 2024).

5.3.2 KMC stage

5.3.2.1 Off-lattice rejection-free kMC, mobile sites and predefined table of events

As discussed in Section 5.2, standard kMC models are lattice-based. In essence, the domain is divided into event sites where elementary processes (e.g., reactions, adsorption/desorption steps) can be performed [221]. To enable off-lattice simulations, PAPRECA introduces event sites attached to atoms. Effectively, atoms act as site centres around which searches for potential atomistic events are performed [270]. Since atoms are displaced during the MD and kMC stages of PAPRECA, the event sites are mobile and their motion is unrestricted in the 3D space. This renders PAPRECA an off-lattice simulator.

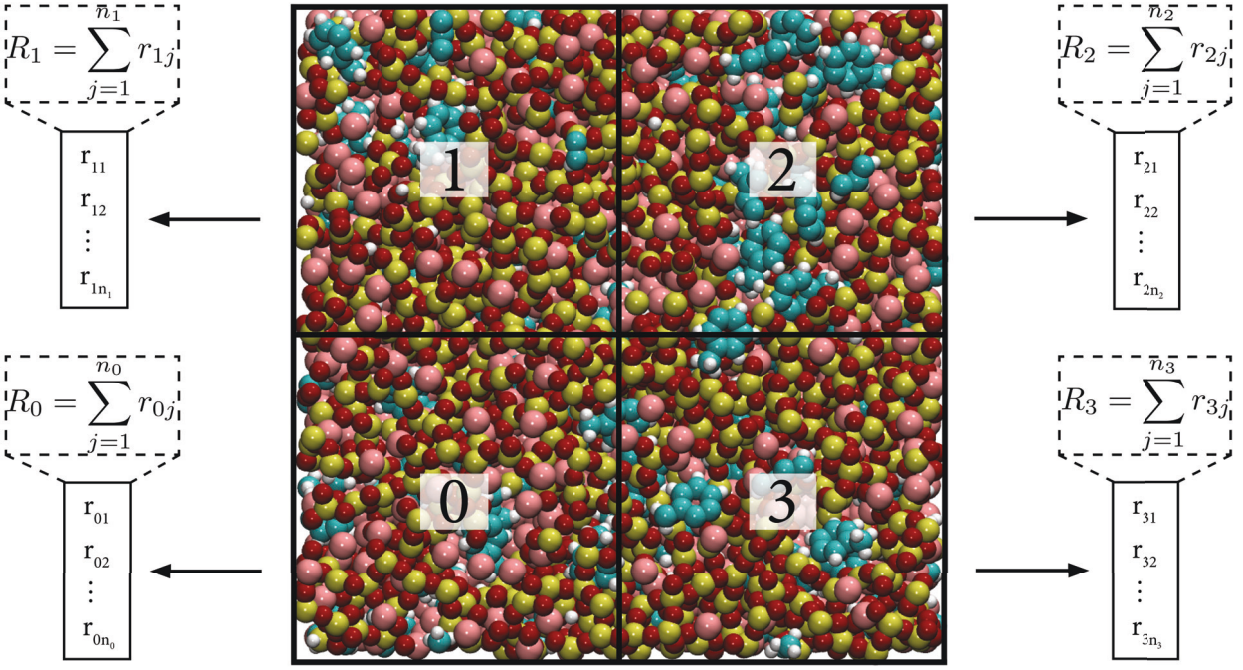


Fig. 5.7: Assembly of local *tables of detected events* on MPI ranks and calculation of cumulative rates of MPI processes (R_i, with i being the MPI rank). Example with 4 MPI processes and n_i discovered events on each rank.

Furthermore, PAPRECA deploys a *predefined table of events* approach. This table is essentially a list containing a finite number of acceptable elementary processes that can be executed during the kMC stage. Such a list stores the rates ($r_{rank,event}$) as well as information related to the event execution (e.g., displacement distances for atoms or the type of bond to be broken after performing the move). In PAPRECA, the *predefined table of events* is a static object that is created at the beginning of the kMC/MD run and remains unchanged throughout the simulation. It is acknowledged that the use of the predefined tables enhances the computational efficiency but reduces the accuracy of PAPRECA relative to AkMC approaches involving dynamic tables of events that are periodically updated and modified during the kMC run [225, 305].

Similarly to the MD stage, the kMC stage of PAPRECA is a memory-distributed application parallelised with MPI. During a kMC stage, each MPI rank discovers acceptable atomistic processes (as defined in the *table of predefined events*) by performing event searches on its "owned" atoms (see Section 5.3.1.2). Each MPI rank retains "ghost" atoms, which are copies of atoms "owned" by other MPI processes. Consequently, to prevent the duplicate discovery of events, no searches

are executed on "ghost" atoms. The discovered events are tabulated and stored locally on each MPI rank in the *table of detected events*. Note that the *table of predefined events* and the *table of detected events* are conceptually different. The former is a static and global (available to all MPI ranks) data structure listing the acceptable events of the run. In contrast, the latter is a local (accessible solely by its parent MPI process) dynamic array storing the discovered events of a specific kMC stage.

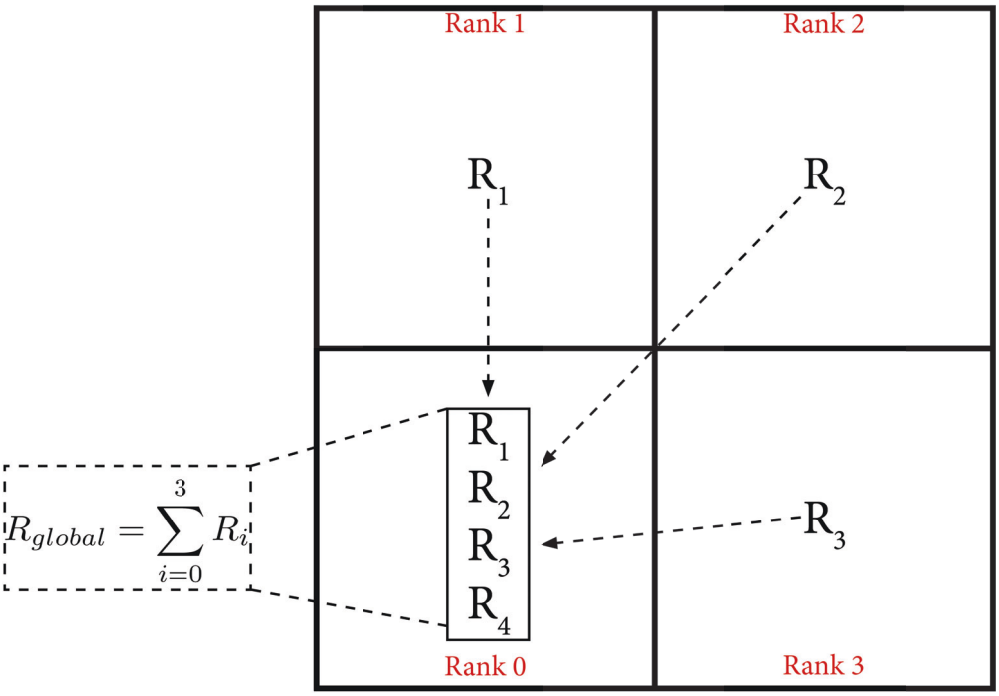


Fig. 5.8: Communication of local cumulative rates R_i to the master MPI process and estimation of global rate of kMC step R_{global}. Example with 4 MPI ranks.

In PAPRECA, the stochastic selection of an elementary process comprises two phases. In the first phase (illustrated in Fig. 5.7), the MPI rank that executes the event is chosen (called the *event rank*). This is done by calculating a local cumulative rate (R_{rank}) for the discovered events of each MPI rank:

$$R_i = \sum_{j=1}^{n_i} r_{ij} \tag{5.2}$$

Where R is the cumulative rate, r is the frequency of an atomistic event, and n is the total number of discovered elementary steps of an MPI process. Indexes i and j refer to MPI ranks and locally detected events, respectively. Recall that the rates of locally discovered atomistic events are retained in each MPI rank within the *table of detected events*:

$$r_i = \begin{bmatrix} r_{i1} & r_{i2} & \dots & r_{in_i} \end{bmatrix} \tag{5.3}$$

The local cumulative rates are estimated locally and subsequently communicated to MPI rank 0 (as depicted in Fig. 5.8). Note that MPI rank 0 acts as the master process of the kMC stage. In any case, rank 0 assembles a *table of rank rates* containing the cumulative rates of each MPI process:

$$R = \begin{bmatrix} R_0 & R_1 & \dots & R_{p-1} \end{bmatrix} \tag{5.4}$$

Where p is the total number of MPI processes (ranks). The master rank additionally computes the global rate (R_{global}) of the kMC step (i.e., sum of local rates) as follows:

$$R_{global} = \sum_{i=0}^{p-1} R_i \tag{5.5}$$

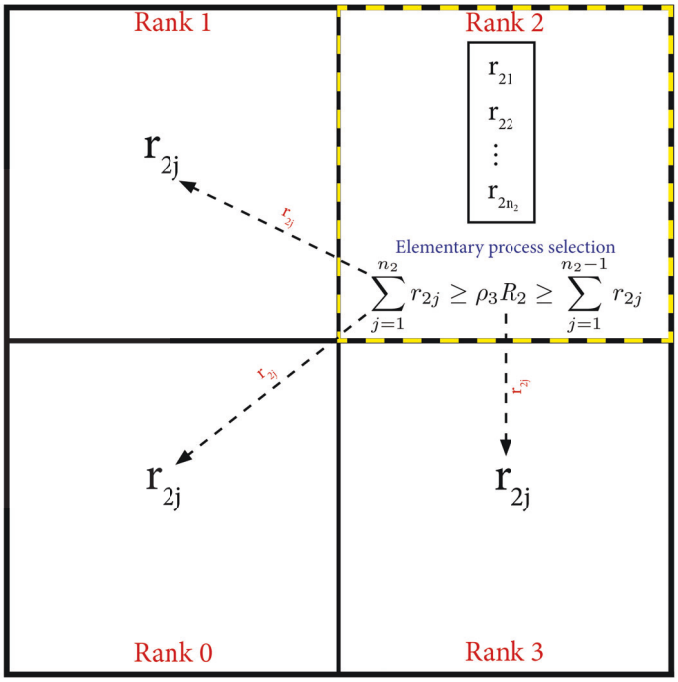


Fig. 5.9: Stochastic selection of elementary event (e.g., reaction, adsorption) on *event rank* and communication of information related to the atomistic process to all MPI ranks. In this example, rank 2 is the *event rank* and there are a total of 4 MPI processes.

By utilising the *table of rank rates* as well as R_{global} together with a rejection-free kinetic Monte Carlo (rkMC) algorithm, rank 0 stochastically selects the *event rank*. In particular, the *event rank* index (i) obeys the following inequality [173]:

$$\sum_{i=0}^{p-1} R_i \geq \rho_1 R_{global} \geq \sum_{i=0}^{p-2} R_i \tag{5.6}$$

Where ρ_1 is a uniformly distributed pseudorandom number between 0 and 1. Then, R_{global} is used to advance the global simulation clock by Δt [173]:

$$\Delta_t = \frac{-ln(\rho_2)}{R_{global}} \tag{5.7}$$

Here, ρ_2 is a second pseudorandom number between 0 and 1. Note that the rest of the MPI processes wait while rank 0 chooses the *event rank* and updates the clock.

In the second phase of elementary process selection, the *event rank* chooses an event from the locally generated and stored *table of detected events*. Once again, an rkMC scheme is deployed [173]. Here, the chosen event index (j) obeys the following inequality:

$$\sum_{j=1}^{n_i} r_{ij} \geq \rho_3 R_i \geq \sum_{j=1}^{n_i-1} r_{ij} \tag{5.8}$$

With ρ_3 being a third pseudorandom number between 0 and 1. Now, every other MPI rank waits while the *event rank* chooses the next kMC step. Finally, the *event rank* communicates information linked to the selected atomistic event (e.g., updated positions and bonds of atoms) back to every other MPI rank (as depicted in Fig. 5.9). This step guarantees that the microstate is consistent and identical across every MPI process following the execution of an atomistic event in the kMC stage. The flowchart provided in Fig. 5.10 is a graphical illustration of the key steps involved in PAPRECA's parallelised rkMC scheme and discussed in this section.

Pseudorandom numbers are always drawn using RANMAR (the generator of Marsaglia, Zaman, and Tsang) [316] as implemented in LAMMPS. This is done by constructing a `LAMMPS_NS::RanMars` object and calling the `uniform()` member function to produce a uniformly distributed number between 0 and 1.

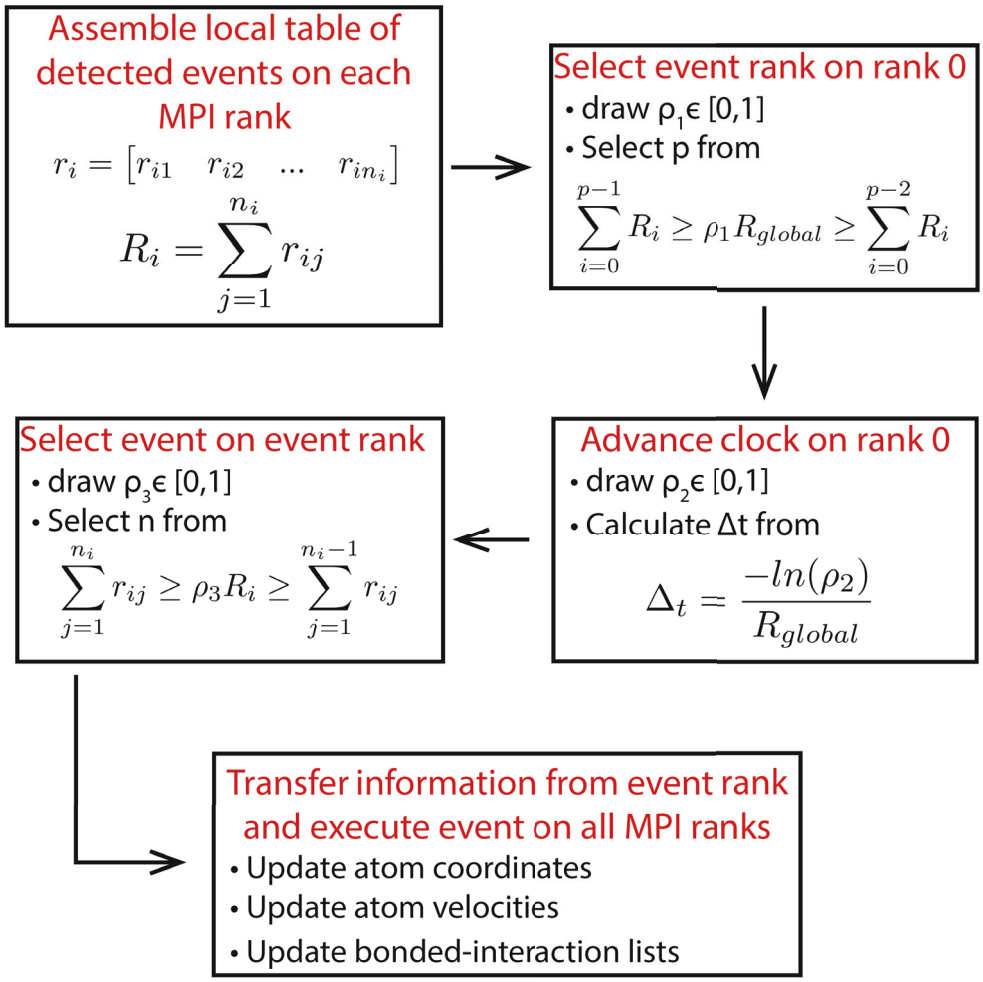


Fig. 5.10: Summary of steps involved in the parallelised kMC stage of PAPRECA.

5.3.2.2 Overview of supported atomistic events

In Section 5.3.2.1, we provided an overview of the algorithms linked to the parallelised kMC stage of PAPRECA. The concepts of mobile event sites, *event rank*, *predefined table of events*, and *table of detected events* were introduced. Here, we delve deeper into the local (per MPI rank) discovery of atomistic processes, the communication of event information from the *event rank* to other MPI ranks and the execution of a kMC step. Since the 17^{th} of September 2024 (version

2.0.0) PAPRECA supports the following classes of predefined events:

i. bond-breaking (reaction).

ii. bond-formation (reaction).

iii. molecular and monoatomic deposition.

iv. monoatomic desorption.

v. diffusion hops.

5.3.2.3 Supported atomistic events: reactions

The reaction (types i and ii) events are intrinsically associated with LAMMPS bonds. Since PAPRECA is built with the LAMMPS library, any bond style (e.g., harmonic) can be deployed as long as it is supported by the selected atom as well as pair styles. This favours the flexibility of PAPRECA. The `PAPRECA::PredefinedReaction` class and its child `PAPRECA::PredefinedBondForm` are utilised to initialise bond-breaking and bond-formation events in the *predefined table of events*, respectively. The event atom types, the corresponding bond type, and the associated reaction rate are required to instantiate a `PAPRECA::PredefinedReaction` object. A *bond distance* (d_{bond}) is additionally required to construct `PAPRECA::PredefinedBondForm` objects. In essence, atoms of the appropriate types (as defined in the *predefined table of events*) separated by less than the *bonding distance* qualify as valid bond-formation candidates.

Additional data structures were introduced in PAPRECA to assist with storing, modifying, and accessing information related to bonded interactions. `PAPRECA::Bond` objects were implemented to retain the IDs and types of bonds. Furthermore, `std::vectors` [317] of `PAPRECA::Bond` objects were deployed to store multiple `PAPRECA::Bond` objects in a dynamic container (called `PAPRECA::BOND_VECTORS`). Note that each pair of atoms is bonded twice (i.e., atom i is retained in the vector of atom j and vice versa). Nonetheless, one of the two bonded atoms is denoted as *head atom* while the other as *tail atom*. Finally, an *std::unordered_map* that maps atom IDs to associated `PAPRECA::BOND_VECTORS` was introduced (called `PAPRECA::atomID2Bonds`). Such a map facilitates the retrieval of atoms bonded to a specific ID without the requirement to loop through the bond list. Note that a LAMMPS bond list retains the IDs and types of multiple interactions linked to every atom in an MPI rank.

PAPRECA accesses information related to bonded interactions as stored by LAMMPS in the final step of the MD stage. To do so, PAPRECA calls the `lammps_gather_bonds` function (defined in the LAMMPS library) to retrieve the locally stored bond lists from all MPI ranks to the master rank. This operation is performed at the beginning of each kMC stage. Then, the gathered bond list is converted to `PAPRECA:Bond` objects that are stored in the corresponding `PAPRECA::BOND_VECTOR` of each atom. Finally, each atom ID is mapped to the associated `PAPRECA:BONDS_VECTOR` using the aforementioned `PAPRECA::atomID2Bonds` unordered map.

MPI ranks detect bond-breaking events (type i) as follows. Firstly, the IDs of "owned" atoms are extracted from the LAMMPS microstate (via a call to `lammps_extract_atom`). Then, the IDs are mapped to the relevant `PAPRECA::BOND_VECTORS` (via the `PAPRECA::atomID2Bonds` container), retaining the IDs of bonded atoms together with associated bond types. Bonds of breakable types

(as listed in the *predefined table of events*) qualify as valid events and are inserted in the *table of detected events* of the parent MPI rank. Note that solely bonds originating from *head atoms* are examined here to prevent the insertion of duplicate bond-breaking events in the *table of detected events*. Whenever a bond-breaking event is selected for execution, the *event rank* broadcasts the atom IDs participating in the bond along with the respective bond type. Then, each MPI rank calls the `delete_bonds` function of LAMMPS to remove the bonded interaction from the system. The central steps linked to the discovery and execution of bond-breaking steps in the kMC stage of PAPRECA are summarised in the flowchart of Fig. 5.11.

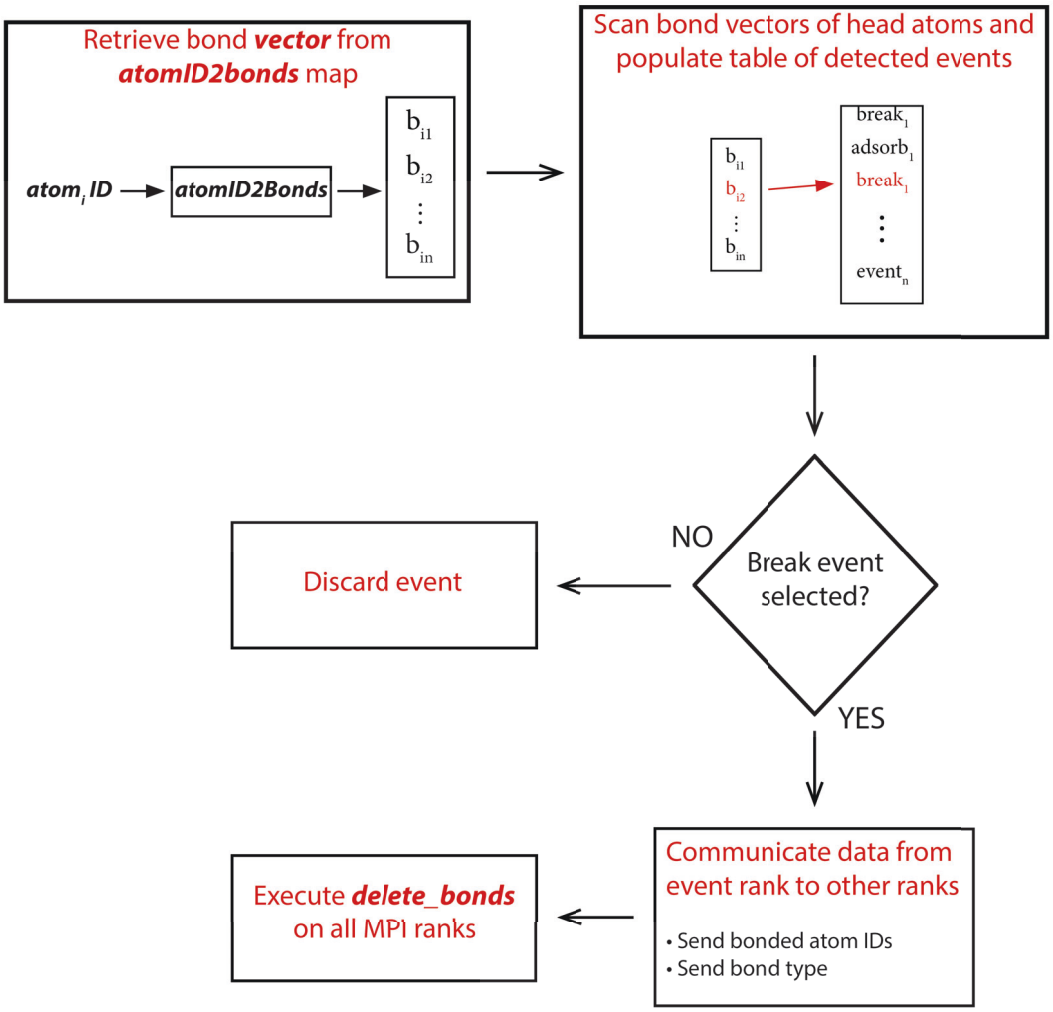


Fig. 5.11: Summary of key steps involved in bond-breaking events (type i).

To enhance the versatility of the software, PAPRECA supports optional features: *catalyzed* and *limited* bond-breaking events. When it comes to *catalyzed* events, bond scission is permitted solely if an atom of a specific type (called *catalyzing type*) is in the vicinity of the *head atom* of the bond. PAPRECA checks for *catalyzing types* as follows. Firstly, the "full" neighbours list generated for PAPRECA (see Section 5.3.1.3) is retrieved. Then, the neighbours of the *head atom* are looped to examine whether any of them is a *catalyzing type*. Note that the use of a "full" neighbours list is necessary in this case. This is justified by considering that each pair of atoms is included in the lists of both neighbours lists and allows looping solely over the *head atom* neighbours to detect *catalyzing types*. In *limited* scission events, bonds can break only if their interatomic

distance is lower than a limiting value (d_{lim}). To test that, a `lammps_extract_atom` function is called to retrieve the spatial coordinates of the bonded atoms from the LAMMPS microstate. Then the relevant separation distance is calculated. When it comes to the calculation of distances, PAPRECA always deploys a wrapper around the `minimum_image()` function of LAMMPS (located in the domain.h header) that accounts for periodic boundaries.

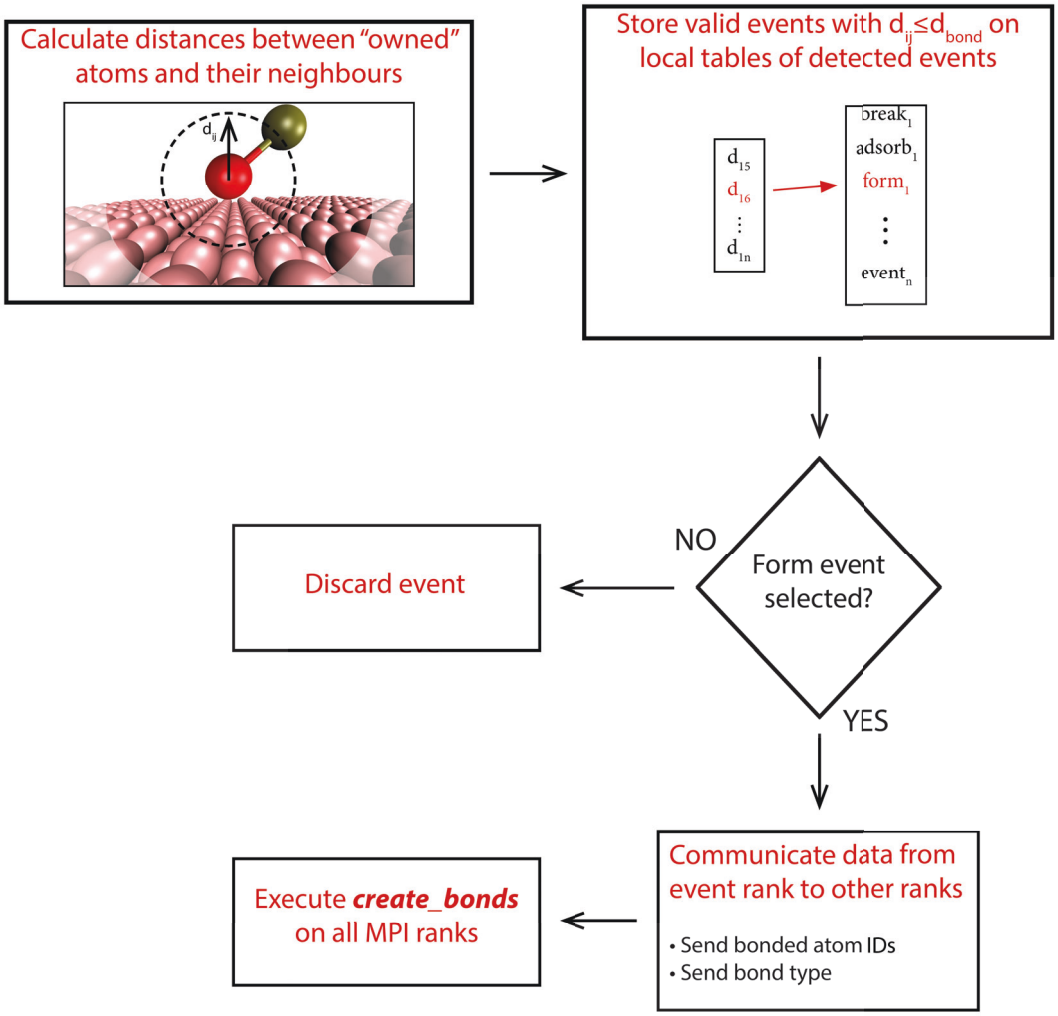


Fig. 5.12: Summary of key steps involved in bond-formation events (type ii). Bond-formation image **(top left)** adapted from our preprint on the hybrid kMC/MD method [233].

To locally detect bond-formation events on MPI ranks, PAPRECA loops over "owned" atoms of bond-forming types (as defined in the *predefined table of events*) on each subdomain. Specifically, the interatomic distances between an "owned" atom and its neighbours are calculated. Valid bond-formation events exhibiting interatomic distances smaller than or equal to the *bond distance* associated with the predefined event are added to the *table of detected events* of the MPI rank:

$$d_{ij} \leq d_{bond_k} \tag{5.9}$$

Where d_{ij} is the minimum image distance between an "owned" atom i and its neighbour atom j, and d_{bond_k} is the bonding distance of the k^{th} bond-formation event included in the *predefined table of events*. Note that bond-formation events utilise the "half" neighbours list of PAPRECA (see Section 5.3.1.3). This is done to favour the computational efficiency of the method and prevent the insertion of event duplicates in the *table of detected events*. If a bond-formation event is selected by

the *event rank*, the bonded atom IDs as well as the bond type are communicated to all other ranks. Then, a `create_bonds single/bond` LAMMPS command is executed collectively to update the bond lists in the system. Overall, the procedure associated with the detection and execution of bond-formation events is graphically presented in Fig. 5.12.

A variety of optional features is available for bond-formation events. The `delete_atoms` option can be utilised to remove bonded atoms following the execution of a formation event. This can be useful to capture volatilisation and evaporation processes. The `delete_atoms` feature has been previously implemented in our kMC/MD study on the decomposition of TCP on iron to remove O_2 molecules formed in the system (see Chapter 3) [270]. The `lone_candidates` option has also been utilised for oxygen species in our kMC/MD study on films from TCP. Such an option considers atoms whose associated bond vectors (`PAPRECA` containers) are empty as valid candidates for a predefined bond-formation event. Additionally, the `same_mol "no"` functionality disables bonding between atoms with the same molecule ID for a predefined bond-formation event. Finally, the `species_maxbonds` and `species_maxbondtypes` options offer control over the coordination of atoms. In particular, `species_maxbonds` can be used to cap the maximum number of bonds for an atom type. On the other hand, the `species_maxbondtypes` feature limits the number of bonds of a specific type for an atom type.

5.3.2.4 Supported atomistic events: molecular and monoatomic deposition

Deposition events (type iii) insert molecules or atoms in the simulation box. PAPRECA deploys molecule templates (as implemented in LAMMPS) to define collections of particles for adsorption events. Such an operation is performed at the beginning of the simulation via the `molecule` LAMMPS command. Note that single-molecule templates can be utilised to model monoatomic adsorption. Using molecule templates offers PAPRECA flexibility for a series of reasons. Firstly, it enables the storing of initial positions, velocities, charges, bonded interactions, special bonds, shake particles [318], and fragments in LAMMPS data structures. Also, more than one molecule or particle can be retained in the molecule template data structures during the simulation. This unlocks sophisticated hybrid kMC/MD models with multiple predefined adsorption events. For example, the deposition of a variety of additive molecules as well as base oils can be simulated to thoroughly investigate the interaction of lubricants [319] with metallic surfaces. Finally, utilisation of molecule templates allows PAPRECA to exploit native LAMMPS functions designed for inserting atoms in the simulation box (e.g., `create_atoms`).

After a molecule template is defined in LAMMPS, kMC deposition events can be initialised and inserted in the *table of predefined events*. Construction of `PAPRECA::PredefinedDeposition` objects demands a variety of inputs as listed below:

- **parent atom type**. This variable defines the type of atoms that can be considered valid mobile sites for predefined deposition events. Effectively, PAPRECA examines if a molecule can be added in the vicinity of specific atom types (i.e., parent atom types for deposition).
- **deposition offset (ΔX)** which defines the separation distance between the position of the parent atom and the centre of mass (COM) of the deposit as defined in LAMMPS.
- **insertion velocity** for each deposited molecule. Note that the velocity of a deposited

molecule is the sum of the insertion velocity and the individual velocities defined for each atom in the molecule template.

- **name of adsorbate** (as defined in the LAMMPS template).
- **rate** of deposition event.

As with any elementary atomistic process in PAPRECA (e.g., bond-formation or bond-breaking), adsorption events are detected locally by each MPI rank. Firstly, the IDs, spatial coordinates, and types of "owned" atoms are extracted from LAMMPS via a `lammps_extract_atom` operation. Then, "owned" atoms are looped and parent atom types (as defined in the *predefined table of events*) are marked as candidate centres for deposition events.

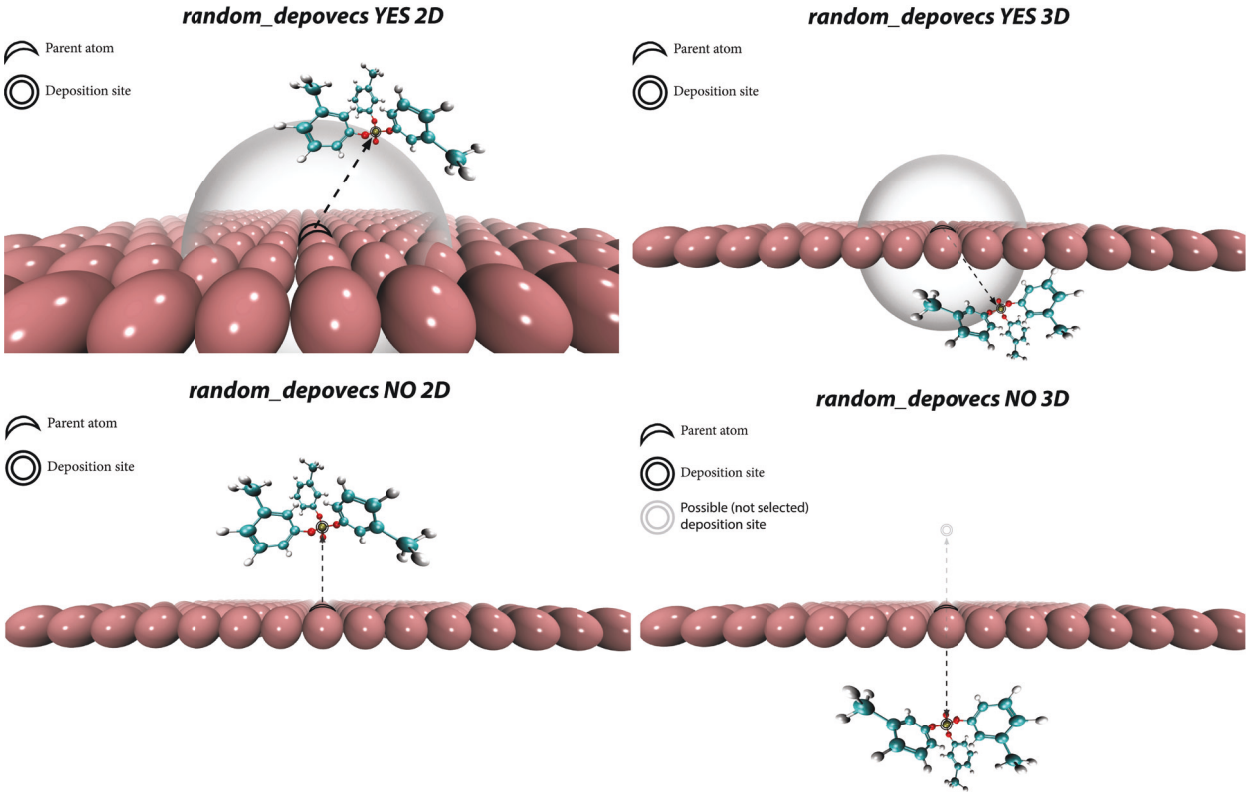


Fig. 5.13: Deposition sites as generated by the `random_depovecs` command. **(Top left):** random_depovecs YES 2D places sites on the surface of the northern hemisphere above the parent atom. **(Top right):** `random_depovecs YES 3D` unlocks sites on both hemispheres. **(Bottom left):** `random_depovecs NO 2D` and **(bottom right):** `random_depovecs NO 3D` generate sites directly above or both above and below the parent atom, respectively.

Defining the deposit site location demands retrieving the coordinates of the atoms involved in the molecule template. Note that the positions of the template atoms are stored in a local coordinate system in the LAMMPS data structures. Therefore, a translation step to convert local atomic coordinates to global coordinates is necessary to ensure consistency with the hybrid kMC/MD simulation box. In any case, the deposition site is offset from the parent atom by a distance of *molecule offset* (as defined for a specific deposition event in the *predefined table of events*). A variety of options are supported by PAPRECA to precisely control the position of the added molecule. The `random_depovecs` option inserts the molecule on the surface of a hemisphere as determined by the following equations:

$$X = x + x_{COM} + \Delta X_k sin(\theta) cos(\phi) \tag{5.10}$$

$$Y = y + y_{COM} + \Delta X_k sin(\theta) sin(\phi) \tag{5.11}$$

$$Z = z + z_{COM} + \Delta X_k cos(\theta) \tag{5.12}$$

Where X, Y, and Z are the coordinates of the deposition site, whereas x, y, and z are the positions of the parent atom. Also, x_{COM}, y_{COM}, z_{COM} are the translated COM coordinates and ΔX_k is the *deposition offset* of the k^{th} deposition event defined in the *predefined table of events*. The angles ϕ and θ are obtained by the relations below:

$$\phi = 2\pi\rho_1 \tag{5.13}$$

$$\theta = \pi\rho_2 \tag{5.14}$$

Where ρ_1 and ρ_2 are two uniformly distributed pseudorandom numbers drawn using the RANMAR generator [316] on the MPI rank that owns the parent atom. Note that `random_depovecs` can be used with the option "2D" which restricts the value of $\theta \in [0, \frac{\pi}{2}]$. On the other hand, utilising option "3D" results in $\theta \in [0, \pi]$. This means that the deposition site can be located either above or below the parent atom. Such an option can become useful for modelling symmetric thin-film growth as it enables deposition sites along both z-directions. Deactivating the `random_depovecs` feature results in a deposition site located directly above or below the parent atom at a separation distance of *molecule offset*. Fig. 5.13 provides examples of different deposition sites as generated by the `random_depovecs` feature.

Overlap tests are performed for each candidate centre to examine whether a molecule (as defined in the molecule template) can be inserted near the parent atom without causing instabilities. This step is vital since small separation distances between atoms can result in excessive interatomic forces, which typically cause runtime errors in the MD stage of PAPRECA [203]. In LAMMPS, this is commonly referred to as an "atom/bond/angle/dihedral/improper missing in the processor" error. Essentially, this means that nearby atoms are being displaced aggressively to the point where neighbours lists stored in individual MPI ranks are not updated properly between time steps. This issue is typical in LJ potentials [205] when interatomic distances are significantly decreased compared to the equilibrium-distance parameter, resulting in elevated repulsive forces.

The "full" PAPRECA neighbours list of the parent atom is obtained to conduct overlap tests. Here, a "full" list is required to guarantee that all possible pairs of atoms are listed in the neighbours list of the parent atom (see Section 5.3.1.3). In any case, overlap tests are performed by estimating the distances between the deposit atoms and the neighbours of the parent atom. Notice that overlap tests are not conducted for each pair of atoms in the system. As such, the modelling of adsorbates characterised by elevated end-to-end distances (e.g., long hydrocarbon chains) can lead to instabilities in PAPRECA. This is justified by considering that overlaps between the neighbours of the parent atom and deposited atoms beyond the neighbours list cutoff distance (see Eq. 5.1) might occur without being detected by overlap tests. However, overlap tests are expected to be successful for molecules whose end-to-end distance is comparable to the neighbours list cutoff distance.

The rationale behind the decision to perform tests on parent atom neighbours was motivated by

computational efficiency considerations. Calculating the distances between each of the potentially inserted molecules in the system and every atom in the simulation box is not a numerically tractable approach. Furthermore, such an approach would necessitate computationally expensive "gather" operations to collect the spatial coordinates of all system atoms in a single MPI rank. This could also impact the scalability of PAPRECA, especially in kMC/MD simulations involving a large number of parent atoms for deposition events.

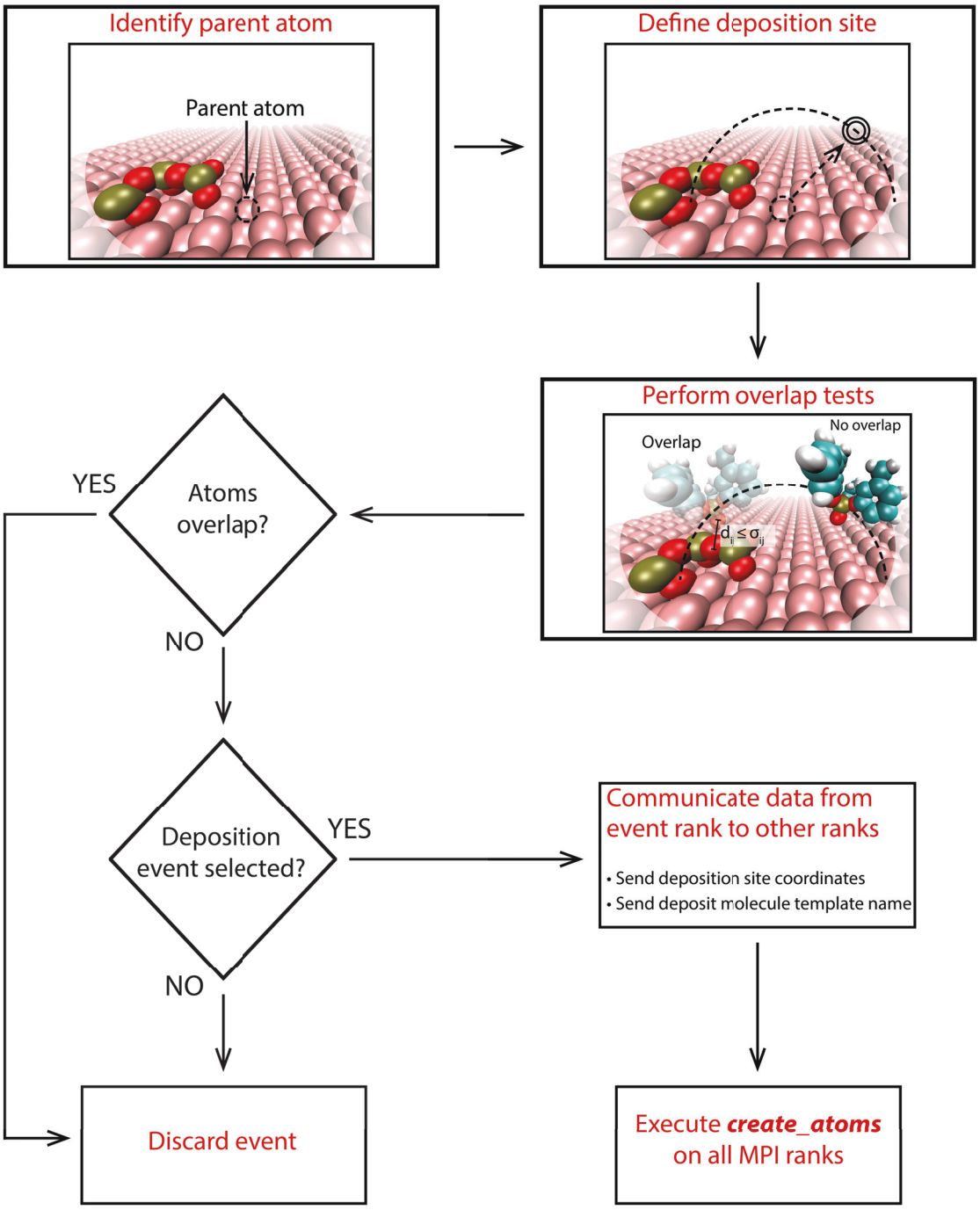


Fig. 5.14: Summary of key steps involved in deposition events (type iii). Overlap and parent atom detection images adapted from our previous work on the hybrid kMC/MD off-lattice method [270].

Overall, valid deposition events exhibit interatomic distances larger than σ_{ij}:

$$d_{ij} > \sigma_{ij} \tag{5.15}$$

Here, σ_{ij} is an equilibrium distance between atom types i and j that is similar to that in the LJ potential [205]. Variable d_{ij} refers to the Euclidean distance (L2 norm) between the parent atom i and the candidate deposited atom j. Once again, a PAPRECA wrapper around the `minimum_image()` function of LAMMPS is deployed to calculate distances while accounting for any PBCs in the simulation box. The σ parameters are initialised in PAPRECA at the beginning of the simulation. In any case, if an overlap is detected, the deposition event is discarded. Alternatively, the valid deposition event is inserted in the local *table of detected events* of the MPI rank.

To account for the influence of the surface coverage on the rate of the growing film, PAPRECA deploys variable sticking coefficients. The sticking coefficient σ is calculated on the master MPI rank following the detection of all deposition events in each subdomain. The coefficient is evaluated using the following equation:

$$\sigma = 1 - \frac{N_{occ}}{N_{total}} \tag{5.16}$$

Where N_{occ} is the fraction of occupied parent atoms for deposition events (i.e., atoms with unsuccessful overlap tests). N_{total} is the total number of sites (i.e., $N_{total} = N_{occ} + N_{free}$) accounting for both occupied and free sites. The estimated sticking coefficient is communicated from the master rank to the other MPI ranks. Then, σ is multiplied by the rates of deposition events in the *table of detected* events. By doing so, elevated surface coverage values are associated with reduced adsorption probabilities. Note that variable-sticking coefficients are utilised by default in PAPRECA. Nonetheless, constant sticking coefficients are also supported through the "constant" `sticking_coeff` option. This option must be passed to the `PAPRECA:PredefinedDeposition` object before its insertion into the *predefined table of events*. A flowchart summarising the central steps of deposition events is given in Fig. 5.14.

When a deposition event is selected for execution, the *event rank* transfers event-related data to all other MPI ranks. Specifically, the deposit site coordinates as well as the name of the molecule template linked to the predefined event are communicated. Finally, a `create_atoms` command with the `mol` option (as implemented in LAMMPS) is executed on all MPI ranks to insert the deposit in the system. By doing so, the `create_atoms` command places the molecule such that the local COM deposit coordinates coincide with the deposit site coordinates. The inserted molecule is not rotated. Therefore, deposited molecules originating from the same predefined deposition event exhibit identical orientation. Nonetheless, the molecule can be rotated at the beginning of the simulation by modifying the local spatial coordinates of atoms in the LAMMPS molecule template.

Notice that because of the use of LAMMPS molecule templates, there is no requirement to transfer the spatial coordinates of each deposited atom or information regarding the bonded interactions (i.e., bonds, angles, dihedrals, impropers) of the molecule from the *event rank* to the rest of the MPI processes. This boosts the computational efficiency and enhances the scalability of the kMC stage of PAPRECA. Moreover, the use of `create_atoms` function eliminates the need to adjust the coordinates of deposited molecules to comply with any PBCs because LAMMPS handles them natively. This lowers the complexity linked to the implementation and execution of predefined deposition events in PAPRECA.

The `depoheights` setting is an optional feature that restricts deposition events to a specific region in the simulation domain. When this setting is activated, parent atoms can only be located

within a cutoff distance (Δh) from the current film height (h):

$$h + \Delta h \geq z \geq h - \Delta h \tag{5.17}$$

Where z is the z-coordinate of the parent atom. Utilising the `depoheights` demands the calculation of the film height at the beginning of each kMC stage. The film-height estimation algorithm used in PAPRECA is discussed in detail in Section 5.3.3.1.

5.3.2.5 Supported atomistic events: monoatomic desorption

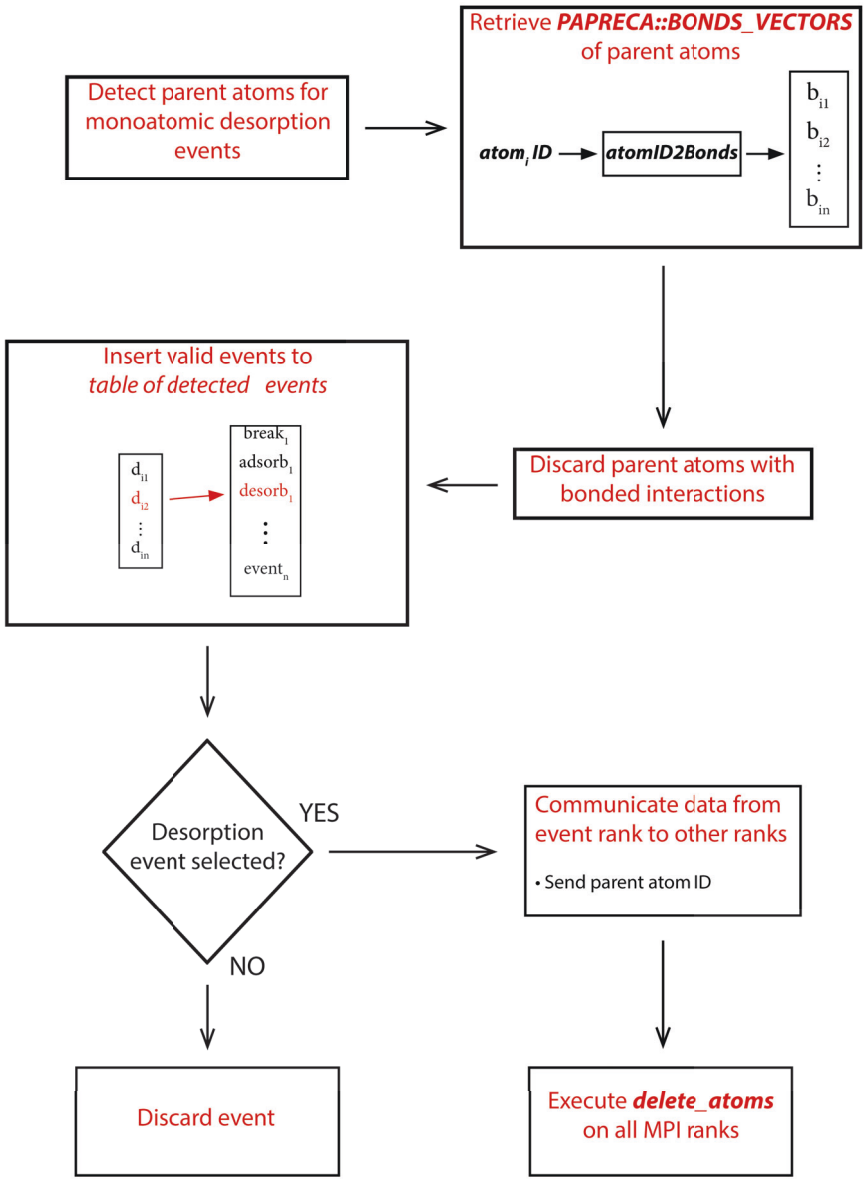


Fig. 5.15: Summary of key steps involved in monoatomic desorption events (type iv).

PAPRECA supports monoatomic desorption events solely for atoms not exhibiting bonded interactions. Hence, only non-bonded terms must be defined for atom types participating in desorption events. The types of atoms that can be parents for monoatomic desorption, as well as the rate of the event, are required to construct `PAPRECA::PredefinedMonoatomicDesorption` objects.

Monoatomic desorption events are discovered locally by each MPI rank. Initially, the types as well as IDs of "owned" atoms are extracted from LAMMPS via a `lammps_extract_atom` operation. Following, atoms are looped and eligible atom types (as defined in the *table of predefined events*) are marked as monoatomic desorption parents. Then, PAPRECA examines whether the valid atom types are "lone" (i.e., do not feature any bonded interactions). This is done by mapping the ID of the atom to the relevant `PAPRECA::BONDS_VECTOR` and then examining if such a vector is an empty container. Valid monoatomic desorption events are inserted into the local *table of detected events*. When the *event rank* selects a monoatomic desorption event for execution, the ID of the parent atom is communicated from the *event rank* to the rest of the MPI ranks. Finally, the event is executed by deleting the parent atom from the simulation box via a `delete_atoms` operation called on all MPI ranks. The key steps involved in the monoatomic desorption events are graphically illustrated in Fig. 5.15.

5.3.2.6 Supported atomistic events: diffusion hops

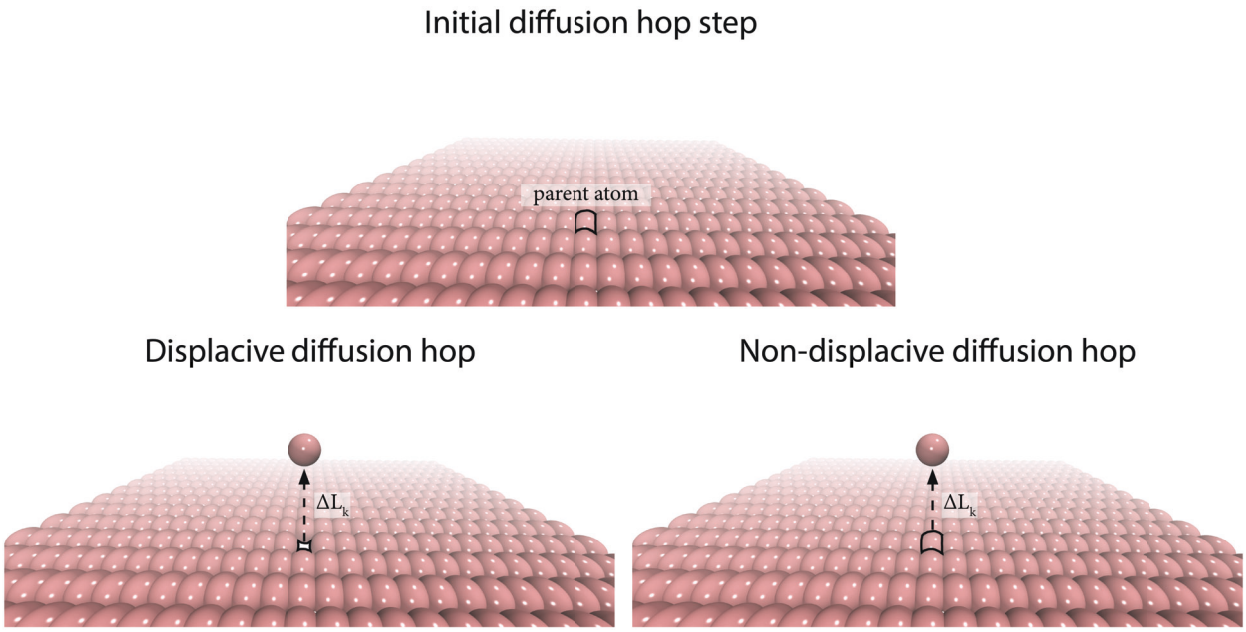


Fig. 5.16: Types of supported diffusion hop events in PAPRECA. **(Top):** initial diffusion hop step with identification of parent atom. **(Bottom left):** *displacive* diffusion hop where the parent atom moves from its initial position. **(Bottom right):** *non-displacive* diffusion hop where the parent atom is not modified and a new atom is placed in the simulation box at a separation distance of ΔL_k.

Diffusion events in PAPRECA displace atoms from their initial position to a different one in the simulation box. PAPRECA replaces fixed lattice sites with mobile event sites (as explained in Section 5.3.2.1). Therefore, atoms are not displaced between strictly defined lattice sites and can move unrestricted within the simulation box. Hence, PAPRECA can become a powerful tool to model diffusion hops through different crystalline phases or even amorphous materials, as well as systems characterised by a low degree of crystallinity. For instance, hybrid kMC/MD simulations can shed light on the diffusion of ions through SEIs in lithium-ion batteries [8]. The following inputs are demanded to initialise a `PAPRECA::PredefinedDiffusionHop` object:

- **parent atom type**. This variable defines the types of atoms that can be displaced.

- **hop distance(ΔL_k)** which defines the characteristic length for diffusion for the k^{th} predefined diffusion hop event.
- **diffusion velocity** can be set to control the velocity of the atom following the execution of the diffusion hop event.
- **diffusion type**. As of September 17^{th} 2024 (version 2.0.0) PAPRECA supports two types of diffusion events. *Displacive* events move the parent atom from its initial position to a different location in the simulation box. *Non-displacive events* spawn a new atom in the system without modifying the properties of the parent atom. *Non-displacive* events can be used to approximate diffusion events in systems exhibiting an immobile substrate. *Non-displacive* events were previously deployed in our hybrid off-lattice study on the decomposition of TCP on iron (see Chapter 3) [270] under the assumption that the mass of the underlying substrate is significantly higher than that of the phosphate film. The two supported types of diffusion hops in PAPRECA are illustrated in Fig. 5.16.
- **diffused type** which dictates the atom type of the diffused atom. This parameter was introduced to elevate the flexibility of PAPRECA. The *diffused type* can be identical to or different from the parent atom type.
- **rate** of diffusion hop event.

The local discovery of diffusion hops begins with calling the `lammps_extract_atom` function to retrieve the spatial coordinates, IDs, and types of "owned" atoms of a given MPI rank. Then, atoms are looped and types linked to `PAPRECA::PredefinedDiffusionHop` objects (as in the *table of predefined events*) are marked as parents to diffusion steps. Then, the diffusion site (i.e., the final location) of each parent type is defined.

The `random_diffvecs` feature controls the location of the diffusion site. Similarly to the sites of deposition events (see Section 5.3.2.4), the diffusion sites can be situated directly above or below the parent atom at a distance of *hop distance* (ΔL_k) by using the `random_diffvecs NO` option. Furthermore, `random_diffvecs NO 2D` discards diffusion hops below (towards the negative z-axis) the parent atom. Alternatively, by utilising `random_diffvecs YES` the parent atom hops to the surface of a sphere of radius ΔL_k as outlined by the equations below:

$$X = x + \Delta L_k sin(\theta) cos(\phi) \tag{5.18}$$

$$Y = y + \Delta L_k sin(\theta) sin(\phi) \tag{5.19}$$

$$Z = z + \Delta L_k cos(\theta) \tag{5.20}$$

Where X, Y, and Z denote the coordinates of the deposition site. Also, angle ϕ is obtained from 5.13 and θ from 5.14. Once again, $\theta \in [0, \frac{\pi}{2}]$ and $\theta \in [0, \pi]$ to define the northern hemisphere and the full sphere around the parent atom in the `random_diffvec YES 2D` and `random_diffvecs YES 3D` cases, respectively. Fig. 5.17 provides illustrated examples of diffusion sites as generated by the different `random_diffvecs` options.

Similarly to the deposition events (see Section 5.3.2.4), overlap tests are performed to discard invalid events that can lead to instabilities in the hybrid kMC/MD simulation. An identical

criterion to that related to deposition events is deployed (see Eq. 5.15). Note that performing overlap tests requires the recovery of the "full" neighbours lists of PAPRECA for the parent atom and estimation of (Euclidean) distances between the diffusion site and atoms in its vicinity. Valid diffusion hop events (i.e., those whose parent atoms obey eq. 5.15) are added to the local *table of detected events*.

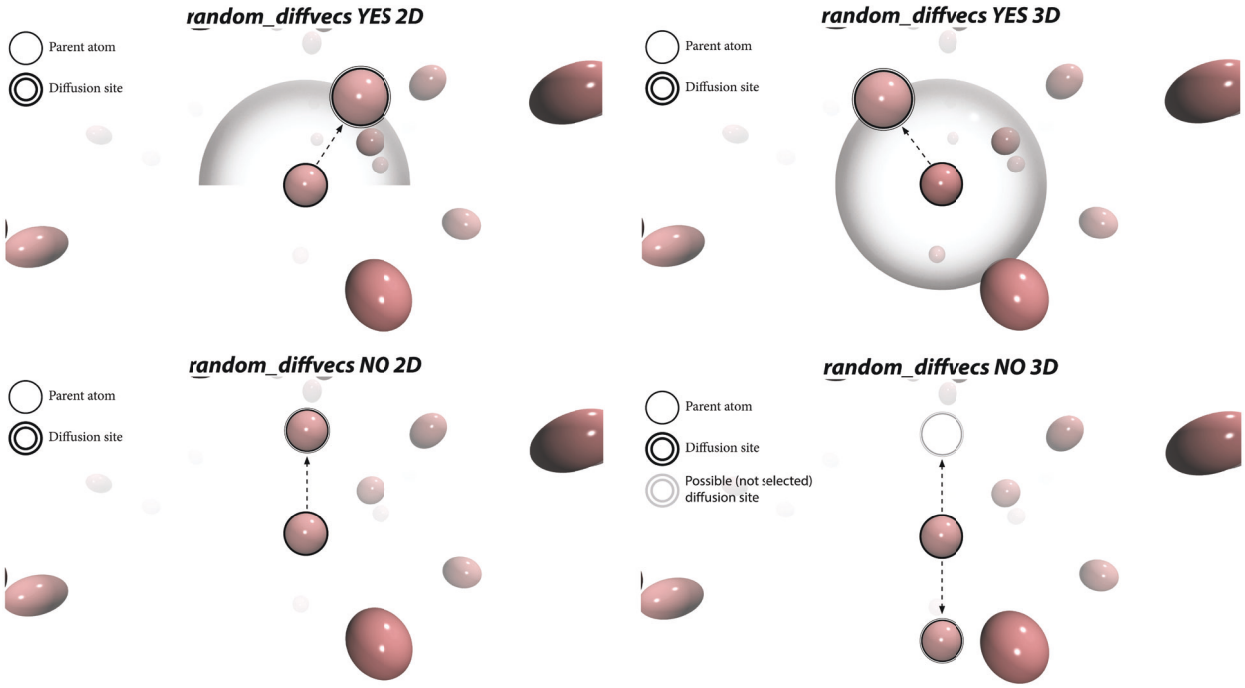


Fig. 5.17: Deposition sites as generated by the `random_diffvecs` command. **(Top left):** random_diffvecs YES 2D places diffusion sites on the surface of the northern hemisphere above the parent atom. **(Top right):** `random_diffvecs YES 3D` unlocks sites on both hemispheres. **(Bottom left):** `random_diffvecs NO 2D` and **(bottom right):** `random_diffvecs NO 3D` generate diffusion sites directly above or both above and below the parent atom, respectively.

The procedure related to the execution of a diffusion event (chosen by the *event rank*) varies based on whether the associated `PAPRECA::PredefinedDiffusionHop` object is linked to a *displacive* or a *non-displacive* move. For *non-displacive* events, the *diffused type* and the spatial coordinates of the diffusion site are communicated from the *event rank* to the remaining MPI processes. Following, the `create_atoms` function is called from all MPI processes to insert a new atom whose centre coincides with the diffusion site. Execution of *displacive* hops additionally requires the transfer of the parent atom ID from the *event rank* to the other MPI ranks. To avoid instabilities in the MD stage of PAPRECA, bonded interactions between the parent atom and neighbouring particles are removed. This operation is performed by calling the `delete_atoms` function of LAMMPS with the "bond yes" option. Then, a call to the `create_atoms` function on all MPI processes adds a new atom of *diffused type* on the diffusion site. In both cases (*displacive* and *non-displacive*), PBCs and the motion of atoms through the edges of the simulation box are handled natively by the `create_atom` function of LAMMPS. The main steps linked to diffusion hop events are summarised in the flowchart of Fig. 5.18.

PAPRECA supports custom diffusion hop steps. In such steps, a user-defined criterion is deployed to determine the validity of diffusion events. As of September 17^{th} 2024 (version 2.0.0), the `Fe_4PO4neib` custom diffusion hop option is available. When this option is utilised, four phosphate

(PO_4) structures must be present in the vicinity of the parent atom. Detecting valid parent atoms for `Fe_4PO4neib` is performed locally on the MPI rank that "owns" the parent atom as follows. Firstly, the "full" neighbours list of the parent atom is accessed. Then, neighbours are looped and their types are extracted via a `lammps_extract_atom` operation. Following, the IDs of atom types linked to phosphorus species are obtained (again through a call to `lammps_extract_atom`) and their `PAPRECA::BONDS_VECTOR` is retrieved using the `PAPRECA::atomID2Bonds` map. Finally, the PO_4 structures are detected by counting the number of $P-O$ bonds of the phosphorus-type atom. Valid `Fe_4PO4neib` custom diffusion hop events (associated with parent atoms with four PO_4 neighbours) are inserted in the *table of detected events* of the relevant MPI rank. A non-parallelised version of the `Fe_4PO4neib` diffusion hop event was firstly introduced in our previous hybrid kMC/MD study on the decomposition of TCP on iron (see Fig. 3.10 in Section 3.3.3 of Chapter 3) [270].

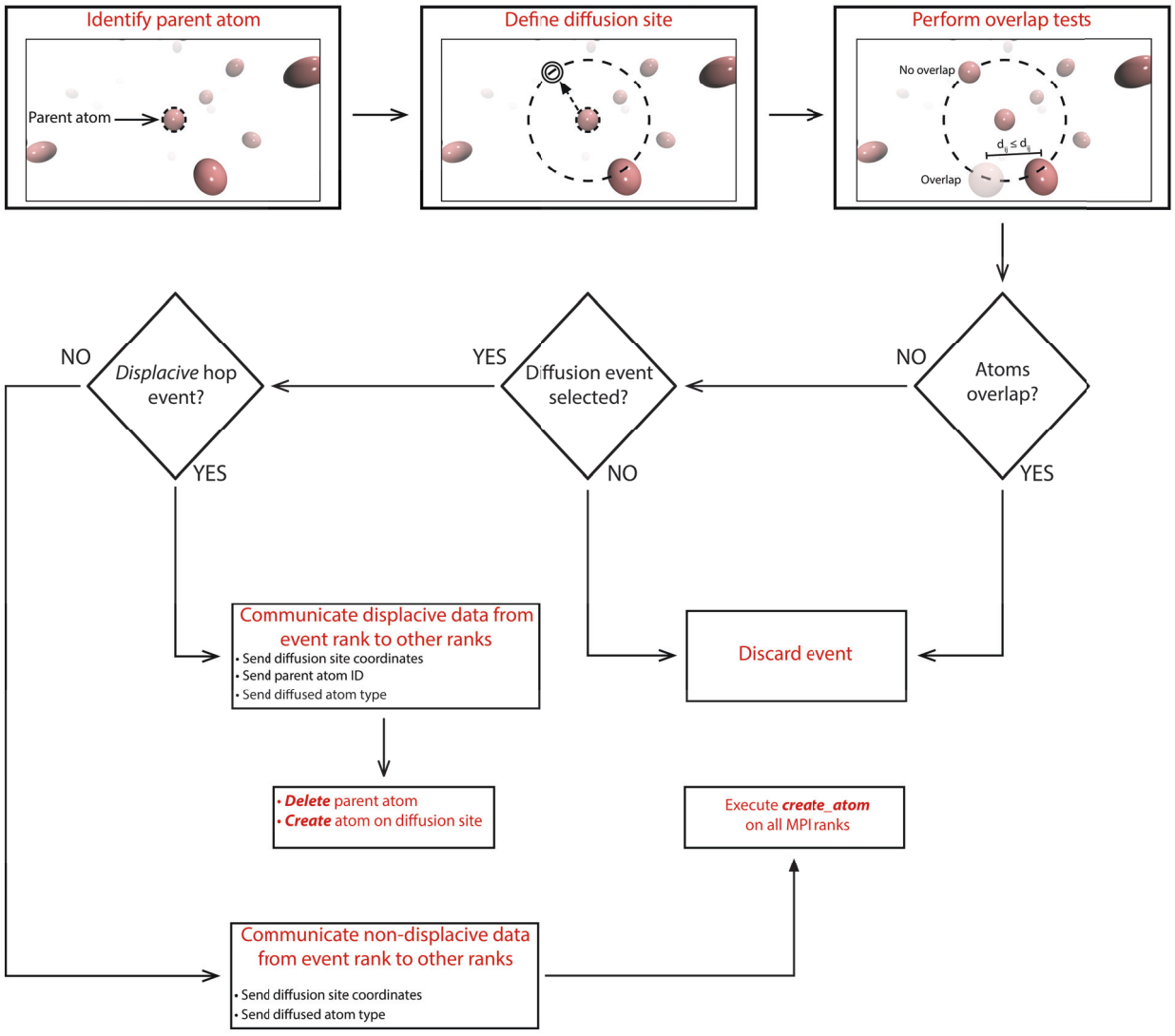


Fig. 5.18: Flowchart summarising the main steps of diffusion hop events.

5.3.3 Utility operations

5.3.3.1 Film-height estimation

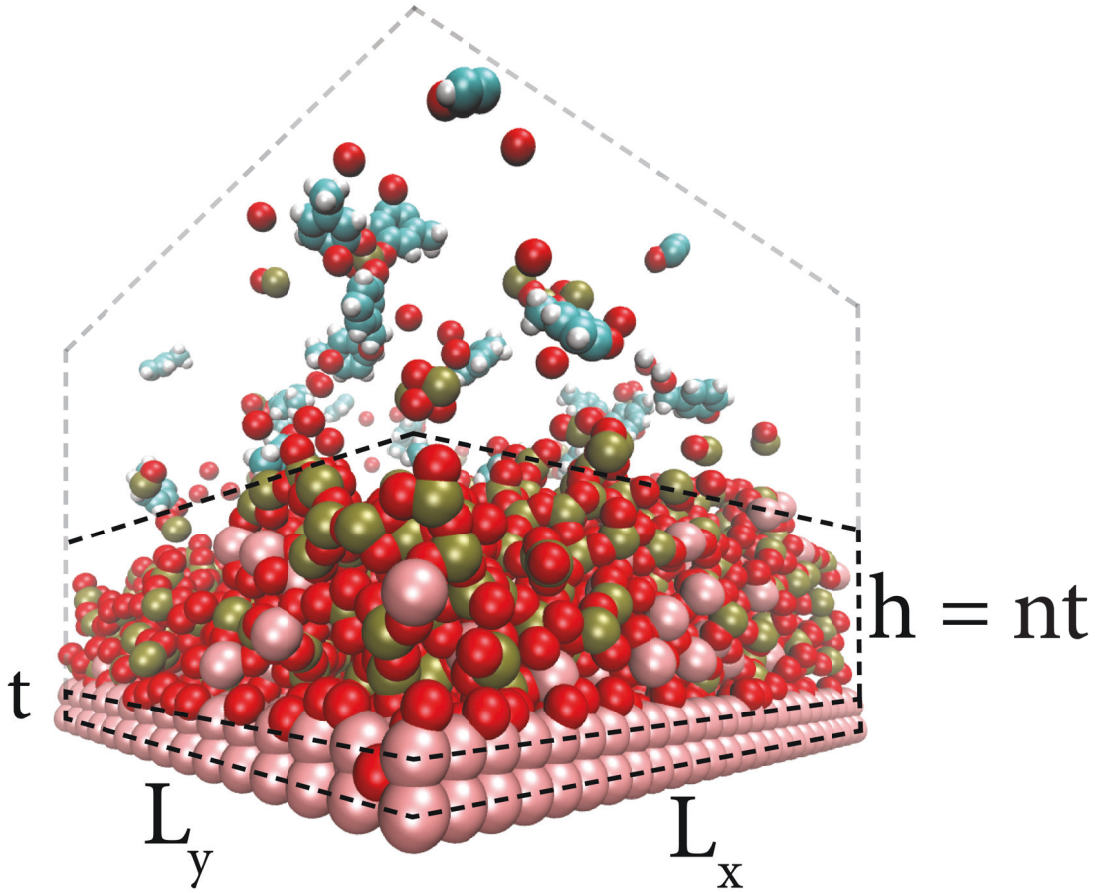


Fig. 5.19: Film height determination on global mass bins (of dimensions L_x, L_y, and t). Image adapted and reproduced under the CC BY NC ND 4.0 license from our preprint on the hybrid kMC/MD method [233].

As of September 17^{th} 2024 (version 2.0.0) PAPRECA deploys a parallel spatial binning algorithm to estimate the film height in the simulation box. This algorithm is called at the beginning of each kMC stage and operates as follows. Firstly, the subdomain linked to each MPI rank is divided into rectangular parallelepiped bins of sides $L_{x,p}$ and $L_{y,p}$ (dimensions of subdomain p along the x- and y-directions). The thickness (t) of the sections is a user-defined parameter. Then, each MPI rank stores the sum of masses of each atom type along with a cumulative mass corresponding to the total mass contained in the bin. Following, the master MPI process creates global mass bins of sides L_x and L_y (dimensions of the full computational domain) and thickness t. An MPI reduce operation is performed to assemble a global mass bins array on the master MPI process (rank 0). Additionally, rank 0 receives the cumulative masses of each MPI process. Finally, the master MPI rank chooses the film height as:

$$h = nt \tag{5.21}$$

With $n \in \mathbb{N}$ being the smallest natural number that satisfies the equation below:

$$\sum_{i}^{n} m_i \geq C m_{tot} \tag{5.22}$$

Where m_i is the mass of the i^{th} bin. C is another user-defined parameter called the *height percentage cutoff*. For instance, a value of 0.95 means that 95% of the total mass of the system is contained between the lower z-boundary of the simulation box and the estimated film height (h). Note that the total mass is obtained from the following equation:

$$m_{tot} = \sum_{i}^{N_{bins}} m_i \tag{5.23}$$

Here N_{bins} represents the total number of bins. The described algorithm is a modified version of the height-estimation procedure described in our preprint on the hybrid off-lattice kMC/MD method for amorphous thin-film growth [233]. Nonetheless, the algorithm presented in this work is parallelised and defines the height of the film through a mass-based criterion. In contrast, the algorithm in our preprint is serial and performs a selection utilising density bins (see Eq. 8 in the relevant preprint) [233]. Fig. 5.19 provides a graphical illustration of the film-height definition step on the master MPI rank.

5.3.3.2 Removal of disconnected atoms

Desorption of molecules from the film to the vacuum region above it can occur during the MD stage of PAPRECA. In such cases, particles can be situated above the current height (of the kMC step) and separated from the film by a distance greater than the force cutoff of the selected interatomic potential (i.e., D_{ff} in Eq. 5.1). This can introduce errors in the film height estimation procedure and result in unrealistically high h (as in eq. 5.21) values. Furthermore, such a phenomenon can elevate the numerical effort of the MD and kMC stages of PAPRECA, as unnecessary calculations are performed on some atoms that are disconnected from the growing film. Finally, the presence of such atoms can bias the rates of deposition events. This is justified by considering that remaining particles can increase the number of detected overlaps, which in turn lowers the sticking coefficient of a deposition event (as defined in Eq. 5.16).

The `desorption` command was introduced to address the above considerations. Note that this is not a predefined event and should not be confused with monoatomic desorption steps (see Section 5.3.2.5). The `desorption` command is a utility operation that periodically deletes groups of atoms from the system. This operation is performed with a user-defined frequency and does not need to be selected by the rkMC scheme (Eq. 5.3.2.1) nor contributes to the global event rate (as in Eq. 5.5). The `desorption` command removes atoms from the simulation box whose z-coordinates obey the following equation:

$$z \geq h_{cut} \tag{5.24}$$

With h_{cut} being a user-defined variable (called the *desorption cutoff*). Particles are deleted immediately after the MD stage of PAPRECA.

Three algorithms were implemented to remove *desorbed atoms* (as defined in PAPRECA) from the simulation domain. The `LAMMPS_region` algorithm is the simplest desorption method in PAPRECA. However, it is solely compatible with shrink-wrapped boundaries on the z-direction of the simulation box. Note that the dimensions of such boundaries are accordingly adjusted to encompass all atoms in the simulation box. The `LAMMPS_region` algorithm leverages that feature

and operates as follows. Firstly, the upper boundary of the simulation box (`boxhi` attribute of the domain object) is extracted from LAMMPS. Then, `boxhi` is compared to h_{cut}. A value of h_{cut} smaller than `boxhi` denotes that particles exist above the user-defined *desorption cutoff*. PAPRECA then uses LAMMPS groups to group all atoms in the simulation box whose z-coordinate is between h_{cut} and `boxhi`. Finally, the collected (in the LAMMPS group) atoms are deleted with a LAMMPS function call to `delete_atoms` on all MPI ranks.

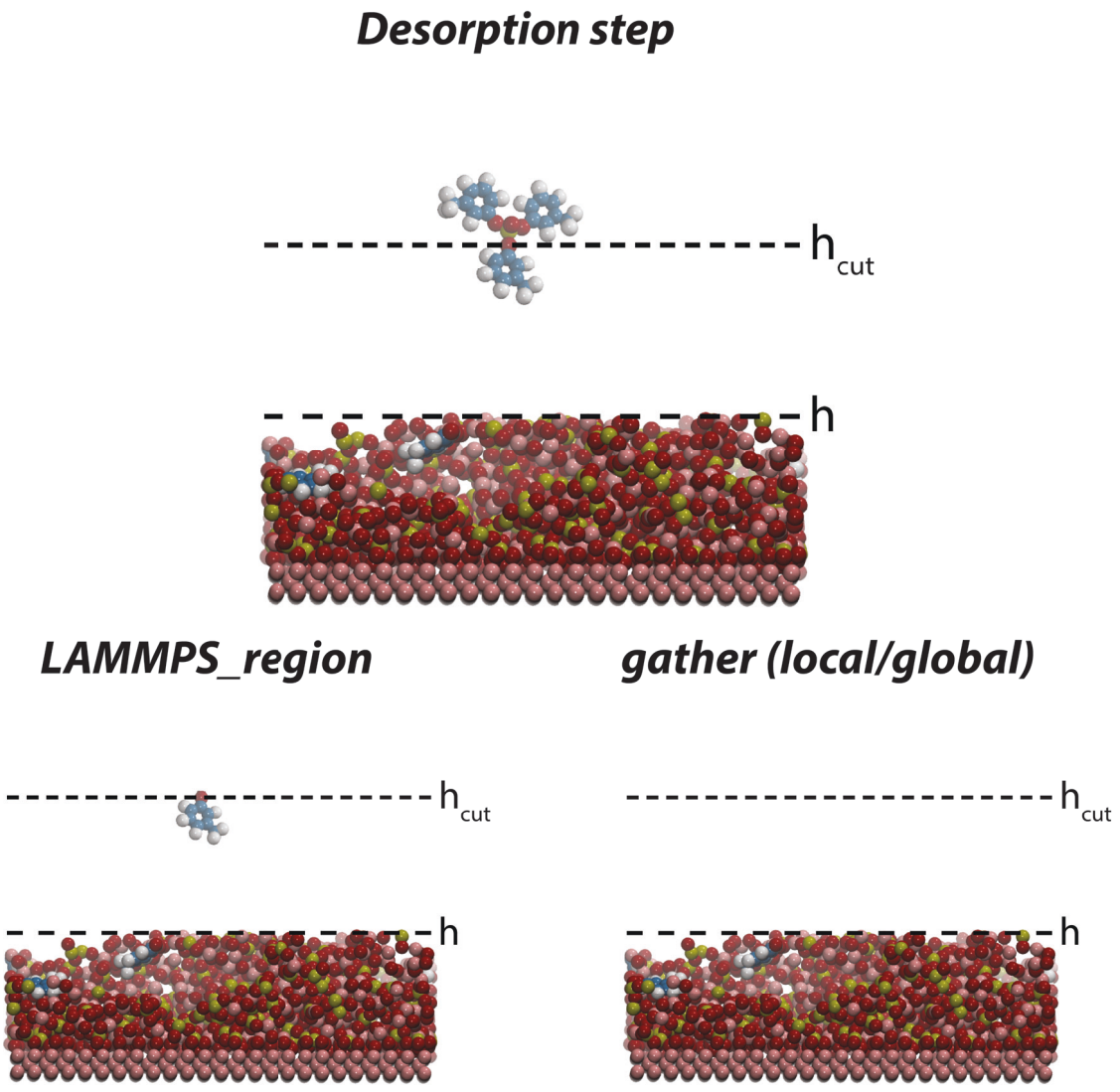


Fig. 5.20: Removal of atoms via the `desorption command`. **(Top):** initial desorption step with identification of atoms located above h_{cut}. **(Bottom left):** `LAMMPS_region` command that solely deletes atoms with $z \geq h_{cut}$. **(Bottom right):** `gather_all` and `gather_local` features removing atoms with $z \geq h_{cut}$ as well as bonded atoms.

Deleting atoms from the computational domain can perturb the forces exerted on neighbouring particles. For instance, deleting an atom but not its bonded pair can result in a force imbalance due to the release of bond energy. Such an instance can lead to the rapid acceleration of the remaining particle and trigger numerical instabilities in the simulation. To circumvent these issues, the `gather_all` and `gather_local` desorption options were introduced in PAPRECA. These features not only delete atoms located above h_{cut} but also any neighbouring atom bonded to them.

The `gather_local` algorithm is a parallelised method in which MPI ranks identify *desorbed*

atom IDs within their local subdomain. Specifically, each MPI rank extracts the coordinates of its "owned" atoms and loops over their z-positions. Atoms obeying Eq. 5.24 are stored in an array of deleted atom IDs. A recursive function is deployed to collect all atoms bonded to the atom IDs marked for deletion. In particular, the `PAPRECA::BONDS_VECTORS` of atoms are retrieved using the `PAPRECA:atomID2bonds` map. Then, the recursive function travels from bonded atom to bonded atom and marks atoms for deletion until a loop is formed or until all bonded atoms are retrieved. A pseudocode of the recursive function described above is provided in Algorithm 1. In any case, the locally collected atom IDs are communicated to the master MPI rank. Then, rank 0 trims duplicate IDs and transfers the processed array back to all other MPI ranks. Finally, the `delete_atoms` function of LAMMPS is called on all MPI ranks to remove the IDs marked for deletion.

Algorithm 1 Recursive Collection of Bonded Atoms

Require: *atom_id* (ID of the starting atom)
Require: *delids* (list of collected atom IDs)
Require: *delids_set* (set of atom IDs marked for deletion)
Require: *atomID2Bonds* (map of atom IDs to `PAPRECA::BONDS_VECTOR`)

```
function collectBondedAtoms(atom_id, delids, delids_set, atomID2Bonds)
    bonds ← atomID2Bonds[atom_id]                ▷ Retrieve PAPRECA::BONDS_VECTOR
    for all bond ∈ bonds do
        bondatom_id ← bond.getBondAtom()
        if bondatom_id ∉ delids_set then          ▷ Check if atom is already processed
            Insert bondatom_id into delids_set
            Append bondatom_id to delids
            collectBondedAtoms(bondatom_id, delids, delids_set, atomID2Bonds)
        end if
    end for
end function
```

The main difference between the `gather_local` and `gather_global` is that the latter deploys solely the master MPI rank to collect atoms obeying Eq. 5.24. Specifically, in the case of `gather_global`, the master MPI rank gathers the IDs, types, and coordinates of particles of all subdomains (using a `lammps_gather_atoms` operation). Then, desorbed atoms together with their bonded pairs are retrieved with a recursive procedure identical to that of `gather_local`, communicated from rank 0 to all other MPI ranks, and deleted via `delete_atoms`. Overall, the `gather_global` and `gather_local` features generate identical trajectories. On the other hand, `LAMMPS_region` deletes a decreased number of atoms compared to the gather commands. Therefore, `LAMMPS_region` samples different microstates than the `gather_local` or `gather_global` commands. Nonetheless, trajectories produced by all three commands are usually similar. This is justified by considering that particles whose bonded pairs are deleted via `LAMMPS_region` typically remain in the `desorption` region (i.e., their coordinates obey Eq. 5.24) and are removed in subsequent kMC steps. A visual representation of `LAMMPS_region` and `gather_all` as well as `gather_local` features for removal of *desorbed atoms* is provided in Fig. 5.20.

5.3.3.3 Files output

A variety of files can be exported by PAPRCEA during the kMC/MD run. In all cases, the master MPI rank writes to a given file while the secondary MPI processes wait. This prevents multiple MPI ranks from simultaneously appending to a file, which can result in file corruption. The "papreca.log" file is generated by default at the beginning of a hybrid kMC/MD run. One line is written to the file immediately after the end of each kMC stage. It contains the hybrid kMC/MD step number, the type of selected event at the current step, and the current global simulation time (in seconds). The "papreca.log" file additionally contains specific information associated with the executed event at the present step. In particular, the IDs as well as the bond type are exported when it comes to reactions (bond-breaking and bond-formation events discussed in Section 5.3.2.3). The deposit site coordinates, insertion velocity, and LAMMPS molecule template name are output for deposition events (see Section 5.3.2.4). The ID as well as the type of the parent atom are output for monoatomic desorption events (see Section 5.3.2.5). Finally, the diffusion site, ID of parent atom, insertion velocity, type of diffusion (*displacive* or *non-displacive*), and atom type of diffused atom (as in Section 5.3.2.6) are exported for diffusion hop events.

The "execTimes.log" file can be optionally activated. A single line is appended to the file at the beginning of a hybrid kMC/MD step with a user-defined printing frequency. The "execTimes.log" file lists the current step number, the total number of atoms at the present step, the walltimes of the kMC as well as MD stages in that step, and the total CPU time of the current step. Since PAPRECA is a parallelised program, different MPI ranks can exhibit varying CPU times. This is justified by considering that an increased number of operations must be executed in the *event rank* to select the executed elementary step or in the master MPI process, which selects the *event rank* and coordinates information from secondary MPI processes (see Section 5.3.2). Moreover, depending on the microstate and the chosen subdomain decomposition scheme (see Section 5.3.1.1), certain MPI processes might perform additional overlap tests (e.g., for deposition or diffusion hop events, see Sections 5.3.2.4 and 5.3.2.6). This raises the computational effort of specific MPI processes. Furthermore, varying walltimes between MPI ranks can be observed when it comes to the MD stage of PAPRECA due to reasons associated with load imbalances and non-uniform atomic density across subdomains (see Section 4.2.1).

To thoroughly investigate the differences in walltimes among MPI ranks, PAPRECA outputs the minimum, maximum, and average CPU times linked to the kMC stage, the MD stage, and the complete hybrid kMC/MD step. This demands coordination of the individual walltimes of MPI processes on the master MPI rank, which appends on the "execTimes.log" file. In particular, calls to the `MPI_Wtime()` function of the MPI library are deployed to insert timestamps and measure the walltime in the different stages of the program (i.e., kMC and MD). Then, MPI reduce operations are performed to collect the minimum, maximum, and average CPU times of the step on the master MPI rank. Finally, the MPI rank prints information to the "execTimes.log" file. Walltime files can be useful in the direction of investigating the scalability aspects of PAPRECA in different applications. For example, the "execTimes.log" file was utilised to examine the scalability of our hybrid kMC/MD model on the thermal decomposition of TCP on iron (illustrated in Fig. 5.33).

If a film-height calculation method (see Section 5.3.3.1) is initialised in a PAPRECA simulation, two different types of optional files can be exported. Firstly, the "heightVtime.log" file can be generated. A user-defined variable controls the printing frequency to the "heightVtime.log" file.

The file contains two columns listing the time as well as the current height at the present step. These files can become useful to capture the kinetic characteristics (e.g., growth rate) of thin films in hybrid kMC/MD applications (see a relevant graph for TCP coatings in Fig. 3.13). Moreover, the use of a spatial binning algorithm dedicated to the estimation of film height (see Section 5.3.3.1) allows for the output of "distribution.log" files. A "distribution.log" file is generated with a user-defined export frequency. Distribution files contain the total number of atoms of each type contained in each bin. Note that solely the global bin (retained in the master rank) is exported since it includes contributions from all MPI processes. As discussed in Section 5.3.3.1, the bins exhibit sides of L_x and L_y and a height of t (a user-defined parameter controlling the thickness of the bins). Mass bins are converted to atom number bins by dividing the mass of an atom type by the total mass of a bin. Distribution files can shed light on the temporal evolution of the elemental distribution of thin films and were previously utilised in our initial hybrid kMC/MD work (see Fig. 3.19) [270].

Finally, the output of "surface_coverage.log" files can be optionally activated with a user-defined printing frequency. These files contain two columns listing the time and surface coverage of system sites. Note that at least one deposition event must be set up in the PAPRECA simulation to enable the generation of "surface_coverage.log" files. This is justified by considering that surface coverage calculations (see Section 5.3.2.4 and Eq. 5.16) are solely triggered when deposition elementary processes are activated and included in the *table of predefined events*.

5.3.3.4 Estimation of event rates

A rate constant is demanded to construct any of the predefined event objects (i.e., `PAPRECA::PredefinedReaction`,`PAPRECA::PredefinedBondForm`, `PAPRECA::PredefinedDeposition`, `PAPRECA::PredefinedMonoatomicDesorption`, and `PAPRECA::PredefinedDiffusionHop` as introduced in Sections 5.3.2.3, 5.3.2.4, 5.3.2.5, and 5.3.2.6, respectively). The `rate_manual` option can be used during the construction of predefined event objects to pass a fixed rate for an elementary process before its inclusion in the *predefined table of events*. Nonetheless, this demands a prior manual rate calculation performed by the PAPRECA user.

To boost the flexibility of the software and favour its user-friendliness, the "rates_calc.h" header was implemented in PAPRECA. This header contains a small library of rate-estimation models appropriate for different classes of atomistic events. Firstly, the `rate_arrhenius` option can be used with any predefined event to retrieve a rate from the Arrhenius equation (see Eq. 3.1). Here, the attempt frequency (ν), activation energy (ΔE), and temperature (T) have to be provided as inputs.

The `rate_hertz` option is designed predominantly for `PAPRECA::PredefinedDeposition` objects and estimates the process rate using the kinetic theory of gases and the Hertz-Knudsen equation (Eq. 3.8) [246]. When "fixed" sticking coefficients are used (see Section 5.3.2.4), the $\sigma(\theta, T)$ parameter is user-provided. In contrast, if the deposition event exhibits a variable sticking coefficient, $\sigma(\theta, T) = 1$ is utilised during the initialisation of the `PAPRECA::PredefinedDeposition` event in the *predefined table of events*. After the calculation of the variable sticking coefficient of the current kMC step, the deposition event rate is properly adjusted by multiplying by σ (as in Eq. 5.16) to account for the influence of surface coverage. Apart from the sticking coefficient, the partial pressure (P) of the adsorbate, surface area (A) of the deposition site, the weight of the deposition (m),

and the associated temperature (T) have to be passed to the `PAPRECA::PredefinedDeposition` object via the `rate_hertz` option.

Finally, PAPRECA supports the `rate_desorb` option. Such an option is appropriate for desorption events (e.g., `PAPRECA::PredefinedMonoatomicDesorption`). The relevant rate is obtained by an Arrhenius-type equation of the following form [320]:

$$r = \frac{\kappa_B T}{h} e^{-\frac{E_{ads}}{\kappa_B T}} \tag{5.25}$$

Where κ_B and h are the Boltzmann and Planck constants, respectively. Also, E_{ads} is the adsorption energy of the adsorbate on a given substrate.

5.3.4 Hybrid kMC/MD implementation

In Sections 5.3.1 and 5.3.2, we analysed specific aspects of the MD and kMC stages of PAPRECA, respectively. Section 5.3.3 offers an overview of the utility functions and operations in PAPRECA. This section discusses PAPRECA as a complete hybrid kMC/MD program. PAPRECA simulations begin with a setup stage. The setup stage comprises three phases. Firstly, an MPI setup phase takes place to initialise MPI with a given number of MPI processes and any optional commands. The number of MPI ranks as well as the optional MPI flags are user inputs passed to the PAPRECA executable at runtime (e.g., via "mpiexec" or "mpirun").

In the second setup phase, LAMMPS is initialised. In the beginning, a `LAMMPS_NS::LAMMPS` (as implemented in the LAMMPS library) object is constructed. This object interfaces the kMC and MD stages of PAPRECA. Through this object, the kMC stage accesses atom-related data structures (e.g., positions or velocities of atoms), retrieves neighbours lists, and calls LAMMPS functions (e.g., `create_atoms` or `delete_atoms`). Following the object construction, the LAMMPS input file is passed to the `LAMMPS_NS::LAMMPS` object. The master MPI rank reads the LAMMPS input file line-by-line, executes a LAMMPS command, and broadcasts the command string to the secondary MPI processes. In turn, secondary MPI processes execute the relevant LAMMPS command. After reading the LAMMPS input file, the MD stage of PAPRECA is fully initialised. This means that MD simulations can be run and LAMMPS functions can be deployed from the main PAPRECA code. The LAMMPS setup phase is responsible for the configuration of the following fundamental parameters and settings of the hybrid kMC/MD run:

- **shape** (e.g., orthogonal or triclinic [26]) and **dimensions** of the simulation box.
- **domain decomposition method** (see Section 5.3.1.1).
- **types of boundaries** (e.g., periodic, fixed or shrink-wrapped as in Section 5.3.1.1).
- **simulation units.**
- **atomic masses**.
- **timestep** for integration of the equations of motion within the MD stage of PAPRECA.
- **atom style** [26]. Note that atom styles in LAMMPS control the type of information retained for each particle in the simulation. For instance, the "atomic" style stores the IDs, types,

spatial coordinates, velocities, forces, image flags (tracking PBCs), and bit masks (used for group assignments and operations). The "molecular" style retains bond, angle, dihedral, and improper data in addition to "atomic" data. The "full" style extends the "molecular" style to include atomic charges.

- **bonded interaction (bond, angle, improper, dihedral)** styles [26] dictating the models used for bonded interactions (e.g., harmonic).
- **pair style** [26] defining the type of force field utilised in the MD stage of PAPRECA (e.g., LJ [205] or ReaxFF [208]).
- **neighbours lists** generation through the "fix papreca all papreca" custom fix for LAMMPS (see Section 5.3.1.3). The rebuild frequency, algorithm deployed for the construction of neighbours lists (e.g., binning method or simple loop through atom pairs), and list parameters (e.g., dimensions of bins) can be controlled through "neighbor" and "neigh_modify" commands of LAMMPS.

The following secondary or optional parameters of the MD stage can be set through the LAMMPS input file and within the LAMMPS initialisation phase of the setup stage of PAPRECA:

- **force field coefficients** (required by the selected pair style).
- **bonded interaction coefficients** (to configure the chosen bonded interaction style).
- **thermostat and barostat** models (e.g., Nosé–Hoover [242, 243])
- **charge equilibration** schemes (e.g., QEq method [207]).
- **minimisation styles** (e.g., CG method [237]).
- **molecule templates** required to initialise `PAPRECA::PredefinedDeposition` objects for kMC stages modelling molecular or atomic deposition (see Section 5.3.2.4).
- **screen outputs** control the frequency and the kind of information (e.g., system temperature, pressure, enthalpy) printed during the MD stage of PAPRECA.
- **file outputs** modifying the frequency and the type of exported files (e.g., trajectory, restart). See Section 5.3.3.3 for additional information.

The LAMMPS input file can also be utilised to create the initial state of the simulation. For instance, a combination of the "lattice" and "create_atoms" commands can be used to initialise a substrate. A minimisation followed by an MD run can prepare the system for subsequent kMC or MD stages. In the final phase of the setup stage, PAPRECA initialises the kMC stage as well as parameters linked to the hybrid kMC/MD simulation. Here, the master MPI rank reads the PAPRECA input file line by line and broadcasts information to the secondary MPI processes (similarly to the LAMMPS setup phase). The following parameters are configured in this phase:

- **total number (or ending time) of kMC steps.** Effectively, this controls the number of elementary processes simulated within the kMC stage of PAPRECA.

- **frequency of MD stages.** Such a variable sets the number of kMC stages per MD stage. For instance, a frequency of ten results in the execution of an MD stage between ten consecutive kMC stages.
- **duration of MD stage.** Sets the number of MD trajectory steps. Note that the timestep as well as other MD-specific parameters (e.g., thermostat or charge equilibration scheme) are configured within the LAMMPS setup phase.
- **equilibration parameters** (e.g., cutoff energy or force utilised in a minimisation scheme). Force minimisations can be deployed before or after an MD stage. Minimisations annihilate residual forces between particles and ensure that the system is at the bottom of a potential energy valley before the next kMC stage. A similar approach was used in our previous work on the hybrid off-lattice kMC/MD method [270].
- **film-height estimation and desorption algorithms along with relevant parameters** (e.g., h_{cut} in Eq. 5.24 introduced in Section 5.3.3.2)
- **equilibrium distances for atom species**. These are required to perform overlap tests (see Sections 5.3.2.4 and 5.3.2.6).
- **predefined events along with their associated parameters** i.e., bond-breaking, bond-formation, deposition, desorption, and diffusion hop events as discussed in Sections 5.3.2.2, 5.3.2.3, 5.3.2.4, 5.3.2.5, and 5.3.2.6.
- **file outputs** of the kMC stage (e.g., height versus time or elemental distribution files).

After the final setup phase, PAPRECA is fully configured and ready to progress to kMC/MD loops - the main part of PAPRECA. Here, MD stages integrate the Newtonian equations of motion to obtain an updated microstate (i.e., positions and velocities of all atoms) separated by a time increment (equal to the chosen timestep) from a previous state. Effectively, MD stages are deployed to simulate fast atomic-scale processes whose associated frequencies are in the order of femtoseconds (i.e., 10^{-15} s). Of course, an appropriate interatomic potential that captures the physics of the underlying system has to be selected. Optionally, minimisations are performed before, after, or both before and after MD stages to relax interatomic forces and prevent instabilities during the propagation of the solution to the equations of motion. MD stages are executed in LAMMPS but controlled from the PAPRECA driver function and via the previously constructed `LAMMPS_NS::LAMMPS` object. The frequency of MD stages (i.e., the number of kMC stages per MD stage) is controlled by a user-defined parameter in the PAPRECA input file. Supplementary PAPRECA operations (e.g., deletion of atoms due to *desorption*, as introduced in Section 5.3.3.2) are performed immediately after MD stages.

Communication between the kMC and MD stages is performed via the `LAMMPS_NS::LAMMPS` object and through native LAMMPS library functions dedicated to accessing LAMMPS data structures. Such an interfacing strategy eliminates the requirement of input files to transfer information between the kMC and MD stages. This favours the computational efficiency and flexibility of our hybrid kMC/MD software and is considered the main advantage of PAPRECA over our initial kMC/MD model presented in Chapter 3 [270]. Specifically, `lammps_extract_atom` operations are utilised to access per-atom information (e.g., IDs, coordinates, types, bonded

interactions of particles). On the other hand, calls to the `lammps_find_fix_neighlist` and `lammps_neighlist_num_elements` functions from the LAMMPS library are deployed to retrieve the LAMMPS neighbours lists generated for the "fix papreca" custom fix.

PAPRECA wrappers around LAMMPS native functions are utilised to interact with LAMMPS objects and call LAMMPS functions that are not directly accessible through LAMMPS library functions. For instance, to calculate Euclidean distances between particles (see sections 5.3.2.4 and 5.3.2.6), PAPRECA calls the `minimum_image` function of LAMMPS by accessing the "domain.h" via the `LAMMPS_NS::LAMMPS` object. Moreover, the `LAMMPS_NS::LAMMPS` object allows the retrieval of LAMMPS molecule templates through calls to the `find_molecule` function of the LAMMPS "molecule.h" header. Finally, the `LAMMPS_NS::LAMMPS` object enables the direct passing of LAMMPS commands to the MD stage and their execution on all MPI ranks. PAPRECA exploits such a feature in a variety of operations. For example, input command strings are constructed by the PAPRECA driver function and communicated to LAMMPS to perform minimisation sequences, create or delete atoms as well as bonds (for predefined events), and handle thermostated groups of atoms in the MD stage.

KMC stages in PAPRECA simulate rare events. Rare events refer to elementary processes (e.g., reactions, adsorption/desorption steps, diffusion hops) whose activation energies are considerably greater than $\kappa_B T$ (i.e., $\Delta E \gg \kappa_B T$). It is assumed that elementary processes are activated with rates described by an Arrhenius-type equation (see Eq. 3.1). Also, the probability of selection of an atomistic event in kMC is proportional to its rate (see Eq. 5.8). Consequently, faster atomistic processes dominate the KMC stage. Hence, the *table of predefined events* has to be meticulously assembled to prevent fast atomic-scale processes from dominating the system and compromising the time-advancing capabilities of the hybrid kMC/MD method. It is generally advised to avoid including elementary events whose rates are comparable to that of molecular vibrations (i.e., 10^{15} s). In any case, fast events (e.g., reactions with ReaxFF [208], diffusion hops or vibrations) can be effectively captured by the MD stage given an appropriate selection of interatomic potential.

KMC stages simulate rare atomistic processes as follows. Firstly, local searches for events are performed on MPI ranks. Each MPI rank stores a copy of the global *predefined table of events* to determine feasible steps in the kMC stage. Discovered kMC events (e.g., reactions, adsorption/desorption steps, diffusion hops) are inserted in the local *tables of detected events* stored in each MPI process. Finally, an elementary atomistic event is selected and executed, and the global simulation clock is advanced by Δt. Executed atomistic events directly access and modify per-atom properties in LAMMPS (e.g., positions and velocities of atoms). This means that subsequent MD and kMC stages can be simulated without further modifications to the system. Details related to the kMC operations are given in Section 5.3.2. At the end of a PAPRECA simulation (i.e., when the final simulation time or the maximum number of kMC stages is reached), a cleanup stage is performed. This stage ensures that allocated resources (e.g., LAMMPS and PAPRECA data structures, MPI communicators and buffers, networks as well as connections) are properly released and that MPI, LAMMPS, and PAPRECA are properly finalised and terminated.

Overall, MD stages capture fast events while kMC events simulate processes linked to elevated activation energies. As such, a variety of atomistic events on different timescales are accessible. This underlines the multiscale nature of hybrid kMC/MD simulations with PAPRECA. A flowchart of PAPRECA is given in Fig. 5.21. Note that an overview of the associated kMC or MD procedures

is provided here. For specific information regarding the kMC and MD stages, the reader is advised to refer to Sections 5.3.1 and 5.3.2, respectively.

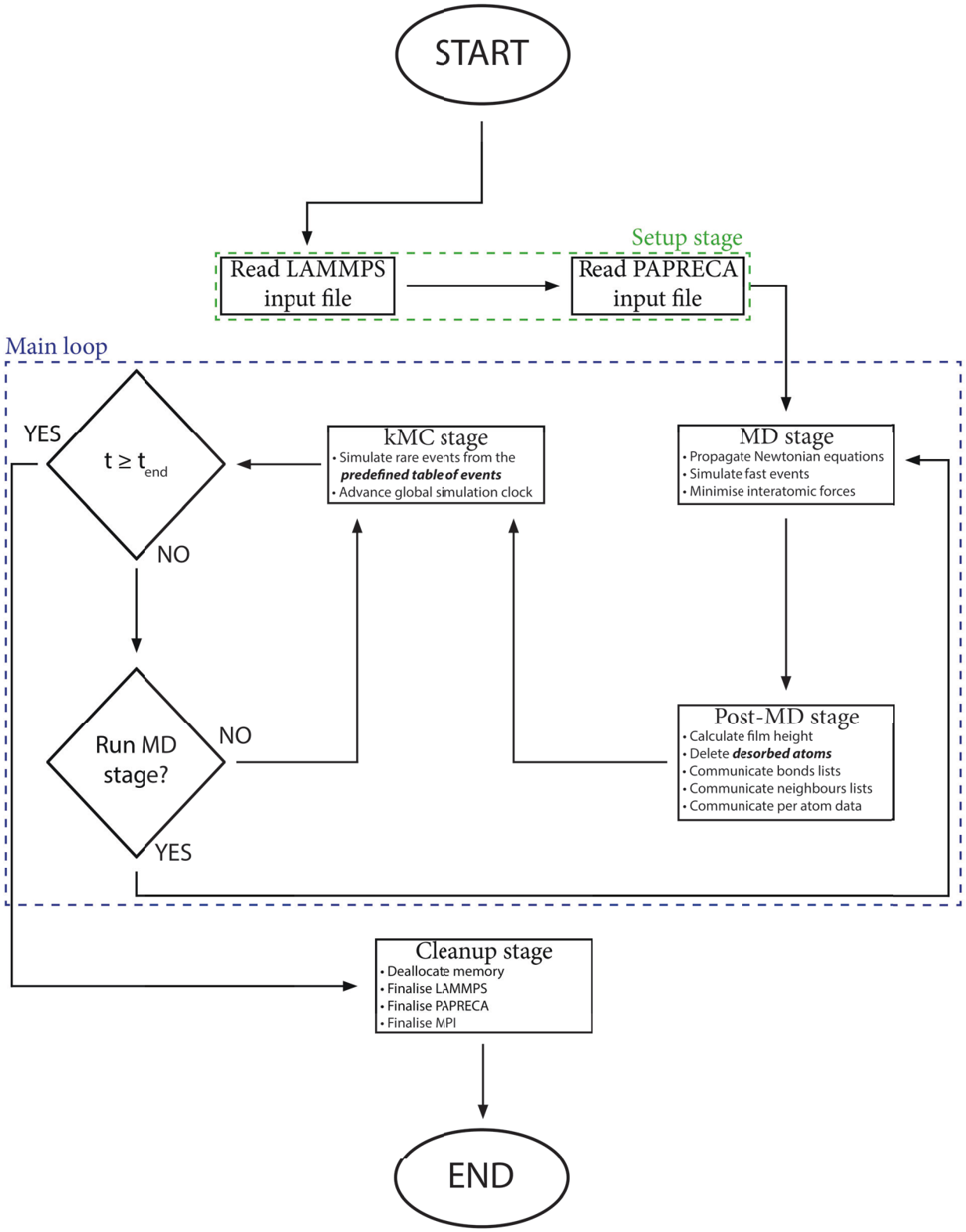


Fig. 5.21: Summary of steps involved in the PAPRECA hybrid off-lattice kMC/MD program.

5.4 Flexible, extendable, and user-friendly design

5.4.1 User interface through input files

As mentioned in Chapter 3, an in-house code written in Fortran95 was used to perform hybrid kMC/MD on the decomposition of TCP on iron [270]. This Fortran95 code was not easily extendable to other systems beyond TCP on iron for a couple of reasons. Firstly, parameters such as the rates of events, diffusion distances, and types of atoms participating in reactions had to be updated in multiple Fortran95 files. Secondly, communication between the MD and kMC stages was performed via a simplistic protocol based on input files. In particular, the driver code written in Fortran95 included functions that exported LAMMPS input (with LAMMPS commands) and data files (containing system trajectory snapshots). Therefore, modifications to the MD stage (e.g., change in atom types or use of a different thermostat) demanded direct access and modification of the source code. This was necessary to ensure that the driver code exported the relevant LAMMPS files in the proper format. Of course, adjusting the source code meant that the Fortran95 project had to be recompiled. This was time-consuming and lowered the user-friendliness of our initial kMC/MD code.

To address the aforementioned issues and promote the extensibility, flexibility, and user-friendliness of PAPRECA, an input file protocol was established. This facilitates effortless communication between the user and the software. The PAPRECA pseudolanguage comprises commands that allow the user to input simulation parameters (e.g., number of kMC stages or ending time of simulation), populate the *table of predefined events* with elementary processes, and overall, initialise the hybrid kMC/MD run without the necessity to modify the source code. This renders PAPRECA easily accessible and allows a broader audience to utilise it more effectively. In practice, no previous experience in C/C++ is required to use PAPRECA, rendering the software suitable for researchers and engineers with varying levels of programming expertise.

The PAPRECA input file controls the kMC stage as well as the hybrid kMC/MD run. On the other hand, PAPRECA utilises LAMMPS input files to initialise the MD stage of the software. Hence, users with prior experience in MD simulations using LAMMPS can easily apply their knowledge when working with PAPRECA. In essence, PAPRECA deploys two input files (PAPRECA and LAMMPS) to control the kMC and MD stages, respectively. Both input files are passed to the PAPRECA executable at launch via an "mpiexec" or "mpirun" command. Consequently, there is no requirement to recompile either the LAMMPS library or PAPRECA. This renders the set-up stage of PAPRECA less time-consuming compared to our initial in-house Fortran95 code.

A variety of PAPRECA input files associated with different applications, along with the accompanying LAMMPS input files, are available on the GitHub repository of the code. A PAPRECA input file to simulate the growth of phosphate films from TCP on Fe(110) is provided in Appendix A. This example input file showcases the PAPRECA pseudolanguage and the ease with which users can initialise the kMC stage of the hybrid kMC/MD simulation.

5.4.2 PAPRECA and LAMMPS libraries

PAPRECA is compiled with the LAMMPS library. As such, the hybrid kMC/MD code is seamlessly integrated with LAMMPS. From a programming perspective, this can become helpful as

PAPRECA developers can readily deploy functions from the `LAMMPS_NS` namespace to perform various tasks. For instance, PAPRECA currently utilises neighbours lists and handles boundary conditions via LAMMPS functions. LAMMPS is an active development project. Additional functionality is periodically added to the software, and a coordinated effort is made to resolve existing bugs and errors. This benefits PAPRECA as it reduces its maintenance requirements and favours its extensibility by using tested and optimised LAMMPS functions.

Of course, the seamless integration of PAPRECA with LAMMPS not only benefits PAPRECA developers. It also supports PAPRECA users intending to utilise the software to perform hybrid kMC/MD simulations in materials science, chemistry, physics, biology, and engineering applications. This is justified by considering that force fields, non-bonded interaction models, and ensembles available to LAMMPS are, by default, accessible to PAPRECA. For example, a DREIDING potential [206] was used in our previous study on the decomposition of TCP on iron [270]. In this work, the iron substrate was fixed, but the Fe atoms interacted with film particles through LJ and coulombic terms. To upgrade the model and introduce mobile substrate atoms, an Embedded atom model (EAM) potential [321] can be deployed to capture Fe-Fe interactions. The computationally efficient DREIDING potential can still be utilised to model non-bonding interactions between film and substrate atoms as well as particles in the film. Implementing such changes in our model is considered straightforward, as both EAM and DREIDING potentials are available in LAMMPS. Specifically, a few commands in the relevant LAMMPS input file are required to initialise a hybrid pair style and configure the force field parameters. The model on thin films from TCP can be extended even further with the use of a barostat that controls the system pressure. Moreover, LAMMPS commands can be deployed to impose sliding speeds on groups of atoms. As such, our initial model can be upgraded and hybrid kMC/MD simulations can be deployed to shed light on the effect of friction on the mechanochemistry of lubricant additives [92, 315].

The above examples showcase the merits of integrating PAPRECA with the LAMMPS library. Specifically, building PAPRECA with LAMMPS provides flexibility not only for PAPRECA developers aiming to extend the code but also for PAPRECA users with no prior programming experience wishing to perform hybrid kMC/MD simulations. Overall, LAMMPS supports approximately 230 pair styles, including bond-order potentials (e.g., Tersoff [322], REBO [323], AIREBO [324]) or reactive force fields (e.g., ReaxFF [208]). Furthermore, it supports charge equilibration schemes (e.g., QEq [207]) and even ML potentials (through the `pair_style mliap` [26]). Note that ML potentials are becoming increasingly popular nowadays and find applications in different fields, including but not limited to crystal structure prediction, nanoparticles, protein unfolding, and water-metal interfaces [325].

The PAPRECA library was created to further boost the extensibility of the software. The main hybrid kMC/MD code (i.e., the PAPRECA driver) is compiled with both LAMMPS and PAPRECA libraries. Specifically, the PAPRECA library includes a collection of subroutines that enable the direct access and modification of per-atom data (e.g., particle spatial coordinates or velocities). Functions in the PAPRECA library can be utilised to insert or remove system particles and molecules, displace atoms, and form or delete bonds (as discussed in Section 5.3.2). Additionally, the PAPRECA library supports a film-height estimation algorithm, methods to estimate rates for events with various models, and approaches to assemble arrays of explicitly bonded atoms (as seen in Section 5.3.3.1). In essence, the PAPRECA driver code deploys the PAPRECA and

LAMMPS libraries to perform operations relevant to the kMC and MD stages, respectively.

The PAPRECA library is a self-contained unit of compiled code. Therefore, development projects can be built with the PAPRECA library to leverage its functionality. In that respect, C++ projects can deploy functions from the `PAPRECA` namespace for the development of hybrid MD applications beyond kMC/MD. For instance, diffusion hops (discussed in Section 5.3.2.6) as implemented in the PAPRECA library can be deployed in an off-lattice hybrid MMC/MD scheme [307]. Generally, the PAPRECA library can become useful for interfacing C++ projects and open-source simulators with LAMMPS.

5.4.3 Object-oriented design

Object-oriented programming (OOP) schemes were implemented in PAPRECA to enhance the flexibility and extensibility of the software. This section briefly analyses the structure as well as inheritance patterns of classes in the `PAPRECA` namespace (i.e., included in the PAPRECA library). A variety of classes are dedicated to the description of predefined events in PAPRECA. The `PAPRECA::PredefinedReaction` class is the base class for reaction events. It is used for predefined bond-breaking events. `PAPRECA::PredefinedBondForm` is a child class of `PAPRECA::Predefined Reaction` that additionally includes a characteristic bond length variable (as described in Section 5.3.2.3). `PAPRECA::PredefinedDeposition`, `PAPRECA::PredefinedMonoatomicDesorption`, and `PAPRECA::DiffusionHop` objects are utilised for deposition, monoatomic desorption, and diffusion hop predefined events, respectively (see Sections 5.3.2.4, 5.3.2.5, 5.3.2.6).

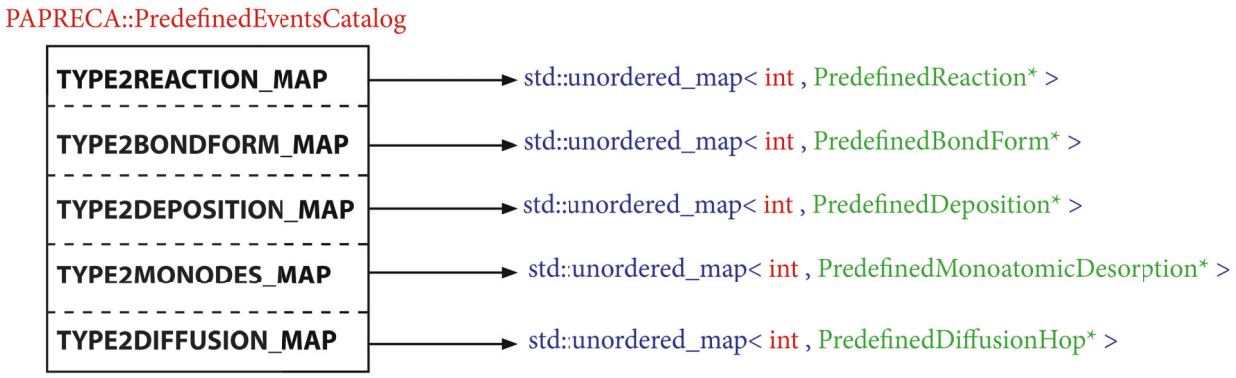


Fig. 5.22: Structure of table of predefined events (PAPRECA::PredefinedEventsCatalog class). The *predefined table of events* contains as many unordered maps as the types of predefined events in PAPRECA (i.e., five corresponding to bond-formation, bond-breaking, deposition, monoatomic desorption, and diffusion hops). Each map maps an atom ID (of integer C++ type) to a pointer to the predefined event object.

The *predefined table of events* is a container implemented in the "event_list.h" header, including objects of the aforementioned classes. This container is stored on all MPI ranks and is essential for the detection of predefined events. Specifically, a class named `PAPRECA::PredefinedEventsCatalog` retains five distinct unordered maps (from the std library) corresponding to the five types of predefined events in PAPRECA (bond-breaking, bond-formation, deposition, monoatomic desorption, and diffusion hop). The unordered maps map atom types to predefined event objects. In practice, the maps are deployed to retrieve valid parent atoms at the event discovery stage, where MPI ranks loop over their "owned" atoms. A graphical representation of the structure of the *predefined table of events* (i.e., the `PAPRECA::PredefinedEventsCatalog` class) storing predefined event objects is provided in Fig. 5.22.

The local *table of detected events* is an std vector container including `PAPRECA::Event` objects. `PAPRECA::Event` is a parent class storing the rate and type of a detected event. A child class inheriting from the `PAPRECA::Event` is implemented for each of the five types of detected events. Specifically, the following classes are used: `PAPRECA::BondBreak`, `PAPRECA::BondForm`, `PAPRECA::Deposition`, `PAPRECA::MonoatomicDesorption`, and `PAPRECA::Diffusion`. Each child class object retains event-specific information along with a pointer to the parent predefined event object. Also, note that detected events are always cast to parent `PAPRECA::Event` class objects for storage in the *table of detected events*. This is practically convenient since it enables the utilisation of a single `std::vector<PAPRECA::Event*>` retaining all locally detected events on the MPI rank instead of deploying multiple vectors for the different types of discovered atomistic processes. The use of a single event vector facilitates the enumeration and event selection operations performed by the kMC stage of PAPRECA (see Section 5.3.2). Of course, the object linked to the atomistic process selected by the *event rank* is cast back to the child class to retrieve the relevant event-specific information and execute the event. The inheritance schematic of `PAPRECA::Event` classes is provided in Fig. 5.23.

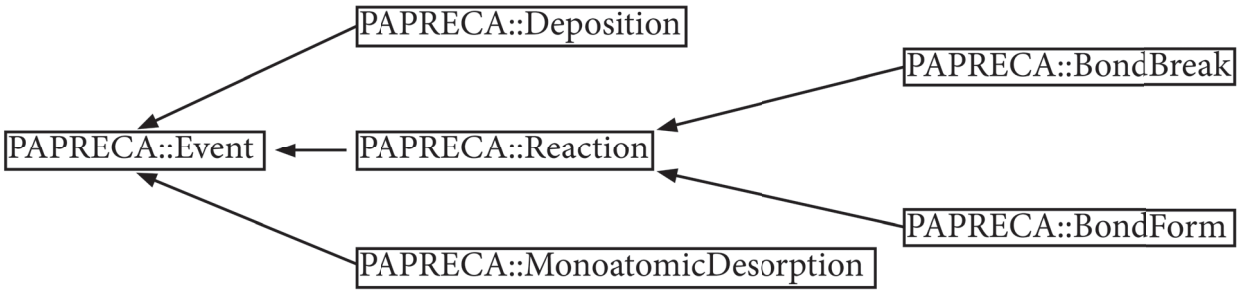


Fig. 5.23: Inheritence tree of `PAPRECA::Event` classes. `PAPRECA::Event` is the parent class of all event classes. `PAPRECA::Reaction` class is the parent of both `PAPRECA::BondForm` and `PAPRECA::BondBreak` classes.

Notice that detected event classes (i.e., `PAPRECA::Event` and its children) and predefined event classes are intrinsically different. Predefined event objects are associated with globally stored predefined events inserted in the *table of predefined events*. They retain basic information related to a predefined event. For instance, `PAPRECA::PredefinedReaction` objects retain the types of atoms and the type of bond associated with a bond-breaking event, while `PAPRECA::PredefinedDiffusionHop` objects store the *types of parent atoms*, *diffusion distance*, *diffusion type*, *diffused type*, and rate of a diffusion event. On the other hand, `PAPRECA::Event` objects contain specific information associated with the detected event. For instance, `PAPRECA::BondBreak` objects store the atom IDs involved in the detected reaction, while `PAPRECA::Diffusion` retains the ID of the parent atom as well as the spatial coordinates of the diffusion site.

The `PAPRECA::Event`, as well as predefined event classes, were designed to enable the effortless extensibility of PAPRECA. In essence, novel types of events for hybrid kMC/MD simulations can be developed in PAPRECA solely by implementing two new classes - a child class inheriting from `PAPRECA::Event` to be utilised with the *table of detected events* and a predefined event class to be used with the *table of predefined events*. Of course, the classes linked to the newly added elementary processes can build upon the existing base classes (as implemented for the five different types of events) through inheritance patterns.

5.4.4 Open source implementation

PAPRECA was inspired by the in-house code written in Fortran95 dedicated to the modelling of the decomposition of TCP molecules on ferrous surfaces. The initial in-house code was a closed-source code and was inaccessible to a broader audience beyond the software developers. In contrast, PAPRECA has been a freely available open-source software since its conceptual design. The open-source philosophy aligns with our desire to provide researchers and engineers with openly distributed tools to perform hybrid kMC/MD simulations on systems in materials science, chemistry, physics, biology, and engineering. We strongly believe that bridging the simulation timescales between MD and the continuum is fundamental to shed light on the properties of systems beyond the traditional limits of atomistic simulations. As such, hybrid kMC/MD simulations promise to accelerate the discovery of next-generation materials associated with applications including but not limited to energy storage [8, 326], lubrication [65, 69, 327], and transportation of hydrocarbon fuels [328–330].

The PAPRECA source code, example input files, test, and an extensive documentation webpage are hosted in the PAPRECA repository on Github [331]. The repository is organised into three branches. Software development takes place on the *main branch*. New features and bug fixes are always pushed on the *main branch*. The updated code is tested for a period of time on the main branch to ensure the stability and scalability of the code, as well as to examine the multi-process (through the MPI protocol) performance of the software. After the testing period, updates are merged to the *release branch* (through a GitHub pull request) to launch a new PAPRECA version. Deploying two branches (i.e., *main* and *release*) is a common practice in software engineering. It guarantees that a stable PAPRECA version is available at all times in the repository (stored in the *release branch*), while it allows uninterrupted code development on the *main branch*. A third branch called *gh-pages* is a utility branch and supports the updating of pages on the PAPRECA documentation website. Note that open-source projects can deploy more than two branches in increasingly convoluted versioning schemes. For instance, LAMMPS utilises four branches for versioning control (i.e., "develop", "release", "stable", and "maintenance") [26].

Of course, GitHub is not solely used for project storage purposes. PAPRECA also leverages GitHub's continuous integration tools suite to actively support the software development process. PAPRECA is built with the LAMMPS library. Consequently, it is vital to periodically check if PAPRECA can be successfully compiled with the newest LAMMPS versions. In addition, it becomes important to examine whether PAPRECA functions as expected when built with the latest LAMMPS version. For instance, modifications to the implementation of the `create_atoms` function of LAMMPS can result in particles inserted in a location of the simulation box different from the defined *deposit site* (as introduced in Section 5.3.2.4). Testing the latest LAMMPS version can be done manually by pulling LAMMPS from the relevant repository branch, building it, and then compiling PAPRECA with the LAMMPS library. Nonetheless, this approach is repetitive, time-consuming, and entails the risk of not detecting incompatible LAMMPS versions promptly.

To provide an automated platform for LAMMPS version testing, PAPRECA deploys GitHub actions. The relevant workflow is scheduled to run daily at midnight and operates as follows. Firstly, the "release" branch of LAMMPS is cloned and the latest release commit SHA (hash) is retrieved. Next, LAMMPS is compiled as a library with the "fix papreca" command (see Section 5.3.1.3). The built executable, along with the LAMMPS library, are saved as artifacts. Note

that each artifact is linked to the relevant release commit hash. Therefore, LAMMPS needs to be compiled solely when the workflow detects a commit hash mismatch between the retained artifact and the previously cloned release branch. In any other case (i.e., if the GitHub cache hit returns "true"), the LAMMPS library and executable are restored from the artifact. After building or retrieving LAMMPS, the PAPRECA project is cloned from the PAPRECA repository and built. If the code compiles successfully, PAPRECA is compatible with the targeted LAMMPS release version.

Then, secondary tests are performed to guarantee that PAPRECA functions operate in a stable manner and generate the expected results with the targeted LAMMPS version. Three classes of secondary tests are performed. Firstly, *event tests* are executed. The *event tests* are written in Python and investigate the correctness of executed elementary processes in PAPRECA. All *event tests* exhibit similar philosophy. Firstly, PAPRECA is initialised from the respective Python script, and a few kMC stages are performed. Following, the Python script exports event-related data from PAPRECA and compares them with system trajectory files output from LAMMPS. Whenever an output mismatch between the files exported from PAPRECA and LAMMPS is detected, the relevant Python script raises an error that results in workflow failure. File mismatches indicate inconsistent communication of data from the kMC stage to LAMMPS, as PAPRECA fails to update the system state after executing a predefined event. Overall, the workflow performs event tests with five random seeds to account for the probabilistic nature of the kMC stage and detect errors originating from different events.

Reaction events are tested by performing four bond-breaking or bond-formation steps. The atom IDs along with the associated bond types of the selected and executed events are output by PAPRECA in a log file. After updating the system to account for the execution of the reaction event, LAMMPS also exports a file containing the IDs and the bond type of the linked atoms. This is done via the `compute bondsinfo all property/local btype batom1 batom2` command. Then, the two files are compared to discover mismatches that trigger errors. The testing procedure for the other classes of PAPRECA events is similar. For instance, the exported PAPRECA and LAMMPS files include the spatial coordinates of the deposition or diffusion site, for `PAPRECA::PredefinedDeposition` and `PAPRECA::PredefinedDiffusionHop` events, respectively. The consistency of the ID of the parent atom is tested when it comes to monoatomic deposition processes.

Source tests is another class of secondary tests. These tests investigate the integrity of key functions implemented in the PAPRECA library (see 5.4.2). The source tests are written in C++ and must be compiled with the LAMMPS and PAPRECA libraries. Firstly, the *source tests* executable examines if the MPI communicator, as well as the `LAMMPS_NS::LAMMPS` object, can be initialised properly without raising any errors. Following, a LAMMPS as well as a PAPRECA input file are read by the code to create a simulation box, initialise a molecule template, and configure predefined events from all five types of atomistic processes supported by PAPRECA (i.e., bond-formation, bond-breaking, deposition, monoatomic desorption, and diffusion).

Then, the correctness of molecule-insertion operations is tested. Specifically, a LAMMPS molecule template is retrieved, and the coordinates of the deposit site are defined for each molecule atom. Following, the molecule is created in the system. Using a `lammps_extract_atom` operation, the spatial coordinates of the molecule atoms are retrieved from the updated configuration

in LAMMPS and compared with the as-defined deposit site coordinates prior to the execution of the event. Any mismatch in atomic coordinates raises an MPI error and prematurely stops the workflow. Furthermore, overlap tests are performed by inserting atoms in the system separated by distances smaller than the user-defined equilibrium interatomic distance parameter (σ_{ij} as introduced in sections 5.3.2.4 and 5.3.2.6). Here, PAPRECA must detect the existing overlaps (as expressed by Eq. 5.15). Note that both deposition as well as overlap tests included in the *source tests* code examine if PBCs are handled properly during the atom insertion and distance calculation operations performed by PAPRECA library functions. Finally, *source tests* initiate random number generator tests that investigate the frequency of overlaps for the uniformly distributed pseudorandom numbers created by RANMARS (drawn from `LAMMPS_NS::RanMars` objects as explained in Section 5.3.2.1). In this case, overlaps refer to the generation of identical pseudorandom numbers on a random sequence originating from a given random seed. For example, if number ρ is the 1^{st} and 101^{st} in the sequence of pseudorandom numbers generated with seed $0 \leq a \leq 900000000$ (limits of RANMARS), an overlap exists with a frequency of 1%. Of course, the performance of the random number generator is inversely proportional to the frequency of detected pseudorandom number overlaps [316].

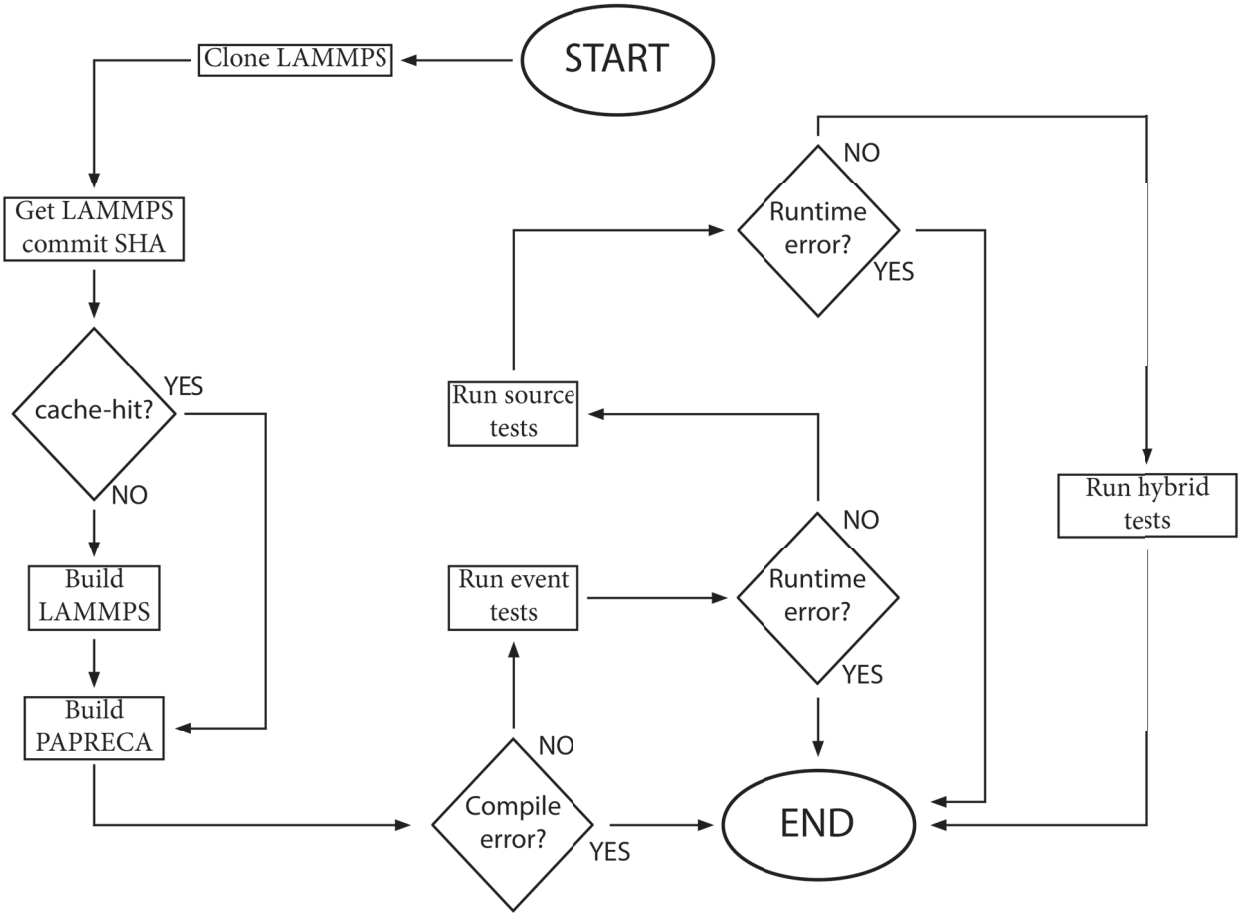


Fig. 5.24: Flowchart of GitHub versioning workflow.

Lastly, the workflow includes *hybrid tests*. Here, PAPRECA is tested as a complete package through a hybrid off-lattice kMC/MD run executed on multiple MPI ranks. In particular, the model associated with the decomposition of TCP on iron (see Chapter 3) is replicated in PAPRECA using appropriate LAMMPS as well as PAPRECA input files. Then, 20 hybrid kMC/MD steps

(i.e., 20 kMC stages followed by 20 MD stages) are performed. Once again, raised errors within the kMC and MD stages or during the communication of data between the different stages result in abrupt workflow termination and signal version incompatibility between PAPRECA and the latest LAMMPS release. A flowchart illustrating the key steps involved in the automated versioning tester is provided in Fig. 5.24. Note that the same workflow can be utilised to not only test the latest LAMMPS release but also to investigate the compatibility of PAPRECA with previous versions of LAMMPS in any of the relevant repository branches. Using this workflow, it was discovered that "version patch_15Sep2022" is the earliest LAMMPS version that is fully compatible with PAPRECA.

PAPRECA deploys a different workflow to generate and update a documentation webpage. This workflow can either be triggered manually or automatically through merges to the *release branch* of PAPRECA. This guarantees that the documentation incorporates the latest software updates. Specifically, the workflow utilises the Doxygen documentation manager to generate a ".html" file directly from the PAPRECA C++ project. Effectively, doxygen reads the PAPRECA source code and builds a webpage that documents all libraries, files, functions, namespaces, classes, and inheritance schemes. Additional webpages are manually included to discuss certain theoretical aspects of kMC/MD, provide installation instructions, and document the commands of the PAPRECA pseudolanguage. A few example applications are also included in the documentation. After building the ".html" file, the relevant workflow uploads the documentation to a public domain hosted on GitHub.

5.5 Example PAPRECA applications

In Sections 5.2, 5.3, 5.4, we introduced PAPRECA, analysed aspects of its hybrid parallel algorithms and discussed the software's design philosophy. In this section, we present certain examples to showcase PAPRECA's capabilities when it comes to modelling systems beyond the thermal decomposition of TCP on iron. Note that this was the proof-of-concept system linked to our initial in-house off-lattice kMC/MD code written in Fortran95.

5.5.1 Diffusion in solvent

5.5.1.1 Background

Through this application, we show how PAPRECA can be utilised to model the kinetics of particles in a periodic box. The physical process captured here is analogous to injecting particles into a confined solvent and allowing them to diffuse and homogenise. Assuming that the homogenisation process is thermally activated, the motion of particles within the solvent can be approximated as independent diffusion hops. The characteristic length associated with each diffusion hop is of the order of magnitude of interatomic equilibrium distances (i.e., $\approx \mathring{A}$). This can be justified by considering that liquids are densely packed. Therefore, diffusion occurs through thermal fluctuations. In essence, particles perform jumps of short lengths as they attempt to escape interatomic interactions within their local environment [202, 332].

Two models are presented in this section. The **first model** is linked to a **pure kMC** setup and displaces atoms through predefined diffusion hop events. Such a model can become useful for

capturing sluggish kinetics. For instance, if the frequency of diffusion events is considerably lower than that of atomic vibrations, then an MD simulation might not be able to appropriately capture the expansion process. Overall, the pure kMC model exhibits that PAPRECA can be used in not only hybrid kMC/MD simulations but also in off-lattice kMC applications with a *predefined table of events*. The **second model** is a **hybrid kMC/MD** setup that deploys predefined diffusion hops through the kMC stage. Furthermore, the MD stage of the second model captures the high-frequency non-bonded interactions between atoms and adds a degree of molecular resolution to the simulation.

5.5.1.2 Methods

A fully periodic cubic simulation box with sides of 30 nm was used for both models. The initial structure was identical for all simulations. Specifically, 300 silicon atoms were randomly inserted within a spherical region of radius 0.5 nm and centred at the origin of the simulation box. To do so, we utilised the `create_atoms` command of LAMMPS with an overlap option that prevented the addition of atoms with an interatomic distance smaller than or equal to 0.1 nm. An equilibration step using the CG method [237] was performed after generating the silicon atoms to annihilate residual forces between atoms and prevent instabilities. The equilibrium distance of the overlap criterion for predefined events (σ_{ij} in Sections 5.3.2.4 and 5.3.2.6) was set to 1.9778 Å. Note that this value corresponds to the σ_{SiSi} parameter of the LJ 12-6 [205] interatomic potential obtained from OpenKIM [333].

Also, a single `PARPECA::PredefinedDiffusionHop` event was utilised. The event considered Si species as parent types for diffusion hops. The random_diffvecs yes 3D option (see Section 5.3.2.6) was used to allow atoms to diffuse on the surface of a sphere of radius ΔL_k centred at the parent atoms. The relevant *hop distance* (ΔL_k) was fixed at 0.5 nm. Such a value is approximately 2.5 times higher than the overlap criterion distance (i.e., 0.19778 nm). This is a valid approximation since the length of diffusion hops of particles in solvents is comparable to interatomic equilibrium distances [202]. The total number of kMC steps of the **pure kMC** model was fixed at 200000.

The frequency linked to the diffusion event was estimated as follows. Firstly, the Stokes–Einstein approximation was utilised to retrieve a diffusion coefficient linked to the motion of silicon particles within the solvent:

$$D = \frac{\kappa_B T}{6\pi\eta r_c} \tag{5.26}$$

Where κ_B is the Boltzmann constant, η is the solvent viscosity, and r_c is the Stokes radius of the diffusion particles. In this example, we used $n = 0.66$ Pa s corresponding to the dynamic viscosity of a SAE 50 motor oil at approximately 300K [334]. A high-viscosity solvent was used in this example to highlight the need for multiscale simulations with PAPRECA. Overall, slower diffusion is expected through viscous solvents. Therefore, the timescales accessible by MD might not be sufficiently long to capture diffusion hop events. Furthermore, the Stokes radius was set at 0.111 nm, which is equal to the covalent radius of Si. The calculated diffusion coefficient was $D = 3.14 \quad 10^{-12} m^2/s$. Note that Eq. 5.26 provides a first-order estimation of the diffusion coefficient associated with the motion of particles in low Reynolds number flows.

Following Fick's law was considered to correlate the hopping frequency to the self-diffusion coefficient and the *hopping length* (ΔL_k). Specifically, recall that:

$$J = -D\frac{\vartheta C}{\vartheta x} \tag{5.27}$$

Where D is the diffusion coefficient, and $\frac{\vartheta C}{\vartheta x}$ represents the slope of the concentration. By definition, for 3-dimensional diffusion and by considering equiprobable jumps across all 6 possible directions, the diffusion coefficient can be expressed as:

$$D = \frac{1}{6} r \Delta {L_k}^2 \tag{5.28}$$

With r being the jump frequency (in units of $[T]^{-1}$) [335]. Consequently, we arrive at the following equation:

$$r = \frac{6D}{\Delta {L_k}^2} \tag{5.29}$$

Substitution of the hopping distance ΔL_k as well as self-diffusion coefficient values for our specific problem resulted in an event frequency of r = 7.54 10^7 Hz.

Note that in the pure kMC model, PAPRECA calls LAMMPS once every 10 stages to generate trajectory file outputs. Nonetheless, this does not affect the system dynamics since no time integration is performed. Furthermore, the pure kMC model used the export_ElementalDistributions function of PAPRECA (see section 5.3.3.1) every 1000 kMC stages with a bin size of 1 nm to generate elemental distribution graphs at different simulation times. This function estimates the distribution of atoms along the z-direction and was initially designed to capture thin-film growth. Nevertheless, through this example, it is demonstrated that the export_ElementalDistributions function can be deployed in fully periodic systems that do not model film growth. In any case, the produced distributions were fitted with the "Gauss" model in Origin Pro software, which implements the following equation:

$$y = y_0 + \frac{A}{w\sqrt{\pi/2}} e^{-2\left(\frac{x-x_c}{w}\right)^2} \tag{5.30}$$

Where y_0, A, w, and x_c are fitting parameters. On the other hand, a normal distribution is described by the following relation:

$$f(x) = \frac{1}{\sqrt{2\pi\sigma^2}} e^{\frac{-(x-x_c)^2}{2\sigma^2}} \tag{5.31}$$

With x_c and σ representing the mean and standard deviation of the distribution, respectively. By comparing the exponents of the expressions above (Eq. 5.30 and Eq. 5.31) we obtained the following correlation between the w parameter of the "Gauss" fit and variance σ^2 of the normal distribution:

$$e^{-2\left(\frac{x-x_c}{w}\right)^2} = e^{\frac{-(x-x_c)^2}{2\sigma^2}} \Rightarrow \frac{2(x-x_c)^2}{w^2} = \frac{(x-x_c)^2}{2\sigma^2} \tag{5.32}$$

So, for any $x \neq x_c$ we obtain the following expression:

$$\sigma^2 = \frac{w^2}{4} \tag{5.33}$$

The setup of the kMC stage of the second model (**hybrid kMC/MD**) was identical to that of the first model. In the MD stage, the universally shifted implementation of the LJ 12-6 potential

(retrieved from OpenKMI [333]) was used to model non-bonded interactions in the system. The velocity-Verlet [203] algorithm with a time step of 1 fs ($10^{-15}s$) was applied to integrate the equations of motion. A Langevin thermostat [336] with a target temperature of 300 K and a damping parameter of 10 fs was imposed on the system to produce trajectories consistent with the canonical (NVT) ensemble. Note that the Langevin thermostat models the motion of silicon atoms through the viscous solvent. The total number of kMC steps of the **hybrid kMC/MD** model was set to 1000000. An MD stage of 100 fs was simulated after each kMC stage. Finally, a pure MD simulation was performed in LAMMPS [26] for comparison purposes. The MD configuration was identical to that of the MD stage of the **hybrid kMC/MD** run performed in PAPRECA. The trajectory duration was fixed at 10^{-7} s, which is equivalent to the total trajectory length of the MD stage (i.e., 100000 kMC stages with 1 MD stage of 100 fs per kMC stage).

5.5.1.3 Results and discussion

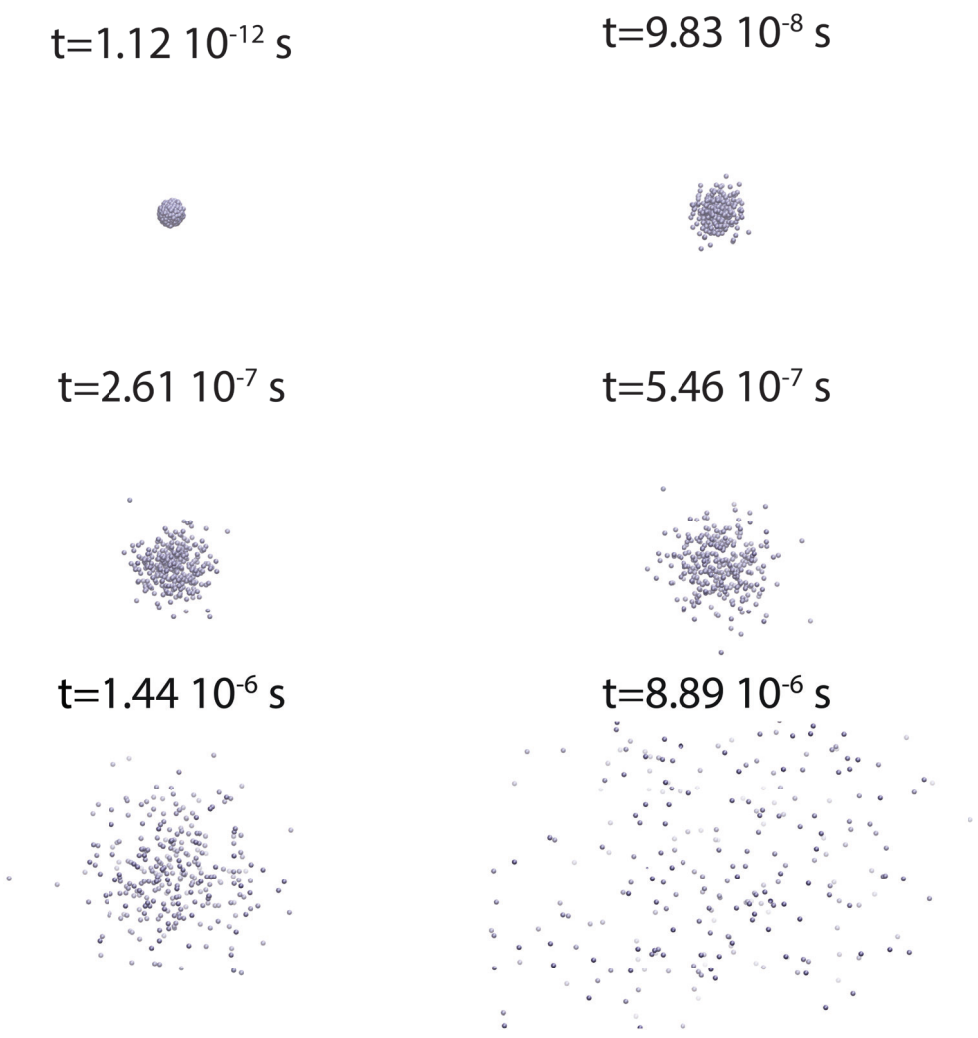


Fig. 5.25: Snapshots of the **pure kMC** model at various timesteps.

Fig. 5.25 provides snapshots of the **pure kMC** model at various times. Note that the time step of PAPRECA is variable (see Eq. 5.7). Therefore, the simulation captures system microstates of timescales spanning over six orders of magnitude. This clearly exhibits the multiscale nature

of kMC simulations in PAPRECA. In any case, we observe that the particles diffuse within the simulation box. The Si atoms move towards the edges of the simulation box and in the end (i.e., at $t = 8.89\ 10^{-6}$ s), we notice that the particles are dispersed in the simulation box. This result is expected since `PAPRECA::PredefinedDiffusionHop` events displace atoms towards regions of the simulation box that do not feature overlaps (as defined in Sections 5.3.2.4 and 5.3.2.6). Consequently, the generated trajectories over sufficiently long timescales are expected to exhibit evenly spaced particles in a completely homogenised system. Note that the **pure KMC** model does not capture attractive or repulsive interatomic interactions between neighbouring atoms. Therefore, the modelled process is physically analogous to a random walk.

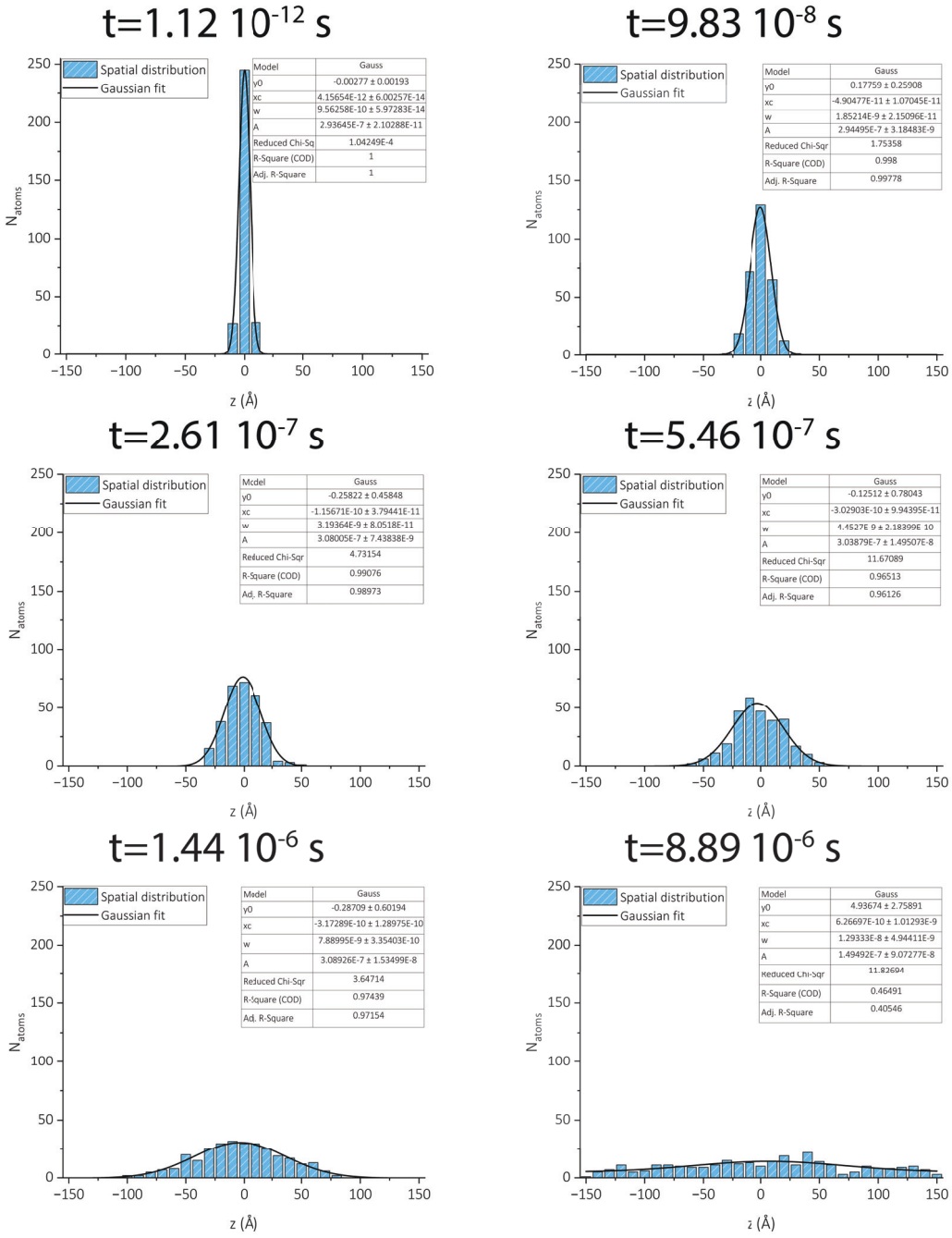


Fig. 5.26: Spatial distributions of the **pure kMC** model at various timesteps. The distributions were procured using spatial binning along the z-direction of the simulation box (as explained in Section 5.3.3.1).

The temporal evolution of the spatial distribution of the system, along with the corresponding Gaussian fits, are presented in Fig. 5.26. Here, it is illustrated that the number of atoms along the z-direction follows a normal distribution. Moreover, the maximum height decreases and the variance of the normal distribution (estimated from Eq. 5.33) increases over time as the particles disperse within the simulation box. In the final snapshot, atoms are completely homogenised, and each bin contains roughly the same number of atoms. This is also confirmed by the broad shape of the relevant Gaussian fit.

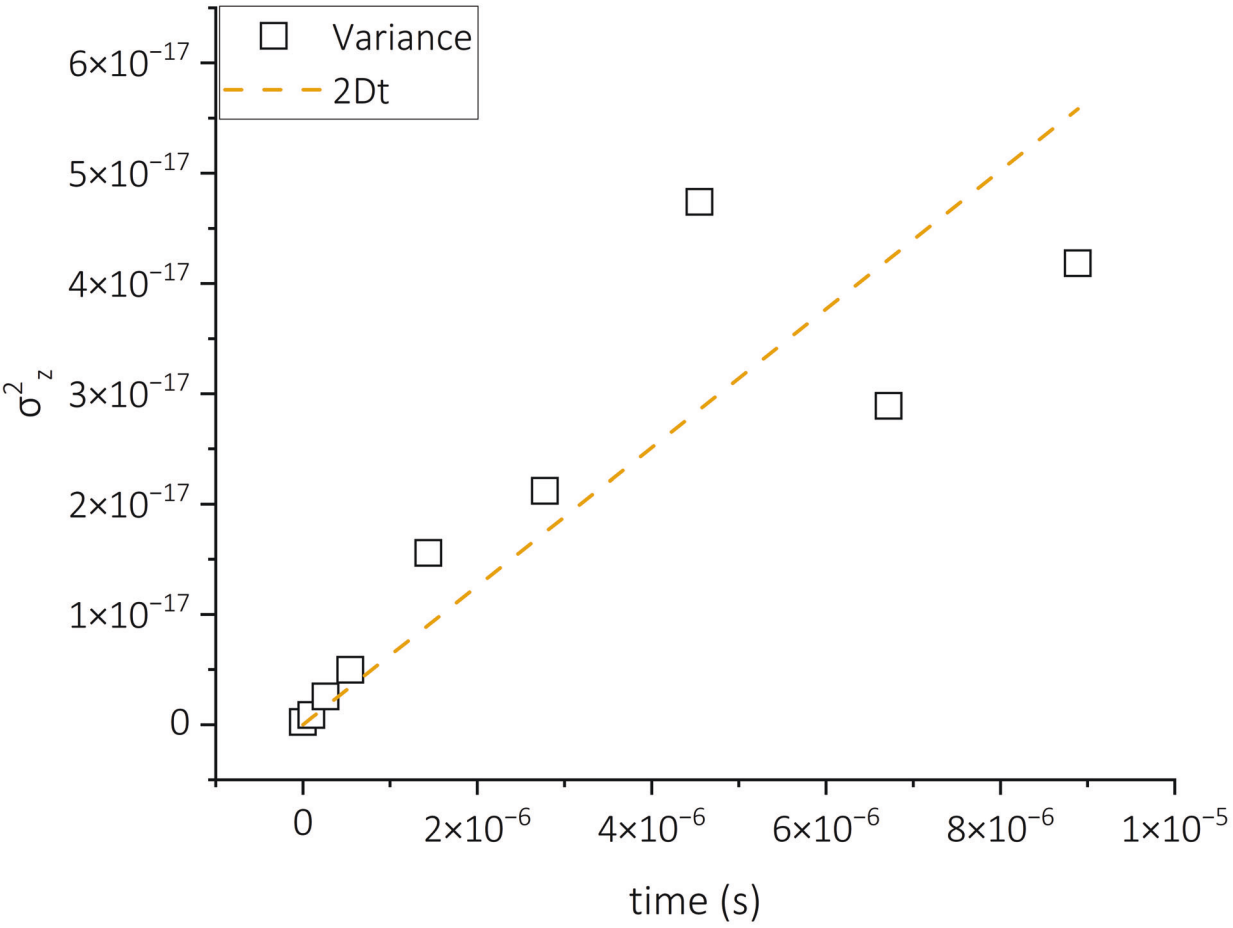


Fig. 5.27: Variance versus time for **pure kMC**. Variances were calculated with Eq. 5.33 from the applied Gaussian fit ("Gauss" model of Origin Pro).

The variance at different simulation times is plotted with black squares in Fig. 5.27. Here, we notice that the variance increases rapidly in the early stages of the simulation and until approximately 2.5 μs. Then, the variance fluctuates about a maximum value as particles approach the edges of the computational domain (of sides L_z=30 nm). Effectively, the plateau value is reached when each bin contains roughly the same number of atoms. The variance cannot exceed this threshold, as the Gaussian distribution approaches its maximum possible breadth for that specific simulation box. An orange dotted line was added to Fig. 5.27 to illustrate the theoretical result linked to Brownian diffusion with $D = 3.14 \quad 10^{-12} m^2/s$. Note that the **pure kMC** result is compared to the 1-D Brownian (i.e., $\sigma^2 = 2Dt$) case since our spatial binning method is solely performed along the z-axis. Of course, the 1-D Brownian diffusion case is described by the $\sigma^2 = 2Dt$ line only under the assumption of spatially isotropic diffusion with each dimension contributing equally to the total variance (i.e., $\sigma^2_{total} = \sigma^2_z + \sigma^2_y + \sigma^2_z = 2Dt + 2Dt + 2Dt = 6Dt$)

[335]. In any case, we observe that the **pure kMC** result matches the analytic solution closely. Slight deviations towards the end of the simulation could be associated with finite-size effects. Performing mean-squared end-to-end distance (MSD) and lag-time (τ) calculations was beyond the scope of this analysis. The complexity of such calculations [337] is elevated compared to that of equivalent calculations from MD trajectories because kMC features variable time steps (see Eq. 5.7). Nevertheless, generating an MSD-τ graph from unwrapped PAPRECA trajectories and correlating with the theoretical result ($2D\tau$) is expected to produce more accurate results and is left as future work.

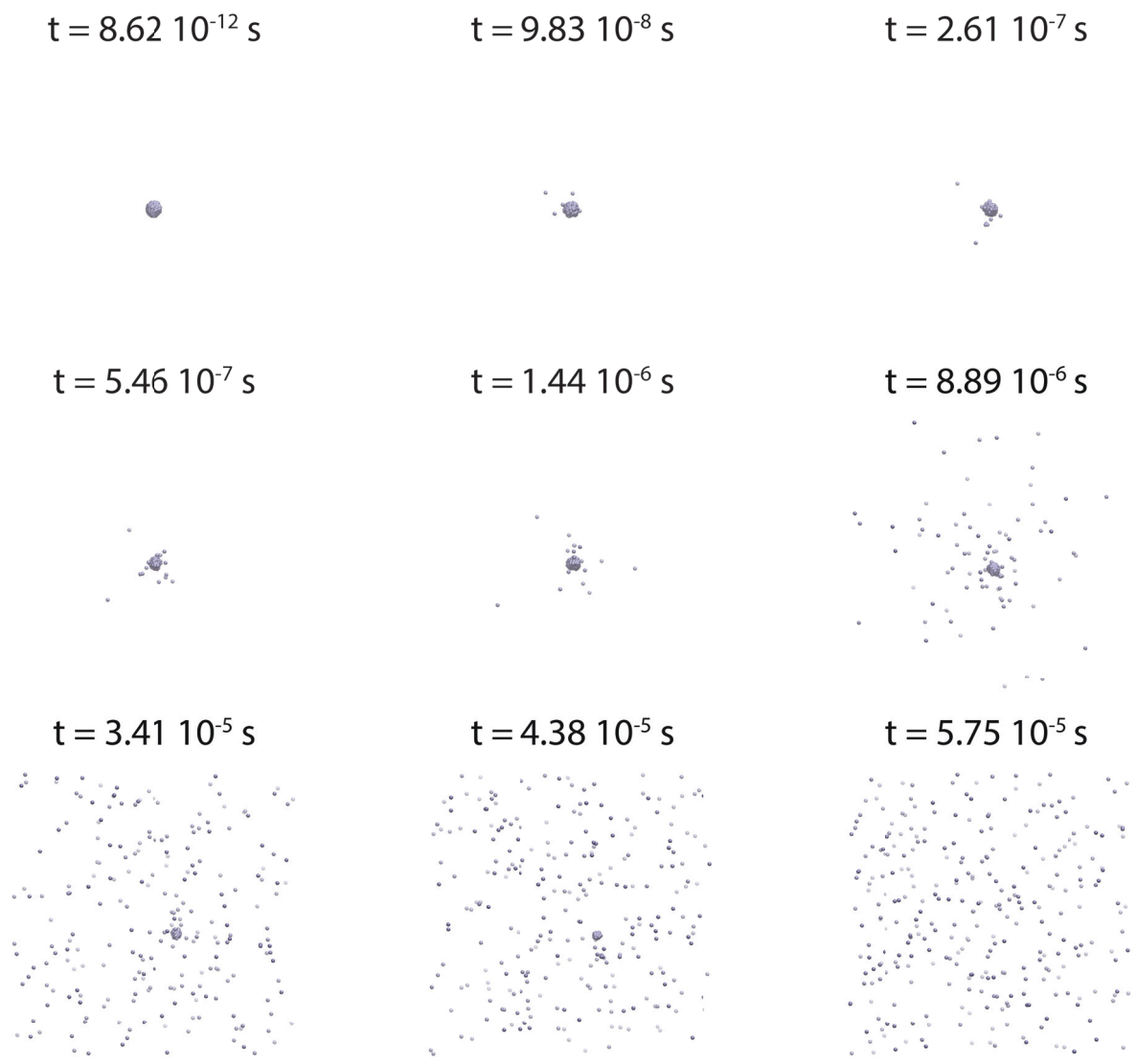


Fig. 5.28: Snapshots of **hybrid kMC/MD** model at different simulation times.

The **pure KMC** model is extended to a **hybrid kMC/MD** scheme that accounts for attractive and repulsive interactions between neighbouring atoms (see 5.5.1.2 for implementation details). Snapshots of the relevant hybrid kMC/MD simulations are provided in Fig. 5.28. Note that the timestep of the kMC stage is variable and that the total number of kMC stages was 200000 and 1000000 for the **pure kMC** and **hybrid kMC/MD** models, respectively. Nevertheless, snapshots at similar simulation times are given in Fig. 5.28 to allow visual comparison

with Fig. 5.25 (corresponding to the **pure kMC** model). In any case, we observe that the **hybrid kMC/MD** simulations feature a cluster of Si atoms that moves within the simulation box. The cluster forms due to LJ interactions captured through the MD stages. Occasionally, particles escape the strong attractive forces from neighbouring atoms through diffusion hops executed in the kMC stage. The escaped particles are further separated from the cluster through subsequent diffusion hops, random-collision forces originating from the Langevin thermostat, or interatomic interactions captured in the MD stage.

Through visual inspection of Figs. 5.25 and 5.28 we observe a couple of differences associated with the temporal evolution of the spatial distribution of Si atoms. Firstly, no mobile cluster is detected in the **pure KMC** model (see Fig. 5.25). In the **pure KMC** model, particles freely expand outwards and no attractive forces are exerted on neighbouring atoms to prevent them from diffusing to the edges of the computational domain. Secondly, we notice that the **hybrid kMC** model requires additional time to reach the fully homogenised state. Specifically, particles necessitate $8.89\,10^{-6}$ s and $5.57\,10^{-5}$ s in the **pure KMC** and **hybrid KMC/MD** schemes, respectively, to disperse in the simulation box. Nonetheless, a discrepancy between the two times is expected. This can be justified by considering that the **hybrid kMC** model involves unsuccessful diffusion hops. These can manifest when the kMC stage displaces an atom away from the cluster, but the same particle is attracted back to the cluster due to attractive LJ forces captured in the MD stage. Hence, an increased number of diffusion hops is neccesary in the **hybrid kMC** model to homogenise the system, which progresses the simulation clock to longer timescales.

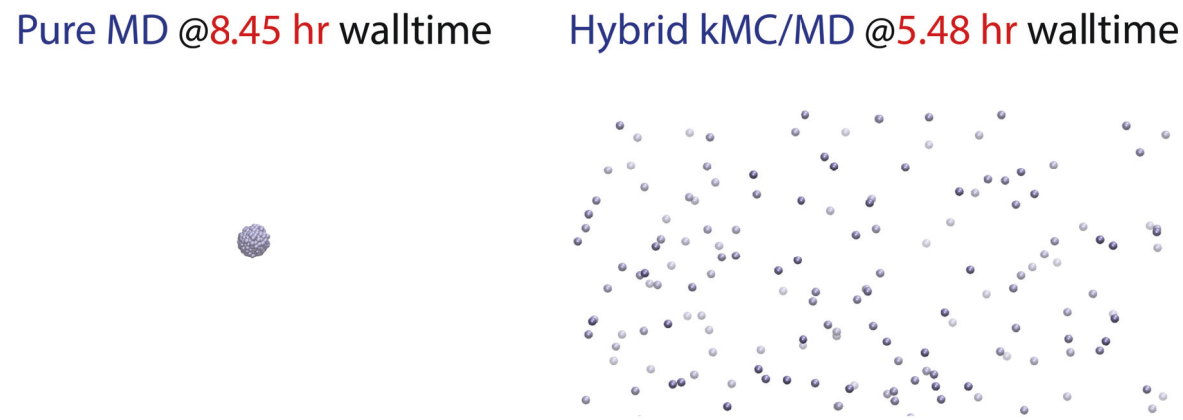


Fig. 5.29: Final snapshot of pure MD **(left)** and hybrid kMC/MD **(right)** simulations. The pure MD model reaches $10^{-7}s$ with 8.54 hours of walltime, while the hybrid kMC/MD scheme in PAPRECA reaches $5.75\,10^{-5}$ s in 5.48 hours.

In any case, the choice of numerical scheme (**pure kMC** or **hybrid kMC/MD**) depends on the modelled example and the underlying physics driving the diffusion of particles. If particles perform a random walk, a **pure kMC** model can be appropriate. In contrast, if no Brownian motion is expected, introducing molecular-level resolution to the model through hybrid kMC/MD simulations can shed light on clustering effects or solvent-particle interactions. Capturing such effects can be important to understand the rate-determining elementary mechanisms in diffusion-dominated systems.

Finally, the advantage of deploying accelerated hybrid kMC/MD instead of pure MD models is demonstrated by performing additional MD simulations in LAMMPS (see 5.5.1.2 for imple-

mentation information). For reference, 100000 hybrid steps comprising 100000 kMC stages and 100000 MD stages of 100 fs each (i.e., $10^{-7}s$ seconds captured in MD) demanded 5.48 hours with 32 cores using the HPC service of Imperial College. On the other hand, 100000 time steps of 100 fs each (same as in the MD stage of the hybrid kMC/MD model) in LAMMPS required 8.54 hours to complete with identical computational resources. The MD reached $10^{-7}s$, while the **hybrid kMC/MD** model reached and $5.75\,10^{-5}$ s. In this example, the **hybrid kMC/MD** and pure MD approaches exhibit time-advancing efficiencies of $9.53\,10^{4}\frac{CPU\ hr}{simulated\ s}$ and $8.54\,10^{7}\frac{CPU\ hr}{simulated\ s}$, respectively. This showcases the ability of PAPRECA to accelerate atomistic simulations, overcoming high-energy barriers. Predefined events, such as diffusion hops, allow PAPRECA to access timescales and system states inaccessible to traditional MD simulations. Fig. 5.29 provides a graphical comparison between the final microstates of the **hybrid kMC/MD** and pure MD simulations. We observe that diffusion hops captured in the **hybrid kMC/MD** model allowed Si atoms to overcome attractive interactions and disperse in the simulation box. In contrast, the MD simulation features a cluster structure at the end of the simulation (i.e., after 10^{-7} s).

5.5.1.4 Conclusions and further work

In this section, we presented two models dedicated to simulating the diffusion of Si particles in motor oil. Firstly, a **pure off-lattice kMC** scheme was deployed that displaced atoms via predefined diffusion hops. The spatial distribution of the system was estimated at different time steps, and Gaussian fits were performed to capture the temporal evolution of the distribution variance. The resulting variance-time data were in good agreement with the theoretical result for Brownian diffusion.

Following, a **hybrid kMC** model was presented. This model was based on the **pure kMC** scheme. The **hybrid kMC/MD** scheme additionally featured an MD stage that simulated non-bonding forces between atoms through an LJ potential and implicit solvent-particle interactions through a Langevin thermostat. Through this added layer of molecular-level resolution, we captured a clustering effect. Furthermore, the modelled LJ interactions delayed the complete dispersion of Si atoms in the simulation as atoms required additional time to overcome the attractive forces exerted on them from the cluster. Finally, the merits linked to hybrid kMC/MD simulations in PAPRECA were highlighted by comparing them to a pure MD model. We observed that the PAPRECA run can theoretically obtain a second of simulated time in $9.53\,10^{4}$ hours of walltime, while LAMMPS requires $8.54\,10^{7}$ hours. In other words, the time-advancing efficiency of the hybrid kMC/MD algorithm was superior to that of the pure MD model by 896.12 times.

A method to evaluate MSD and lagtimes in kMC simulations featuring variable time steps will yield supplementary insights on the effect of diffusion mechanisms (e.g., Brownian, or restricted by interatomic attractive interactions) in the temporal evolution of the spatial distribution of species. Moreover, finite-size effects have to be explored to examine the influence of simulation box size on the mobility of particles. Finally, the hybrid kMC/MD model can be extended to explicitly model solvent-particle interactions instead of capturing them implicitly through the Langevin thermostat. This will shed light on the elementary processes leading to clustering, aggregation, and diffusion of atoms through the solvent.

5.5.2 Monoatomic adsorption and desorption

5.5.2.1 Background

In this section, we demonstrate how PAPRECA can be used to investigate monoatomic desorption and adsorption processes on a substrate. The presented example shows how the software can capture the surface dynamics of a monolayer. Additionally, the application of this section exhibits how the proper deployment of predefined events and functions allows PAPRECA to perform lattice-based simulations.

5.5.2.2 Methods

This is a pure kMC example. Nonetheless, a LAMMPS input file was utilised to initialise atom types, the adsorption molecule template (see Section 5.3.2.4), and generate the starting structure. Specifically, a simulation box of lengths $L_x = L_y = L_z = 6$ nm was set. PBCs were deployed on the x- and y-direction edges. A shrink-wrapped edge was applied in the z-direction to allow for box adjustments due to the insertion of atoms. Two atom types were used in the simulation. The first type was associated with frozen substrate atoms, and the second one was linked to particles capable of adsorbing and desorbing on the substrate. The overlap criterion distances for adsorption events (see Section 5.3.2.4) were fixed to $\sigma_{11} = 2.15597$Å and $\sigma_{22} = 1.17599$Å for types 1 and 2, respectively. Note that such distances correspond to the LJ [205] σ parameters of aluminium and oxygen species parameters from OpenKIM [333]. The Lorentz–Barthelot mixing rules were utilised to estimate the σ_{12} cross term. An FCC substrate of lattice spacing $d = 4.046$ Å comprising type 1 species was generated via the `lattice` and `create_atoms` commands in LAMMPS. Moreover, an MD stage was periodically performed to export trajectory files for visualisation purposes. Similarly to the pure kMC model of Section 5.5.1.2, the MD stage had no impact on the system dynamics since no time integration was performed.

A `PAPRECA::PredefinedDeposition` predefined event was added in the PAPRECA input file to capture monoatomic adsorption steps in the kMC stage. As explained in Section 5.3.2.4, monoatomic adsorption can be simulated using LAMMPS molecule templates containing a single atom. Also, a height calculation method with mass bins was implemented with a mass cutoff of 95% and a bin width of 1 Å (see Section 5.3.3.1). Type 1 atoms acted as parent types and type 2 particles as depositing types for the predefined deposition event. The sticking coefficient was fixed at 1. The `random_depovecs NO 2D` option was used for the deposition event, which places deposition sites directly above the parent atom at a distance of ΔX (i.e., the deposition offset introduced in section 5.3.2.4). Here, ΔX was fixed at 4.046 Å , which is equal to the lattice spacing. Since deposition sites are placed directly above parent atoms, the example presented here resembles that of a classic lattice-based kMC application with fixed event sites. In essence, this underlines the extensibility of PAPRECA and its capabilities for modelling not only off-lattice, but also lattice-based systems. A `PAPRECA::PredefinedMonoatomicDesorption` predefined event was also inserted in the PAPRECA input file to model monoatomic desorption processes. Here, atoms of type 2 were considered as valid parent types for the relevant predefined event.

Note that this is a parametric study investigating the influence of adsorption/desorption rates on the steady-state surface coverage. The temporal evolution of surface coverage was monitored through ”surface_coverage.log” files (see Section 5.3.3.3). In practice, a series of PAPRECA simu-

lations were performed for the following adsorption/desorption rates $\frac{r_{ads}}{r_{des}} = [0.1\ 0.25\ 0.5\ 1\ 5\ 10]$. A termination criterion was used in the PAPRECA input file via the `time_end` command to terminate the simulations at $t_{sim} = 50$ s.

An analytic solution for the temporal evolution of the monolayer surface coverage was derived for comparison purposes. For the complete derivation, the reader is redirected to Appendix B. Below, we present the non-equilibrium result:

$$\theta(t) = \frac{r_a}{r_a + r_d}(1 - e^{-(r_a + r_d)t}) \tag{5.34}$$

The steady state solution is also given:

$$\lim_{t \to \infty} \theta(t) = \frac{r_a}{r_a + r_d} \tag{5.35}$$

5.5.2.3 Results and discussion

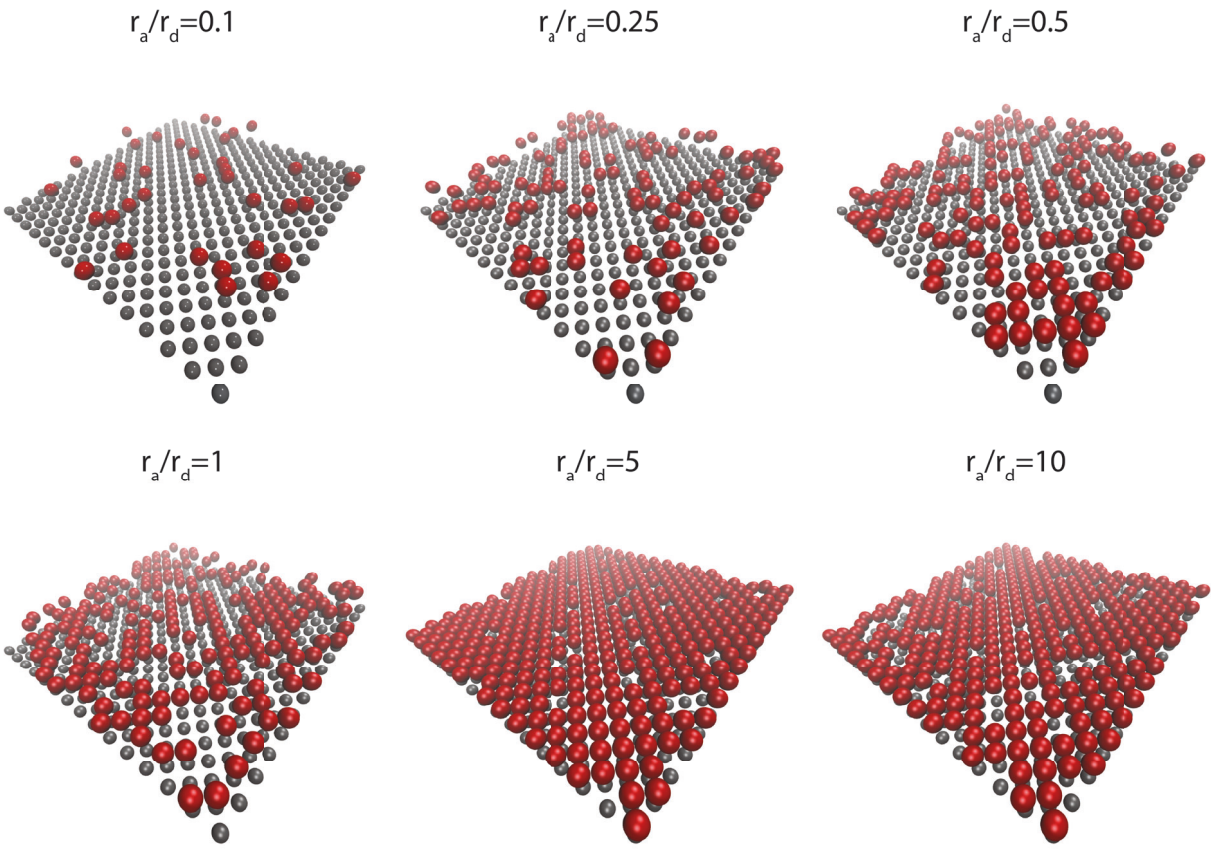


Fig. 5.30: Final (steady state) snapshots (at $t = 50$ s) of kMC simulations for different ratios of adsorption/desorption rates (r_a/r_d). Type 1 and type 2 atoms are illustrated as grey and red, respectively.

Fig. 5.30 illustrates final snapshots for the kMC simulations with different adsorption/desorption ratios. We observe that higher r_a/r_d values lead to elevated steady-state coverages. This is expected since the rate of each adsorption event increases relatively to that of desorption events as r_a/r_d rises. Hence, adsorption events are selected more often by the kMC algorithm at higher r_a/r_d values. Recall that the probability of selection in the kMC stage is biased by the rate of the event (see Section 5.3.2).

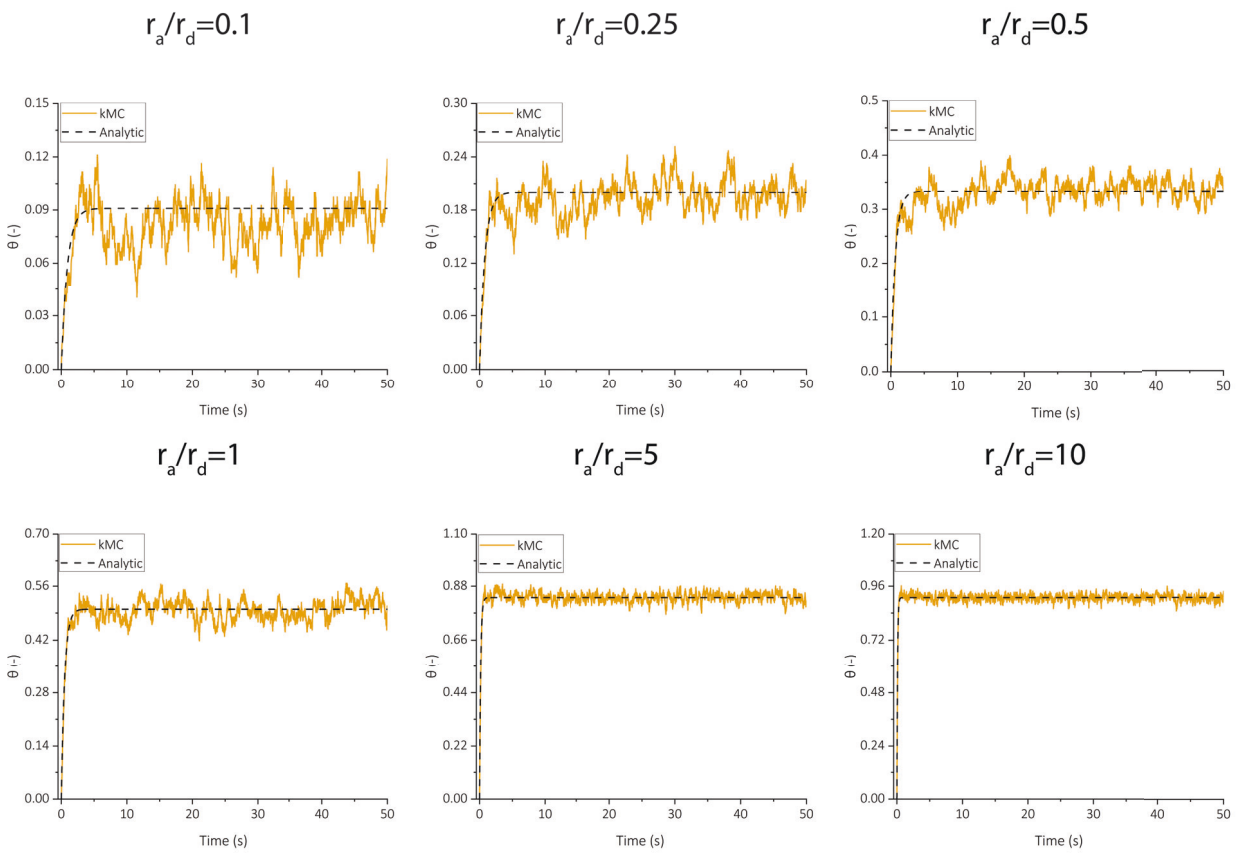


Fig. 5.31: Surface coverage (θ) as a function of time for different ratios of adsorption/desorption rates (r_a/r_d). The kMC data and theoretical solution (see Eq. 5.34) are depicted with solid orange and dotted black lines, respectively.

The surface coverages for different r_a/r_d are given in Fig. 5.31. Here, we observe that the kMC model matches the theoretical result (derived in Eq. 5.34) for any tested r_a/r_b ratio. A linear slope is observed at the initial stages of deposition. The slope of θ is proportional to $\frac{r_a}{r_a+r_b}$. Furthermore, the exponential term in Eq. 5.34 exhibits a decay that scales with the $r_a + r_b$. Consequently, the greater the value of r_a/r_b, the earlier the system reaches a state of dynamic equilibrium. In such a state, the cumulative probability of adsorption events becomes roughly equal to that of desorption events. The surface composition is variable. However, the surface coverage fluctuates about the steady state result ($\theta = \frac{r_a}{r_a+r_b}$ in Eq. 5.35) as sites are continuously freed and reoccupied.

Also, it can be observed that as the r_a/r_b ratio decreases, the amplitude of oscillations of θ about the analytical value increases. Effectively, the mean solution error increases at diminished values of r_a/r_b. Such an effect is depicted in Fig. 5.32. This phenomenon can be justified by considering that during dynamic equilibrium, the surface coverage is more sensitive to changes in the surface structure. For instance, the equilibrium value for $r_a/r_b = 0.1$ is $\theta_{analytic} = 0.0909$. Our kMC simulations featured a total of 421 sites. For $r_a/r_b = 0.1$ and at $t = 50$ s, 36 of them were occupied, leading to a surface coverage of $\theta_{kMC} = 0.0855$ corresponding to an error of 5.94%. Now, if a monoatomic desorption event is executed, the surface coverage will drop to a value of 0.0831, which is associated with an error of 8.55%. Effectively, this means that the error increased by 2.61% after solely one kMC step. In contrast, $\theta_{analytical} = 0.909$ and $\theta_{kMC} = 0.912$ at $t = 50$ s (with 384 out of 424 deposition sites occupied) for $r_a/r_b = 10$. This is linked to an error of 0.33%. By analogy, a subsequent monoatomic desorption event will lower the surface coverage at 0.910,

which is associated with an error of 0.071%. Hence, the difference in solution error caused by the monoatomic desorption event is 0.256%. This value is by an order of magnitude lower than 2.61%, corresponding to a r_a/r_d ratio of 0.1. In essence, this renders the errors and the fluctuations of kMC solutions about the analytic result more prominent at lower values of r_a/r_d.

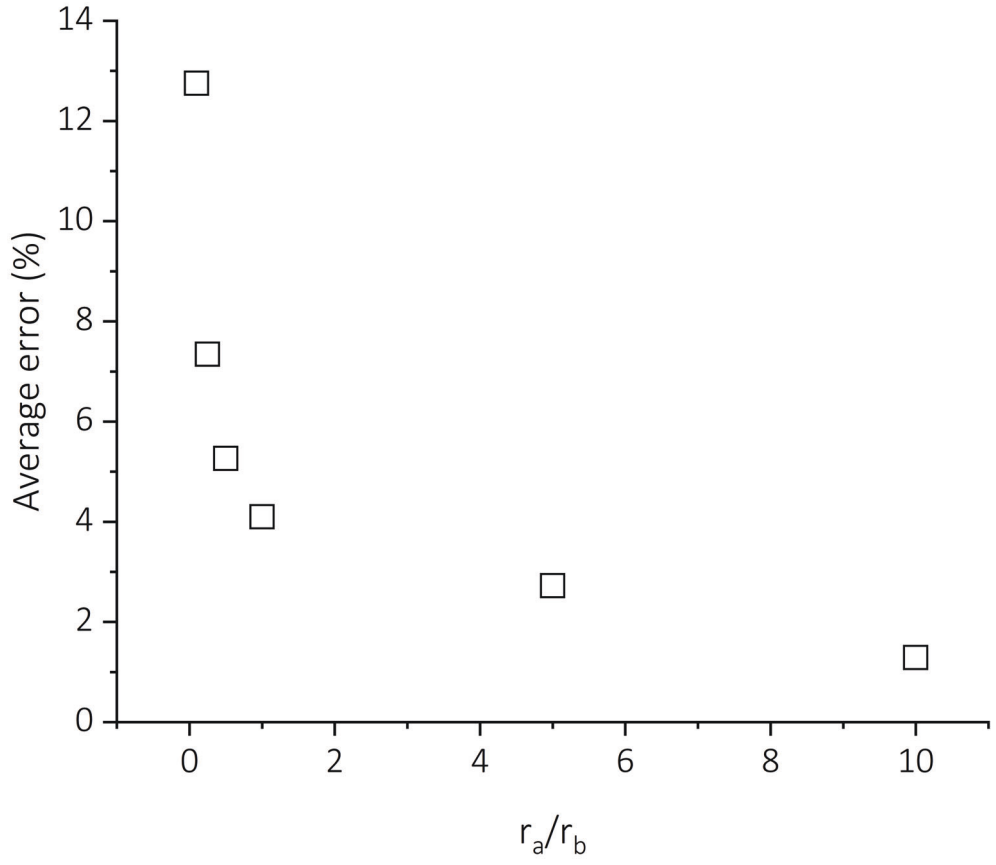


Fig. 5.32: Average error for different ratios of adsorption to desorption (r_a/r_b). The error at each time step was calculated as $\frac{|\theta_{analytic}-\theta_{kMC}|}{\theta_{analytic}}$

5.5.2.4 Conclusions and further work

In this section, we exhibited how PAPRECA can be used to perform pure kMC simulations on the growth of a monolayer. PAPRECA is, by design, an off-lattice simulator. Nevertheless, it is demonstrated that the `random_despotives 2D NO` feature coupled with a frozen substrate can be exploited to initialise and execute lattice-based simulations with fixed lattice-sites. To examine the applicability of PAPRECA in lattice-based problems, an FCC lattice was created, and monoatomic adsorption and desorption predefined events were utilised in the *predefined table of events* of kMC. Simulations were performed for ratios of adsorption to desorption rates (r_a/r_b) ranging from 0.1 to 10, and the relevant surface coverages were estimated by PAPRECA and exported via the `export_SurfaceCoverage` available in the software. The kMC results for surface coverage were compared to an analytic solution. It was shown that the surface coverage estimated by PAPRECA matches the analytic result closely. Also, it was demonstrated that higher r_a/r_d ratios lead to diminished errors in the kMC solution. This was mainly attributed to the fact that when the equilibrium θ is low at decreased r_a/r_d ratios, a single adsorption or desorption event represents a

larger fractional change in θ, making fluctuations more pronounced.

The applicability of this example is restricted to systems where interactions between adsorbed species are insignificant. In the future, the model can be extended to include surface reactions. This can unlock realistic simulations on catalysis or chemical vapour deposition [137, 338] processes with PAPRECA. Furthermore, these types of simulations can be extended even further to hybrid kMC/MD schemes with short-range atomistic interactions captured by an appropriate interatomic potential in the MD stage.

5.6 Scalability of PAPRECA

The scalability of PAPRECA was investigated by performing hybrid kMC/MD simulations on thin films grown from the decomposition of lubricant additive TCP molecules on an Fe(110) substrate. For further information regarding the system setup, refer to Chapter 3 and our previous study [270]. Here, the relevant model was replicated for hybrid kMC/MD simulations in the PAPRECA simulator.

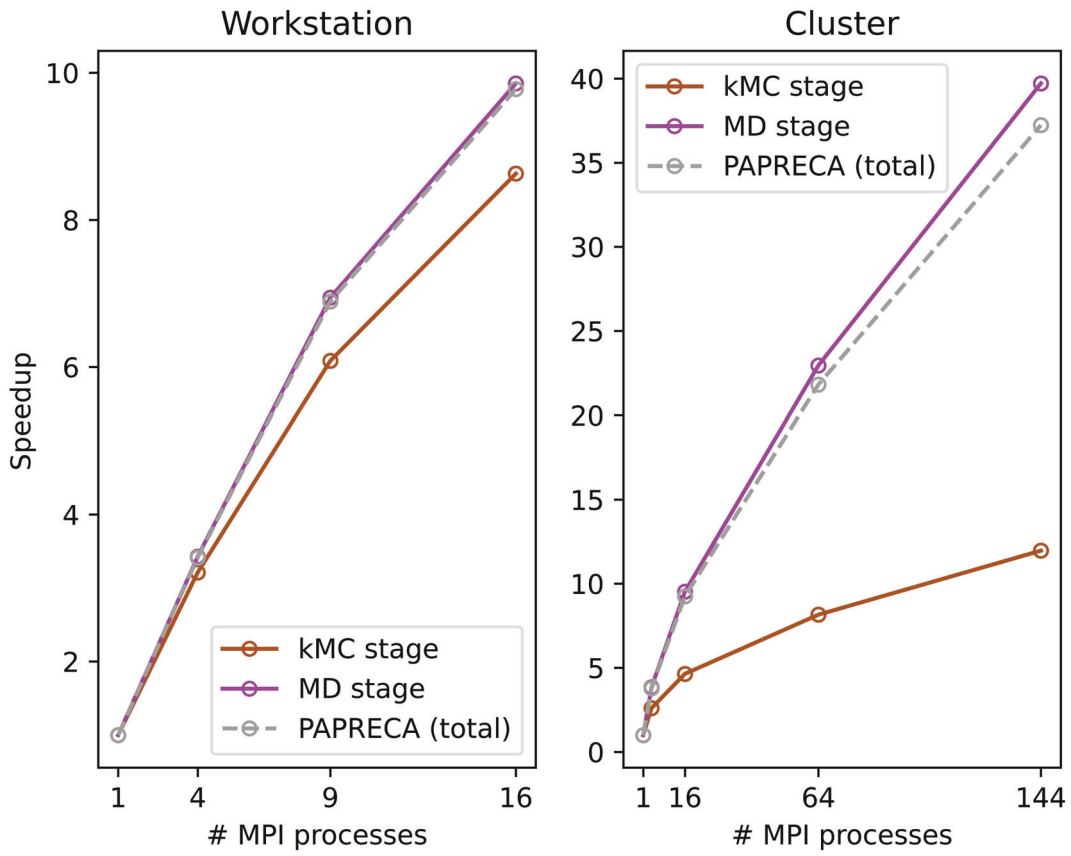


Fig. 5.33: Hybrid kMC/MD scalability tests of PAPRECA for TCP on Fe(110) conducted on a workstation **(left)** and on the CX3 cluster at Imperial College **(right)**.

Two independent scalability tests were performed. The first scalability test was conducted locally, on a personal computer (CPU: Intel(R) Core(TM) i9-10980XE CPU @ 3.00GHz, RAM: 128 Gb DDR4 @ 3200 MHz). Four runs were performed with 1, 4, 9, and 16 MPI processes, respectively. The local tests simulated 1000 PAPRECA steps, with a PAPRECA step comprising

a kMC stage where a predefined event is executed, followed by an MD stage where the system is relaxed. The second scalability test was performed on the CX3 cluster managed by the Research Computing Service at Imperial College London (CPU: 2xAMD EPYC 7742 with 128 cores per node, RAM: 1TB per node, interconnect: 100GbE Ethernet). This scalability test was conducted with the same parameters as the local one but with a different number of total PAPRECA steps (i.e., 9000 instead of 1000). Also, five runs were performed with 1, 4, 16, 64, and 144 MPI processes. Since the phosphate thin film grew along the z-direction of the simulation box, an NxNx1 processor grid (along the x-, y-, and z-directions, respectively) was utilised for all local and HPC tests. Figure 5.33 illustrates the results of both tests.

Here, the speedup value of N MPI processes was calculated as $t_N = \frac{T_1}{T_N}$, with T_1 being the total walltime of 1 MPI process. For this specific system (i.e., phosphates example), it can be observed that the kMC stage does not scale as effectively as the MD stage (performed in LAMMPS). Nonetheless, the total speedup (i.e., combined kMC and MD) of a hybrid PAPRECA run is comparable to the MD stage speedup. This can be justified by the fact that the kMC stages require significantly less CPU time than the MD stages, regardless of the number of MPI processes. For instance, the total walltimes of the kMC and MD stages of the 64 MPI processes example (second scalability test on the CX3 cluster) were 0.226 and 2.71 hours, respectively.

5.7 Limitations and further plans for development

One of the central limitations of PAPRECA is the use of a *predefined table of events* to model elementary processes. This introduces semi-empiricism to the method and requires a priori knowledge of dominant atomistic events (e.g., reactions, diffusion hops, adsorption/desorption events). In some cases, the presence of a database of events created through extensive experimental or computational investigations diminishes the complexity associated with the assembly of *predefined table of events*. Nevertheless, in other practical applications, such a database is not available. Therefore, rate-determining processes must be discovered.

Typically, methods with atomic-scale resolution are deployed to shed light on the crucial elementary events. Nonetheless, discovering key atomistic processes is not trivial. For instance, an appropriate force field that accurately captures interatomic interactions between a solvent and a solute must be selected to estimate the MSD and derive the diffusion coefficient and hopping rate for a dissolved molecule. An accurate reactive potential (e.g., ReaxFF [208]) must be utilised to retrieve the activation energies and attempt frequencies for bond-formation or bond-breaking events. This was performed in our initial study on the decomposition of TCP on iron (see Chapter 3) [270]. However, representative reactive force field parameters may not be available in the literature for the studied species or the system under investigation. Also, note that important elementary processes that dominate a system in experimentally-relevant scales might not manifest in classical or ab-initio MD simulations due to timescale limitations (see Section 2.1.2). Finally, methods estimating activation energies from basins on the PES (e.g., DFT with NEB [231] or the activation relaxation technique [228]) neglect the influence of entropic effects on the kinetics of detected atomistic processes.

The aforementioned remarks highlight the necessity for a prior thorough understanding of system dynamics and kinetics. In essence, PAPRECA is a powerful tool to unlock experimentally

relevant timescales. However, prospective users are reminded that PAPRECA cannot be used nor has it been designed to elucidate elementary atomistic events manifesting in femtosecond timescales. For that task, other available methods, such as DFT, ab-initio MD, and traditional MD that possess the required accuracy, should be utilised (see Section 2.1.2). Additionally, the intrinsic difficulties linked to event discovery showcase the necessity for a multiscale approach dedicated to the retrieval of activation energies and attempt frequencies of elementary processes. Effectively, a combination of DFT and MD simulations has to be performed to gain an in-depth understanding of the mechanisms driving system evolution and populate the *predefined table of events* of PAPRECA. In that respect, establishing a multiscale framework to retrieve the rates of dominant system events is of paramount importance to boost the extensibility of the software in chemistry, physics, materials science, and engineering applications. The development of such a framework is beyond the scope of this PhD thesis, but it is left for future work. For instance, the framework could provide automated tools to train machine learning potentials on DFT data and subsequently, launch MD simulations with the trained force field to capture atomistic events. The same framework could additionally offer methods (e.g., based on ML approaches) to detect patterns from MD trajectories and discover reactions, diffusion hops, adsorption/desorption steps. The same framework can aid towards the initialisation of the relevant *table of predefined events* associated with the system. Overall, the development of such a framework promises to render PAPRECA attractive to a wider audience, not only in academia but also in the industrial sector (e.g., inFUSE prosperity partners).

Another limitation of PAPRECA derives from practical considerations associated with the execution of predefined events. Of course, not all systems can be accurately modelled as a sequence of decoupled diffusion hops, deposition steps, and bond-breaking or bond-formation events of fixed frequencies. Certain systems can evolve through reaction pathways and concerted atomic moves. For example, kMC simulations on the formation and growth of SEIs in lithium-ion batteries require the modelling of various reduction, opening, pairing, and dimerisation processes [98]. To address that, predefined events featuring concerted atom moves will be prioritised in future versions of PAPRECA. Additionally, *event chains* will be implemented to provide users with approaches to capture events that occur in stages over multiple timesteps (e.g., reaction pathways). Effectively, the concept of *event chains* can be viewed as a generalisation of the REACTER protocol currently implemented in LAMMPS [26, 339]. Nevertheless, REACTER is specifically designed to handle reaction pathways through bond-formation and bond-breaking events. In contrast, *event chains* will involve different classes of predefined events. For instance, the *event chains* concept will be capable of modelling the evolution of a system through adsorption-reaction-diffusion cycles.

The presence of a *predefined table of events* does not strictly demand the use of fixed rates for events. The concept of *variable event rates* is, to a limited extent, already available in PAPRECA. *Variable event rates* assist in capturing competitive elementary steps that can influence the rates of other detected events in the local atomic environment. For example, the rates of deposition events can be scaled with the sticking coefficient (see Section 5.3.2.4). Also, the rates for diffusion events can be set to zero if there are fewer than four phosphate structures in the neighbourhood of the parent atom (see `Fe_4PO4neib` option in Section 5.3.2.6). Finally, the rates of bond-formation events can be zeroed via the `catalyzed` command designed for `PAPRECA::PredefinedBondBreak` events. Nevertheless, in future iterations of PAPRECA, we aim to introduce further functional-

ity dedicated to imposing *variable event rates*. For instance, the activation energy of adsorption and bond-breaking events can be a function of the adsorbate orientation and bond distance, respectively. Furthermore, the rates of events can be continuously updated by exploiting derived properties from LAMMPS and the MD stage of PAPRECA in hybrid kMC/MD simulations. For example, a reaction rate can be altered to reflect local or global changes in temperature, pressure, friction, viscosity, etc. Such an addition to PAPRECA can become useful in the accurate modelling dynamics of lubricated surfaces under friction. For instance, the activation energy of a $P-O$ bond-breaking event in ferrous surfaces in contact with lubricant additive TCP molecules can be correlated to the sliding speed or pressure [92, 315].

Moreover, note that PAPRECA is, by design, an off-lattice simulator. Consequently, the software is not expected to be the most numerically efficient or most accurate tool in applications involving crystalline materials. In such systems, other open-source tools such as SPPARKS [296] can be used. However, crystalline structure and short-range order can be modelled in PAPRECA via a couple of approaches. Firstly, structure can be captured from an appropriate interatomic potential and within the MD stage in hybrid kMC/MD simulations with PAPRECA. Secondly, adsorption/desorption or diffusion hop events can be executed on fixed lattice sites with proper use of the `random_depovecs 2D` (see example in Section 5.5.2) or `radom_diffvecs 2D` commands, respectively. Nonetheless, it is acknowledged that the lattice structures captured by the aforementioned commands are rather simplistic to be accurate in most practical applications. Hence, additional functionality will be added in future versions of PAPRECA to enable fixed deposition and diffusion sites that are not directly above or below the parent atom. This added functionality will assist hybrid kMC/MD and pure kMC simulations in ordered systems and potentially unlock realistic PAPRECA models for multiphase crystalline materials.

To enable simulations of molecules featuring elevated end-to-end distances, certain algorithms linked to `PAPRECA::PredefinedDeposition` event have to be revisited and improved. Firstly, the overlap-detection method has to be generalised. Note that solely overlaps between neighbours of the parent atom and molecule atoms are currently identified in PAPRECA (as explained in Section 5.3.2.4). Nonetheless, this can result in instabilities in the MD stage since long adsorbates can overlap with particles not included in the neighbours list of the parent atom. Future versions of PAPRECA should incorporate algorithms dedicated to the detection of long-range overlaps. This will enable hybrid kMC/MD simulations on the deposition of long hydrocarbon chains, which are important in lubrication applications [340]. Additionally, note that a film-height identification scheme based on a fixed mass cutoff parameter is implemented in PAPRECA (see Section 5.3.3.1). A more sophisticated height calculation algorithm is required to provide a better estimate for the film height at each timestep. For example, the film height can be determined by starting from the bottom layer of the film and progressively considering additional atoms within a cutoff distance until a vacuum region is detected.

Furthermore, we believe that each additional second captured with hybrid kMC/MD simulations improves even further our understanding of materials interfaces. Consequently, improving the numerical efficiency and enhancing the scalability of PAPRECA to enable faster simulations in bigger systems will be our primary goal for future development. In that respect, we aim to involve additional parallelisation schemes in the software. Note that PAPRECA currently selects an *event MPI rank* which executes a single event at each kMC stage (see Section 5.3.2). By

postulating that atomistic steps discovered by each MPI rank are independent, a parallelisation scheme could fire an event on each processor at every kMC stage. This can accelerate kMC simulations as each kMC stage will execute as many predefined events as the number of MPI ranks in the simulation. A similar parallelisation approach is available for on-lattice kMC in SPPARKS [296]. In any case, the implementation of such a parallelisation scheme in PAPRECA can become challenging due to the requirement to handle multiply-detected events on subdomain boundaries. Moreover, implementation complexities can arise from the necessity to design algorithms dedicated to treating conflicting elementary steps in different MPI ranks. For instance, a bond-formation and a monoatomic desorption event involving one of the bonded particles cannot be performed simultaneously on neighbouring subdomains at the same kMC stage. This would result in a "bond atoms missing" error in LAMMPS as the rank executing the formation event will attempt to bond an existing atom with a particle removed from the adjacent MPI rank.

The computational efficiency of PAPRECA can be further elevated through the implementation of parallel software engineering protocols. For instance, intra-processor parallelisation can be achieved with OpenMP. OpenMP can be deployed to vectorise and reduce the cost of numerically expensive loops of the kMC stage. For instance, overlaps for deposition and diffusion hop events (see Sections 5.3.2.4 and 5.3.2.6) can be detected through single instruction, multiple data (SIMD) data processing schemes instead of traditional iterative approaches. Finally, CUDA parallelisation can reduce the numerical cost of critical tasks in the kMC stage (e.g., the aforementioned overlap-detection loops) and boost the scalability of the software, enabling PAPRECA simulations with bigger systems.

Finally, we aim to improve the user interface of PAPRECA. Note that the *PAPRECA pseudolanguage* is currently utilised to initialise a PAPRECA simulation and communicate with the user and the software. It is acknowledged that mastering the *PAPRECA pseudolanguage* and becoming familiar with the various commands controlling the hybrid kMC/MD simulation can become time-consuming. To render PAPRECA more attractive to a wide audience, we aim to provide interfacing through Python programming. In essence, Python wrappers around PAPRECA functions will be implemented to allow the user to initialise and run PAPRECA directly from a Python script. Introducing PAPRECA to the Python ecosystem can aid towards the democratisation of the developed hybrid kMC/MD simulator due to the recent popularity of Python for scientific computing purposes.

5.8 Summary and conclusions

In this chapter, we introduced a kMC software called PAPRECA. PAPRECA enables atomistic simulations beyond the timescale limits of MD. PAPRECA was inspired by a previous in-house code written in Fortran95 that was dedicated to the modelling of TCP decomposition on ferrous substrates (see Chapter 3). In contrast to the closed-source and specialised code written in Fortran95, PAPRECA is a general and open-source software that can be utilised to model various systems in chemistry, physics, materials science, and engineering. A hybrid kMC/MD scheme is implemented in the software. High activation energy atomistic processes (e.g., reactions, diffusion hops, adsorption/desorption steps) are captured by a kMC simulator, while high-frequency processes such as atomic vibrations are modelled in an MD stage. The MD stage is performed in

LAMMPS - a popular open-source software for MD. To the best of our knowledge, PAPRECA is the only available hybrid off-lattice kMC/MD simulator available in open-source repositories.

In the first sections of this chapter (i.e., 5.1 and 5.2), we discussed the motivation of PAPRECA and formally introduced the software. In Section 5.3, an in-depth analysis with regard to the parallel algorithms of PAPRECA was performed. The specifics of the MD stage (performed in LAMMPS) were discussed in Section 5.3.1. Section 5.3.2 discussed the parallel algorithms of the kMC stage. Emphasis was given on the discovery, selection, and execution of the different families of atomistic processes accessible to the software (i.e., bond-formation, bond-breaking, diffusion hops, molecular as well as atomic deposition, and monoatomic desorption). In section 5.4, we discussed user-interfacing, software libraries, as well as aspects of object-oriented programming and open-source implementations.

In section 5.5, the applicability of PAPRECA in systems beyond the thermal decomposition of TCP on iron was exhibited through examples. In the first example, an off-lattice kMC and an off-lattice hybrid kMC/MD scheme were deployed to model the diffusion of Si particles in a viscous solvent (see Section 5.5.1). The pure kMC results for the temporal evolution of the variance of the spatial distribution matched the analytic result for Brownian diffusion. The pure kMC model was also extended to a hybrid kMC/MD scheme that not only captured diffusion hops through the kMC stage, but also captured interatomic interactions through an LJ potential. It was demonstrated that the hybrid kMC/MD simulations in PAPRECA allowed the system to overcome high-energy diffusion barriers. Overall, the kMC/MD model advanced the simulation clock by three orders of magnitude faster than equivalent MD simulations.

A second application that simulated monoatomic desorption and adsorption on a fixed lattice was presented in Section 5.5.2. Simulations were performed for different values of adsorption to desorption ratios. The relevant results for the evolution of surface coverage agreed well with the analytic solution. Furthermore, this example illustrates that the existing functionality in PAPRECA can be useful in performing lattice-based kMC studies. This showcases the ability of PAPRECA to perform both off-lattice and lattice-based simulations.

Then, in Section 5.6, the scalability of PAPRECA was investigated through tests performed at a local workstation and the HPC service of Imperial College London. It was demonstrated that the scalability of PAPRECA is similar to that of LAMMPS. This result is promising, since LAMMPS is a massively parallelised and optimised simulator that has been under continuous development since the 1990s [26].

In Section 5.7, we discussed the limitations of the software and addressed plans for further development. Specifically, we focused on constraints associated with the use of a *predefined table of events* and underlined the importance of the development of a novel framework to discover atomistic events and estimate their respective rates. Moreover, we discussed ideas towards the improvement of the computational efficiency of PAPRECA through parallelisation schemes. We also introduced ideas to enhance the applicability of the method to additionally complex systems in the energy sector (e.g., SEIs) through *event chains* or *variable event rates*. Finally, we discussed plans to improve existing functionality (e.g., film-height calculation methods) and addressed the need for software democratisation through user-interfacing based on Python scripting.

Overall, PAPRECA was designed to allow researchers and engineers in both academia and industry to extend atomistic simulations to experimentally-relevant timescales. Enabling off-lattice

simulations that capture both low- and high-frequency atomistic processes can accelerate materials discovery and shed light on the driving atomic-scale mechanisms in critical interfaces in the energy sector. PAPRECA is a complete package that can readily simulate the system evolution through bond-breaking, bond-formation, adsorption/desorption steps, and diffusion hops. Further plans for development promise to broaden PAPRECA's area of applicability even further to systems featuring complex reaction pathways.

Data availability

PAPRECA's open-source code, including example input scripts and tests, is available on GitHub: https://github.com/sntioudis/papreca [331].

Chapter 6

Revisiting the model for thin films from lubricant additives

6.1 Introduction

In Chapter 3, the hybrid kMC/MD methodology was introduced. The methodology was validated through an example from tribology and lubrication. Specifically, we simulated the thermal decomposition of TCP molecules on an iron substrate. In Chapter 4, an experimental study was performed to investigate the accuracy of the proposed hybrid kMC/MD methodology. The experimental results were compared with relevant data available in the literature, as well as data generated from the hybrid kMC/MD methodology. In Chapter 5, an open-source as well as fully parallelised hybrid kMC/MD simulator was presented. In the present chapter, we will explore further the validity of our model related to the thermal decomposition of TCP on ferrous surfaces. In particular, we will deploy the scalable software presented in the previous section (i.e., PAPRECA) to perform hybrid kMC/MD runs on the decomposition of TCP. Different temperatures will be tested to accurately match the experimental conditions (as outlined in Section 4). Moreover, a sensitivity analysis on the diffusion length parameter for hopping events (i.e, ΔL_k defined in Section 5.5.1) will be performed. Finally, the thermal decomposition model will be extended to capture shear and compressive stress effects. Effectively, those can be considered as our initial attempts to perform realistic tribological simulations capturing mechanochemical interactions at experimentally relevant timescales with hybrid kMC/MD schemes.

6.2 Thermal decomposition of TCP on iron

6.2.1 Methods

For the most part, the simulation details are identical to the ones utilised for the thermal decomposition model of Chapter 3. Here, the details are briefly summarised and subtle changes to the model are analysed. Recall that the model of Chapter 3 deployed reflective walls on the edge of the simulation box along the z-direction (see Section 3.3.3). In contrast, no reflective walls were implemented in this section's model. Instead, the `LAMMPS_region` recursive algorithm presented in Section 5.3.3.2 (see Algorithm 1) was deployed to remove disconnected atoms separated from the current film height by 20 Å or more. The `mass_bins` method (discussed in Section 5.3.3.1)

was utilised with a mass cutoff of 95% and a bin width of 1Å to estimate the current film height at the beginning of each kMC stage. A shrink-wrapped boundary was implemented along the z-direction to dynamically adjust the edges of the simulation box, while periodic boundaries were utilised along the x- and y-directions.

A DREIDING interatomic potential [206] and the QEq charge equilibration method [207] were used for the MD stage of PAPRECA with identical coefficients to our previous study on the thermal decomposition of TCP (see Section 3). The Nosé–Hoover [242, 243] thermostat was utilised with a damping parameter of 50 fs to produce trajectories consistent with the NVT ensemble. The timestep was fixed at 0.5 fs. The initial structure featured an iron substrate that was generated via the `lattice` and `create_atoms` commands of LAMMPS. Specifically, a face-centred cubic (FCC) lattice was created, and the z-axis of the simulation box was oriented towards the (110) crystallographic direction. This enabled film growth along the Fe(110) plane. Note that, similarly to our initial model, the substrate remained frozen during the MD as well as kMC stages of the PAPRECA run. 200 fs were simulated in the MD stage after every kMC stage, while a longer trajectory of 1000 fs was captured every 200 kMC stages. The CG method [237] was deployed to zero interatomic forces and ensured that the system was at a local minimum on the PES before and after each kMC stage. The hybrid kMC/MD simulations were performed for 185 °C, 190 °C, 195 °C, 200 °C, 205 °C to match the temperatures tested with our experimental setup (see Chapter 4). All simulations were run up to 350 seconds.

`PAPRECA::PredefinedDeposition` events (see Section 5.3.2.4) were deployed to capture deposition events for mmm-TCP molecules. Similarly to our initial model, any atom type could be a parent to deposition events. Therefore, a `PAPRECA::PredefinedDeposition` event was used for every atom type. The `depoheights` option was implemented (see Eq. 5.17) to restrict deposition events 5Å above or below the current film height. Also, the `random_depovecs NO 2D` option was imposed to generate deposition sites directly above the parent atom types. The deposition offset (ΔX) was fixed at $\sigma_{ij} + 0.1$ Å, with σ_{ij} representing the equilibrium interatomic distance parameter of the DREIDING potential. A variable sticking coefficient was utilised via the option `sticking_coeff variable` (as outlined in Section 5.3.2.4). The velocity of inserted TCP molecules was fixed at 0 Å/fs. Note that an insertion velocity of -0.02 Å/fs was utilised in our initial model on the decomposition of TCP on iron. In the model presented in this section, the use of velocity biasing was not preferred as it was found to be linked to instabilities in thin films larger than approximately 30 Å (the maximum thickness of systems studied in our initial model).

`PAPRECA::PredefinedBondBreak` events for P-O, as well as C-O bonds, were inserted in the *predefined table of events* of the hybrid kMC/MD simulation. The `catalyzed` option (see Section 5.3.2.3) was imposed to solely break bonds between pairs of atoms that feature at least one Fe neighbour in their respective neighbours lists. `PAPRECA::PredefinedBondForm` events formed P-O, P=O, Fe-O, Fe=O, and O-O bonds in the kMC stage of the simulation. The `delete_atoms` option was implemented to remove bonded oxygen atoms resulting from O-O bonding events. The `species_maxbonds` option was imposed to restrict the maximum number of bonds for substrate Fe, C, O, P, H, and film Fe species to 3, 2, 2, 4, 1, and 6, respectively. Furthermore, the `species_maxbondtypes` option was utilised to permit solely a single oxygen-surface Fe bonding event. Note that the options for formation events were identical to those used in our initial study on the decomposition of TCP (see Section 3.3.4). For additional information regarding the

limit settings for `PAPRECA::PredefinedBondForm` events, the reader is advised to refer to Section 5.3.2.3.

A `PAPRECA::PredefinedDiffusionHop` event was inserted in the *predefined table of events* to simulate the diffusion of surface Fe atoms towards the growing film. Similar to our previous model on the decomposition of TCP, Fe atoms remained frozen, and new iron particles were inserted into the simulation box. This was modelled with `non-displacive` diffusion type events (see Section 5.3.2.6) in PAPRECA. The diffusion velocity was fixed at 0 Å/fs, and the `random_diffvecs NO 2D` option was implemented to place inserted particles directly above the parent atom. Furthermore, the custom `Fe_4PO4neib` diffusion option was deployed to reject event parents with fewer than 4 PO_4 structures in their neighbourhood. An identical rule was implemented in the Fortran95 code used for our initial investigation on the decomposition of TCP (see Section 3).

Recall that a diffusion hopping distance value of 4.14468 Å $(\sigma_{ij} + 0.1)$ was utilised in our previous model. Moreover, recall that the temporal evolution of film height in our initial model on the decomposition of TCP featured a plateau at approximately 3 nm (see Fig. 3.13 of 3.3.7). It was concluded that this plateau was a direct consequence of unreacted TCP molecules attaching to the surface at the later stages of the simulation. Note that P-O and C-O bonds were allowed to break only if an iron atom was present in the neighbours list of either atom of the bonded pair. To the best of our understanding, increasing the hopping distance for Fe atoms is expected to result in an elevated number of iron atoms in the film due to fewer interatomic overlaps (see Section 5.3.2.6 for a definition of an overlap). The insertion of additional Fe atoms in the film can lead to a rise in bond-breaking events between P-O and C-O species, which in turn favours the formation of longer iron polyphosphate chains. This enables the growth of thicker films. After acknowledging the remarks above, we decided to perform a simplistic sensitivity analysis on the hopping distance ΔL_k with values larger than 4.14468 Å (which led to a plateau at 3 nm). Specifically, we tested ΔL_k values of 5.14468 and 7.14468 Å.

The base rates for the bond-breaking, bond-formation, and diffusion events were estimated from the Arrhenius equation (i.e., Eq. 3.1) via the `rate_arrhenius` option (see Section 5.3.3.4). The ΔE and ν values were identical to the ones utilised in our initial model on the decomposition of TCP (see Section 3.3.4). Of course, the temperature varied based on the simulation temperature. The base rate of deposition events was estimated through the `rate_hertz` option (see Section 5.3.3.4 and Eq. 3.8) with m = 368.37 g/mol, $A = 7.648\text{Å}^2$ (as discussed in Section 3.3.4). A partial adsorbate pressure of P=0.01 atm was utilised in the Hertz-Knudsen equation (Eq. 3.8) to provide a realistic representation of the conditions of our experimental work. Recall that our experiments were performed at ambient pressure and with mixtures of 1% TCP. Consequently, under ideal mixing conditions, the partial pressure of TCP molecules in solution would be 0.01 atm.

6.2.2 Results and discussion

Appendix C includes height versus time graphs for a ΔL_k value of 5.14468 Å. A plateau of approximately 3 nm is illustrated at the late stages of growth and for any tested temperature. This work will focus on simulations performed with a hopping distance of ΔL_k=7.14468 Å. This decision was motivated after observing that the generated height-time graphs with ΔL_k=7.14468 Å exhibit linear growth instead of a plateau at the late stages of the simulation.

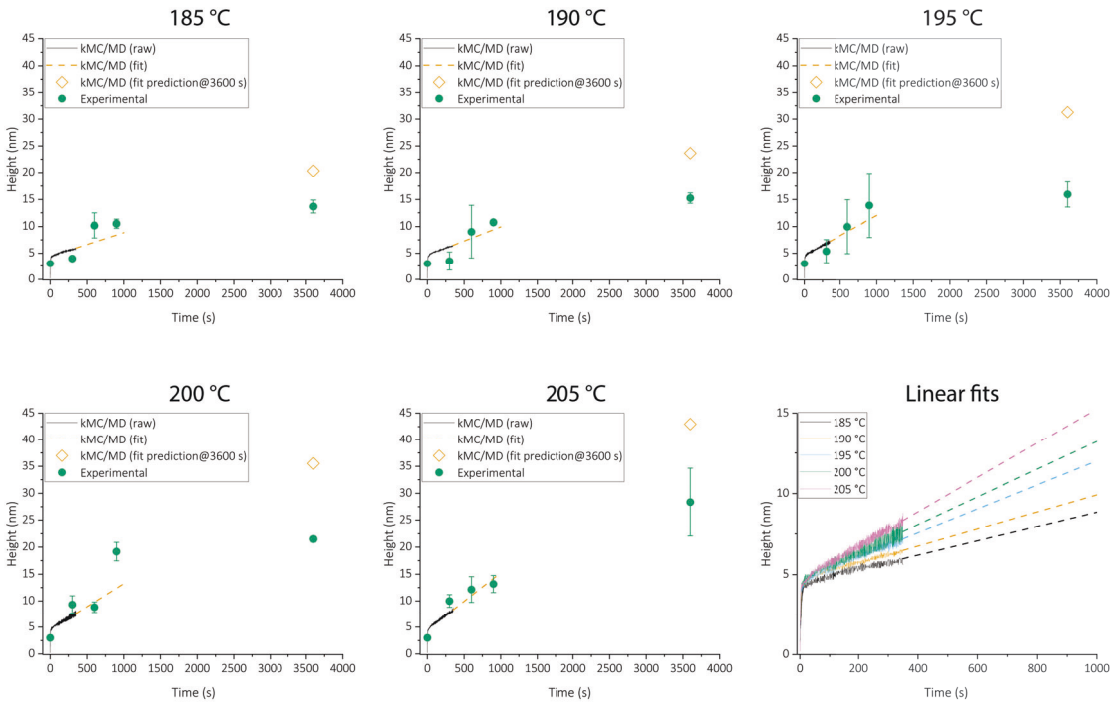


Fig. 6.1: Height versus time for different temperatures with a diffusion hopping distance for substrate iron atoms (ΔL_k) fixed at 7.14468 Å. Results from hybrid kMC/MD simulations in PAPRECA. Extrapolating lines and fit predictions at 3600 s are obtained from linear fits on the final 100 seconds of the respective run. Experimental results come from our investigation presented in Chapter 4.

Table 6.1: Hybrid kMC/MD simulation output data for different temperatures. Revisited model for the thermal decomposition of TCP on Fe(110).

Temperature (°C)	Thickness @ 350s (nm)	Extrapolated thickness @ 1hr (nm)	Linear growth rate (nm/s)
185	6.0	20.3	0.0044
190	6.5	23.6	0.0053
195	7.2	31.3	0.0074
200	7.6	35.5	0.0086
205	8.3	43.0	0.0107

Fig. 6.1 illustrates the generated growth profiles for different temperatures. In the absence of an analytic fitting expression, the growth profiles are extrapolated with linear fits on the linear segment of each height versus time graph. Data from our experimental investigation on the decomposition of TCP (see Chapter 4) are also presented in the graph. For completeness, a separate graph illustrating the graphs and linear fits is also given in Fig. 6.1. For any tested temperature, a steep growth is initially observed up to 5 nm. Then, the thin films exhibit linear growth, and the growth rate is proportional to the system temperature. At the end of the simulation (i.e., 350 seconds), the thin films at 185 °C, 190 °C, 195 °C, 200 °C, and 205 °C feature a thickness of 5.969, 6.486, 7.196, 7.647, and 8.33 nm, respectively. On the other hand, the growth rates (estimated from the slope of the linear interpolations) are 0.00442, 0.00528, 0.00741, 0.00858, and 0.01066 nm for 185 °C, 190 °C, 195 °C, 200 °C, and 205 °C, respectively. The relevant data are summarised in Table 6.1. Overall, the results of the hybrid kMC/MD simulations are in good agreement with data obtained from our MTM analysis on 52100.

The atomic percentages of Fe, P, O, and C species estimated from the hybrid kMC/MD model are illustrated in Fig. 6.2. The elemental distributions at any temperature are similar to those obtained from our initial study on the decomposition of TCP (see Fig. 3.19 in Chapter 3). The

simulations of the current chapter can capture the carbon peak near the iron substrate (at about 0.5 nm). This peak was previously observed in the Auger depth profile experiments of Johnson et al. [67] on thermally decomposed t-BPP molecules (see Fig. 3.19.b). Recall that our initial hybrid kMC/MD investigation on the same system (in Chapter 3) did not feature the relevant carbon peak, potentially due to our model design that ejected m-cresol fragments from the system after certain C-O bond scission events [270]. In contrast, the model presented in this section does not delete fragmented m-cresol groups and exhibits a near-surface elemental composition that agrees better with experimental data on phosphate-containing films.

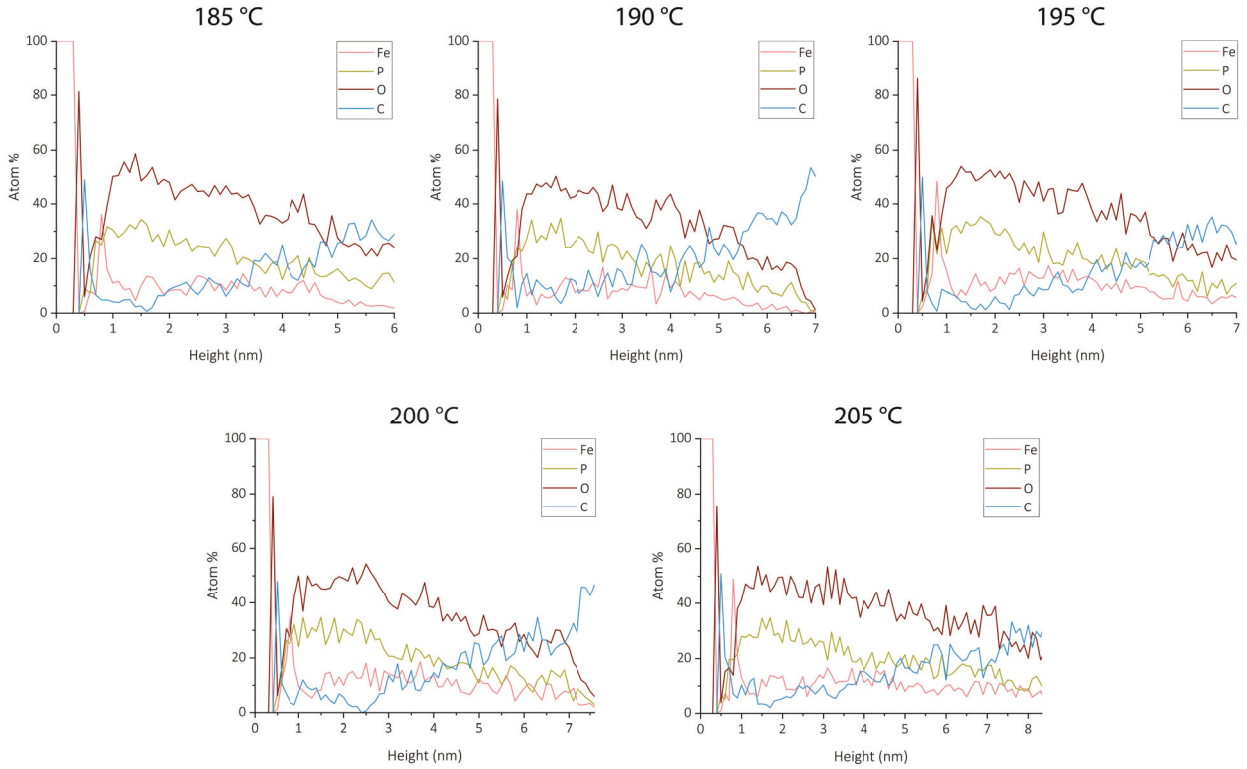


Fig. 6.2: Elemental distribution across the film thickness as calculated from the hybrid kMC/MD model on the decomposition of TCP on Fe(110) and at different temperatures. All distributions were generated from the final snapshot (i.e., at 350 s) and for a thickness range of $[0,h_m]$, where h_m is the maximum film height of the run.

In the current study, the hopping distance for substrate iron diffusion events (ΔL_k) was fixed at 7.14468 Å. This led to an increase in the number of Fe atoms in the system compared to our initial investigation on the same system that used a ΔL_k value of 4.14468 Å. Recall that in our previous study, Fe species moved up to approximately 1.5-2.0 nm at a temperature of 528.15 K. In contrast, in the model presented here, iron atoms propagate further than 2 nm at any tested temperature. Moreover, Fe atoms reach the upper film layers at higher temperatures. This is potentially linked to enhanced atom mobility at elevated temperatures, accelerating Fe diffusion during the MD stage of PAPRECA. Finally, the final film height (at 350 s) is proportional to the system temperature (see table 6.1). Note that this behaviour was also observed in our experimental analysis with SLIM (see Section 4.3.2). The dependence of film thickness on the system temperature can be associated with the amount of iron present at the film-vacuum interface. The higher the percentage of iron species, the greater the probability of C-O as well as P-O bond-breaking events. Recall that the `catalyzed` option was utilised for these bonds to model the catalytic role of Fe atoms. In any case,

the relevant scission events generate dangling oxygen bonds that enable further iron polyphosphate film growth through subsequent Fe-O and P-O bond-formation events. The significance of Fe species in the formation and growth of films from the decomposition of phosphate-containing additives was previously discussed in Chapter 2 (see Section 2.1.1.3). Finally, a slight increase in the carbon content is illustrated in the upper film layers for any tested temperature. This observation agrees well with our previous XPS results (see Fig. 4.4 in Chapter 4), which showed that the surface of the TCP film was dominated by carbonaceous compounds. Example micrograph segments of the different regions of the thin film generated at 205 °C are given in Fig. 6.3.

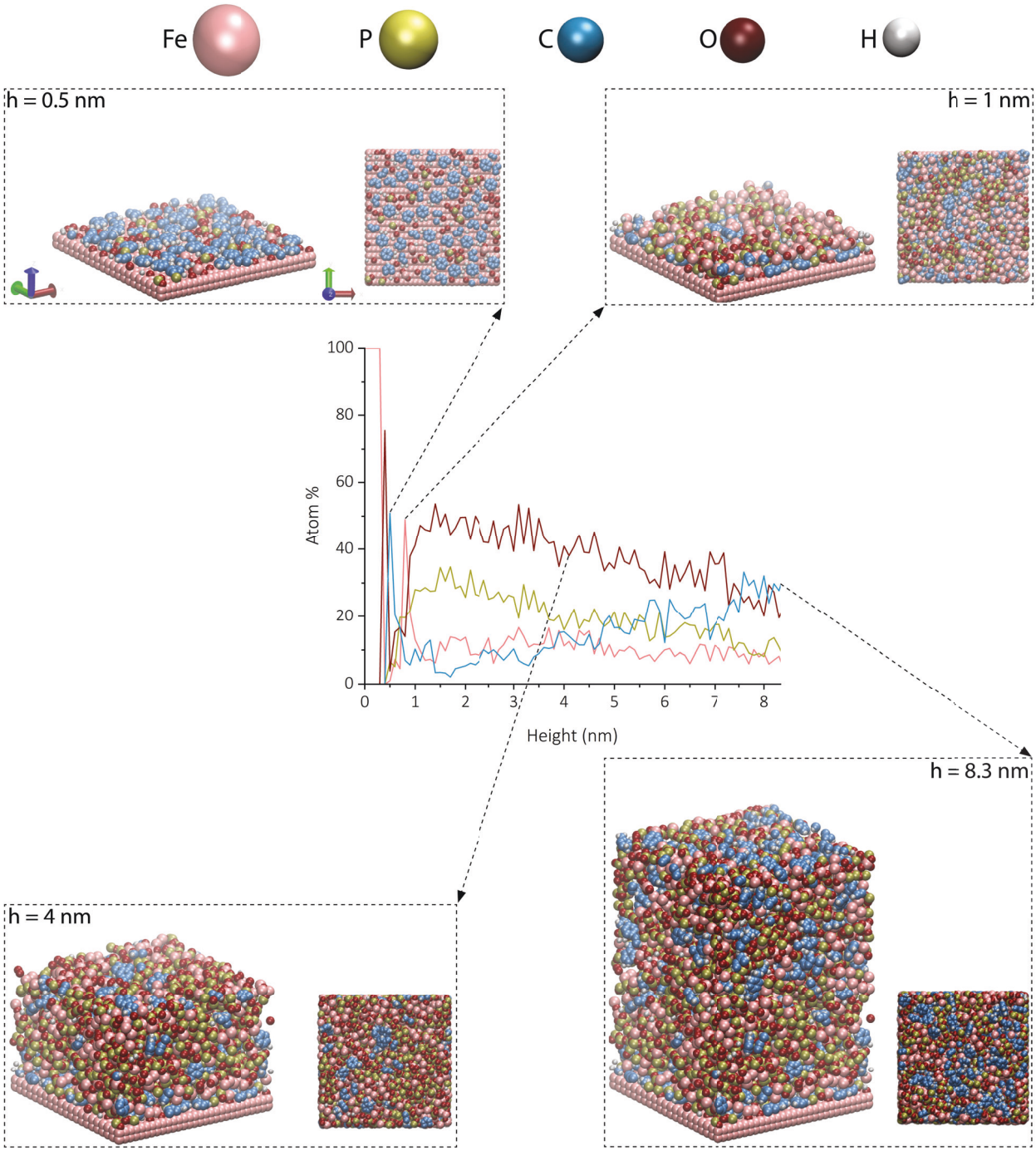


Fig. 6.3: Example micrograph segments for 205 °C at 0.5, 1, 4, and 8.3 nm.

6.2.3 Conclusions and future work

In this section, we revisited the model investigating the thermal decomposition of TCP on a Fe(110) substrate. A hybrid kMC/MD model shedding light on the long-timescale growth of the relevant lubricant additive was first presented in Chapter 3. In the current section, we fine-tuned the diffusion hopping distance for substrate Fe species. We also modified the C-O as well as P-O bond-breaking events to retain fragmented m-cresol groups in the system. All simulations were performed in PAPRECA - the scalable (see Fig. 5.33) hybrid kMC/MD simulator presented in Chapter 5.

The aforementioned model ramifications enabled film growth beyond the maximum height of about 3 nm obtained in our initial study on the decomposition of TCP. The height versus time curves obtained from the kMC/MD model and for different temperatures were in good agreement with equivalent experimental data collected in Chapter 4. Furthermore, the improved model of this section revealed a dependence of the maximum film height on the system temperature. This is associated with elevated Fe atom mobility, allowing catalytic iron species to propagate to upper layers of the thin film and enable further growth. Finally, the new decomposition model appears to provide a more representative description of the near-surface elemental composition, which is dominated by the carbon species of m-cresol groups.

Overall, the elemental composition as well as temporal evolution results presented in this section agree with our experimental data. Nevertheless, further work has to be performed with lower-scale simulations (e.g., ReaxFF MD and DFT) to revise the *table of predefined events* of the model. This will provide a more realistic description of the rare events driving the formation and growth of thin films from TCP. Also, the near-surface chemistry can be upgraded by introducing mobile surface atoms. Furthermore, a simplistic sensitivity analysis presented in this section revealed that specific event parameters such as the hopping distance (ΔL_K) for diffusion events can influence key hybrid kMC/MD results such as the final film height. In future model iterations of the model, the hopping and adsorption distances (see Sections 5.3.2.4 and 5.3.2.6) must be fine-tuned through additional lower-level simulations or advanced sensitivity analyses involving feedback loops on experimental datasets [341].

6.3 Mechanochemistry of TCP molecules on ferrous surfaces

In this section, we will upgrade the model presented in Section 6.2 to provide elementary insights on the mechanochemical decomposition of TCP on iron.

6.3.1 Methods

The starting configuration consisted of 48 TCP molecules randomly inserted between two Fe slabs. Note that the starting configuration is equivalent to that utilised in the ReaxFF study of Ogbomo et al. [92]. The two Fe(110) slabs were generated using the `create_atoms` (similarly to Section 6.3.1). The length of each slab across the x- and y-dimensions was $L_x = 48$ Å, $L_y = 48$ Å. Each slab featured 11 Fe monolayers and a gap of 43 Å was initially present between them. The DREIDING potential [206] and the QEq method [207] were used with parameters identical to those of Section 6.2.1. The velocity-Verlet [203] algorithm was utilised to integrate the equations of motion.

The starting structure was prepared as follows. In the beginning, the iron slabs were frozen, and the CG method [237] was deployed to zero residual interatomic forces. Then, an average force was applied on the atoms of the top slab equivalent to a normal pressure of 1 GPa. Note that the bottom slab remained frozen throughout the simulation (both in kMC and MD stages). On the other hand, the upper slab was allowed to perform rigid body displacements. Nevertheless, both slabs were allowed to exert forces on the atoms of TCP molecules through LJ as well as Coulombic interactions. In any case, the upper slab was compressed for 25 ps to achieve a liquid density of TCP of approximately 1.2 ± 0.1 $\frac{g}{cm^3}$ [92]. Then, the normal load was removed, and a velocity of 10 m/s was applied to every atom of the upper slab across the y-direction. A short run of 25 ps was executed to stabilise the system. Both preparatory runs of 25 ps were performed with a timestep of 0.25 fs.

An MD stage of 100 fs was simulated after each kMC stage to capture atomic vibrations and move the upper slab with a velocity of 10 m/s. Once again, a timestep of 0.25 fs was used. The CG algorithm [237] was deployed before and after each MD stage to annihilate any remaining stresses between atoms and prevent instabilities in the hybrid kMC/MD run. The Nosé–Hoover [242, 243] thermostat was utilised with a damping parameter of 25 fs to produce trajectories consistent with the NVT ensemble. Bond-formation as well as bond-breaking templates were inserted in the *predefined table of events* of the KMC stage. Data regarding the type and frequencies of rate-determining reactions were kindly shared by Egheosa Ogbomo (PhD student in the Tribology group of Imperial College). The relevant data are unpublished but originate from the work of Ogbomo et al. [92] on the mechanochemistry of TCP on ferrous surfaces.

Table 6.2: Summary of reaction events used for the PAPRECA study of mechanochemical decomposition of TCP on iron. The rate-determining reactions and their relevant rates correspond to 1 GPa normal pressure and 10 m/s sliding speeds. Data were retrieved using ReaxFF simulations by Egheosa Ogbomo [92] and kindly shared with permission to be included in the current PhD thesis.

Event	Base rate (Hz)	Notes
P-O formation	$1.175\ 10^{11}$	1 per oxygen atom, maximum 4 per phosphorus atom
P=O formation	$1.175\ 10^{11}$	1 per oxygen atom, maximum 4 per phosphorus atom
Fe-O formation	$2.553\ 10^{9}$	1 per oxygen atom
Fe=O formation	$2.553\ 10^{9}$	1 per oxygen atom
Fe-C formation	$1.352\ 10^{9}$	1 per oxygen atom
P-O scission	$7.144\ 10^{10}$	only for $d_{bond} \leq 1.694$ Å
C-O scission	$5.976\ 10^{9}$	only for $d_{bond} \leq 1.485$ Å

A `PAPRECA::PredefinedBondBreak` event was used to capture the scission of the P-O bond of the TCP molecules. A second `PAPRECA::PredefinedBondBreak` was utilised to dissociate the C-O bonds of TCP. P-O, P=O formation events for film species were simulated through `PAPRECA::PredefinedBondForm` templates. Additional `PAPRECA::PredefinedBondForm` templates were introduced to model Fe-O, Fe=O, and Fe-C bond-formation events between substrate Fe atoms and oxygen as well as carbon atoms present between the iron slabs. The types of reaction events and their frequencies as utilised in this hybrid kMC/MD study are given in Table 6.2. The `species_maxbonds` option of PAPRECA was used to prevent atom over-coordination. In particular, the maximum number of bonds for a specific P and O atom was limited to 4 and 2, respectively. Furthermore, the `species_maxbondtypes` option was deployed to restrict surface bonds. Specifically, each C or O species was permitted to form a single bond with surface Fe atoms. Finally, the

`create_ElementalDistributions` command with a bin width of 1 Å was deployed to generate elemental distribution. Simulations were performed for a total of 10000 hybrid kMC/MD steps.

6.3.2 Results and discussion

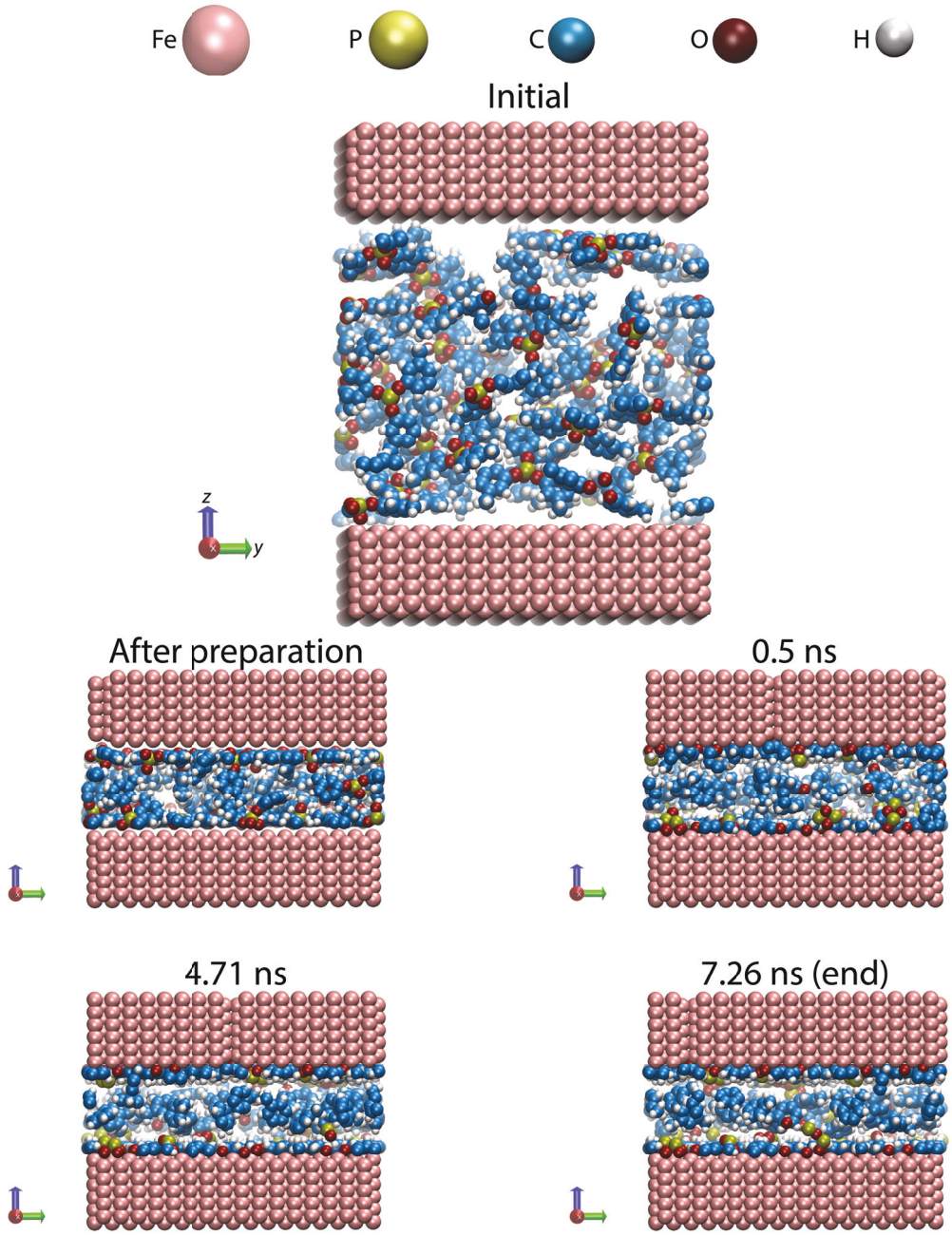


Fig. 6.4: Mechanochemical system snapshots at different stages of the simulation.

Overall, PAPRECA required 40 hours on 32 processors to complete 10000 hybrid kMC/MD steps and reach 7.26 ns. Effectively, the time-advancing efficiency of the system of this section is 1.98 10^{13} CPU s/s or 6.20 10^{11} CPU s/(s processor). Note that the time-advancing efficiency of the hybrid kMC/MD simulations presented in this section is inferior to that of the thermal decomposition model (271.94 CPU sec/sec as discussed in Section 3.3.6). This can be justified by the fact that the time step (Δt) of PAPRECA is inversely proportional to the cumulative event rate (see Eq.

5.7). The predefined events of the mechanochemical simulations (see Table 6.2) feature frequencies of the order of $10^9 - 10^{11}$ Hz. On the other hand, the thermal decompositions simulations included predefined events with rates in the order of 10^3 Hz (TCP adsorption with sticking coefficient of 1 as in Section 3.3.4). Therefore, the Δt corresponding to the mechanochemical system is by orders of magnitude smaller than the Δt of the thermal decomposition setup.

Nevertheless, the PAPRECA simulations exhibit superior time-advancing efficiency than the equivalent ReaxFF runs that demanded 48 hours on 80 processors to reach 1 ns. This accounts for a ReaxFF time-advancing efficiency of 1.73 10^{14} CPU s/(s processor), which is by three orders of magnitude lower than the PAPRECA efficiency of 6.20 10^{11} CPU s/(s processor). This highlights the time-advancing capabilities of PAPRECA even in cases where experimentally relevant timescales cannot be reached due to intrinsic limitations associated with the rates of predefined events.

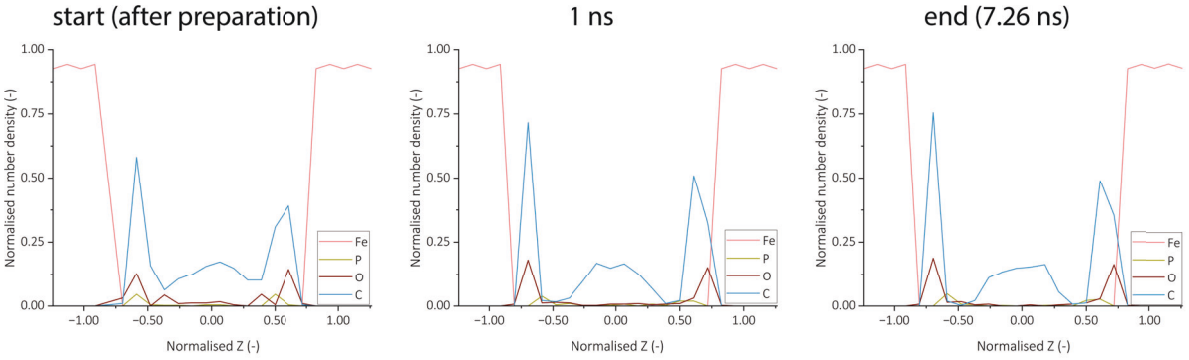


Fig. 6.5: Normalised number densities obtained from hybrid kMC/MD runs and at different stages of the simulation.

System snapshots at various stages of the simulation are given in 6.4. TCP molecules migrate towards the iron surfaces after the preparatory compression and sliding steps. Following, TCP molecules decompose on the frozen substrates through P-O as well as C-O scission events. The film-growth sequence continues with bond-formation events involving carbon and oxygen radicals and surface iron atoms. Then, P-O bonding events are executed to form a P-O-P polyphosphate chain network. Note that iron polyphosphate structures have been reported in relevant studies in the literature and recent MD simulations using the ReaxFF force field [92] (see Section 2.1.1.3). After approximately 4.71 ns the system reaches a state of dynamic equilibrium. Specifically, the system evolves through polymerisation and depolymerisation steps involving P-O bonds that result in the rearrangement of polyphosphate chains. Similar behaviour featuring iron-catalysed polymerisation/depolymerisation steps has been observed in rubbing experiments with phosphate-containing ZDDP additives [58, 59]. At the end of the simulation (7.26 ns), all phosphate chains are attached to the iron substrates with a monolayer of toluene molecules (decomposition products) separating the two surfaces.

The normalised number density for volumetric segments of 2304 Å^3 (i.e., 48x48x1 Å^3) at the start and end of the simulation are presented in Fig. 6.5. The number density at 1 ns is also given in Fig. 6.5 for comparison purposes. Specifically, the elemental composition at 1 ns from our PAPRECA simulations is compared to a normalised kernel density estimation (KDE) graph at 1 ns from the ReaxFF MD study of Ogbomo et al. [92]. Note that the KDE (averaged over 100 ps)

graph for a temperature of 500 K and a normal load of 1 GPa (as in Fig. 6.6) was not originally published in the relevant paper and was kindly shared by Egheosa Ogbomo with permission to be included in this thesis.

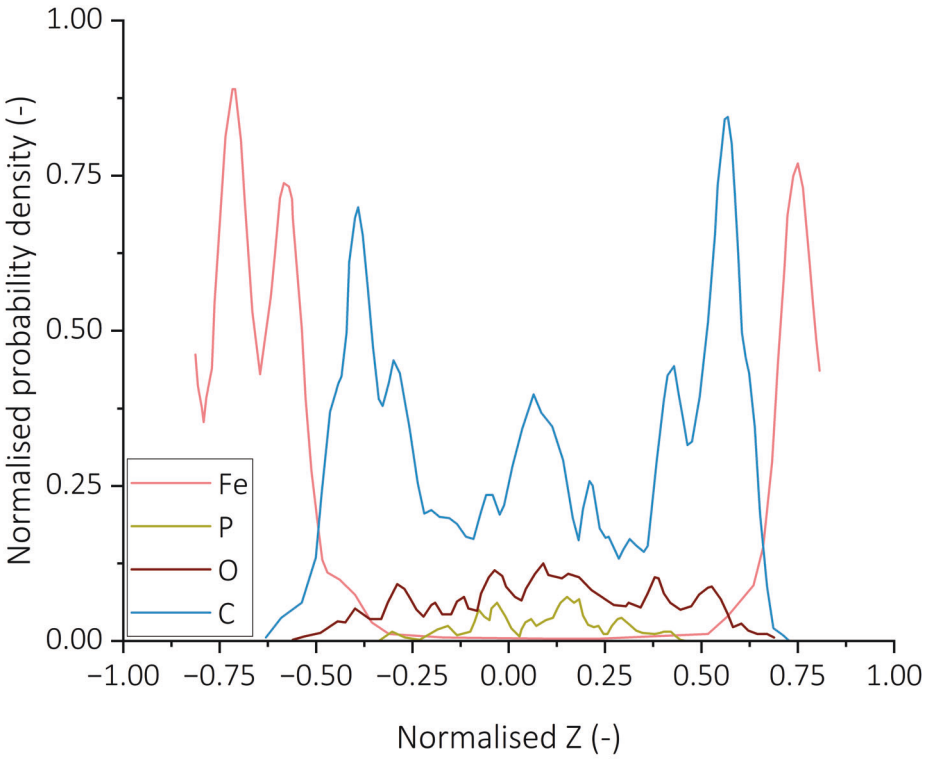


Fig. 6.6: Normalised probability density from ReaxFF simulations on the mechanochemistry of TCP on iron. Data were retrieved using ReaxFF simulations by Egheosa Ogbomo [92] and kindly shared with permission to be included in the current PhD thesis.

In any case, we observe that the structure generated from the hybrid kMC/MD simulations at 1 ns (middle Fig. 6.5) agrees qualitatively with that obtained from the ReaxFF run (Fig. 6.6). The distribution of carbon atoms is similar, with sharp peaks at the TCP/substrate interface. Oxygen and phosphorus atoms appear to be dispersed between the ferrous surfaces at the end of the ReaxFF runs. On the other hand, O and C species are segregated near the iron substrate in the hybrid kMC/MD simulations. Such discrepancies in the elemental distribution of oxygen and carbon atoms can be attributed to the use of different interatomic potentials in the PAPRECA (DREIDING) and MD (ReaxFF) simulations. Furthermore, it has to be acknowledged that the hybrid kMC/MD simulations execute a predefined event (i.e., bond-formation or scission) during each kMC stage. Effectively, this leads to the total decomposition of TCP molecules in the system. This can elevate the mobility and subsequently accelerate the diffusion of carbon as well as oxygen atoms towards the iron surfaces, leading to the observed C and P peaks in the middle image of Fig. 6.5. Finally, we notice a mismatch concerning the distributions of Fe species. This can be explained by recalling that the ferrous substrates are frozen in the PAPRECA simulations, while iron monolayers are mobile (except for the bottom/top ones) in the ReaxFF runs [92].

6.3.3 Conclusions and future work

In this section, we extended the model presented in Sections 3 and 6.2 to study the mechanochemical decomposition of TCP between iron slabs. A system comprising 48 TCP molecules confined between two Fe(110) slabs was used as proof of concept. The confined TCP molecules were pressurised at 1 GPa, and a sliding speed of 10 m/s was imposed on the upper Fe(110) slab. The number density (i.e., structure) calculated from the hybrid kMC/MD at 1 ns is in reasonable agreement with relevant ReaxFF simulations. The PAPRECA simulations additionally replicate a polymerisation/depolymerisation sequence occurring at the late stages of the simulations that has been observed in rubbing experiments involving phosphate esters. In the future, supplementary PAPRECA simulations must be performed with unfrozen substrate atoms to improve the accuracy of predicted hybrid kMC/MD structures.

In contrast to the thermal decomposition model (see sections 3 and 6.2), the setup presented in this section cannot reach experimentally relevant timescales. This is a direct consequence of the scission and bond-formation events of elevated rates ($\approx 10^9 - 10^{11}$ Hz) included in the *predefined table of events* of the kMC stage. In that respect, further simulations at lower scales must be performed to discover slow-rate events. This can result in a *table of predefined events* that realistically describes the crucial elementary atomistic processes. Hence, the hybrid kMC/MD algorithm could be capable of reaching longer timescales via larger Δt increments. In any case, the PAPRECA simulations demonstrate superior time-advancing efficiency than the equivalent ReaxFF runs. This enables reactive simulations on tribological systems beyond the limits of ReaxFF. Such elevated efficiency can be exploited to model bigger systems (featuring more than 48 TCP molecules) to further investigate the polyphosphate linking and rearrangement phenomena.

The merit of PAPRECA can be further demonstrated by accelerating mechanochemical simulations at temperatures and pressures lower than those utilised in ReaxFF MD models. Also, hybrid kMC/MD simulations can be proven valuable when it comes to modelling experimentally relevant sliding speeds. In that respect, a novel predefined event class has to be introduced in PAPRECA to slide substrates within the kMC stage. Moreover, the PAPRECA software can be extended to investigate the dynamic growth of thin films under friction and sliding. This can be done as follows. Firstly, molecule deposition events can be introduced in the kMC stage of mechanochemical hybrid kMC/MD simulations. Secondly, the upper substrate can be removed to create space for adsorbate insertion. Finally, a series of boundary conditions acting on atoms situated at the top of the simulation box can be implemented to guarantee mass as well as energy equilibria and realistically capture sliding, compression, and substrate-fluid interactions. Of course, performing the relevant simulations requires lower-level calculations (e.g., using DFT) to investigate the near-surface charge distributions between film atoms and substrate atoms.

Chapter 7

Summary, conclusions, and future work

Each chapter of this thesis contains specific conclusions and suggestions for further work. In this chapter, we summarise the central thesis conclusions and additionally provide ideas for the development and application of novel hybrid multiscale simulation techniques.

7.1 Summary and key thesis conclusions

In Chapter 2, we explored a few critical systems of the energy sector featuring materials interfaces. Specifically, we discussed SEIs, materials for CO_2 adsorption, and thin films formed from lubricant additives. A variety of relevant computational and experimental studies are present in the literature. Nonetheless, a gap was identified when it comes to structure-property relationships for energy materials. There was also an opportunity to link between atomistic processes (e.g., adsorption/desorption, diffusion, reactions) and key properties such as capacitance for SEIs, CO_2 selectivity for carbon adsorption materials, and film roughness for coatings from lubricant additives. Addressing the aforementioned gaps necessitates multiscale models of atomistic resolution capable of reaching experimentally relevant timescales. Chapter 2 also includes a review on multiscale simulation schemes deployed to extend the timescales, lengthscales, or both spatiotemporal scales beyond the limits of traditional methods of atomistic resolution (e.g., AIMD, DFT). Hybrid kMC/MD simulations appear attractive due to their ability to model timescales ranging from fs up to seconds, minutes, or even hours with a degree of molecular-level resolution. However, to the best of our knowledge, hybrid off-lattice kMC/MD schemes typically focus on reaction events and cannot simulate adsorption, desorption, diffusion, and concerted elementary events.

In Chapter 3, we introduced a novel hybrid off-lattice kMC/MD algorithm capable of capturing not only reactions (bond-formation/bond-breaking) but also molecular adsorption and diffusion hops. The model was benchmarked using a popular system involving materials interfaces in the field of tribology. Specifically, we investigated the thermal decomposition of TCP molecules on an iron substrate over timescales of tens of seconds. The growth rate, surface roughness, elemental composition, and phosphate chain length results were in good agreement with previous experimental and computational studies on thin films from ester-containing lubricant additives. Overall, we concluded that the developed hybrid kMC/MD model is a suitable tool when it comes to providing

long-timescale atomistic insights on coatings generated from the thermal decomposition of TCP on iron.

In Chapter 4, we performed an experimental investigation on the decomposition of TCP on 52100 bearing steel. An in-house experimental setup was developed to grow thin films from lubricant additives in solution. SLIM was deployed for the ex-situ estimation of thin-film thickness at different growth times. This enabled the calculation of representative growth rates. The relevant growth rates were compared with existing data in the literature and our benchmark simulation (performed in Chapter 3), and good agreement was observed. Furthermore, we performed XPS to elucidate the structure of the thin films. We concluded that the surface structure of the protective coatings was rich in carbon-based and iron oxide compounds. A diminished content of phosphates was also identified on the surface of the films.

In Chapter 5, the specialised hybrid kMC/MD scheme was upgraded to a general hybrid kMC/MD simulator. The new software was named PAPRECA and is available on GitHub for license-free use. The decision to freely distribute PAPRECA was inspired by our open-source philosophy and our motivation to democratise multiscale atomistic tools for further use in critical interfaces of interest in the energy sector. PAPRECA uses LAMMPS for the MD stage of hybrid kMC/MD simulations, while a fully parallelised kMC algorithm written in C++ is responsible for the kMC stage. A C++ interface communicates information between the kMC and MD stages. An input file-based user interface facilitates the initialisation and execution of PAPRECA simulations. A variety of predefined elementary events are supported in the kMC stage, such as adsorption, desorption, reactions, and diffusion hops. Overall, the user-friendly and extensible design of PAPRECA encourages further software development and application of the hybrid kMC/MD method to not only thin films from lubricant additives but also other materials interfaces such as SEIs or CO_2 capture devices (see Section 2.1.1). The applicability of PAPRECA beyond the decomposition of TCP on iron was demonstrated through a couple of simple examples (diffusion through a viscous fluid and monolayer growth).

In Chapter 6, we revisited the model for the thermal decomposition of TCP on iron. This time, fully parallelised hybrid kMC/MD simulations with PAPRECA were performed. Initially, we investigated the effects of diffusion hopping distance and concluded that a distance of 7.1 Å enables thin film growth up to approximately 8 nm. Furthermore, we observed that higher temperatures lead to increased final film thickness. Note that this was also evident in our experimental analysis using SLIM (given in Chapter 4). Moreover, we noticed that retaining m-cresol groups after C-O decomposition reactions leads to a near-surface elemental distribution that agrees better with previous studies on thin film growth from ester-containing lubricant additives. The thermal decomposition model was later extended to investigate the mechanochemical decomposition of TCP between sliding iron slabs. To the best of our knowledge, this is the first hybrid kMC/MD investigation of the mechanochemistry of lubricant additives. Using PAPRECA simulations, we illustrated that the hybrid kMC/MD simulator is capable of capturing similar early-stage tribofilm compositions to ReaxFF schemes. Furthermore, the PAPRECA model exhibited superior time-advancing efficiency than equivalent bond-order (e.g., ReaxFF) MD simulations.

7.2 Further work

The fidelity of the hybrid kMC/MD model on the decomposition of TCP on iron has to be improved. Firstly, additional lower-scale simulations (e.g., DFT, AIMD, or ReaxFF) must be performed to acquire more representative event rates for the predefined events. Additional lower-scale simulations will also aid in the direction of a more representative *table of predefined events*, including the rate-determining elementary processes dictating the formation and growth of thin films from TCP. Moreover, an in-depth sensitivity analysis is necessary to investigate the effect of event-specific parameters such as the diffusion hop or deposition distance and the molecular orientation for adsorption events. Furthermore, the hybrid kMC/MD model can be exploited to provide long-timescale atomistic insights on different substrates (e.g., $Fe_3C(010)$ and $Fe_3O_4(001)$ [92]). Later, the decomposition model can be utilised to accelerate the study and subsequent discovery of ashless lubricant additives.

As far as the upgraded model on the mechanochemical decomposition of TCP is concerned, the model must be validated against varying normal load as well as sliding speed conditions. Also, deposition and diffusion events must be included for a more realistic representation of the tribofilm formation. On the other hand, longer hybrid kMC/MD simulations are necessary to shed light on the link between atomistic events and surface morphology descriptors (e.g., RMS roughness or fractal dimension) at experimentally relevant timescales. Once again, the hybrid kMC/MD model can be extended to investigate different substrates, varying surface roughness, and other additives (e.g., ZDDP, TBPP, and TNBP, as discussed in Section 2.1.1.3). Deploying PAPRECA simulations on such additives requires a thorough prior understanding of the relevant rate-determining decomposition mechanisms. Recent advances in ML-based force fields [325], however, promise to enhance the fidelity of MD simulations and significantly accelerate the population of predefined event tables in hybrid kMC/MD frameworks.

Our experimental investigation can be continued with further XPS experiments coupled with ion-sputtering techniques. This will allow us to capture the elemental composition of thermally grown thin films from TCP as a function of thickness and enable further model validation. In-situ experiments can also become beneficial to dynamically monitor the surface structure as well as the thickness of the growing films.

Finally, PAPRECA is an ongoing development project. As such, we aim to maintain it and increase its functionality over time. Added parallelisation will be introduced in future iterations of PAPRECA. Specifically, novel algorithms to achieve concurrent predefined event execution will be designed and implemented. Note that similar event execution schemes are available in SPPARKS [296]. Also, PAPRECA will be further parallelised by exploiting the CUDA and OpenMP interfaces. Furthermore, PAPRECA will benefit from added predefined event functionality. For instance, *event chains* can capture complex groups of predefined events executed sequentially (e.g., reaction chains or adsorption followed by bond-breaking). Introducing functionality for variable event rates will also aid towards a more realistic description of elementary processes. Moreover, sophisticated algorithms to describe long-range molecular overlaps and calculate film thickness need to be implemented in future versions of PAPRECA. The PAPRECA user interface will also transition from input file-based to Python script-based. The aforementioned software improvements will allow PAPRECA simulations to reach longer timescales and investigate different energy

interfaces, such as SEIs, thin films from ashless lubricant additives, and materials for CO_2 capture. We believe that PAPRECA has the potential to become a freely accessible, extendable, and transferable platform to conduct multiscale simulations in critical interfaces of the energy sector.

Bibliography

[1] United Nations. CNet Zero Coalition, 2025. URL https://www.un.org/en/climatechange/net-zero-coalition. [Accessed: 24th Feburary 2025].

[2] Zaera, Francisco. Probing Liquid/Solid Interfaces at the Molecular Level. *Chemical Reviews*, 112:2920–2986, 2012. doi: 10.1021/cr2002068. URL https://pubs.acs.org/doi/10.1021/cr2002068.

[3] Keal, Thomas W. and Elena, Alin Marin and Sokol, Alexey A. and Stoneham, Karen and Probert, Matt I.J. and Cucinotta, Clotilde S. and Willock, David J. and Logsdail, Andrew J. and Zen, Andrea and Hasnip, Phil J. and Bush, Ian J. and Watkins, Matthew and Alfe, Dario and Skylaris, Chris Kriton and Curchod, Basile F.E. and Cai, Qiong and Woodley, Scott M. Materials and Molecular Modeling at the Exascale. *Computing in Science and Engineering*, 24:36–45, 2022. doi: 10.1109/MCSE.2022.3141328. URL https://ieeexplore.ieee.org/document/9674861.

[4] Cresce, Arthur V. and Russell, Selena M. and Baker, David R. and Gaskell, Karen J. and Xu, Kang. In Situ and Quantitative Characterization of Solid Electrolyte Interphases. *Nano Letters*, 14(3):1405–1412, 2014. doi: 10.1021/nl404471v. URL https://doi.org/10.1021/nl404471v.

[5] Goodenough, John B. and Park, Kyu-Sung. The Li-Ion Rechargeable Battery: A Perspective. *Journal of the American Chemical Society*, 135(4):1167–1176, 2013. doi: 10.1021/ja3091438. URL https://doi.org/10.1021/ja3091438.

[6] Xu, Kang. Nonaqueous Liquid Electrolytes for Lithium-Based Rechargeable Batteries. *Chemical Reviews*, 104(10):4303–4418, 2004. doi: 10.1021/cr030203g. URL https://doi.org/10.1021/cr030203g.

[7] Patil, Arun and Patil, Vaishali and Wook Shin, Dong and Choi, Ji-Won and Paik, Dong-Soo and Yoon, Seok-Jin. Issue and challenges facing rechargeable thin film lithium batteries. *Materials Research Bulletin*, 43(8):1913–1942, 2008. ISSN 0025-5408. doi: 10.1016/j.materresbull.2007.08.031. URL https://www.sciencedirect.com/science/article/pii/S0025540807003868.

[8] An, Seong Jin and Li, Jianlin and Daniel, Claus and Mohanty, Debasish and Nagpure, Shrikant and Wood, David L. The state of understanding of the lithium-ion-battery graphite solid electrolyte interphase (SEI) and its relationship to formation cycling. *Carbon*, 105:52–

76, August 2016. doi: 10.1016/j.carbon.2016.04.008. URL https://www.sciencedirect.com/science/article/pii/S0008622316302676.

[9] Winter, Martin. The solid electrolyte interphase – the most important and the least understood solid electrolyte in rechargeable li batteries. *Zeitschrift für Physikalische Chemie*, 223 (10-11):1395–1406, 2009. doi: 10.1524/zpch.2009.6086. URL https://doi.org/10.1524/zpch.2009.6086.

[10] Peled, E. and Golodnitsky, D. and Ardel, G. Advanced Model for Solid Electrolyte Interphase Electrodes in Liquid and Polymer Electrolytes. *Journal of The Electrochemical Society*, 144(8):L208, aug 1997. doi: 10.1149/1.1837858. URL https://dx.doi.org/10.1149/1.1837858.

[11] Aurbach, D. and Markovsky, B. and Levi, M. D. and Levi, E. and Schechter, A. and Moshkovich, M. and Cohen, Y. New insights into the interactions between electrode materials and electrolyte solutions for advanced nonaqueous batteries. *Journal of Power Sources*, 81-82:95–111, 1999. doi: 10.1016/S0378-7753(99)00187-1. URL https://www.sciencedirect.com/science/article/pii/S0378775399001871.

[12] Harris, Stephen J. and Lu, Peng. Effects of Inhomogeneities—Nanoscale to Mesoscale—on the Durability of Li-Ion Batteries. *The Journal of Physical Chemistry C*, 117(13):6481–6492, 2013. doi: 10.1021/jp311431z. URL https://doi.org/10.1021/jp311431z.

[13] Joho, Felix and Rykart, Beat and Blome ,Andreas and Novák, Petr and Wilhelm, Henri and Spahr ,Michael E. Relation between surface properties, pore structure and first-cycle charge loss of graphite as negative electrode in lithium-ion batteries. *Journal of Power Sources*, 97-98:78–82, 2001. doi: 10.1016/S0378-7753(01)00595-X. URL https://www.sciencedirect.com/science/article/pii/S037877530100595X. Proceedings of the 10th International Meeting on Lithium Batteries.

[14] Li,Mengya and Wu,Yang and Zhao,Fei and Wei,Yang and Wang,Jiaping and Jiang,Kaili and Fan,Shoushan. Cycle and rate performance of chemically modified super-aligned carbon nanotube electrodes for lithium ion batteries. *Carbon*, 69:444–451, 2014. ISSN 0008-6223. doi: 10.1016/j.carbon.2013.12.047. URL https://www.sciencedirect.com/science/article/pii/S0008622313012025.

[15] Ping, Ping and Wang, Qingsong and Sun, Jinhua and Feng, Xuyong and Chen, Chunhua. Effect of sulfites on the performance of LiBOB/γ-butyrolactone electrolytes. *Journal of Power Sources*, 196(2):776–783, 2011. ISSN 0378-7753. doi: 10.1016/j.jpowsour.2010.07.064. URL https://www.sciencedirect.com/science/article/pii/S0378775310012875.

[16] Zhang, S. S. and Xu, K. and Jow, T. R. EIS study on the formation of solid electrolyte interface in Li-ion battery. *Electrochimica Acta*, 51(8):1636–1640, 2006. ISSN 0013-4686. doi: 10.1016/j.electacta.2005.02.137. URL https://www.sciencedirect.com/science/article/pii/S0013468605007966. Electrochemical Impedance Spectroscopy.

[17] Cui, Xiaoling and Zhang, Hongming and Li, Shiyou and Li, Xiatong and Feng, Huixia.

Electrochemical performances of a novel lithium bis(oxalate)borate-based electrolyte for lithium-ion batteries with $LiFePO_4$ cathodes. *Ionics*, 20:789–794, 2014. doi: 10.1007/s11581-013-1034-7. URL https://doi.org/10.1007/s11581-013-1034-7.

[18] Tasaki, Ken and Kanda, Katsuya and Kobayashi, Takao and Nakamura, Shinichiro and Ue, Makoto. Theoretical Studies on the Reductive Decompositions of Solvents and Additives for Lithium-Ion Batteries near Lithium Anodes. *Journal of The Electrochemical Society*, 153 (12):A2192, 2006. doi: 10.1149/1.2354460. URL https://dx.doi.org/10.1149/1.2354460.

[19] Bhattacharya, Sandeep and Riahi, A. Reza and Alpas, Ahmet T. Thermal cycling induced capacity enhancement of graphite anodes in lithium-ion cells. *Carbon*, 67:592–606, 2014. doi: 10.1016/j.carbon.2013.10.032. URL https://www.sciencedirect.com/science/article/pii/S0008622313009792.

[20] Soto, Fernando A. and Balbuena, Perla B. Elucidating Oligomer-Surface and Oligomer-Oligomer Interactions at a Lithiated Silicon Surface. *Electrochimica Acta*, 220:312–321, 2016. ISSN 0013-4686. doi: 10.1016/j.electacta.2016.10.082. URL https://www.sciencedirect.com/science/article/pii/S0013468616321697.

[21] Zvereva, Elena and Caliste, Damien and Pochet, Pascal. Interface identification of the solid electrolyte interphase on graphite. *Carbon*, 111:789–795, 2017. doi: 10.1016/j.carbon.2016.10.063. URL https://www.sciencedirect.com/science/article/pii/S0008622316309253.

[22] (Youngman) Chusid and Ein Ely, E. and Aurbach, D. and Babai, M. and Carmeli, Y. Electrochemical and spectroscopic studies of carbon electrodes in lithium battery electrolyte systems. *Journal of Power Sources*, 43(1):47–64, 1993. doi: 10.1016/0378-7753(93)80101-T. URL https://www.sciencedirect.com/science/article/pii/037877539380101T.

[23] Wang, Aiping and Kadam, Sanket and Li, Hong and Shi, Siqi and Qi, Yue. Review on modeling of the anode solid electrolyte interphase (SEI) for lithium-ion batteries. *npj Computational Materials*, 4(15), 2018. doi: 10.1038/s41524-018-0064-0. URL https://doi.org/10.1038/s41524-018-0064-0.

[24] Islam, Md Mahbubul and van Duin, Adri C. T. Reductive Decomposition Reactions of Ethylene Carbonate by Explicit Electron Transfer from Lithium: An eReaxFF Molecular Dynamics Study. *The Journal of Physical Chemistry C*, 120(48):27128–27134, 2016. doi: 10.1021/acs.jpcc.6b08688. URL https://doi.org/10.1021/acs.jpcc.6b08688.

[25] Jorn, Ryan and Kumar, Revati and Abraham, Daniel P. and Voth, Gregory A. Atomistic Modeling of the Electrode–Electrolyte Interface in Li-Ion Energy Storage Systems: Electrolyte Structuring. *The Journal of Physical Chemistry C*, 117(8):3747–3761, 2013. doi: 10.1021/jp3102282. URL https://doi.org/10.1021/jp3102282.

[26] Thompson, Aidan P. and Aktulga, H. Metin and Berger, Richard and Bolintineanu, Dan S. and Brown, W. Michael and Crozier, Paul S. and In 't Veld, Pieter J. and Kohlmeyer, Axel and Moore, Stan G. and Nguyen, Trung Dac and Shan, Ray and Stevens, Mark J. and Tranchida, Julien and Trott, Christian and Plimpton, Steven J. LAMMPS - a flex-

ible simulation tool for particle-based materials modeling at the atomic, meso, and continuum scales. *Computer Physics Communications*, 271:108171, February 2022. doi: 10.1016/j.cpc.2021.108171. URL https://www.sciencedirect.com/science/article/pii/S0010465521002836.

[27] Jacobs, Tevis D. B. and Junge, Till and Pastewka, Lars. Quantitative characterization of surface topography using spectral analysis. *Surface Topography: Metrology and Properties*, 5 (1):013001, January 2017. doi: 10.1088/2051-672X/aa51f8. URL https://dx.doi.org/10.1088/2051-672X/aa51f8.

[28] IPCC. Special Report on Carbon Dioxide Capture and Storage. *Cambridge*, 2005. URL https://www.ipcc.ch/report/carbon-dioxide-capture-and-storage/. [Accessed: 11th March 2025].

[29] D'Alessandro, Deanna M. and Smit, Berend and Long, Jeffrey R. Carbon Dioxide Capture: Prospects for New Materials. *Angewandte Chemie International Edition*, 49(35):6058–6082, 2010. doi: 10.1002/anie.201000431. URL https://onlinelibrary.wiley.com/doi/abs/10.1002/anie.201000431.

[30] Schmitt, Tommy and Leptinsky, Sarah and Turner, Marc and Zoelle, Alexander and White, Charles W. and Hughes, Sydney and Homsy, Sally and Woods, Mark and Hoffman, Hannah and Shultz, Travis and others. Cost and Performance Baseline for Fossil Energy Plants Volume 1: Bituminous Coal and Natural Gas to Electricity. Technical report, National Energy Technology Laboratory (NETL), Pittsburgh, PA, Morgantown, WV, and Albany, OR (United States), 10 2022. URL https://www.osti.gov/biblio/1893822.

[31] Chue, K. T. and Kim, J. N. and Yoo, Y. J. and Cho, S. H. and Yang, R. T. Comparison of Activated Carbon and Zeolite 13X for CO2 Recovery from Flue Gas by Pressure Swing Adsorption. *Industrial & Engineering Chemistry Research*, 34(2):591–598, 1995. doi: 10.1021/ie00041a020. URL https://doi.org/10.1021/ie00041a020.

[32] Choi, Sunho and Drese, Jeffrey H. and Jones, Christopher W. Adsorbent Materials for Carbon Dioxide Capture from Large Anthropogenic Point Sources. *ChemSusChem*, 2(9):796–854, 2009. doi: 10.1002/cssc.200900036. URL https://chemistry-europe.onlinelibrary.wiley.com/doi/abs/10.1002/cssc.200900036.

[33] Tao, Z. and Tian, Y. and Wu, W. and Liu, Zhendong and Fu, Weiqi and Kung, Chung-Kei and Shang, Jin. Development of zeolite adsorbents for CO2 separation in achieving carbon neutrality. *npj Materials Sustainability*, 2(20), 2024. doi: 10.1038/s44296-024-00023-x. URL https://doi.org/10.1038/s44296-024-00023-x.

[34] Mazumder, S. and van Hemert, P. and Busch, A. and Wolf, K-H.A.A. and Tejera-Cuesta, P. Flue gas and pure CO2 sorption properties of coal: A comparative study. *International Journal of Coal Geology*, 67(4):267–279, 2006. ISSN 0166-5162. doi: 10.1016/j.coal.2005.12.001. URL https://www.sciencedirect.com/science/article/pii/S0166516205002090.

[35] Thallapally, Praveen K. and McGrail, B. Peter and Atwood, Jerry L. and Gaeta, Carmine and

Tedesco, Consiglia and Neri, Placido. Carbon Dioxide Capture in a Self-Assembled Organic Nanochannels. *Chemistry of Materials*, 19(14):3355–3357, 2007. doi: 10.1021/cm0709121. URL https://doi.org/10.1021/cm0709121.

[36] Babarao, Ravichandar and Jiang, Jianwen. Molecular Screening of Metal-Organic Frameworks for CO_2 storage. *Langmuir*, 24(12):6270–6278, 2008. doi: 10.1021/la800369s. URL https://doi.org/10.1021/la800369s.

[37] Bae, Youn-Sang and Farha, Omar K. and Hupp, Joseph T. and Snurr, Randall Q. Enhancement of co2/n2 selectivity in a metal-organic framework by cavity modification. *Journal of Materials Chemistry*, 19:2131–2134, 2009. doi: 10.1039/B900390H. URL http://dx.doi.org/10.1039/B900390H.

[38] Millward, Andrew R. and Yaghi, Omar M. Metal-Organic Frameworks with exceptionally high capacity for storage of carbon dioxide at room temperature. *Journal of the American Chemical Society*, 127(51):17998–17999, 2005. doi: 10.1021/ja0570032. URL https://pubs.acs.org/doi/10.1021/ja0570032.

[39] Comotti, Angiolina and Bracco, Silvia and Sozzani, Piero and Horike, Satoshi and Matsuda, Ryotaro and Chen, Jinxi and Takata, Masaki and Kubota, Yoshiki and Kitagawa, Susumu. Nanochannels of Two Distinct Cross-Sections in a Porous Al-Based Coordination Polymer. *Journal of the American Chemical Society*, 130(41):13664–13672, 2008. doi: 10.1021/ja802589u. URL https://doi.org/10.1021/ja802589u.

[40] Li, Xinghua and Wang, Jianjian and Liu, Xin and Liu, Lingmei and Cha, Dongkyu and Zheng, Xinliang and Yousef, Ali A. and Song, Kepeng and Zhu, Yihan and Zhang, Daliang and Han, Yu. Direct Imaging of Tunable Crystal Surface Structures of MOF MIL-101 Using High-Resolution Electron Microscopy. *Journal of the American Chemical Society*, 141(30):12021–12028, 2019. doi: 10.1021/jacs.9b04896. URL https://doi.org/10.1021/jacs.9b04896.

[41] Yazaydın, A. Özgür and Benin, Annabelle I. and Faheem, Syed A. and Jakubczak, Paulina and Low, John J. and Willis, Richard R. and Snurr, Randall Q. Enhanced CO2 Adsorption in Metal-Organic Frameworks via Occupation of Open-Metal Sites by Coordinated Water Molecules. *Chemistry of Materials*, 21(8):1425–1430, 2009. doi: 10.1021/cm900049x. URL https://doi.org/10.1021/cm900049x.

[42] Hicks, Jason C. and Drese, Jeffrey H. and Fauth, Daniel J. and Gray, McMahan L. and Qi, Genggeng and Jones, Christopher W. Designing Adsorbents for CO2 Capture from Flue Gas-Hyperbranched Aminosilicas Capable of Capturing CO2 Reversibly. *Journal of the American Chemical Society*, 130(10):2902–2903, 2008. doi: 10.1021/ja077795v. URL https://doi.org/10.1021/ja077795v.

[43] Lu, Xiaobin and Khonsari, M. M. and Gelinck, E. R. M. The Stribeck Curve: Experimental Results and Theoretical Prediction. *Journal of Tribology*, 128(4):789–794, 04 2006. doi: 10.1115/1.2345406. URL https://doi.org/10.1115/1.2345406.

[44] Spikes, H. A. Boundary Lubrication and Boundary Films. In *Thin Films in Tribology*, volume 25 of *Tribology Series*, pages 331–346. Elsevier, 1993. doi: 10.1016/S0167-8922(08)70389-4. URL https://www.sciencedirect.com/science/article/pii/S0167892208703894.

[45] Spikes, H. A. Mixed lubrication — an overview. *Lubrication Science*, 9(3):221–253, 1997. doi: 10.1002/ls.3010090302. URL https://onlinelibrary.wiley.com/doi/abs/10.1002/ls.3010090302.

[46] Spikes, H. A. and Zhang, Jie. History, Origins and Prediction of Elastohydrodynamic Friction. *Tribology Letters*, 56(1):1–25, 10 2014. doi: 10.1007/s11249-014-0396-y.

[47] Hori, Y. *Friction, Wear, and Lubrication*. Springer Tokyo, 2006. doi: 10.1007/4-431-27901-6_1. URL https://doi.org/10.1007/4-431-27901-6_1.

[48] Hutchings, I. and Shipway, P. *Tribology: Friction and wear of engineering materials: Second Edition*. Butterworth-Heinemann, 2017.

[49] Braun, Jürgen. *Additives*, chapter 6, pages 117–152. John Wiley & Sons, Ltd, 2017. doi: 10.1002/9783527645565.ch6. URL https://onlinelibrary.wiley.com/doi/abs/10.1002/9783527645565.ch6.

[50] Spikes, H. A. The history and mechanism of ZDDP. *Tribology Letters*, 17:469–489, 10 2004. doi: 10.1023/B:TRIL.0000044495.26882.b5. URL https://link.springer.com/article/10.1023/B:TRIL.0000044495.26882.b5.

[51] Fujita, H. and Spikes, H. A. The formation of zinc dithiophosphate antiwear films. *Proceedings of the Institution of Mechanical Engineers, Part J*, 218(4):265–278, 2004. doi: 10.1243/1350650041762677. URL https://doi.org/10.1243/1350650041762677.

[52] Hershberger, J. and Ajayi, O. O. and Fenske, G. R. Zinc content of ZDDP films formed thermally and mechanically. *Tribology International*, 38(3):299–303, 2005. ISSN 0301-679X. doi: 10.1016/j.triboint.2004.08.013. URL https://www.sciencedirect.com/science/article/pii/S0301679X04001707. Boundary Lubrication.

[53] Pauli, M. D. and Rufael, T. S. and Mowlem, J. K. and Weinert, M. and Saldin, D. K. and Tysoe, W. T. X-ray absorption near-edge structure analysis of the chemical environment of zinc in the tribological film formed by zinc dialkyl dithiophosphate decomposition on steel. *Tribology International*, 38(2):195–204, 2005. ISSN 0301-679X. doi: 10.1016/j.triboint.2004.08.007. URL https://www.sciencedirect.com/science/article/pii/S0301679X04001616.

[54] Dorgham, Abdel and Parsaeian, Pourya and Azam, Abdullah and Wang, Chun and Morina, Ardian and Neville, Anne. Single-asperity study of the reaction kinetics of P-based triboreactive films. *Tribology International*, 133:288–296, 2019. ISSN 0301-679X. doi: 10.1016/j.triboint.2018.11.029. URL https://www.sciencedirect.com/science/article/pii/S0301679X18305693.

[55] Zhang, Jie and Ewen, James P. and Ueda, Mao and Wong, Janet S. S. and Spikes, Hugh A. Mechanochemistry of Zinc Dialkyldithiophosphate on Steel Surfaces under Elastohydrodynamic Lubrication Conditions. *ACS Applied Materials & Interfaces*, 12(5):6662–6676, 2020. doi: 10.1021/acsami.9b20059. URL https://doi.org/10.1021/acsami.9b20059.

[56] Fujita, Glovnea, H. R. P. and Spikes, H. A. Study of Zinc Dialkydithiophosphate Antiwear Film Formation and Removal Processes, Part I: Experimental. *Tribology Transactions*, 48 (4):558–566, 2005. doi: 10.1080/05698190500385211. URL https://doi.org/10.1080/05698190500385211.

[57] Dawczyk, Joanna and Ware, Ecaterina and Ardakani, Mahmoud and Russo, Joe and Spikes, Hugh. Use of FIB to Study ZDDP Tribofilms. *Tribology Letters*, 66(155), 11 2018. doi: 10.1007/s11249-018-1114-y. URL https://link.springer.com/article/10.1007/s11249-018-1114-y.

[58] Spikes, H. A. Mechanisms of ZDDP—An Update. *Tribology Letters*, 73(38), 02 2025. doi: 10.1007/s11249-025-01968-3. URL https://link.springer.com/article/10.1007/s11249-025-01968-3.

[59] Heuberger, Roman and Rossi, Antonella and Spencer, Nicholas D. XPS study of the influence of temperature on ZnDTP tribofilm composition. *Tribology Letters*, 25(3):185–196, March 2007. doi: 10.1007/s11249-006-9166-9. URL https://doi.org/10.1007/s11249-006-9166-9.

[60] Mosey, Nicholas J. and Müser, Martin H. and Woo, Tom K. Molecular Mechanisms for the Functionality of Lubricant Additives. *Science*, 307(5715):1612–1615, 2005. doi: 10.1126/science.1107895. URL https://www.science.org/doi/abs/10.1126/science.1107895.

[61] Peeters, Stefan and Barlini, Alberto and Jain, Jayant and Gosvami, Nitya and Righi, M. Clelia. Adsorption and decomposition of ZDDP on lightweight metallic substrates: Ab initio and experimental insights. *Applied Surface Science*, 600:153947, 06 2022. doi: 10.1016/j.apsusc.2022.153947. URL https://www.sciencedirect.com/science/article/pii/S0169433222014908.

[62] Benini, Francesca and Restuccia, Paolo and Righi, M. Clelia. Zinc dialkyldithiophosphates adsorption and dissociation on ferrous substrates: An ab initio study. *Applied Surface Science*, 642:158419, 2024. ISSN 0169-4332. doi: 10.1016/j.apsusc.2023.158419. URL https://www.sciencedirect.com/science/article/pii/S0169433223020998.

[63] Bodek, Kristian M. and Wong, Victor V. The Effects of Sulfated Ash, Phosphorus and Sulfur on Diesel Aftertreatment Systems - A Review. In *JSAE/SAE International Fuels & Lubricants Meeting*. SAE International, 2007. doi: 10.4271/2007-01-1922. URL https://doi.org/10.4271/2007-01-1922.

[64] Spikes, Hugh. Low- and zero-sulphated ash, phosphorus and sulphur anti-wear additives for engine oils. *Lubrication Science*, 20(2):103–136, 2008. doi: 10.1002/ls.57. URL https://onlinelibrary.wiley.com/doi/abs/10.1002/ls.57.

[65] Johnson, David W. and Hils, John E. Phosphate Esters, Thiophosphate Esters and Metal Thiophosphates as Lubricant Additives. *Lubricants*, 1(4):132–148, 2013. doi: 10.3390/lubricants1020048. URL https://www.mdpi.com/2075-4442/1/4/132.

[66] Devlin, Mark T. and Guevremont, Jeffrey and Sheets, Roger and Loper, John and Guinther, Greg and Thompson, Karen and Jao, Tze-Chi. Effect of metal-free phosphorus anti-wear compounds on passenger car emissions and fuel economy. *Lubrication Science*, 20(2):151–161, 2008. doi: 10.1002/ls.44. URL https://onlinelibrary.wiley.com/doi/abs/10.1002/ls.44.

[67] Johnson, David W. and Morrow, Samantha and Forster, Nelson H. and Saba, Costandy S. Vapor-Phase Lubrication: Reaction of Phosphate Ester Vapors with Iron and Steel. *Chemistry of Materials*, 14(9):3767–3775, September 2002. doi: 10.1021/cm010921o. URL https://doi.org/10.1021/cm010921o.

[68] Hageman, G. and Mackenzie Ross, S. J. and Nihom, J. and van der Laan, G. Aerotoxic syndrome: A new occupational disease caused by contaminated cabin air? In *Advances in Neurotoxicology*, volume 7, pages 77–132. Academic Press, Cambridge, MA, USA, January 2022. doi: 10.1016/bs.ant.2022.04.001. URL https://www.sciencedirect.com/science/article/abs/pii/S2468748022000017.

[69] Guan, Bihan and Pochopien, Bernadeta A. and Wright, Dominic S. The chemistry, mechanism and function of tricresyl phosphate (TCP) as an anti-wear lubricant additive. *Lubrication Science*, 28(5):257–265, August 2016. doi: 10.1002/ls.1327. URL https://doi.org/10.1002/ls.1327.

[70] Graham, E. E. and Klaus, E. E. Lubrication from the Vapor Phase at High Temperatures. *A S L E Transactions*, 29(2):229–234, January 1986. doi: 10.1080/05698198608981682. URL https://www.tandfonline.com/doi/abs/10.1080/05698198608981682.

[71] Sung, Dougyong and Kim, Donggun and Gellman, Andrew J. The surface chemistry of vapor phase lubricants: tricresylphosphate on Ni(1 0 0). *Tribology International*, 38(2):151–157, February 2005. doi: 10.1016/j.triboint.2004.07.023. URL https://www.sciencedirect.com/science/article/pii/S0301679X04001537.

[72] Van Treuren, K. W. and Barlow, D. N. and Heiser, W. H. and Wagner, M. J. and Forster, N. H. Investigation of Vapor-Phase Lubrication in a Gas Turbine Engine. *Journal of Engineering for Gas Turbines Power*, 120(2):257–262, April 1998. doi: 10.1115/1.2818113. URL https://doi.org/10.1115/1.2818113.

[73] Wagner, M. J. and Forster, N. H. Vapor phase lubrication for expendable gas turbine engines. *Journal of Engineering for Gas Turbines Power*, 122(2):185–190, 2023. doi: 10.1115/99-GT-028. URL https://asmedigitalcollection.asme.org/GT/proceedings/GT1999/78583/V001T01A002/248044.

[74] Godfrey, Douglas. The Lubrication Mechanism of Tricresyl Phosphate on Steel. *A S L E Transactions*, 8(1):1–11, 1965. doi: 10.1080/05698196508972073. URL https://doi.org/

10.1080/05698196508972073.

[75] Bieber, H. E. and Klaus, E. E. and Tewksbury, E. J. A Study of Tricresyl Phosphate as an Additive for Boundary Lubrication. *A S L E Transactions*, 11(2):155–161, 1968. doi: 10.1080/05698196808972218. URL https://doi.org/10.1080/05698196808972218.

[76] Gauthier, A. and Montes, H. and Georges, J. M. Boundary Lubrication with Tricresylphosphate (TCP). Importance of Corrosive Wear. *A S L E Transactions*, 25(4):445–455, 1982. doi: 10.1080/05698198208983112. URL https://doi.org/10.1080/05698198208983112.

[77] Saba, C. S. and Forster, N. H. Reactions of Aromatic Phosphate Esters with Metals and Their Oxides. *Tribology Letters*, 12(2):135–146, February 2002. doi: 10.1023/A:1014081523491. URL https://link.springer.com/article/10.1023/A:1014081523491.

[78] Sung, D. and Gellman, A. J. The surface chemistry of alkyl and arylphosphate vapor phase lubricants on Fe foil. *Tribology International*, 35(9):579–590, September 2002. doi: 10.1016/S0301-679X(02)00045-2. URL https://www.sciencedirect.com/science/article/pii/S0301679X02000452.

[79] Pavelko, G. F. The mechanism of iron phosphide formation during boundary friction in the presence of organic phosphates and phosphites. *Journal of Friction and Wear*, 33(2):115–123, April 2012. doi: 10.3103/S1068366612020092. URL https://doi.org/10.3103/S1068366612020092.

[80] Goldblatt, I. L. and Appeldoorn, J. K. The Antiwear Behavior of TCP in Different Atmospheres and Different Base Stocks. *A S L E Transactions*, 13(3):203–214, 1970. doi: 10.1080/05698197008972296. URL https://doi.org/10.1080/05698197008972296.

[81] Klaus, E. E. and Phillips, J. and Lin, S. C. and Wu, N. L. and Duda, J. L. Structure of Films Formed During the Deposition of Lubrication Molecules on Iron and Silicon Carbide. *Tribology Transactions*, 33(1):25–32, January 1990. doi: 10.1080/10402009008981926. URL https://www.tandfonline.com/doi/abs/10.1080/10402009008981926.

[82] Metla, Sai Bhavani Sravan and Rouhani, Mehdir and Hobley, Jonathan and Ou, Hsin-Hung and Jeng, Yeau-Ren. The reaction of the oil additive tricresylphosphate on steel: The solution to an enduring 100-year-old mystery. *Applied Materials Today*, 39:102324, 2024. ISSN 2352-9407. doi: 10.1016/j.apmt.2024.102324. URL https://www.sciencedirect.com/science/article/pii/S2352940724002695.

[83] Forster, Nelson H. Rolling Contact Testing of Vapor Phase Lubricants-Part III: Surface Analysis. *Tribology Transactions*, 42(1):1–9, January 1999. doi: 10.1080/10402009908982183. URL https://www.tandfonline.com/doi/abs/10.1080/10402009908982183.

[84] Sasaki, Keiji and Inayoshi, Naruhiko and Tashiro, Kohji. Friction-induced dynamic chemical changes of tricresyl phosphate as lubricant additive observed under boundary lubrication with 2D fast imaging FTIR-ATR spectrometer. *Wear*, 268(7):911–916, March 2010. doi: 10.1016/j.wear.2009.12.017. URL https://www.sciencedirect.com/science/article/pii/

S0043164809006395.

[85] Wheeler, Donald R. and Faut, Owen D. The adsorption and thermal decomposition of tricresylphosphate (TCP) on iron and gold. *Applied Surface Science*, 18(1):106–122, May 1984. doi: 10.1016/0378-5963(84)90040-0. URL https://www.sciencedirect.com/science/article/pii/0378596384900400.

[86] Shaeffer, S. K. High temperature reaction of aryl phosphate esters on an iron film. *Tribology Transactions*, 46:332–338, 2003. doi: 10.1080/10402000308982634. URL https://www.tandfonline.com/doi/abs/10.1080/10402000308982634.

[87] Arezzo, Franco. Oil-Aging Mechanism on 52100 Steel with Hydrocarbon Oils Containing Tricresyl Phosphate (TCP). *ASLE Transactions*, 28(2):203–212, January 1985. doi: 10.1080/05698198508981612. URL https://www.tandfonline.com/doi/abs/10.1080/05698198508981612.

[88] Arezzo, Franco and Moore, Richard L. Reactions between 52100 steel and tricresyl phosphate neat and mixed with hydrocarbon oil. *Surface Coatings Technoly*, 33:235–242, December 1987. doi: 10.1016/0257-8972(87)90191-5. URL https://www.sciencedirect.com/science/article/pii/0257897287901915.

[89] Acharya, B. and Pardue, T. N. and Avva, K. S. and Krim, J. In situ, real time studies of thermal reaction film formation temperatures for iron and 304SS surfaces immersed in 5% tricresyl phosphate in base oil. *Tribology International*, 126:106–115, October 2018. doi: 10.1016/j.triboint.2018.04.034. URL https://www.sciencedirect.com/science/article/pii/S0301679X18302275.

[90] Osei-Agyemang, Eric and Berkebile, Stephen and Martini, Ashlie. Decomposition Mechanisms of Anti-wear Lubricant Additive Tricresyl Phosphate on Iron Surfaces Using DFT and Atomistic Thermodynamic Studies. *Tribology Letters*, 66(1):48–22, February 2018. doi: 10.1007/s11249-018-0998-x. URL https://doi.org/10.1007/s11249-018-0998-x.

[91] Khajeh, Arash and Bhuiyan, Fakhrul Hasan and Mogonye, Jon-Erik and Pesce-Rodriguez, Rose A. and Berkebile, Stephen and Martini, Ashlie. Thermal Decomposition of Tricresyl Phosphate on Ferrous Surfaces. *Journal of Physical Chemistry C*, 125(9):5076–5087, March 2021. doi: 10.1021/acs.jpcc.0c10789. URL https://doi.org/10.1021/acs.jpcc.0c10789.

[92] Ogbomo, Egheosa and Bhuiyan, Fakhrul H. and Latorre, Carlos Ayestarán and Martini, Ashlie and Ewen, James P. Effects of surface chemistry on the mechanochemical decomposition of tricresyl phosphate. *Physical Chemistry Chemical Physics*, 26(1):278–292, 2024. doi: 10.1039/D3CP05320B. URL https://pubs.rsc.org/en/content/articlehtml/2023/cp/d3cp05320b.

[93] Oulego, P. and Blanco, D. and Ramos, D. and Viesca, J. L. and Díaz, M. and Hernández Battez, A. Environmental properties of phosphonium, imidazolium and ammonium cation-based ionic liquids as potential lubricant additives. *Journal of Molecular Liquids*, 272:937–947, 2018. ISSN 0167-7322. doi: 10.1016/j.molliq.2018.10.106. URL https://www.

sciencedirect.com/science/article/pii/S0167732218345501.

[94] Peguiron, Anke and Moras, Gianpietro and Walter, Michael and Uetsuka, Hiroshi and Pastewka, Lars and Moseler, Michael. Activation and mechanochemical breaking of C–C bonds initiate wear of diamond (110) surfaces in contact with silica. *Carbon*, 98:474–483, 2016. ISSN 0008-6223. doi: 10.1016/j.carbon.2015.10.098. URL https://www.sciencedirect.com/science/article/pii/S0008622315304115.

[95] Deng, Jie and Morgan, Dane and Szlufarska, Izabela. Kinetic Monte Carlo simulation of the effective diffusivity in grain boundary networks. *Computational Materials Science*, 93:36–45, 2014. ISSN 0927-0256. doi: 10.1016/j.commatsci.2014.06.028. URL https://www.sciencedirect.com/science/article/pii/S092702561400439X.

[96] Jalali, Mohammad Hadi and Ghayour, Mostafa and Ziaei-Rad, Saeed and Shahriari, Behrooz. Dynamic analysis of a high speed rotor-bearing system. *Measurement*, 53:1–9, 2014. ISSN 0263-2241. doi: 10.1016/j.measurement.2014.03.010. URL https://www.sciencedirect.com/science/article/pii/S0263224114001043.

[97] Phlipot, Gregory P. and Kochmann, Dennis M. A quasicontinuum theory for the nonlinear mechanical response of general periodic truss lattices. *Journal of the Mechanics and Physics of Solids*, 124:758–780, 2019. doi: 10.1016/j.jmps.2018.11.014. URL https://www.sciencedirect.com/science/article/pii/S0022509618304071.

[98] Abbott, Joseph W. and Hanke, Felix. Kinetically Corrected Monte Carlo–Molecular Dynamics Simulations of Solid Electrolyte Interphase Growth. *Journal of Chemical Theory and Computation*, 18(2):925–934, February 2022. doi: 10.1021/acs.jctc.1c00921. URL https://doi.org/10.1021/acs.jctc.1c00921.

[99] Chacón, Enrique and Bresme, Fernando and Tarazona, Pedro. Elasticity of bilayer lipid membranes from their density correlation function. *Molecular Physics*, 122(21-22):e2346262, 2024. doi: 10.1080/00268976.2024.2346262. URL https://doi.org/10.1080/00268976.2024.2346262.

[100] Trageser, Jeremy E. and Mitchell, John A. and Johnson, Kyle L. and Rodgers, Theron M. A Bézier curve fit to melt pool geometry for modeling additive manufacturing microstructures. *Computer Methods in Applied Mechanics and Engineering*, 415:116208, 2023. ISSN 0045-7825. doi: 10.1016/j.cma.2023.116208. URL https://www.sciencedirect.com/science/article/pii/S0045782523003328.

[101] Wiriyasart, S. and Hommalee, C. and Sirikasemsuk, S. and Prurapark, R. and Naphon, P. Thermal management system with nanofluids for electric vehicle battery cooling modules. *Case Studies in Thermal Engineering*, 18:100583, 2020. ISSN 2214-157X. doi: 10.1016/j.csite.2020.100583. URL https://www.sciencedirect.com/science/article/pii/S2214157X19304836.

[102] Weiand, Erik and Rodriguez-Ropero, Francisco and Roiter, Yuri and Koenig, Peter H. and Angioletti-Uberti, Stefano and Dini, Daniele and Ewen, James P. Effects of surfac-

tant adsorption on the wettability and friction of biomimetic surfaces. *Physical Chemistry Chemical Physics*, 25:21916–21934, 2023. doi: 10.1039/D3CP02546B. URL http://dx.doi.org/10.1039/D3CP02546B.

[103] O'Malley, Alexander J. and Logsdail, A. J. and Sokol, A. A. and Catlow, C. R. A. Modelling metal centres, acid sites and reaction mechanisms in microporous catalysts. *Faraday Discussions*, 188:235–255, 2016. doi: 10.1039/C6FD00010J. URL http://dx.doi.org/10.1039/C6FD00010J.

[104] Reuter, Karsten and Scheffler, Matthias. First-Principles Atomistic Thermodynamics for Oxidation Catalysis: Surface Phase Diagrams and Catalytically Interesting Regions. *Physical Review Letters*, 90:046103, Jan 2003. doi: 10.1103/PhysRevLett.90.046103. URL https://link.aps.org/doi/10.1103/PhysRevLett.90.046103.

[105] Xuerong Zhang, James Pugh, and Philip Ross. Computation of Thermodynamic Oxidation Potentials of Organic Solvents Using Density Functional Theory. *Journal of The Electrochemical Society*, 148:E183–E188, 05 2001. doi: 10.1149/1.1362546. URL https://iopscience.iop.org/article/10.1149/1.1362546.

[106] Li, Tao and Balbuena, Perla B. Theoretical studies of the reduction of ethylene carbonate. *Chemical Physics Letters*, 317(3):421–429, 2000. ISSN 0009-2614. doi: 10.1016/S0009-2614(99)01374-3. URL https://www.sciencedirect.com/science/article/pii/S0009261499013743.

[107] Dzubak, Allison L. and Lin, Li-Chiang and Kim, Jihan and Swisher, Joseph A. and Poloni, Roberta and Maximoff, Sergey N. and Smit, Berend and Gagliardi, Laura. Ab initio carbon capture in open-site metal-organic frameworks. *Nature Chemistry*, 4(10):810–816, Oct 2012. doi: 10.1038/nchem.1432. URL https://doi.org/10.1038/nchem.1432.

[108] Tuckerman, Mark E. Ab initio molecular dynamics: basic concepts, current trends and novel applications. *Journal of Physics: Condensed Matter*, 14:R1297 – R1355, 2002. URL https://api.semanticscholar.org/CorpusID:118340535.

[109] Schwegler, Eric and Galli, Giulia and Gygi, François and Hood, Randolph Q. Dissociation of Water under Pressure. *Physical Review Letters*, 87:265501, Dec 2001. doi: 10.1103/PhysRevLett.87.265501. URL https://link.aps.org/doi/10.1103/PhysRevLett.87.265501.

[110] Diraison, M. and Martyna, G. J. and Tuckerman, M. E. Simulation studies of liquid ammonia by classical ab initio, classical, and path-integral molecular dynamics. *The Journal of Chemical Physics*, 111(3):1096–1103, 07 1999. doi: 10.1063/1.479194. URL https://doi.org/10.1063/1.479194.

[111] Hoang, Vo and Nguyen, Ngoclinh and Hung, N. Structure and dynamics of liquid and amorphous Al2O3.2SiO2. *The European Physical Journal Applied Physics*, 37:111 – 118, 01 2007. doi: 10.1051/epjap:2006137. URL https://www.epjap.org/articles/epjap/abs/2007/01/ap06122/ap06122.html.

[112] Saitta, A. Marco and Soper, Paul D. and Wasserman, E. and Klein, Michael L. Influence of a knot on the strength of a polymer strand. *Nature*, 399(6731):46–48, May 1999. doi: 10.1038/19935. URL https://doi.org/10.1038/19935.

[113] Piana, Stefano and Sebastiani, Daniel and Carloni, Paolo and Parrinello, Michele. Ab Initio Molecular Dynamics-Based Assignment of the Protonation State of Pepstatin A/HIV-1 Protease Cleavage Site. *Journal of the American Chemical Society*, 123(36):8730–8737, 2001. doi: 10.1021/ja003145e. URL https://doi.org/10.1021/ja003145e.

[114] Tuckerman, M. and Laasonen, K. and Sprik, M. and Parrinello, M. Ab initio molecular dynamics simulation of the solvation and transport of hydronium and hydroxyl ions in water. *The Journal of Chemical Physics*, 103(1):150–161, 07 1995. doi: 10.1063/1.469654. URL https://doi.org/10.1063/1.469654.

[115] Duan, Yong and Kollman, Peter A. Pathways to a Protein Folding Intermediate Observed in a 1-Microsecond Simulation in Aqueous Solution. *Science*, 282(5389):740–744, 1998. doi: 10.1126/science.282.5389.740. URL https://www.science.org/doi/abs/10.1126/science.282.5389.740.

[116] Marrink, S. J. and Mark, A. E. Effect of Undulations on Surface Tension in Simulated Bilayers. *The Journal of Physical Chemistry B*, 105(26):6122–6127, 2001. doi: 10.1021/jp0103474. URL https://doi.org/10.1021/jp0103474.

[117] Li, Zongyi and Saurabh, Suman and Hollowell, Peter and Kalonia, Cavan K. and Waigh, Thomas A. and Li, Peixun and Webster, John R. P. and Seddon, John M. and Bresme, Fernando and Lu, Jian Ren. pH-Dependent Conformational Plasticity of Monoclonal Antibodies at the SiO2/Water Interface: Insights from Neutron Reflectivity and Molecular Dynamics. *ACS Applied Materials & Interfaces*, 16(51):70231–70241, 2024. doi: 10.1021/acsami.4c14407. URL https://doi.org/10.1021/acsami.4c14407.

[118] Carman, Fionn and Ewen, James P. and Bresme, Fernando and Wu, Billy and Dini, Daniele. Molecular Simulations of Thermal Transport across Iron Oxide–Hydrocarbon Interfaces. *ACS Applied Materials & Interfaces*, 16(43):59452–59467, 2024. doi: 10.1021/acsami.4c09434. URL https://doi.org/10.1021/acsami.4c09434.

[119] Mees, Jan and O'Connor, Thomas C. and Pastewka, Lars. Entropic stress of grafted polymer chains in shear flow. *The Journal of Chemical Physics*, 159(9):094902, 09 2023. doi: 10.1063/5.0158245. URL https://doi.org/10.1063/5.0158245.

[120] Ewen, James P. and Latorre, Carlos Ayestarán and Gattinoni, Chiara and Khajeh, Arash and Moore, Joshua D. and Remias, Joseph E. and Martini, Ashlie and Dini, Daniele. Substituent Effects on the Thermal Decomposition of Phosphate Esters on Ferrous Surfaces. *Journal of Physical Chemistry C*, 124(18):9852–9865, May 2020. doi: 10.1021/acs.jpcc.9b11787. URL https://doi.org/10.1021/acs.jpcc.9b11787.

[121] Khajeh, Arash and Hu, Xiaoli and Mohammadtabar, Karen and Shin, Yun Kyung and van Duin, Adri C. T. and Berkebile, Stephen and Martini, Ashlie. Statistical Analysis

of Tri-Cresyl Phosphate Conversion on an Iron Oxide Surface Using Reactive Molecular Dynamics Simulations. *Journal of Physical Chemistry C*, 123(20):12886–12893, May 2019. doi: 10.1021/acs.jpcc.9b02394. URL https://doi.org/10.1021/acs.jpcc.9b02394.

[122] Cahn, John W. and Hilliard, John E. Free Energy of a Nonuniform System. I. Interfacial Free Energy. *The Journal of Chemical Physics*, 28(2):258–267, 02 1958. doi: 10.1063/1.1744102. URL https://doi.org/10.1063/1.1744102.

[123] Allen, Samuel M. and Cahn, John W. A microscopic theory for antiphase boundary motion and its application to antiphase domain coarsening. *Acta Metallurgica*, 27(6): 1085–1095, 1979. ISSN 0001-6160. doi: 10.1016/0001-6160(79)90196-2. URL https://www.sciencedirect.com/science/article/pii/0001616079901962.

[124] Chen, Long-Qing. Phase-Field Models for Microstructure Evolution. *Annual Review of Materials Research*, 32:113–140, 2002. doi: 10.1146/annurev.matsci.32.112001.132041. URL https://www.annualreviews.org/content/journals/10.1146/annurev.matsci.32.112001.132041.

[125] Wheeler, A. A. and Boettinger, W. J. and McFadden, G. B. Phase-field model for isothermal phase transitions in binary alloys. *Physical Review A*, 45:7424–7439, May 1992. doi: 10.1103/PhysRevA.45.7424. URL https://link.aps.org/doi/10.1103/PhysRevA.45.7424.

[126] Galenko, Peter and Lebedev, Vladimir. Non-equilibrium effects in spinodal decomposition of a binary system. *Physics Letters A*, 372(7):985–989, 2008. ISSN 0375-9601. doi: 10.1016/j.physleta.2007.08.070. URL https://www.sciencedirect.com/science/article/pii/S0375960107012601.

[127] Wang, Y. and Khachaturyan, A. G. Three-dimensional field model and computer modeling of martensitic transformations. *Acta Materialia*, 45(2):759–773, 1997. ISSN 1359-6454. doi: 10.1016/S1359-6454(96)00180-2. URL https://www.sciencedirect.com/science/article/pii/S1359645496001802.

[128] Li, Y. L. and Hu, S. Y. and Liu, Z. K. and Chen, L. Q. Phase-field model of domain structures in ferroelectric thin films. *Applied Physics Letters*, 78(24):3878–3880, 06 2001. ISSN 0003-6951. doi: 10.1063/1.1377855. URL https://doi.org/10.1063/1.1377855.

[129] Kazaryan, A. and Wang, Y. and Dregia, S. A. and Patton, Bruce R. Generalized phase-field model for computer simulation of grain growth in anisotropic systems. *Physical Review B*, 61: 14275–14278, Jun 2000. doi: 10.1103/PhysRevB.61.14275. URL https://link.aps.org/doi/10.1103/PhysRevB.61.14275.

[130] Kazaryan, A. and Wang, Y. and Dregia, S. A. and Patton, Bruce R. Grain growth in systems with anisotropic boundary mobility: Analytical model and computer simulation. *Physical Review B*, 63:184102, Apr 2001. doi: 10.1103/PhysRevB.63.184102. URL https://link.aps.org/doi/10.1103/PhysRevB.63.184102.

[131] Aranson, I. S. and Kalatsky, V. A. and Vinokur, V. M. Continuum Field Description of Crack

Propagation. *Physical Review Letters*, 85:118–121, Jul 2000. doi: 10.1103/PhysRevLett.85.118. URL https://link.aps.org/doi/10.1103/PhysRevLett.85.118.

[132] Karma, Alain and Kessler, David A. and Levine, Herbert. Phase-Field Model of Mode III Dynamic Fracture. *Physical Review Letters*, 87:045501, Jul 2001. doi: 10.1103/PhysRevLett.87.045501. URL https://link.aps.org/doi/10.1103/PhysRevLett.87.045501.

[133] Levitas, Valery I. and Javanbakht, Mahdi. Advanced phase-field approach to dislocation evolution. *Physical Review B*, 86:140101, Oct 2012. doi: 10.1103/PhysRevB.86.140101. URL https://link.aps.org/doi/10.1103/PhysRevB.86.140101.

[134] Landau, David P. and Binder, Kurt. *A Guide to Monte Carlo Simulations in Statistical Physics*. Cambridge University Press, Cambridge, England, UK, November 2014. ISBN 978-1-10707402-6. URL https://assets.cambridge.org/97811084/90146/frontmatter/9781108490146_frontmatter.pdf.

[135] Battaile, C. C. and Srolovitz, D. J. and Butler, J. E. A kinetic Monte Carlo method for the atomic-scale simulation of chemical vapor deposition: Application to diamond. *Journal of Applied Physics*, 82(12):6293–6300, December 1997. doi: 10.1063/1.366532. URL https://pubs.aip.org/aip/jap/article-abstract/82/12/6293/490064/.

[136] Cheimarios, Nikolaos and To, Deifilia and Kokkoris, George and Memos, George and Boudouvis, Andreas G. Monte Carlo and Kinetic Monte Carlo Models for Deposition Processes: A Review of Recent Works. *Frontiers in Physics*, 9:631918, 2021. doi: 10.3389/fphy.2021.631918. URL https://www.frontiersin.org/articles/10.3389/fphy.2021.631918.

[137] Stamatakis, Michail and Vlachos, Dionisios G. Unraveling the Complexity of Catalytic Reactions via Kinetic Monte Carlo Simulation: Current Status and Frontiers. *ACS Catalysis*, 2(12):2648–2663, December 2012. doi: 10.1021/cs3005709. URL https://doi.org/10.1021/cs3005709.

[138] Stamatakis, Michail and Piccinin, Simone. Rationalizing the Relation between Adlayer Structure and Observed Kinetics in Catalysis. *ACS Catalysis*, 6(3):2105–2111, 2016. doi: 10.1021/acscatal.5b02876. URL https://doi.org/10.1021/acscatal.5b02876.

[139] Pineda, M. and Stamatakis, M. Kinetic Monte Carlo simulations for heterogeneous catalysis: Fundamentals, current status, and challenges. *Journal of Chemical Physics*, 156:120902, 3 2022. doi: 10.1063/5.0083251. URL https://aip.scitation.org/doi/10.1063/5.0083251.

[140] Turner, C. Heath and Lei, Yu and Bao, Yuping. Modeling the atomistic growth behavior of gold nanoparticles in solution. *Nanoscale*, 8(17):9354–9365, April 2016. doi: 10.1039/C6NR01881E. URL http://dx.doi.org/10.1039/C6NR01881E.

[141] Cuppen, H. M. and Karssemeijer, L. J. and Lamberts, T. The kinetic Monte Carlo method as a way to solve the master equation for interstellar grain chemistry. *Chemicals Reviews*, 113:8840–8871, 2013. doi: 10.1021/cr400234a. URL https://pubs.acs.org/doi/10.1021/

cr400234a.

[142] Zienkiewicz, O. C. Achievements and some unsolved problems of the finite element method. *International Journal for Numerical Methods in Engineering*, 47(1-3):9–28, 2000. URL https://onlinelibrary.wiley.com/doi/abs/10.1002/%28SICI%291097-0207%2820000110/30%2947%3A1/3%3C9%3A%3AAID-NME793%3E3.0.CO%3B2-P.

[143] Zienkiewicz, O. C. and Taylor, R. L. and Zhu, J. Z. *The Finite Element Method: Its Basis and Fundamentals*. Butterworth-Heinemann, Oxford, seventh edition, 2013. ISBN 978-1-85617-633-0. doi: 10.1016/B978-1-85617-633-0.00019-8. URL https://www.sciencedirect.com/science/article/pii/B9781856176330000198.

[144] Bower, A. F. and Guduru, P. R. A simple finite element model of diffusion, finite deformation, plasticity and fracture in lithium ion insertion electrode materials. *Modelling and Simulation in Materials Science and Engineering*, 20(4):045004, apr 2012. doi: 10.1088/0965-0393/20/4/045004. URL https://dx.doi.org/10.1088/0965-0393/20/4/045004.

[145] Lyu, Bugao and Zhang, Limin and Meng, Xianghui and Wang, Chengen. A Boundary Lubrication Model and Experimental Study Considering ZDDP Tribofilms on Reciprocating Friction Pairs. *Tribology Letters*, 70(2):65, 2022. doi: 10.1007/s11249-022-01607-1. URL https://doi.org/10.1007/s11249-022-01607-1.

[146] Ardah, Suhaib and Profito, Francisco J. and Dini, Daniele. An integrated finite volume framework for thermal elasto-hydrodynamic lubrication. *Tribology International*, 177:107935, 2023. doi: 10.1016/j.triboint.2022.107935. URL https://www.sciencedirect.com/science/article/pii/S0301679X22005060.

[147] Shirazian, S. and Pishnamazi, M. and Rezakazemi, M. and Nouri, A. and Jafari, M. and Noroozi, S. and Marjani, A. Implementation of the Finite Element Method for Simulation of Mass Transfer in Membrane Contactors. *Chemical Engineering & Technology*, 35(6):1077–1084, 2012. doi: 10.1002/ceat.201100397. URL https://onlinelibrary.wiley.com/doi/abs/10.1002/ceat.201100397.

[148] Yuan, Tian and Gao, Ling and Zhan, Wenbo and Dini, Daniele. Effect of Particle Size and Surface Charge on Nanoparticles Diffusion in the Brain White Matter. *Pharmaceutical Research*, 39(4):767–781, 2022. ISSN 1573-904X. doi: 10.1007/s11095-022-03222-0. URL https://doi.org/10.1007/s11095-022-03222-0.

[149] Bramley, Gabriel Adrian and Beynon, Owain Tomos and Stishenko, Pavel Viktorovich and Logsdail, Andrew James. The application of QM/MM simulations in heterogeneous catalysis. *Physical Chemistry Chemical Physics*, 25:6562–6585, 2023. doi: 10.1039/D2CP04537K. URL http://dx.doi.org/10.1039/D2CP04537K.

[150] Faheem, Muhammad and Heyden, Andreas. Hybrid Quantum Mechanics/Molecular Mechanics Solvation Scheme for Computing Free Energies of Reactions at Metal–Water Interfaces. *Journal of Chemical Theory and Computation*, 10(8):3354–3368, 2014. doi: 10.1021/ct500211w. URL https://doi.org/10.1021/ct500211w.

[151] Nastase, S. A. F. and O'Malley, A. J. and Catlow, C. R. A. and Logsdail, A. J. Computational QM/MM investigation of the adsorption of MTH active species in H-Y and H-ZSM-5. *Physical Chemistry Chemical Physics*, 21:2639–2650, 2019. doi: 10.1039/C8CP06736H. URL http://dx.doi.org/10.1039/C8CP06736H.

[152] Ananikov, Valentine P. and Musaev, Djamaladdin G. and Morokuma, Keiji. Real size of ligands, reactants and catalysts: Studies of structure, reactivity and selectivity by ONIOM and other hybrid computational approaches. *Journal of Molecular Catalysis A: Chemical*, 324 (1):104–119, 2010. doi: 10.1016/j.molcata.2010.03.015. URL https://www.sciencedirect.com/science/article/pii/S1381116910001123.

[153] Zhang, Sen and Zhang, Xu and Jiang, Guangming and Zhu, Huiyuan and Guo, Shaojun and Su, Dong and Lu, Gang and Sun, Shouheng. Tuning Nanoparticle Structure and Surface Strain for Catalysis Optimization. *Journal of the American Chemical Society*, 136(21):7734–7739, 2014. doi: 10.1021/ja5030172. URL https://doi.org/10.1021/ja5030172.

[154] Chen, Zhengzheng and Zhang, Xu and Lu, Gang. Multiscale Computational Design of Core/Shell Nanoparticles for Oxygen Reduction Reaction. *The Journal of Physical Chemistry C*, 121(3):1964–1973, 2017. doi: 10.1021/acs.jpcc.6b11337. URL https://doi.org/10.1021/acs.jpcc.6b11337.

[155] Reinhardt, P. and Causà, M. and Marian, C. M. and He S, B. A. Adsorption of CO on TiO_2 (110) studied by means of a cluster model surrounded by multipoles obtained from slab calculations. *Physical Reviews B*, 54:14812–14821, Nov 1996. doi: 10.1103/PhysRevB.54.14812. URL https://link.aps.org/doi/10.1103/PhysRevB.54.14812.

[156] Nasluzov, Vladimir A. and Ivanova, Elena A. and Shor, Alexei M. and Vayssilov, Georgi N. and Birkenheuer, Uwe and Rösch, Notker. Elastic Polarizable Environment Cluster Embedding Approach for Covalent Oxides and Zeolites Based on a Density Functional Method. *The Journal of Physical Chemistry B*, 107(10):2228–2241, 2003. doi: 10.1021/jp026742r. URL https://doi.org/10.1021/jp026742r.

[157] Berger, Daniel and Oberhofer, Harald and Reuter, Karsten. First-principles embedded-cluster calculations of the neutral and charged oxygen vacancy at the rutile TiO_2(110) surface. *Physical Review B*, 92:075308, Aug 2015. doi: 10.1103/PhysRevB.92.075308. URL https://link.aps.org/doi/10.1103/PhysRevB.92.075308.

[158] Andreoni, W. and Curioni, A. and Mordasini, T. DFT-based molecular dynamics as a new tool for computational biology: First applications and perspective. *IBM Journal of Research and Development*, 45(3.4):397–407, 2001. doi: 10.1147/rd.453.0397. URL https://ieeexplore.ieee.org/document/5389048.

[159] Rovira, Carme and Parrinello, Michele. First-principles molecular dynamics simulations of models for the myoglobin active center. *International Journal of Quantum Chemistry*, 80(6):1172–1180, 2000. doi: 10.1002/1097-461X(2000)80:6⟨1172::AID-QUA4⟩3.0.CO;2-E. URL https://onlinelibrary.wiley.com/doi/abs/10.1002/1097-461X%282000%

2980%3A6%3C1172%3A%3AAID-QUA4%3E3.0.CO%3B2-E.

[160] Rovira, Carme and Schulze, Brita and Eichinger, Markus and Evanseck, Jeffrey D. and Parrinello, Michele. Influence of the Heme Pocket Conformation on the Structure and Vibrations of the Fe-CO Bond in Myoglobin: A QM/MM Density Functional Study. *Biophysical Journal*, 81(1):435–445, 2001. doi: 10.1016/S0006-3495(01)75711-6. URL https://www.sciencedirect.com/science/article/pii/S0006349501757116.

[161] Elliott, James. Novel Approaches to Multiscale Modelling in Materials Science. *International Materials Reviews*, 56:207–225, 07 2011. doi: 10.1179/1743280410Y.0000000002. URL https://journals.sagepub.com/doi/10.1179/1743280410Y.0000000002.

[162] Hénin, Jérôme and Lelièvre, Tony and Shirts, Michael and Valsson, Omar and Delemotte, Lucie. Enhanced Sampling Methods for Molecular Dynamics Simulations [Article v1.0]. *Living Journal of Computational Molecular Science*, 4, 08 2022. doi: 10.33011/livecoms.4.1.1583. URL https://livecomsjournal.org/index.php/livecoms/article/view/v4i1e1583.

[163] Wang, Fugao and Landau, D. P. Efficient, Multiple-Range Random Walk Algorithm to Calculate the Density of States. *Physical Review Letters*, 86:2050–2053, Mar 2001. doi: 10.1103/PhysRevLett.86.2050. URL https://link.aps.org/doi/10.1103/PhysRevLett.86.2050.

[164] Torrie, G. M. and Valleau, J. P. Nonphysical sampling distributions in Monte Carlo free-energy estimation: Umbrella sampling. *Journal of Computational Physics*, 23(2):187–199, 1977. ISSN 0021-9991. doi: 10.1016/0021-9991(77)90121-8. URL https://www.sciencedirect.com/science/article/pii/0021999177901218.

[165] Berg, Bernd A. and Neuhaus, Thomas. Multicanonical ensemble: A new approach to simulate first-order phase transitions. *Physical Review Letters*, 68:9–12, Jan 1992. doi: 10.1103/PhysRevLett.68.9. URL https://link.aps.org/doi/10.1103/PhysRevLett.68.9.

[166] Voter, Arthur F. A method for accelerating the molecular dynamics simulation of infrequent events. *The Journal of Chemical Physics*, 106(11):4665–4677, 03 1997. ISSN 0021-9606. doi: 10.1063/1.473503. URL https://doi.org/10.1063/1.473503.

[167] Voter, Arthur F. and Montalenti, Francesco and Germann, Timothy C. Extending the Time Scale in Atomistic Simulation of Materials. *Annual Review of Materials Research*, 32:321–346, 2002. doi: 10.1146/annurev.matsci.32.112601.141541. URL https://www.annualreviews.org/content/journals/10.1146/annurev.matsci.32.112601.141541.

[168] Darve, Eric and Rodríguez-Gómez, David and Pohorille, Andrew. Adaptive biasing force method for scalar and vector free energy calculations. *The Journal of Chemical Physics*, 128 (14):144120, 04 2008. doi: 10.1063/1.2829861. URL https://doi.org/10.1063/1.2829861.

[169] Corral-Casas, Carlos and Ayestarán Latorre, Carlos and Gattinoni, Chiara and Brewer, Mark and Karl, Jörn and Dini, Daniele and Ewen, James P. Molecular Insights into the Adsorption of Deposit Control Additives from Hydrocarbon Fuels. *Langmuir*, 41(3):1900–1913, 2025. doi:

10.1021/acs.langmuir.4c04368. URL https://doi.org/10.1021/acs.langmuir.4c04368.

[170] Acero, Pablo Navarro and Mohr, Stephan and Bernabei, Marco and Fernández, Carlos and Domínguez, Beatriz and Ewen, James P. Molecular Simulations of Surfactant Adsorption on Iron Oxide from Hydrocarbon Solvents. *Langmuir*, 37(50):14582–14596, 2021. doi: 10.1021/acs.langmuir.1c02133. URL https://doi.org/10.1021/acs.langmuir.1c02133.

[171] Voter, Arthur F. and Sørensen, Mads R. Accelerating Atomistic Simulations of Defect Dynamics: Hyperdynamics, Parallel Replica Dynamics, and Temperature-Accelerated Dynamics. *MRS Proceedings*, 538, jan 1998. doi: 10.1557/proc-538-427. URL https://doi.org/10.1557/proc-538-427.

[172] Martínez, E. and Perriot, R. and Kober, E. M. and Bowlan, P. and Powell, M. and McGrane, S. and Cawkwell, M. J. Parallel replica dynamics simulations of reactions in shock compressed liquid benzene. *The Journal of Chemical Physics*, 150(24):244108, 06 2019. doi: 10.1063/1.5092209. URL https://doi.org/10.1063/1.5092209.

[173] Fichthorn, Kristen A. and Weinberg, W. H. Theoretical foundations of dynamical Monte Carlo simulations. *Journal of Chemical Physics*, 95(2):1090–1096, July 1991. doi: 10.1063/1.461138. URL https://doi.org/10.1063/1.461138.

[174] Nagaoka, Masataka and Suzuki, Yuichi and Okamoto, Takuya and Takenaka, Norio. A hybrid MC/MD reaction method with rare event-driving mechanism: Atomistic realization of 2-chlorobutane racemization process in DMF solution. *Chemical Physics Letters*, 583:80–86, September 2013. doi: 10.1016/j.cplett.2013.08.017. URL https://www.sciencedirect.com/science/article/pii/S0009261413010257.

[175] Gissinger, Jacob R. and Jensen, Benjamin D. and Wise, Kristopher E. REACTER: A Heuristic Method for Reactive Molecular Dynamics. *Macromolecules*, 53(22):9953–9961, 2020. doi: 10.1021/acs.macromol.0c02012. URL https://doi.org/10.1021/acs.macromol.0c02012.

[176] Tschöp, W. and Kremer, K. and Batoulis, J. and Bürger, T. and Hahn, O. Simulation of polymer melts. I. Coarse-graining procedure for polycarbonates. *Acta Polymerica*, 49(2-3):61–74, 1998. doi: 10.1002/(SICI)1521-4044(199802)49:2/3⟨61::AID-APOL61⟩3.0.CO;2-V. URL https://onlinelibrary.wiley.com/doi/abs/10.1002/%28SICI%291521-4044%28199802%2949%3A2/3%3C61%3A%3AAID-APOL61%3E3.0.CO%3B2-V.

[177] Baschnagel, Jörg and Binder, Kurt and Doruker, Pemra and Gusev, Andrei and Hahn, Oliver and Kremer, Kurt and Mattice, Wayne and Müller-Plathe, Florian and Murat, Michael and Paul, Wolfgang and Santos, Serge and Suter, Ulrich and Tries, Volker. *Bridging the Gap Between Atomistic and Coarse-Grained Models of Polymers: Status and Perspectives*, volume 152, pages 41–156. Springer, 04 2000. ISBN 978-3-540-66735-3. doi: 10.1007/3-540-46778-5_2. URL https://colab.ws/articles/10.1007%2F3-540-46778-5_2.

[178] Müller-Plathe, Florian. Coarse-Graining in Polymer Simulation: From the Atomistic to the Mesoscopic Scale and Back. *ChemPhysChem*, 3(9):754–769, 2002. doi: 10.1002/1439-7641(20020916)3:9⟨754::AID-CPHC754⟩3.0.CO;2-U. URL

https://chemistry-europe.onlinelibrary.wiley.com/doi/abs/10.1002/1439-7641%2820020916%293%3A9%3C754%3A%3AAID-CPHC754%3E3.0.CO%3B2-U.

[179] Voth, Gregory A., editor. *Coarse-Graining of Condensed Phase and Biomolecular Systems*. CRC Press, 1st edition, 2008. doi: 10.1201/9781420059564. URL https://www.taylorfrancis.com/books/mono/10.1201/9781420059564/coarse-graining-condensed-phase-biomolecular-systems-gregory-voth.

[180] Kmiecik, Sebastian and Gront, Dominik and Kolinski, Michal and Wieteska, Lukasz and Dawid, Aleksandra Elzbieta and Kolinski, Andrzej. Coarse-Grained Protein Models and Their Applications. *Chemical Reviews*, 116(14):7898–7936, 2016. doi: 10.1021/acs.chemrev.6b00163. URL https://doi.org/10.1021/acs.chemrev.6b00163.

[181] Elliott, James A. and Paddison, Stephen J. Modelling of morphology and proton transport in PFSA membranes. *Physical Chemistry Chemical Physics*, 9:2602–2618, 2007. doi: 10.1039/B701234A. URL http://dx.doi.org/10.1039/B701234A.

[182] Praprotnik, Matej and Site, Luigi Delle and Kremer, Kurt. Multiscale Simulation of Soft Matter: From Scale Bridging to Adaptive Resolution. *Annual Review of Physical Chemistry*, 59:545–571, 2008. doi: 10.1146/annurev.physchem.59.032607.093707. URL https://www.annualreviews.org/content/journals/10.1146/annurev.physchem.59.032607.093707.

[183] Weiand, Erik and Ewen, James P. and Koenig, Peter H. and Roiter, Yuri and Page, Steven H. and Angioletti-Uberti, Stefano and Dini, Daniele. Coarse-grained molecular models of the surface of hair. *Soft Matter*, 18:1779–1792, 2022. doi: 10.1039/D1SM01720A. URL http://dx.doi.org/10.1039/D1SM01720A.

[184] Marrink, Siewert J. and Risselada, H. Jelger and Yefimov, Serge and Tieleman, D. Peter and de Vries, Alex H. The MARTINI Force Field: Coarse Grained Model for Biomolecular Simulations. *The Journal of Physical Chemistry B*, 111(27):7812–7824, 2007. doi: 10.1021/jp071097f. URL https://doi.org/10.1021/jp071097f.

[185] Smith, E. R. and Trevelyan, D. J. and Ramos-Fernandez, E. and Sufian, A. and O'Sullivan, C. and Dini, D. CPL library — A minimal framework for coupled particle and continuum simulation. *Computer Physics Communications*, 250:107068, 2020. doi: 10.1016/j.cpc.2019.107068. URL https://www.sciencedirect.com/science/article/pii/S0010465519303819.

[186] Fish, Jacob and Wagner, Gregory J. and Keten, Sinan. Mesoscopic and multiscale modelling in materials. *Nature Materials*, 20(6):774–786, June 2021. doi: 10.1038/s41563-020-00913-0. URL https://doi.org/10.1038/s41563-020-00913-0.

[187] Tadmor, E. B. and Ortiz, M. and Phillips, R. Quasicontinuum analysis of defects in solids. *Philosophical Magazine A*, 73(6):1529–1563, 1996. doi: 10.1080/01418619608243000. URL https://doi.org/10.1080/01418619608243000.

[188] Kohlhoff, S. and Gumbsch, P. and Fischmeister, H. F. Crack propagation in b.c.c. crystals

studied with a combined finite-element and atomistic model. *Philosophical Magazine A*, 64(4):851–878, 1991. doi: 10.1080/01418619108213953. URL https://doi.org/10.1080/01418619108213953.

[189] Nair, A.K. and Warner, D.H. and Hennig, Richard and Curtin, W.A. Coupling quantum and continuum scales to predict crack tip dislocation nucleation. *Scripta Materialia*, 63:1212–1215, 01 2010. doi: 10.1016/j.scriptamat.2010.08.038. URL https://www.sciencedirect.com/science/article/abs/pii/S1359646210005750?via%3Dihub.

[190] Kochmann, Dennis M. and Hopkins, Jonathan B. and Valdevit, Lorenzo. Multiscale modeling and optimization of the mechanics of hierarchical metamaterials. *MRS Bulletin*, 44(10):773–781, 2019. doi: 10.1557/mrs.2019.228. URL https://doi.org/10.1557/mrs.2019.228.

[191] Knapek, S. Matrix-Dependent Multigrid Homogenization for Diffusion Problems. *SIAM Journal on Scientific Computing*, 20(2):515–533, 1998. doi: 10.1137/S1064827596304848. URL https://doi.org/10.1137/S1064827596304848.

[192] Fish, Jacob and Belsky, Vladimir. Multi-grid method for periodic heterogeneous media Part 2: Multiscale modeling and quality control in multidimensional case. *Computer Methods in Applied Mechanics and Engineering*, 126(1):17–38, 1995. doi: 10.1016/0045-7825(95)00812-F. URL https://www.sciencedirect.com/science/article/pii/004578259500812F.

[193] Miehe, C. and Bayreuther, Claus. On multiscale FE analyses of heterogeneous structures: From homogenization to multigrid solvers. *International Journal for Numerical Methods in Engineering*, 71:1135 – 1180, 09 2007. doi: 10.1002/nme.1972. URL https://onlinelibrary.wiley.com/doi/10.1002/nme.1972.

[194] Plimpton, Steve. Computational limits of classical molecular dynamics simulations. *Computational Materials Science*, 4(4):361–364, 1995. doi: 10.1016/0927-0256(95)00037-1. URL https://www.sciencedirect.com/science/article/pii/0927025695000371. Proceedings of the Workshop on Glasses and The Glass Transition:1 Challenges in Materials Theory and Simulation.

[195] Elber, Ron. Perspective: Computer simulations of long time dynamics. *The Journal of Chemical Physics*, 144(6):060901, 02 2016. doi: 10.1063/1.4940794. URL https://doi.org/10.1063/1.4940794.

[196] Ingólfsson, Helgi I. et al. Machine Learning-Driven Multiscale Modeling: Bridging the Scales with a Next-Generation Simulation Infrastructure. *Journal of Chemical Theory and Computation*, 19(9):2658–2675, 2023. doi: 10.1021/acs.jctc.2c01018. URL https://doi.org/10.1021/acs.jctc.2c01018.

[197] Marconi, Umberto Marini Bettolo and Tarazona, Pedro. Dynamic density functional theory of fluids. *The Journal of Chemical Physics*, 110(16):8032–8044, 04 1999. ISSN 0021-9606. doi: 10.1063/1.478705. URL https://doi.org/10.1063/1.478705.

[198] Stanton, L. G. and Oppelstrup, T. and Carpenter, T. S. and Ingólfsson, H. I. and Surh, M. P. and Lightstone, F. C. and Glosli, J. N. Dynamic density functional theory of multicomponent cellular membranes. *Physical Review Research*, 5:013080, Feb 2023. doi: 10.1103/PhysRevResearch.5.013080. URL `https://link.aps.org/doi/10.1103/PhysRevResearch.5.013080`.

[199] Bhatia, Harsh and Carpenter, Timothy S. and Ingólfsson, Helgi I. and Dharuman, Gautham and Karande, Piyush and Liu, Shusen and Oppelstrup, Tomas and Neale, Chris and Lightstone, Felice C. and Van Essen, Brian and Glosli, James N. and Bremer, Peer-Timo. Machine-learning-based dynamic-importance sampling for adaptive multiscale simulations. *Nature Machine Intelligence*, 3(5):401–409, May 2021. doi: 10.1038/s42256-021-00327-w. URL `https://doi.org/10.1038/s42256-021-00327-w`.

[200] Holey, Hannes and Gumbsch, Peter and Pastewka, Lars. Active learning for parameter-free multiscale modeling of boundary lubrication, 2025. URL `https://arxiv.org/abs/2503.09619`.

[201] Rasmussen, Carl Edward and Williams, Christopher K. I. *Gaussian Processes for Machine Learning*. The MIT Press, 11 2005. doi: 10.7551/mitpress/3206.001.0001. URL `https://doi.org/10.7551/mitpress/3206.001.0001`.

[202] Allen, P. Michael and Tidelsey, J. Dominic. *Computer Simulation of Liquids*, volume 26. Oxford University Press, Oxford, England, UK, apr 1986. doi: 10.1093/oso/9780198803195.001.0001. URL `https://doi.org/10.1093/oso/9780198803195.001.0001`.

[203] Verlet, Loup. Computer "Experiments" on Classical Fluids. I. Thermodynamical Properties of Lennard-Jones Molecules. *Physical Review*, 159(1):98–103, July 1967. doi: 10.1103/PhysRev.159.98. URL `https://link.aps.org/doi/10.1103/PhysRev.159.98`.

[204] Müser, Martin H. and Sukhomlinov, Sergey V. and Pastewka, Lars. Interatomic potentials: achievements and challenges. *Advances in Physics: X*, 8(1):2093129, 2023. doi: 10.1080/23746149.2022.2093129. URL `https://doi.org/10.1080/23746149.2022.2093129`.

[205] Jones, J. E. On the determination of molecular fields.-II. From the equation of state of a gas. *Proceedings of the Royal Society A*, 106(738):463–477, 1924. doi: 10.1098/rspa.1924.0082. URL `https://royalsocietypublishing.org/doi/10.1098/rspa.1924.0082#`.

[206] Mayo, Stephen L. and Olafson, Barry D. and Goddard, William A. DREIDING: a generic force field for molecular simulations. *Journal of Physical Chemistry*, 94(26):8897–8909, December 1990. doi: 10.1021/j100389a010. URL `https://doi.org/10.1021/j100389a010`.

[207] Rappe, Anthony K. and Goddard, William A. III. Charge equilibration for molecular dynamics simulations. *Journal of Physical Chemistry*, 95(8):3358–3363, April 1991. doi: 10.1021/j100161a070. URL `https://doi.org/10.1021/j100161a070`.

[208] van Duin, Adri C. T. and Dasgupta, Siddharth and Lorant, Francois and Goddard, William A. ReaxFF: A Reactive Force Field for Hydrocarbons. *Journal of Physical Chemistry A*, 105

(41):9396–9409, October 2001. doi: 10.1021/jp004368u. URL https://doi.org/10.1021/jp004368u.

[209] Senftle, Thomas P. and Hong, Sungwook and Islam, Md Mahbubul and Kylasa, Sudhir B. and Zheng, Yuanxia and Shin, Yun Kyung and Junkermeier, Chad and Engel-Herbert, Roman and Janik, Michael J. and Aktulga, Hasan Metin and Verstraelen, Toon and Grama, Ananth and van Duin, Adri C. T. The ReaxFF reactive force-field: development, applications and future directions. *npj Computational Materials*, 2(15011):1–14, March 2016. doi: 10.1038/npjcompumats.2015.11. URL https://doi.org/10.1038/npjcompumats.2015.11.

[210] Chen, Chao and Zhao, Lingling and Wang, Jingfan and Lin, Shangchao. Reactive Molecular Dynamics Simulations of Biomass Pyrolysis and Combustion under Various Oxidative and Humidity Environments. *Industrial & Engineering Chemistry Research*, 56(43):12276–12288, November 2017. doi: 10.1021/acs.iecr.7b01714. URL https://doi.org/10.1021/acs.iecr.7b01714.

[211] Si, Ting and Huang, Kai and Lin, Yuyu and Gu, Mingyan. ReaxFF Study on the Effect of CaO on Cellulose Pyrolysis. *Energy & Fuels*, 33(11):11067–11077, November 2019. doi: 10.1021/acs.energyfuels.9b02583. URL https://doi.org/10.1021/acs.energyfuels.9b02583.

[212] Ongari, Daniele and Boyd, Peter G. and Kadioglu, Ozge and Mace, Amber K. and Keskin, Seda and Smit, Berend. Evaluating Charge Equilibration Methods To Generate Electrostatic Fields in Nanoporous Materials. *Journal of Chemical Theory and Computation*, 15(1):382–401, 2019. doi: 10.1021/acs.jctc.8b00669. URL https://doi.org/10.1021/acs.jctc.8b00669.

[213] Parr, Robert G. and Donnelly, Robert A. and Levy, Mel and Palke, William E. Electronegativity: The density functional viewpoint. *The Journal of Chemical Physics*, 68(8):3801–3807, 04 1978. doi: 10.1063/1.436185. URL https://doi.org/10.1063/1.436185.

[214] Sanderson, R. T. Electronegativity and bond energy. *Journal of the American Chemical Society*, 105(8):2259–2261, 1983. doi: 10.1021/ja00346a026. URL https://doi.org/10.1021/ja00346a026.

[215] Tolman, Richard C. The Principle of Microscopic Reversibility. *Proceedings of the National Academy of Sciences*, 11(7):436–439, July 1925. doi: 10.1073/pnas.11.7.436. URL https://doi.org/10.1073/pnas.11.7.436.

[216] Trochet, Mickaël and Mousseau, Normand and Béland, Laurent Karim and Henkelman, Graeme. Off-Lattice Kinetic Monte Carlo Methods. In *Handbook of Materials Modeling: Methods: Theory and Modeling*, pages 715–743. Springer, Cham, Switzerland, March 2020. ISBN 978-3-319-44677-6. doi: 10.1007/978-3-319-44677-6_29. URL https://doi.org/10.1007/978-3-319-44677-6_29.

[217] Bortz, A. B. and Kalos, M. H. and Lebowitz, J. L. A new algorithm for Monte Carlo simulation of Ising spin systems. *Journal of Computational Physics*, 17(1):10–18, Jan-

uary 1975. doi: 10.1016/0021-9991(75)90060-1. URL https://www.sciencedirect.com/science/article/pii/0021999175900601.

[218] Gillespie, Daniel T. A general method for numerically simulating the stochastic time evolution of coupled chemical reactions. *Journal of Computational Physics*, 22(4):403–434, December 1976. doi: 10.1016/0021-9991(76)90041-3. URL https://www.sciencedirect.com/science/article/pii/0021999176900413.

[219] Margraf, Johannes T. and Reuter, Karsten. Systematic Enumeration of Elementary Reaction Steps in Surface Catalysis. *ACS Omega*, 4(2):3370–3379, February 2019. doi: 10.1021/acsomega.8b03200. URL https://doi.org/10.1021/acsomega.8b03200.

[220] Campbell, Charles T. The Degree of Rate Control: A Powerful Tool for Catalysis Research. *ACS Catalysis*, 7(4):2770–2779, April 2017. doi: 10.1021/acscatal.7b00115. URL https://pubs.acs.org/doi/10.1021/acscatal.7b00115.

[221] Andersen, Mie and Panosetti, Chiara and Reuter, Karsten. A practical guide to surface kinetic Monte Carlo simulations. *Frontiers in Chemistry*, 7:202, 2019. doi: 10.3389/fchem.2019.00202. URL https://doi.org/10.3389/fchem.2019.00202.

[222] Zheng, Xiaoping and Zhang, Peifeng. Kinetic Monte Carlo simulation of surfactant-mediated Cu thin-film growth. *Computational Materials Science*, 50(1):6–9, November 2010. doi: 10.1016/j.commatsci.2010.05.054. URL https://www.sciencedirect.com/science/article/pii/S0927025610003447.

[223] Nita, F. and Mastail, C. and Abadias, G. Three-dimensional kinetic Monte Carlo simulations of cubic transition metal nitride thin film growth. *Physical Review B*, 93(6):064107, February 2016. doi: 10.1103/PhysRevB.93.064107. URL https://link.aps.org/doi/10.1103/PhysRevB.93.064107.

[224] Cantrell, Rebecca A. and Clancy, Paulette. A New Kinetic Monte Carlo Algorithm for Heteroepitactical Growth: Case Study of C60 Growth on Pentacene. *Journal of Chemical Theory and Computation*, 8(3):1048–1057, March 2012. doi: 10.1021/ct200819r. URL https://doi.org/10.1021/ct200819r.

[225] Henkelman, Graeme and Jónsson, Hannes. Long time scale kinetic Monte Carlo simulations without lattice approximation and predefined event table. *Journal of Chemical Physics*, 115(21):9657–9666, December 2001. doi: 10.1063/1.1415500. URL https://doi.org/10.1063/1.1415500.

[226] Xu, Haixuan and Osetsky, Yury N. and Stoller, Roger E. Simulating complex atomistic processes: On-the-fly kinetic Monte Carlo scheme with selective active volumes. *Physical Review B*, 84(13):132103, October 2011. doi: 10.1103/PhysRevB.84.132103. URL https://link.aps.org/doi/10.1103/PhysRevB.84.132103.

[227] Li, Lei and Li, Xinyu and Duan, Zhiyao and Meyer, Randall J. and Carr, Rob and Raman, Sumathy and Koziol, Lucas and Henkelman, Graeme. Adaptive kinetic Monte Carlo simu-

lations of surface segregation in PdAu nanoparticles. *Nanoscale*, 11(21):10524–10535, May 2019. doi: 10.1039/C9NR01858A. URL http://dx.doi.org/10.1039/C9NR01858A.

[228] El-Mellouhi, Fedwa and Mousseau, Normand and Lewis, Laurent J. Kinetic activation-relaxation technique: An off-lattice self-learning kinetic Monte Carlo algorithm. *Physical Review B*, 78(15):153202, October 2008. doi: 10.1103/PhysRevB.78.153202. URL https://link.aps.org/doi/10.1103/PhysRevB.78.153202.

[229] Henkelman, Graeme and Jónsson, Hannes. A dimer method for finding saddle points on high dimensional potential surfaces using only first derivatives. *Journal of Chemical Physics*, 111 (15):7010–7022, October 1999. doi: 10.1063/1.480097. URL https://doi.org/10.1063/1.480097.

[230] Sörensen, Mads R. and Voter, Arthur F. Temperature-accelerated dynamics for simulation of infrequent events. *Journal of Chemical Physics*, 112(21):9599–9606, June 2000. doi: 10.1063/1.481576. URL https://doi.org/10.1063/1.481576.

[231] Henkelman, Graeme and Uberuaga, Blas P. and Jónsson, Hannes. A climbing image nudged elastic band method for finding saddle points and minimum energy paths. *Journal of Chemical Physics*, 113(22):9901–9904, December 2000. doi: 10.1063/1.1329672. URL https://doi.org/10.1063/1.1329672.

[232] Xu, Lijun and Mei, Donghai and Henkelman, Graeme. Adaptive kinetic Monte Carlo simulation of methanol decomposition on Cu(100). *Journal of Chemical Physics*, 131(24): 244520, December 2009. doi: 10.1063/1.3281688. URL https://pubs.aip.org/aip/jcp/article-abstract/131/24/244520/189850/.

[233] Ntioudis, Stavros and Ewen, James Patrick and Dini, Daniele and Turner, Christoffer Heath. A hybrid off-lattice kinetic Monte Carlo/molecular dynamics method for amorphous thin film growth. *ChemRxiv*, April 2023. doi: 10.26434/chemrxiv-2023-9fl0k-v2. URL https://chemrxiv.org/engage/chemrxiv/article-details/642ececf736114c96305c329.

[234] Orr, B. G. and Kessler, D. and Snyder, C. W. and Sander, L. A Model for Strain-Induced Roughening and Coherent Island Growth. *Europhysics Letters*, 19(1):33, May 1992. doi: 10.1209/0295-5075/19/1/006. URL https://dx.doi.org/10.1209/0295-5075/19/1/006.

[235] Lam, Chi-Hang and Lee, Chun-Kin and Sander, Leonard M. Competing Roughening Mechanisms in Strained Heteroepitaxy: A Fast Kinetic Monte Carlo Study. *Physical Review Letters*, 89(21):216102, November 2002. doi: 10.1103/PhysRevLett.89.216102. URL https://link.aps.org/doi/10.1103/PhysRevLett.89.216102.

[236] Van Swygenhoven, Helena and Weertman, Julia R. Deformation in nanocrystalline metals. *Materials Today*, 9(5):24–31, May 2006. doi: 10.1016/S1369-7021(06)71494-8. URL https://www.sciencedirect.com/science/article/pii/S1369702106714948.

[237] Hestenes, Magnus R. and Stiefel, Eduard. Methods of conjugate gradients for solving linear systems. *Journal of Research of the National Institute of Standards and Technology*, 49:409–

435, 1952. URL https://nvlpubs.nist.gov/nistpubs/jres/049/jresv49n6p409_a1b.pdf.

[238] Milman, V. and Winkler, B. and White, J. A. and Pickard, C. J. and Payne, M. C. and Akhmatskaya, E. V. and Nobes, R. H. Electronic structure, properties, and phase stability of inorganic crystals: A pseudopotential plane-wave study. *International Journal of Quantum Chemistry*, 77(5):895–910, January 2000. doi: 10.1002/(SICI)1097-461X(2000)77:5⟨895::AID-QUA10⟩3.0.CO;2-C. URL https://doi.org/10.1002/(SICI)1097-461X(2000)77:5%3C895::AID-QUA10%3E3.0.CO%3B2-C.

[239] Mosey, Nicholas J. and Woo, Tom K. Finite Temperature Structure and Dynamics of Zinc Dialkyldithiophosphate Wear Inhibitors A Density Functional Theory and ab Initio Molecular Dynamics Study. *Journal of Physical Chemistry A*, 107(25):5058–5070, 2003. doi: 10.1021/jp034085c. URL https://pubs.acs.org/doi/10.1021/jp034085c.

[240] Patiño , Carlos Miguel and Alzate-Vargas , Lorena and Li , Chunyu and Haley , Benjamin P and Strachan , Alejandro. LAMMPS Data-File Generator, 2017. URL https://nanohub.org/resources/struc2lammpsdf. [Accessed: 30th January 2025].

[241] Di Tommaso, Devis and Ainsworth, Richard I. and Tang, Emilia and de Leeuw, Nora H. Modelling the structural evolution of ternary phosphate glasses from melts to solid amorphous materials. *Journal of Materials Chemistry B*, 1(38):5054–5066, September 2013. doi: 10.1039/C3TB20662A. URL https://pubs.rsc.org/en/content/articlehtml/2013/tb/c3tb20662a.

[242] Nosé, Shūichi. A molecular dynamics method for simulations in the canonical ensemble. *Molecular Physics*, 52(2):255–268, June 1984. doi: 10.1080/00268978400101201. URL https://www.tandfonline.com/doi/abs/10.1080/00268978400101201.

[243] Hoover, William G. Canonical dynamics: Equilibrium phase-space distributions. *Physical Review A*, 31(3):1695–1697, March 1985. doi: 10.1103/PhysRevA.31.1695. URL https://link.aps.org/doi/10.1103/PhysRevA.31.1695.

[244] Manousiouthakis, Vasilios I. and Deem, Michale W. Strict detailed balance is unnecessary in Monte Carlo simulation. *The Journal of Chemical Physics*, 110(6):2753–2756, 1999. doi: 10.1063/1.477973. URL https://pubs.aip.org/aip/jcp/article-abstract/110/6/2753/474590.

[245] Martínez, L. and Andrade, R. and Birgin, E. G. and Martínez, J. M. PACKMOL: A package for building initial configurations for molecular dynamics simulations. *Journal of Computational Chemistry*, 30(13):2157–2164, October 2009. doi: 10.1002/jcc.21224. URL https://doi.org/10.1002/jcc.21224.

[246] Laidler, K. J. and Keith, J. *Chemical Kinetics*. Harper & Row, 1987. URL https://scholar.google.com/scholar_lookup?title=Chemical%20Kinetics&publication_year=1987&author=J.%20Laidler&author=J.%20Keith.

[247] Xu, Lang and Kirvassilis, Demetrios and Bai, Yunhai and Mavrikakis, Manos. Atomic and molecular adsorption on Fe(110). *Surface Science*, 667:54–65, January 2018. doi: 10.1016/j.susc.2017.09.002. URL https://www.sciencedirect.com/science/article/pii/S0039602817305988.

[248] Erley, W. and Ibach, H. Vibrational excitations and structure of oxygen on Fe(110). *Solid State Communications*, 37(12):937–942, March 1981. doi: 10.1016/0038-1098(81)91190-X. URL https://www.sciencedirect.com/science/article/pii/003810988191190X.

[249] Wight, A. and Condon, N. G. and Leibsle, F. M. and Worthy, G. and Hodgson, A. Initial stages of Fe(110) oxidation at 300 K: kinetics and structure. *Surface Science*, 331-333:133–137, July 1995. doi: 10.1016/0039-6028(95)00176-X. URL https://www.sciencedirect.com/science/article/pii/003960289500176X.

[250] Ossowski, Tomasz and Kiejna, Adam. Oxygen adsorption on Fe(110) surface revisited. *Surface Science*, 637-638:35–41, July 2015. doi: 10.1016/j.susc.2015.03.001. URL https://www.sciencedirect.com/science/article/pii/S0039602815000618.

[251] Chenoweth, Kimberly and van Duin, Adri C. T. and Goddard, William A. ReaxFF Reactive Force Field for Molecular Dynamics Simulations of Hydrocarbon Oxidation. *Journal of Physical Chemistry A*, 112(5):1040–1053, February 2008. doi: 10.1021/jp709896w. URL https://doi.org/10.1021/jp709896w.

[252] Stoch, Pawel and Stoch, Agata and Ciecinska, Malgorzata and Krakowiak, Ireneusz and Sitarz, Maciej. Structure of phosphate and iron-phosphate glasses by DFT calculations and FTIR/Raman spectroscopy. *Journal of Non-Crystalline Solids*, 450:48–60, October 2016. doi: 10.1016/j.jnoncrysol.2016.07.027. URL https://www.sciencedirect.com/science/article/pii/S002230931630299X.

[253] Kuss, Christian and Liang, Guoxian and Schougaard, Steen B. Atomistic modeling of site exchange defects in lithium iron phosphate and iron phosphate. *Journal of Materials Chemistry*, 22(47):24889–24893, November 2012. doi: 10.1039/C2JM35538H. URL http://dx.doi.org/10.1039/C2JM35538H.

[254] Zeng, Yuewu. Role of PO4 tetrahedron in LiFePO4 and FePO4 system. *Microscopy Research and Technique*, 78(6):462–471, June 2015. URL https://pubmed.ncbi.nlm.nih.gov/25846750/.

[255] Fichthorn, Kristen A. and Lin, Yangzheng. A local superbasin kinetic Monte Carlo method. *The Journal of Chemical Physics*, 138(16):164104, 04 2013. doi: 10.1063/1.4801869. URL https://pubs.aip.org/aip/jcp/article-abstract/138/16/164104/71495.

[256] Humphrey, William and Dalke, Andrew and Schulten, Klaus. VMD: Visual molecular dynamics. *Journal of Molecular Graphics*, 14(1):33–38, February 1996. doi: 10.1016/0263-7855(96)00018-5. URL https://www.sciencedirect.com/science/article/pii/0263785596000185.

[257] Persson, B. N. J. and Albohr, O. and Tartaglino, U. and Volokitin, A. I. and Tosatti, E. On the nature of surface roughness with application to contact mechanics, sealing, rubberfriction and adhesion. *Journal of Physics: Condensed Matter*, 17(1):R1, December 2004. doi: 10.1088/0953-8984/17/1/R01. URL https://dx.doi.org/10.1088/0953-8984/17/1/R01.

[258] Cohen, P. I. and Petrich, G. S. and Pukite, P. R. and Whaley, G. J. and Arrott, A. S. Birth-death models of epitaxy: I. Diffraction oscillations from low index surfaces. *Surface Science*, 216(1):222–248, June 1989. doi: 10.1016/0039-6028(89)90655-9. URL https://www.sciencedirect.com/science/article/pii/0039602889906559.

[259] Röttger, Michael C. and Sanner, Antoine and Thimons, Luke A. and Junge, Till and Gujrati, Abhijeet and Monti, Joseph M. and Nöhring, Wolfram G. and Jacobs, Tevis D. B. and Pastewka, Lars. Contact.engineering-Create, analyze and publish digital surface twins from topography measurements across many scales. *Surface Topography: Metrology Properties*, 10:035032, 9 2022. doi: 10.1088/2051-672X/ac860a. URL https://iopscience.iop.org/article/10.1088/2051-672X/ac860a.

[260] Persson, B. N. J. On the Fractal Dimension of Rough Surfaces. *Tribology Letters*, 54(1): 99–106, April 2014. doi: 10.1007/s11249-014-0313-4. URL https://doi.org/10.1007/s11249-014-0313-4.

[261] Dorgham, Abdel and Azam, Abdullah and Parsaeian, Pourya and Wang, Chun and Morina, Ardian and Neville, Anne. An Assessment of the Effect of Relative Humidity on the Decomposition of the ZDDP Antiwear Additive. *Tribology Letters*, 69(2):72–12, May 2021. doi: 10.1007/s11249-021-01446-6. URL https://doi.org/10.1007/s11249-021-01446-6.

[262] Al-Hasni, Bushra and Mountjoy, Gavin. Structural investigation of iron phosphate glasses using molecular dynamics simulation. *Journal of Non-Crystalline Solids*, 357(15):2775–2779, July 2011. doi: 10.1016/j.jnoncrysol.2010.10.010. URL https://www.sciencedirect.com/science/article/pii/S0022309310007751.

[263] Hoppe, U. and Walter, G. and Barz, A. and Stachel, D. and Hannon, A. C. The P-O bond lengths in vitreous probed by neutron diffraction with high real-space resolution. *Journal of Physics: Condensed Matter*, 10(2):261, January 1998. doi: 10.1088/0953-8984/10/2/004. URL https://iopscience.iop.org/article/10.1088/0953-8984/10/2/004.

[264] Zhang, Liying and Brow, Richard K. A Raman Study of Iron–Phosphate Crystalline Compounds and Glasses. *Journal of the American Ceramic Society*, 94(9):3123–3130, September 2011. doi: 10.1111/j.1551-2916.2011.04486.x. URL https://doi.org/10.1111/j.1551-2916.2011.04486.x.

[265] Stoch, Pawel and Szczerba, Wojciech and Bodnar, Wiktor and Ciecinska, Malgorzata and Burkel, Eberhard. Structural properties of iron-phosphate glasses: Spectroscopic studies and ab initio simulations. *Physical Chemistry Chemical Physics*, 16(37):19917, August 2014. doi: 10.1039/c4cp03113j. URL https://pubs.rsc.org/en/content/articlelanding/2014/cp/c4cp03113j.

[266] Karabulut, M. and Marasinghe, G. K. and Ray, C. S. and Day, D. E. and Waddill, G. D. and Booth, C. H. and Allen, P. G. and Bucher, J. J. and Caulder, D. L. and Shuh, D. K. An investigation of the local iron environment in iron phosphate glasses having different Fe(II) concentrations. *Journal of Non-Crystalline Solids*, 306(2):182–192, August 2002. doi: 10.1016/S0022-3093(02)01053-0. URL https://www.sciencedirect.com/science/article/pii/S0022309302010530.

[267] Hoppe, U. and Karabulut, M. and Metwalli, E. and Brow, R. K. and Jóvári, P. The Fe–O coordination in iron phosphate glasses by x-ray diffraction with highenergy photons. *Journal of Physics: Condensed Matter*, 15(36):6143, August 2003. doi: 10.1088/0953-8984/15/36/305. URL https://dx.doi.org/10.1088/0953-8984/15/36/305.

[268] Ntioudis, Stavros and Ewen, James Patrick and Dini, Daniele and Turner, Christian Heath. Off-lattice hybrid kinetic Monte Carlo/molecular dynamics simulations on iron polyphosphate films from tricresyl phosphate molecules. *Mendeley Data V1*, 2023. doi: 10.17632/p8bjyrg5jh.1. URL https://data.mendeley.com/datasets/p8bjyrg5jh/1.

[269] Metla, Sai Bhavani Sravan and Rouhani, Mehdi and Hobley, Jonathan and Ou, Hsin-Hung and Jeng, Yeau-Ren. The reaction of the oil additive tricresylphosphate on steel: The solution to an enduring 100-year-old mystery. *Applied Materials Today*, 39:102324, August 2024. doi: 10.1016/j.apmt.2024.102324. URL https://www.sciencedirect.com/science/article/pii/S2352940724002695.

[270] Ntioudis, Stavros and Ewen, James P. and Dini, Daniele and Turner, C. Heath. A hybrid off-lattice kinetic Monte Carlo/molecular dynamics method for amorphous thin film growth. *Computational Materials Science*, 229:112421, October 2023. doi: 10.1016/j.commatsci.2023.112421. URL https://www.sciencedirect.com/science/article/pii/S0927025623004159.

[271] Fry, Benjamin M. and Moody, Gareth and Spikes, Hugh and Wong, Janet S. S. Effect of Surface Cleaning on Performance of Organic Friction Modifiers. *Tribology Transactions*, 63(2):305–313, March 2020. doi: 10.1080/10402004.2019.1687797. URL https://www.tandfonline.com/doi/full/10.1080/10402004.2019.1687797.

[272] Flaticon. Free icons, January 2025. URL https://www.flaticon.com/free-icons/. [Accessed: 8th January 2025].

[273] Vecteezy. Vector art, January 2025. URL https://www.vecteezy.com/vector-art/. [Accessed: 8th January 2025].

[274] Cann, P. M. and Spikes, H. A. and Hutchinson, J. The Development of a Spacer Layer Imaging Method (SLIM) for Mapping Elastohydrodynamic Contacts. *Tribology Transactions*, 39(4):915–921, January 1996. doi: 10.1080/10402009608983612. URL https://www.tandfonline.com/doi/abs/10.1080/10402009608983612.

[275] Jung, Youngsuk and Kline, R. Joseph and Fischer, Daniel A. and Lin, Eric K. and Heeney, Martin and McCulloch, Iain and DeLongchamp, Dean M. The Effect of Interfacial Roughness

on the Thin Film Morphology and Charge Transport of High-Performance Polythiophenes. *Advanced Functional Materials*, 18(5):742–750, March 2008. doi: 10.1002/adfm.200701089. URL https://doi.org/10.1002/ADFM.200701089.

[276] AZoM. AISI 52100 Alloy Steel (UNS G52986), September 2012. URL https://www.azom.com/article.aspx?ArticleID=6704. [Accessed: 7th January 2025].

[277] Shell. Shell XHVI 3 Revision 4, 2023. URL https://www.shell.com/content/dam/shell/assets/en/business-functions/energy-and-innovation/documents/chs-shell-xhvi-3-rev-4.pdf. [Accessed: 7th January 2025].

[278] Jain, Varun and Biesinger, Mark C. and Linford, Matthew R. The Gaussian-Lorentzian Sum, Product, and Convolution (Voigt) functions in the context of peak fitting X-ray photoelectron spectroscopy (XPS) narrow scans. *Applied Surface Science*, 447:548–553, July 2018. doi: 10.1016/j.apsusc.2018.03.190. URL https://www.sciencedirect.com/science/article/pii/S0169433218308766.

[279] ThermoFisher Scientific. Table of elements, January 2025. URL https://www.thermofisher.com/uk/en/home/materials-science/learning-center/periodic-table.html. [Accessed: 20th January 2025].

[280] National Institute of Standards and Technology. NIST Standard Reference Database Number 20, January 2000. URL https://dx.doi.org/10.18434/T4T88K. [Accessed: 20th January 2025].

[281] MacLaren, Alexander and LaMascus, Parker and Carpick, Robert W. Enhancing the Range and Reliability of the Spacer Layer Imaging Method. *Tribology Letters*, 72(3):95–21, July 2024. doi: 10.1007/s11249-024-01890-0. URL https://link.springer.com/article/10.1007/s11249-024-01890-0.

[282] Spikes, H. A. and Cann, P. M. The development and application of the spacer layer imaging method for measuring lubricant film thickness. *Proceedings of the Institution of Mechanical Engineers, Part J: Journal of Engineering Tribology*, 215(3):261–277, March 2001. doi: 10.1243/1350650011543529. URL https://journals.sagepub.com/doi/10.1243/1350650011543529.

[283] Hartl, Martin and Krupka, Ivan and Liska, Miroslav. Differential colorimetry: tool for evaluation of chromatic interference pattern. *Optical Engineering*, 36(9):2384–2391, September 1997. doi: 10.1117/1.601415. URL https://doi.org/10.1117/1.601415.

[284] Makki, J. F. and Graham, E. E. Vapor Phase Deposition on High Temperature Surfaces. *Tribology Transactions*, 33(4):595–603, January 1990. doi: 10.1080/10402009008981994. URL https://www.tandfonline.com/doi/abs/10.1080/10402009008981994.

[285] Lara, J. and Molero, H. and Ramirez-Cuesta, A. and Tysoe, W. T. Structure and Growth Kinetics of Films Formed by the Thermal Decomposition of CCl4 on Iron Surfaces. *Langmuir*, 12(10):2488–2494, January 1996. doi: 10.1021/la9503515. URL https://pubs.acs.org/

doi/10.1021/la9503515.

[286] Cabrera, N. and Mott, N. F. Theory of the oxidation of metals. *Reports on Progress in Physics*, 12(1):163, January 1949. doi: 10.1088/0034-4885/12/1/308. URL https://iopscience.iop.org/article/10.1088/0034-4885/12/1/308.

[287] Adams, A. C. and Smith, T. E. and Chang, C. C. The Growth and Characterization of Very Thin Silicon Dioxide Films. *Journal of Electrochemical Society*, 127(8):1787, August 1980. doi: 10.1149/1.2130002. URL https://iopscience.iop.org/article/10.1149/1.2130002.

[288] Chen, J. and Qin, Z. and Shoesmith, D. W. Kinetics of Corrosion Film Growth on Copper in Neutral Chloride Solutions Containing Small Concentrations of Sulfide. *Journal of Electrochemical Society*, 157(10):C338, August 2010. doi: 10.1149/1.3478570. URL https://iopscience.iop.org/article/10.1149/1.3478570.

[289] CPP Scripts. Fortran vs C++: A Quick Comparison Guide, 2025. URL https://cppscripts.com/fortran-vs-cpp. [Accessed: 2nd Feburary 2025].

[290] Leetmaa, Mikael and Skorodumova, Natalia V. KMCLib: A general framework for lattice kinetic Monte Carlo (KMC) simulations. *Computional Physics Communications*, 185(9):2340–2349, September 2014. doi: 10.1016/j.cpc.2014.04.017. URL https://www.sciencedirect.com/science/article/pii/S0010465514001519.

[291] Morgan, Benjamin J. lattice_mc: A Python Lattice-Gas Monte Carlo Module. *Journal of Open Source Software*, 2(13):247, May 2017. doi: 10.21105/joss.00247. URL https://joss.theoj.org/papers/10.21105/joss.00247.

[292] Heiber, Michael C. KMC_Lattice v2.0: An Object-Oriented C++ Library for Custom Kinetic Monte Carlo Simulations. *Journal of Open Source Software*, 4(33):1168, January 2019. doi: 10.21105/joss.01168. URL https://joss.theoj.org/papers/10.21105/joss.01168.

[293] Heiber, Michael C. Excimontec v1.0: An Open-Source Software Tool for Kinetic Monte Carlo Simulations of Organic Electronic Devices. *Journal of Open Source Software*, 5(53):2307, September 2020. doi: 10.21105/joss.02307. URL https://joss.theoj.org/papers/10.21105/joss.02307.

[294] Jørgensen, Mikkel and Grönbeck, Henrik. MonteCoffee: A programmable kinetic Monte Carlo framework. *Journal of Chemical Physics*, 149(11), September 2018. doi: 10.1063/1.5046635. URL https://pubmed.ncbi.nlm.nih.gov/30243278/.

[295] Martin, Pablo and Gaitero, Juan J. and Dolado, Jorge S. and Manzano, Hegoi. KIMERA: A Kinetic Montecarlo Code for Mineral Dissolution. *Minerals*, 10(9):825, September 2020. ISSN 2075-163X. doi: 10.3390/min10090825. URL https://www.mdpi.com/2075-163X/10/9/825.

[296] Mitchell, John A. and Abdeljawad, Fadi and Battaile, Corbett and Garcia-Cardona, Cristina

and Holm, Elizabeth A. and Homer, Eric R. and Madison, Jon and Rodgers, Theron M. and Thompson, Aidan P. and Tikare, Veena and Webb, Ed and Plimpton, Steven J. Parallel simulation via SPPARKS of on-lattice kinetic and Metropolis Monte Carlo models for materials processing. *Modeling and Simulation in Materials Science and Engineering*, 31(5): 055001, May 2023. doi: 10.1088/1361-651X/accc4b. URL `https://iopscience.iop.org/article/10.1088/1361-651X/accc4b`.

[297] Reuter, Karsten and Savara, Aditya and Hoffmann, Max J. and Matera, Sebastian and Lorenzi, Juan M. and Andersen, Mie and Bajdich, Michal and Garhammer, Andreas. kmcos: Kinetic Monte Carlo of Systems, January 2020. URL `https://github.com/kmcos/kmcos`. [Accessed: 28th January 2025].

[298] Pasumarthi, Viswanath. Python-based Charge Dynamics (PyCD), January 2017. URL `https://github.com/vpasumarthi/PyCD/`. [Accessed: 28th January 2025].

[299] Grabowski, Frederic and Kochanczyk, Marek. VIS-A-VIS: agent-based simulator of viral infection spread and viral infection self-containment in a monolayer of cell, January 2022. URL `https://github.com/grfrederic/visavis`. [Accessed: 28th January 2025].

[300] Helleboid, Remi. MulSKIPS: A Kinetic Monte Carlo super-Lattice code, January 2021. URL `https://github.com/MulSKIPS/MulSKIPS`. [Accessed: 28th January 2025].

[301] Jansson, Ville. Kimocs - Kinetic Monte Carlo for Surfaces, January 2016. URL `https://gitlab.com/vjansson/Kimocs`. [Accessed: 28th January 2025].

[302] Nandipati, Giridhar. KSOME: Kinetic Simulations of Microstructural Evolution, January 2021. URL `https://gitlab.osti.gov/giridharnandipati/ksome`. [Accessed: 28th January 2025].

[303] Deng, Zeyu. kMCpy: Kinetic Monte Carlo Simulation using Python, January 2022. URL `https://github.com/caneparesearch/kMCpy`. [Accessed: 28th January 2025].

[304] Alberdi, Joseba and Albi, Julen. Morphokinetics, January 2018. URL `https://github.com/dipc-cc/Morphokinetics`. [Accessed: 28th January 2025].

[305] Chill, Samuel T. and Welborn, Matthew and Terrell, Rye and Zhang, Liang and Berthet, Jean-Claude and Pedersen, Andreas and Jónsson, Hannes and Henkelman, Graeme. EON: software for long time simulations of atomic scale systems. *Modeling and Simulation in Materials Science and Engineering*, 22(5):055002, May 2014. doi: 10.1088/0965-0393/22/5/055002. URL `https://iopscience.iop.org/article/10.1088/0965-0393/22/5/055002`.

[306] Van Swygenhoven, Helena and Weertman, Julia R. Deformation in nanocrystalline metals. *Materials Today*, 9(5):24–31, May 2006. doi: 10.1016/S1369-7021(06)71494-8. URL `https://www.sciencedirect.com/science/article/pii/S1369702106714948`.

[307] Barhaghi, Mohammad Soroush and Crawford, Brad and Schwing, Gregory and Hardy, David J. and Stone, John E. and Schwiebert, Loren and Potoff, Jeffrey and Tajkhor-

shid, Emad. py-MCMD: Python Software for Performing Hybrid Monte Carlo/Molecular Dynamics Simulations with GOMC and NAMD. *Journal of Chemical Theory and Computation*, 18(8):4983–4994, August 2022. doi: 10.1021/acs.jctc.1c00911. URL https://pubs.acs.org/doi/10.1021/acs.jctc.1c00911.

[308] Nejahi, Younes and Barhaghi, Mohammad Soroush and Mick, Jason and Jackman,Brock and Rushaidat, Kamel and Li, Yuanzhe and Schwiebert, Loren and Potoff, Jeffrey. GOMC: GPU Optimized Monte Carlo for the simulation of phase equilibria and physical properties of complex fluids. *SoftwareX*, 9:20–27, 2019. doi: 10.1016/j.softx.2018.11.005. URL https://www.sciencedirect.com/science/article/pii/S2352711018301171.

[309] James C. Phillips, David J. Hardy, Julio D. C. Maia, John E. Stone, João V. Ribeiro, Rafael C. Bernardi, Ronak Buch, Giacomo Fiorin, Jérôme Hénin, Wei Jiang, Ryan McGreevy, Marcelo C. R. Melo, Brian K. Radak, Robert D. Skeel, Abhishek Singharoy, Yi Wang, Benoît Roux, Aleksei Aksimentiev, Zaida Luthey-Schulten, Laxmikant V. Kalé, Klaus Schulten, Christophe Chipot, and Emad Tajkhorshid. Scalable molecular dynamics on CPU and GPU architectures with NAMD. *Journal of Chemical Physics*, 153(4), July 2020. doi: 10.1063/5.0014475. URL https://pubs.aip.org/aip/jcp/article-abstract/153/4/044130/1064953/.

[310] Martin, Marcus G. and Siepmann, J. Ilja. Novel Configurational-Bias Monte Carlo Method for Branched Molecules. Transferable Potentials for Phase Equilibria. 2. United-Atom Description of Branched Alkanes. *Journal of Physical Chemistry B*, 103(21):4508–4517, May 1999. doi: 10.1021/jp984742e. URL https://pubs.acs.org/doi/10.1021/jp984742e.

[311] Chen, Yunjie and Roux, Benoît. Generalized Metropolis acceptance criterion for hybrid nonequilibrium molecular dynamics—Monte Carlo simulations. *Journal of Chemical Physics*, 142(2), January 2015. doi: 10.1063/1.4904889. URL https://pubs.aip.org/aip/jcp/article-abstract/142/2/024101/605217/.

[312] The MPI Forum, CORPORATE. MPI: a message passing interface. In *Proceedings of the 1993 ACM/IEEE Conference on Supercomputing*, Supercomputing '93, page 878–883, New York, NY, USA, 1993. Association for Computing Machinery. doi: 10.1145/169627.169855. URL https://doi.org/10.1145/169627.169855.

[313] Plimpton, Steve. Fast Parallel Algorithms for Short-Range Molecular Dynamics. *Journal of Computational Physics*, 117(1):1–19, March 1995. doi: 10.1006/jcph.1995.1039. URL https://www.sciencedirect.com/science/article/pii/S002199918571039X.

[314] Ewen, James P. and Spikes, Hugh A. and Dini, Daniele. Contributions of Molecular Dynamics Simulations to Elastohydrodynamic Lubrication. *Tribology Letters*, 69(1):24–15, February 2021. doi: 10.1007/s11249-021-01399-w. URL https://doi.org/10.1007/s11249-021-01399-w.

[315] Ayestarán Latorre, Carlos and Remias, Joseph E. and Moore, Joshua D. and Spikes, Hugh A. and Dini, Daniele and Ewen, James P. Mechanochemistry of phosphate esters confined

between sliding iron surfaces. *Communications Chemistry*, 4(178):1–11, December 2021. doi: 10.1038/s42004-021-00615-x. URL https://doi.org/10.1038/s42004-021-00615-x.

[316] James, F. A review of pseudorandom number generators. *Computer Physics Communications*, 60(3):329–344, October 1990. doi: 10.1016/0010-4655(90)90032-V. URL https://www.sciencedirect.com/science/article/pii/001046559090032V.

[317] C++ reference. C++ reference, 2024. URL https://en.cppreference.com/w/. [Accessed: 9th Feburary 2025].

[318] Ryckaert, Jean-Paul and Ciccotti, Giovanni and Berendsen, Herman J. C. Numerical-Integration of Cartesian Equations of Motion of a System with Constraints – Molecular-Dynamics of N-Alkanes. *Journal of Computational Physics*, 23(3):327–341, March 1977. doi: 10.1016/0021-9991(77)90098-5. URL https://www.sciencedirect.com/science/article/abs/pii/0021999177900985?via%3Dihub.

[319] Braun, Jürgen. *Additives*, chapter 6, pages 117–152. John Wiley & Sons, Ltd, 2017. doi: https://doi.org/10.1002/9783527645565.ch6. URL https://onlinelibrary.wiley.com/doi/abs/10.1002/9783527645565.ch6.

[320] Weckman, Timo and Shirazi, Mahdi and Elliott, Simon D. and Laasonen, Kari. Kinetic Monte Carlo Study of the Atomic Layer Deposition of Zinc Oxide. *Journal of Physical Chemistry C*, 122(47):27044–27058, November 2018. doi: 10.1021/acs.jpcc.8b06909. URL https://doi.org/10.1021/acs.jpcc.8b06909.

[321] Daw, Murray S. and Foiles, Stephen M. and Baskes, Michael I. The embedded-atom method: a review of theory and applications. *Materials Science Reports*, 9(7):251–310, March 1993. doi: 10.1016/0920-2307(93)90001-U. URL https://www.sciencedirect.com/science/article/pii/092023079390001U.

[322] Tersoff, J. New empirical approach for the structure and energy of covalent systems. *Physical Review B*, 37(12):6991 – 7000, 1988. doi: 10.1103/PhysRevB.37.6991. URL https://journals.aps.org/prb/abstract/10.1103/PhysRevB.37.6991.

[323] Brenner, Donald W. and Shenderova, Olga A. and Harrison, Judith A. and Stuart, Steven J. and Ni, Boris and Sinnott, Susan B. A second-generation reactive empirical bond order (REBO) potential energy expression for hydrocarbons. *Journal of Physics Condensed Matter*, 14(4):783 – 802, 2002. doi: 10.1088/0953-8984/14/4/312. URL https://iopscience.iop.org/article/10.1088/0953-8984/14/4/312.

[324] Stuart, Steven J. and Tutein, Alan B. and Harrison, Judith A. A reactive potential for hydrocarbons with intermolecular interactions. *Journal of Chemical Physics*, 112(14):6472 – 6486, 2000. doi: 10.1063/1.481208. URL https://doi.org/10.1063/1.481208.

[325] Friederich, Pascal and Häse, Florian and Proppe, Jonny and Aspuru-Guzik, Alán. Machine-learned potentials for next-generation matter simulations. *Nature Materials*, 20:750–761, 2021. doi: 10.1038/s41563-020-0777-6. URL https://www.nature.com/articles/

s41563-020-0777-6.

[326] Aberle, Armin G. Thin-film solar cells. *Thin Solid Films*, 517:4706–4710, 7 2009. doi: 10.1016/j.tsf.2009.03.056. URL https://www.sciencedirect.com/science/article/pii/S0040609009005124.

[327] Luiz, Juli Felicio and Spikes, Hugh. Tribofilm Formation, Friction and Wear-Reducing Properties of Some Phosphorus-Containing Antiwear Additives. *Tribology Letters*, 68(3): 75–24, July 2020. doi: 10.1007/s11249-020-01315-8. URL https://doi.org/10.1007/s11249-020-01315-8.

[328] Sun, C. Y. and Peng, B. Z. and Dandekar, A. and Ma, Q. L. and Chen, G. J. Studies on hydrate film growth. *Annual Reports Section "C" (Physical Chemistry)*, 106:77–100, June 2010. doi: 10.1039/B811053K. URL http://dx.doi.org/10.1039/B811053K.

[329] Morrissy, Shane A. and McKenzie, Angus J. and Graham, Brendan F. and Johns, Michael L. and May, Eric F. and Aman, Zachary M. Reduction of Clathrate Hydrate Film Growth Rate by Naturally Occurring Surface Active Components. *Energy Fuels*, 31(6):5798–5805, June 2017. doi: 10.1021/acs.energyfuels.6b02942. URL https://pubs.acs.org/doi/10.1021/acs.energyfuels.6b02942.

[330] Ahmad, Ehsan A. and Chang, Hao-Yeh and Al-Kindi, Mohammed and Joshi, Gaurav R. and Cooper, Karyn and Lindsay, Robert and Harrison, Nicholas M. Corrosion Protection through Naturally Occurring Films: New Insights from Iron Carbonate. *ACS Applied Material Interfaces*, 11:33435–33441, 2019. doi: 10.1021/acsami.9b10221. URL https://pubs.acs.org/doi/10.1021/acsami.9b10221.

[331] Ntioudis, Stavros and Ewen, James P. and Dini, Daniele and Turner, C. Heath. PAPRECA, January 2024. URL https://github.com/sntioudis/papreca. [Accessed: 20th January 2025].

[332] Tavenner, Jacob P. and Mendelev, Mikhail I. and Lawson, John W. Molecular dynamics based kinetic Monte Carlo simulation for accelerated diffusion. *Computational Materials Science*, 218:111929, February 2023. doi: 10.1016/j.commatsci.2022.111929. URL https://www.sciencedirect.com/science/article/pii/S0927025622006401.

[333] Lennard-Jones, John. Efficient 'universal' shifted Lennard-Jones model for all KIM API supported species developed by Elliott and Akerson (2015) v003, 2018. URL https://doi.org/10.25950/962b4967.

[334] Engineering Toolbox. Motor Oils - Dynamic Viscosities, 2011. URL https://www.engineeringtoolbox.com/dynamic-viscosity-motor-oils-d_1759.html. [Accessed: 2nd March 2025].

[335] Reed-Hill, Robert E. and Abbaschian, Reza. *Physical metallurgy principles* . PWS-Kent Pub, Boston, Mass, 3rd ed. edition, 1992. ISBN 0534921736. URL https://www.nrc.gov/docs/ML1533/ML15337A236.pdf.

[336] Schneider, T. and Stoll, E. Molecular-dynamics study of a three-dimensional one-component model for distortive phase transitions. *Physical Review B*, 17:1302–1322, Feb 1978. doi: 10.1103/PhysRevB.17.1302. URL https://link.aps.org/doi/10.1103/PhysRevB.17.1302.

[337] Pranami, Gaurav and Lamm, Monica H. Estimating Error in Diffusion Coefficients Derived from Molecular Dynamics Simulations. *Journal of Chemical Theory and Computation*, 11 (10):4586–4592, 2015. doi: 10.1021/acs.jctc.5b00574. URL https://doi.org/10.1021/acs.jctc.5b00574.

[338] Battaile, Corbett C. and Srolovitz, David J. Kinetic Monte Carlo Simulation of Chemical Vapor Deposition. *Annual Review of Materials Research*, 32:297–319, 2002. doi: 10.1146/annurev.matsci.32.012102.110247. URL https://www.annualreviews.org/content/journals/10.1146/annurev.matsci.32.012102.110247.

[339] Gissinger, Jacob R. and Jensen, Benjamin D. and Wise, Kristopher E. Molecular modeling of reactive systems with REACTER. *Computer Physics Communications*, 304:109287, 2024. ISSN 0010-4655. doi: 10.1016/j.cpc.2024.109287. URL https://www.sciencedirect.com/science/article/pii/S0010465524002108.

[340] Dresel, Wilfried. *Synthetic Base Oils*, chapter 5, pages 83–116. John Wiley & Sons, Ltd, 2017. doi: 10.1002/9783527645565.ch5. URL https://onlinelibrary.wiley.com/doi/abs/10.1002/9783527645565.ch5.

[341] Shields, Benjamin J. and Stevens, Jason and Li, Jun and Parasram, Marvin and Damani, Farhan and Alvarado, Jesus I. Martinez and Janey, Jacob M. and Adams, Ryan P. and Doyle, Abigail G. Bayesian reaction optimization as a tool for chemical synthesis. *Nature*, 590(7844):89–96, 2021. doi: 10.1038/s41586-021-03213-y. URL https://doi.org/10.1038/s41586-021-03213-y.

Appendices

Appendix A: Example PAPRECA input files: Phosphate Film Growth from TCP on Fe110

```
#Basic settings
KMC_steps 20000 #total number of kMC stages
KMC_per_MD 10 #frequency of executed MD stages
random_seed 1234124
fluid_atomtypes 7 2 3 4 5 6 7 8 #sets types of mobile atoms in the MD stage
frozen_atomtypes 1 1 #sets types of frozen atoms in the MD stage

#Height Calculation and desorption
height_calculation mass_bins 0.94 1.0 #sets height calculation method with bins
desorption 20 LAMMPS_region #deletes disconnected (by 20 angstroms) atoms

#Sigmas for types
sigmas_options LAMMPS #retrieves equilibrium interatomic distances from LAMMPS

#Set max bonds for types
species_maxbonds 1 3 #Fe surface
species_maxbonds 2 2 #C_3
species_maxbonds 3 2 #C_R
species_maxbonds 4 2 #O single-bonded
species_maxbonds 5 4 #P
species_maxbonds 6 2 #O double-bonded
species_maxbonds 7 1 #Hydrogen
species_maxbonds 8 6 #Fe film

#Set max bonds of specific bond type for atom types
species_maxbondtypes 4 10 1 #Single-bonded oxygen with surface irons
species_maxbondtypes 6 10 1 #Double-bonded oxygen with surface irons

#Equilibration
minimize_prior yes minimize 1.0e-3 1.0e-5 100 1000 #minimisation before MD stage
minimize_after yes minimize 1.0e-3 1.0e-5 100 1000 #minimisation after MD stage
```

```
trajectory_duration 200 #total timesteps for each MD stage

#Predefined events

#Bond-breakings
create_BondBreak 4 5 7 rate_arrhenius 13.68 6.99e10 528.15 catalyzed 2 1 8
create_BondBreak 3 4 6 rate_arrhenius 20.54 1.56e10 528.15 catalyzed 2 1 8

#Bond-formations
create_BondForm 5 4 8 3.7588562 no no no rate_manual 1.0e13
create_BondForm 5 6 9 3.7588562 no no no rate_manual 1.0e13
create_BondForm 1 4 10 3.9315243 no no no rate_manual 1.0e13
create_BondForm 1 6 10 3.9315243 no no no rate_manual 1.0e13
create_BondForm 8 4 11 3.9315243 no no no rate_manual 1.0e13
create_BondForm 8 6 11 3.9315243 no no no rate_manual 1.0e13
create_BondForm 4 4 12 3.4045958 yes yes yes rate_manual 1.0e13

#Diffusion hops
create_DiffusionHop 1 0.0 4.14468 no 8 rate_arrhenius 11.53 1.4e13 528.15 custom
↪  Fe_4PO4neib 1 5
random_diffvecs no

#Depositions
create_Deposition 1 3.60259 0.00 mmmTCP rate_hertz 0.0001 7.640648 368.37 528.15
↪  sticking_coeff variable
create_Deposition 2 3.34563 0.00 mmmTCP rate_hertz 0.0001 7.640648 368.37 528.15
↪  sticking_coeff variable
create_Deposition 3 3.34563 0.00 mmmTCP rate_hertz 0.0001 7.640648 368.37 528.15
↪  sticking_coeff variable
create_Deposition 4 3.13315 0.00 mmmTCP rate_hertz 0.0001 7.640648 368.37 528.15
↪  sticking_coeff variable
create_Deposition 5 3.44877 0.00 mmmTCP rate_hertz 0.0001 7.640648 368.37 528.15
↪  sticking_coeff variable
create_Deposition 6 3.13315 0.00 mmmTCP rate_hertz 0.0001 7.640648 367.37 528.15
↪  sticking_coeff variable
create_Deposition 7 3.03830 0.00 mmmTCP rate_hertz 0.0001 7.640648 367.37 528.15
↪  sticking_coeff variable
create_Deposition 8 3.60259 0.00 mmmTCP rate_hertz 0.0001 7.640648 368.37 528.15
↪  sticking_coeff variable
depoheights 5 20
random_depovecs no

#File Exports
```

```
export_HeightVtime 10
export_ElementalDistributions 500 bin_width 1.0
export_ExecutionTimes 1
```

Appendix B: Analytic solution for non-reactive monolayer surface coverage

An analytic solution for the monolayer surface coverage can be derived by assuming non-interacting surface species and uncorrelated adsorption as well as desorption events. Under these assumptions, the temporal evolution of surface coverage can be described by the following differential equation:

$$\frac{d\theta}{dt} = r_a(1-\theta) - r_d\theta \tag{1}$$

With $\theta(t)$ representing the surface coverage (i.e., the ratio of occupied to total system sites $\theta = \frac{n_{occ}}{n_{total}}$) and r_a as well as r_d being the adsorption and desorption rates, respectively. Effectively, this equation expresses a mass balance and states that the accumulation of particles in the system (i.e., $\frac{d\theta}{dt}$) is linked to the difference between the input (i.e., r_a for adsorption) and output (i.e., r_d for desorption) rates. Note that the input rate is scaled by $(1-\theta)$ as the lower the surface coverage the greater the number of available sites for deposition. In contrast, the output rate scales directly with the surface coverage (i.e., $\theta_{out} = r_d\theta$) since solely deposited atoms can subsequently desorb through monoatomic desorption events. In any case, Eq. 1 can be manipulated as below:

$$\frac{d\theta}{dt} + (r_a + r_d)\theta = r_a \tag{2}$$

This is a non-homogeneous differential equation with a general solution of:

$$\theta(t) = \theta_h + \theta_p \tag{3}$$

Here, θ_h and θ_p represent the homogeneous and particular solutions, respectively. Firstly, we begin by solving the homogeneous equation:

$$\frac{d\theta_h}{dt} + \theta_h(r_a + r_d) = 0 \Rightarrow d\theta_h \frac{1}{\theta_h} = -(r_a + r_d)dt \Rightarrow \int \frac{1}{\theta_h} d\theta_h = \int -(r_a + r_d)dt \Rightarrow \tag{4}$$

$$\Rightarrow \ln\theta_h = -(r_a + r_d)t + C \Rightarrow \theta_h = e^{-(r_a+r_d)t+C} \Rightarrow \theta_h = Ce^{-(r_a+r_d)t}$$

For the particular equation, we assume the following solution:

$$\theta_p = \nu(t)e^{-(r_a+r_d)t} \tag{5}$$

Where $\nu(t)$ is a function that has to be determined. Now, we substitute Eq. 5 to Eq. 2:

$$\frac{d(\nu(t)e^{-(r_a+r_d)t})}{dt} + (r_a + r_b)\nu(t)e^{-(r_a+r_d)t} = r_a \Rightarrow \tag{6}$$

$$\Rightarrow \frac{d\nu(t)}{dt}e^{-(r_a+r_d)t} - (r_a + r_d)\nu(t)e^{-(r_a+r_d)t} + (r_a + r_d)\nu(t)e^{-(r_a+r_d)t} = r_a \Rightarrow$$

$$\Rightarrow \frac{d\nu(t)}{dt}e^{-(r_a+r_d)t} = r_a \Rightarrow \nu(t) = \int r_a e^{(r_a+r_d)t}dt \Rightarrow \nu(t) = \frac{r_a}{r_a + r_d}e^{(r_a+r_d)t}$$

At this point we can substitute $\nu(t)$ (as derived in Eq. 6) to Eq. 5 and obtain a solution for θ_p:

$$\theta_p = \frac{r_a}{r_a + r_d} \tag{7}$$

Finally, the total solution for $\theta(t)$ is retrieved by substituting the homogeneous and particular solutions (from Eq. 4 and 7) to Eq. 3:

$$\theta(t) = \frac{r_a}{r_a + r_d} + Ce^{-(r_a+r_d)t} \tag{8}$$

Note that $\theta(t = 0) = 0$. Consequently:

$$C = -\frac{r_a}{r_a + r_d} \tag{9}$$

Hence:

$$\theta(t) = \frac{r_a}{r_a + r_d}(1 - e^{-(r_a+r_d)t}) \tag{10}$$

A steady state solution for Eq. 10 can be obtained by calculating the limit of $\theta(t)$ as $t \to \infty$:

$$\lim_{t\to\infty} \theta(t) = \frac{r_a}{r_a + r_d} \tag{11}$$

Appendix C: Decomposition of TCP on iron: Growth profiles for hopping distance of 5.14468 Å

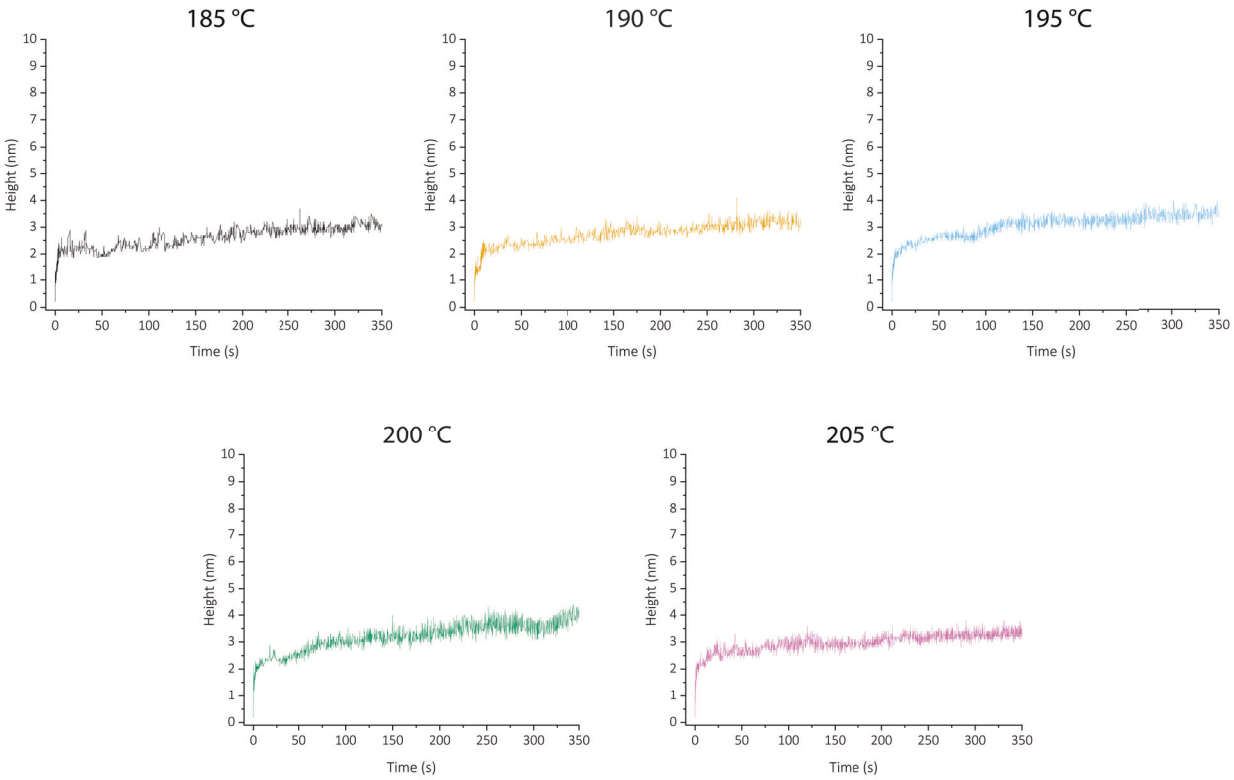


Fig. C.1: Height versus time for different temperatures with a diffusion hopping distance for substrate iron atoms (ΔL_k) fixed at 5.14468 Å. Results from the refined model for the study of the thermal decomposition of TCP on iron (see Chapter 6).

Appendix D: Copies of permission documents to reproduce copyrighted material

16/4/25, 12:14 μ.μ. RightsLink Printable License

ELSEVIER LICENSE
TERMS AND CONDITIONS

Apr 16, 2025

This Agreement between Stavros Ntioudis, Imperial College London ("You") and Elsevier ("Elsevier") consists of your license details and the terms and conditions provided by Elsevier and Copyright Clearance Center.

License Number	6010740428372
License date	Apr 16, 2025
Licensed Content Publisher	Elsevier
Licensed Content Publication	Tribology International
Licensed Content Title	In situ, real time studies of thermal reaction film formation temperatures for iron and 304SS surfaces immersed in 5% tricresyl phosphate in base oil
Licensed Content Author	B. Acharya,T.N. Pardue,K.S. Avva,J. Krim
Licensed Content Date	Oct 1, 2018

https://s100.copyright.com/AppDispatchServlet 1/10

Licensed Content Volume	126
Licensed Content Issue	n/a
Licensed Content Pages	10
Start Page	106
End Page	115
Type of Use	reuse in a thesis/dissertation
Portion	figures/tables/illustrations
Number of figures/tables/illustrations	1
Format	both print and electronic
Are you the author of this Elsevier article?	No
Will you be translating?	No
Title of new work	A multiscale modelling framework to capture atomically resolved interfacial processes at experimentally relevant timescales

Institution name	Imperial College london
Expected presentation date	Jun 2025
Portions	Fig. 7
The Requesting Person / Organization to Appear on the License	Stavros Ntioudis, Imperial College London
Requestor Location	Mr. Stavros Ntioudis Requestor's Address (confidential) Requestor's Address (confidential) United Kingdom
Publisher Tax ID	GB 494 6272 12
Total	0.00 GBP

Terms and Conditions

INTRODUCTION

1. The publisher for this copyrighted material is Elsevier. By clicking "accept" in connection with completing this licensing transaction, you agree that the following terms and conditions apply to this transaction (along with the Billing and Payment terms and conditions established by Copyright Clearance Center, Inc. ("CCC"), at the time that you opened your RightsLink account and that are available at any time at https://myaccount.copy_right.com).

GENERAL TERMS

2. Elsevier hereby grants you permission to reproduce the aforementioned material subject to the terms and conditions indicated.

3. Acknowledgement: If any part of the material to be used (for example, figures) has appeared in our publication with credit or acknowledgement to another source, permission must also be sought from that source. If such permission is not obtained then that material may not be included in your publication/copies. Suitable acknowledgement to the source must be made, either as a footnote or in a reference list at the end of your publication, as follows:

"Reprinted from Publication title, Vol /edition number, Author(s), Title of article/ title of chapter, Pages No., Copyright (Year), with permission from Elsevier [OR APPLICABLE SOCIETY COPYRIGHT OWNER]." Also Lancet special credit- "Reprinted from The Lancet, Vol. number, Author(s), Title of article, Pages No., Copyright (Year), with permission from Elsevier."

4. Reproduction of this material is confined to the purpose and/or media for which permission is hereby given. The material may not be reproduced or used in any other way, including use in combination with an artificial intelligence tool (including to train an algorithm, test, process, analyse, generate output and/or develop any form of artificial intelligence tool), or to create any derivative work and/or service (including resulting from the use of artificial intelligence tools).

5. Altering/Modifying Material: Not Permitted. However figures and illustrations may be altered/adapted minimally to serve your work. Any other abbreviations, additions, deletions and/or any other alterations shall be made only with prior written authorization of Elsevier Ltd. (Please contact Elsevier's permissions helpdesk here). No modifications can be made to any Lancet figures/tables and they must be reproduced in full.

6. If the permission fee for the requested use of our material is waived in this instance, please be advised that your future requests for Elsevier materials may attract a fee.

7. Reservation of Rights: Publisher reserves all rights not specifically granted in the combination of (i) the license details provided by you and accepted in the course of this licensing transaction, (ii) these terms and conditions and (iii) CCC's Billing and Payment terms and conditions.

8. License Contingent Upon Payment: While you may exercise the rights licensed immediately upon issuance of the license at the end of the licensing process for the transaction, provided that you have disclosed complete and accurate details of your proposed use, no license is finally effective unless and until full payment is received from

you (either by publisher or by CCC) as provided in CCC's Billing and Payment terms and conditions. If full payment is not received on a timely basis, then any license preliminarily granted shall be deemed automatically revoked and shall be void as if never granted. Further, in the event that you breach any of these terms and conditions or any of CCC's Billing and Payment terms and conditions, the license is automatically revoked and shall be void as if never granted. Use of materials as described in a revoked license, as well as any use of the materials beyond the scope of an unrevoked license, may constitute copyright infringement and publisher reserves the right to take any and all action to protect its copyright in the materials.

9. Warranties: Publisher makes no representations or warranties with respect to the licensed material.

10. Indemnity: You hereby indemnify and agree to bold harmless publisher and CCC, and their respective officers, directors, employees and agents, from and against any and all claims arising out of your use of the licensed material other than as specifically authorized pursuant to this license.

11. No Transfer of License: This license is personal to you and may not be sublicensed, assigned, or transferred by you to any other person without publisher's written permission.

12. No Amendment Except in Writing: This license may not be amended except in a writing signed by both parties (or, in the case of publisher, by CCC on publisher's behalf).

13. Objection to Contrary Terms: Publisher hereby objects to any terms contained in any purchase order, acknowledgment, check endorsement or other writing prepared by you, which terms are inconsistent with these terms and conditions or CCC's Billing and Payment terms and conditions. These terms and conditions, together with CCC's Billing and Payment terms and conditions (which are incorporated herein), comprise the entire agreement between you and publisher (and CCC) concerning this licensing transaction. In the event of any conflict between your obligations established by these terms and conditions and those established by CCC's Billing and Payment terms and conditions, these terms and conditions shall control.

14. Revocation: Elsevier or Copyright Clearance Center may deny the permissions described in this License at their sole discretion, for any reason or no reason, with a full refund payable to you. Notice of such denial will be made using the contact information provided by you. Failure to receive such notice will not alter or invalidate the denial. In no event will Elsevier or Copyright Clearance Center be responsible or liable for any costs, expenses or damage incurred by you as a result of a denial of your permission

16/4/25, 12:14 µ.µ. Rightslink Printable License

request, other than a refund of the amount(s) paid by you to Elsevier and/or Copyright Clearance Center for denied permissions.

LIMITED LICENSE

The following terms and conditions apply only to specific license types:

15. **Translation:** This permission is granted for non-exclusive world **English** rights only unless your license was granted for translation rights. If you Licensed translation rights you may only translate this content into the languages you requested. A professional translator must perform all translations and reproduce the content word for word preserving the integrity of the article.

16. **Posting licensed content on any Website:** The following terms and conditions apply as follows: Licensing material from an Elsevier journal: All content posted to the web site must maintain the copyright information line on the bottom of each image; A h$_{y\,p}$ er-text must be included to the Homepage of the journal from which you are licensing at http://www.sciencedirect.com/science/journal/xxxxx or the Elsevier homepage for books at h11P-://www.elsevier.com; Central Storage: This license does not include permission for a scanned version of the material to be stored in a central repository such as that provided by Heron/XanEdu.

Licensing material from an Elsevier book: A hyper-text link must be included to the Elsevier homepage at h11P-://www.elsevier.com. All content posted to the web site must maintain the copyright information line on the bottom of each image.

Posting licensed content on Electronic reserve: In addition to the above the following clauses are applicable: The web site must be password-protected and made available only to bona fide students registered on a relevant course. This permission is granted for 1 year only. You may obtain a new license for future website posting.

17. **For journal authors:** the following clauses are applicable in addition to the above:

Preprints:

A preprint is an author's own write-up of research results and analysis, it has not been peer-reviewed, nor has it bad any other value added to it by a publisher (such as formatting, copyright, technical enhancement etc.).

Authors can share their preprints anywhere at any time. Preprints should not be added to or enhanced in any way in order to appear more like, or to substitute for, the final versions

https://s100.copyright.com/AppDispatchServlet 6/10

16/4/25, 12:14 μ.μ. Rightslink Printable License

of articles however authors can update their preprints on arXiv or RePEc with their Accepted Author Manuscript (see below).

If accepted for publication, we encourage authors to link from the preprint to their formal publication via its DOI. Millions of researchers have access to the formal publications on ScienceDirect, and so links will help users to find, access, cite and use the best available version. Please note that Cell Press, The Lancet and some society-owned have different preprint policies. Information on these policies is available on the journal homepage.

Accepted Author Manuscripts: An accepted author manuscript is the manuscript of an article that has been accepted for publication and which typically includes author-incorporated changes suggested during submission, peer review and editor-author communications.

Authors can share their accepted author manuscript:

- immediately
  - via their non-commercial person homepage or blog
  - by updating a preprint in arXiv or RePEc with the accepted manuscript
  - via their research institute or institutional repository for internal institutional uses or as part of an invitation-only research collaboration work-group
  - directly by providing copies to their students or to research collaborators for their personal use
  - for private scholarly sharing as part of an invitation-only work group on commercial sites with which Elsevier has an agreement
- After the embargo period
  - via non-commercial hosting platforms such as their institutional repository
  - via commercial sites with which Elsevier has an agreement

In all cases accepted manuscripts should:

- link to the formal publication via its DOI
- bear a CC-BY-NC-ND license - this is easy to do
- if aggregated with other manuscripts, for example in a repository or other site, be shared in alignment with our hosting policy not be added to or enhanced in any way to appear more like, or to substitute for, the published journal article.

Published journal article **(JPA):** A published journal article (PJA) is the definitive final record of published research that appears or will appear in the journal and embodies all value-adding publishing activities including peer review co-ordination, copy-editing, formatting, (if relevant) pagination and online enrichment.

https://s100.copyright.com/AppDispatchServlet 7/10

16/4/25, 12:14 µ.µ. Rightslink Printable License

Policies for sharing publishing journal articles differ for subscription and gold open access articles:

Subscrintion Articles: If you are an author, please share a link to your article rather than the full-text. Millions of researchers have access to the formal publications on ScienceDirect, and so links will help your users to find, access, cite, and use the best available version.

Theses and dissertations which contain embedded PJAs as part of the formal submission can be posted publicly by the awarding institution with DOI links back to the fonnal publications on ScienceDirect.

If you are affiliated with a library that subscribes to ScienceDirect you have additional private sharing rights for others' research accessed under that agreement. This includes use for classroom teaching and internal training at the institution (including use in course packs and courseware programs), and inclusion of the article for grant funding purposes.

Gold OP-en Access Articles: May be shared according to the author-selected end-user license and should contain a CrossMark logQ, the end user license, and a DOI link to the formal publication on ScienceDirect.

Please refer to Elsevier's gosting_policx for further information.

18. **For book authors** the following clauses are applicable in addition to the above: Authors are permitted to place a brief summary of their work online only. You are not allowed to download and post the published electronic version of your chapter, nor may you scan the printed edition to create an electronic version. **Posting to a repository:** Authors are permitted to post a summary of their chapter only in their institution's repository.

19. **Thesis/Dissertation:** If your license is for use in a thesis/dissertation your thesis may be submitted to your institution in either print or electronic form. Should your thesis be published commercially, please reapply for permission. These requirements include permission for the Library and Archives of Canada to supply single copies, on demand, of the complete thesis and include p e r ffssion for Proquest/UMl to supply single copies, on demand, of the complete thesis. Should your thesis be published commercially, please reapply for permission. Theses and dissertations which contain embedded PJAs as part of the formal submission can be posted publicly by the awarding institution with DOI links back to the formal publications on ScienceDirect.

https://s 100.copyright.com/AppDispatchServlet 8/10

16/4/25, 12:14 µ.µ. Rightslink Printable License

Elsevier Onen Access Terms and Conditions

You can publish open access with Elsevier in hundreds of open access journals or in nearly 2000 established subscription journals that support open access publishing. Permitted third party re-use of these open access articles is defined by the author's choice of Creative Commons user license. See our QP-en access license P-OlicY. for more information.

Terms & Conditions applicable to aU Open Access articles published with Elsevier:

Any reuse of the article must not represent the author as endorsing the adaptation of the article nor should the article be modified in such a way as to damage the author's honour or reputation. If any changes have been made, such changes must be clearly indicated.

The author(s) must be appropriately credited and we ask that you include the end user license and a DOI link to the formal publication on ScienceDirect.

If any part of the material to be used (for example, figures) has appeared in our publication with credit or acknowledgement to another source it is the responsibility of the user to ensure their reuse complies with the terms and conditions determined by the rights holder.

Additional Terms & Conditions applicable to each Creative Commons user license:

CC BY: The CC-BY license allows users to copy, to create extracts, abstracts and new works from the Article, to alter and revise the Article and to make commercial use of the Article (including reuse and/or resale of the Article by commercial entities), provided the user gives appropriate credit (with a link to the formal publication through the relevant DOI), provides a link to the license, indicates if changes were made and the licensor is not represented as endorsing the use made of the work. The full details of the license are available at httP-://creativecommons.orgLlicenseslbY./4.0.

CC BY NC SA: The CC BY-NC-SA license allows users to copy, to create extracts, abstracts and new works from the Article, to alter and revise the Article, provided this is not done for commercial purposes, and that the user gives appropriate credit (with a link to the formal publication through the relevant DOI), provides a link to the license, indicates if changes were made and the licensor is not represented as endorsing the use made of the work. Further, any new works must be made available on the same conditions. The full details of the license are available at htw://creativecommons.orgl!icenseslbY.-nc-sa/4.0.

https://s100.copyright.com/AppDispatchServlet 9/10

16/4/25, 12:14 μ.μ. Rightslink Printable License

CC BY NC ND: The CC BY-NC-ND license allows users to copy and distribute the Article, provided this is not done for commercial purposes and further does not permit distribution of the Article if it is changed or edited in any way, and provided the user gives appropriate credit (with a link to the formal publication through the relevant DOI), provides a link to the license, and that the licensor is not represented as endorsing the use made of the work. The full details of the license are available at ht:tp://creativecommons.orgl!icenses/by-nc-nd/4.0. Any commercial reuse of Open Access articles published with a CC BY NC SA or CC BY NC ND license requires permission from Elsevier and will be subject to a fee.

Commercial reuse includes:

- Associating advertising with the full text of the Article
- Charging fees for document delivery or access
- Article aggregation
- Systematic distribution via e-mail lists or share buttons

Posting or linking by commercial companies for use by customers of those companies.

20. **Other Conditions:**

v1.10

Questions? customercare@copyright.com.

https://s100.copyright.com/AppDispatchServlet 10/10

16/4/25, 1:19 μ.μ. Rightslink Printable License

ELSEVIER LICENSE
TERMS AND CONDITIONS

Apr16,2025

This Agreement between Stavros Ntioudis, Imperial College London ("You") and Elsevier ("Elsevier") consists of your license details and the terms and conditions provided by Elsevier and Copyright Clearance Center.

License Number	6010761433470
License date	Apr 16, 2025
Licensed Content Publisher	Elsevier
Licensed Content Publication	Computational Materials Science
Licensed Content Title	Kinetic Monte Carlo simulation of the effective diffusivity in grain boundary networks
Licensed Content Author	Jie Deng,Dane Morgan,Izabela Szlufarska
Licensed Content Date	Oct 1, 2014
Licensed Content Volume	93

https://s100.copyright.com/AppDispatchServlet 1/10

16/4/25, 1:19 μ.μ. Rightslink Printable License

Licensed Content Issue	n/a
Licensed Content Pages	10
Start Page	36
End Page	45
Type of Use	reuse in a thesis/dissertation
Portion	figures/tables/illustrations
Number of figures/tables/illustrations	1
Format	both print and electronic
Are you the author of this Elsevier article?	No
Will you be translating?	No
Title of new work	A multiscale modelling framework to capture atomically resolved interfacial processes at experimentally relevant timescales
Institution name	Imperial College london

https://s100.copyright.com/AppDispatchServlet 2/10

Expected presentation date	Jun2025
Portions	Fig. I.(a)
The Requesting Person I Organization to Appear on the L.1cense	Stavros Ntiouws, lmpena1Co1lege London
Requestor Location	Mr. Stavros Ntioudis Requestor's Address (confidential) Requestor's Address (confidential) United Kingdom
Publisher Tax ID	GB 494 6272 12
Total	0.O0GBP

Terms and Conditions

INTRODUCTION

1. The publisher for this copyrighted material is Elsevier. By clicking "accept" in connection with completing this licensing transaction, you agree that the following terms and conditions apply to this transaction (along with the Billing and Payment terms and conditions established by Copyright Clearance Center, Inc. ("CCC"), at the time that you opened your RightsLink account and that are available at any time at htrns://myaccount.copyright.com).

GENERAL TERJ."1S

2. Elsevier hereby grants you permission to reproduce the aforementioned material subject to the terms and conditions indicated.

3. Acknowledgement: If any part of the material to be used (for example, figures) has appeared in our publication with credit or acknowledgement to another source, permission must also be sought from that source. If such permission is not obtained then that material may not be included in your publication/copies. Suitable acknowledgement to the source must be made, either as a footnote or in a reference list at the end of your publication, as follows:

"Reprinted from Publication title, Vol /edition number, Author(s), Title of article/ title of chapter, Pages No., Copyright (Year), with permission from Elsevier [OR APPLICABLE SOCIETY COPYRIGHT OWNER]." Also Lancet special credit- "Reprinted from The Lancet, Vol. number, Author(s), Title of article, Pages No., Copyright (Year), with permission from Elsevier."

4. Reproduction of this material is confined to the purpose and/or media for which permission is hereby given. The material may not be reproduced or used in any other way, including use in combination with an artificial intelligence tool (including to train an algorithm, test, process, analyse, generate output and/or develop any form of artificial intelligence tool), or to create any derivative work and/or service (including resulting from the use of artificial intelligence tools).

5. Altering/Modifying Material: Not Permitted. However figures and illustrations may be altered/adapted minimally to serve your work. Any other abbreviations, additions, deletions and/or any other alterations shall be made only with prior written authorization of Elsevier Ltd. (Please contact Elsevier's permissions helpdesk here). No modifications can be made to any Lancet figures/tables and they must be reproduced in full.

6. If the permission fee for the requested use of our material is waived in this instance, please be advised that your future requests for Elsevier materials may attract a fee.

7. Reservation of Rights: Publisher reserves all rights not specifically granted in the combination of (i) the license details provided by you and accepted in the course of this licensing transaction, (ii) these terms and conditions and (iii) CCC's Billing and Payment terms and conditions.

8. License Contingent Upon Payment: While you may exercise the rights licensed immediately upon issuance of the license at the end of the licensing process for the transaction, provided that you have disclosed complete and accurate details of your proposed use, no license is finally effective unless and until full payment is received from you (either by publisher or by CCC) as provided in CCC's Billing and Payment terms and conditions. If full payment is not received on a timely basis, then any license preliminarily granted shall be deemed automatically revoked and shall be void as if never

granted. Further, in the event that you breach any of these terms and conditions or any of CCC's Billing and Payment terms and conditions, the license is automatically revoked and shall be void as if never granted. Use of materials as described in a revoked license, as well as any use of the materials beyond the scope of an unrevoked license, may constitute copyright infringement and publisher reserves the right to take any and all action to protect its copyright in the materials.

9. War anties: Publisher makes no representations or warranties with respect to the licensed material.

10. Indemnity: You hereby indemnify and agree to hold harmless publisher and CCC, and their respective officers, directors, employees and agents, from and against any and all claims arising out of your use of the licensed material other than as specifically authorized pursuant to this license.

11. No Transfer of License: This license is personal to you and may not be sublicensed, assigned, or transferred by you to any other person without publisher's written p e r ſssion.

12. No Amendment Except in Writing: This license may not be amended except in a writing signed by both parties (or, in the case of publisher, by CCC on publisher's behalf).

13. Objection to Contrary Terms: Publisher hereby objects to any terms contained in any purchase order, acknowledgment, check endorsement or other writing prepared by you, which terms are inconsistent with these terms and conditions or CCC's Billing and Payment terms and conditions. These terms and conditions, together with CCC's Billing and Payment terms and conditions (which are incorporated herein), comprise the entire agreement between you and publisher (and CCC) concerning this licensing transaction. In the event of any conflict between your obligations established by these terms and conditions and those established by CCC's Billing and Payment terms and conditions, these terms and conditions shall control.

14. Revocation: Elsevier or Copyright Clearance Center may deny the permissions described in this License at their sole discretion, for any reason or no reason, with a full refund payable to you. Notice of such denial will be made using the contact information provided by you. Failure to receive such notice will not alter or invalidate the denial. In no event will Elsevier or Copyright Clearance Center be responsible or liable for any costs, expenses or damage incurred by you as a result of a denial of your permission request, other than a refund of the amount(s) paid by you to Elsevier and/or Copyright Clearance Center for denied permissions.

LIMITED LICENSE

16/4/25, 1:19 μ.μ. Rightslink Printable License

The following terms and conditions apply only to specific license types:

15. **Translation:** This pennission is granted for non-exclusive world **English** rights only unless your license was granted for translation rights. If you licensed translation rights you may only translate this content into the languages you requested. A professional translator must perform all translations and reproduce the content word for word preserving the integrity of the article.

16. **Posting licensed content on any Website:** The following terms and conditions apply as follows: Licensing material from an Elsevier journal: All content posted to the web site must maintain the copyright information line on the bottom of each image; A h$_{y\ p}$ er-text must be included to the Homepage of the journal from which you are licensing at htm://www.sciencedirect.com/science/journal/xxxxx or the Elsevier homepage for books at htm://www.elsevier.com; Central Storage: This license does not include permission for a scanned version of the material to be stored in a central repository such as that provided by Heron/XanEdu.

Licensing material from an Elsevier book: A hyper-text link must be included to the Elsevier homepage at htm://www.elsevier.com . All content posted to the web site must maintain the copyright information line on the bottom of each image.

Posting licensed content on Electronic reserve: In addition to the above the following clauses are applicable: The web site must be password-protected and made available only to bona fide students registered on a relevant course. Tbjs permission is granted for 1 year only. You may obtain a new license for future website posting.

17. **For journal authors:** the following clauses are applicable in addition to the above:

Preprints:

A preprint is an author's own write-up of research results and analysis, it has not been peer-reviewed, nor has it had any other value added to it by a publisher (such as formatting, copyright, technical enhancement etc.).

Authors can share their preprints anywhere at any time. Preprints should not be added to or enhanced in any way in order to appear more like, or to substitute for, the final versions of articles however authors can update their preprints on arXiv or RePEc with their Accepted Author Manuscript (see below).

If accepted for publication, we encourage authors to link from the preprint to their formal publication via its DOI. Millions of researchers have access to the formal publications on

https://s100.copyright.com/AppDispatchServlet 6/10

16/4/25, 1:19 μ.μ. Rightslink Printable License

ScienceDirect, and so links will help users to find, access, cite and use the best available version. Please note that Cell Press, The Lancet and some society-owned have different preprint policies. Information on these policies is available on the journal homepage.

Accepted Author Manuscripts: An accepted author manuscript is the manuscript of an article that has been accepted for publication and which typically includes author-incorporated changes suggested during submission, peer review and editor-author communications.

Authors can share their accepted author manuscript:

- immediately
  - via their non-commercial person homepage or blog
  - by updating a preprint in arXiv or RePEc with the accepted manuscript
  - via their research institute or institutional repository for internal institutional uses or as part of an invitation-only research collaboration work-group
  - directly by providing copies to their students or to research collaborators for their personal use
  - for private scholarly sharing as part of an invitation-only work group on commercial sites with which Elsevier has an agreement
- After the embargo period
  - via non-commercial hosting platforms such as their institutional repository
  - via commercial sites with which Elsevier has an agreement

In all cases accepted manuscripts should:

- link to the formal publication via its DOI
- bear a CC-BY-NC-ND license - this is easy to do
- if aggregated with other manuscripts, for example in a repository or other site, be shared in alignment with our hosting policy not be added to or enhanced in any way to appear more like, or to substitute for, the published journal article.

Published journal article (JPA): A published journal article (PJA) is the definitive final record of published research that appears or will appear in the journal and embodies all value-adding publishing activities including peer review co-ordination, copy-editing, formatting, (if relevant) pagination and online enrichment.

Policies for sharing publishing journal articles differ for subscription and gold open access articles:

Subscrintion Articles: If you are an author, please share a link to your article rather than the full-text. Millions of researchers have access to the formal publications on

https://s100.copyright.com/AppDispatchServlet 7/10

16/4/25, 1:19 μ.μ. Rightslink Printable License

ScienceDirect, and so links will help your users to find, access, cite, and use the best available version.

Theses and dissertations which contain embedded PJAs as part of the formal submission can be posted publicly by the awarding institution with DOI links back to the formal publications on ScienceDirect.

If you are affiliated with a library that subscribes to ScienceDirect you have additional private sharing rights for others' research accessed under that agreement. Thjs includes use for classroom teaching and internal training at the institution (including use in course packs and courseware programs), and inclusion of the article for grant funding purposes.

Gold Onen Access Articles: May be shared according to the author-selected end-user license and should contain a CrossMark logQ, the end user license, and a DOI link to the formal publication on ScienceDirect.

Please refer to Elsevier's P-OstingP-olicY. for further information.

18. **For book authors** the following clauses are applicable in addition to the above: Authors are permitted to place a brief summary of their work online only. You are not allowed to download and post the published electronic version of your chapter, nor may you scan the printed edition to create an electronic version. **Posting to a repository:** Authors are permitted to post a summary of their chapter only in their institution's repository.

19. **Thesis/Dissertation:** If your license is for use in a thesis/dissertation your thesis may be submitted to your institution in either print or electronic form. Should your thesis be published commercially, please reapply for permission. These requirements include permission for the Library and Archives of Canada to supply single copies, on demand, of the complete thesis and include permission for Proquest/UMI to supply single copies, on demand, of the complete thesis. Should your thesis be published commercially, please reapply for permission. Theses and dissertations which contain embedded PJAs as part of the formal submission can be posted publicly by the awarding institution with DOI links back to the formal publications on ScienceDirect.

Elsevier Onen Access Terms and Conditions

You can publish open access with Elsevier in hundreds of open access journals or in nearly 2000 established subscription journals that support open access publishing. Permitted third party re-use of these open access articles is defined by the author's choice

https://s100.copyright.com/AppDispatchServlet 8/10

16/4/25, 1:19 μ.μ. Rightslink Printable License

of Creative Commons user license. See our Open access license policy_ for more information.

Terms & Conditions applicable to all Open Access articles published with Elsevier:

Any reuse of the article must not represent the author as endorsing the adaptation of the article nor should the article be modified in such a way as to damage the author's honour or reputation. If any changes have been made, such changes must be clearly indicated.

The author(s) must be appropriately credited and we ask that you include the end user license and a DOI link to the formal publication on ScienceDirect.

If any part of the material to be used (for example, figures) has appeared in our publication with credit or acknowledgement to another source it is the responsibility of the user to ensure their reuse complies with the terms and conditions determined by the rights holder.

Additional Terms & Conditions applicable to each Creative Commons user license:

CC BY: The CC-BY license allows users to copy, to create extracts, abstracts and new works from the Article, to alter and revise the Article and to make commercial use of the Article (including reuse and/or resale of the Article by commercial entities), provided the user gives appropriate credit (with a link to the formal publication through the relevant DOI), provides a link to the license, indicates if changes were made and the licensor is not represented as endorsing the use made of the work. The full details of the license are available at htm://creativecornmons.org/licenses/by_/4.0.

CC BY NC SA: The CC BY-NC-SA license allows users to copy, to create extracts, abstracts and new works from the Article, to alter and revise the Article, provided this is not done for commercial purposes, and that the user gives appropriate credit (with a link to the formal publication through the relevant DOI), provides a link to the license, indicates if changes were made and the licensor is not represented as endorsing the use made of the work. Further, any new works must be made available on the same conditions. The full details of the license are available at htm://creativecommons.orgllicenses/by_-nc-sa/4.0.

CC BY NC ND: The CC BY-NC-ND license allows users to copy and distíbute the Article, provided this is not done for commercial purposes and further does not permit distribution of the Article if it is changed or edited in any way, and provided the user gives appropriate credit (with a link to the formal publication through the relevant DOI), provides a link to the license, and that the licensor is not represented as endorsing the use made of the work. The full details of the license are available at

https://s100.copyright.com/AppDispatchServlet 9/10

htm://creativecommons.orgl!icensesfbY.-nc-nd/4.0. Any commercial reuse of Open Access articles published with a CC BY NC SA or CC BY NC ND license requires permission from Elsevier and will be subject to a fee.

Commercial reuse includes:

- Associating advertising with the full text of the Article
- Charging fees for document delivery or access
- Article aggregation
- Systematic distribution via e-mail lists or share buttons

Posting or linking by commercial companies for use by customers of those companies.

20. Other Conditions:

vl.10

Questions? customercare@copY-right.com.

16/4/25, 1:23 μ.μ. Rightslink Printable License

ELSEVIER LICENSE
TERMS AND CONDITIONS

Apr16,2025

This Agreement between Stavros Ntioudis, Imperial College London ("You") and Elsevier ("Elsevier") consists of your license details and the terms and conditions provided by Elsevier and Copyright Clearance Center.

License Number	6010770163408
License date	Apr 16, 2025
Licensed Content Publisher	Elsevier
Licensed Content Publication	Measurement
Licensed Content Title	Dynamic analysis of a high speed rotor-bearing system
Licensed Content Author	Mohammad Hadi Jalali,Mostafa Ghayour,Saeed Ziaei-Rad,Behrooz Shahriari
Licensed Content Date	Jul 1,2014
Licensed Content Volume	53

https://s100.copyright.com/AppDispatchServlet 1/10

Licensed Content Issue	n/a
Licensed Content Pages	9
Start Page	1
End Page	9
Type of Use	reuse in a thesis/dissertation
Portion	figures/tables/illustrations
Number of figures/tables/illustrations	1
Format	both print and electronic
Are you the author of this Elsevier article?	No
Will you be translating?	No
Title of new work	A multiscale modelling framework to capture atomically resolved interfacial processes at experimentally relevant timescales
Institution name	Imperial College london

Expected presentation date	Jun2025
Portions	Fig. 2
The Requesting Person I Organization to Appear on the L.license	Stavros Ntiouws, lmpena1Co1lege London
Requestor Location	Mr. Stavros Ntioudis Requestor's Address (confidential) Requestor's Address (confidential) United Kingdom
Publisher Tax ID	GB 494 6272 12
Total	0.O0GBP

Terms and Conditions

INTRODUCTION

1. The publisher for this copyrighted material is Elsevier. By clicking "accept" in connection with completing this licensing transaction, you agree that the following terms and conditions apply to this transaction (along with the Billing and Payment terms and conditions established by Copyright Clearance Center, Inc. ("CCC"), at the time that you opened your RightsLink account and that are available at any time at htrns://myaccount.copyright.com).

GENERAL TERJ."1S

2. Elsevier hereby grants you permission to reproduce the aforementioned material subject to the terms and conditions indicated.

16/4/25, 1:23 μ.μ. Rightslink Printable License

3. Acknowledgement: If any part of the material to be used (for example, figures) has appeared in our publication with credit or acknowledgement to another source, permission must also be sought from that source. If such permission is not obtained then that material may not be included in your publication/copies. Suitable acknowledgement to the source must be made, either as a footnote or in a reference list at the end of your publication, as follows:

"Reprinted from Publication title, Vol /edition number, Author(s), Title of article/ title of chapter, Pages No., Copyright (Year), with permission from Elsevier [OR APPLICABLE SOCIETY COPYRIGHT OWNER]." Also Lancet special credit- "Reprinted from The Lancet, Vol. number, Author(s), Title of article, Pages No., Copyright (Year), with permission from Elsevier."

4. Reproduction of this material is confined to the purpose and/or media for which permission is hereby given. The material may not be reproduced or used in any other way, including use in combination with an artificial intelligence tool (including to train an algorithm, test, process, analyse, generate output and/or develop any form of artificial intelligence tool), or to create any derivative work and/or service (including resulting from the use of artificial intelligence tools).

5. Altering/Modifying Material: Not Permitted. However figures and illustrations may be altered/adapted minimally to serve your work. Any other abbreviations, additions, deletions and/or any other alterations shall be made only with prior written authorization of Elsevier Ltd. (Please contact Elsevier's permissions helpdesk here). No modifications can be made to any Lancet figures/tables and they must be reproduced in full.

6. If the permission fee for the requested use of our material is waived in this instance, please be advised that your future requests for Elsevier materials may attract a fee.

7. Reservation of Rights: Publisher reserves all rights not specifically granted in the combination of (i) the license details provided by you and accepted in the course of this licensing transaction, (ii) these terms and conditions and (iii) CCC's Billing and Payment terms and conditions.

8. License Contingent Upon Payment: While you may exercise the rights licensed immediately upon issuance of the license at the end of the licensing process for the transaction, provided that you have disclosed complete and accurate details of your proposed use, no license is finally effective unless and until full payment is received from you (either by publisher or by CCC) as provided in CCC's Billing and Payment terms and conditions. If full payment is not received on a timely basis, then any license preliminarily granted shall be deemed automatically revoked and shall be void as if never

https://s100.copyright.com/AppDispatchServlet 4/10

granted. Further, in the event that you breach any of these terms and conditions or any of CCC's Billing and Payment terms and conditions, the license is automatically revoked and shall be void as if never granted. Use of materials as described in a revoked license, as well as any use of the materials beyond the scope of an unrevoked license, may constitute copyright infringement and publisher reserves the right to take any and all action to protect its copyright in the materials.

9. War anties: Publisher makes no representations or warranties with respect to the licensed material.

10. Indemnity: You hereby indemnify and agree to hold harmless publisher and CCC, and their respective officers, directors, employees and agents, from and against any and all claims arising out of your use of the licensed material other than as specifically authorized pursuant to this license.

11. No Transfer of License: This license is personal to you and may not be sublicensed, assigned, or transferred by you to any other person without publisher's written p e r ſssion.

12. No Amendment Except in Writing: This license may not be amended except in a writing signed by both parties (or, in the case of publisher, by CCC on publisher's behalf).

13. Objection to Contrary Terms: Publisher hereby objects to any terms contained in any purchase order, acknowledgment, check endorsement or other writing prepared by you, which terms are inconsistent with these terms and conditions or CCC's Billing and Payment terms and conditions. These terms and conditions, together with CCC's Billing and Payment terms and conditions (which are incorporated herein), comprise the entire agreement between you and publisher (and CCC) concerning this licensing transaction. In the event of any conflict between your obligations established by these terms and conditions and those established by CCC's Billing and Payment terms and conditions, these terms and conditions shall control.

14. Revocation: Elsevier or Copyright Clearance Center may deny the permissions described in this License at their sole discretion, for any reason or no reason, with a full refund payable to you. Notice of such denial will be made using the contact information provided by you. Failure to receive such notice will not alter or invalidate the denial. In no event will Elsevier or Copyright Clearance Center be responsible or liable for any costs, expenses or damage incurred by you as a result of a denial of your permission request, other than a refund of the amount(s) paid by you to Elsevier and/or Copyright Clearance Center for denied permissions.

LIMITED LICENSE

16/4/25, 1:23 μ.μ. Rightslink Printable License

The following terms and conditions apply only to specific license types:

15. **Translation:** This pennission is granted for non-exclusive world **English** rights only unless your license was granted for translation rights. If you licensed translation rights you may only translate this content into the languages you requested. A professional translator must perform all translations and reproduce the content word for word preserving the integrity of the article.

16. **Posting licensed content on any Website:** The following terms and conditions apply as follows: Licensing material from an Elsevier journal: All content posted to the web site must maintain the copyright information line on the bottom of each image; A h$_{y\ p}$ er-text must be included to the Homepage of the journal from which you are licensing at htm://www.sciencedirect.com/science/journal/xxxxx or the Elsevier homepage for books at htm://www.elsevier.com; Central Storage: This license does not include permission for a scanned version of the material to be stored in a central repository such as that provided by Heron/XanEdu.

Licensing material from an Elsevier book: A hyper-text link must be included to the Elsevier homepage at htm://www.elsevier.com . All content posted to the web site must maintain the copyright information line on the bottom of each image.

Posting licensed content on Electronic reserve: In addition to the above the following clauses are applicable: The web site must be password-protected and made available only to bona fide students registered on a relevant course. Tbjs permission is granted for 1 year only. You may obtain a new license for future website posting.

17. **For journal authors:** the following clauses are applicable in addition to the above:

Preprints:

A preprint is an author's own write-up of research results and analysis, it has not been peer-reviewed, nor has it had any other value added to it by a publisher (such as formatting, copyright, technical enhancement etc.).

Authors can share their preprints anywhere at any time. Preprints should not be added to or enhanced in any way in order to appear more like, or to substitute for, the final versions of articles however authors can update their preprints on arXiv or RePEc with their Accepted Author Manuscript (see below).

If accepted for publication, we encourage authors to link from the preprint to their formal publication via its DOI. Millions of researchers have access to the formal publications on

https://s100.copyright.com/AppDispatchServlet 6/10

16/4/25, 1:23 μ.μ. Rightslink Printable License

ScienceDirect, and so links will help users to find, access, cite and use the best available version. Please note that Cell Press, The Lancet and some society-owned have different preprint policies. Information on these policies is available on the journal homepage.

Accepted Author Manuscripts: An accepted author manuscript is the manuscript of an article that has been accepted for publication and which typically includes author-incorporated changes suggested during submission, peer review and editor-author communications.

Authors can share their accepted author manuscript:

- immediately
  - via their non-commercial person homepage or blog
  - by updating a preprint in arXiv or RePEc with the accepted manuscript
  - via their research institute or institutional repository for internal institutional uses or as part of an invitation-only research collaboration work-group
  - directly by providing copies to their students or to research collaborators for their personal use
  - for private scholarly sharing as part of an invitation-only work group on commercial sites with which Elsevier has an agreement
- After the embargo period
  - via non-commercial hosting platforms such as their institutional repository
  - via commercial sites with which Elsevier has an agreement

In all cases accepted manuscripts should:

- link to the formal publication via its DOI
- bear a CC-BY-NC-ND license - this is easy to do
- if aggregated with other manuscripts, for example in a repository or other site, be shared in alignment with our hosting policy not be added to or enhanced in any way to appear more like, or to substitute for, the published journal article.

Published journal article (JPA): A published journal article (PJA) is the definitive final record of published research that appears or will appear in the journal and embodies all value-adding publishing activities including peer review co-ordination, copy-editing, formatting, (if relevant) pagination and online enrichment.

Policies for sharing publishing journal articles differ for subscription and gold open access articles:

Subscrintion Articles: If you are an author, please share a link to your article rather than the full-text. Millions of researchers have access to the formal publications on

https://s100.copyright.com/AppDispatchServlet 7/10

16/4/25, 1:23 µ.µ. Rightslink Printable License

ScienceDirect, and so links will help your users to find, access, cite, and use the best available version.

Theses and dissertations which contain embedded PJAs as part of the formal submission can be posted publicly by the awarding institution with DOI links back to the formal publications on ScienceDirect.

If you are affiliated with a library that subscribes to ScienceDirect you have additional private sharing rights for others' research accessed under that agreement. Thjs includes use for classroom teaching and internal training at the institution (including use in course packs and courseware programs), and inclusion of the article for grant funding purposes.

Gold Onen Access Articles: May be shared according to the author-selected end-user license and should contain a CrossMark logQ, the end user license, and a DOI link to the formal publication on ScienceDirect.

Please refer to Elsevier's P-OstingP-olicY. for further information.

18. **For book authors** the following clauses are applicable in addition to the above: Authors are permitted to place a brief summary of their work online only. You are not allowed to download and post the published electronic version of your chapter, nor may you scan the printed edition to create an electronic version. **Posting to a repository:** Authors are permitted to post a summary of their chapter only in their institution's repository.

19. **Thesis/Dissertation:** If your license is for use in a thesis/dissertation your thesis may be submitted to your institution in either print or electronic form. Should your thesis be published commercially, please reapply for permission. These requirements include permission for the Library and Archives of Canada to supply single copies, on demand, of the complete thesis and include permission for Proquest/UMI to supply single copies, on demand, of the complete thesis. Should your thesis be published commercially, please reapply for permission. Theses and dissertations which contain embedded PJAs as part of the formal submission can be posted publicly by the awarding institution with DOI links back to the formal publications on ScienceDirect.

Elsevier Onen Access Terms and Conditions

You can publish open access with Elsevier in hundreds of open access journals or in nearly 2000 established subscription journals that support open access publishing. Permitted third party re-use of these open access articles is defined by the author's choice

https://s100.copyright.com/AppDispatchServlet 8/10

16/4/25, 1:23 μ.μ. Rightslink Printable License

of Creative Commons user license. See our Open access license policy_ for more information.

Terms & Conditions applicable to all Open Access articles published with Elsevier:

Any reuse of the article must not represent the author as endorsing the adaptation of the article nor should the article be modified in such a way as to damage the author's honour or reputation. If any changes have been made, such changes must be clearly indicated.

The author(s) must be appropriately credited and we ask that you include the end user license and a DOI link to the formal publication on ScienceDirect.

If any part of the material to be used (for example, figures) has appeared in our publication with credit or acknowledgement to another source it is the responsibility of the user to ensure their reuse complies with the terms and conditions determined by the rights holder.

Additional Terms & Conditions applicable to each Creative Commons user license:

CC BY: The CC-BY license allows users to copy, to create extracts, abstracts and new works from the Article, to alter and revise the Article and to make commercial use of the Article (including reuse and/or resale of the Article by commercial entities), provided the user gives appropriate credit (with a link to the formal publication through the relevant DOI), provides a link to the license, indicates if changes were made and the licensor is not represented as endorsing the use made of the work. The full details of the license are available at htm://creativecornmons.org/licenses/by_/4.0.

CC BY NC SA: The CC BY-NC-SA license allows users to copy, to create extracts, abstracts and new works from the Article, to alter and revise the Article, provided this is not done for commercial purposes, and that the user gives appropriate credit (with a link to the formal publication through the relevant DOI), provides a link to the license, indicates if changes were made and the licensor is not represented as endorsing the use made of the work. Further, any new works must be made available on the same conditions. The full details of the license are available at htm://creativecommons.orgllicenses/by_-nc-sa/4.0.

CC BY NC ND: The CC BY-NC-ND license allows users to copy and distíbute the Article, provided this is not done for commercial purposes and further does not permit distribution of the Article if it is changed or edited in any way, and provided the user gives appropriate credit (with a link to the formal publication through the relevant DOI), provides a link to the license, and that the licensor is not represented as endorsing the use made of the work. The full details of the license are available at

https://s100.copyright.com/AppDispatchServlet 9/10

16/4/25, 1:23 μ.μ. Rightslink Printable License

htm://creativecommons.orgl!icensesfbY.-nc-nd/4.0. Any commercial reuse of Open Access articles published with a CC BY NC SA or CC BY NC ND license requires permission from Elsevier and will be subject to a fee.

Commercial reuse includes:

- Associating advertising with the full text of the Article
- Charging fees for document delivery or access
- Article aggregation
- Systematic distribution via e-mail lists or share buttons

Posting or linking by commercial companies for use by customers of those companies.

20. Other Conditions:

vl.10

Questions? customercare@copY-right.com.

https://s100.copyright.com/AppDispatchServlet 10/10

16/4/25, 12:34 μ.μ. Rightslink Printable License

SPRINGER NATURE LICENSE
TERMS AND CONDITIONS

Apr16,2025

This Agreement between Stavros Ntioudis, Imperial College London ("You") and Springer Nature ("Springer Nature") consists of your license details and the terms and conditions provided by Springer Nature and Copyright Clearance Center.

License Number	6010750284033
License date	Apr 16, 2025
Licensed Content Publisher	Springer Nature
Licensed Content Publication	Tribology Letters
Licensed Content Title	Decomposition Mechanisms of Anti-wear Lubricant Additive Tricresyl Phosphate on Iron Surfaces Using DPT and Atomistic Thermodynamic Studies
Licensed Content Author	Eric Osei-Agyemang et al
Licensed Content Date	Feb 10, 2018

https://s100.copyright.com/AppDispatchServlet 1/9

16/4/25, 12:34 µ.µ. Rightslink Printable License

Type of Use	Thesis/Dissertation
Requestor type	academic/university or research institute
Format	print and electronic
Portion	figures/tables/illustrations
Number of figures/tables/illustrations	1
Will you be translating?	no
Circulation/distribution	1 - 29
Author of this Springer Nature content	no
Title of new work	A multiscale modelling framework to capture atomically resolved interfacial processes at experimentally relevant timescales
Institution name	Imperial College london
Expected presentation date	Jun 2025
Portions	Fig. 10

https://s100.copyright.com/AppDispatchServlet 2/9

The Requesting Person/ Organization to Appear on the L.license	Stavros Nr oud.ls, Impena1 Co1lege London
Requestor Location	Mr. Stavros Ntioudis Requestor's Address (confidential) Requestor's Address (confidential) United Kingdom
Billing Type	Invoice
Billing Address	Mr. Stavros Ntioudis Requestor's Address (confidential) Requestor's Address (confidential)
Total	0.00GBP

Terms and Conditions

Springer Nature Customer Service Centre GmbH Terms and Conditions

The following te-m s and conditions ("Terms and Conditions") together with the terms specified in your [RightsLink] constitute the License ("License") between you as Licensee and Springer Nature Customer Service Centre GmbH as Licensor. By clicking 'accept' and completing the transaction for your use of the material ("Licensed Material"), you confirm your acceptance of and obligation to be bound by these Terms and Conditions.

1. Grant and Scope of License

1. 1. The Licensor grants you a personal, non-exclusive, non-transferable, non-sublicensable, revocable, world-wide License to reproduce, distribute, communicate to the public, make available, broadcast, electronically transmit or create derivative works using the Licensed Material for the purpose(s) specified in your RightsLink Licence Details only. Licenses are granted for the specific use requested in the order and for no other use, subject to these Terms and Conditions. You acknowledge and agree that the rights granted to you under this License do not include the right to modify, edit, translate, include in collective works, or create derivative works of the Licensed Material in whole or in part unless expressly stated in your RightsLink Licence Details. You may use the Licensed Material only as permitted under this Agreement and will not reproduce, distribute, display, perform, or otherwise use or exploit any Licensed Material in any way, in whole or in part, except as expressly permitted by this License.

1. 2. You may only use the Licensed Content in the manner and to the extent permitted by these Terms and Conditions, by your RigbtsLink Licence Details and by any applicable laws.

1. 3. A separate license may be required for any additional use of the Licensed Material, e.g. where a license has been purchased for print use only, separate permission must be obtained for electronic re-use. Similarly, a License is only valid in the language selected and does not apply for editions in other languages unless additional translation rights have been granted separately in the License.

1. 4. Any content within the Licensed Material that is owned by third parties is expressly excluded from the License.

1. 5. Rights for additional reuses such as custom editions, computer/mobile applications, film or TV reuses and/or any other derivative rights requests require additional permission and may be subject to an additional fee. Please apply to jouma1P-ermissions@ P-ringemature.com or bookP.ermissions gringemature.com for these rights.

2. Reser'ation of Rights

Licensor reserves all rights not expressly granted to you under this License. You acknowledge and agree that nothing in this License limits or restricts Licensor's rights in or use of the Licensed Material in any way. Neither this License, nor any act, omission, or statement by Licensor or you, conveys any ovroership right to you in any Licensed Material, or to any element or portion thereof. As between Licensor and you, Licensor owns and retains all right, title, and interest in and to the Licensed Material

16/4/25, 12:34 µ.µ. Rightslink Printable License

subject to the license granted in Section 1.1. Your permission to use the Licensed Material is expressly conditioned on you not impairing Licensor's or the applicable copyright owner's rights in the Licensed Material in any way.

3. Restrictions on use

3. 1. Minor editing privileges are allowed for adaptations for stylistic purposes or formatting purposes provided such alterations do not alter the original meaning or intention of the Licensed Material and the new figure(s) are still accurate and representative of the Licensed Material. Any other changes including but not limited to, cropping, adapting, and/or omitting material that affect the meaning, intention or moral rights of the author(s) are strictly prohibited.

3. 2. You must not use any Licensed Material as part of any design or trademark.

3. 3. Licensed Material may be used in Open Access Publications (OAP), but any such reuse must include a clear acknowledgment of this permission visible at the same time as the figures/tables/illustration or abstract and which must indicate that the Licensed Material is not part of the governing OA license but has been reproduced with permission. This may be indicated according to any standard referencing system but must include at a minimum 'Book/Journal title, Author, Journal Name (if applicable), Volume (if applicable), Publisher, Year, reproduced with permission from SNCSC'.

4. STM Permission Guidelines

4. 1. An alternative scope of license may apply to signatories of the STM Permissions Guidelines ("STM PG") as amended from time to time and made available at https://www.stm-assoc.org[intellectual-P-TOP-etlY.Lnermissions/nermissions-gyidelines/.

4. 2. For content reuse requests that qualify for permission under the STM PG, and which may be updated from time to time, the STM PG supersede the terms and conditions contained in this License.

4. 3. If a License has been granted under the STM PG, but the STM PG no longer apply at the time of publication, further permission must be sought from the Rightsholder. Contact joumalgermissions@.:mringernature.com or bookgermissions@ gringemature.com for these rights.

https://s 100.copyright.com/AppDispatchServlet 5/9

5. Duration of License

5. 1. Unless otherwise indicated on your License, a License is valid from the date of purchase ("License Date") until the end of the relevant period in the below table:

Reuse in a medical communications project	Reuse up to distribution or time period indicated in License
Reuse in a dissertation/thesis	Lifetime of thesis
Reuse in a journal/magazine	Lifetime ofjournal/magazine
Reuse in a book/textbook	Lifetime of edition
Reuse on a website	I year unless otherwise specified in the License
Reuse in a presentation/slide kit/poster	Lifetime of presentation/slide kit/poster. Note: publication whether electronic or in print of presentation/slide kit/poster may require further tpermission.
Reuse in conference proceedings	Lifetime of conference proceedings
Reuse in an annual report	Lifetime of annual report
Reuse in training/CME materials	Reuse up to distribution or time period indicated in License
Reuse in newsrnedia	Lifetime of newsmedia
Reuse in coursepack/classroom materials	Reuse up to distribution and/or time period indicated in license

6. Acknowledgement

6. 1. The Licensor's permission must be acknowledged next to the Licensed Material in print. In electronic form, this acknowledgement must be visible at the same time as the figures/tables/illustrations or abstract and must be hyperlinked to the journal/book's homepage.

6. 2. Acknowledgement may be provided according to any standard referencing system and at a minimum should include "Author, Article/Book Title, Journal name/Book imprint, volume, page number, year, Springer Nature".

16/4/25, 12:34 µ.µ. Rightslink Printable License

7. Reuse in a dissertation or thesis

7. 1. Where 'reuse in a dissertation/thesis' has been selected, the following terms apply: Print rights of the Version of Record are provided for; electronic rights for use only on institutional repository as defined by the Sherpa guideline (www.sherga.ac.uk/romeoD and only up to what is required by the awarding institution.

7. 2. For theses published under an ISBN or ISSN, separate permission is required. Please contact journalP-ermissions@.s.P-ringemature.com or bookperrnissions@.s.P.ringemature.com for these rights.

7. 3. Authors must properly cite the published manuscript in their thesis according to current citation standards and include the following acknowledgement: *'Reproduced with permission from Springer Nature'.*

8. License Fee

You must pay the fee set forth in the License Agreement (the "License Fees"). All amounts payable by you under this License are exclusive of any sales, use, withholding, value added or similar taxes, government fees or levies or other assessments. Collection and/or remittance of such taxes to the relevant tax authority shall be the responsibility of the party who has the legal obligation to do so.

9. Warranty

9. 1. The Licensor warrants that it has, to the best of its knowledge, the rights to license reuse of the Licensed Material. **You are solely responsible for ensuring that the material you wish to license is original to the Licensor and does not carry the copyright of another entity or third party (as credited in the published version).** If the credit line on any part of the Licensed Material indicates that it was reprinted or adapted with permission from another source, then you should seek additional permission from that source to reuse the material.

9. 2. EXCEPT FOR TIIE EXPRESS WARRANTY STATED HEREIN AND TO THE EXTENT PERMITTED BY APPLICABLE LAW, LICENSOR PROVIDES THE LICENSED MATERIAL "AS IS" AND MAKES NO OTHER REPRESENTATION OR WARRANTY. LICENSOR EXPRESSLY DISCLAIMS ANY LIABILITY FOR ANY CLAIM ARISING FROM OR OUT OF THE CONTENT, INCLUDING BUT NOT LIMITED TO ANY ERRORS, INACCURACIES, OMISSIONS, OR DEFECTS CONTAINED THEREIN, AND

https://s 100.copyright.com/AppDispatchServlet 7/9

16/4/25, 12:34 µ.µ. Rightslink Printable License

ANY IMPLIED OR EXPRESS WARRANTY AS TO MERCHANTABILITY OR FITNESS FOR A PARTICULAR PURPOSE. IN NO EVENT SHALL LICENSOR BE LIABLE TO YOU OR ANY OTHER PARTY OR ANY OTHER PERSON OR FOR ANY SPECIAL, CONSEQUENTIAL, INCIDENTAL, INDIRECT, PUNITIVE, OR EXEMPLARY DAMAGES, HOWEVER CAUSED, ARISING OUT OF OR IN CONNECTION WITH THE DOWNLOADING, VIEWING OR USE OF THE LICENSED MATERIAL REGARDLESS OF THE FORM OF ACTION, WHETHER FOR BREACH OF CONTRACT, BREACH OF WARRANTY, TORT, NEGLIGENCE, INFRINGEMENT OR OTHERWISE (INCLUDING, WITHOUT LIMITATION, DAMAGES BASED ON LOSS OF PROFITS, DATA, FILES, USE, BUSINESS OPPORTUNITY OR CLAIMS OF THIRD PARTIES), AND WHETHER OR NOT THE PARTY HAS BEEN ADVISED OF THE POSSIBILITY OF SUCH DAMAGES. THIS LIMITATION APPLIES NOTWITHSTANDING ANY FAILURE OF ESSENTIAL PURPOSE OF ANY LIMITED REMEDY PROVIDED HEREIN.

10. Termination and Cancellation

10. 1. The License and all rights granted hereunder will continue until the end of the applicable period shown in Clause 5.1 above. Thereafter, this license will be terminated and all rights granted hereunder will cease.

10. 2. Licensor reserves the right to terminate the License in the event that payment is not received in full or if you breach the terms of this License.

11. General

11. 1. The License and the rights and obligations of the parties hereto shall be construed, interpreted and determined in accordance with the laws of the Federal Republic of Germany without reference to the stipulations of the CISG (United Nations Convention on Contracts for the International Sale of Goods) or to Germany's choice-of-law principle.

11. 2. The parties acknowledge and agree that any controversies and disputes arising out of this License shall be decided exclusively by the courts of or having jurisdiction for Heidelberg, Germany, as far as legally permissible.

11. 3. This License is solely for Licensor's and Licensee's benefit. It is not for the benefit of any other person or entity.

https://s100.copyright.com/AppDispatchServlet 8/9

16/4/25, 12:34 µ.µ. Rightslink Printable License

Questions? For questions on Copyright Clearance Center accounts or website issues please contact :mringematuresupport@copY.right.com or+1-855-239-3415 (toll free in the US) or+1-978-646-2777. For questions on Springer Nature licensing please visit hllP-s://www.springernature.com/gpJpartners/rights-nerrnissions-third-nany-distribution

Other Conditions:

Version 1.4 - Dec 2022

Questions? customercare@cov.Y.right.com.

https://s100.copyright.com/AppDispatchServlet 9/9

16/4/25, 12:53 µ.µ. Rightslink Printable License

ELSEVIER LICENSE
TERMS AND CONDITIONS

Apr16,2025

This Agreement between Stavros Ntioudis, Imperial College London ("You") and Elsevier ("Elsevier") consists of your license details and the terms and conditions provided by Elsevier and Copyright Clearance Center.

License Number	6010751412862
License date	Apr 16, 2025
Licensed Content Publisher	Elsevier
Licensed Content Publication	Carbon
Licensed Content Title	Activation and mechanochemical breaking of C - C bonds initiate wear of diamond (l l0) surfaces in contact with silica
Licensed Content Author	Anke Peguiron,Gianpietro Moras,Michael Walter,Hiroshj Uetsuka,Lars Pastewka,Michael Moseler
Licensed Content Date	Mar I,2016

https://s 100.copyright.com/AppDispatchServlet 1/10

16/4/25, 12:53 µ.µ. Rightslink Printable License

Licensed Content Volume	98
Licensed Content Issue	n/a
Licensed Content Pages	10
Start Page	474
End Page	483
Type of Use	reuse in a thesis/dissertation
Portion	figures/tables/illustrations
Number of figures/tables/illustrations	1
Format	both print and electronic
Are you the author of this Elsevier article?	No
Will you be translating?	No
Title of new work	A multiscale modelling framework to capture atomically resolved interfacial processes at experimentally relevant timescales

https://s100.copyright.com/AppDispatchServlet 2/10

Institution name	Imperial College london
Expected presentation date	Jun 2025
Portions	Fig. I
The Requesting Person / Organization to Appear on the License	Stavros Ntioudis, Imperial College London
Requestor Location	Mr. Stavros Ntioudis Requestor's Address (confidential) Requestor's Address (confidential) United Kingdom
Publisher Tax ID	GB 494 6272 12
Total	0.00 GBP

Terms and Conditions

INTRODUCTION

1. The publisher for this copyrighted material is Elsevier. By clicking "accept" in connection with completing this licensing transaction, you agree that the following terms and conditions apply to this transaction (along with the Billing and Payment terms and conditions established by Copyright Clearance Center, Inc. ("CCC"), at the time that you opened your RightsLink account and that are available at any time at https://myaccount.copy_right.com).

GENERAL TERMS

2. Elsevier hereby grants you permission to reproduce the aforementioned material subject to the terms and conditions indicated.

3. Acknowledgement: If any part of the material to be used (for example, figures) has appeared in our publication with credit or acknowledgement to another source, permission must also be sought from that source. If such permission is not obtained then that material may not be included in your publication/copies. Suitable acknowledgement to the source must be made, either as a footnote or in a reference list at the end of your publication, as follows:

"Reprinted from Publication title, Vol /edition number, Author(s), Title of article/ title of chapter, Pages No., Copyright (Year), with permission from Elsevier [OR APPLICABLE SOCIETY COPYRIGHT OWNER]." Also Lancet special credit- "Reprinted from The Lancet, Vol. number, Author(s), Title of article, Pages No., Copyright (Year), with permission from Elsevier."

4. Reproduction of this material is confined to the purpose and/or media for which permission is hereby given. The material may not be reproduced or used in any other way, including use in combination with an artificial intelligence tool (including to train an algorithm, test, process, analyse, generate output and/or develop any form of artificial intelligence tool), or to create any derivative work and/or service (including resulting from the use of artificial intelligence tools).

5. Altering/Modifying Material: Not Permitted. However figures and illustrations may be altered/adapted minimally to serve your work. Any other abbreviations, additions, deletions and/or any other alterations shall be made only with prior written authorization of Elsevier Ltd. (Please contact Elsevier's permissions helpdesk here). No modifications can be made to any Lancet figures/tables and they must be reproduced in full.

6. If the permission fee for the requested use of our material is waived in this instance, please be advised that your future requests for Elsevier materials may attract a fee.

7. Reservation of Rights: Publisher reserves all rights not specifically granted in the combination of (i) the license details provided by you and accepted in the course of this licensing transaction, (ii) these terms and conditions and (iii) CCC's Billing and Payment terms and conditions.

8. License Contingent Upon Payment: While you may exercise the rights licensed immediately upon issuance of the license at the end of the licensing process for the transaction, provided that you have disclosed complete and accurate details of your proposed use, no license is finally effective unless and until full payment is received from

you (either by publisher or by CCC) as provided in CCC's Billing and Payment terms and conditions. If full payment is not received on a timely basis, then any license preliminarily granted shall be deemed automatically revoked and shall be void as if never granted. Further, in the event that you breach any of these terms and conditions or any of CCC's Billing and Payment terms and conditions, the license is automatically revoked and shall be void as if never granted. Use of materials as described in a revoked license, as well as any use of the materials beyond the scope of an unrevoked license, may constitute copyright infringement and publisher reserves the right to take any and all action to protect its copyright in the materials.

9. Warranties: Publisher makes no representations or warranties with respect to the licensed material.

10. Indemnity: You hereby indemnify and agree to bold harmless publisher and CCC, and their respective officers, directors, employees and agents, from and against any and all claims arising out of your use of the licensed material other than as specifically authorized pursuant to this license.

11. No Transfer of License: This license is personal to you and may not be sublicensed, assigned, or transferred by you to any other person without publisher's written permission.

12. No Amendment Except in Writing: This license may not be amended except in a writing signed by both parties (or, in the case of publisher, by CCC on publisher's behalf).

13. Objection to Contrary Terms: Publisher hereby objects to any terms contained in any purchase order, acknowledgment, check endorsement or other writing prepared by you, which terms are inconsistent with these terms and conditions or CCC's Billing and Payment terms and conditions. These terms and conditions, together with CCC's Billing and Payment terms and conditions (which are incorporated herein), comprise the entire agreement between you and publisher (and CCC) concerning this licensing transaction. In the event of any conflict between your obligations established by these terms and conditions and those established by CCC's Billing and Payment terms and conditions, these terms and conditions shall control.

14. Revocation: Elsevier or Copyright Clearance Center may deny the permissions described in this License at their sole discretion, for any reason or no reason, with a full refund payable to you. Notice of such denial will be made using the contact information provided by you. Failure to receive such notice will not alter or invalidate the denial. In no event will Elsevier or Copyright Clearance Center be responsible or liable for any costs, expenses or damage incurred by you as a result of a denial of your permission

16/4/25, 12:53 µ.µ. Rightslink Printable License

request, other than a refund of the amount(s) paid by you to Elsevier and/or Copyright Clearance Center for denied permissions.

LIMITED LICENSE

The following terms and conditions apply only to specific license types:

15. **Translation:** This permission is granted for non-exclusive world **English** rights only unless your license was granted for translation rights. If you Licensed translation rights you may only translate this content into the languages you requested. A professional translator must perform all translations and reproduce the content word for word preserving the integrity of the article.

16. **Posting licensed content on any Website:** The following terms and conditions apply as follows: Licensing material from an Elsevier journal: All content posted to the web site must maintain the copyright information line on the bottom of each image; A h$_{y\,p}$ er-text must be included to the Homepage of the journal from which you are licensing at http://www.sciencedirect.com/science/journal/xxxxx or the Elsevier homepage for books at h11P-://www.elsevier.com; Central Storage: This license does not include permission for a scanned version of the material to be stored in a central repository such as that provided by Heron/XanEdu.

Licensing material from an Elsevier book: A hyper-text link must be included to the Elsevier homepage at h11P-://www.elsevier.com. All content posted to the web site must maintain the copyright information line on the bottom of each image.

Posting licensed content on Electronic reserve: In addition to the above the following clauses are applicable: The web site must be password-protected and made available only to bona fide students registered on a relevant course. This permission is granted for 1 year only. You may obtain a new license for future website posting.

17. **For journal authors:** the following clauses are applicable in addition to the above:

Preprints:

A preprint is an author's own write-up of research results and analysis, it has not been peer-reviewed, nor has it bad any other value added to it by a publisher (such as formatting, copyright, technical enhancement etc.).

Authors can share their preprints anywhere at any time. Preprints should not be added to or enhanced in any way in order to appear more like, or to substitute for, the final versions

https://s100.copyright.com/AppDispatchServlet 6/10

16/4/25, 12:53 μ.μ. Rightslink Printable License

of articles however authors can update their preprints on arXiv or RePEc with their Accepted Author Manuscript (see below).

If accepted for publication, we encourage authors to link from the preprint to their formal publication via its DOI. Millions of researchers have access to the formal publications on ScienceDirect, and so links will help users to find, access, cite and use the best available version. Please note that Cell Press, The Lancet and some society-owned have different preprint policies. Information on these policies is available on the journal homepage.

Accepted Author Manuscripts: An accepted author manuscript is the manuscript of an article that has been accepted for publication and which typically includes author-incorporated changes suggested during submission, peer review and editor-author communications.

Authors can share their accepted author manuscript:

- immediately
  - via their non-commercial person homepage or blog
  - by updating a preprint in arXiv or RePEc with the accepted manuscript
  - via their research institute or institutional repository for internal institutional uses or as part of an invitation-only research collaboration work-group
  - directly by providing copies to their students or to research collaborators for their personal use
  - for private scholarly sharing as part of an invitation-only work group on commercial sites with which Elsevier has an agreement
- After the embargo period
  - via non-commercial hosting platforms such as their institutional repository
  - via commercial sites with which Elsevier has an agreement

In all cases accepted manuscripts should:

- link to the formal publication via its DOI
- bear a CC-BY-NC-ND license - this is easy to do
- if aggregated with other manuscripts, for example in a repository or other site, be shared in alignment with our hosting policy not be added to or enhanced in any way to appear more like, or to substitute for, the published journal article.

Published journal article **(JPA):** A published journal article (PJA) is the definitive final record of published research that appears or will appear in the journal and embodies all value-adding publishing activities including peer review co-ordination, copy-editing, formatting, (if relevant) pagination and online enrichment.

https://s100.copyright.com/AppDispatchServlet 7/10

16/4/25, 12:53 µ.µ. Rightslink Printable License

Policies for sharing publishing journal articles differ for subscription and gold open access articles:

Subscrintion Articles: If you are an author, please share a link to your article rather than the full-text. Millions of researchers have access to the formal publications on ScienceDirect, and so links will help your users to find, access, cite, and use the best available version.

Theses and dissertations which contain embedded PJAs as part of the formal submission can be posted publicly by the awarding institution with DOI links back to the fonnal publications on ScienceDirect.

If you are affiliated with a library that subscribes to ScienceDirect you have additional private sharing rights for others' research accessed under that agreement. This includes use for classroom teaching and internal training at the institution (including use in course packs and courseware programs), and inclusion of the article for grant funding purposes.

Gold OP-en Access Articles: May be shared according to the author-selected end-user license and should contain a CrossMark logQ, the end user license, and a DOI link to the formal publication on ScienceDirect.

Please refer to Elsevier's gosting_policx for further information.

18. **For book authors** the following clauses are applicable in addition to the above: Authors are permitted to place a brief summary of their work online only. You are not allowed to download and post the published electronic version of your chapter, nor may you scan the printed edition to create an electronic version. **Posting to a repository:** Authors are permitted to post a summary of their chapter only in their institution's repository.

19. **Thesis/Dissertation:** If your license is for use in a thesis/dissertation your thesis may be submitted to your institution in either print or electronic form. Should your thesis be published commercially, please reapply for permission. These requirements include permission for the Library and Archives of Canada to supply single copies, on demand, of the complete thesis and include p e r ffssion for Proquest/UMl to supply single copies, on demand, of the complete thesis. Should your thesis be published commercially, please reapply for permission. Theses and dissertations which contain embedded PJAs as part of the formal submission can be posted publicly by the awarding institution with DOI links back to the formal publications on ScienceDirect.

https://s 100.copyright.com/AppDispatchServlet 8/10

16/4/25, 12:53 µ.µ. Rightslink Printable License

Elsevier Onen Access Terms and Conditions

You can publish open access with Elsevier in hundreds of open access journals or in nearly 2000 established subscription journals that support open access publishing. Permitted third party re-use of these open access articles is defined by the author's choice of Creative Commons user license. See our QP-en access license P-OlicY. for more information.

Terms & Conditions applicable to aU Open Access articles published with Elsevier:

Any reuse of the article must not represent the author as endorsing the adaptation of the article nor should the article be modified in such a way as to damage the author's honour or reputation. If any changes have been made, such changes must be clearly indicated.

The author(s) must be appropriately credited and we ask that you include the end user license and a DOI link to the formal publication on ScienceDirect.

If any part of the material to be used (for example, figures) has appeared in our publication with credit or acknowledgement to another source it is the responsibility of the user to ensure their reuse complies with the terms and conditions determined by the rights holder.

Additional Terms & Conditions applicable to each Creative Commons user license:

CC BY: The CC-BY license allows users to copy, to create extracts, abstracts and new works from the Article, to alter and revise the Article and to make commercial use of the Article (including reuse and/or resale of the Article by commercial entities), provided the user gives appropriate credit (with a link to the formal publication through the relevant DOI), provides a link to the license, indicates if changes were made and the licensor is not represented as endorsing the use made of the work. The full details of the license are available at httP-://creativecommons.orgLlicenseslbY./4.0.

CC BY NC SA: The CC BY-NC-SA license allows users to copy, to create extracts, abstracts and new works from the Article, to alter and revise the Article, provided this is not done for commercial purposes, and that the user gives appropriate credit (with a link to the formal publication through the relevant DOI), provides a link to the license, indicates if changes were made and the licensor is not represented as endorsing the use made of the work. Further, any new works must be made available on the same conditions. The full details of the license are available at htw://creativecommons.orgl!icenseslbY.-nc-sa/4.0.

https://s100.copyright.com/AppDispatchServlet 9/10

CC BY NC ND: The CC BY-NC-ND license allows users to copy and distribute the Article, provided this is not done for commercial purposes and further does not permit distribution of the Article if it is changed or edited in any way, and provided the user gives appropriate credit (with a link to the formal publication through the relevant DOI), provides a link to the license, and that the licensor is not represented as endorsing the use made of the work. The full details of the license are available at ht:tp://creativecommons.orgl!icenses/by-nc-nd/4.0. Any commercial reuse of Open Access articles published with a CC BY NC SA or CC BY NC ND license requires permission from Elsevier and will be subject to a fee.

Commercial reuse includes:

- Associating advertising with the full text of the Article
- Charging fees for document delivery or access
- Article aggregation
- Systematic distribution via e-mail lists or share buttons

Posting or linking by commercial companies for use by customers of those companies.

20. **Other Conditions:**

v1.10

Questions? customercare@copyright.com.

16/4/25, 2:25 μ.μ. Rightslink Printable License

ELSEVIER LICENSE
TERMS AND CONDITIONS

Apr16,2025

This Agreement between Stavros Ntioudis, Imperial College London ("You") and Elsevier ("Elsevier") consists of your license details and the terms and conditions provided by Elsevier and Copyright Clearance Center.

License Number	6010790883284
License date	Apr 16, 2025
Licensed Content Publisher	Elsevier
Licensed Content Publication	Journal of the Mechanics and Physics of Solids
Licensed Content Title	A quasicontinuum theory for the nonlinear mechanical response of general periodic truss lattices
Licensed Content Author	Gregory P. Phlipot,Dennis M. Kochmann
Licensed Content Date	Mar 1, 2019
Licensed Content Volume	124

https://s100.copyright.com/AppDispatchServlet 1/10

16/4/25, 2:25 μ.μ. Rightslink Printable License

Licensed Content Issue	n/a
Licensed Content Pages	23
Start Page	758
End Page	780
Type of Use	reuse in a thesis/dissertation
Portion	figures/tables/illustrations
Number of figures/tables/illustrations	1
Format	both print and electronic
Are you the author of this Elsevier article?	No
Will you be translating?	No
Title of new work	A multiscale modelling framework to capture atomically resolved interfacial processes at experimentally relevant timescales
Institution name	Imperial College london

https://s100.copyright.com/AppDispatchServlet 2/10

Expected presentation date	Jun2025
Portions	Fig. 14.(c)
The Requesting Person I Organization to Appear on the L.1cense	Stavros Ntiouws, lmpena1Co1lege London
Requestor Location	Mr. Stavros Ntioudis Requestor's Address (confidential) Requestor's Address (confidential) United Kingdom
Publisher Tax ID	GB 494 6272 12
Total	0.O0GBP

Terms and Conditions

INTRODUCTION

1. The publisher for this copyrighted material is Elsevier. By clicking "accept" in connection with completing this licensing transaction, you agree that the following terms and conditions apply to this transaction (along with the Billing and Payment terms and conditions established by Copyright Clearance Center, Inc. ("CCC"), at the time that you opened your RightsLink account and that are available at any time at htrns://myaccount.copyright.com).

GENERAL TERJ."1S

2. Elsevier hereby grants you permission to reproduce the aforementioned material subject to the terms and conditions indicated.

3. Acknowledgement: If any part of the material to be used (for example, figures) has appeared in our publication with credit or acknowledgement to another source, permission must also be sought from that source. If such permission is not obtained then that material may not be included in your publication/copies. Suitable acknowledgement to the source must be made, either as a footnote or in a reference list at the end of your publication, as follows:

"Reprinted from Publication title, Vol /edition number, Author(s), Title of article/ title of chapter, Pages No., Copyright (Year), with permission from Elsevier [OR APPLICABLE SOCIETY COPYRIGHT OWNER]." Also Lancet special credit- "Reprinted from The Lancet, Vol. number, Author(s), Title of article, Pages No., Copyright (Year), with permission from Elsevier."

4. Reproduction of this material is confined to the purpose and/or media for which permission is hereby given. The material may not be reproduced or used in any other way, including use in combination with an artificial intelligence tool (including to train an algorithm, test, process, analyse, generate output and/or develop any form of artificial intelligence tool), or to create any derivative work and/or service (including resulting from the use of artificial intelligence tools).

5. Altering/Modifying Material: Not Permitted. However figures and illustrations may be altered/adapted minimally to serve your work. Any other abbreviations, additions, deletions and/or any other alterations shall be made only with prior written authorization of Elsevier Ltd. (Please contact Elsevier's permissions helpdesk here). No modifications can be made to any Lancet figures/tables and they must be reproduced in full.

6. If the permission fee for the requested use of our material is waived in this instance, please be advised that your future requests for Elsevier materials may attract a fee.

7. Reservation of Rights: Publisher reserves all rights not specifically granted in the combination of (i) the license details provided by you and accepted in the course of this licensing transaction, (ii) these terms and conditions and (iii) CCC's Billing and Payment terms and conditions.

8. License Contingent Upon Payment: While you may exercise the rights licensed immediately upon issuance of the license at the end of the licensing process for the transaction, provided that you have disclosed complete and accurate details of your proposed use, no license is finally effective unless and until full payment is received from you (either by publisher or by CCC) as provided in CCC's Billing and Payment terms and conditions. If full payment is not received on a timely basis, then any license preliminarily granted shall be deemed automatically revoked and shall be void as if never

granted. Further, in the event that you breach any of these terms and conditions or any of CCC's Billing and Payment terms and conditions, the license is automatically revoked and shall be void as if never granted. Use of materials as described in a revoked license, as well as any use of the materials beyond the scope of an unrevoked license, may constitute copyright infringement and publisher reserves the right to take any and all action to protect its copyright in the materials.

9. War anties: Publisher makes no representations or warranties with respect to the licensed material.

10. Indemnity: You hereby indemnify and agree to hold harmless publisher and CCC, and their respective officers, directors, employees and agents, from and against any and all claims arising out of your use of the licensed material other than as specifically authorized pursuant to this license.

11. No Transfer of License: This license is personal to you and may not be sublicensed, assigned, or transferred by you to any other person without publisher's written p e r ſssion.

12. No Amendment Except in Writing: This license may not be amended except in a writing signed by both parties (or, in the case of publisher, by CCC on publisher's behalf).

13. Objection to Contrary Terms: Publisher hereby objects to any terms contained in any purchase order, acknowledgment, check endorsement or other writing prepared by you, which terms are inconsistent with these terms and conditions or CCC's Billing and Payment terms and conditions. These terms and conditions, together with CCC's Billing and Payment terms and conditions (which are incorporated herein), comprise the entire agreement between you and publisher (and CCC) concerning this licensing transaction. In the event of any conflict between your obligations established by these terms and conditions and those established by CCC's Billing and Payment terms and conditions, these terms and conditions shall control.

14. Revocation: Elsevier or Copyright Clearance Center may deny the permissions described in this License at their sole discretion, for any reason or no reason, with a full refund payable to you. Notice of such denial will be made using the contact information provided by you. Failure to receive such notice will not alter or invalidate the denial. In no event will Elsevier or Copyright Clearance Center be responsible or liable for any costs, expenses or damage incurred by you as a result of a denial of your permission request, other than a refund of the amount(s) paid by you to Elsevier and/or Copyright Clearance Center for denied permissions.

LIMITED LICENSE

16/4/25, 2:25 μ.μ. Rightslink Printable License

The following terms and conditions apply only to specific license types:

15. **Translation:** This pennission is granted for non-exclusive world **English** rights only unless your license was granted for translation rights. If you licensed translation rights you may only translate this content into the languages you requested. A professional translator must perform all translations and reproduce the content word for word preserving the integrity of the article.

16. **Posting licensed content on any Website:** The following terms and conditions apply as follows: Licensing material from an Elsevier journal: All content posted to the web site must maintain the copyright information line on the bottom of each image; A h$_{y\ p}$ er-text must be included to the Homepage of the journal from which you are licensing at htm://www.sciencedirect.com/science/journal/xxxxx or the Elsevier homepage for books at htm://www.elsevier.com; Central Storage: This license does not include permission for a scanned version of the material to be stored in a central repository such as that provided by Heron/XanEdu.

Licensing material from an Elsevier book: A hyper-text link must be included to the Elsevier homepage at htm://www.elsevier.com . All content posted to the web site must maintain the copyright information line on the bottom of each image.

Posting licensed content on Electronic reserve: In addition to the above the following clauses are applicable: The web site must be password-protected and made available only to bona fide students registered on a relevant course. Tbjs permission is granted for 1 year only. You may obtain a new license for future website posting.

17. **For journal authors:** the following clauses are applicable in addition to the above:

Preprints:

A preprint is an author's own write-up of research results and analysis, it has not been peer-reviewed, nor has it had any other value added to it by a publisher (such as formatting, copyright, technical enhancement etc.).

Authors can share their preprints anywhere at any time. Preprints should not be added to or enhanced in any way in order to appear more like, or to substitute for, the final versions of articles however authors can update their preprints on arXiv or RePEc with their Accepted Author Manuscript (see below).

If accepted for publication, we encourage authors to link from the preprint to their formal publication via its DOI. Millions of researchers have access to the formal publications on

https://s 100.copyright.com/AppDispatchServlet 6/10

16/4/25, 2:25 μ.μ. Rightslink Printable License

ScienceDirect, and so links will help users to find, access, cite and use the best available version. Please note that Cell Press, The Lancet and some society-owned have different preprint policies. Information on these policies is available on the journal homepage.

Accepted Author Manuscripts: An accepted author manuscript is the manuscript of an article that has been accepted for publication and which typically includes author-incorporated changes suggested during submission, peer review and editor-author communications.

Authors can share their accepted author manuscript:

- immediately
  - via their non-commercial person homepage or blog
  - by updating a preprint in arXiv or RePEc with the accepted manuscript
  - via their research institute or institutional repository for internal institutional uses or as part of an invitation-only research collaboration work-group
  - directly by providing copies to their students or to research collaborators for their personal use
  - for private scholarly sharing as part of an invitation-only work group on commercial sites with which Elsevier has an agreement
- After the embargo period
  - via non-commercial hosting platforms such as their institutional repository
  - via commercial sites with which Elsevier has an agreement

In all cases accepted manuscripts should:

- link to the formal publication via its DOI
- bear a CC-BY-NC-ND license - this is easy to do
- if aggregated with other manuscripts, for example in a repository or other site, be shared in alignment with our hosting policy not be added to or enhanced in any way to appear more like, or to substitute for, the published journal article.

Published journal article (JPA): A published journal article (PJA) is the definitive final record of published research that appears or will appear in the journal and embodies all value-adding publishing activities including peer review co-ordination, copy-editing, formatting, (if relevant) pagination and online enrichment.

Policies for sharing publishing journal articles differ for subscription and gold open access articles:

Subscrintion Articles: If you are an author, please share a link to your article rather than the full-text. Millions of researchers have access to the formal publications on

https://s100.copyright.com/AppDispatchServlet 7/10

16/4/25, 2:25 μ.μ. Rightslink Printable License

ScienceDirect, and so links will help your users to find, access, cite, and use the best available version.

Theses and dissertations which contain embedded PJAs as part of the formal submission can be posted publicly by the awarding institution with DOI links back to the formal publications on ScienceDirect.

If you are affiliated with a library that subscribes to ScienceDirect you have additional private sharing rights for others' research accessed under that agreement. Thjs includes use for classroom teaching and internal training at the institution (including use in course packs and courseware programs), and inclusion of the article for grant funding purposes.

Gold Onen Access Articles: May be shared according to the author-selected end-user license and should contain a CrossMark logQ, the end user license, and a DOI link to the formal publication on ScienceDirect.

Please refer to Elsevier's P-OstingP-olicY. for further information.

18. **For book authors** the following clauses are applicable in addition to the above: Authors are permitted to place a brief summary of their work online only. You are not allowed to download and post the published electronic version of your chapter, nor may you scan the printed edition to create an electronic version. **Posting to a repository:** Authors are permitted to post a summary of their chapter only in their institution's repository.

19. **Thesis/Dissertation:** If your license is for use in a thesis/dissertation your thesis may be submitted to your institution in either print or electronic form. Should your thesis be published commercially, please reapply for permission. These requirements include permission for the Library and Archives of Canada to supply single copies, on demand, of the complete thesis and include permission for Proquest/UMI to supply single copies, on demand, of the complete thesis. Should your thesis be published commercially, please reapply for permission. Theses and dissertations which contain embedded PJAs as part of the formal submission can be posted publicly by the awarding institution with DOI links back to the formal publications on ScienceDirect.

Elsevier Onen Access Terms and Conditions

You can publish open access with Elsevier in hundreds of open access journals or in nearly 2000 established subscription journals that support open access publishing. Permitted third party re-use of these open access articles is defined by the author's choice

https://s100.copyright.com/AppDispatchServlet 8/10

16/4/25, 2:25 μ.μ. Rightslink Printable License

of Creative Commons user license. See our Open access license policy_ for more information.

Terms & Conditions applicable to all Open Access articles published with Elsevier:

Any reuse of the article must not represent the author as endorsing the adaptation of the article nor should the article be modified in such a way as to damage the author's honour or reputation. If any changes have been made, such changes must be clearly indicated.

The author(s) must be appropriately credited and we ask that you include the end user license and a DOI link to the formal publication on ScienceDirect.

If any part of the material to be used (for example, figures) has appeared in our publication with credit or acknowledgement to another source it is the responsibility of the user to ensure their reuse complies with the terms and conditions determined by the rights holder.

Additional Terms & Conditions applicable to each Creative Commons user license:

CC BY: The CC-BY license allows users to copy, to create extracts, abstracts and new works from the Article, to alter and revise the Article and to make commercial use of the Article (including reuse and/or resale of the Article by commercial entities), provided the user gives appropriate credit (with a link to the formal publication through the relevant DOI), provides a link to the license, indicates if changes were made and the licensor is not represented as endorsing the use made of the work. The full details of the license are available at htm://creativecornmons.org/licenses/by_/4.0.

CC BY NC SA: The CC BY-NC-SA license allows users to copy, to create extracts, abstracts and new works from the Article, to alter and revise the Article, provided this is not done for commercial purposes, and that the user gives appropriate credit (with a link to the formal publication through the relevant DOI), provides a link to the license, indicates if changes were made and the licensor is not represented as endorsing the use made of the work. Further, any new works must be made available on the same conditions. The full details of the license are available at htm://creativecommons.orgllicenses/by_-nc-sa/4.0.

CC BY NC ND: The CC BY-NC-ND license allows users to copy and distíbute the Article, provided this is not done for commercial purposes and further does not permit distribution of the Article if it is changed or edited in any way, and provided the user gives appropriate credit (with a link to the formal publication through the relevant DOI), provides a link to the license, and that the licensor is not represented as endorsing the use made of the work. The full details of the license are available at

https://s100.copyright.com/AppDispatchServlet 9/10

16/4/25, 2:25 μ.μ. RightsLink Printable License

http://creativecommons.org/licenses/by-nc-nd/4.0. Any commercial reuse of Open Access articles published with a CC BY NC SA or CC BY NC ND license requires permission from Elsevier and will be subject to a fee.

Commercial reuse includes:

- Associating advertising with the full text of the Article
- Charging fees for document delivery or access
- Article aggregation
- Systematic distribution via e-mail lists or share buttons

Posting or linking by commercial companies for use by customers of those companies.

20. **Other Conditions**:

v1.10

Questions? customercare@copyright.com.

https://s100.copyright.com/AppDispatchServlet 10/10